# STRAPDOWN INERTIAL NAVIGATION
# LECTURE NOTES

**Paul G Savage**

**Strapdown Associates, Inc.**

**January 10, 2010**

**(Seventh Printing)**

Strapdown Associates, Inc.
4727 South Lake Sarah Drive
Maple Plain, Minnesota 55359

Telephone: (763) 479-1981
email: pgs@strapdownassociates.com

# FOREWORD

This Lecture Notes book is a compilation of strapdown inertial navigation material I prepared from 1975 and 1985. The primary element of the book is a set of lecture notes I used from 1977 - 1978 as handout material for an after hours course given while at Honeywell on LINS (Laser Inertial Navigation System) analytical theory of operation. The book also includes four technical papers presented from 1976 - 1984 on strapdown systems, analytics, and sensors. The first two papers describes the state-of-the-art of strapdown inertial navigation system and sensor technology in the 1976 - 1978 time frame, before strapdown systems became operational on military and commercial aircraft. The last two papers were prepared in 1984 - 1986 after strapdown inertial technology had been accepted for general aircraft application; the first providing an update on the 1978 inertial sensor paper, the second providing a detailed description of computational routines embedded as software in typical strapdown systems to perform the attitude/velocity/position inertial navigation computation functions. The 1976 systems paper is particularly interesting because it contains sensor and system test data that convinced many in the aerospace industry of the readiness of laser gyro strapdown inertial navigation technology to enter the production development cycle.

Lecture Notes was prepared as background handout material for attendees of my Introductory Course On Strapdown Inertial Systems offered to the aerospace industry from 1981 - 2009. Lecture Notes presents the theoretical basis for technical material overviewed in the course on overhead slides, as also provided to course attendees in the book:

**Introduction To Strapdown Inertial Navigation Systems**

Now that the Introductory Strapdown Course is no longer being offered, the Lecture Notes and Introduction books can be purchased directly from my company Strapdown Associates, Inc. by telephone (763-479-1918) or email (pgs@strapdownassociates.com).

Paul G Savage

**NOTES**

# CONTENTS

**EARLY PAPERS FOR BACKGROUND**

1976 PAPER - LASER GYROS IN STRAPDOWN
INERTIAL NAVIGATION SYSTEMS

1978 PAPER - STRAPDOWN SENSORS

## NOTES

# LASER GYROS IN STRAPDOWN INERTIAL NAVIGATION SYSTEMS

Paul G Savage
Staff Engineer, Navigation Systems
Honeywell Government and Aeronautical Products Division
1625 Zarthan Avenue
St. Louis Park, Minnesota 55416

Presented at the
IEEE Position Location and Navigation Symposium
Hilton Inn
San Diego, California

November 1-3, 1976

# LASER GYROS IN STRAPDOWN INERTIAL NAVIGATION SYSTEMS

By Paul G. Savage
Staff Engineer, Navigation Systems
Honeywell Government and Aeronautical Products Division
1625 Zarthan Avenue
St. Louis Park, Minnesota 55416

## ABSTRACT

For more than a decade, the advent of strapdown systems has been forecasted as the solution to the problems of high cost (acquisition and life cycle) experienced with traditional gimbaled inertial navigation platforms. Until only recently, however, basic limitations in computers (high costs for strapdown high-speed requirements) and gyros (dynamic range) have limited the advancement of strapdown techology to the concept feasibility development phase. The advent of the high-speed, low-cost computer in the 1970's, and most recently, performance breakthroughs in the laser gyro, make today's strapdown technology a viable contender for the inertial navigation system of the 1980's.

This paper reviews strapdown as contrasted with gimbaled inertial navigation system technology with emphasis on the requirements imposed on the inertial sensors (in particular, the gyros). The theory of operation and performance characteristics of the laser gyro are discussed relative to the strapdown system requirements, and contrasted with spinning mass gyros (the single-degree-of-freedom floated rate integrating gyro, the tuned rotor gyro, and the electrostatic gyro).

The paper begins with a review of the basic concepts of strapdown inertial navigation, identifying computational elements and interfaces with the strapdown sensors (gyros and accelerometers). The mechanisms for sensor-to-system error propagation are addressed. A comparison is made between the equivalent gimbaled and strapdown inertial navigation system mechanization approaches in terms of the demands on the inertial sensors for achieving a given level of system performance. In particular, the higher demands for the strapdown sensors are identified and quantified (maximum rate capability, bias and scale factor accuracy, bandwidth, quantization level, stability of the alignment angles between the sensors, reaction time, and calibration interval).

The basic theory of laser gyro operation is reviewed with emphasis on the distinction between mechanization approaches currently used for compensating lock-in. The alternative momentum wheel strapdown gyro configurations are described for comparison with the laser gyro. The laser gyro is then analyzed with regard to its compatibility with the strapdown system requirements compared to the spinning wheel strapdown gyro configurations in the areas of cost, reliability, size, and performance. Recently published flight test data on systems using tuned rotor and electrostatic gyros are analyzed and compared with equivalent laser gyro flight test data taken with the Honeywell LINS (Laser Inertial Navigation System).

The impact of laser gyro strapdown inertial systems in advanced hybrid aided configurations (such as with GPS) is addressed and contrasted with spinning mass gyro systems, both gimbaled and strapdown. The complexity and accuracy requirements for the sensor error model are reviewed relative to ultimate performance capabilities achievable in hybrid aided systems using Kalman filters. Included in the paper is a discussion of the extended use of strapdown sensor signals for other than navigation functions in advanced multifunction integrated strapdown avionics applications, and the associated impact on sensor requirements and tradeoffs.

The paper concludes that on the basis of cost, reliability, and performance in both unaided and advanced hybrid aided systems, the laser gyro is superior to the other strapdown sensors for general aircraft application. Acquisition and life-cycle costs for laser gyro systems should be significantly lower than for traditional gimbaled navigation systems, with comparable performance in the 1 nmi/h class. These advantages, coupled with the extended capabilities of the laser gyro and strapdown technology in advanced multifunction applications, should make the laser gyro strapdown navigation system the preferred inertial mechanization approach for the 1980's.

## INTRODUCTION

The state of the art in strapdown inertial navigation technology has achieved a level of maturity in recent years that makes it a serious contender for general avionics use in the near future. Computer limitations, which handicapped strapdown compared to gimbaled technology in the past, are now virtually nonexistent due to the advent of the low-cost, high-speed minicomputer. Recent advances in gyro technology, most notably in the ring laser gyro,[1] have virtually eliminated the dynamic range problems that previously limited the accuracy potential of strapdown systems. The capabilities of today's strapdown technology have been demonstrated to be in the classical 1 nmi/h gimbaled performance category, with production system costs projected to be one half that of gimbaled systems with comparable accuracy. The traditional strapdown versus gimbaled tradeoffs used by strapdown proponents for the last decade to tout the advantages of strapdown technology must now be given more serious evaluation. Due to the assortment of strapdown gyro types available today, the tradeoff analyses must extend to the sensor level such that overall system capabilities can be assessed for the particular strapdown mechanizations available.

The purpose of this paper is threefold:

- To introduce the uninitiated to the general field of strapdown as contrasted with gimbaled inertial navigation technology, emphasizing the fundamental distinctions in implementation, performance characteristics, and associated demands on the inertial components for the two mechanization approaches.
- To provide a funtional description and performance analysis of the laser gyro in a strapdown system such that the capabilities, advantages, and limitations of this unique sensor can be understood on a system-level basis and contrasted with the capabilities of gimbaled systems and momentum wheel gyro strapdown technology.
- To present the rationale that has led the author to believe that the laser gyro strapdown system is the preferred inertial mechanization approach for general aircraft application in the 1980's. In this regard, fairly detailed discussions are presented illustrating the tradeoffs between the laser gyro strapdown system and the alternates available. The intent is to provide the reader with a thorough understanding of the principal tradeoffs involved such that he may draw his own conclusions.

The approach used in the paper for performance analyses is to avoid rigorous (and complex) mathematical descriptions wherever possible. Instead, performance characteristics are described on an intuitive level, and examples are used to illustrate typical situations and magnitudes of the performance variables. The intent is to provide a basic understanding of the principal performance characteristics of strapdown as contrasted with gimbaled inertial navigation systems. For a more rigorous analysis, the reader is referred to the classical inertial navigation texts.[2, 3, 4, 5]

For comparative purposes, the classical "1 nmi/h" inertial navigation requirement is used throughout the paper as a basis for judging performance requirements and capabilities for the candidate systems analyzed. Selection of different performance levels may modify some of the quantitative tradeoffs presented; however, the basic performance characteristics described are still representative of inertial navigation systems in general.

The analysis of the alternate strapdown gyro systems for contrast with laser gyro systems is a difficult task due to the general inaccessibility of detailed performance data between sensor/systems manufacturers. (The author is employed at Honeywell, a laser gyro system manufacturer that is in competition with other inertial sensor/system suppliers.) The approach taken here is to emphasize the fundamental characteristics and limitations of the technologies, avoiding the details of performance peculiarities associated with particular vendor designs, and assuming that the system design can be accomplished to achieve manufacturer-stated performance, cost, and reliability goals. Hence, when limited data is available, the approach taken is to error on the side favoring the alternate approach. Regarding the single-degree-of-freedom floated rate integrating gyro, the author has first-hand experience at Honeywell with this class of instrument as with the laser gyro; hence, performance comparisons with the laser gyro are somewhat more detailed.

Notably absent in this paper is the standard treatise on strapdown algorithm errors and associated computer loading. Algorithm analyses and selection is an important aspect of the software design process for strapdown systems that must be accomplished during the normal development cycle. On the basis of the author's experience on the Honeywell LINS (Laser Inertial Navigation System) Program, strapdown software can be developed for today's minicomputer that has negligible impact on the system error budget. Associated computer costs are minimal and of secondary importance in system cost tradeoffs.

## STRAPDOWN SYSTEM CONFIGURATIONS

Figures 1 and 2 illustrate the mechanization of typical strapdown navigation systems, identifying computational elements and interfaces with the strapdown sensors (gyros and accelerometers). Figures 1 and 2 differ in the type of gyro used (rate or attitude). For the attitude gyro configuration (Figure 2), sensor assembly attitude relative to a reference coordinate frame (the gyro rotor reference) is measured directly from the gyros. For the rate gyro configuration (Figure 1), the attitude of the sensor assembly relative to a reference space is calculated in the system computer by processing the rate gyro signals. In other respects, Figures 1 and 2 are equivalent.

Referring to Figure 1, the interface between the sensors and system computer is a digital integration process over the computer attitude computation interval. The up-down counters in Figure 1 provide the integration function of counting

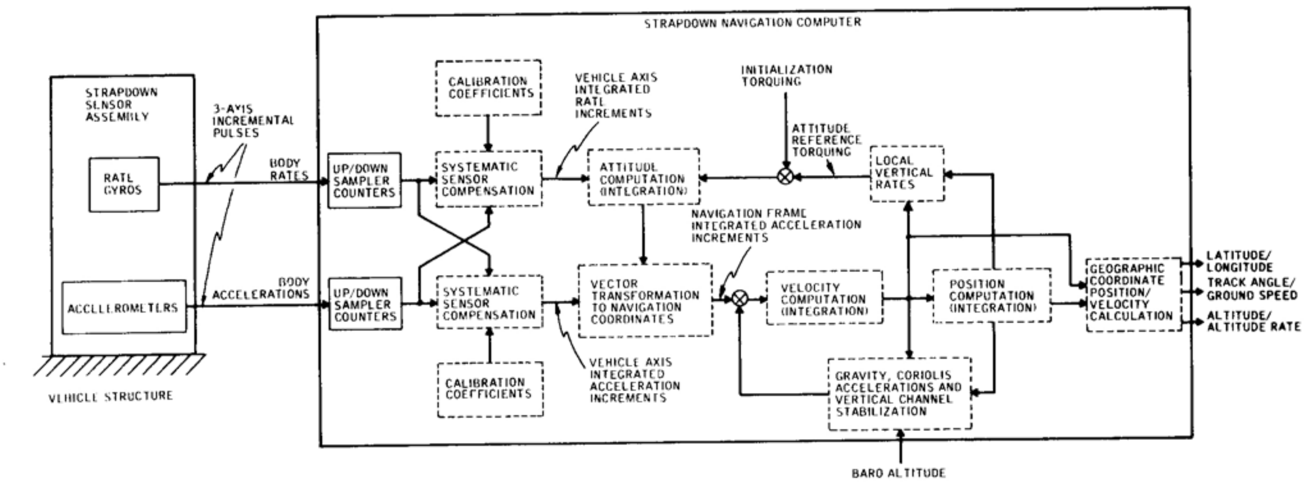


Figure 1. Rate Gyro Strapdown Inertial Navigation System

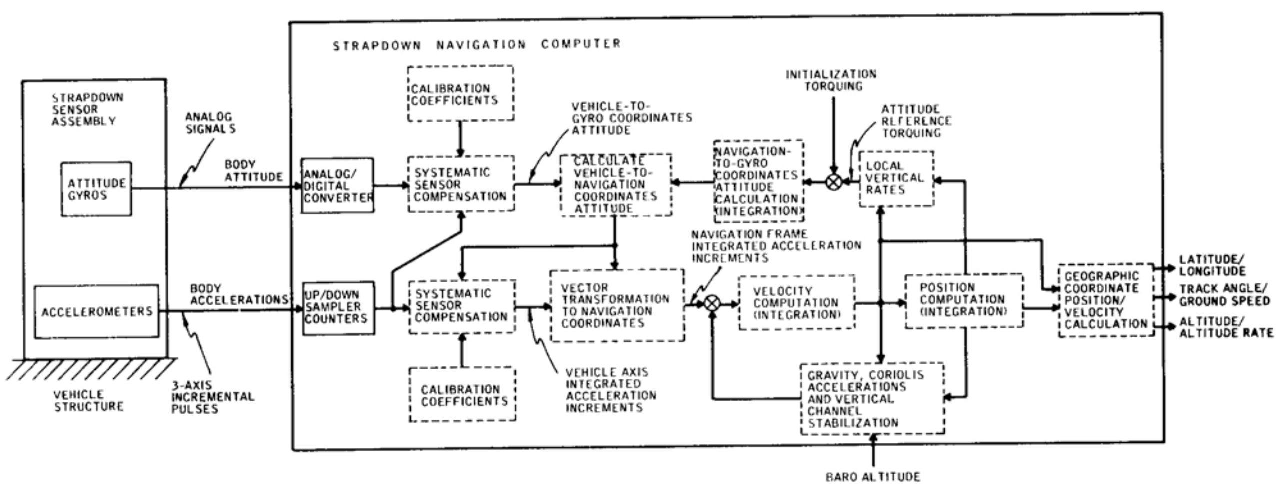


Figure 2. Attitude Gyro Strapdown Inertial Navigation System

the output pulses from the strapdown sensors over the computer iteration interval. The gyros and accelerometers are mechanized to output pulses, the occurance and phase sense of which indicate that a prescribed increment of integrated vehicle axis rate and/or acceleration has been accumulated in a specified direction. The accumulations from the up-down counters are sampled simultaneously into holding registers once each computer iteration interval and are reset for the next interval accumulation. The sampled counts are serially loaded into the computer memory during each computation interval for processing.

The integrated rate samples (Figure 1) are compensated in the system computer for known systematic errors and then used to update the calculated attitude of the sensor assembly relative to navigation coordinates (typically local level azimuth wander).[4] The attitude data is used to transform the accelerometer count vector (after applying compensation) from sensor axes to its equivalent vector form in navigation coordinates. In the attitude gyro configuration (Figure 2), the equivalent acceleration transformation function is performed using attitude data provided directly from the attitude gyros, after first applying an attitude rotation to account for the orientation of the gyro reference relative to the navigation coordinate frame.

The computed navigation coordinate frame integrated acceleration increments are then accumulated to compute earth-referenced velocity. Included are correction terms (gravity, Coriolis) to correct for acceleration effects not directly measurable by the specific force-sensing accelerometers. For the vertical velocity channel, a barometric altimeter feedback from the altitude computation loop is included to prevent vertical channel divergence.

The velocity vector is integrated to determine vehicle earth-referenced position and altitude. Computed position is used to calculate the components of earth rate in the local level navigation coordinate frame. These signals summed with the angular rate of the position vector relative to the earth (calculated from the horizontal velocity components) are used to precess the navigation attitude reference to maintain its horizontal orientation with respect to the local vertical. In the case of the Figure 1 rate gyro configuration, this is accomplished by torquing the analytical attitude reference directly. In the case of the Figure 2 attitude gyro configuration, this is accomplished by rotating the gyro attitude reference matrix. Vehicle geographic latitude/longitude angular coordinates are determined directly from the computed position data for output information. The azimuth orientation of the locally level navigation frame relative to earth geographic (North/East) coordinates is also determined as part of the position computation process. This data is used to resolve the horizontal velocity vector from navigation coordinates to determine ground speed and track angle relative to North.

The initial value for the attitude matrix in Figure 1 (and gyro attitude relative to navigation coordinates in Figure 2) is typically determined during the preflight alignment process while the vehicle is stationary. Conceptually, the method is to deduce the initial attitude using the gyros and accelerometers to measure the orientation of the sensor assembly relative to the sensed earth rate and gravity reaction force vectors. The analytical method for achieving the measurement differs between systems. In general, the process is a filtering operation that implicitly seeks the gravity/earth rate signals in the presence of sensor noise and aircraft dynamic disturbances (principally acceleration). Insertion of aircraft initial latitude and longitude to the system is included in the preflight procedures.

Figures 1 and 2 illustrate typical mechanization approaches used in strapdown inertial navigation systems. For a particular application, variations will exist. However, for performance analysis purposes, the Figure 1 and 2 configurations adequately represent the sensor/computer interface for analyzing error characteristics of particular sensor types.

## GIMBALED SYSTEM CONFIGURATION

Figure 3 illustrates a typical inertial navigation system using a gimbaled platform to isolate the sensor assembly from the user vehicle. The gimbal servos in Figure 3 are slaved to the outputs of attitude or rate integrating gyros mounted on the stable element. In this manner, the gyro outputs are constrained to null, thereby attitude stabilizing the accelerometers, which are also mounted on the stable element. Torquing signals generated in the system computer operate on the gyros in a prescribed manner to control the orientation of the stable element relative to earth coordinates.

As the stable element is torqued on command from the system computer, the orientation of the stable element (and accelerometers) is known in the computer, and the accelerometer signals can be interpreted in a known coordinate frame. For the common case where the platform is controlled to be parallel with navigation axes (e.g., azimuth wander), the acceleration signals from the platform can be integrated directly in the system computer to obtain navigational velocity data. Hence, for this case, the accelerometer outputs in Figure 3 are analogous to the analytically transformed acceleration signals in Figures 1 and 2. The position/velocity computation functions in Figures 1, 2, and 3, therefore, are equivalent or identical.

For sensor error analysis purposes, the gimbaled system configuration considered in the paper is of the locally level azimuth wander type. This is the traditional approach used in most systems today. It should be recognized, however, that several of the system errors (notably those created by fixed biases in level axis gyros and accelerometers) can be cancelled through the addition of an azimuth turn-table to the platform assembly on which the level axis sensors are mounted (e.g., the Delco Carousel system). Rotation of the turn-table at a fixed rate (typically

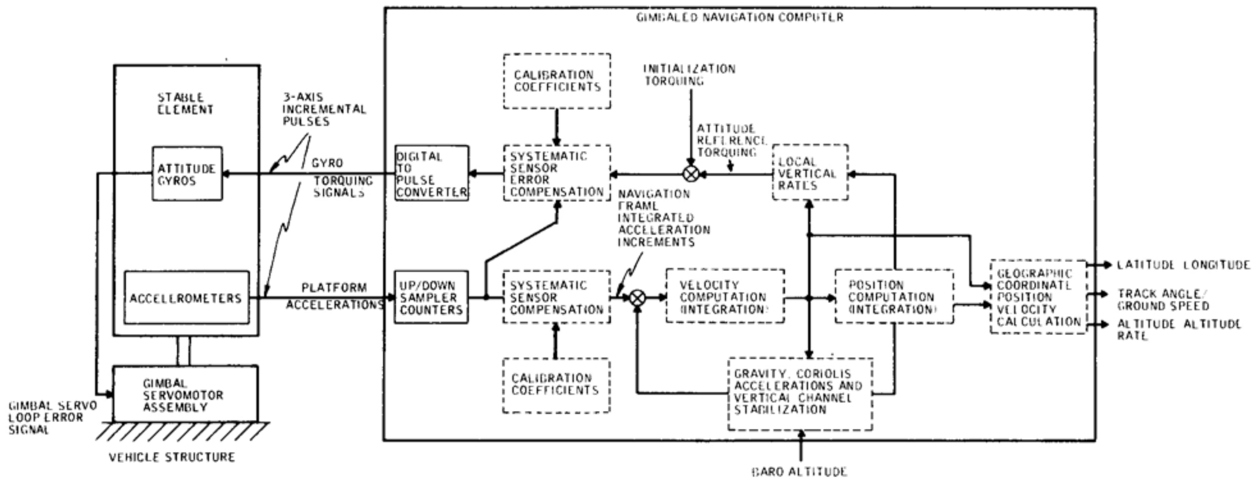


Figure 3. Gimbaled Inertial Navigation System

one revolution per minute) averages away the bias effects on navigation error due to the rotation of the lines of action of the sensor error vectors relative to navigation coordinates, and the resulting conversion of constant sensor errors to oscillatory inputs to the navigation equations. Although this approach relieves performance requirements for the level sensors, it also results in a cost/complexity penalty due to the addition of the turn-table.

## COMPARISON BETWEEN STRAPDOWN AND GIMBALED SYSTEM MECHANIZATIONS

Comparisons between Figures 1, 2, and 3 illustrate the fundamental distinctions between strapdown and gimbaled implementations:

1. An increase in computer complexity for the strapdown system to analytically perform the accelerometer attitude stabilization function provided implicitly by the mechanical gimbal assembly.

2. A decrease in mechanical complexity for the strapdown system due to the elimination of the gimbal assembly.

3. An increase in the performance requirements for the strapdown compared to the gimbaled sensors to provide equivalent system-level performance in a more severe vehicle mounted rate environment.

Items 1 and 2 are the classical strapdown versus gimbaled tradeoffs that strapdown proponents have traditionally used to prove the cost and reliability advantages of the strapdown approach. It has only been in recent years, however, with the advent of low-cost, high-speed digital computers that the tradeoff favors the strapdown approach.

Of more significance is Item 3, which underlies the basis for the gimbaled mechanization concept. The gimbal assembly in a gimbaled navigation system is used for the express purpose of shielding the inertial sensors on the stable element from the rotational environment of the user vehicle, hence reducing sensor performance requirements to meet a given level of system accuracy. The corrolary is that for a particular inertial sensor, the gimbaled mechanization approach will be more accurate than its strapdown equivalent. Therefore, to achieve equivalent system-level performance, the strapdown sensor generally requires a higher performance capability than its gimbaled counterpart. Two avenues can be pursued to achieve the performance improvement:

- Modifying the gimbaled sensor for strapdown application to achieve higher performance levels. A sensor cost increase would result that would partially offset the strapdown savings of eliminating the gimbal assembly. The technical feasibility depends on advancements in gimbaled sensor technology that make possible what was originally (10 years ago) unachievable.

- Development of new sensors with the required strapdown performance levels with comparable (or lower) costs compared to traditional gimbaled sensors.

Today's sensor technology provides the inertial system designer with four choices that can be considered for the above alternatives: floated rate integrating gyros, tuned rotor gyros, electrostatic gyros, and laser gyros. The first three devices are based on the inertial properties of spinning mass and are suitable for use in both strapdown and gimbaled systems. The laser gyro is based on the relativistic properties of light and is uniquely compatible with only strapdown applications due to its inherent digital pulse output. The suitability of either type of device in a strapdown system depends on its performance level in application environments compared with the performance requirements for a specified level of system accuracy.

## STRAPDOWN SENSOR PERFORMANCE REQUIREMENTS

This section discusses some of the more significant sensor error sources affecting strapdown as contrasted with gimbaled system performance and identifies typical sensor requirements to meet a general 1 nmi/h system accuracy specification. The quantitative values presented for the error mechanisms can be easily derived through kinematic reasoning or through use of the simplified analytical error models in the classical navigation texts.[2,3,4,5]

The particular angular rate and linear acceleration followed by an aircraft in a given mission has a major effect on the composite navigation error generated in the inertial navigation system. Depending on the direction and time phasing of the maneuvers (relative to the Schuler frequency for example), error effects can accumulate or cancel each other. The performance figures presented here are representative of strapdown and gimbaled system 1 nmi/h requirements in general and serve to illustrate the relative differences between the two mechanization approaches. Precise requirements for a particular application can only be determined through detailed error analyses for the class of missions and equipment types being considered for that application.

In the discussion to follow, the reader should be aware of the fundamental distinction between two characteristic errors in an inertial navigation system: 1) the average position error rate and 2) the velocity error. Average position error rate is a term traditionally used to classify system navigation positioning accuracy. It represents the average slope of the position error curve over the total navigation period and is usually measured in nautical miles per hour. The velocity error is a measure of the instantaneous slope of the position error curve during flight and is usually measured in knots or feet per second. The position error is a measure of the accuracy in the ability to estimate current vehicle location at any point in time; the velocity error is a measure of how accurately the inertial system can predict the instantaneous speed and flight path direction of the vehicle. In general, due principally to the Schuler oscillatory characteristics associated with inertial navigation systems,[2,3,4,5] the velocity error and average position error rates are unequal. On an ensemble basis, the velocity error is typically larger than the position error rate by a factor of about 3 for gimbaled systems and 3 to 5 for strapdown systems.

One further point should be noted regarding the definition of sensor errors used in the paper. Sensor error or accuracy requirements refer to the error residuals left in the system after the sensor signals have been compensated for known systematic (calibratable) effects (Figures 1, 2, and 3 compensation operations). As such, sensor errors as used here represent performance deviations after calibration due to calibration errors and sensor performance anomalies.

### Gyro Rate Capability

Depending on the type of vehicle, the angular rate range over which performance must be maintained can vary from 100 deg/s (for large commercial aircraft) to 400 deg/s (for military fighter aircraft). Strapdown sensors, which are mounted directly to a vehicle, are exposed to the full vehicle rates; gimbaled sensors, which are isolated from an air frame by the gimbal assembly, are only exposed to the relatively low rates of the computer torquing signals (typically 1 deg/min maximum).

### Gyro Bias Accuracy

The effect of gyro bias error on an inertial navigation system is to generate a position error with a systematic drift component proportional to the gyro bias and a velocity error that oscillates around the average position error slope at the Schuler frequency (84 minute period). The effect has two causes: drift input to the attitude reference during flight, and a heading misalignment during flight created by gyro bias during preflight alignment. In general, gyro bias errors in the 0.01 deg/h range are compatible with overall 1 nmi/h system position error requirements. As illustrated by the following examples, the exact error magnitudes are dependent on the flight profiles anticipated and the system mechanization used (strapdown or gimbaled).

Because the sensors are fixed to the stable element in a gimbaled system, their orientation during the early flight phase (first hour or two) is parallel to their orientation during alignment (for a wander azimuth system). The result is that the North component of position drift created by bias during early flight partially cancels the effect of the initial heading misalignment, because both errors are caused by the same gyro drift. In the strapdown system, where the sensors are fixed to the vehicle, there is no correlation between the orientation of the sensors during flight and alignment, and the navigation and heading errors appear statistically independent. Thus, no systematic cancellation occurs. On the other hand, because the strapdown sensors are fixed to the vehicle, drift rates on outbound and return legs of a circular flight can have a cancelling effect. In the gimbaled system, where the sensors are fixed to the stable element, no such cancellation will occur.

For both gimbaled and strapdown systems, navigation over a spherical earth has a bounding effect on cross-range position error growth. The effect can be visualized by considering the cross-range navigation error that would be generated when traveling on a great circle trajectory that deviates from a desired great circle flight path. Initially, the cross-range error will have a linear growth rate. After traversing 90 degrees of inertial range angle, a cross-range position error will have been accumulated, but the off-nominal and nominal flight paths will now be parallel; hence the cross-range position error rate will be zero. Continued travel will actually decrease the position error. This bounding characteristic of terrestrial inertial navigation systems is an important consideration when error budgeting for long-range flights.

To achieve 1 nmi/h overall system performance, somewhat improved bias performance is required of the strapdown gyro to provide a greater budget for other sensor errors that have a larger effect on strapdown system accuracy (due to the more difficult body-mounted rate environment). Performance improvements are desirable in the areas of g-sensitivity and thermal sensitivity. These two effects can be a major source of error for gimbaled gyros under dynamic flight conditions (fast warm-ups and high-g maneuvers).

## Gyro Wide-band Rate Noise

Wide-band rate noise from a gyro in an inertial navigation system (a white noise random drift rate) has two deleterious effects: an increase in the system alignment time to achieve a given level of initial heading accuracy, and an rms growth rate in a position/velocity Schuler oscillation during navigation. The latter effect, generally, is of more concern from a velocity accuracy standpoint. For a gyro white noise rate with rms density of $\sigma_G$ (deg/h$^{1/2}$), an alignment time $T_A$, and a navigation time t, the rms initial heading error ($\sigma_H$) and Schuler velocity error ($\sigma_V$) are given by:

$$\sigma_H = \frac{\sigma_G}{\Omega T_A^{1/2} \cos \lambda_A}$$

$$\sigma_V = \sigma_G \frac{R\omega_o}{\sqrt{2}} t^{1/2} \left(1 - \frac{\sin 2\omega_o t}{2\omega_o t}\right)^{1/2}$$

where $\Omega$ is earth's rotational rate, $\lambda_A$ is aircraft latitude during alignment, R is earth's radius to the vehicle during cruise, and $\omega_o$ is the Schuler frequency (84 minute period).

For a gyro random noise of 0.002 deg/h$^{1/2}$, an alignment time of 5 minutes, and an alignment latitude of 45 degrees, this translates into an initial heading error of 2 arc minutes and a velocity error at 1 hour of 0.6 ft/s. These figures are generally consistent with "1 nmi/h navigator" performance requirements.

## Gyro Scale Factor Accuracy

Operation over wide rate ranges where large net attitude excursions can occur over a given flight imposes a severe requirement on strapdown rate gyro (Figure 1) scale factor accuracy. Of particular significance are large unidirectional maneuvers. For example, for a 360 degree unidirectional turn (heading rotation) with a 0.005 percent gyro scale factor error, a 0.018 degree heading error is produced in the strapdown attitude reference. The impact on navigational accuracy for typical aircraft velocities (750 knots combined effect of earth and aircraft motion) is to generate an average 0.23 nmi/h cross-track position drift. A more severe case is a 360 degree roll maneuver generating a 0.018 verticality error in the attitude reference. The impact is a bounded cross-track Schuler oscillation having a ±8 ft/s velocity error and a position error that oscillates between 0 and 2 nautical miles.

These maneuvers vividly illustrate the need for high scale factor accuracy in rate gyro strapdown systems where severe vehicle maneuvering is prominant. The exact requirements are a function of the number and type of maneuvers expected for the missions to be flown, the direction and time phasing of the maneuvers, and most importantly, the navigational (position and velocity) requirements for all points along the mission (i.e., an overall 1 nmi/h requirement is a gross oversimplification). An important point to be noted regarding maneuver profiles is that rotations in the direction opposite to a previous maneuver (about the same axis) cancel the scale factor errors of the previous maneuver. In general, it would appear that a 0.0005 percent scale factor accuracy capability for a strapdown rate gyro meets most mission requirements where "1 nmi/h performance" is the stated goal.

A potentially more severe scale factor accuracy requirement for the strapdown rate gyro (Figure 1) is the effect of scale factor nonlinearities, particularly near the null input rate region (±1 deg/sec). Typical user vehicles are in a continual state of angular oscillatory motion due to autopilot limit cycling and vehicle interactions with the air mass. A ±1 deg/s oscillation (zero mean) activity level is a common environmental condition. Consider the effect of a gyro nonlinearity in scale factor near the null region (i.e., a slightly different scale factor for positive rates than for negative rates). The effect on the oscillatory rate input is to generate a systematic bias error output proportional to the product of the input rate amplitude with the nonlinearity. For an equivalent bias accuracy requirement of less than 0.01 deg/h, gyro scale factor nonlinearities around null must be held to 1 part in $10^6$ to avoid rectifying 1 deg/sec oscillatory errors. Depending on the strapdown gyro configuration used, this effect could be more severe than the desired 0.0005 percent overall scale factor accuracy limit, as its presence is continually felt, not only under maneuvering flight conditions.

For the gimbaled attitude type gyro, scale factor accuracy refers to torquer performance (Figure 3).

The torquer operates on the rate commands from the navigation computer, which maintains the platform level. Because the pickoff is continually servoed to null by the gimbal operation, the pickoff scale factor error is not critical for navigation accuracy (as contrasted with the strapdown attitude gyro). If a torquer scale factor error exists, a gyro drift rate is generated proportional to the torquing rate, which for a local vertically maintained platform is proportional to the angular rate of travel of the vehicle over the earth. The result is a navigation position error rate proportional to vehicle translational rate. For typical vehicle rates of 750 knots (including earth's motion) and a 0.03 percent torquer scale factor error, a 0.23 nmi/h position error rate is generated. Compared to 1 nmi/h accuracy requirements, this is acceptable performance.

For the strapdown attitude gyro (Figure 2), scale factor error is included in the wide-angle readout accuracy performance figure.

Attitude Gyro Wide-Angle Readout Accuracy

An error source peculiar to the attitude-type strapdown gyro configuration (Figure 2) is the accuracy of the attitude output signal over the full range for wide-angle (spherical) readout. A readout error of 20 arc seconds corresponds to peak position and velocity oscillatory errors of 0.7 nautical miles and 2.5 ft/s. For missions requiring good velocity accuracy, angle readout errors should be constrained to 10 arc seconds.

Rate Gyro Bandwidth

The requirement to calculate attitude from digital body rate integration increments in the rate gyro strapdown system (Figure 1) imposes unique requirements on gyro bandwidth. Due to the noncomutative nature of attitude motion as a function of body rate, sinusoidal rate components in two body axes at a given frequency, if out of phase, generate an attitude rate along the third axis that has a constant component.[6] Hence, if such out-of-phase motion (coning) is present at a significant level, it must be measured by the strapdown gyros and properly accounted for in the strapdown computer. Otherwise, a systematic attitude drift error will result about the third axis.

To be capable of measuring the high-frequency coning motion anticipated from vehicle vibrations, the strapdown rate sensor should have sufficient bandwidth. Bandwidth limitations in the rate sensor have to be overcome by either ensuring that coning vibrations will not be generated outside the gyro pass band (a difficult analytical problem in view of the uncertainties involved) or by shock mounting the sensor assembly to ensure that angular vibrations outside the gyro pass band will be attenuated. The latter alternative introduces a penalty in size and cost, an error in the ability to precisely know the alignment of the sensor assembly relative to the vehicle (for attitude output purposes), and places a limitation on the ability of the strapdown sensors to measure wideband body rate for other than navigation purposes.

Typical bandwidth requirements for strapdown rate gyros are difficult to define due to their close dependence on particular vehicle vibration and sensor mount characteristics. In general, bandwidths from 30 to 300 Hz may be required, depending on the application.

Rate Gyro Quantization

For the strapdown rate gyro, the quantization level (pulse size) of the integrated rate output increments has a bearing on the attitude computation accuracy in the strapdown computer. The quantization level has to be sized to accurately account for coning-type motion over the anticipated frequency range of expected input vibrations.

For a gyro pulse size E, a coning amplitude E, and a coning frequency F, a worst case order-of-magnitude estimate for the coning error generated by pulse quantization is $\pi E^2 F$. For a pulse size and coning amplitude of 3 arc seconds with 20 Hz frequency (not unreasonable for a high-performance vehicle), this translates into a 0.003 deg/h error. This is an acceptable error for a 1 nmi/h navigation system.

Depending on the vehicle vibration level, and the mechanical interface between the strapdown sensor assembly and the vehicle, high-frequency coning motion may or may not exist. A frustrating aspect of this phenomenon is the inability to adequately model and analyze the effect prior to installation in the user vehicle. As for the bandwidth requirement, an expedient solution to the problem is to shock mount the sensor assembly to ensure that high frequencies are attenuated. The alternatives are to select a gyro with a fine pulse size (order of 2 arc second) or to use a large pulse (e.g., 10 arc seconds) with the hope of never seeing large rectifying coning effects in practice.

Accelerometer Error

The effect of accelerometer bias in an inertial system during navigation is to introduce a Schuler oscillation into the velocity and position data. For a 50μg bias on an accelerometer in a fixed horizontal attitude, peak velocity and position errors of 1.3 ft/s and 0.34 nautical mile result. These figures are generally consistent with 1 nmi/h inertial navigation system requirements and are representative of performance in either strapdown or gimbaled applications.

Another effect of accelerometer bias is to introduce an initial tilt into the attitude reference due to the preflight alignment process that also uses the accelerometers for sensing vertical. The effect of initial tilt during navigation is identical in magnitude to the bias error effect described previously; however, its direction is along the initial accelerometer input axis direction. For a strapdown implementation, the direction of an accelerometer during flight has no correlation with its direction during alignment. Hence, the two errors, although caused by the same source, appear as independent quantities that on a statistical basis have an rms effect $\sqrt{2}$ times larger than either error acting independently. For the gimbaled system, where the sensors are mounted on the stable element, their orientation during the early phase of flight (first hour or two) is parallel to their orientation during alignment. The result is that the tilt effect cancels the bias effect early in flight. For long flight times (several hours), the rotation of the platform uncouples the two effects (for a wander azimuth mechanization) resulting in performance equivalent to the strapdown system. Hence, from a long-term navigation standpoint, the overall accelerometer bias effects for strapdown and gimbaled systems are equivalent. For short missions, however, the gimbaled system has the advantage in performance for a given accelerometer.

An additional error source associated with accelerometers that should not be overlooked is the short-term transient bias trending characteristic following turn-on. A changing accelerometer bias during system alignment cannot be distinguished from a platform heading variation from North (and the resulting attitude reference torquing rates generated in the system to maintain verticality on a rotating earth). Hence, accelerometer bias trending during alignment is interpreted as a heading deviation, and a heading error results. Quantitatively, 0.01 μg/sec trending (not unusual for today's instruments) generates a 0.7 arc minute heading error, which is generally consistent with 1 nmi/h navigation requirements. For strapdown systems requiring fast reaction times, the stabilization time to minimize heading errors in alignment due to accelerometer bias trending is an important consideration in accelerometer selection.

Regarding the strapdown system, scale factor trending during alignment can have the same effect as bias trending if the sensor assembly is oriented at an angle relative to the local vertical. For a 5 degree angle, 0.1 ppm/sec scale factor trending will produce the equivalent of the 0.01 μg/sec bias effect described. For a gimbaled system, in which the accelerometers are leveled as part of the alignment process, no such error exists.

Sensor Alignment Accuracies

Alignment uncertainties between the input axes of the sensors in an inertial navigation system generate navigation errors due to erroneous interpretation by the navigation computer of the orientation of the accelerometer sensing axes relative to navigation coordinates. As an example, for a system (strapdown or gimbaled) with a misalignment between a nominally parallel gyro and accelerometer, consider the effect of a rotation about an axis perpendicular to the accelerometer input axis. If the rotation axis lies in the plane of the misaligned gyro-accelerometer axes, the gyro will sense a portion of the rotation, indicating erroneously to the system computer that the accelerometer has rotated about an axis that is tipped from the true rotation axis by the misalignment angle. The result is that the sensed accelerations are interpreted in the system computer to be rotated by an error angle from the true sensing direction.

The magnitude of this effect is proportional to the size of the angular movements of the sensor assembly over the anticipated mission profiles, and the sensor misalignment uncertainties. For a gimbaled system, the angular motion of the platform is typically on the order of angular distance traveled over the earth; hence, the platform attitude error and resulting navigation error is proportional to range angle. For a 1 arc minute misalignment, a navigation error on the order of 0.03 percent of distance traveled results (or 0.03 percent of average velocity in terms of navigation error rate), which is generally consistent with 1 nmi/h inertial navigation system requirements.

In the strapdown system, where the sensor assembly is attached to the vehicle, it can be rotated through large angles very rapidly, introducing the potential of large cross-coupling effects over the mission length due to misalignments. For example, a 10 arc second misalignment error between a nominally parallel gyro and accelerometer, coupled with a 180-degree rotation normal to the accelerometer input axis, will generate a 20 arc second attitude dispersion in the computer in interpreting the accelerometer signals. If an angular error in verticality is produced, a Schuler oscillation will be generated in the navigation computer with peak velocity errors of ±2.5 ft/s and a position error that oscillates between 0 and 0.7 nautical mile.

An important characteristic of the latter error phenomenon is that for a complete rotation (360 degrees) no net attitude error accumulates. For an attitude-type strapdown gyro (Figure 2), this characteristic applies for all maneuvers that end at the same attitude orientation, independent of attitude history during the maneuver (i.e., the attitude error that can develop for a particular maneuver is determined by the final attitude only and is at maximum for a 180 degree rotation). However, for the strapdown rate gyro configuration (Figure 1), due to the nature of the attitude update equations in the strapdown computer, the attitude error is a function of the way in which the maneuver was executed. As a result, complex sequential maneuvers, or complete rotational maneuvers about an axis that is not along one of the cardinal sensor assembly axis, can generate residual attitude errors, even if the maneuver ends at the same attitude at which it originated. For example, consider a maneuver consisting of a +90 degree roll followed in succession by a +90 degree pitch, -180 degree roll, +90 degree pitch, and +90 degree roll. The aircraft attitude at completion of the maneuver is as it was originally. However, a net attitude error will be left in the rate gyro strapdown computer if the gyros were misaligned relative to one another during the maneuver due to cross-coupling effects introduced as the maneuver progressed.

Depending on the anticipated mission envelopes to be flown, the effect of this residual error buildup must be included in the error budget to determine the strapdown rate gyro alignment requirement. Also included must be an assessment of mission needs as a function of time in the mission. In general, it appears that 5 to 10 arc second alignment accuracy is required between strapdown sensors to be consistent with 1 nmi/h system accuracy requirements. For the attitude gyro strapdown system, 10 arc seconds appears acceptable.

### Reaction Time

A traditional problem with inertial navigation systems has been the time required for warm-up and alignment before the navigation mode can be entered. In the past, 15 minutes for these operations was not uncommon. The warm-up requirement is dictated by the time period for performance to stabilize in the inertial sensors, at least to a predictable level. The alignment time is limited by sensor noise characteristics and expected vehicle acceleration disturbances (wind buffeting and fuel loading) during alignment. A desired improvement for all inertial components, gimbaled or strapdown, is reduction in the reaction time to less than 5 minutes.

### Sensor Calibration Interval

Sensor accuracies of the magnitudes discussed are not easily achieved with conventional instruments on a long-term basis. Periodic calibrations are typically required to achieve the required performance levels during mission times.

For gimbaled systems, calibrations of the instruments can be achieved through the built-in expedient of using the gimbal assembly as a platform test table in a special system calibrate test mode. The method is to command the stable element to rotate to different attitudes while recording and comparing system/sensor readings. The movement of the sensor assembly relative to local gravity and earth's rate permits the sensor errors to be separated from the true earth rate and gravity reaction force measurements, thereby calibrating the sensors. The advantage of this approach is that the calibration can be performed without removing the system from the stationary user vehicle.

For the strapdown sensors, no mechanism exists for automatically positioning the sensor assembly without moving the vehicle. Further, vehicle motion on the ground is limited to heading changes; hence, if used, many error sources are not observable (cannot be calibrated). The ability to accurately and conveniently measure sensor errors therefore, is severely limited for the strapdown system.

It should be noted that a composite gyro bias compensation method has been demonstrated on strapdown floated rate integrating gyros [7, 8] through the measurement and comparison of system performance with the gyro spin motors operating at two different speeds (i.e., forward and reversed[8]). For the wheel reversal method, this has an effect equivalent to a 180 degree rotation of the gyros. This calibration mechanism is limited by its inability to separate g-insensitive from g-sensitive error terms, the inability to accurately measure gyro scale factor errors, and the problem of predicting vehicle movement during the period when the gyro spin motors are being changed such that performance can be compared in equivalent reference frames.

In general, it can be stated that long-term stability requirements are more severe for the strapdown than for the gimbaled sensors due to the lack of a convenient on-board calibration mechanism and to the general unacceptability of regular system removals from the user vehicle. Thus, not only are the accuracy requirements generally more difficult to achieve for strapdown sensors for a given mission; they must also be achieved without the luxury of frequent calibrations, which can be afforded with gimbaled systems.

### Summary

Table 1 is a summary of the strapdown as contrasted with gimbaled sensor requirements for the error sources considered in a "1 nmi/h navigator" application. For degraded navigation performance, the requirements diminish proportionally.

| Performance Parameter | Typical Values for 1 nmi/h System Accuracy | | |
|---|---|---|---|
| | Gimbaled | Rate Gyro Strapdown | Attitude Gyro Strapdown |
| Gyro Rate Range (deg/s) | 0.02 | 100-400[a] | 100-400[a] |
| Gyro Bias Accuracy (deg/h) | 0.01[b] | 0.01 | 0.01 |
| Gyro Wide-Band Random Rate Noise ($deg/h^{1/2}$) | 0.002 | 0.002 | 0.002 |
| Gyro Scale Factor Accuracy (percent) | 0.03 | 0.0005 - 0.005[a] | N/A |
| Attitude Gyro Wide-Angle Readout Accuracy (arc second) | N/A | N/A | 10 |
| Rate Gyro Bandwidth (Hz) | N/A | 30-300[a] | N/A |
| Rate Gyro Quantization (arc second) | N/A | 2-10[a] | N/A |
| Accelerometer Bias Accuracy (µg) | 100 | 50 | 50 |
| Accelerometer Short-Term Bias Trending (µg/s) | 0.01 | 0.01 | 0.01 |
| Accelerometer Short-Term Scale Factor Trending (PPM/s) | N/A | 0.1 | 0.1 |
| Sensor-to-Sensor Alignment Accuracy (arc second) | 60 | 5-10[a] | 10 |
| System Reaction Time, Warm-up and Alignment (min) | 5 | 5 | 5 |
| System Calibration Interval (months) | 1 | 6 | 6 |

[a] Depending on severity of dynamic environment.
[b] Degraded under dynamic conditions from indicated figure.

Table 1. Typical Strapdown Versus Gimbaled Sensor Performance Requirements

THE RING LASER GYRO

Of the strapdown gyro types available today and in the immediate future, the ring laser gyro has the capability for best achieving the performance requirements given in Table 1. This unique instrument has no moving parts and is extremely simple in construction, providing the required low cost and high reliability in projected production configurations. Its accuracy relies on the constancy of the speed of light. Reference 9 describes this unique instrument, its mechanization approach, and performance characteristics.

Figure 4 depicts the basic operating elements in a laser gyro: a closed optical cavity containing two beams of correlated (single-frequency) light. The beams travel continuously between the reflecting surfaces of the cavity in a closed triangular path; one beam travels in the clockwise direction, the other in the counterclockwise direction, each occupying the same physical space in the cavity. The light beams are generated from the lasing action of a helium-neon gas discharge within the optical cavity. The reflecting surfaces are dielectric mirrors designed to selectively reflect the frequency associated with the particular helium-neon transition being used.

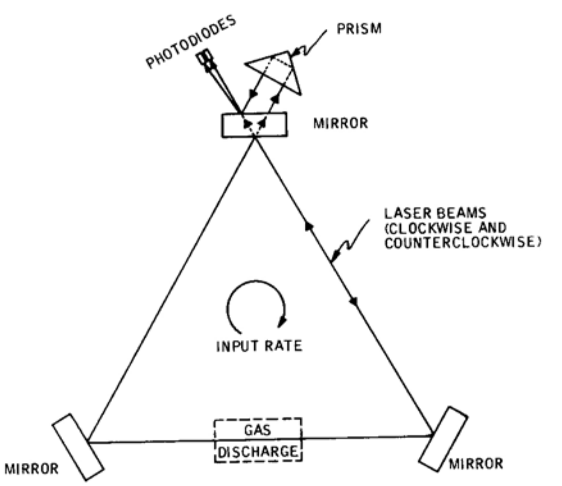


Figure 4. Laser Gyro Operating Principles

To understand the principle of operation of the laser gyro, consider the effect of cavity rotation to an observer rotating with the cavity. Relative to the observer, it would take longer for a wave of light to transverse the distance around the optical path in the direction of rotation than in the direction opposite to the rotation. Due to the constancy of the speed of light, this effect is interpreted by the observer as a lengthening of the net optical path length in the direction of rotation, and a shortening of the path length in the opposite direction. Because a fixed integral number of light waves must exist around the path at any instant of time (the beams are continuous, closing on themselves), the path length shift must also be accompanied by a frequency shift in the opposite sense. The frequency difference between the two beams, thereby, becomes a measure of rotation rate.

The frequency difference is measured in the laser gyro by allowing a small percentage of the laser radiation to escape through one of the mirrors (Figure 4). A prism is used to reflect one of the beams such that it crosses the other in almost the same direction at a small angle (wedge angle). Due to the finite width of the beams, the effect of the wedge angle is to generate an optical fringe pattern in the readout zone. When the frequencies between the two laser beams are equal (under zero rate conditions), the fringes are stationary relative to the observer. When the frequencies of the two beams are different (under rotational rates), the fringe pattern moves relative to the observer at a rate and direction proportional to the frequency difference (i.e., proportional to the angular rate). More importantly, the passage of each fringe indicates that the integrated frequency difference (integrated input rate) has changed by a specified increment. Hence, each fringe passage is a direct indication of an incremental integrated rate movement, the exact form of the output needed for a rate gyro strapdown navigation system (Figure 1).

The mechanism for generating digital integrated rate increment pulses from the laser gyro consists of two photodiodes mounted in the fringe area and spaced 90 degrees apart (in fringe space). As the fringes pass by the diodes, sinusoidal output signals are generated, with each cycle of a sine wave corresponding to the movement of one fringe over the diodes. By observing which diode output is leading the other (by 90 degrees), the direction of rotation is determined. Simple digital pulse triggering and direction logic operating on the photodiode outputs convert the sinusoidal signals to digital pulses for computer input.

The pulse size (quantization) for the laser gyro depends on the wave length of the laser beam and the path length between the mirrors. For typical laser gyros with 0.63 μm wavelength and distances between mirrors (each leg) on the order of 4 inches, the pulse size is 2 arc seconds.

## Laser Gyro Construction

The accuracy of the laser gyro depends on the ability to keep the laser beam independent of the influences of the lasing cavity. A key requirement in this regard is that the average of the path lengths around the lasing triangle for the clockwise and counterclockwise beams be constant and equal to the value for peak lasing power (averaged between the two beams). In regard to the latter requirement it is recognized that many of the key error parameters for the laser gyro are stationary for small variations in path length about the nominal for peak average power.[10]

To achieve a high degree of path length stability, the laser gyro optical cavity is constructed of Cer Vit material, which has an extremely low coefficient of thermal expansion. Figure 5 illustrates Honeywell's mechanization concept. A single Cer Vit structure is used to contain the helium neon gas with the lasing mirrors and electrodes forming the seals. High voltage (typically 1500 volts) applied across the electrodes (one cathode and two anodes) ionizes the helium neon gas mixture, thereby providing the required laser pumping action. Figure 6 illustrates the interface between the block assembly and the gyro electronics.

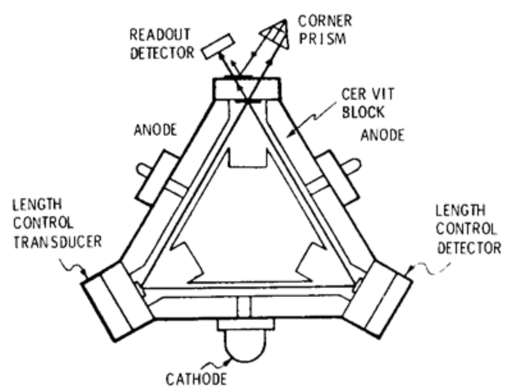


Figure 5. Laser Gyro Block Assembly

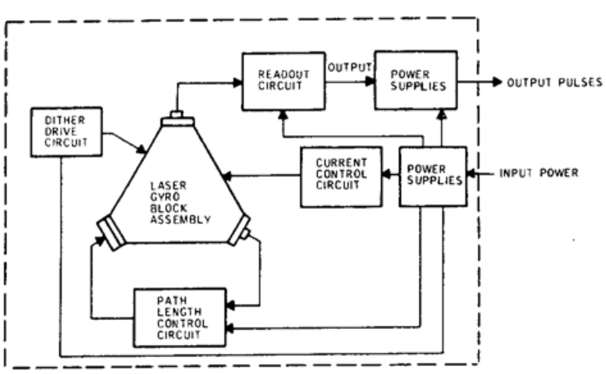


Figure 6. Laser Gyro Electronic Assemblies

A piezoelectric transducer mounted on one of the mirror substrates is used to control the path length of the cavity (Figures 5 and 6). The control signal for the transducer is proportional to the deviation from the peak of the average power in the laser beams; hence, the control loop is designed to maintain a path length that produces peak average lasing power. The average beam power is measured by a photodiode mounted on one of the mirrors that senses the radiation from both the clockwise and counterclockwise beams.

Flow phenomena in the laser gyro can cause bias shifts due to differential changes in the index of refraction of light along the forward and reverse beam paths.[11] To reduce the possibility of net circular flow phenomena in the gyro, circuitry is provided to maintain the net current flow in the two ionization paths constant (see Figure 6).

## Laser Gyro Packaging

Figure 7 illustrates the packaging concept used for Honeywell laser gyros. The electronics to control the laser and to provide readout pulses are mounted with the laser block in a single box. Included is the high voltage supply for gyro operations (regulated low level voltages are gyro inputs). The box is hermetically sealed to avoid problems associated with high voltage arcing at high altitudes.

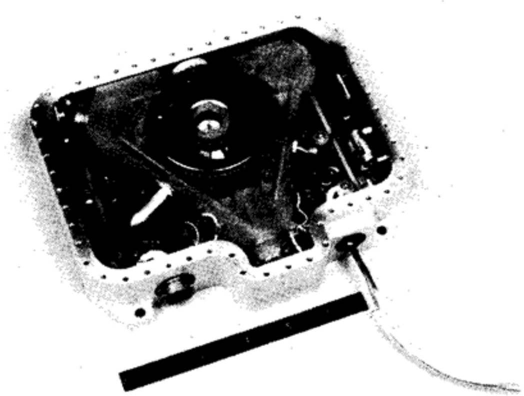

Figure 7. Honeywell GG1300 Laser Gyro

## Laser Gyro Lock-In

The phenomenon of lock-in in the laser gyro has historically been its most prominent error source and the most difficult to handle. The means for compensating its effects is the principal factor determining the configuration and performance of laser gyros from different manufacturers.

The phenomenon of laser gyro lock-in arises because of imperfections in the lasing cavity, principally the mirrors, that produce backscattering from one laser beam into the other.[12] The resulting coupling action tends to hold the frequencies of the two beams together at low rates producing a dead zone. When the gyro input rate exceeds a threshold known as the lock-in rate, the beams separate in frequency and begin to produce output pulses.

The magnitude of the lock-in effect depends on the quality of the mirrors used. In general, the limit of today's technology at Honeywell results in lock-in rates on the order of 0.01 to 0.1 deg/s. Compared with 0.01 deg/h navigation requirements, this is a serious error source that must be overcome.

Honeywell's approach for overcoming lock-in is the simple expedient method of mechanically dithering the laser block at high frequency through a dither flexure suspension built into the gyro assembly. The spoked wheel-like structure in Figure 7 is a torsional spring. One on each side of the laser block torsionally suspends it from the center post. Piezoelectric transducers on one of the springs provide the dither motor drive mechanism (Figure 6) to torsionally oscillate the lasing block at its resonant frequency through a small angle. This creates enough motion in the gyro to ensure that the dwell time in the lock-in zone is short such that lock-in will never develop. The result is a gyro that has continuous resolution over the complete rate range. The residual effect of lock-in is a small random error in the gyro output (random rate noise) that is introduced each time the block passes through lock-in (at twice the dither frequency).

By mounting the readout reflector prism on the gyro case and the readout photodiodes on the block (Figure 5), a simple mechanism is provided to remove the dither signal from the gyro output. If the gyro center of rotation is selected properly, the translation of the dither beam across the prism causes a fringe motion at the detector that identically cancels the dither rate sensed by the block. The result is an output signal that accurately measures the rotation of the gyro case, free from the dither oscillation.

Other Methods for Lock-In Compensation

Other methods used for lock-in compensation have been electrical in nature and have had the unfortunate effect of introducing other errors into the laser gyro that have degraded its bias and scale factor accuracy.

The original alternative to mechanical dither was use of a Faraday cell within the lasing cavity[10]. This method for overcoming lock-in introduces a controlled differential shift in the index of refraction of light into the cavity between the clockwise and counterclockwise beams. The result is an imposed constant gyro bias (usually alternating in sign) that is used to keep the gyro out of lock-in. The index of refraction shift is generated by applying a magnetic field to the Faraday cell, with magnitude and phase proportional to the desired bias. The bias, being known and constant, is removed from the output by digital subtraction.

A recently introduced alternate to the Faraday cell approach is the magnetic mirror concept in which a special outer coating is applied to the laser mirrors.[13] By applying a magnetic field to the mirrors, a differential phase shift is introduced between the reflected clockwise and counterclockwise beams, which appears as a differential path length change around the cavity. The result is a bias imposed on the gyro output that is controllable by the applied magnetic field.

The principal difficulty in the Faraday cell and magnetic mirror bias approaches has been the introduction of thermal sensitivities and bias uncertainties into the gyro through the same mechanism used to introduce the electrical bias. Data available on laser gyros using this biasing technique indicate that at least an order of magnitude performance improvement is needed before the 1 nmi/h requirements of Table 1 can be achieved.[14,15]

Another approach for overcoming lock-in has been the differential laser gyro (DILAG) concept.[16] This method also incorporates a Faraday bias cell, but in a manner that tends to cancel the effects of bias shift generated by the intrusion of the cell into the laser cavity. The method is to use a polarizing crystal in the cavity that creates two sets of counterrotating beams, each set polarized in a different direction. Hence, two laser gyros are created in the same cavity, each being separable through use of a polaroid filter on the output. The effect of the polarization difference between the two laser sets is to make each respond in the opposite sense to the applied Faraday bias. Hence, one gyro output is biased in the opposite direction from the other. Averaging the two signals theoretically cancels the Faraday bias from the output, including the deleterious effects of bias uncertainties.

The accuracy of the DILAG approach hinges on the bias effects in each gyro being equal and opposite. The limited data vailable on DILAG suggests that further development is needed before the concept can be seriously considered for 1 nmi/h navigation applications.[17]

## ALTERNATE STRAPDOWN GYROS

Other than the laser gyro, three gyro types can be considered for high-accuracy strapdown inertial navigation: the single-degree-of-freedom floated rate integrating gyro, the tuned rotor gyro, and the electrostatic gyro (ESG). The first two types of gyros have reached a high level of production maturity on gimbaled inertial navigation system programs. The electrostatic gyro is an advanced development technology instrument being considered for strapdown and high-accuracy gimbaled applications.

Unlike the laser gyro, each of these devices relies on the classical method for inertially sensing angular motion: use of a proof angular momentum device as a reference and measurement of angular motion relative to it (for attitude) or the torque needed to rotate it (to measure rate). The accuracy of all such devices is dependent on the accuracy by which the momentum device can be contained without introducing unknown torques (drift rates).

Single-Degree-of-Freedom Floated Rate Integrating Gyro

The floated rate integrating gyro, pictured schematically in Figure 8 and described in more detail in References 2, 3, and 5, is the gyro with the longest production history and is the original high-accuracy platform gyro. The device consists of a cylindrical hermetically sealed momentum wheel/spinmotor assembly (float) mounted on delicate pivots in a cylindrical case. The cavity between the case and float is filled with a high viscosity fluid that serves the dual purpose of suspending the float at neutral buoyancy and providing damping to resist relative float/case angular motion about the pivots.

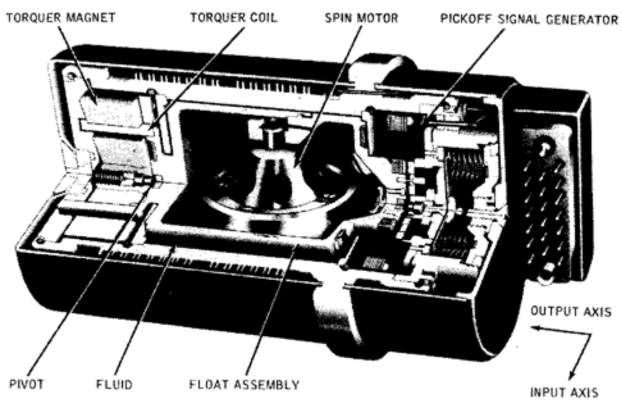


Figure 8. Single-Degree-of-Freedom Floated Rate Integrating Gyro

A pickoff assembly is provided that outputs an electrical signal proportional to the displacement of the float relative to the case about the pivot (output) axis. Also included is a torquer assembly consisting of a coil attached to the float assembly and a permanent magnet fixed to the case. By inputting electrical current to the torquer coil, known torques can be applied to the float assembly about the output axis. Delicate flex leads between the case and float are used to transmit the current for the motor and torquer coils.

The device senses rate through the gyroscopic reaction torque generated about the output axis when the gyro is rotated about is input axis (see Figure 8). The reaction torque is provided by the damping fluid, which generates a torque proportional to the relative rate developed between the float and case (rate of change of angle sensed by the pickoff as a gyroscopic response to input axis rate). As a result, a rate of change of the pickoff angle is generated proportional to the input axis rotation rate. The pickoff angle, thereby, becomes a measure of the integrated input rate.

To operate the gyro in a strapdown mode, the float is caged to the case by a torquing signal proportional to the pickoff output. The torquing signal forces the float assembly to track the input axis motion, and the torquer current becomes proportional to the input axis rate. Further, due to the integrating nature of the device, the integral of the torquer current becomes proportional to the integrated input axis rate. A measure of the torquer current, thereby, provides integrated rate information for a rate gyro strapdown navigation system.

In general, there are two alternatives for quantizing the integrated rate current gyro torquing signal to provide the required incremental pulse form for the strapdown computer (Figure 1). The first alternative is to quantize the torquer current at known integrated current increments (digital rebalance). The occurrence of a rebalance increment into the gyro, therefore, indicates that an integrated rate increment has been sensed. Digital pulses generated in the torquer current gating logic provide the output signals for the strapdown computer. The other alternative incorporates an analog gyro loop, with a measure of the analog torquer current used for input to an electronic integrator. The integrator is rebalanced incrementally in a manner analogous to the digital gyro loop rebalance scheme, with the occurrence of a pulse representing the sensed integrated rate increment.

The tradeoff between the two approaches generally hinges on the amount of current required to cage the gyro and the associated difficulties in generating high-frequency, high-current pulses (for the digital rebalance) versus the complexity of the analog electronic pulse rebalance integrator (external to an analog gyro loop) to maintain low drift rates.

Tuned Rotor Gyro

The tuned rotor gyro is the most advanced gyro in production today for aircraft 1 nm/h gimbaled platforms. Due to its simplicity compared to the floated rate integrating gyro, it is theoretically lower in cost and more reliable. A schematic diagram of the tuned rotor gyro wheel assembly is shown in Figure 9 (see Reference 18 for a more detailed description).

The gyro consists of a momentum wheel (rotor) connected by a flexible gimbal to a case fixed spinmotor drive shaft. The gimbal is attached to the motor and rotor through members that are torsionally flexible but laterally rigid. (Figure 9 illustrates the tuned rotor principle. The particular mechanization used for the rotor assembly varies between manufacturers.) A two-axis pickoff is included (not shown in Figure 9) that measures the angular deviation of the rotor (in two axes) relative to the case (to which the motor is attached). Also included (not shown) is a two-axis magnetic torquer assembly that allows the rotor to be torqued relative to the case on current command.

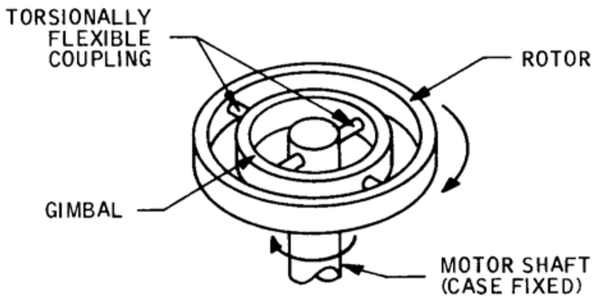


Figure 9. Tuned Rotor Gyro Concept

As for all angular momentum-based rate sensing devices, the key design feature of the gyro is the means by which it can contain the reference momentum (the spinning rotor) without introducing spurious torques (drift rates) in the process. For the tuned rotor, the method is linked to the dynamic effect of the flexible gimbal attachment between the rotor and the motor. Geometrical reasoning reveals that when the rotor is spinning at an angle that deviates from the motor shaft direction, the gimbal is driven into a cyclic oscillation in and out of the rotor plane at twice the rotor frequency. Dynamic analysis shows that the reaction torque on the rotor to sustain this motion has a systematic component along the angular deviation vector that is proportional to the angular displacement, but that acts as a spring with a negative spring constant.[18] The flexible pivots between the rotor and gimbal, on the other hand, provide a similar spring torque to the rotor, but of opposite sign. Hence. to free the rotor from systematic torques associated with the angular displacement, it is only necessary to set the gimbal pivot springs such that their effect cancels the inverse spring effect of the gimbal. The result (tuning) is a rotor suspension that is insensitive to angular movement of the case. Hence, the pickoff outputs represent the angular deviation of the case relative to the rotor reference.

Use of the tuned rotor in a strapdown mode parallels the technique used for the floated rate integrating gyro. Exceptions are that damping must be provided electrically in the caging loop, as there is no fluid, and that the gyro must be caged in two axes simultaneously. The latter effect couples the two caging loops together due to the gyroscopic cross-axis reaction of the rotor to applied torques.

Proponents of the tuned rotor technology point to its advantages compared to the floated gyro: fewer parts, two axes per gyro, elimination of the need for the fluid suspension and associated error mechanisms, elimination of flex lead error torques, elimination of spinmotor axial mass unbalance as an error source, and more predictable instrument warm-up characteristics. These advantages are partially offset by the addition of drift terms caused by extraneous torques and forces at twice spin frequency, the addition of errors caused by imperfect rotor tuning, windage torques and drift errors associated with dynamic viscous coupling of the off-null gimbal motion with the surrounding gas, and motor bearing lubricant containment problems if a near vacuum is held around the rotor to eliminate the latter gas dynamic effects.[19]

Electrostatic Gyro (ESG)

Of the three angular momentum devices considered, the ESG comes closest to achieving the theoretically ideal suspension system. In the ESG, a spherical rotor is suspended in a vacuum by an electrostatic field, which is generated by case-fixed electrodes; hence, there is no physical contact with the rotor assembly. Pickoffs on the case sense the orientation of the case relative to the rotor.

Mechanizations of the ESG pickoff have used optical devices that sense scribe marks etched on the rotor. For such an approach, the rotor is a hollow shell, 1 to 2 inches in diameter. Alternatively, a small, solid rotor (typically 1 cm in diameter) can be used with a radially offset mass. The resulting modulation in the suspension field (due to the mass unbalance) is used to determine the relative case/rotor orientation. Each of these approaches is being considered for gimbaled application;[20,21] however, only the latter approach, which uses the small rotor, is being considered for strapdown application.[20,22] In a strapdown configuration, the ESG is used as an attitude gyro (Figure 2); hence, the accuracy of the pickoff is a key performance parameter (Table 1).

For a specified case orientation relative to the rotor, and with accurate thermal controls, ESG errors can be very predictable and compensatable. However, for a strapdown application where the case can be at arbitrary orientations relative to the rotor, compensation becomes more difficult. Due to the nonprecise mechanical nature and large size (relative to the rotor) of the suspension coils, it is difficult to manufacture a gyro that has a fixed center of suspension in the rotor cavity for all orientations of the rotor, case, and specific force vector. Consequently, to avoid excessive drift torques (fixed and g-sensitive), complex modeling is needed in three dimensions for bias calibration coefficients.[22] The calibration problem is further complicated by movements of the mechanical assemblies caused by gyro thermal expansion. To compensate for this effect, additional modeling can be used; however, thermal control seems to be the only accurate method.

To overcome some of these difficulties, Autonetics, the principal proponent of the ESG for strapdown inertial navigation, is developing a turn-table assembly for their MICRON strapdown ESG system, on which the inertial sensors are mounted. The turn-table is rotated at a known rate relative to the system chassis. The result is an averaging of the bias error effects (assumed case correlated) such that the integrated navigation error is improved.

## RING LASER GYRO PERFORMANCE

This section analyzes the performance capabilities of the laser gyro against the requirements for strapdown navigation presented in Table 1. The analysis is based exclusively on Honeywell GG1300 laser gyro performance characteristics due to the wealth of data currently available on this instrument. The GG1300 (Figure 7) has a lasing triangle 5.7 inches on a leg, operates on a 0.63 μm helium-neon transition, and has a pulse size of 1.57 arc seconds. The packaged device including its electronics (Figure 7) is 8.7 inches long, 6.7 inches wide, and 2.1 inches in depth.

In general, laser gyro performance is a strong function of the size of the lasing cavity, larger gyros having higher accuracy. The GG1300 is the largest laser gyro currently being produced by Honeywell and has demonstrated the highest performance levels thus far achieved with laser gyro technology. To meet the small size constraints of tomorrow's high-performance military aircraft, the GG1342 laser gyro is currently in development at Honeywell. The GG1342 has a 4.2 inch path length, and outside dimensions of 6.8 inches by 5.8 inches by 2.1 inches deep. Recent developments in laser gyro technology at Honeywell provide the basis for performance projections for the new device that equal what has been achieved to date with the GG1300. On this basis, the performance data and conclusions drawn for the GG1300 in the following section are expected to be also representative of the capabilities of the newer GG1342 technology.

### Rate Capability

The rate capability of the laser gyro is limited only by the bandwidth of the readout electronics. Output frequencies of 1 MHz are readily achievable within the current state of the art in low-noise, high-gain readout amplifiers operating on the laser gyro photodiode output signals. For the Honeywell GG1300 size gyro (1.5 arc seconds pulse size), this translates into a 400 deg/s capability that meets the full requirement presented in Table 1. Smaller gyros (and a linearly proportional pulse size increase) yield higher rate capabilities.

### Bias

Test data on several Honeywell GG1300 laser gyros in 1974-1975 has demonstrated outstanding long-term bias stability in the 0.01 deg/h category including turn-on to turn-on, thermal, and vibration exposures.[23] The bias stability characteristic of the laser gyro was vividly illustrated by a long-term test conducted over a two-year period on a GG1300 laser gyro in which over 6000 operating hours were accumulated, and during which time no calibrations were made. The results, shown in Figure 10, indicate a long-term stability of better than 0.01 deg/h. The data in Figure 10 is the total data sample taken (no editing). Each data point represents the average drift over the first 4 hours of operation (from turn-on) computed as the four-hour pulse count divided by four. At least 3 hours of off time preceded each test.

There is no known g-sensitivity in the laser gyro bias. References 24, 25, and 26 describe rocket sled and severe vibrational exposure tests performed on Honeywell laser gyros that demonstrate the g-insensitive performance capabilities.

Figure 11 illustrates the bias sensitivity of Honeywell's current GG1300 laser gyro technology to start-up and severe thermal transients. Figure 11 also includes similar test data obtained on Honeywell's older technology laser gyros (1974-1975). A comparison between the Figure 11 data sets illustrates the technology improvements achieved over the last year in laser gyro thermal insensitivity. As can be seen from Figure 11, the effect of thermal environments on gyro bias accuracy relative to 0.01 deg/h requirements is barely noticeable for today's instrument. In addition, performance data analyses at Honeywell have demonstrated that the residual thermal effects are easily modeled using temperature measurements from each gyro. The result is that the compensated bias performance in today's gyro is virtually constant, independent of start-up and thermal transient effects.

### Gyro Wide-Band Random Rate Noise

Random wide-band rate noise in the laser gyro is caused by mechanically dithering the gyro block through the lock-in zone twice each dither cycle. As a result, a random angle error is generated at twice the dither frequency, which is uncorrelated from half cycle to half cycle. The effect is a rate-noise-like signal on the gyro output that has zero mean and short correlation time. For error analysis purposes, the effect can be accurately modeled as white noise.

The effect of the white noise is notable in both Figure 11 data sets. These data sets are plots of average rate samples using a 1 minute averaging window (the integral of the gyro output, or pulse count, over a one minute period). The noise in the data is the average rate noise from the gyro for the one minute averages. The rms value of the noise for both sets of data is on the

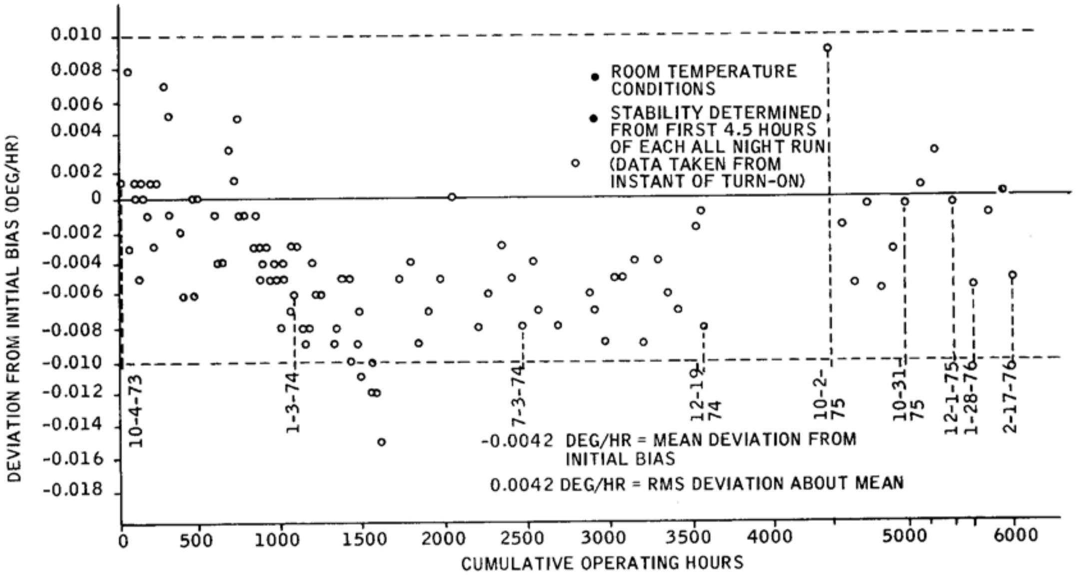


Figure 10. GG1300 Laser Gyro Long-Term Bias Stability

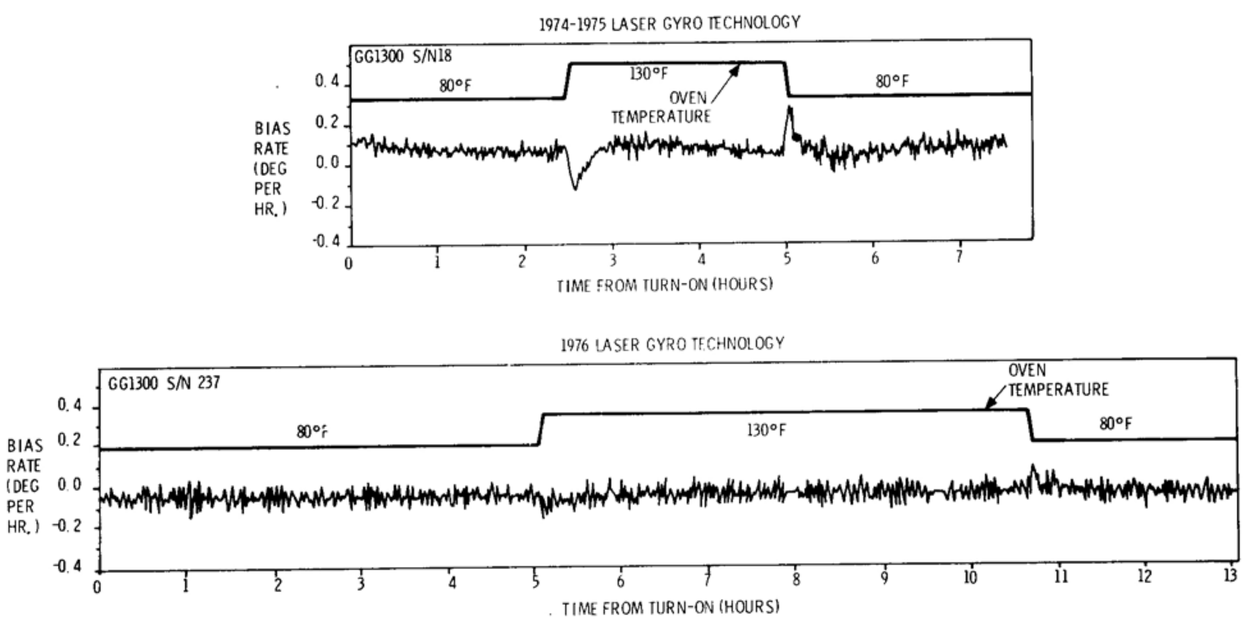


Figure 11. GG1300 Laser Gyro Start-up and Thermal Transient Bias Sensitivity

order of 0.025 deg/h. The corresponding random noise spectral coefficient is obtained by multiplying this figure by the square root of the averaging time. The result is 0.003 deg/$h^{1/2}$ compared to the 0.002 deg/$h^{1/2}$ requirement in Table 1.

Random noise for laser gyros is a function of the mirror quality and manufacturer's experience. Current Honeywell technology is capable of producing GG1300 gyros with random noise coefficients in the 0.002 to 0.005 deg/$h^{1/2}$ range. With the benefits of learning as the laser gyro technology phases into production, 0.002 deg/$h^{1/2}$ or lower should be standard performance.

Scale Factor Accuracy

The laser gyro's scale factor accuracy is one of its principal attributes. Figure 12 illustrates the scale factor temperature sensitivity and high rate linearity characteristics of the GG1300 laser gyro. Table 2 shows the scale factor stability of several GG1300 laser gyros over a six month period. The data in Figure 12 and Table 2 was taken during 1974-1975 and is considered typical for laser gyros of that time. Higher performance levels have been demonstrated with several of today's laser gyro instruments. On this basis,

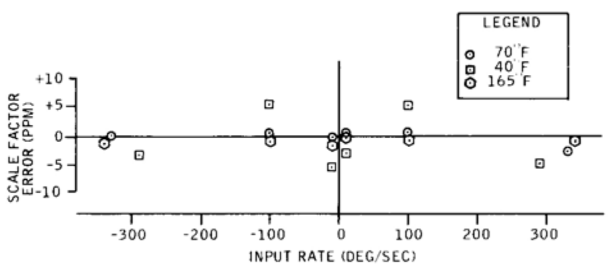


Figure 12. 1974-1975 GG1300 Laser Gyro Technology Scale Factor Thermal Sensitivity and High Rate Linearity

| Gyro Serial Number | Test Period (Weeks) | Number of Scale Factor Measurements Over Test Period[a] | Measured RMS Scale Factor Deviation (PPM) |
|---|---|---|---|
| 1 | 20 | 5 | 2.3 |
| 2 | 17 | 17 | 2.2 |
| 3 | 13 | 12 | 3.2 |
| 4 | 18 | 14 | 3.3 |
| 5 | 9 | 6 | 1.2 |
| 6 | 25 | 24 | 1.7 |

[a] Gyros were turned off between test measurements.

Table 2. 1974-1975 GG1300 Laser Gyro Technology Scale Factor Stability

it can be concluded that the stringent 0.0005 percent scale factor accuracy requirement of Table 1 should be readily achievable.

The laser gyro is unique in the symmetry of its scale factor characteristics. There is no known mechanism in the instrument for creating a scale factor that differs for plus or minus rate inputs. Theoretically, the gyro has zero asymmetry error. A dramatic demonstration of this phenomenon can be seen by placing the gyro on a rate table and violently oscillating it about its input axis while accumulating output counts. If the table is returned to its original position after completion of the test, the accumulated counts will be indistinguishable from a similar run performed with the table stationary. Figure 13 illustrates the results of such a test performed on a GG1300 gyro for 10 minute sampling periods with table rate oscillations from 0.1 to 50 deg/s. The results are indistinguishable from the random noise scatter visible in the control runs at zero rate. It can be easily seen from the data that the corresponding asymmetrical error to produce the same scatter level is less than 0.1 part per million. Hence, the Table 1 requirement for low asymmetrical scale factor error around null (1 PPM) is easily achievable with the laser gyro.

Bandwidth

There is no bandwidth limiting mechanism in the laer gyro. The output represents the integral of angular rate (incrementally) with no dynamic lag (other than the quantization delay associated with the digitization process).

Quantization

The fine pulse size naturally available from the laser gyro (1.5 to 3.0 arc seconds depending on the gyro size) easily meets the requirements of Table 1. An even finer level of pulse size is achievable if required under unusual circumstances by triggering outputs at the positive and negative zero crossings of both output photodiodes. A factor of four finer pulse size can be obtained by this technique for a given gyro block configuration. The penalty is a proportional decrease in maximum rate capability (or increased readout electronics complexity for increased bandwidth to maintain the same rate capability).

Sensor Alignment Accuracy

The alignment stability between the sensor axes of a strapdown system is determined by the gyro and accelerometer instrument stabilities as well as the stability of their mounts. For a Honeywell laser gyro strapdown system (LINS - Laser Inertial Navigation System) tested at Holloman Air Force Base in 1975 (tests to be described subsequently), alignment stabilities for the three month test period and four months thereafter (before and after tests) including mild temperature variations (±30°F), were within 10 arc seconds. This was achieved without

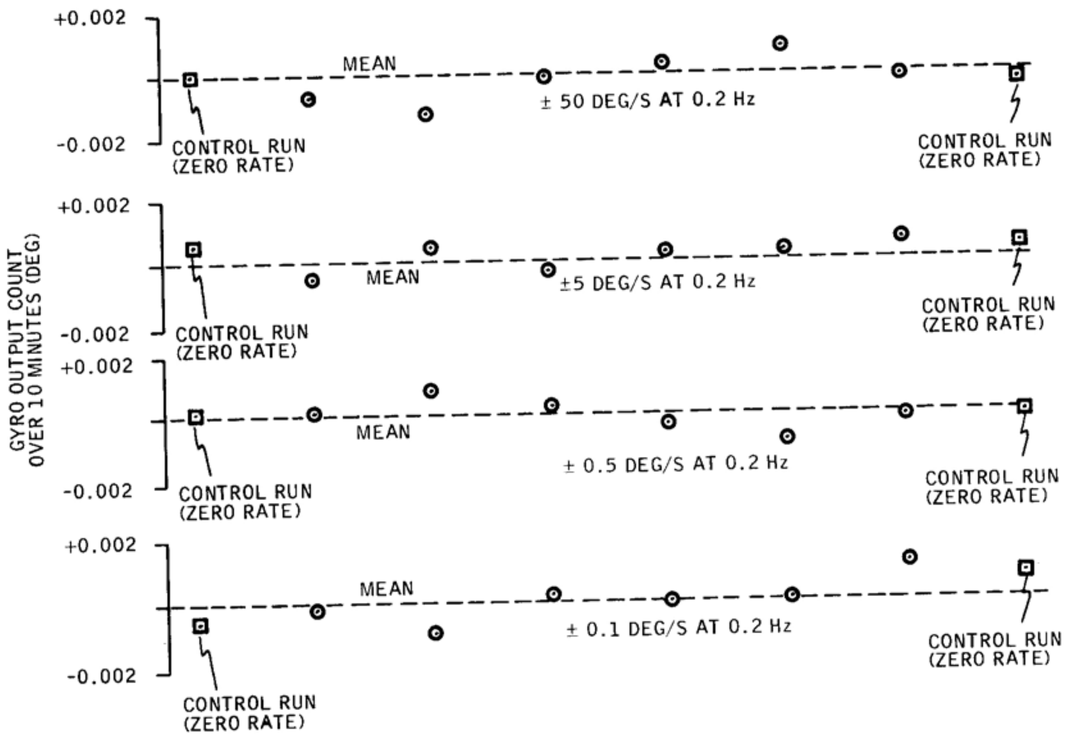


Figure 13. GG1300 Laser Gyro Low Rate Asymmetry Error

special design provisions in the engineering hardware to maintain good alignment stability. (The primary purpose for the tests was to demonstrate navigation positioning accuracy, not velocity accuracy, which is more susceptible to sensor misalignment effects.) Prototype system/gyro hardware currently in design at Honeywell should provide a 5 to 10 arc second alignment stability or better over long term including standard military temperature exposures. The Table 1 requirement should, therefore, be achievable.

Reaction Time

Due to the insensitivity of the laser gyro bias to thermal start-up transients, nominal performance is achieved at turn-on. Demonstrated noise levels of 0.002 deg/h$^{1/2}$ for the device require 5 minutes of system alignment filtering to achieve 1 nmi/h accuracy and 2 to 5 minutes for 1 to 2 nmi/h performance. With additional performance improvements through production learning, it is reasonable to expect overall reaction times for production laser gyro 1 nmi/h strapdown inertial navigators in the 1980's to be less than the 5 minute performance goal given in Table 1.

Sensor Calibration Interval

The ultimate feasibility of a strapdown sensor hinges on its ability to maintain its accuracy over long periods of time without regularly scheduled calibration/removals. In this regard, the laser gyro excels, having demonstrated long-term stabilities of several thousand hours for its system critical performance parameters.

Flight Test Results

A composite of the overall performance capabilities of 1974-1975 Honeywell laser gyro technology is vividly illustrated by the results of a series of flight tests conducted in 1975 at Holloman Air Force Base CIGTF (Central Inertial Guidance Test Facility) on a brassboard engineering hardware version of the Honeywell LINS. The test results are summarized in Reference 23 and detailed in Reference 27. The abstract in Reference 27 states:

"The Honeywell Laser Inertial Navigation System (LINS), an engineering model of a ring laser gyro strapdown inertial navigation system, was subject to developmental testing at the Central Inertial Guidance Test Facility (CIGTF), 658th Test Group, Holloman Air Force Base, New Mexico, during the period 14 April 1975 to 24 July 1975. The tests were requested by the 666A Program Office, Air Force Avionics Laboratory.

A total of 20 laboratory tests, 13 flights in an NC-141A cargo aircraft test bed, and one van test were accomplished. Of these, 12 laboratory tests and 11 flight tests were used in the analysis to determine navigation performance accuracy. The analysis indicated that the LINS appears to be better than a 'one nautical mile per hour' navigator when operating unaided, except for barometric altimeter inputs.

The radial position error CEP rate had a value of 0.89 nm/h for the flight test ensemble used in the computation; the radial position error CEP rate for the laboratory test ensemble was 0.83 nm/h. The radial position error 90th percentile rates were 1.62 nm/h and 1.36 nm/h for the flight and laboratory tests, respectively.

The LINS was operated for a total of 229 hours with 42 turn-ons without failure. Navigation time was 207 hours.

Reaction time was 20 minutes for all tests that were analyzed.

The tests demonstrated the successful application of ring laser gyros to strapdown inertial navigation system technology."

Velocity accuracies in the LINS Holloman tests were in the 5 to 6 ft/s range (rms per axis at one hour) due principally to random noise and residual thermal effects in 1974-1975 technology gyros. Laser gyro technology advancements demonstrated in 1976 at Honeywell in these areas should provide 3 to 5 ft/s and 1 nmi/h performance levels in both fighter and cargo aircraft in future LINS systems, as well as reducing the reaction time to 5 minutes or less.

### Summary

The laser gyro has the performance capabilities needed to meet or better the difficult requirements of Table 1 for the 1 nmi/h inertial navigation system. Its use in strapdown applications, then, depends on its performance capabilities and cost compared to the alternate strapdown gyro approaches.

## THE LASER GYRO COMPARED TO THE ALTERNATE STRAPDOWN SENSOR CANDIDATES

A comparison between the laser gyro and other strapdown sensors is difficult due to limited data in the available literature and the differing conditions associated with the available data. Basic factors to be traded off are cost, reliability, size, and performance (not necessarily in that order of importance) in unaided as well as hybrid aided system applications. An additional area for comparison is in the capability of the sensors to meet the requirements of the multifunction strapdown sensor assembly, a sensor-sharing concept being considered for advanced avionics systems as a means for lowering aircraft life-cycle costs through net sensor count reduction.[28,29,30] This unique capability of strapdown system technology may prove to be its principal advantage over the gimbaled inertial navigation system.

### Cost Comparisons

From a cost standpoint, the laser gyro should be lower in cost per axis than the floated or tuned rotor gyro. On the basis of Honeywell experience, production costs for an inertial navigation grade strapdown floated gyro including strapdown electronics is approximately $8K, or $24K for the three gyros in a system. Teledyne estimates that a strapdown tuned rotor gyro would cost $6.7K. With strapdown electronics, this figure is probably closer to $8K per gyro, or $16K for the two gyros in a system. These figures can be compared directly to Honeywell's estimate of $3K to $3.5K for a laser gyro in production or $9K to $10.5K for the three gyros in a system.

Similar data on the sensor level could not be found for the ESG; however, on a system basis, costs for a strapdown ESG navigator (without the turn-table) have been estimated to be $35K.[20,22] With a turn-table, the figure must be somewhat higher (closer to $40K). Estimates for tuned rotor strapdown systems are also in the $40K category.[31,32] Honeywell's estimate for a production LINS is $30K to $40K, depending on the functions required.

Compared to the gimbaled system, strapdown systems using either of the available gyros should be lower in cost. Typical gimbaled system costs are in the $60K to $80K range. This compares with $30K to $50K for strapdown systems in general, with laser gyro system costs at the low end of the spectrum, and floated gyro system costs at the high end.

### Reliability Comparisons

From a reliability standpoint, the basic construction of the key element in the laser gyro, the block assembly, makes it an extremely reliable device. Based on accelerated life tests on the block elements, Honeywell projects MTBFs for the laser gyro block assembly on the order of 50 000 hours. To this must be added the failure rates associated with the electronic assemblies, including high-voltage supplies and piezoelectric drivers. The resulting overall MTBF projected for the laser gyro including electronics is 20 000 hours.

Honeywell's experience with floated rate integrating gyros using ball-bearing spinmotors is that 8000 hours is typical for the MTBF in such devices. To this must be added the failure rates for the strapdown electronics, bringing the overall MTBF to approximately 6000 hours, or 2000 hours net MTBF for the three gyros in a strapdown system. Gas bearing floated gyros may have somewhat higher reliabilities in the area of 10 000 hours (including electronics). For the three gyros in a system, this translates into a net gyro MTBF of 3300 hours.

For the tuned rotor gyro, ball-bearing spin-motors are also used. However, larger bearings, lower preloads, and slower wheel speeds can be used compared to the floated gyro due to the reduced criticality of bearing stability on gyro accuracy. Based on these assumptions, a reliability estimate of 10 000 hours MTBF may be expected for the strapdown tuned rotor gyro with electronics. A similar estimate is obtained in Reference 31. For the two gyros in a system, this is equivalent to a combined MTBF of 5000 hours. This compares with 6700 hours combined MTBF for the three laser gyros required in a system.

On a system basis, Autonetics has projected its original strapdown MICRON ESG system to have an MTBF of 2000 hours.[22] The addition of a turn-table will reduce this figure somewhat. Honeywell projects the reliability of the laser gyro LINS system to be greater than 2000 hours MTBF.

Regarding reliability, the ESG is unique among all of the strapdown sensors considered in that the catastrophic effect of losing suspension voltage and "dropping the ball" is possible, while the rotor is spinning. Safeguards must be built into systems using the ESG to avoid this possibility, and the large repair costs associated with it.

It is important to categorize a failure type by whether or not it is catastrophic to a particular function. The failure rates considered have tacitly assumed that loss of navigation accuracy constitutes a failure. One of the unique aspects of the laser gyro is that a large percentage of its possible failure modes are electronic and only degrade performance below navigation requirements. For example, the effect of a dither drive failure is to introduce a 0.02 deg/s dead zone (lock-in) into the gyro output. If the gyro output is being used for additional functions in an aircraft (e.g., flight control), this failure may not be catastrophic to those functions. Hence, the reliability of the laser gyro in these cases is considerably higher than the 20 000 hour figure quoted, from a flight safety/mission success standpoint. This factor has an important bearing on the multifunction aspects of the laser gyro. For the other strapdown sensors, most failures are catastrophic to basic functional operation; hence, the navigation reliability figures apply to other functions as well.

In general, reliability figures in the 800 to 2500 hour MTBF category should be achievable with strapdown systems, with laser gyro systems being the most reliable. Gimbaled system manufacturers are quick to point out that reliability levels of 2000 hours have already been demonstrated by gimbaled systems in commercial applications.[33] Further, for the failure rates experienced, a relatively low percentage are caused by the gimbal assembly.[34] The corollary is that electronic failures in a gimbaled system dominate the failure history; hence, strapdown systems, which are of equal or greater electronic complexity, should have no better reliability. The argument ignores one key point. A gimbal assembly failure is a much more expensive item to repair than an electrical failure. A gimbal assembly failure generally requires shipment back to the manufacturer, teardown, rebuild, and retest. Electrical failures, on the other hand, are generally serviced at the intermediate level by the procuring agency, typically requiring only a replacement of an electronic card or part. Hence, in terms of overall maintenance costs, mechanical failures have far more impact than electrical failures. The larger percentage of mechanical parts and corresponding mechanical failures in the gimbaled compared to the strapdown system should, therefore, result in a lower maintenance cost for the strapdown system.

Size Comparisons

The deficiency of today's laser gyro is its size. The Honeywell GG1300 laser gyro has a volume of 115 cubic inches (Figure 7). Honeywell's GG1342 reduced-size, high-accuracy laser gyro now in development is 84 cubic inches. Comparable figures for the alternate strapdown gyro configurations are generally less than half the volume of a GG1342 (including electronics) on a per axis basis. Hence, for the state of the art, an overall volume penalty of 100 to 150 cubic inches generally results for a system using three laser gyros as contrasted with systems using the alternate strapdown gyros.

On a system level, Honeywell projects the size of a production LINS Inertial Navigation Unit (equivalent functionally to an ARINC 561 INU)[35] using the newer GG1342 gyros to be approximately 1000 cubic inches in volume. This size appears to be generally acceptable for most applications and is generally consistent with existing gimbaled INU sizes. (A unique exception is the Litton LN-40 system using the new miniature P-4 platform.)[36]

Performance Comparisons

General comparisons can be made between the laser gyro and alternate strapdown sensors regarding their underlying mechanization concepts and projected abilities to perform to the Table 1 requirements. In addition, recent (1975) flight test results on tuned rotor and ESG technology systems can be analyzed to obtain an overall composite performance comparison against the 1975 Honeywell LINS flight tests at Holloman. For further analysis, References 2, 3, 5, 19, and 37 can be consulted for mathematical definitions of the error mechanisms in floated and tuned rotor gyros.

Rate Capabilities -- Each of the alternate strapdown gyros can achieve the 400 deg/s requirement. In the case of the floated rate integrating and tuned rotor gyros, performance and cost penalties are incurred as rate requirements increase.

Gyro Bias -- For each of the alternate strapdown gyros, the bias error is g-sensitive and has long-term trending characteristics due to mechanical instabilities and manufacturing tolerances. Thermal effects on bias in the ESG and floated rate integrating gyro are significant, requiring thermal controls (and a warm-up penalty) for compensation. Each of the alternate instruments has several dynamic error effects that are predictable and can consequently be modeled out in the computer. However, depending on the dynamic environment involved, such modeling imposes an added burden on the system computer and sensor interface that should not be overlooked.

For the tuned rotor gyro, bias instabilities can be overcome largely through increased angular momentum, with additional complexity in the torquing loop due to the higher current levels needed for angular momentum caging. Based on the 1 nmi/h system-level performance obtained in transport aircraft using strapdown tuned rotor gyros with large angular momentum wheels, it can be assumed that the bias performance levels of Table 1 are achievable in benign flight environments.[41, 42] In dynamic flight environments, bias g-sensitive effects will degrade performance to some extent.

In the case of the floated rate integrating gyro, increasing angular momentum creates additional error torques due to the need for heavier flex leads for a larger torquer coil (to handle the increased momentum), added mass unbalance instabilities due to the larger coil cup assembly, and stiffer pivots to handle the increased momentum reaction torque loading under output axis rotations. The net result is that increased momentum has a limited capability in solving the floated gyro bias stability problems, and some form of regular calibration is probably needed to achieve the required long-term stability. A concept such as the dual-speed spinmotor technique appears necessary for calibrating these gyros frequently if the requirements in Table 1 are to be approached. The inability for this calibration technique to separate g-sensitive from g-insensitive errors, however, probably restricts the floated gyros to strapdown applications in fairly benign flight environments if unaided performance approaching 1 nmi/h is to be achieved.

In the case of the ESG, long-term bias stability has been a problem.[39] Also of concern has been the difficulty in calculating the many coefficients needed to characterize the ESG error sources.[22, 39] The turn-table concept being incorporated in new strapdown ESG systems (by Autonetics), in addition to gyro improvements to reduce thermal gradient effects, will hopefully provide the long-term performance needed to meet the requirements of strapdown navigation in the future.

The laser gyro easily meets the requirements of Table 1 over long term without performance degradation due to dynamic or thermal effects.

Gyro Wide-Band Random Rate Noise -- The wide-band random noise rate characteristic in the alternate strapdown gyros appears to be negligible compared to 0.002 $deg/h^{1/2}$ requirements. Hence, for laser gyros, this effect (on the order of 0.002 $deg/h^{1/2}$) is a handicap that partially offsets some of its advantages in bias stability and environmental immunity compared to the other sensors.

Scale Factor Accuracy -- Of the three strapdown rate sensors being analyzed, only the laser gyro has the capabilities for meeting the Table 1 requirements. Due principally to thermal sensitivities and aging effects in the torquer magnetics, scale factor accuracies in torque rebalance instruments are generally limited to 0.005 percent. The 0.005 percent figure assumes that torquer scale factor temperature compensation is included, either passively as an integral part of the gyro, or actively through temperature measurements and associated computer compensation. Compared to Table 1 requirements, the 0.005 percent limitation places a serious handicap on the tuned rotor and floated gyros for high-performance applications. Relative to the 1 PPM low-rate asymmetry requirement for the rate gyros, Honeywell's experience with a GG1009H floated gyro, and Boeing's experience with a tuned rotor gyro,[38] showed that this performance level is achievable, but not without careful design work. For the laser gyro, no asymmetrical error exists due to the inherent characteristics of the device.

Attitude Gyro Wide Angle Readout Accuracy -- For the strapdown ESG, wide-angle readout accuracies of 18 arc seconds have been achieved.[20, 22] This performance is somewhat marginal in high-velocity accuracy applications. However, it is reasonable to assume that improvements will be made such that the Table 1 10 arc second goal is achieved in future production units.

Rate Gyro Bandwidth -- The laser gyro has no bandwidth limitation relative to attitude determination accuracy. Due to the torque rebalance nature of the floated and tuned rotor gyros, each has a bandwidth limitation regarding rate input sensing capabilities. As a result, sensor assembly coning rate vibration frequencies near or above the bandwidth of these sensors will result in attitude drift errors unless the vibration levels are naturally small or intentionally attenuated (through shock mounts).

Honeywell's experience with a strapdown GG1009H navigation-grade floated rate integrating gyro has shown that 80 Hz bandwidths are readily achievable. For strapdown tuned rotor gyros, 75 Hz bandwidths have been achieved,[38] and Litton[40] claims that bandwidths in excess of 85 percent of spin speed are achievable using new caging techniques. For typical tuned rotor spin rates, this translates into a bandwidth in the 50 to 150 Hz area.

Rate Gyro Quantization -- Gyro quantization error primarily affects strapdown rate instruments. Hence, the ESG, being an attitude gyro, does not have this as an error source. The laser gyro quantization level is naturally small and easily meets the requirements of Table 1. For the floated and tuned rotor gyros, the quantization level is limited by the ability to accurately generate precision electrical rebalance pulses with the gyro digitizer electronics at high frequency. Dual scaling techniques (coarser pulse at high rates where errors can be tolerated due to short operating periods) can be used to achieve a finer pulse during normal system operating periods. An even finer quantization level can be attained by sampling the residual integrator analog signal in the pulse rebalance loop and by transmitting this signal into the computer as a pulse count correction at the time when the gyro pulse counts are sampled. Through the use of these aids, the required levels of quantization should be achievable for tuned rotor and floated gyros. It should be noted, however, that the cost for the associated electronics must increase as the requirements become more severe (finer pulse/higher rate).

Accelerometer Error -- The impact on strapdown systems using either of the gyro types is the same: tighter requirements on other sensor error parameters to compensate for accelerometer errors, if significant. The 50 $\mu g/s$, 0.01 $\mu g/s$, and 0.1 PPM/s requirements given in Table 1 are achievable today. However, this performance level is a significant portion of the error budget for systems requiring good velocity accuracy during the first hour of flight (i.e., military tactical aircraft). What is needed is a new accelerometer designed for strapdown application with superior performance levels. In this way, other sensor performance requirements can be somewhat relieved to achieve a given level of system accuracy.

Sensor Alignment Accuracy -- Strapdown systems using either of the four sensors considered should have comparable capabilities in alignment stability. On a system basis, 10 arc seconds sensor-to-sensor alignment accuracy (Table 1) should be achievable. For the rate gyro sensors, the more difficult 5-arc second requirement (compared to 10 arc seconds for attitude gyros like the ESG) may be achievable in the future with careful design work.

Reaction Time -- A key advantage for the laser gyro is its ability to perform at required accuracy levels within a few seconds from turn-on. With the low random rate noise projected for production laser gyros, system alignment times of 5 minutes should be achievable with full 1 nmi/h accuracy.

System-level tests with tuned rotor gyros in 1975 have demonstrated reaction times of 7 to 8 minutes.[38] Assuming modest design improvements, it is reasonable to project reaction time capabilities of 5 minutes for future production tuned rotor gyro systems.

Reaction times for the ESG have been a significant problem area in the past due to the sensitivity of gyro performance to temperature effects and the difficulty of spinning up the gyros and thermally stabilizing the system (with required temperature controls) in a reasonable time period.[39] Recent improvements in gyro design (for reduced thermal gradients) and the introduction of a turn-table for error averaging will hopefully allow reasonable reaction times (less than 10 minutes) for new strapdown ESG systems.

For the floated gyro, error modeling is difficult due to the nonlinear characteristics of its suspension system at off-nominal flotation and fluid reaction torques in the presence of thermal gradients. As a result, thermal controls are needed to maintain the flotation fluid at nominal operating temperature before accurate performance is achievable. A warm-up time delay of 5 to 10 minutes is thereby introduced, to allow time for the gyro to come up to temperature and stabilize. To this must be added an additional 5 to 10 minutes for alignment and calibration (i.e., using spinmotor reversal). An overall system reaction time on the order of 15 to 20 minutes results. Compared to Table 1 requirements, this level of performance shows no improvement over the reaction time capabilities of older gimbaled technology.

Sensor Calibration Interval -- Calibration intervals of several thousand hours are projected for laser gyros, and it is believed that they have the potential for requiring no calibrations for the lifetime of the device (following initial factory calibration), if production units display the same ensemble characteristics measured on individual engineering units. For systems using tuned rotor gyros with large angular momentum wheels, calibration intervals of greater than six months have been experienced.[41, 42]

For the ESG, the effect of case rotations through use of the turn-table will hopefully eliminate the need for regularly scheduled sensor calibrations, following initial factory calibration. In the case of the floated gyro, regular calibration appears to be a requirement. However, calibration can largely be done without system removals through use of the dual-speed spinmotor reversal method. Note that this same technique should be applicable to the tuned rotor gyro if necessary.

It can be concluded that each of the strapdown gyro types are projected to have calibration requirements that are reasonable for normal flight operations. Of the four gyro types, the laser gyro appears to have the greatest potential for achieving the longest interval between calibrations, and possibly the ultimate capability of requiring no calibrations for the lifetime of the unit.

Flight Test Comparisons -- Flight tests of an Autonetics MICRON (Micro-Navigator) ESG system, a Boeing strapdown tuned rotor gyro system, and the Honeywell LINS laser gyro system, all conducted in 1975, provide a unique opportunity for comparing the capabilities of the three strap-down sensors on a system level at a common time in their development cycle.

In the case of the Honeywell and Autonetics systems, the flight test program was conducted by the same Government agency (Holloman Air Force Base Central Inertial Guidance Test Facility - CIGTF) aboard a C-141 cargo aircraft. For the MICRON system, additional tests were also conducted in a UH-1 helicopter. The wealth of flight and laboratory test results obtained and the similarity of test conditions provide the ability to compare these systems in many cases on a one for one basis. The overall composite results of the test programs are provided in References 27 and 39, and are summarized in Tables 3 and 4.

On a performance basis, the LINS and MICRON systems performed remarkably similar, each displaying capabilities below the classical 1 nmi/h accuracy requirement for traditional inertial

Table 3. LINS CIGTF Flight Test Summary

| | Lab | Flight (Cargo) | Van | Total |
|---|---|---|---|---|
| Radial Position Error CEP Rate (nmi/h) | 0.83 | 0.89[a] | N/A[b] | N/A |
| Radial Position Error 90th Percentile Rate (nmi/h) | 1.36 | 1.62[a] | N/A[b] | N/A |
| Radial Velocity Error 50th Percentile Rate/Y-Intercept (ft/s per h, ft/s)[c] | 0.42, 2.70 | 1.86, 2.93 | N/A[b] | N/A |
| Number of System Turn-Ons | 25 | 15 | 2 | 42 |
| Number of System Operating Hours | 133 | 90 | 6 | 229 |
| Number of Flight Hours | N/A | 66 | N/A | 66 |
| Number of Navigation Hours | 118 | 84 | 5 | 207 |
| Number of Navigation Hours for Valid Tests[e] | 109.6 | 68.6 | 5 | 183.2 |
| Number of Valid Tests[e] | 20 | 11 | 1 | 32 |
| Number of Tests Used for Performance Analysis | 12 | 11 | N/A[b] | 23 |
| Reaction Time Used (hours) | 0.33[d] | 0.33[d] | 0.33[d] | N/A |
| Number of Calibrations Over Test Duration | ← None → | | | |
| Test Period | 14 April 1975 to 24 July 1975 | | | |

[a] Based on first 4 hours of the flight test ensembles. For all data in the ensemble, CEP = 0.65 n/mi/h and 90th percentile equals 1.2 nmi/h.[6]

[b] Single run: 0.75 nmi/h; 1.43 ft/s/h, 2.5 ft/s

[c] Slope and t = 0 value of best fit straight line to ensemble.

[d] Ten minutes warm-up, 10 minutes for alignment for all tests.

[e] Valid tests are tests that generate navigation performance data

Table 4. MICRON CIGTF Flight Test Summary

| | Lab | Flight (Cargo) | Flight (Helicopter) | Total |
|---|---|---|---|---|
| Radial Position Error CEP Rate (nmi/h) | 1.23 | 0.60[a] | 0.92[a] | N/A |
| Radial Position Error 90th Percentile Rate (nmi/h) | 2.02 | 0.96[a] | 1.46[a] | N/A |
| Radial Velocity Error 50th Percentile Rate/Y-Intercept (ft/s per h, ft/s)[b] | 3.83, 0.37 | 2.63, -0.19 | 2.96, 0.44 | N/A |
| Number of System Turn-Ons | 46 | 15 | 11 | 72 |
| Number of System Operating Hours | 213 | 118.3 | 61.7 | 393 |
| Number of Flight Hours | N/A | Not Available | Not Available | 74.9 |
| Number of Navigation Hours | 77.1 | 81.5 | 34.4 | 193.0 |
| Number of Navigation Hours for Valid Tests[d] | 29.8 | 79.6 | 30.4 | 139.8 |
| Number of Valid Tests[d] | 11 | 14 | 10 | 35 |
| Number of Tests Used for Performance Analysis | 6 | 11 | 7 | 24 |
| Reaction Time Used (hours) | 2-3[c] | 2-3[c] | 2-3[c] | N/A |
| Number Calibrations Over Test Duration | ← 6 → | | | |
| Test Period | 7 October 1974 to 16 July 1975 | | | |

[a] Based on all data in ensemble.

[b] Slope and t=o value of best fit straight line to ensemble.

[c] No restrictive time limit was imposed and extra time is included.

[d] Valid tests are tests that generate navigation performance data.

systems. From an operational suitability basis, the MICRON system experienced calibration stability and thermal warm-up difficulties, which necessitated a long reaction time and several calibrations. For LINS, no temperature controls were used, no calibrations were performed for the three month test interval, and, although not required due to the developmental classification of the tests, 20 minutes was used for the LINS reaction time (the limit imposed by Holloman for verification testing).

Both the LINS and MICRON systems tested at Holloman Air Force Base were engineering developmental units; hence, performance characteristics during 1975 tests should be somewhat degraded from what is projected in future production units (with the benefits of technology advances and learning). Nevertheless, the test results serve to dramatically illustrate the capabilities and limitations of ESG and laser gyro systems at a common time in their development cycles, and provide a basis for judging the extent of development improvements needed in the two technologies to meet required operational performance objectives.

In the case of the tuned rotor gyro, References 41 and 42 describe a flight test program of a Boeing-designed strapdown engineering development system using Teledyne tuned rotor gyros. The tests were conducted by Boeing in 727 and 747 transport aircraft. Test results are summarized in Table 5.

| | 727 Aircraft | 747 Aircraft |
|---|---|---|
| Radial Position Error CEP Rate (nmi/h) | 1.6 | 0.7 |
| Radial Position Error 90th Percentile Rate (nmi/h) | 2.5 | 1.3 |
| Radial Velocity Error 50th Percentile Average (ft/s)[b] | Not Available | 5.91 |
| Number of Flight Hours | 6.5 | 8.5 |
| Number of Navigation Hours | 8.2 | 12.1 |
| Number of Navigation Hours for Valid Tests[c] | 8.2 | 12.1 |
| Number of Valid Tests[c] | 3 | 4 |
| Number of Tests Used for Performance Analysis | 3 | 4 |
| Reaction Time Used (Hours) | 0.167 | 0.167 |
| Number of Calibrations Over Test Duration | ← None[a] → | |
| Test Period | 23 July 1975 to 24 January 1976 | |

[a] With the exception of a scale factor calibration due to a design modification incorporated into the gyro range switching electronics after the 727 tests and prior to 747 tests.

[b] Ensemble average for all data points for all flights.

[c] Valid tests are tests that generate navigation performance data.

Table 5. Boeing Tuned Rotor Strapdown Flight Test Summary

A comparison between Tables 3, 4, and 5 shows equivalent performance for the tuned rotor system, also in the 1 nmi/h category. From an operational suitability standpoint, the performance described in Table 5 was achieved using a 10 minute reaction time, with no temperature controls, and without calibrations for the duration of the 6 month test period. On the basis of these results, it can be concluded that in 1975, the capabilities of the tuned rotor and laser gyro technologies were equivalent in transport flight environments.

Recent flight test data on floated rate integrating gyro strapdown inertial grade systems is not available. Flight test results of tests conducted in 1965 at Holloman AFB on a Honeywell system yielded 2 to 4 nmi/h CEP unaided performance.[43] These results are not necessarily representative of what is attainable with today's technology; however, it is believed that 1 nmi/h accuracies for floated rate integrating gyro strapdown systems are not quite achievable.

Performance Comparison Summary -- A summary of the performance capabilities of the sensors considered compared with Table 1 requirements is presented in Table 6. From Table 6, it can be concluded that of the four gyros considered, the laser gyro has the greatest potential for meeting or exceeding the requirements for general aircraft application.

## Comparisons in Hybrid Aided Applications

An important aspect of the error characteristics of inertial instruments is their predictability in hybrid aided applications. Future global positioning system (GPS) aids promise to have the capability to provide extremely accurate position and velocity data. If the INS that interfaces with a GPS has well defined stable error characteristics, outstanding calibration capabilities will be achievable in flight. The result is that the inertial system will have the capability for operating extremely accurately for long periods of time in the event of GPS jamming or of a receiver failure.

One of the unique advantages of a laser gyro strapdown system is the accuracy of its error model and the stability of its principal error sources (gyro and accelerometer bias, scale factor, and input axis alignment). Potentially, the stability of these errors will be sufficient between system turn-ons to enable precise unaided inertial performance from the instant of take-off (using the last set of calibration data obtained from a previous aided flight). The overall invulnerability of the GPS/strapdown navigation system would, thereby, be further enhanced. Alternatively, this capability could be used to relax the long-term accuracy requirements for the strapdown sensor alignment stabilities, permitting field maintenance at the sensor level and calibration in flight. Reduced life-cycle costs result.

| Performance Parameter | Requirements for 1 nmi/h System Accuracy | | Projected Strapdown Sensor/System Capabilities | | | |
|---|---|---|---|---|---|---|
| | Rate Gyro Strapdown | Attitude Gyro Strapdown | Laser Gyro | Floated Rate Integrating Gyro | Tuned Rotor Gyro | ESG |
| Gyro Rate Range (deg/s) | 100-400[a] | 100-400[a] | 400 | 100-400[b] | 100-400[b] | 400 |
| Gyro Bias Accuracy (deg/h) | 0.01 | 0.01 | < 0.01 | 0.01-0.02[c,e] | 0.01[c] | < 0.01[c,f] |
| Gyro Wide-Band Random Rate Noise (deg/h$^{1/2}$) | 0.002 | 0.002 | 0.002 | < 0.002 | < 0.002 | < 0.002 |
| Gyro Scale Factor Accuracy (percent) | 0.0005-0.005[a] | N/A | <0.0005 | 0.005 | 0.005 | N/A |
| Rate Gyro Scale Factor Low Rate Asymmetry (PPM) | 1 | N/A | 0 | 1[b] | 1[b] | N/A |
| Attitude Gyro Wide Angle Readout Accuracy (arc sec) | N/A | 10 | N/A | N/A | N/A | 10[d] |
| Rate Gyro Bandwidth (Hz) | 30-300[a] | N/A | Unlim. | 30-150[b] | 30-150[b] | N/A |
| Rate Gyro Quantization (arc sec) | 2-10[a] | N/A | 2 | 2-10[b] | 2-10[b] | N/A |
| Accelerometer Bias Accuracy (μg) | 50 | 50 | 50 | 50 | 50 | 50 |
| Accelerometer Short-Term Bias Trending (μg/s) | 0.01 | 0.01 | 0.01 | 0.01 | 0.01 | 0.01 |
| Accelerometer Short-Term Scale Factor Trending (PPM/s) | 0.1 | 0.1 | 0.1 | 0.1 | 0.1 | 0.1 |
| Sensor-to-Sensor Alignment Accuracy (arc sec) | 5-10[a] | 10 | 5[d] | 5[d] | 5[d] | 10 |
| System Reaction Time (Warm-up and Alignment-min) | 5 | 5 | 5 | 15-20[e] | 5 | < 10[f] |
| System Calibration Interval (months) | 6 | 6 | >6 | 6[e] | 6 | 6[f] |

[a] Depending on severity of dynamic environment.

[b] Designed for application with associated complexity increase for tighter requirements.

[c] Degraded from level indicated under dynamic flight conditions.

[d] Assumes factor of two improvement over demonstrated capabilities.

[e] Assumes use of preflight calibration (e.g. - spin motor reversal).

[f] Assumes use of turn-table and gyro improvements.

Table 6. Comparison Summary of Projected Strapdown Sensor Capabilities Against System Requirements

Compared to the other strapdown sensors (or traditional 1 nmi/h gimbaled systems), only the laser gyro has the required error source stability (scale factor and bias) over thermal, dynamic, and day-to-day turn-on cycles to achieve significant navigation performance improvements with this approach.

An important aspect of the design of an aided inertial navigation system is the complexity of the Kalman filter required for the aiding function and the associated flight computer requirements in terms of memory and execution speed. Depending on the accuracies required, the complexity of the system error models, and the characteristic response times for the error source dynamics, requirements on the Kalman filter can vary considerably. For precision aided applications, such as with GPS where a precise, long-term, stand-alone capability may be required for extended time periods (under jammed conditions for example), it is important that all significant error sources in the inertial system be accurately modeled. Only in this way will the GPS be capable of calibrating the INS while aiding, such that the required high accuracies will be achievable when the aiding capability is interrupted.

A disadvantage for strapdown compared to gimbaled systems is the complexity of the error model required to accurately account for the dominant error states. Depending on the required accuracies and in-flight calibration capabilities (through the aiding process), a strapdown inertial system error model could, in an extreme case, require up to 30 states (three attitude, three velocity, three position, six gyro misalignments, three gyro scale factors, three gyro biases, three accelerometer biases, three accelerometer scale factors, and three accelerometer misalignments). In addition, the dynamic effects associated with some of these states are significant (i.e., the misalignment coupling error effects in rate gyro strapdown systems), requiring high rate calculations in the aiding computer to properly evaluate the elements of the state-transition matrix for the Kalman filter update.[44] If the strapdown sensors have significant g-sensitive error terms (such as the tuned rotor and ESG), even more states may be required. The gimbaled system error model, on the other hand, could conceivably ignore the sensor misalignment and accelerometer bias errors, for example, as their effects are less severe, potentially resulting in equivalent performance with 18 states.

The example given is an extreme case, set forth to illustrate a point. In a real situation, the difference between the strapdown and gimbaled approaches would not be as severe. (For example, some of the misalignment errors for the strapdown system are not critical, and in the case of laser gyro systems, the gyro bias states can be ignored, with achieved performance comparable to gimbaled systems that include gyro bias states.) Nevertheless, the computer requirements for the strapdown hybrid aided system should generally be more severe than for the gimbaled approach for a given level of high-accuracy performance.

These considerations illustrate the classical strapdown versus gimbaled tradeoff as applied to hybrid aided inertial systems: increased computer complexity for the strapdown system to analytically account for effects that are passively controlled in the gimbaled system through use of the complex gimbaled assembly. For today's computer technology, the cost/speed burden of a Kalman filter with 20 or more states is not trivial. However, with continuing advances in low-cost, high-speed computer technology, the computer penalty for a strapdown system in precise, hybrid aided applications will be as trivial tomorrow as it is today in unaided applications. This is consistent with the time table for introduction of GPS hybrid aided systems in the 1980's.

## Comparisons in Multifunction Applications

For advanced multifunction applications, strapdown system requirements are to provide rate and acceleration outputs in aircraft coordinates as well as the normal attitude, velocity, position data for other aircraft functional use.[28,29,30] The three strapdown rate gyro configurations (laser gyro, tuned rotor gyro, and floated rate integrating gyro) are each capable of providing the body rate output signals directly, as this is the natural form of their output signal.

The ESG, being a strapdown attitude gyro, does not have the rate signal as a natural output. Deriving rate analytically in an ESG system (a nontrivial function of the calculated rate of change of the acceleration transformation matrix in Figure 2) provides a noisy signal (due to differentiated attitude pickoff noise) that must be filtered for reasonable low-noise rate output performance. The resulting dynamic lag introduces stability problems in high-performance aircraft applications.

It should be noted that the rate gyro configurations also have noise on the rate outputs (due to pulse quantization, for example, if the rates are calculated as a pulse count over the rate sampling period). Due to the fineness of the pulse sizes involved, these effects are generally small (particularly for the laser gyro) and can be circumvented if required, in the case of the tuned rotor or floated gyros, by sampling the analog signals available in the gyro loop.

An interesting aspect of the multifunction strapdown system is the added need for redundancy to satisfy the flight safety/mission success requirements associated with the avionics systems using the system outputs. A particularly intriguing aspect of strapdown technology is the possibility of using skewed sensor geometries as a means for achieving specified levels of system redundancy without requiring an equal level of sensor redundancy per system axis.[29,30,45,46] The concept relies on the principle that three axes of orthogonal sensor vector data can be derived analytically in the system computer from the measurements of three sensors whose axes are nonorthogonal (skewed). All that is required is that the computer know the relative orientation of the sensors (and that the skewed sensor axes be noncoplanar). Hence, four skewed (non-orthogonal) axes of input data can be used to achieve a full level of system redundancy. (Three-axis orthogonal data can be derived from any three of the four skewed sensors; thus, three axes of orthogonal data can still be developed after any single sensor failure.) The result is that each level of required system redundancy can be achieved with the addition of only one additional axis of sensor data. This contrasts with the traditional block-level redundancy approach that requires a complete duplication of all system sensors for each system redundancy level.

Use of the skewed redundancy concept in terrestrial vehicles will require that, in general, the sensors be skewed relative to the gravity reaction force vector. If the sensors have g-sensitive drift terms, this can cause performance problems.[47] A classical, expedient to g-sensitive drift errors has been to orient the sensors relative to the average vehicle force vector such that the error effects tend to be unexcited. Normally, a cardinal orientation relative to the aircraft axes results. The added constraint of skewed sensor geometries will preclude use of this expedient, generally resulting in degraded performance.

In the case of the ESG, tuned rotor, and floated gyros, their g-sensitivity will cause performance degradation in multifunction applications using skewed redundant sensor arrays. Due to the g-insensitivity of the laser gyro, no such performance shift should occur.

# CONCLUSIONS

From the analyses presented, the following general conclusions can be drawn regarding the tradeoffs between strapdown systems using the laser gyro, tuned rotor gyro, ESG, and floated rate integrating gyro, in contrast with gimbaled system technology.

### Cost

The cost of the systems using either of the strapdown sensors should range in the $30K to $50K category, with laser gyro systems at the lower end of the spectrum and systems with floated rate integrating gyros at the high end. This provides a significant cost advantage over gimbaled systems with comparable performance in the $60K to $80K price range.

### Reliability

From a reliability standpoint, strapdown systems should have reliabilities on the order of 800 to 2500 hours, with laser gyro systems having the highest reliability. Gimbaled systems have achieved reliabilities approaching these figures; however, associated maintenance costs for the strapdown systems should be lower due to the lower cost of repair for electrical as compared to mechanical failures, and a lower percentage of mechanical failures in the strapdown compared to the gimbaled systems.

### Size

At present, laser gyro strapdown systems have a size penalty compared with systems using other sensor types, including gimbaled systems. At the current state of the art, 100 to 150 additional cubic inches per system are typically required due to the laser gyro size. With projected technology advances through production learning and engineering development (laser gyro technology is still in its infancy), the size penalty should disappear. With the current laser gyro size, 1000 cubic inches is projected for a complete strapdown INU, which still compares favorably with the size of contemporary gimbaled INUs (750 to 1500 cubic inches).

### Performance

Of the strapdown sensors considered, only the laser gyro meets the overall Table 1 requirements for 1 nmi/h performance. The g- and thermally insensitive wide bandwidth characteristics of the laser gyro make this performance achievable over the spectrum of dynamic environments encountered in commercial and military aircraft, without thermal controls, over long term (without calibrations), and for reaction times of less than 5 minutes (warm-up and alignment).

The tuned rotor and floated rated integrating gyros have limited performance capabilities in moderate to severe dynamic environments due principally to scale factor inaccuracy. In the case of the floated gyro, general performance capabilities (gyro bias accuracy) are questionable for applications requiring 1 nmi/h accuracy. The ESG and floated gyros have reaction time disadvantages due to the need for thermal controls and subsequent warm-up delays. For the floated gyro, the reaction time delay is compounded by a potential requirement for a calibration mode as a part of normal preflight initialization procedures to compensate for long-term stability limitations. In the case of the tuned rotor, ESG, and floated gyros, g-sensitive bias terms further restrict their accuracy capabilities in dynamic environments.

Compared to the gimbaled system, only the laser gyro strapdown system appears capable of providing equivalent performance. This is due to the g-insensitive performance of the laser compared to gimbaled gyros, and the subsequent improvement in bias accuracy that compensates for other strapdown sensor errors not present with gimbaled systems.

### Hybrid Aided Applications

Due to the unusually high stability characteristics of its error sources and accuracy of its error model, laser gyro performance in hybrid aided applications should be superior to strapdown systems using other sensors and to traditional gimbaled systems. The complexity of the Kalman filter and associated computer loading is more severe for a strapdown compared to a gimbaled system in precision hybrid aided applications due to the greater number of strapdown error sources and associated states. However, computer technology advances should eliminate this disadvantage in the 1980's.

### Multifunction Applications

For advanced multifunction strapdown applications, only laser gyro systems have the characteristics to provide the proper output signals (body rate, body acceleration, attitude, position, velocity) at the required accuracy, over the spectrum of dynamic environments experienced in commercial and military aircraft. The g-insensitivity of the laser gyro enhances its utility in skewed redundant multifunction strapdown applications, where reaction forces become applied to the sensors in a noncardinal sense, thereby degrading the performance of sensors with g-sensitive errors.

### Summary

On the basis of cost, reliability, and performance in unaided and advanced hybrid aided systems, the laser gyro is superior to the other strapdown sensors for general aircraft application. Costs for laser gyro systems (acquisition and life cycle) should be significantly lower than for traditional gimbaled navigators, with comparable performance in the 1 nmi/h class. These advantages, coupled with the extended capabilities of the laser gyro and strapdown technology in advanced multifunction applications, should make the laser gyro strapdown navigation system the preferred inertial mechanization approach for the 1980's.

REFERENCES


1. Philip J. Klass, "Laser Gyro Reemerges as INS Contender,"Aviation Week and Space Technology, January 13, 1975.

2. George R. Pitman, Jr. ed., Inertial Guidance, John Wiley and Sons, 1962.

3. Cornelius T. Leondes ed., Guidance and Control of Aerospace Vehicles, McGraw-Hill, 1963.

4. Kenneth R. Britting, Inertial Navigation System Analysis, John Wiley and Sons, 1971.

5. George R. Macomber and Manuel Fernandes, Inertial Guidance Engineering, Prentice-Hall, 1962.

6. "A Study of Critical Computational Problems Associated with Strapdown Inertial Navigation Systems," Prepared by Hamilton Standard under Contract NASA CR-968, April 1968.

7. James P. Roantree , "Advancements in Strapdown Navigation," NAECON Conference, Dayton, Ohio, 1974.

8. A. J. Eberlein, "Inertial Navigation Interim Report," Honeywell Internal Interoffice Correspondence, May 3 1972.

9. Joseph Killpatrick, "The Laser Gyro," IEEE Spectrum, October 1967.

10. Frederick Arronowitz, "The Laser Gyro," Laser Applications, Vol. 1, Academic Press, 1971.

11. Ted J. Podgorski and Fred Arronowitz, "Langmuir Flow Effects in the Laser Gyro," IEEE Journal of Quantum Electronics. Vol. QE-4, No. 1, January 1968.

12. Frederick Arronowitz and R. J. Collins, "Mode Coupling Due to Back Scattering in a HeNe Traveling Wave," Applied Physics Letters, Vol. 9, No. 1, July 1 1966.

13. Robert F. Morrison, "Laser Gyro Reaction Time Investigation Program," prepared under Contract No. F33 (615)-73-C-1054, Report No. AFAL-TR-74-189, September 1974.

14. Donald J. Pasik, Morris I. Gneses, and George R. Taylor, "A Ring Laser Gyro Strapdown Inertial Navigation System: Performance Analysis and Test Results," AIAA Guidance and Control Conference, Boston, Massachusetts, August 20-22, 1975.

15. Julius Feldman, David Gootkind, and Stephan Helfant, "Sperry ASLG 15 Laser-Gyro Performance and Error Model, Final Report," CSDL Report R-989, Prepared Under Contract NAS1-13958, July 1976.

16. James P. Roantree, John E. Burns, and Robert W. McAdory, "Differential Laser Gyro Technology," NAECON Conference, Dayton, Ohio, 1975.

17. W. K. Stowell, R. W. McAdory, and J. P. Roantree, "Differential Laser Gyro," IEEE Southeast Conference, Clemson, South Carolina, April 5-7, 1976.

18. Robert J. G. Craig, "Theory of Operation of Elastically Supported Tuned Gyroscope," IEEE Transactions on Aerospace and Electronic Systems, Vol. AES-8, No. 3, May 1972.

19. Robert J. G. Craig, "Theory of Errors of a Multigimbal, Elastically Supported, Tuned Gyroscope," IEEE Transactions on Aerospace and Electronic Systems, Vol. AES-8, No. 3, May 1972.

20. Captain Robert R. Warzynski and Ronald L. Ringo, "The Evolution of ESG Technology," Agard Symposium, June 1971.

21. N. T. Bold, H. J. Engebretson, and J. P. Moore, "Universal Marine System Gyro-ESG," ION Conference, Long Island, New York, October 23-24, 1973.

22. Robert R. Duncan, "MICRON - A Strapdown Inertial Navigator Using Miniature Electrostatic Gyros," SAE Aerospace Control and Guidance Systems Committee, Paradise Valley, Arizona, May 15-17, 1974.

23. Paul G. Savage and Mario B. Ignagni, "Honeywell Laser Inertial Navigation System (LINS) Test Results," Ninth Joint Services Data Exchange Group for Inertial Systems, St. Petersburg, Florida, November 18-19, 1975.

24. "ATIGS Final Report," Prepared by Central Inertial Guidance Test Facility, 6585th Test Group, Holloman Air Force Base, Planned for Publication in November, 1976.

25. "Upstage Technology Report," Laser Triad Rate Gyro, Mc Donnell Douglas Report G3236, August 1972.

26. "ABMDA UPSTAGE Experiment," Presentation to Congress by U.S. Department of Defense, Directorate of Development, Research, and Engineering, Advanced Research Projects Agency, October 1972.

27. "Developmental Test of the Honeywell Laser Inertial Navigation System (LINS), Final Report," ADTC-TR-75-74, Prepared by Central Inertial Guidance Test Facility, 6585th Test Group, Holloman Air Force Base, November 1975.

28. Captain Edwin V. Harrington, Jr., Jackie W. Bell, and Major George H. Raroha, "MIRA: A New Approach to Integrated Reference Systems," NAECON Conference, Dayton, Ohio, May 18-20, 1976.

29. A. J. Eberlein and P. G. Savage, "Strapdown Cost Trend Study and Forecast, Prepared Under Contract NAS2-8065, Report No. CR-137585.

30. Jack C. Shaw, "Benefits of Strapdown Over Gimbal Systems for Aircraft Application," NAECON Conference, Dayton, Ohio, May 18-20, 1976.

31. "Investigation of Application of Two-Degree-of-Freedom Dry Tuned-Gimbal Gyroscopes to Strapdown Navigation Systems, Final Report," Prepared by Teledyne Under Contract NAS1-12175, Report No. NASA CR-132419, April 1974.

32. H. Halamandaris, "Strapdown Inertial Navigation Practical Considerations," NAECON Conference, Dayton, Ohio, May 14-16, 1973.

33. "INS Maintainability/Reliability Session," Dr. Roger Phaneuf, Chairman, Eighth Joint Services Data Exchange for Inertial Systems, Charles Stark Draper Laboratory, Cambridge, Massachusetts, August 19-21, 1974.

34. Roland Peterson, "Advantages of Gimbaled Inertial Navigation Systems," NAECON Conference, Dayton, Ohio, May 18-20, 1976.

35. "Air Transport Inertial Navigation System-INS, ARINC Characteristics No. 561-9," Prepared by the Airlines Electronic Engineering Committee, Aeronautical Radio, Inc., February 1, 1973.

36. J. S. Lipman, "LN-40-The Fourth-Generation LITTON Inertial Navigation System," NAECON Conference, Dayton, Ohio, June 10-12, 1975.

37. "Dynamic Errors in Strapdown Inertial Navigation Systems," Prepared by the Analytical Sciences Corporation, Under Contract NAS12-508, Report No. NASA CR-1962, December 1971.

38. "Development Test Results of Boeing ISADS System," Informal Discussions with Jack C. Shaw (Boeing) regarding design experience during the development of the Boeing Integrated Strapdown Air Data System, a strapdown navigation system utilizing Teledyne tuned rotor gyros with Boeing-designed gyro electronics (Flight Test Results Reported in References 41 and 42).

39. "Development Flight Testing of the N-57A Inertial Navigation System, Final Report," ADTC-TR-75-86, Prepared by Central Inertial Guidance Test Facility, 6585th Test Group, Holloman Air Force Base, November 1975.

40. Robert J. G. Craig and James G. Russel, "Cost Considerations in a Strapdown Navigation System Using Dry-Tuned Instruments," INTERCON 1975, New York City, New York, April 8-10, 1975.

41. "Strapdown 727 Flight Test Summary Results," Boeing Report B-8182-5-48A, October 1975.

42. "Strapdown 747 Flight Test Summary Results," Boeing Report B-8182-6-3A, January 1976.

43. "Flight Test of the Sign III Kalman Inertial Doppler System, Final Report," AFSWC-TR-71-74, Prepared by Central Inertial Guidance Test Facility, 6585th Test Group, Holloman Air Force Base, April 1967.

44. Arthur Gelb ed., Applied Optimal Estimation, MIT Press, 1974.

45. D. H. Barnhill and D. C. Susens, "Digital Attitude Reference-Redundancy and Temperature Control Considerations," A1AA/JACC Guidance and Control Conference, Seattle, Washington, August 15-17, 1966.

46. J. P. Gilmore, "A Non-Orthogonal Gyro Configuration," MIT/IL Report T-472, January 1967.

47. A. J. Pejsa, "Optimum Skewed Redundant Inertial Navigators," A1AA Paper No. 73-850, August 1973.

## NOTES

# STRAPDOWN SENSORS

Paul G Savage
Staff Engineer, Navigation Systems
Honeywell Avionics Division
2600 Ridgeway Parkway NE
Minneapolis, Minnesota 55413

Presented in the United Kingdom,
Italy, Norway, Germany and Denmark
as part of
AGARD Lecture Series No. 95
STRAPDOWN INERTIAL SYSTEMS -
THEORY AND APPLICATIONS
San Diego, California

June, 1978

STRAPDOWN SENSORS

By

Paul G. Savage
Staff Engineer, Navigation Systems
Honeywell Inc., Avionics Division
2600 Ridgway Parkway NE
Minneapolis, Minnesota 55413

SUMMARY

Gyros and accelerometers currently available for strapdown-digital-system application are described and compared. Instruments discussed are the single-degree-of-freedom floated rate-integrating gyro, the tuned-rotor gyro, the electrostatic gyro, the laser gyro, and the pendulous accelerometer. For each sensor, the theory of operation and mechanization approach is described, an analytical error model is developed, performance characteristics are analyzed (relative to the other sensors), advantages and limitations are discussed, and application areas identified. A section is included describing torque-loop electronic design approaches that have been utilized with the torque-rebalance strapdown sensors (the floated gyro, tuned-rotor gyro, and the pendulous accelerometer).

## 1. INTRODUCTION

The state of the art in strapdown inertial navigation technology has achieved a level of maturity in recent years that makes it a serious contender for general avionics usage in the near future. Computer limitations, which handicapped strapdown compared to gimbaled technology in the past, are now virtually nonexistent due to the advent of the low-cost, high-speed minicomputer. Recent advances in gyro technology, particularly the laser gyro, (1, 2) have virtually eliminated the dynamic-range problems that previously limited the accuracy potential of strapdown systems. The capabilities of today's strapdown technology have been demonstrated to be in the classical 1-nmi/h gimbaled performance category, (3, 4, 5, 6) with production system costs projected to be one half that of gimbaled systems with comparable accuracy (7, 8, 9). The traditional strapdown versus gimbaled tradeoffs used by strapdown proponents for the past decade to tout the advantages of strapdown technology must now be given more serious evaluation. Due to the assortment of strapdown sensor types available today, the tradeoff analyses must extend to the sensor level such that overall system capabilities can be assessed for the particular strapdown mechanizations available.

This paper describes the operating characteristics, performance capabilities, and limitations of the inertial sensors (gyros and accelerometers) that are available for strapdown application. The primary focus is on the available gyro technology, since this has traditionally been the determining factor for strapdown (and gimbaled) system performance. Accelerometers are also addressed because, more-so than in gimbaled applications, strapdown accelerometers can have a significant impact on overall system performance, particularly the effect of accelerometer bias and alignment error on system velocity accuracy (10, 11). Strapdown gyro technology has now advanced to the point where the accelerometer has become a major portion of the system error budget. As the gyro technology further evolves, the accelerometer may well become the limiting error source for strapdown systems unless new accelerometer designs are developed specifically for strapdown application. Work in this regard has been initiated, although not yet at the level of funding dedication being afforded to the strapdown gyro.

Gyros analyzed in this paper are the floated rate-integrating gyro, tuned-rotor gyro, electrostatic gyro, and the laser gyro. The discussion on accelerometers is limited to the pendulous torque-to-balance type because this instrument, originally designed for gimbaled applications, continues to be the mainstream acceleration-sensing device being utilized for strapdown applications. A separate section is included on torque-loop electronics mechanization approaches for torque-to-balance instruments. Three of the sensors discussed require such electronics as an integral part of their operation (and performance) in strapdown applications.

For each of the sensors, a functional description is provided defining the basic hardware configuration of the device and its principle of operation. An analytical description is presented which defines the input/output characteristics of each unit, identifying its error sources and dynamic characteristics. Finally, a performance assessment is provided that categorizes the sensor accuracy capabilities, limitations, and associated application areas.

## 2. SENSOR PERFORMANCE REQUIREMENTS

Table 1 defines the accuracy capabilities typically required from strapdown sensors in two application areas: the 1-nmi/h accuracy long-term (1 to 10 hours) terrestrial strapdown inertial navigation system (INS), and the strapdown Attitude and Heading Reference System (AHRS). The performance figures in Table 1 for the two systems represent the upper and lower ends of the performance requirements spectrum for strapdown sensors in general. The INS application is the most demanding and has only recently been achievable; the AHRS area is representative of a broader class of strapdown applications, some of which have been in production for the past few years (e. g., tactical missile midcourse guidance).

With regard to rate-gyro bandwidth requirements in Table 1, the indicated levels are needed in the high-performance area in severe vibration dynamic environments to assure that adequate data is provided to the system computer defining the angular vibrations of the sensor assembly. Failure to account for correlated out-of-phase angular vibrations in two axes (i. e., coning) produces an error in the system computer due to the inability to account for actual attitude movement developed about the third axis from kinematic rectification (or noncommutativity). (13, 60) For the AHRS-type applications, bandwidth is generally determined by strapdown rate signal output requirements for other vehicle functions (e.g., stabilization).

Table 1. Typical Strapdown Sensor Performance Requirements

| Performance Parameter | Performance Requirements | |
|---|---|---|
| | Inertial Navigator | AHRS |
| Gyro Rate Range (deg/sec) | 100-400 | 100-400 |
| Gyro Bias Uncertainty (deg/hr) | 0.01 | 1.0-10.0 |
| Gyro Random Noise (deg/$\sqrt{hr}$)* | 0.003 | 0.2 |
| Rate-Gyro Scale-Factor Uncertainty (ppm) | 5-50 | 100-1000 |
| Rate-Gyro Scale-Factor Low Rate Assymetry (ppm) | 1 | 100 |
| Rate-Gyro Bandwidth (Hz) | 30-300 | 30-80 |
| Rate-Gyro Output-Pulse Quantization ($\widehat{sec}$) | 2-10 | 10-100 |
| Attitude Gyro Readout Uncertainty ($\widehat{sec}$) | 10 | 200 |
| Accelerometer Bias Uncertainty (μg) | 50 | 1000 |
| Accelerometer Scale-Factor Uncertainty (ppm) | 200 | 1000 |
| Sensor Alignment Uncertainty ($\widehat{sec}$) | 5 | 200 |
| Sensor Warm-Up Time (min) | 1-5 | 0.5-1.0 |
| Sensor Minimum Calibration Interval (yr) | 0.5 | 2 |

*Note: This error source is a characteristic principally of laser gyros (see Section 7.2). It should be noted that the other gyros also have random noise output errors, but generally with a narrower-bandwidth and lower-amplitude power-spectral-density compared to the laser gyro.

The calibration interval requirement in Table 1 is an important performance consideration for strapdown systems in high-accuracy applications due to the need to remove the sensor assembly from the user vehicle when calibration is necessary (for turntable testing to excite the measurable sensor errors and to separate g-sensitive errors and earth-rate input effects)*. In essence, a strapdown sensor assembly calibration requirement imposes the same burden on the user as any other maintenance action; hence, it is generally considered a part of the equipment Mean-Time-Between-Removals (MTBR) reliability figure. For gimbaled systems, the gimbal assembly can be utilized to perform the test turntable function, and the system can be calibrated aboard the user vehicle through a special built-in-test mode.

## 3. SINGLE-DEGREE-OF-FREEDOM FLOATED RATE-INTEGRATING GYRO

The floated rate-integrating gyro (16, 17, 18, 19, 20, 12) pictured schematically in Figure 1 is the gyro with the longest production history and is the original high-accuracy gimbaled-platform gyro. The device consists of a cylindrical hermetically sealed momentum-wheel/spinmotor assembly (float) contained in a cylindrical hermetically sealed case. The float is interfaced to the case by a precision suspension assembly that is laterally rigid (normal to the cylinder axis) but allows "frictionless" angular movement of the float relative to the case about the cylinder axis. The cavity between the case and float is filled with a fluid that serves the dual purpose of suspending the float at neutral buoyancy, and providing viscous damping to resist relative float-case angular motion about the suspension axis.

A ball-bearing or gas-bearing synchronous-hysteresis spinmotor is utilized in the float to maintain constant rotor spinspeed, hence constant float angular momentum. A signal-generator/pickoff provides an electrical output signal from the gyro proportional to the angular displacement of the float relative to the case. An electrical torque generator provides the capability for applying known torques to the float about the suspension axis proportional to an applied electrical input current. Delicate flex leads are used to transmit electrical signals and power between the case and float.

Under applied angular rates about the input axis, the gyro float develops a precessional rate about the output axis (rotation rate of the angle sensed by the signal-generator/pickoff, see Figure 1). The pickoff-angle rate generates a viscous torque on the float about the output axis (due to the damping fluid) which sums with the electrically applied torque-generator torque to precess the float about the input axis

*It should be noted that a composite-bias calibration procedure has been demonstrated on single-degree-of-freedom floated rate-integrating gyros (14, 15) that can be accomplished statically and therefore, in the user vehicle. Conceptually, the method is to measure the gyro output with the spinmotor operating at two different speeds (e.g., forward and reverse). A comparison between the two readings allows the gyro-bias to be separated from earth-rate input. This calibration technique is limited by its inability to separate g-insensitive from g-sensitive error terms, the inability to measure gyro scale factor errors, and the problem of predicting user vehicle movement during the period when the gyro spinmotor speed is being changed such that performance can be compared in equivalent reference frames.

at the gyro input rate. The pickoff-angle rate thereby becomes proportional to the difference between the input rate and the torque-generator precessional rate; hence the pickoff angle becomes proportional to the integral of the difference between the input and torque-generator rates.

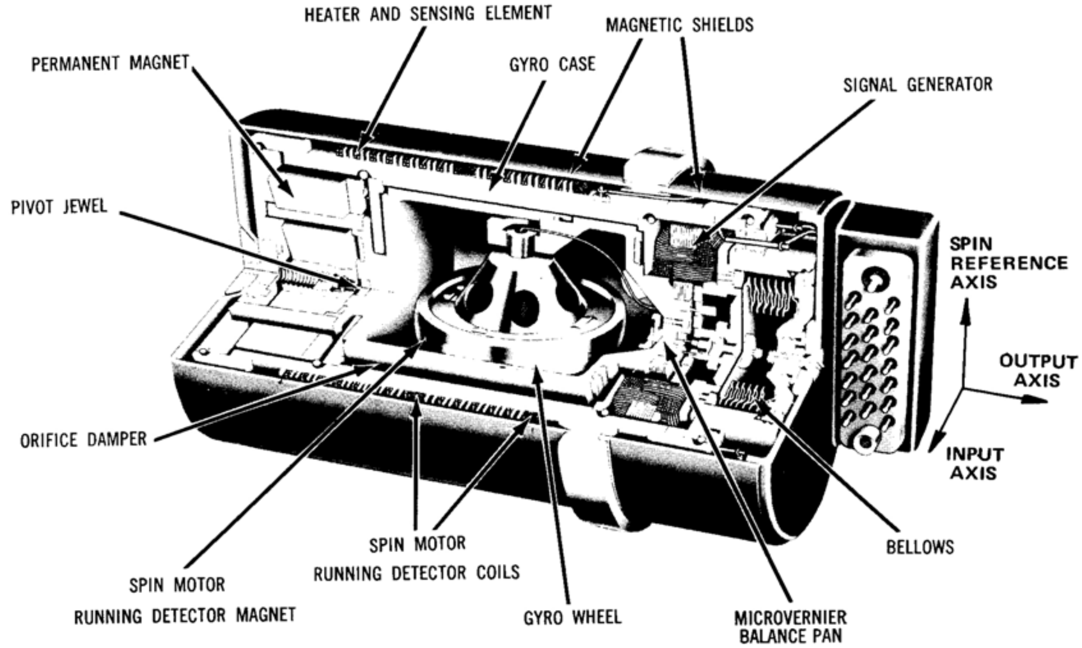


Figure 1. Honeywell GG87 single-degree-of-freedom floated-rate-integrating gyro.

To operate the gyro in a strapdown mode, the pickoff angle is electrically servoed to null by the torque generator which is driven by the signal-generator/pickoff output (through suitable compensation and amplifier electronics). The time integral of the difference between the input and torque-generator precessional rates is thereby maintained at zero, and the integral of the torque-generator rate becomes proportional to the integral of the input rate. Thus, the integral of the torque-generator electrical current provides a measure of the integral of input rate for a rate-gyro strapdown inertial navigation system.

### 3.1 General Design Considerations

The suspension assembly for the floated gyro is typically of the pivot-and-jewel type. Some units additionally employ a magnetic suspension around the pivots to eliminate friction under benign flight conditions, and to compensate for off-nominal flotation.

The signal-generator/pickoff is either of the moving-coil or variable-reluctance type. For the moving-coil pickoff, a small receiver coil is mounted to the float and an a-c excitation coil is attached to the case. Movement of the float relative to the case modifies the flux linkage sensed by the receiver coil; hence, a d-c voltage-output is generated from the receiver coil proportional to float-case angular displacement. For the variable-reluctance pickoff, the excitation and receiver coils are mounted to the case, and a soft-iron assembly is attached to the float in the flux return path between the excitation and receiver coils. Movement of the float relative to the case varies the orientation of the soft iron in the excitation field, thereby modifying the return flux to the receiver coil. The receiver-coil voltage thereby becomes proportional to float-case angular displacement. The tradeoff between the two pickoff approaches is the addition of two flex leads (and associated error-torque uncertainties on the float) for the moving-coil pickoff versus increased error-torque magnetic sensitivity (to internally generated fields) for the variable-reluctance pickoff.

The floated gyro torque-generator is either of the permanent-magnet or electromagnetic (microsyn) type. For the permanent-magnet torquer, a coil cup is attached to the float (or case) and a permanent magnet is mounted to the case (or float). Applied electrical current to the torquer coil generates magnetic flux which interacts with the permanent-magnet field, thereby producing a torque on the float. The tradeoff between a case-versus float-mounted magnet is the addition of two flex leads (for the case-mounted magnet) versus increased float size and increased error-torque magnetic sensitivity to internally generated fields (for the float-mounted magnet). For the electro-magnetic torquer, a soft iron assembly is mounted to the float, and an electromagnetic coil is attached to the case. Applied current to the coil generates a magnetic field that interacts with the iron to produce the desired torque on the float. The advantage of the electromagnetic torquer is the elimination of the permanent magnet and associated scale-factor variations due to aging (field strength decay), and the ability to implement the torque generator without flex leads. Disadvantages are increased torquer scale-factor nonlinearities and thermal sensitivities, and increased float magnetic-error-torque susceptability to internally generated fields.

### 3.2 Analytical Description and Error Model

Consider the float assembly for the single-degree-of-freedom floated rate-integrating gyro, and define a coordinate frame for it with z along the rotor spin axis, y along the float suspension axis, and x to complete the orthogonal triad (as shown in Figure 2). The torque-momentum transfer equation for the float assembly about the float (y) axis is

$$\tau_y = J_y\dot{\omega}_y + (J_x - J_z)\,\omega_z\omega_x - \omega_x J_r \omega_r \tag{1}$$

where

$\tau_y$ = net torque on the float assembly about the y axis

$\omega_x, \omega_y, \omega_z$ = inertial angular rates of rotation of the float assembly about the x, y, and z axes

$\omega_r$ = angular rate of the rotor relative to the float (about z)

$J_x, J_y, J_z$ = moments of inertia of the float assembly (including the rotor) about the x, y, and z axes

$J_r$ = moment of inertia of the rotor about the spinmotor axis

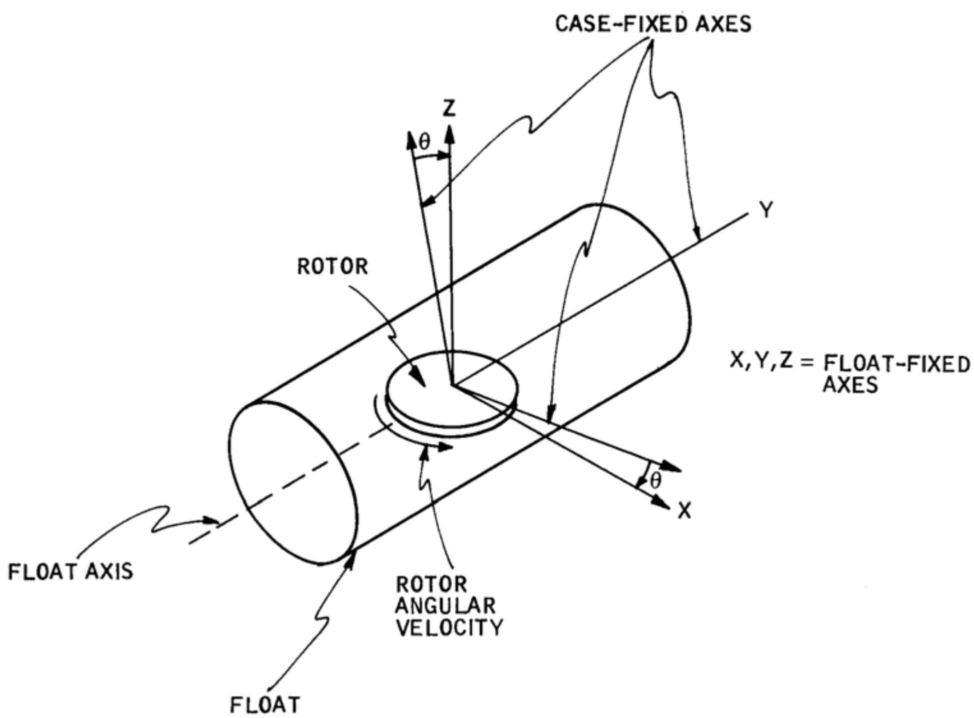


Figure 2. Gyro gimbal and case axes.

The corresponding momentum-transfer equation for the rotor about the spin axis is

$$J_r(\dot{\omega}_z - \dot{\omega}_r) = \tau_r = f(\delta\omega_r) \tag{2}$$

with

$$\delta\omega_r = \omega_r - \omega_o \tag{3}$$

where

$\omega r_o$ = nominal spinmotor rotor speed

$\delta\omega_r$ = variation in the rotor speed from nominal

$\tau_r$ = rotor spinmotor torque designed to maintain nominal rotor speed (i. e., hold $\delta\omega_r$ at null)

$f(\delta\omega_r)$ = functional operator indicating that the spinmotor torque is a function of the deviation of the rotor speed from nominal

The torque on the float assembly ($\tau_y$ in Eq. (1)) is composed of three terms: viscous flotation-fluid torques due to rotation rates of the float about the float axis relative to the gyro case; torques intentionally applied to the float assembly through the electromagnetic torque-generator; and unwanted torques due to imperfections in the gyro from its idealized theoretical configuration

$$\tau_y = -C\dot{\theta} + \tau_T + \tau_e \tag{4}$$

where

$C$ = viscous torque coefficient

$\theta$ = angle of the gyro relative to the gyro case (that would be sensed by the gyro signal-generator/pickoff)

$\tau_T$ = applied torque-generator torque

$\tau_e$ = unwanted error-torque

The torque-generator torque in Eq. (4) is defined in terms of the input axis (x) precessional rate it is intended to generate (a torquer-input command-rate) with an associated torquer scale-factor error (the error in realizing the torquer command-rate)

$$\begin{aligned} H_o &= J_r \omega r_o \\ \tau_T &= -\frac{H_o}{(1+\epsilon)}\,\omega_T \end{aligned} \tag{5}$$

where

$H_o$ = nominal gyro angular momentum

$\omega_T$ = intended torque-generator-induced precessional rate

$\epsilon$ = torque-generator (and associated electronics) scale-factor error

The unwanted error-torque in Eq. (4) is equated to a bias rate which is defined as the torque-generator-input command-rate needed to nullify the effect of the error torque on the float

$$\tau_e = \frac{H_o}{(1+\epsilon)}\,\omega_B \tag{6}$$

where

$\omega_B$ = gyro bias rate

The float angular rates in Eq. (1) can be related to angular rates along nominal gyro axes*. The float is misaligned from the gyro case by the pickoff angle ($\theta$) and the gyro case may be misaligned from the nominal gyro axes (due to imperfections in the gyro mounting surfaces and the gyro-system mounting), hence

$$\begin{aligned} \omega_x &= \omega_{IA} + \gamma_{SRA}\omega_{OA} - (\gamma_{OA} + \theta)\,\omega_{SRA} \\ \omega_y &= \omega_{OA} + \gamma_{IA}\omega_{SRA} - \gamma_{SRA}\omega_{IA} + \dot{\theta} \\ \omega_z &= \omega_{SRA} + (\gamma_{OA} + \theta)\,\omega_{IA} - \gamma_{IA}\omega_{OA} \end{aligned} \tag{7}$$

where

IA, OA, SRA = nominal gyro axes (IA = input axis, OA = output axis, SRA = spin-reference axis, Figure 1)

$\omega_{IA}, \omega_{OA}, \omega_{SRA}$ = angular rates of the gyro about the nominal gyro axes

$\gamma_{IA}, \gamma_{OA}, \gamma_{SRA}$ = misalignments of the gyro case axes relative to nominal gyro axes

---

*Nominal gyro axes are defined as the gyro axis orientation assumed in the strapdown system computer.

Eq. (3) through (7) are now substituted into Eq. (1) to obtain the input/output equation for the single-degree-of-freedom floated rate-integrating gyro. After neglecting higher-order effects and rearranging, the result is

$$\omega_T = (1 + \epsilon)\left[\omega_{IA} + \gamma_{SRA}\omega_{OA} - (\gamma_{OA} + \theta)\,\omega_{SRA} + \frac{(J_z - J_x)}{H_o}\,\omega_{SRA}\,\omega_{IA} + \frac{J_r}{H_o}\omega_{IA}\,\delta\omega_r\right] + \omega_B - \frac{1}{H_o}\left[J_y(\dot{\omega}_{OA} + \ddot{\theta}) + C\dot{\theta}\right] \tag{8}$$

The associated equation for the $\delta\omega_r$ spinmotor rate variation is similarly obtained from Eq. (2) and (3)

$$\delta\dot{\omega}_r = \dot{\omega}_s - \frac{1}{J_r}\,f(\delta\omega_r) \tag{9}$$

Equation (8) shows that the command rate ($\omega_T$) input to the gyro torque generator is proportional to the gyro input rate ($\omega_{IA}$), plus dynamic and cross-coupling effects, the principal one being the $C\dot{\theta}$ term. The integral of Eq. (8) can be rearranged to show that the pickoff angle ($\theta$) is principally proportional to the integral of the difference between the torque-generator command rate and the gyro input rate.

The floated rate-integrating gyro can be utilized in two basic modes of operation: open loop and closed loop. For open-loop operation, the gyro pickoff angle ($\theta$) is used to measure single-axis attitude variations from nominal of a platform to which the device is mounted. The nominal attitude is the integral of the command-rate ($\omega_T$). For such applications, the platform attitude about the gyro input-axis is controlled (e. g., by servomotors in the case of a gimbaled inertial navigation platform) to maintain the gyro pickoff angle at null. The platform can then be made to rotate at a specified rate about the input-axis by torquing the gyro with $\omega_T$ equal to the desired rotation rate. The platform controller will drive the platform to maintain $\theta$ at null, thereby driving $\omega_{IA}$, the platform rate, to equal $\omega_T$ in the integral sense.

The closed-loop mode of operation is utilized in strapdown applications where the gyro is used to sense input rate. In the closed-loop mode, the gyro is electrically caged by generating a command rate into the torque-generator to maintain the pickoff angle $\theta$ at null. Figure 3 is a block diagram of Eq. (8) and (9) illustrating this concept. From the block diagram it should be apparent that for proper dynamic characteristics designed into the gyro torque-generator electronics, the pickoff angle can be maintained near null with the resulting torque-generator command-rate ($\omega_T$) becoming proportional to the input rate ($\omega_{IA}$) in the integral sense (plus additional error terms). The bandwidth (or dynamic response time) of the instrument (output $\omega_T$ compared to input $\omega_{IA}$) is determined by the gain and form of the command-electronics mechanization. Several approaches are possible as described in Section 4.

The input-error terms in Figure 3 that corrupt the accuracy of the gyro in measuring $\omega_I$ are the mechanical misalignment errors ($\gamma_{OA}$ and $\gamma_{SRA}$), the float-to-case misalignment angle error ($\theta$), output-axis angular acceleration ($\dot{\omega}_{OA}$), anisoinertia effects ($J_z - J_x$), spinmotor loop dynamics ($f(\delta\omega_r)$), torque-generator/electronics scale-factor error ($\epsilon$), and gyro bias errors ($\omega_B$). The float-to-case misalignment error is caused by signal-generator/pickoff angle bias (pickoff null different from $\theta$ null), and dynamic effects in the torque loop. (12) The anisoinertia, spinmotor dynamic, and angular acceleration effects, as well as the bandwidth limitations of the device (which impacts the pickoff misalignment error), are design limitations intrinsic to the basic gyro concept. The remaining errors (mechanical misalignment, pickoff-angle detector bias, scale-factor error, and bias error) are caused by imperfections in the gyro that deviate from the theoretically perfect design.

A typical model of the scale-factor error for the floated gyro in the strapdown closed-loop mode of operation is given by

$$\epsilon = \epsilon_o + \epsilon_1 \frac{\omega_{IA}}{|\omega_I|} + \epsilon_2\,\omega_{IA} + \epsilon_3\,\omega_{IA}^{\,2} \tag{10}$$

where

$\epsilon_o$ = basic "fixed" scale-factor error

$\epsilon_1$ = scale factor asymmetry error (positive scale factor different from negative scale factor)

$\epsilon_2, \epsilon_3$ = linearity-error effects that modify the scale-factor error under high rates

The scale-factor-linearity errors are functions of the torque-loop mechanization approach utilized, and, for a permanent-magnet torque-generator, the tightness of the torquing loop (ability to minimize pickoff angle movement which could produce variations in the electromagnetic interface between the gyro-torquer-coil and torquer-magnets). The presence of the $\epsilon_1$ coefficient depends on the torque-loop electronics implementation utilized (see Section 4.). If the term exists, it can be particularly troublesome due to its ability to rectify low rate oscillatory inputs (such as vehicle limit-cycling). The $\epsilon_o$ coefficient is dependent on the torque-generator temperature (due principally to torquer magnetic-field-strength thermal sensitivity), and to scale-factor error in the torque-loop electronics.

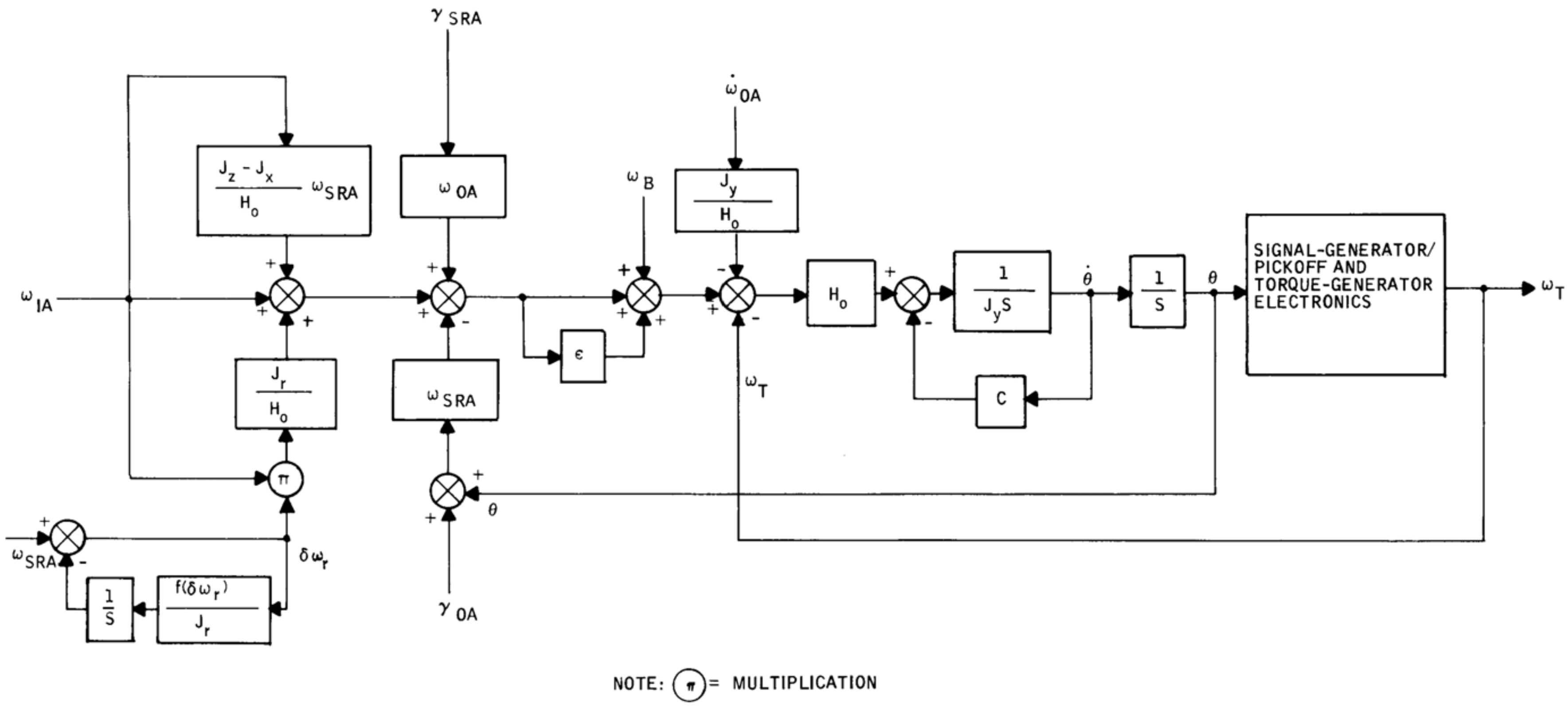


Figure 3. Single-degree-of-freedom floated-rate-integrating gyro analytical response diagram.

The $\omega_B$ bias error includes several effects associated with manufacturing tolerances and electromechanical instabilities. A typical error model for the bias is illustrated by Eq. (11)

$$\omega_B = B_0 + B_1 a_{IA} + B_2 a_{SRA} + B_3 a_{IA} a_{SRA} + n \tag{11}$$

where

$a_{IA}$, $a_{SRA}$ = accelerations of the gyro along the input (IA) and spin-reference (SRA) axes

$B_0$ = g-insensitive bias error

$B_1$ = g-sensitive bias coefficient created from gyro float mass unbalance (relative to the gimbal pivots) along the spinmotor axis. (A principal error source in this regard is movement of the rotor along the spin axis due to spinmotor bearing compliance.)

$B_2$ = g-sensitive bias coefficient created from float mass-unbalance along the input axis

$B_3$ = anisoelastic bias error coefficient created by unequal compliance of the gyro float assembly along the input and spin axes

n = zero-mean random bias term representable as a stochastic noise process

For the floated rate-integrating gyro, the $B_0$ term is typically caused by residual flex-lead torques, residual thermal gradients across the gyro that produce flotation-fluid flow around the float assembly, magnetic torques on the float assembly caused by eddy current fields from the gyro case (generated from stray spinmotor fields entering the case), pivot torques due to off-nominal flotation in gyros without magnetic suspensions (caused by fluid temperature variations and float manufacturing tolerances), pivot stiction due to pivot reaction torque under gyro rotations about the output axis (the torque needed to precess the float about the input axis), and torque-loop/pulse-electronics bias errors (for binary torque-loops, or analog torque-loops with follow-up analog-to-digital conversion: see Section 4).

Random noise is created by zero mean instabilities in the gyro that have short correlation times (i.e., minutes or less). Examples are variations in the g-insensitive bias due to variations in pivot friction, and variations in the g-sensitive bias due to random movements of the rotor along the spin axis.

In general, the B and $\epsilon$ coefficients in Eq. (10) and (11) have predictable and unpredictable components. The predictable components can be measured a priori and used in the inverse sense to correct (compensate) the gyro-output data (typically in the system computer where the gyro data is input). The B, $\epsilon$ coefficients can be modeled in the computer as simple constants, or in the more sophisticated applications, can include predictable temperature variations as functions of sensor temperature measurements. The degree to which the measured coefficients characterize the actual gyro errors is, in general, a function of time, temperature/vibration exposure, input profile, and number of device turn-ons. The time period for which the measured coefficients accurately characterize the gyro constitutes the long-term stability of the gyro and its associated calibration interval (to remeasure and correct the error coefficients).

The dynamic errors in Figure 3 can also be compensated in the same manner as the bias and scale-factor errors within the bandwidth limitations of the uncompensated sensor-output signals (the signals utilized in the system computer sensor-compensation models). With regard to bandwidth limitations of dynamic compensation, the anisoinertia, spinmotor dynamic, and pickoff angle dynamic cross-coupling effects can be particularly troublesome because of their ability to rectify high-frequency inputs about the spin and input axes (12) (a similar problem exists for the anisoelastic bias error). The pickoff-angle cross-coupling rectification error is caused by the torque-loop bandwidth limitation through the dynamic servo error ($\theta$) generated under high-frequency input-axis angular-rate, and the resulting cross-coupling of spin-axis rate into the gyro output (see Figure 3). Compensation for spinmotor effects can have additional inaccuracies because of the difficulty in accurately modeling the motor-speed control-loop dynamics.

### 3.3 Performance and Application Areas

Simplified low-cost versions of the floated gyro have been successfully utilized in tactical missile and spacecraft booster guidance applications where the AHRS sensor figures from Table 1 are representative of gyro performance requirements. Examples are the midcourse systems employed on the Harpoon and Standard Missile-2 tactical missiles, the booster inertial guidance systems on the Agena and Delta launch vehicles, the backup guidance system utilized in the Apollo Lunar Module, and the guidance and navigation system utilized in the Prime Reentry Vehicle (the first nondevelopmental strapdown guidance system application). To the author's knowledge, floated-gyro performance consistant with Table 1 1-nmi/hr strapdown navigator requirements has yet to be demonstrated in a statistically valid system flight test. Results of flight tests conducted in 1965 at Holloman Air Force Base on a Honeywell system using high-quality floated gyros yielded 2- to 4-nmi/hr CEP unaided performance. (21) These results are not necessarily representative of what is attainable with today's technology; however, sceptics believe that 1-nmi/hr accuracies for floated rate-integrating gyro strapdown systems are not quite achievable with reasonably priced instruments.* Particulars regarding the capability of the floated gyro in meeting the Table 1 sensor requirements are discussed in the following paragraphs.

---

*Some floated gyro enthusiasts believe that the more sophisticated strapdown floated gyro configurations can meet 1-nmi/hr navigation system requirements. Floated gyro manufacturers, however, are not promoting the use of these instruments today for 1-nmi/hr strapdown applications because of their higher cost and/or performance deficiencies (in the case of the lower cost units) compared to the other available strapdown gyro types.

The bias error for the floated rate-integrating gyro (both g-sensitive and g-insensitive effects) has long-term trending characteristics that require calibration to achieve high-accuracy performance compatible with Table 1 INS requirements. Thermal effects on the bias error are significant, and difficult to accurately model for compensation (e.g., pickoff null movement and associated flex-lead error-torque variations; spinmotor axial shifts due to motor-bearing preload variations; and off-nominal fluid temperature, hence off-nominal flotation, a problem for non-magnetic float suspensions). As a result, thermal controls are generally required to achieve high accuracy*, and a warmup time penalty is incurred. Care must be taken in using the device to assure that input vibration levels and vector direction (linear and angular) do not rectify the dynamically sensitive bias terms (anisoelasticity, anisoinertia, spinmotor dynamics, pickoff angle dynamic response error) beyond application performance limits. An unfortunate aspect of the latter consideration is that vibration profiles at the sensor or even system level are difficult to obtain during the development cycle (particularly regarding angular vibrations and linear-vibration vector direction). Computer compensation can be employed to reduce dynamic errors for low-frequency inputs (within the bandwidth of the sensor torque loop).

Increasing angular momentum [to reduce bias error, see Eq. (6)] also creates additional error torques on the float due to stiffer pivots to handle the increased-momentum reaction-torque loading under output axis rotations; a larger float assembly (for the larger spinmotor and larger torque generator to precess the increased angular momentum) with an associated increase in mass unbalance, float-case electromagnetic-interraction error torques, and float-suspension error torques; heavier flex leads for the larger spinmotor; and (for a permanent-magnet torque-generator with float-mounted coil) heavier flex leads for the larger torquer-coil assembly. The net result is that increased momentum has only a limited capability in reducing floated-gyro bias error, and some form of regular calibration is probably needed to achieve the long-term stability needed to meet Table 1 INS requirements. A concept such as the dual-speed spinmotor technique (see Section 2) appears necessary for conveniently calibrating these gyros frequently if the requirements in Table 1 are to be met. The inability for this calibration technique to separate g-sensitive from g-insensitive errors, however, probably restricts the floated gyro to strapdown applications in fairly benign flight environments if unaided 1-nmi/hr performance is to be achieved. For lower-performance applications (such as the AHRS in Table 1), performance requirements are readily achievable.

Due to torque-generator thermal sensitivities and, in the case of the permanent-magnet torquer, aging effects in the torquer magnet, scale factor accuracies in torque-rebalance instruments (such as the floated gyro) are generally limited to 50 ppm. Compared to Table 1 requirements, the 50-ppm limitation places a serious handicap on torque-rebalance gyros for high performance applications. Relative to the 1-ppm low-rate asymmetry requirement for rate gyros, Honeywell's experience with a GG1009H floated gyro has shown that this performance level is achievable with careful design practice.

Due to its torque-rebalance nature, the floated gyro has a limited-bandwidth input-rate-sensing capability. As a result, sensor-assembly coning-rate vibration frequencies near or above the bandwidth of this sensor will result in attitude drift errors unless the vibration levels are naturally small or intentionally attenuated (through shock mounts). Honeywell's experience with a strapdown GG1009H navigation-grade floated rate-integrating gyro has shown that 80-Hz bandwidths are easily achieved, including a factor of 7 rise in torque-loop stiffness at low (0-5 Hz) frequencies (i.e. lag-lead compensation). For most applications, this bandwidth level is sufficient to meet system needs. Care must be taken in severe vibration applications, however, to assure that unanticipated coning effects will not constitute a major error source.

Alignment stabilities of 5 seconds of arc (the Table 1 requirement) may be achievable with the floated gyro, but not without careful design work. Mechanical instabilities of the gyro-system mount, gimbal pivot, and spinmotor axis; torque-loop servo errors; and pickoff detector null shifts, all contribute to the alignment error. The overall alignment error must remain within allowable limits for several months, over thermal, vibration, angular rate, and linear acceleration environments so that frequent calibration is not required. Thermal modeling may be needed to compensate for pickoff null movement.

The random noise from the floated gyro is generally well within the Table 1 requirements; hence, it does not constitute a major error source. The required rate capability is designed into the unit (through specification of the angular momentum and torque-generator design) and, as such, can be selected to meet the Table 1 requirements. Higher rate requirements impact gyro accuracy through a larger torque-generator requirement and associated bias error effects (e.g., mass unbalance).

Due to the need for thermal controls in high-accuracy applications, a warmup time delay of 5 to 10 minutes is needed to allow the floated gyro to come up to temperature and stabilize. To this must be added an additional 5 minutes for calibration (e.g., using spinmotor reversal). An overall warmup time of 15 minutes results which generally is not compatible with high-performance system requirements. For the lower-performance applications, gyro accuracy is acceptable without heaters (or the output accuracy is acceptable during gyro warmup); hence, the "warmup" time limit is the time for spinmotor run-up, which is typically achievable in 30 seconds.

---

*Another reason for temperature controls in high-performance floated gyros is to maintain nominal damping characteristics in the damping fluid [i.e., the C-coefficient in Eq. (8)] to retain nominal dynamic response performance in the torque-rebalance loop. Typical flotation fluids vary their damping characteristics significantly with temperature and lose their fluid characteristics at low temperatures. Mechanical devices (e.g., orifice dampers) can be utilized in the gyro float-case cavity that provide passive control of damping, and achieve high damping levels with thinner fluids. Unfortunately, these devices also add residual error torques and, therefore, are typically utilized in only the lower-performance application areas.

Quantization levels achievable with the floated gyro depend on the torque-loop/pulse-electronics implementation utilized (see Section 4) which can be selected to meet Table 1 requirements.

## 4. TORQUE LOOP MECHANIZATION APPROACHES FOR TORQUE-REBALANCE INSTRUMENTS

The implementation of the torque loop for torque-to-balance instruments (such as the floated rate-integrating gyro) can be performed using either of two basic approaches: digital torque rebalance, or analog torque rebalance with follow-up analog-to-digital conversion. Both concepts are illustrated in Figure 4.

### 4.1 Digital-Torque Rebalance

For the digital-rebalance concept, precision time-amplitude current pulses are generated and gated into the sensor torquer to maintain the pickoff angle at null. Dynamic analog compensation is utilized in the torque loop (if necessary) to provide sufficient wide-bandwidth stable performance (pickoff angle maintained at null under expected dynamic input-rate conditions).

Each current pulse input to the torque generator has the same time-amplitude content; hence, the integral per pulse of the current into the torquer is fixed. This corresponds to an equivalent integral quantum of input data to the sensor (input rate in the case of a gyro) that caused the pulse to be generated (through the forward pickoff/current-command loop). Hence, the occurrence of a rebalance pulse provides a digital indication (to the system computer) that (for a gyro) the device has been rotated through a known fixed quantum of angle about its input axis. For an accelerometer, the pulse occurrence represents a fixed incremental velocity change. Implementation approaches for the pulse command logic vary, depending on sensor-application requirements. In general, two methods are possible: pulse-on-demand and binary torquing.

For the pulse-on-demand concept, a pulse is only input to the torquer when it is needed to drive the analog input to the pulse-command logic toward null. Otherwise, the torquer current is maintained at

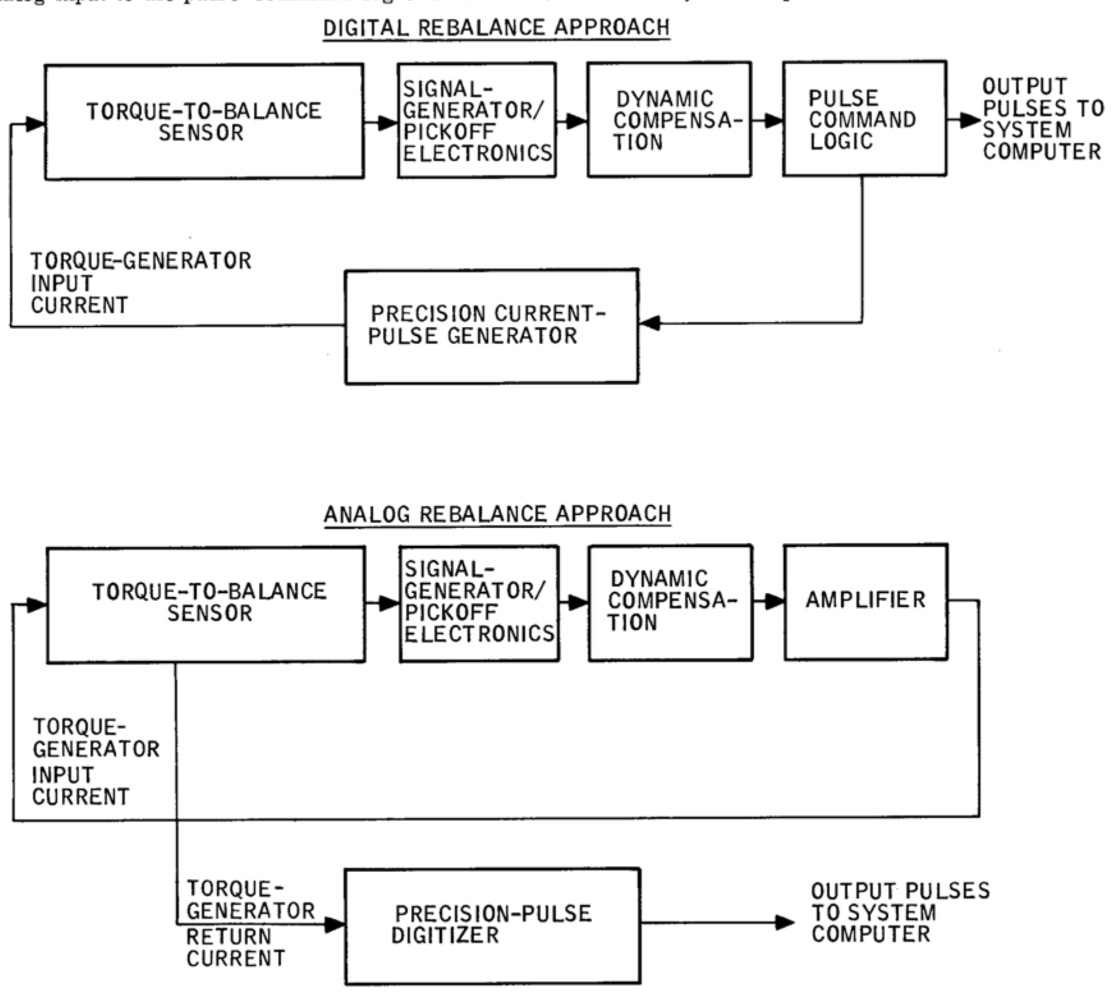


Figure 4. Torque-rebalance-loop concepts.

zero. Figure 5 illustrates two commonly used methods for implementing the pulse-on-demand logic. For the approach at the top of Figure 5, a pulse is issued when the analog-input-signal magnitude exceeds a specified threshold. After the threshold is exceeded, pulses are generated at a constant rate into the sensor torquer with a phase sense (plus or minus) to drive the input signal (through the sensor response) below the threshold limit. The pulse size is set so that for the pulse-frequency capability of the current-pulse generator, sufficient current is generated through the torquer to maintain sensor pick-off null capture under maximum sensor-input conditions. For each pulse transmitted to the torquer, a pulse is output to the system computer to indicate that an incremental change in the sensor input has occurred and has been rebalanced electrically.

For the approach in the lower half of Figure 5, pulses are generated into the torquer at a rate (frequency) proportional to the analog-signal input level. The pulse size for this approach is also set to hold the pickoff at null under maximum input conditions for which the voltage-to-pulse-frequency converter generates its maximum output pulse frequency.

In general, the tradeoff between the two pulse-on-demand logic approaches in Figure 5 hinges on the effective bandwidth in the overall sensor torque loop versus the torque-loop accuracy under zero and dynamic input conditions (off-null pickoff angle, which leads to cross-coupling errors (see Figure 3), and pulse limit-cycling, which indicates erroneous attitude oscillations to the system computer).

For the binary pulse-command logic approach, constant-amplitude pulses are applied to the sensor torque-generator at a constant rate. The percentage of positive (compared to negative) pulses is controlled to balance the sensor input. Figure 6 illustrates two common binary-torquing configurations: fixed-pulse-width torquing, and pulse-width-modulated torquing.

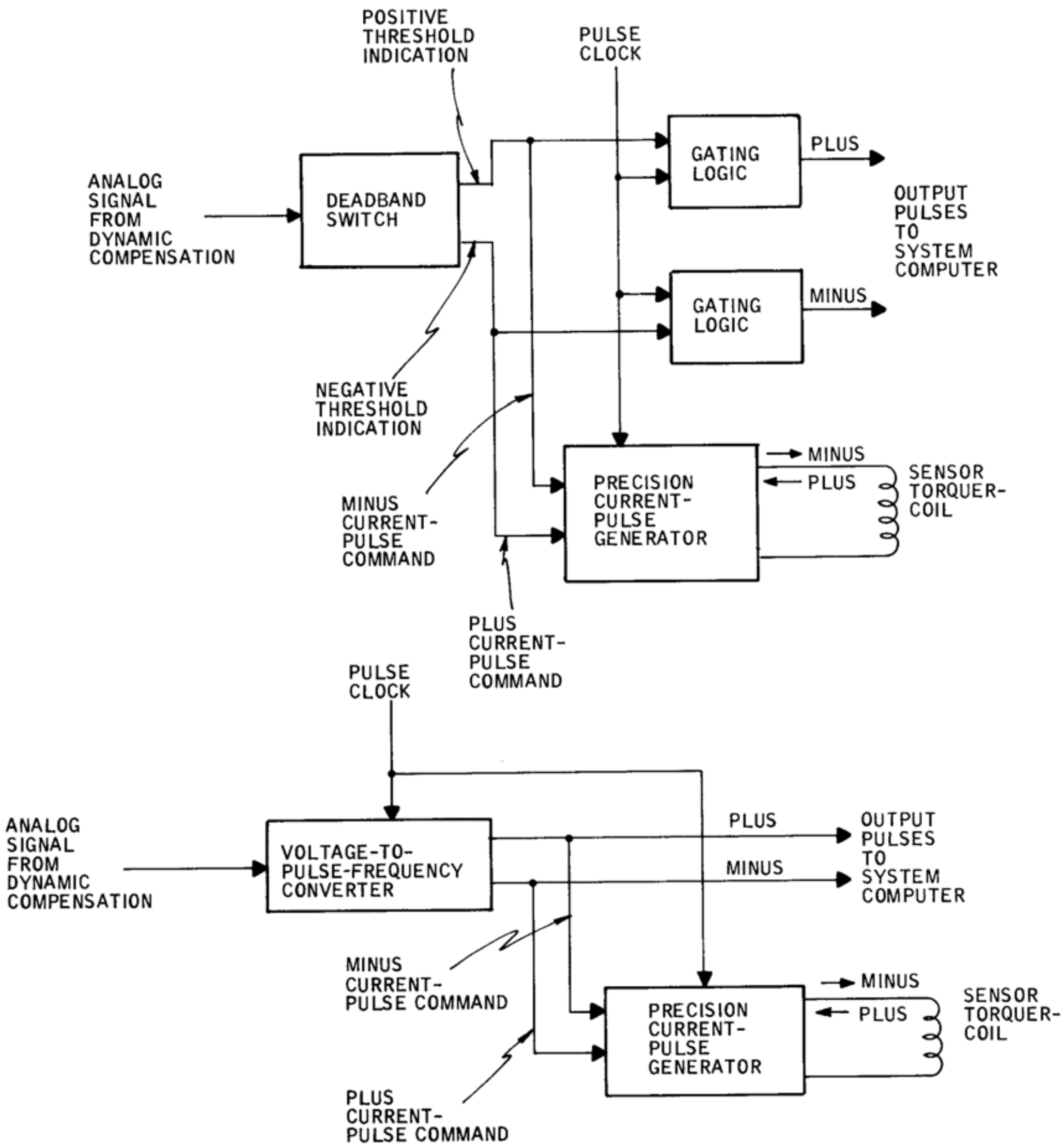


Figure 5. Pulse-on-demand torquer-current command-logic concepts.

For the binary fixed-pulse-width concept, constant-amplitude constant-width pulses are continuously gated into the torque generator in the positive or negative sense, depending on the phasing of the input signal to the command logic (see Figures 4 and 6). With no input to the sensor, the pulse logic establishes a torque-loop limit-cycle condition in which half the pulses delivered to the torque generator are positive and half are negative (i.e., no net torque is delivered on the average). When an input is applied to the sensor, a larger percentage of pulses is generated with phasing that balances the sensor input. The average difference between the positive and the negative pulses delivered per unit time becomes proportional to the sensor input, and the average pulse-count (positive minus negative) becomes proportional to the integral of the sensor input. The pulse size is established so that for the torque-loop pulse-frequency utilized, sufficient current is generated under maximum sensor input conditions to balance the sensor input.

For the binary pulse-width-modulated torque loop approach (59) (Figure 6), a constant-frequency, constant-amplitude variable-width square-wave is generated by the torque-command electronics, with the difference between the plus and minus wave widths proportional to the input to the command logic (see Figure 4). The variable-width square wave is edge-synchronized with a high-frequency clock, and then used to gate a precision constant current into the sensor torque-generator: positive for the positive cycle of the square-wave, negative for the negative cycle. Thus, the average current into the torquer becomes proportional to the difference between the square-wave positive and negative wave-widths, and

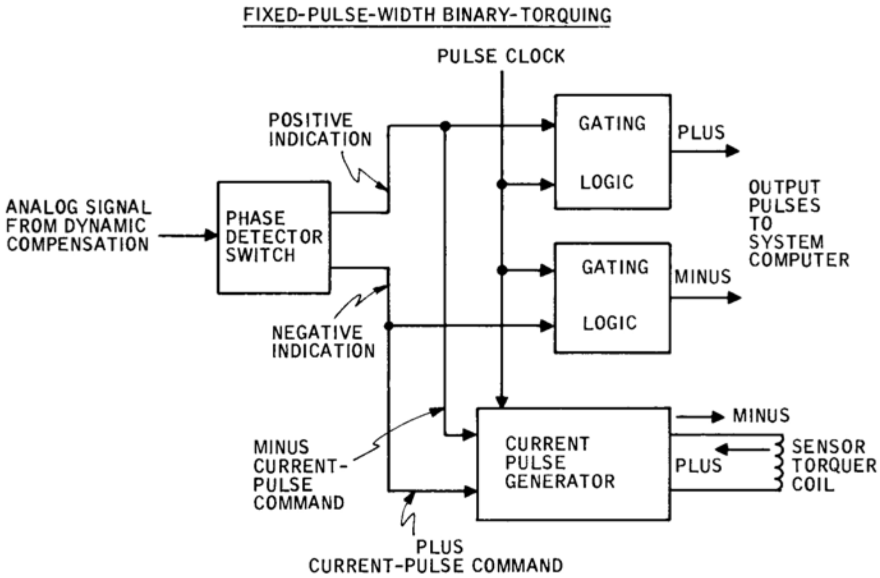


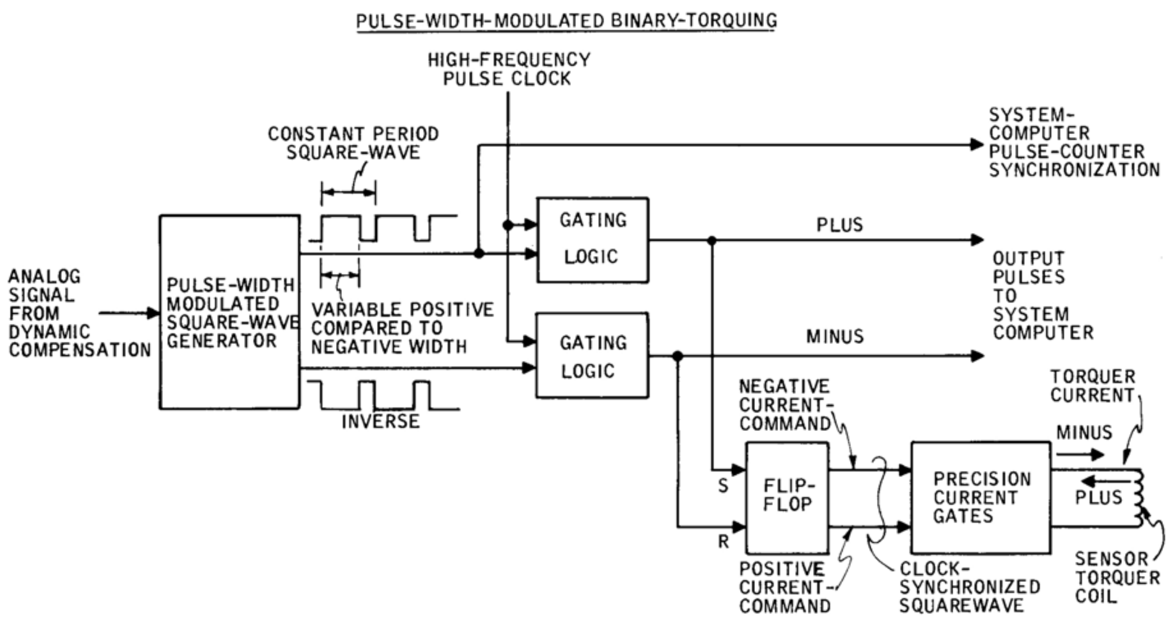


Figure 6. Binary torquer-current command-logic concepts.

thereby proportional to the command-logic input signal. During the time that positive current is being commanded, the high-frequency pulse clock is gated as the gyro pulse output along the positive output line, and conversely for negative current. Since the torquing current square wave is edge synchronized with the high-frequency clock, the total time period for a current pulse (positive or negative) into the torquer is proportional to an integral number of high-frequency pulse counts. As a result, each high-frequency pulse represents a quantum of known integrated torquer current-time (the high-frequency clock period times the torquer current). By counting the positive minus the negative high-frequency pulses in the system computer over each square wave cycle (a count synchronizer is needed; see Figure 6), a fine resolution measure of integrated sensor input is obtained.

An advantage of the binary pulse-width-modulated concept compared to the pulse-on-demand or binary fixed-pulse-width approaches is that finer pulse size (resolution) is achievable with the former. The pulse size for each concept is determined by the maximum torquing rate divided by the maximum pulse frequency (at maximum rate). For the binary pulse-width-modulated concept, the maximum output-pulse frequency is established by the pulse clock, and is independent of the torquing pulse frequency (established by the square-wave period; see Figure 6). For example, for a 400-degree-per-second maximum rate requirement and a 1-MHz pulse clock (not untypical), the pulse size is $400 \times 10^{-6}$ degrees or 1.5 sec of arc. For the pulse-on demand or binary fixed-pulse-width concepts, the output and torquer pulse-frequencies are equivalent since both are generated from the same source (the pulse clock in Figures 5 and 6). As a result, the output-pulse frequency must be limited to the maximum frequency for which torquer-current pulses can be accurately generated (a function of electronic delays, inductive torquer-coil transients, and the current levels needed for the particular torque-generator design). For strapdown gyros, 5 KHz is a typical maximum torque-rebalance pulse-frequency. For strapdown accelerometers, higher pulse-torquing frequencies are attainable due to the lower current levels involved (e.g., 20 KHz). Hence, the pulse resolution for the pulse-on-demand or binary fixed-pulse-width schemes is generally one to two orders of magnitude coarser than for the binary pulse-width-modulated approach for the same maximum torquing-rate capability. Finer resolution can be achieved with the pulse-on-demand or binary fixed-pulse-width approaches by switching to a lower current level under low sensor input conditions, a design complication that still does not provide fine resolution at high sensor inputs if required. Alternatively, the residual analog signal on the sensor output can be sampled and brought into the system computer through an analog-to-digital converter as a correction to the sensor pulse count accumulated in the computer. The accuracy of this technique is limited by the error (principally scale factor) of the sensor signal-generator/pickoff, generally a poor-quality signal for high-accuracy attitude measurement.

Another advantage for the binary torquing schemes is that total current load into the sensor torque generator is maintained at a constant value (sum of absolute positive and negative current), hence, the thermal effect on the sensor torquer is constant. Since torquer scale-factor accuracy is a function of torquer temperature, operation at a constant thermal load condition tends to minimize torquer scale-factor variations due to thermal gradient loading. For the pulse-on-demand implementation, since average current delivered to the torquer is proportional to input rate, torquer heating becomes proportional to input rate, and thermal transient scale factor variations can be introduced as a function of sensor input. Torquer scale-factor temperature-error effects can be compensated to some extent by installing a thermal detector in the sensor torque generator and using the output signal to correct for device scale-factor variations (either electronically in the actual sensor, or through software in the system computer). The technique can be utilized in unheated sensor applications to improve performance (for both pulse-on-demand and binary torque loops). It also partially compensates for the added thermal transient error that occurs for the pulse-on-demand scheme under dynamic input conditions.

The principal disadvantage of the binary rebalance scheme is the need to operate continuously at maximum positive and negative current loads into the torquer, even at zero sensor-input conditions. As a result, the torque-loop scale-factor symmetry (plus compared to minus current/torque transfer) must be extremely accurate to avoid generating a net large bias error. For example, for a gyro torque loop designed to handle a 400-deg/sec input rate, a 1-ppm asymmetry results in an equivalent bias error of $400 \times 10^{-6} \times 3600$ or 1.4-deg/hr under zero input-rate conditions.

The advantage of digital rebalance schemes in general (either pulse-on-demand or binary) compared to the analog rebalance approach discussed in Section 4.2 is that the torquer current-pulse waveforms have two fixed shapes (positive or negative pulse or square-wave), independent of the average torquing rate. As a result, torquer-linearity error effects [the $\epsilon_2$, $\epsilon_3$ terms in Eq. (10)] are largely absent. Care must still be taken, however, for the pulse-on-demand implementation to assure that the $\epsilon_1$ asymmetry error is small (a function of the positive and negative torquer-current electronics design match) so that normal low-level oscillatory sensor inputs will not rectify into a bias error. For the binary torque-loop schemes, the $\epsilon_1$ symmetry is not an error source (torque-loop asymmetry generates the bias-error effect described in the previous paragraph).

### 4.2 Analog Torque-Rebalance with Follow-Up Analog-to-Digital Conversion

The alternate to digital rebalance is capture of the sensor element with an analog torque loop (Figure 4). The analog current into the torque generator becomes a continuous measure (in the integral sense) of sensor input. To develop the incremental pulse signals required by the computer, a digitizer circuit is utilized. The digitizer circuit integrates the analog input signal from the torquer, and incrementally rebalances the integrator with fixed current-time (or voltage-time depending on implementation) increments to maintain the integrator output at null. For each rebalance pulse issued to the integrator, an output pulse is issued to the system computer indicating that a known increment of integrated torquer current has been accrued; hence, the integral of the sensor input has also incremented by a known value. The digitizer circuit is typically implemented in much the same manner as the pulse-on-demand digital torque-loop scheme at the top of Figure 5, with the digitizer electronic integrator operating as the sensor does in Figure 5.

An advantage of the analog-torquing loop approach is that wider bandwidth performance is easily achieved and tighter sensor nulls can generally be held compared with the digital-rebalance schemes where continuous off-null oscillatory operation is produced through the pulse-torquing (i.e., the sensor pickoff-angle is nulled within a pulse). In addition, the design of the digital-rebalance portion of the digitizer can be simplified by operating at lower maximum current levels (through scaling of the integrator input), a technique that is prohibitive with digital rebalance where the torquer current to sustain sensor-element capture must be maintained by the digital pulses. Another advantage for analog torquing is that the design of the sensor torque-loop electronics is simplified and essentially uncoupled from the more sophisticated digital-pulse circuitry. As a result, the design of the digitizer can be accomplished independently from the sensor and a common digitizer design configuration may be compatible with several different sensors (e.g., the gyros and accelerometers in a system, or different manufacturer designs for one class of sensor in multiple-source procurements).

Disadvantages of the analog-rebalance concept are the added error (particularly bias) associated with the digitizer, and the sensor scale-factor errors associated with high-rate linearity and torquer heating as a function of input magnitude. Regarding the bias-error effect, the state of the art in analog circuitry has progressed to the point where low bias accuracies (relative to sensor bias) can be achieved with careful design practice. Regarding the scale-factor-error effects, dynamic compensation can be utilized to virtually eliminate the scale-factor-linearity error. Thermal transient error can be eliminated to a degree by thermal measurement and modeling, the adequacy depending on the dynamic-rate environment and accuracy requirements for the particular application. Since mechanization approaches for the digitizer parallel those for the pulse-on-demand digital-rebalance concept, tradeoffs associated with resolution capabilities also apply. It should be noted that the rescaling technique utilized with pulse-on-demand torquing (similarly applicable to the digitizer to increase resolution under low input conditions) also reduces the effective digitizer bias error under low rate conditions (due to rescaling of the digitizer input-signal relative to the sensor rebalance current and digitizer-integrator input-offset current or voltage). In the case of a digitizer based on current input (utilized to reduce integrator bias), a current-input rescaling may be required under high input conditions due to limitations in low-drift electronic integrator amplifiers to absorb the total torquer current from the sensor.

## 5. TUNED-ROTOR GYRO

The tuned-rotor gyro (22, 23, 24, 25, 26) is the most advanced gyro in large-scale production today for aircraft 1-nmi/hr gimbaled platforms. Due to its simplicity (compared to the floated rate-integrating gyro), the tuned-roto gyro is theoretically lower in cost and more reliable. A drawing of a representative tuned-rotor gyro is presented in Figure 7. Figure 8 is a schematic illustration of the gyro rotor assembly.

The gyro consists of a momentum wheel (rotor) connected by a flexible gimbal to a case-fixed synchronous-hysteresis ball-bearing spinmotor drive shaft. The gimbal is attached to the motor and rotor through members that are torsionally flexible but laterally rigid. A two-axis variable-reluctance signal-generator/pickoff is included that measures the angular deviation of the rotor (in two axes) relative to the case (to which the motor is attached). Also included is a two-axis permanent-magnet torque generator that allows the rotor to be torqued relative to the case on current command. The torquer magnets are attached to the rotor, and the torquer coils are attached to the gyro case.

As for all angular-momentum-based rate-sensing devices, the key design feature of the gyro is the means by which it can contain the reference momentum (the spinning rotor), without introducing torques (drift rates) in the process. For the tuned-rotor gyro, the method is linked to the dynamic effect of the flexible gimbal attachment between the rotor and the motor. Geometrical reasoning reveals that when the rotor is spinning at an angle that deviates from the motor-shaft direction, the gimbal is driven into a cyclic oscillation in and out of the rotor plane at twice the rotor frequency. Dynamic analysis shows that the reaction torque on the rotor to sustain this motion has a systematic component along the angular-deviation vector that is proportional to the angular displacement, but that acts as a spring with a negative spring constant. The flexible pivots between the rotor and gimbal, on the other hand, provide a similar spring torque to the rotor, but of opposite sign. Hence, to free the rotor from systematic torques associated with the angular displacement, it is only necessary to set the gimbal pivot springs such that their effect cancels the inverse spring effect of the gimbal. The result (tuning) is a rotor suspension that is insensitive to angular movement of the case.

Use of the tuned-rotor gyro in a strapdown mode parallels the technique used for the floated rate-integrating gyro. Exceptions are that damping must be provided electrically in the caging loop, as there is no fluid, and that the gyro must be caged in two axes simultaneously. The latter effect couples the two caging loops together due to the gyroscopic cross-axis reaction of the rotor to applied torques.

### 5.1 Analytical Description and Error Model

Consider the rotor assembly for the tuned-rotor gyro and define four coordinate frames for it as shown in Figure 9: one attached to the rotor (R), one attached to the gimbal (G), one attached to the gyro case (C), and pickoff axes (P) defined with X and Y axes in the plane of the rotor, but displaced from the case axes by small-angle Euler rotations $\theta_x$ and $\theta_y$. These are the pickoff angles for the gyro. The Y-axis of the gimbal frame is along the inner torsional flexure that connects the gimbal to the spinmotor shaft. The gimbal-frame X-axis is displaced angularly about the Z-axis from the gyro-case axes by the motor-shaft angle $\phi$. The gimbal X-Y plane is displaced from the case X-Y plane by the flexure angle $\beta$. The X-axis of the rotor is aligned with the outer flexure axis that connects the rotor to the gimbal. The rotor axes are displaced from the gimbal frame by the flexure angle $\alpha$.

From the geometry in Figure 9, the kinematic constraint relations for the pickoff and flexure angles can be written as

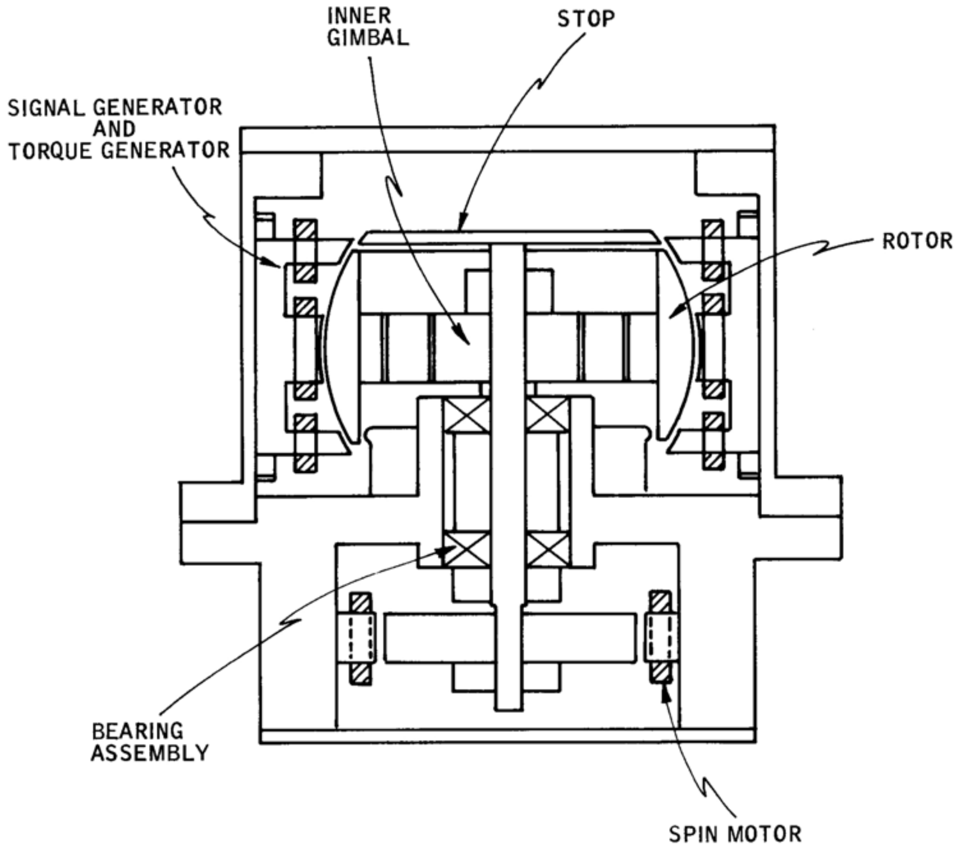


Figure 7. Typical tuned-rotor gyro configuration.

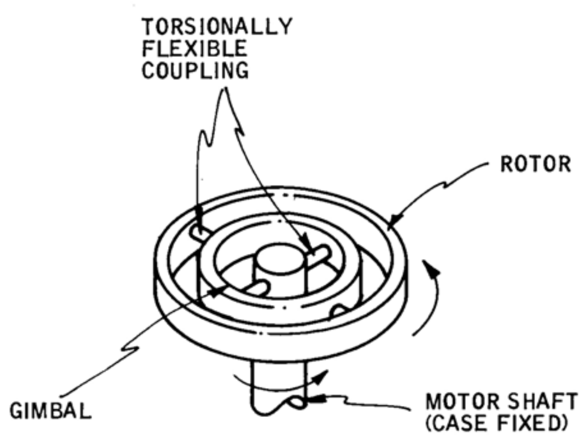


Figure 8. Tuned-rotor-gyro rotor assembly.

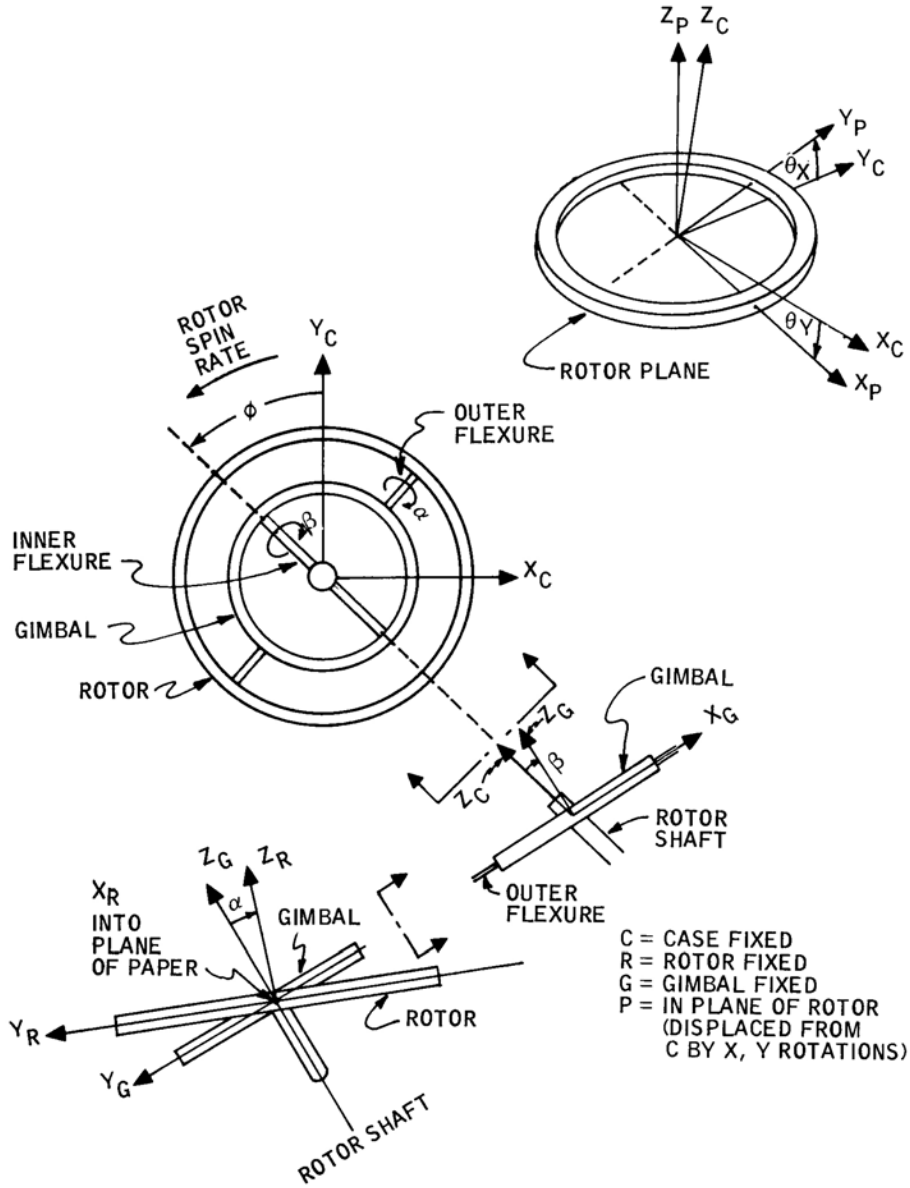


Figure 9. Tuned-rotor-gyro coordinate-frame geometry.

$$\begin{aligned} \alpha &= \theta_x \cos\phi + \theta_y \sin\phi \\ \beta &= \theta_y \cos\phi - \theta_x \sin\phi \end{aligned} \tag{12a}$$

and their inverse

$$\begin{aligned} \theta_x &= \alpha \cos\phi - \beta \sin\phi \\ \theta_y &= \beta \cos\phi + \alpha \sin\phi \end{aligned} \tag{12b}$$

The torque equation for the gimbal and rotor about the gimbal Y-axis is

$$\tau^G_{G_y} = \tau^G_{G\alpha_y} - C_\beta\dot{\beta} - K_\beta\beta + \tau^G_{Ge_y}$$

or

$$\tau^G_{G\alpha_y} = \tau^G_{G_y} + C_\beta\dot{\beta} + K_\beta\beta - \tau^G_{Ge_y} \tag{13}$$

where

$\tau^G_{G_y}$ = total torque on the gimbal about the gimbal (superscript) Y-axis

$K_\beta$ = torsional spring constant for the $\beta$ flexure

$C_\beta$ = torsional damping torque associated with $\beta$ flexure movement (e.g., caused by interaction of the gimbal with the surrounding gas)

$\tau^G_{G\alpha_y}$ = Y-axis reaction torque on the gimbal at the $\alpha$ flexure junction

$\tau^G_{Ge_y}$ = spurious (unwanted) error producing torques on the gimbal about the gimbal Y-axis

Torques on the rotor can be similarly written along gimbal X, Y, and Z axes

$$\begin{aligned}
\tau^G_{R_x} &= \tau^G_{RT_x} - C_\alpha\dot{\alpha} - K_\alpha\alpha + \tau^G_{Re_x} \\
\tau^G_{R_y} &= \tau^G_{RT_y} + \tau^G_{R\alpha_y} + \tau^G_{Re_y} = \tau^G_{RT_y} + \tau^G_{Re_y} - \tau^G_{G\alpha_y} \\
\tau^G_{R_z} &= \tau^G_{RT_z} + \tau^G_{R\alpha_z} + \tau^G_{Re_z}
\end{aligned} \tag{14}$$

where

$\tau^G_{R_i}$ = total torque on the rotor about the gimbal i-axis (i = X, Y, or Z)

$K_\alpha$ = torsional spring constant for the $\alpha$ flexure

$C_\alpha$ = damping torque associated with $\alpha$ flexure movement

$\tau_{R\alpha_i}$ = reaction torque on the rotor at the $\alpha$ flexure junction about the gimbal i-axis (i = Y or Z)

$\tau^G_{Re_i}$ = error torque on the rotor about the gimbal i-axis (i = X, Y, or Z)

$\tau^G_{RT_i}$ = electrically applied torque-generator torque on the rotor about the gimbal i- axis (i = X, Y, or Z) intentionally applied through the gyro torquer

The Y-axis component of Eq. (14) relates the Y-axis torque on the rotor at the $\alpha$ flexure ($\tau^G_{R\alpha_y}$) to the negative of the equivalent reaction torque on the gimbal ($\tau^G_{G\alpha_y}$) given by Eq. (13).

Equations (14) with (13) can now be transformed to their equivalent form in pickoff coordinates

$$\underline{\tau}^P_R = C^P_G\left(\underline{\tau}^G_{RT} + \underline{\tau}^G_{Re} + \begin{bmatrix} -\ C_\alpha\dot{\alpha} - K_\alpha\alpha \\ -\left(\tau^G_{G_y} + K_\beta\beta + C_\beta\dot{\beta}\right) + \tau^G_{Ge_y} \\ \tau^G_{R\alpha_z} \end{bmatrix}\right) \tag{15}$$

where

$C^P_G$ = direction cosine matrix relating gimbal and pickoff coordinate axes

$\underline{\tau}^G_{RT}, \underline{\tau}^G_{Re}$ = vectors with Eq. (14) gimbal-frame components $\tau^G_{RT_x}$, $\tau^G_{RT_y}$, etc.

$\underline{\tau}^P_R$ = net rotor torque in pickoff axes

Using small-angle theory (for $\alpha$, $\beta$), the $C^P_G$ matrix can be shown to be

$$C^P_G = \begin{bmatrix} \cos\phi & -\sin\phi & -\alpha\sin\phi \\ \sin\phi & \cos\phi & \alpha\cos\phi \\ 0 & -\alpha & 1 \end{bmatrix}$$

Substituting in Eq. (15) and expanding

$$\tau_{R_x}^P = \tau_{RT_x}^P + (\tau_{Re_x}^P - \tau_{Ge_y}^G \sin \phi) - (C_\alpha \dot{\alpha} + K_\alpha \alpha) \cos \phi$$

$$+ (\tau_{G_y}^G + C_\beta \dot{\beta} + K_\beta \beta) \sin \phi - \tau_{R\alpha_z}^G \alpha \sin \phi$$

$$\tau_{R_y}^P = \tau_{RT_y}^P + (\tau_{Re_y}^P + \tau_{Ge_y}^G \cos \phi) - (C_\alpha \dot{\alpha} + K_\alpha \alpha) \sin \phi \tag{16}$$

$$- (\tau_{G_y}^G + C_\beta \dot{\beta} + K_\beta \beta) \cos \phi + \tau_{R\alpha_z}^G \alpha \cos \phi$$

$$\tau_{R_z}^P = (\tau_{Re_z}^P - \alpha \, \tau_{Ge_y}^G) + \tau_{R\alpha_z}^G + \alpha \, (\tau_{G_y}^G + K_\beta \beta + C_\beta \dot{\beta})$$

where

$\tau_{R_i}^P, \tau_{RT_i}^P, \tau_{Re_i}^P$ = components of $\underline{\tau}_R^P, \underline{\tau}_{RT}^P, \underline{\tau}_{Re}^P$

Note that the Z component of $\underline{\tau}_{RT}^P$ is absent in Eq. (16). This is because the gyro torquer is designed to apply torque to only the rotor in the rotor plane.

The Z expression in Eq. (16) can be used to solve for $\tau_{R\alpha_z}^G$ for substitution in the X, Y equations. After dropping $\alpha$-squared terms as second order, the result is

$$\tau_{R_x}^P = \tau_{RT_x}^P - \tau_{R_z}^P \alpha \sin \phi - (C_\alpha \dot{\alpha} + K_\alpha \alpha) \cos \phi$$

$$+ (\tau_{G_y}^G + C_\beta \dot{\beta} + K_\beta \beta) \sin \phi + \tau_{e_x} \tag{17}$$

$$\tau_{R_y}^P = \tau_{RT_y}^P + \tau_{R_z}^P \alpha \cos \phi - (C_\alpha \dot{\alpha} + K_\alpha \alpha) \sin \phi$$

$$- (\tau_{G_y}^G + C_\beta \dot{\beta} + K_\beta \beta) \cos \phi + \tau_{e_y}$$

In Eq. (17), the $\tau_{e_x}$ and $\tau_{e_y}$ terms are the composite of all the error effects in the X, Y torque equations.

The momentum transfer equations relating the torques in Eq. (17) to rotational movement of the rotor assembly are now developed to obtain the input/output equations for the tuned-rotor gyro.

The angular rate of the gimbal in gimbal axes is given by

$$\underline{\omega}_G^G = C_C^G (\underline{\omega}_C^C + \underline{\omega}_r^C) + \dot{\underline{\beta}}^G \tag{18}$$

where

$\underline{\omega}_G^G$ = gimbal inertial angular rate vector in gimbal axes

$\underline{\omega}_C^C$ = gyro case angular rate vector in case axes

$\underline{\omega}_r^C$ = spin-motor rate vector in case axes

$\dot{\underline{\beta}}^G$ = rate of change of the $\beta$ angle-vector ($\underline{\beta}^G$) in gimbal axes

$C_C^G$ = direction-cosine matrix relating case and gimbal axes

The $C_C^G$ matrix is given from Figure 9 by

$$C_C^G = \begin{bmatrix} \cos \phi & \sin \phi & -\beta \\ -\sin \phi & \cos \phi & 0 \\ \beta \cos \phi & \beta \sin \phi & 1 \end{bmatrix} \tag{19}$$

The momentum-transfer equation for the gimbal in gimbal axes is given by

$$\underline{\tau}_G^G = I_G^G \, \dot{\underline{\omega}}_G^G + \underline{\omega}_G^G \times (I_G^G \, \underline{\omega}_G^G) \tag{20}$$

where

$I_G^G$ = inertia tensor for the gimbal in gimbal axes

With Figure 9, the components of the elements in Eq. (18) and (20) can be defined as

$$\underline{\omega}_C^C = \begin{pmatrix} \omega_\mu \\ \omega_\nu \\ \omega_\xi \end{pmatrix}$$

$$\underline{\omega}_r^C = \begin{pmatrix} 0 \\ 0 \\ \omega_r \end{pmatrix} \qquad (21)$$

$$\dot{\underline{\beta}}^G = \begin{pmatrix} 0 \\ \dot{\beta} \\ 0 \end{pmatrix}$$

$$I_G^G = \begin{bmatrix} I_G & 0 & 0 \\ 0 & I_G & 0 \\ 0 & 0 & J_G \end{bmatrix}$$

where

$\omega_\mu$, $\omega_\nu$, $\omega_\xi$ = X, Y, Z components of case rate $\underline{\omega}_C$ in case axes

$\omega_r$ = spinmotor rate

$I_G$, $J_G$ = gimbal moments of inertia about the X, Y axes, and about the Z polar axis

Substituting Eq. (18), (19), and (21) into Eq. (20), noting that $\dot{\phi} = \omega_r$, and neglecting $\beta$-squared effects as second-order yields the expression for the gimbal Y-axis torque for Eq. (17)

$$\tau_{G_y}^G = I_G \left[ \ddot{\beta} + (\dot{\omega}_\nu - \omega_r \omega_\mu) \cos \phi - (\dot{\omega}_\mu + \omega_r \omega_\nu) \sin \phi \right] + (I_G - J_G) \left[ -\beta \omega_r^2 + \omega_r (\omega_\mu \cos \phi + \omega_\nu \sin \phi - 2 \beta \omega_\xi) + \omega_\xi (\omega_\mu \cos \phi + \omega_\nu \sin \phi) \right] \qquad (22)$$

The $\dot{\alpha}$, $\dot{\beta}$, $\ddot{\beta}$ expressions for Eq. (17) and (22) are obtained by differentiating Eq. (11)

$$\begin{aligned} \dot{\alpha} &= \dot{\theta}_x \cos \phi + \dot{\theta}_y \sin \phi + \omega_r \beta \\ \dot{\beta} &= \dot{\theta}_y \cos \phi - \dot{\theta}_x \sin \phi - \omega_r \alpha \\ \ddot{\beta} &= \ddot{\theta}_y \cos \phi - \ddot{\theta}_x \sin \phi - \alpha \dot{\omega}_r - 2 \omega_r (\dot{\theta}_y \sin \phi + \dot{\theta}_x \cos \phi) - \omega_r^2 \beta \end{aligned} \qquad (23)$$

To develop an expression for the rotor torque-momentum-transfer equation (for $\tau_{R_x}^P$ and $\tau_{R_y}^P$ in Eq. (17)), the net rotor angular rate in the P frame is first defined as the sum of its consecutive (Euler) angular-rate-vector components

$$\underline{\omega}_R^P = C_C^P (\underline{\omega}_C^C + \underline{\omega}_r^C) + C_G^P (\dot{\underline{\alpha}}^G + \dot{\underline{\beta}}^G) \qquad (24)$$

where

$\underline{\omega}_R^P$ = total rotor inertial angular rate in P coordinates

$\dot{\underline{\alpha}}^G$ = rate of change of the $\alpha$ torsion flexure angle-vector in gimbal-frame coordinates

$C_C^P$, $C_G^P$ = direction-cosine matrices relating P, C, and G

The pickoff angle $\theta$ is the angle between case and pickoff axes, hence, the first term in Eq. (24) assuming small angles is

$$C_C^P(\underline{\omega}_C^C + \underline{\omega}_r^C) = \underline{\omega}_C^C + \underline{\omega}_r^C - \underline{\theta}^C \times (\underline{\omega}_C^C + \underline{\omega}_r^C) \tag{25}$$

If the $\alpha,\beta$ effects in $C_G^P$ are neglected as second order, $C_G^P$ in Eq. (24) can be approximated by the cosine matrix for Z-axis $\phi$ angle rotation generated by $\omega_r$ (see Figure 9). Recognizing that $\underline{\theta}$ is the vector sum of $\underline{\alpha}$ and $\underline{\beta}$, the second term in Eq. (24) can be written as

$$C_G^P(\underline{\dot{\beta}}^G + \underline{\dot{\alpha}}^G) = C_G^P\,\underline{\dot{\theta}}^G \approx \underline{\dot{\theta}}^C + \underline{\theta}^C \times \underline{\omega}_r^C \tag{26}$$

where

$\underline{\dot{\theta}}^c$ = rate of change of the pickoff angle $\underline{\theta}$ as measured in case (or pickoff) coordinates

Substituting Eq. (25) and (26) into Eq. (24) defines the rotor rate in terms of known matrix quantities

$$\underline{\omega}_R^P = \underline{\omega}_C^C + \underline{\omega}_r^C - \underline{\theta}_C^C \times \underline{\omega}_C^C \tag{27}$$

An expression for the P frame rotation rate as measured in the P frame is obtained similarly

$$\underline{\omega}_P^P = C_C^P\underline{\omega}_C^C + \underline{\dot{\theta}}^C = \underline{\omega}_C^C + \underline{\dot{\theta}}^C - \underline{\theta}^C \times \underline{\dot{\omega}}_C^C \tag{28}$$

The momentum transfer equation for the rotor can be written in P coordinates as

$$\underline{\tau}_R^P = I_R^P\,\underline{\dot{\omega}}_R^P + \underline{\omega}_P^P \times (I_R^P\,\underline{\omega}_R^P) \tag{29}$$

where

$\underline{\tau}_R^P$ = net torque on the rotor assembly in P coordinates

$I_R^P$ = inertia tensor for the rotor in P coordinates

Particular vector and matrix elements in Eq. (27) through (29) are defined as

$$\underline{\theta}^C = \begin{pmatrix} \theta_x \\ \theta_y \\ 0 \end{pmatrix}$$

$$\underline{\dot{\theta}}^C = \begin{pmatrix} \dot{\theta}_x \\ \dot{\theta}_y \\ 0 \end{pmatrix}$$

$$I_R^P = \begin{bmatrix} I_R & 0 & 0 \\ 0 & I_R & 0 \\ 0 & 0 & J_R \end{bmatrix}$$

With Eq. (21) for the remaining vector definitions, Eq. (29) can be expanded to obtain the desired scalar expressions for the torque-momentum-transfer equations along P frame axes

$$\begin{aligned}
\tau_{R_x}^P &= I_R(\dot{\omega}_\mu + \ddot{\theta}_x - \dot{\theta}_y\,\omega_\xi - \theta_y\,\dot{\omega}_\xi) + J_R\,\omega_r(\omega_\nu + \dot{\theta}_y + \theta_x\,\omega_\xi) + (J_R - I_R)\,\omega_\xi(\omega_\nu + \dot{\theta}_y) \\
\tau_{R_y}^P &= I_R(\dot{\omega}_\nu + \ddot{\theta}_y + \dot{\theta}_x\,\omega_\xi + \theta_x\,\dot{\omega}_\xi) - J_R\,\omega_r(\omega_\mu + \dot{\theta}_x - \theta_y\,\omega_\xi) - (J_R - I_R)\,\omega_\xi(\omega_\mu + \dot{\theta}_x) \\
\tau_{R_z}^P &\approx J_R(\dot{\omega}_r + \dot{\omega}_\xi)
\end{aligned} \tag{30}$$

Equations (17), (22), and (30), with Eq. (12a) and (23) in combination define the dynamic response relations for the tuned-rotor gyro. Before combining, additional nomenclature is introduced to simplify the form of the final result and to account for gyro-case misalignments.

The $\alpha$ and $\beta$ torsion-flexure spring constants are defined to be equal to a nominal value $K_o$ plus small error variations

$$\begin{aligned}
K_\alpha &= K_o + \Delta K_\alpha \\
K_\beta &= K_o + \Delta K_\beta
\end{aligned} \tag{31}$$

The following definitions are introduced for the inertia terms

$$
\begin{aligned}
J &= J_R + \frac{1}{2} J_G \\
I &= I_R + \frac{1}{2} I_G \\
L_G &= I_G - \frac{1}{2} J_G
\end{aligned}
\tag{32}
$$

The spinmotor rate is defined as a nominal value ($\omega_{r_o}$) plus a variation ($\delta_{\omega_r}$) due to motor dynamics; and a nominal gyro angular momentum ($H_o$) is defined

$$
\begin{aligned}
\omega_r &= \omega_{r_o} + \delta_{\omega_r} \\
H_o &= J\omega_{r_o}
\end{aligned}
\tag{33}
$$

The torque-generator torque is defined in terms of a gyroscopic precessional command rate with a scale-factor and cross-coupling error; and the error torque is equated to a bias rate defined as the torque-generator command-rate needed to nullify the effect of the error torque on the rotor

$$
\begin{aligned}
\tau_{RT_x} &= \frac{H_o}{(1+\epsilon_y)} \omega_{T_y} + \beta_{y_x} \omega_{T_x} \\
\tau_{RT_y} &= -\frac{H_o}{(1+\epsilon_x)} \omega_{T_x} + \beta_{x_y} \omega_{T_y} \\
\tau_{e_x} &= -\frac{H_o}{(1+\epsilon_y)} \omega_{\beta_y} \\
\tau_{e_y} &= \frac{H_o}{(1+\epsilon_x)} \omega_{\beta_x}
\end{aligned}
\tag{34}
$$

where

$\omega_{T_x}, \omega_{T_y}$ = X- and Y-axis torquer command rates

$\beta_{y_x}, \beta_{x_y}$ = torquer cross-coupling errors (Y command rate into X-axis, and X command rate into Y-axis)

$\epsilon_x, \epsilon_y$ = X- and Y-axis torquer scale-factor errors

$\omega_{B_x}, \omega_{B_y}$ = gyro X- and Y-axis bias rates

The gyro case axes may be misaligned from nominal gyro axes by small misalignment angles $\gamma_x$, $\gamma_y$, and $\gamma_z$

$$
\begin{aligned}
\omega_\mu &= \omega_x + \gamma_z \omega_y - \gamma_y \omega_z \\
\omega_\nu &= \omega_y + \gamma_x \omega_z - \gamma_z \omega_x \\
\omega_\xi &= \omega_z + \gamma_y \omega_x - \gamma_x \omega_y
\end{aligned}
\tag{35}
$$

Finally, the following trigonometric identities are noted

$$
\begin{aligned}
\sin^2 \phi &= \frac{1}{2} - \frac{1}{2} \cos 2\phi \\
\cos^2 \phi &= \frac{1}{2} + \frac{1}{2} \cos 2\phi \\
\sin \phi \cos \phi &= \frac{1}{2} \sin 2\phi
\end{aligned}
\tag{36}
$$

With Eq. (31) through (36), Eq. (11), (17), (22), (23), and (30) can now be combined to yield the input/output equations for the tuned-rotor gyro. Upon combination, rearrangement, introducing the fact that the gimbal inertia is significantly less than the rotor inertia, neglecting higher-order effects, and assuming that angular vibration inputs at exactly twice spin-frequency have negligible liklihood, yields the results in Eq. (37a) and (37b).

$$\omega_{T_x} = (1+\epsilon_x)\,[(\omega_x+\dot{\theta}_x) + \gamma_z\,\omega_y - (\gamma_y+\theta_y)\,\omega_z + \beta_{x_y}\,\omega_{T_y} - \frac{I}{H_o}(\dot{\omega}_y + \ddot{\theta}_y) + \frac{(J-I)}{H_o}\,\omega_z\,(\omega_x+\dot{\theta}_x)$$

$$+ \frac{J}{H_o}(\omega_x+\dot{\theta}_x)\,\delta_{\omega_r}] + \omega_{B_x} - \frac{1}{H_o}[(K_o - L_G\,\omega_{r_o}^2) - 2L_G\,\omega_{r_o}\,\delta\omega_r + \frac{1}{2}(\Delta K_\alpha + \Delta K_\beta)]\theta_y \qquad (37a)$$

$$+ \frac{1}{2J}(C_\alpha + C_\beta)\,\theta_x$$

$$\omega_{T_y} = (1+\epsilon_y)\,[(\omega_y+\dot{\theta}_y) - \gamma_z\,\omega_x + (\gamma_x+\theta_x)\,\omega_z - \beta_{y_x}\,\omega_{T_x} + \frac{I}{H_o}(\dot{\omega}_x + \ddot{\theta}_x) + \frac{(J-I)}{H_o}\,\omega_z\,(\omega_y+\dot{\theta}_y) \qquad (37b)$$

$$+ \frac{J}{H_o}(\omega_y+\dot{\theta}_y)\,\delta\omega_r] + \omega_{B_y} + \frac{1}{H_o}[(K_o - L_G\,\omega_{r_o}^2) - 2L_G\,\omega_{r_o}\,\delta\omega_r + \frac{1}{2}(\Delta K_\alpha - \Delta K_\beta)]\,\theta_x$$

$$+ \frac{1}{2J}(C_\alpha + C_\beta)\,\theta_y$$

The $\delta\omega_r$ term in Eq. (37a)and (37b) is a function of the spinmotor dynamics, and can be described analytically by considering the rotor-gimbal assembly as the inertial load to the spinmotor. Neglecting gimbal-angle and misalignment effects as second order, and assuming that the rotor inertia is much larger than the gimbal inertia, provides the result given by Eq. (38)

$$J(\omega_z + \delta\omega_r) = \tau_r = f(\delta\omega_r) \qquad (38)$$

where

$\tau_r$ = spinmotor torque designed to maintain the rotor at nominal speed $\omega_{r_o}$

$f(\delta\omega_r)$ = functional operator indicating that the spinmotor torque is a function of the deviation of the rotor speed from nominal

Equations (37a) and (37b) show that the X and Y torquer command rates to the gyro ($\omega_{T_x}$, $\omega_{T_y}$) are proportional to the X- and Y-axis gyro input rates ($\omega_x$, $\omega_y$) plus dynamic and cross-coupling effects, the principal one being the pickoff-angle ($\theta_x$, $\theta_y$) nominal spring dynamic effect $[(K_o - L_G\omega_{r_o}^2)\theta]$. Due to the magnitude of $K_o$ and $L_G\,\omega_{r_o}^2$, this term could generate a significant rate error in the gyro for off-null pickoff operation (which is generally the case due to the inability to operate the gyro ideally with the pickoff angle held precisely at zero). To eliminate this as an error source, the nominal torsional-flexure spring constant $K_o$ is designed to cancel the dynamic term $L_G\,\omega_{r_o}^2$

$$K_o = L_G\,\omega_{r_o}^2 \qquad (39)$$

Setting the gimbal spring rates as specified by Eq. (39), the condition known as tuning, cancels the spring dynamic effect, and makes the rotor appear to be free of the gimbal case under off-null pickoff-angle conditions. Hence, the rotor is effectively uncoupled from the gyro case without the use of special pivots or flotation fluid as with the single-degree-of-freedom floated rate-integrating gyro. Note that the rotor-case freedom effect can be seen directly from Eq. (37a) and (37b) if the error terms and command rates are equated to zero. Under these conditions the equations collapse to the simplified form

$$\dot{\theta}_x = -\omega_x$$
$$\dot{\theta}_y = -\omega_y \qquad (40)$$

Hence, the pickoff angle becomes equal to the negative of the integral of the gyro-case motion, or equivalently, the gyro rotor is fixed inertially with the pickoff angle providing a direct measure of the gyro-case angular motion (i.e., the gyro acts as an ideal two-degree-of-freedom attitude sensor).

In strapdown applications the pickoff angle is maintained near null through closed-loop torquing, with the torquer command signals thereby becoming measures of input rate (in the integral sense). Such a scheme is illustrated by the analytical block diagram in Figure 10 which is a schematic representation of Eq. (37a), (37b), and (38) with Eq. (39).

If Eq. (37a), (38), and Figure 10 for the tuned-rotor gyro are compared with Eq. (8), (9), and Figure 3 for the single-degree-of-freedom floated rate-integrating gyro, it will be apparent that the two gyros contain similar dynamic error terms ($\gamma_y$, $\gamma_z$, $\theta_y$ misalignment coupling, $\dot{\omega}_y$ and $\ddot{\theta}_y$ angular acceleration effects, $\omega_z\,\omega_x$ anisoinertia, and $\omega_x\,\delta\omega_r$ motor dynamics). In addition, the tuned-rotor gyro contains the cross-coupling rate term ($\dot{\theta}_x$), torquer cross-coupling effects ($\beta_{xy}$), gimbal damping effects ($C_\alpha + C_\beta$), and the residual spring torque terms due to off-nominal tuning(the ($\Delta K_\alpha + \Delta K_\beta$) effect with nominal gyro spin speed and the effect of $\delta\omega_r$ spin-speed error with nominal spring constants)). It should also be apparent that the torque loops for the tuned rotor are dynamically more complex (due to two-axis cross-coupling) and undamped (the $C\dot{\theta}$ term for the floated gyro is not present in the tuned rotor). Hence, additional compensation electronics are required in the Figure 10 command electronics to achieve wide-bandwidth stable performance. In other respects, mechanization approaches for the torque loops are as described previously for torque-to-balance instruments in general.

The scale-factor-error model for the tuned-rotor gyro operating in the strapdown mode is given by Eq. (41) and is entirely equivalent to that for the floated rate-integrating gyro [Eq. (10)].

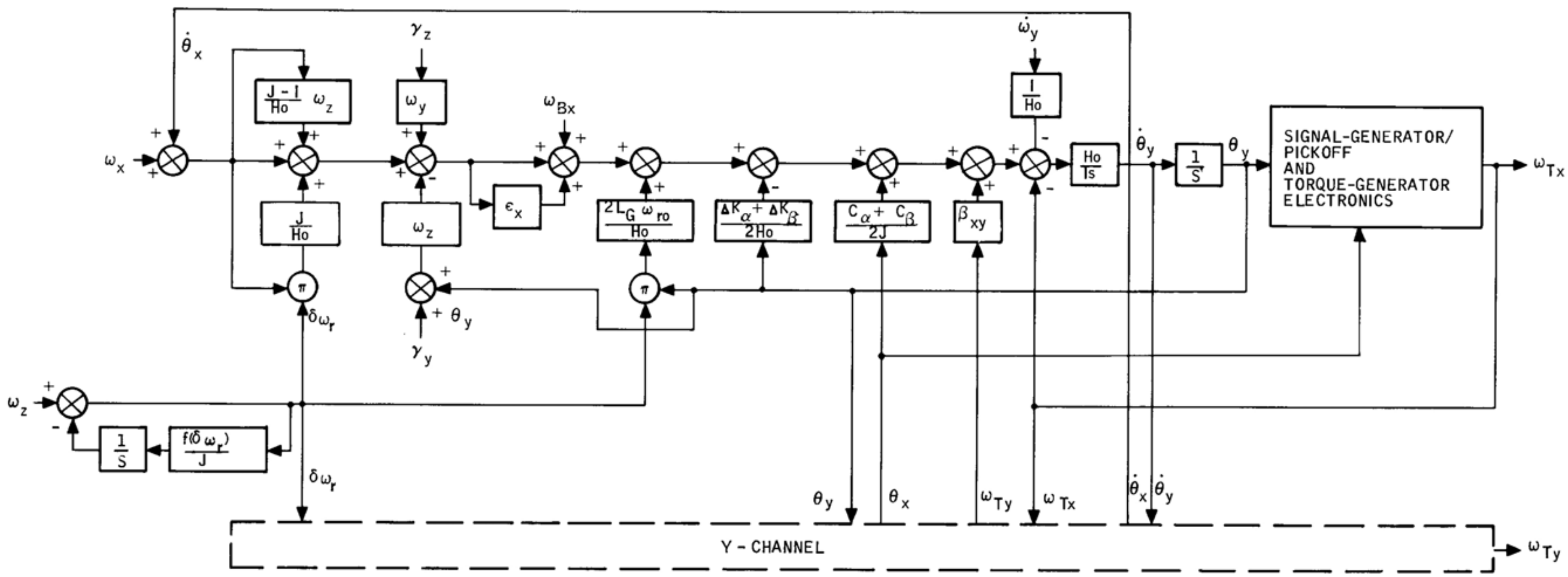


NOTE: (π) = MULTIPLICATION

Figure 10. Tuned-rotor-gyro analytical response diagram.

$$
\begin{aligned}
\varepsilon_x &= \varepsilon_{0_x} + \varepsilon_{1_x} \frac{\omega_x}{|\omega_x|} + \varepsilon_{2_x}\, \omega_x + \varepsilon_{3_x}\, \omega_x^2 \\
\varepsilon_y &= \varepsilon_{0_y} + \varepsilon_{1_y} \frac{\omega_y}{|\omega_y|} + \varepsilon_{2_y}\, \omega_y + \varepsilon_{3_y}\, \omega_y^2
\end{aligned} \tag{41}
$$

The bias errors for the tuned-rotor gyro ($\omega_{B_x}$ and $\omega_{B_y}$) can modeled (25, 26) as

$$
\begin{aligned}
\omega_{B_x} &= B_{0_x} + B_1\, a_x + B_2\, a_y + B_3\, a_x\, a_z + n_x \\
\omega_{B_y} &= B_{0_y} + B_1\, a_y - B_2\, a_x + B_3\, a_y\, a_z + n_y
\end{aligned} \tag{42}
$$

where

$a_x, a_y, a_z$ = accelerations of the gyro along the x, y, and z nominal gyro axes.

Note that the acceleration-sensitive bias coefficients in Eq. (42) are identical between axes (because they are caused by rotor-assembly effects which are common to X, Y channel outputs). A comparison between Eq. (42) and Eq. (11) (for the floated gyro) shows that the bias-error equations are of the same form. Sources of $B_0$ bias error for the tuned-rotor gyro are stray internally generated magnetic fields that interact with the rotor-mounted torquer magnet, and torque-loop/pulse-electronics bias errors (for binary torque loops or analog torque loops with follow-up analog-to-digital conversion, see Section 4). The effects of off-nominal tuning and gimbal damping in Eq. (37a) and (37b) are usually included as part of the $B_0$ bias error (in conjunction with pickoff-angle offsets caused, for example, by spinmotor-shaft misalignments or signal-generator/pickoff bias). Additional, but unlikely $B_0$ bias errors for the tuned-rotor gyro are caused by acceleration inputs at spin frequency along the spin axis rectifying radial mass-unbalance effects in the rotor assembly (relative to the center of torsional support for the rotor assembly), acceleration inputs at twice spin frequency normal to the spin axis rectifying gimbal mass-unbalance along the spin axis, and rectification of twice spin-speed angular-rate inputs to the gyro due to alternating inertial/spring reaction loads of the rotor-gimbal assembly relative to the motor shaft. (25, 26) The latter effect is predictable by the expressions used to develop Eq. (37a) and (37b) (neglected in the final Eq. (37a) and (37b) forms presented).

The $B_1$ g-sensitive coefficient is caused by mass-unbalance of the rotor assembly along the spin axis, and the $B_2$ coefficient, by geometrical imperfections in the torsional elements. (25, 27) The $B_3$ coefficient is the anisoelastic effect for the gyro caused by unequal compliance of the rotor assembly along the X, Y, Z directions. The n noise terms are stochastic errors that have relatively short correlation times (caused, for example, by spinmotor-shaft orientation changes due to ball bearing preload variations and resulting error torques created by off-nominal tuning).

As with the floated gyro, several errors in the tuned-rotor gyro are inherent in the basic instrument design (bandwidth limitation, anisoinertia, and angular acceleration sensitivity). The remaining errors are caused by imperfections in the gyro manufacture, many of which are predictable over long time intervals. System-level software compensation can be utilized to remove the predictable error effects within the bandwidth limitations of the uncompensated sensor-output signals (the signals utilized to compensate the dynamic-error effects).

### 5.2 Performance and Application Areas

The strapdown version of the tuned-rotor gyro has been developed for applications requiring performance in, or close to, the 1-nmi/hr category (refer to Table 1). Applications receiving the greatest attention have been for transport aircraft as a navigation system that also (and in some cases, primarily) provides high-quality outputs for flight-control-system use (Schuler-tuned attitude, inertially derived heading, body rates and accelerations, horizontal and vertical velocity) (8, 28). Enthusiasts for the strapdown tuned-rotor technology envision its ultimate utilization in higher-performance military aircraft (29). The lower-performance application areas (such as for tactical missile midcourse guidance) have not been pursued by tuned-rotor technologists, probably because of difficulties in competing with the lower-cost floated-gyro technologies that currently dominate this area. Some consideration is being given to the utilization of tuned-rotor inertial strapdown systems for spacecraft booster guidance, a small specialized area from a production standpoint, and one that has traditionally utilized high-quality floated rate-integrating gyros for implementation.

Specific performance capabilities of the tuned-rotor gyro parallel those for the floated gyro, with some notable exceptions. The tuned-rotor gyro was developed to eliminate some of the problems (in cost and performance) associated with older floated rate-integrating gyro technology. Proponents of the tuned-rotor technology point to its advantages compared to the floated gyro: fewer parts, two axes per gyro, elimination of the need for the fluid suspension and associated error mechanisms, elimination of flex-lead-error torques, elimination of spinmotor axial mass unbalance as an error source and associated simplifications in spinmotor bearing design, and more predictable instrument warmup characteristics. These advantages are partially offset by the addition of errors caused by imperfect rotor tuning, windage torques and drift errors associated with dynamic viscous coupling of the off-null gimbal motion with the surrounding gas; and rotor heating and motor bearing lubricant containment problems if a near vacuum is held around the rotor to eliminate the latter gas-dynamic effects.

For the tuned-rotor gyro, bias instabilities can be overcome largely through increased angular momentum [see Eq. (34)], with additional complexity in the torque loops due to the higher current levels needed for angular momentum caging. Based on the 1-nmi/hr system-level performance obtained in transport aircraft using strapdown tuned-rotor gyros with large angular momentum wheels, (4, 5) it can be assumed that the bias performance levels of Table 1 are achievable in benign flight environments using temperature modeling for compensation (without thermal controls). In dynamic flight environments, g-sensitive bias effects will degrade performance to some extent. Potential rectification errors that contribute to bias in the floated gyro are also present in the tuned rotor. As such, the potential for large bias error also exists for the tuned rotor in high linear- and angular-vibration environments (due to anisoinertia, spinmotor dynamics, anisoelasticity, pickoff-angle dynamic error, and bandwidth limitations for compensation).

Rate capability, bandwidth, and scale-factor accuracy for the strapdown tuned-rotor gyro (a torque-to-balance instrument) directly parallel that for the strapdown floated gyro with similar limitations (high vibration and angular rates). Bandwidths of 75 Hz and scale-factor accuracies of 50 ppm (with thermal modeling for compensation) have been achieved for tuned-rotor gyros at Boeing (30), and Litton (31) claims that bandwidths in excess of 85 percent of spin speed are achievable using new caging techniques. For typical tuned-rotor spin rates, this translates into a bandwidth in the 50- to 150-Hz area.

Alignment errors for tuned-rotor gyros are caused by pickoff null shift, torquer input-axis misalignment, dynamic torque-rebalance servo error, and gyro-system-mount misalignment. Due to the absence of the gimbal pivot and spinmotor-axis misalignment errors associated with the floated gyro, 5-seconds-of-arc alignment accuracy should be more easily achievable with the tuned-rotor gyro. As with the floated gyro, random noise is not a major error source for the tuned-rotor gyro.

For systems using tuned-rotor gyros with large angular momentum wheels, calibration intervals of greater than 6-months have been experienced for 1-nmi/hr benign environment system applications. (4, 5) Note, that if needed, the dual-speed spinmotor calibration technique developed for the floated gyro (see Section 2) can also be used with the tuned rotor, if necessary, to reduce the frequency of removals for system recalibration. Warmup times in the 2- to 5-minute category (for spinmotor runup and thermal stabilization) have been demonstrated by high-accuracy tuned-rotor gyros with thermal modeling for error compensation. (4, 5)

## 6. ELECTROSTATIC GYRO

Of the three angular-momentum devices considered in this paper, the electrostatic gyro comes closest to achieving the theoretically ideal suspension system. In the electrostatic gyro, a spherical rotor is suspended in a vacuum by an electrostatic field generated by case-fixed electrodes; hence, there is no physical contact with the rotor assembly. Pickoffs on the case sense the orientation of the case relative to the rotor. Figure 11 illustrates the implementation concept.

Some mechanizations of the electrostatic-gyro pickoff (17) have used optical detectors that sense scribe marks etched on the rotor. For such an approach, the rotor is a hollow shell, 1 to 2 inches in diameter (see Figure 11). Alternatively, a small solid rotor (typically 1 centimeter in diameter) can be used with a radially offset mass. (32) The resulting modulation in the suspension field (due to the mass unbalance) is used to determine the relative case/rotor orientation. Each of these approaches is being considered for gimbaled application. (32, 33, 34) However, only the small solid rotor approach is being considered today for strapdown application. (9, 34)

The electrostatic gyro can be used only as an attitude gyro (there is no torque-to-balance concept for the instrument); hence, in strapdown applications where large angular motion is common, the accuracy of the pickoff (which must sense the total attitude) is a key performance parameter. In this respect, the gyro differs from the floated and tuned-rotor instruments that are operated in strapdown applications with the pickoff-angle held near null.

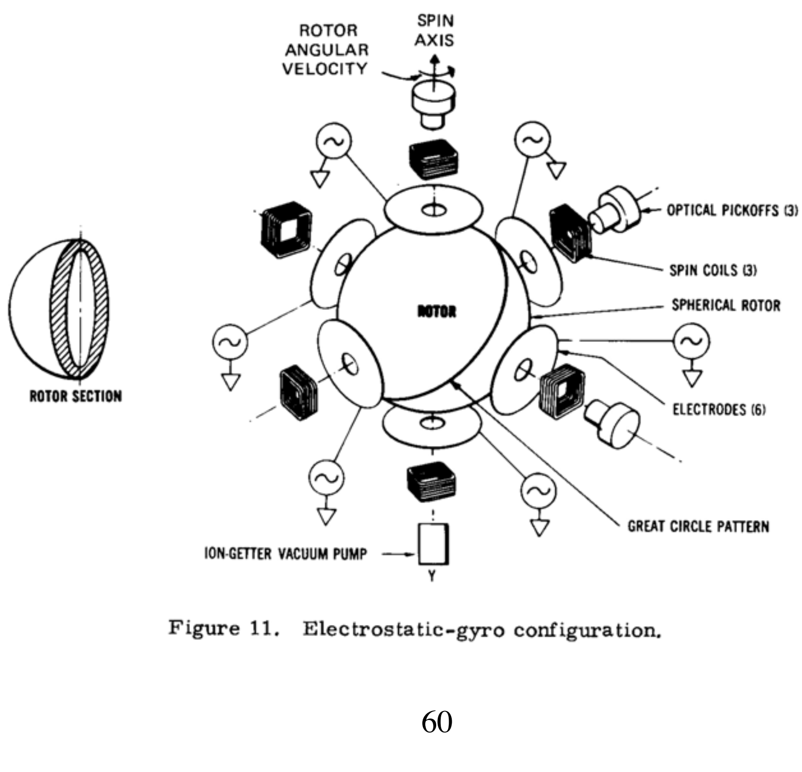


Figure 11. Electrostatic-gyro configuration.

One of the principal advantages of the electrostatic gyro compared to the other spinning-mass instruments is the elimination of mechanical friction producing mechanisms (i. e., spinmotor bearings) and associated reliability problems. A disadvantage for the electrostatic gyro from a reliability standpoint is the potential damage to the rotor and case that can result during a momentary loss in gyro-rotor suspension voltage while the rotor is spinning.

## 6.1 Analytical Description and Error Model

In one respect, the analytical model for the electrostatic gyro is much simplified compared to the torque-to-balance strapdown gyros (tuned-rotor and floated rate-integrating gyros) due to the lack of dynamic-error terms implicit in the design of the latter instruments. If the electrostatic gyro could be manufactured perfectly with ideal materials, it would have no error effects, and its output would be a true indication of the orientation of the gyro case relative to an inertially fixed rotor spin-axis (i. e., an ideal two-degree-of-freedom attitude gyro). However, due to imperfections that must exist in any real device, errors are present in the instrument that can be divided into two categories: bias errors, and (for strapdown applications) attitude readout errors. In very general terms, these errors can be represented as

$$
\begin{aligned}
\omega_{B_x} &= f_x(a_x, a_y, a_z, u_x, u_y, u_z) \\
\omega_{B_y} &= f_y(a_x, a_y, a_z, u_x, u_y, u_z) \\
\omega_{B_z} &= f_z(a_x, a_y, a_z, u_x, u_y, u_z) \\
\delta u_x &= g_x(u_x, u_y, u_z) + \gamma_z u_x - \gamma_x u_z \\
\delta u_y &= g_y(u_x, u_y, u_z) + \gamma_x u_y - \gamma_y u_x \\
\delta u_z &= g_z(u_x, u_y, u_z) + \gamma_y u_z - \gamma_z u_y
\end{aligned}
\tag{43}
$$

where

$\omega_{B_x}, \omega_{B_y}, \omega_{B_z}$ = components of gyro bias rate (in case axes); the bias vector represents the precessional rate of the rotor, and is normal to the rotor spin-axis

$a_x, a_y, a_z$ = three-axis acceleration components of the gyro case (in case axes)

$u_x, u_y, u_z$ = cosines of the angles between the rotor spin-axis and gyro-case axes (i. e., the attitude information sensed by the read-out detectors)

$f_x(\,), f_y(\,), f_z(\,)$ = functional operators indicating a functional dependence of the bias numerical values on the bracketed quantities

$\delta u_x, \delta u_y, \delta u_z$ = net attitude readout errors

$g_x(\,), g_y(\,), g_z(\,)$ = functional operators associated with the gyro readout mechanism indicating a functional dependence of the numerical values on the bracketed quantities

$\gamma_x, \gamma_y, \gamma_z$ = misalignments of gyro-case axes from nominal gyro axes

Due principally to the full spherical attitude operating mode of the strapdown electrostatic gyro, the bias and attitude readout error effects are complex functions of case-rotor orientation and accelerations in three dimensions. The bias attitude sensitivity is caused by the different orientation of the gyro suspension coils relative to the rotor and associated variations in the electrostatic suspension field (from nominal) in the rotor cavity that produces a net moment on the spinning rotor. Acceleration-induced bias-sensitivity effects are caused by the center of electrostatic suspension force on the rotor not coinciding with the rotor center of mass, also a function of the orientation of the case relative to the rotor. Attitude readout errors are caused by electronic instabilities and attitude nonlinearities in the pickoff over the full spherical readout range.

The f ( ) and g( ) elements in Eq. (43) are typically expressed as a set of compensation models that analytically characterize the error phenomena as a function of sensed acceleration ($a_x$, $a_y$, $a_z$), rotor-axis cosines ($u_x$, $u_y$, $u_z$), and gyro parameters (e. g., rotor case-envelope, and suspension-servo characteristics). (9) The gyro parameters in the models are the measurable quantities that characterize each gyro for calibration purposes (i. e., calibration coefficients). The stability of the coefficients from turn-on to turn-on, over temperature, vibration, and acceleration, as well as the complexity (number of terms) in the error model utilized, ultimately determines the performance capabilities of the gyro (and the complexity and frequency of calibration).

## 6.2 Performance and Application Areas

The principal focus for strapdown electrostatic gyro application has been in the 1-nmi/hr navigation system area where its proponents point to the cost and reliability advantages it affords compared to equivalent gimbaled INS technologies. However, because the electrostatic gyro is inherently an attitude-sensing instrument, its utility in other strapdown application areas (28, 29, 35) is limited (compared to the other strapdown gyros) due to its inability to also provide a rate-signal output. Deriving rate analytically in the electrostatic-gyro system computer (a nontrivial function of the calculated rate of change of the computed attitude data) provides a noisy signal (due to differentiated attitude pickoff noise) that must be filtered for reasonable low-noise rate-output performance. The resulting dynamic lag can introduce stability problems (in flight-control systems, for example) where the rate signal is utilized.

For a specified case orientation relative to the rotor (as in gimbaled applications), and with accurate thermal controls, electrostatic-gyro errors can be remarkably predictable and compensatible. However, for strapdown applications where the case can be at arbitrary orientations relative to the rotor, compensation is difficult. Due to the nonprecise mechanical nature and large size (relative to the rotor) of the suspension coils, it is difficult to manufacture a gyro that has a fixed center of suspension in the rotor cavity for all orientations of the rotor, case, and specific-force vector (hence, the problem of complex three-dimensional modeling for bias calibration coefficients. (6, 9). The calibration problem is further complicated by thermal expansion movement of the mechanical assemblies, and associated variations in the error coefficients. To compensate for this effect, thermal modeling has been used, but with limited success. Thermal control for the electrostatic gyro appears to be the only accurate method for direct bias-error control in strapdown applications.

To overcome some of these difficulties, Autonetics, the principal proponent of the electrostatic gyro for strapdown inertial navigation, has developed a turntable assembly for their MICRON strapdown electrostatic-gyro system, on which the inertial sensors are mounted. The turntable is rotated at a known rate relative to the system chassis, typically about the user vehicle yaw axis. The result is an averaging of the case-correlated bias-error effects such that the overall navigation error is improved. The effect of case rotation is expected to eliminate the need for the frequent calibrations that have accompanied the performance instabilities experienced in the past with the strapdown electrostatic gyro.

Reaction times for the electrostatic gyro have been a significant problem area in the past due to the sensitivity of gyro performance to temperature effects, and the difficulty in spinning up the gyros and thermally stabilizing the system (with temperature controls) in a reasonable time period. (6) Recent improvements in gyro design (for reduced thermal gradients) and the introduction of the turntable for error averaging are expected to allow reasonable reaction times (less than 10 minutes at the system level) for new strapdown electrostatic-gyro systems.

An important advantage for the electrostatic gyro in maneuvering applications is that direct attitude readout is provided and is, therefore, not subject to the unbounded computational attitude-error-buildup effects associated with rate-sensing strapdown gyros where attitude is calculated in the system computer (through a rate-integration process that also integrates the effects of rate-gyro scale factor error, misalignment cross-coupling, pulse-output quantization uncertainty, and finite bandwidth*). As a result, the alignment (and pickoff) accuracy requirements for the electrostatic gyro are somewhat relaxed compared to the other strapdown gyros because the associated attitude error over short maneuver times (relative to the Schuler period) is bounded (i.e., equals the bias on the gyro attitude-output signal).

For the strapdown solid-rotor electrostatic gyro, wide-angle readout accuracies of 18 seconds of arc have been achieved in the past (9, 34). This performance is somewhat marginal in high velocity-accuracy applications. However, it is reasonable to assume that improvements will be made such that the 10-second-of-arc goal in Table 1 is achieved in future production units. The alignment accuracy for the instrument is determined by the stability of the gyro-system mount, which should be well within Table 1 requirements.

The bandwidth and rate-gyro scale-factor accuracy requirements in Table 1 are not applicable to the electrostatic gyro. Random noise for the instrument is not a significant error source.

# 7. RING LASER GYRO

Unlike the gyros that utilize rotating mass for angular-measurement reference, the laser-gyro operating principal is based on the relativistic properties of light. The device has no moving parts; hence, it has the potential for extremely high reliability. References 36 and 37 describe this unique instrument, its mechanization approach, and performance characteristics.

Figure 12 depicts the basic operating elements in a laser gyro: a closed optical cavity containing two beams of correlated (single-frequency) light. The beams travel continuously between the reflecting surface of the cavity in a closed optical-path; one beam travels in the clockwise direction, the other in the counterclockwise direction, each occupying the same physical space in the cavity. The light beams are generated from the lasing action of a helium-neon gas discharge within the optical cavity. The reflecting surfaces are dielectric mirrors designed to selectively reflect the frequency associated with the particular helium-neon transition being used.

---

*The extent to which these error-effects accumulate in the rate-gyro strapdown-system computer is determined by the user vehicle angular-rate (and vibration) profile.

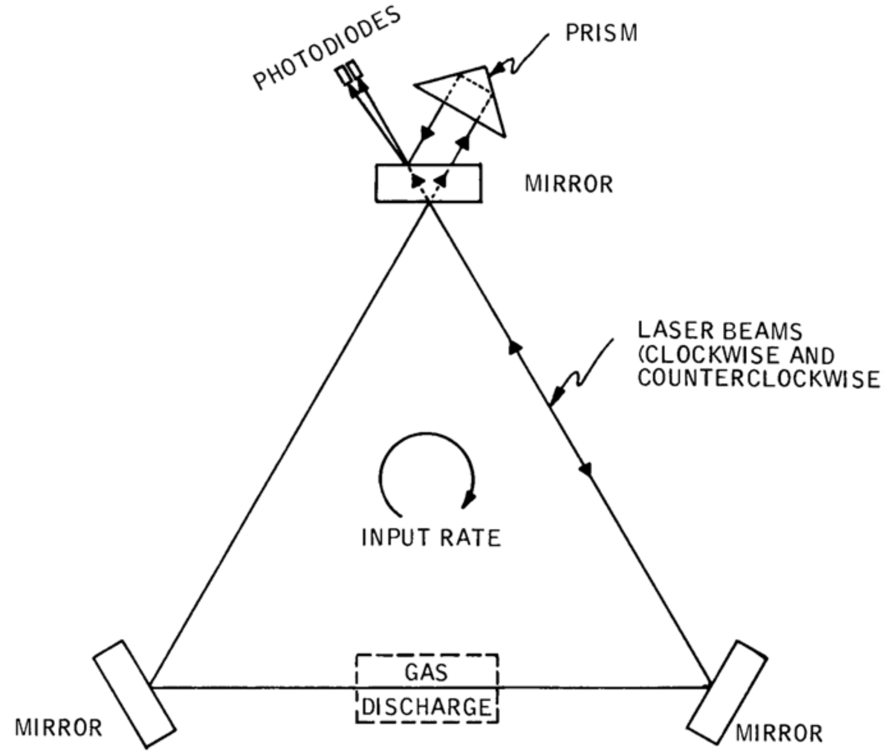


Figure 12. Laser-gyro operating elements.

To understand the operation of the laser gyro, consider the effect of cavity rotation on an observer rotating with the cavity. Relative to the observer, it takes longer for a wave of light to traverse the distance around the optical path in the direction of rotation than in the direction opposite to the rotation. Due to the constancy of the speed of light, this effect is interpreted by the observer as a lengthening of the net optical path length in the direction of rotation, and a shortening of the path length in the opposite direction. Because a fixed integral number of light waves must exist around the path at any instant of time (the beams are continuous, closing on themselves), the path-length shift must also be accompanied by a frequency shift in the opposite sense. The frequency difference between the two beams thereby becomes a measure of rotation rate.

The frequency difference is measured in the laser gyro by allowing a small percentage of the laser radiation to escape through one of the mirrors (Figure 12). A prism is typically used to reflect one of the beams such that it crosses the other in almost the same direction at a small angle (wedge angle). Due to the finite width of the beams, the effect of the wedge angle is to generate an optical fringe pattern in the readout zone. When the frequencies between the two laser beams are equal (under zero rate conditions), the fringes are stationary relative to the observer. When the frequencies of the two beams are different (under rotational rates), the fringe pattern moves relative to the observer at a rate and direction proportional to the frequency difference (i. e., proportional to the angular rate). More importantly, the passage of each fringe indicates that the integrated frequency difference (integrated input rate) has changed by a specified increment. Hence, each fringe passage is a direct indication of an incremental integrated rate movement, the exact form of the output needed for a rate-gyro strapdown navigation system.

Digital integrated-rate-increment pulses are generated from the laser gyro from the outputs of two photodiodes mounted in the fringe area and spaced 90 degrees apart (in fringe space). As the fringes pass by the diodes, sinusoidal output signals are generated, with each cycle of a sine wave corresponding to the movement of one fringe over the diodes. By observing which diode output is leading the other (by 90 degrees), the direction of rotation is determined. Simple digital-pulse triggering and direction logic operating on the photodiode outputs convert the sinusoidal signals to digital pulses for computer input.

The pulse size (quantization) for the laser gyro depends on the wavelength of the laser beam and the path length between the mirrors. For a typical triangular-optical-path laser gyro with 0.63 micron wavelength and pathlength between mirrors (each leg of the triangle) of 4.2 inches, the pulse size is 2 seconds of arc.*

*This pulse sizing assumes pulse triggering at the positive-going zero-crossing of one of the photodiode outputs. A factor of four finer pulse size is attainable if required by triggering output pulses at the positive- and negative-going zero crossings from both photodiode output signals. The penalty is a proportional decrease in maximum rate capability (or increased readout electronics complexity for increased bandwidth to maintain the same rate capability).

7.1 General Design Considerations

7.1.1 Construction -- The accuracy of the laser gyro depends on the manner in which the laser beams are affected by the influences of the lasing cavity. A key requirement in this regard is that the average of the path lengths around the lasing triangle for the clockwise and counterclockwise beams be constant and equal to the value for peak average lasing power. The peak-laser-power condition corresponds to the laser frequency being centered at the peak of the helium-neon gas-discharge Doppler gain curve. (38) Many of the error parameters in the laser gyro are stationary for small variations in gyro operation about the center of the Doppler gain curve. (37)

To achieve a high degree of path-length stability, the laser-gyro optical cavity is typically constructed of ceramic-vitreous (Cervit) material, which has an extremely low coefficient of thermal expansion. Figure 13 illustrates a typical laser-gyro mechanization concept. A Cervit structure is used to contain the helium-neon gas, with the lasing mirrors and electrodes forming the seals. High voltage (typically 1500 volts) applied across the electrodes (one cathode and two anodes) ionizes the helium-neon gas mixture, thereby providing the required laser pumping action. High-quality optical seals must be used in the Figure 13 configuration to avoid introducing contaminants into the helium-neon mixture, thereby degrading performance and ultimately limiting lifetime. Alternatively, a gain tube that contains the helium-gas can be inserted in the cavity, with optical windows (Brewster windows) provided for laser beam entry and exit (39). The advantage of the gain-tube approach is that the beam-cavity seal requirement (particularly for the mirrors) can be relaxed, since the helium-neon is no longer in contact with the mirror seals. The disadvantage is the addition of seals for the gain tube (Brewster window seals), and the introduction of acceleration and thermally sensitive gyro bias uncertainties due to differential phase shifts and energy losses (between the two laser beams) generated from birefringent (40) and anisotropic optical effects in the Brewster window optics.

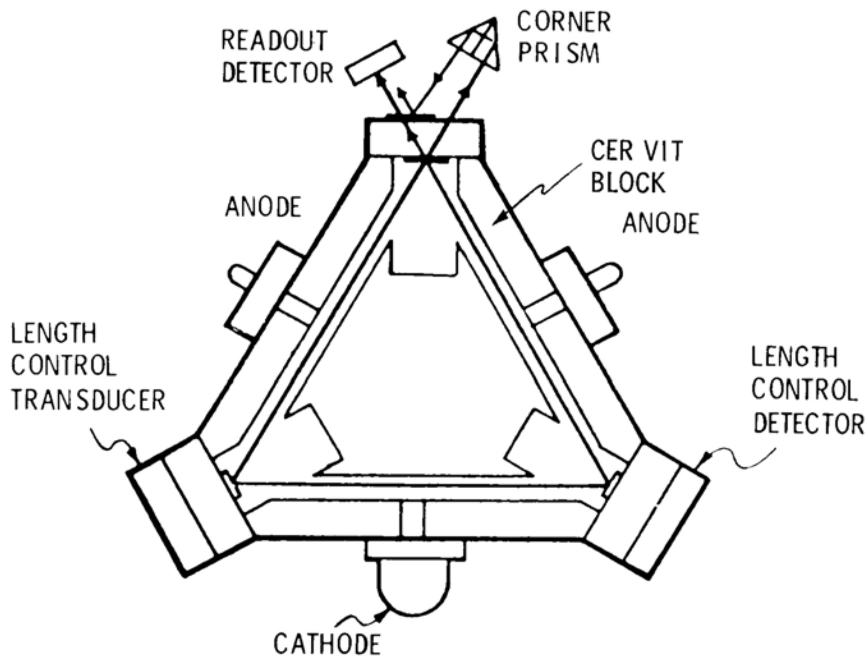


Figure 13. Laser-gyro block assembly.

Figure 14 illustrates the interface between a typical laser-gyro block assembly and the gyro electronics. A piezoelectric transducer mounted on one of the mirror substrates is typically used to control the path length of the cavity (Figures 13 and 14). The control signal for the transducer is proportional to the deviation from the peak of the average power in the laser beams; hence, the control loop is designed to maintain a path length that produces peak average lasing power. The average beam power is measured by a photodiode mounted on one of the mirrors that senses a small percentage of the radiation from both the clockwise and counterclockwise beams.

Flow phenomena in the laser gyro (e.g., Langmuir flow) can cause bias shifts due to differential changes in the index of refraction of light along the forward and reverse beam-paths. (37, 41) To reduce the possibility of net circular-flow phenomena in the gyro, circuitry is typically provided to maintain a constant balance between the net current flows in each of the two ionization paths (see Figure 14).

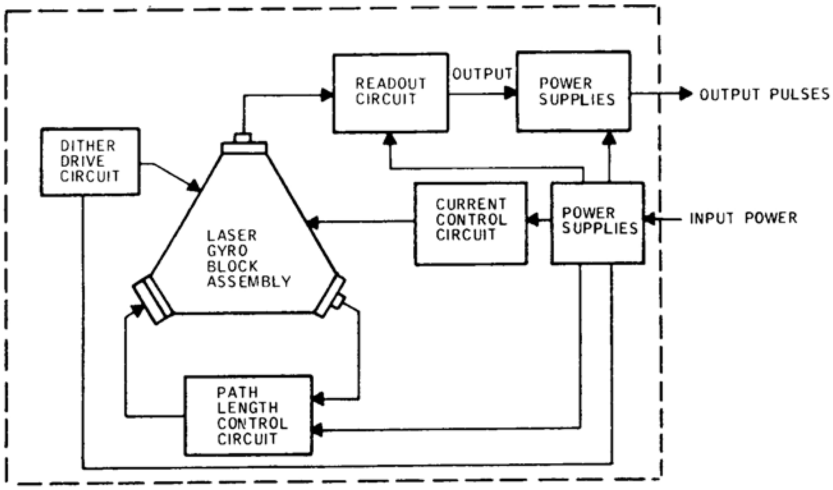


Figure 14. Laser-gyro electronic elements.

7.1.2 Packaging -- Figure 15 illustrates a typical laser gyro packaging concept. The electronics to control the laser and to provide readout pulses are mounted with the laser block in a single box. The high-voltage supply is included for gyro operations (regulated low-level voltages are gyro inputs). The box is hermetically sealed to avoid problems associated with high-voltage arcing at high altitudes.

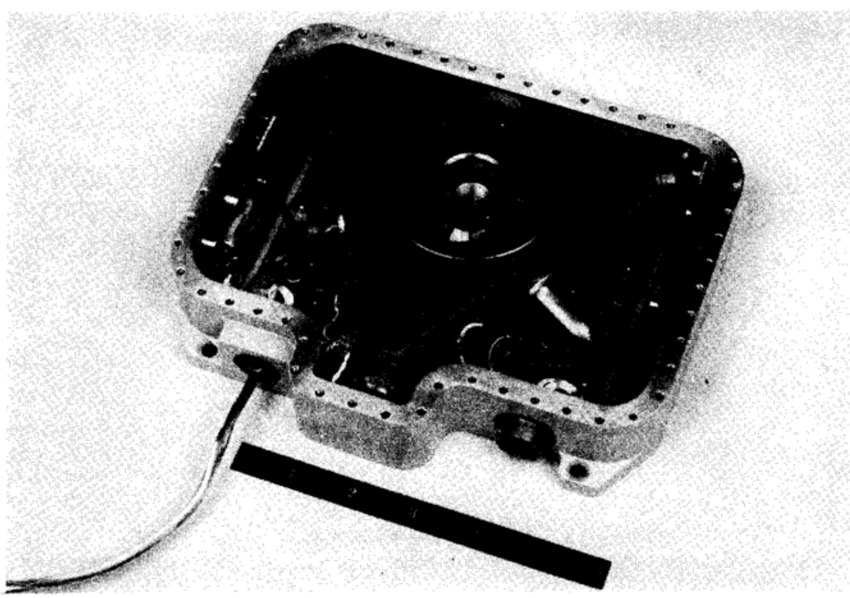

Figure 15. Honeywell GG1300 laser gyro.

Alternative packaging approaches incorporate three laser cavities in a single block of Cervit (e.g., Figure 16 or References 42 and 43). The advantage of the latter integrated concept is precise alignment-stability between gyro axes, and small size due to the ability to interweave the laser triangles. Disadvantages are the inability to replace a single gyro for maintenance actions, and difficulties in implementing mechanical dither for lock-in compensation.

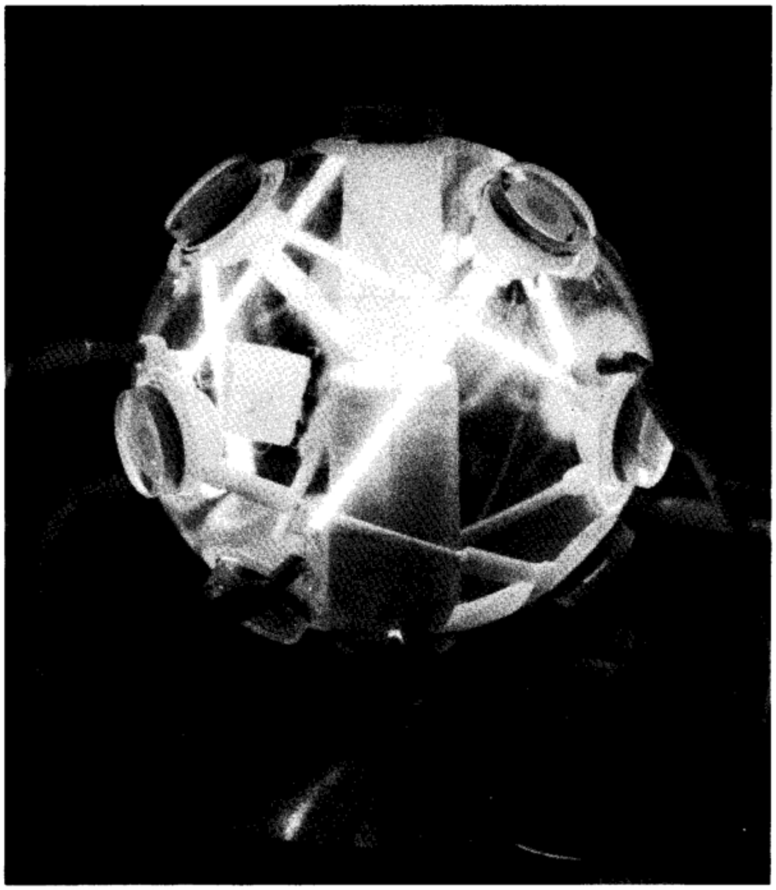

Figure 16. Honeywell GG1330 laser triad rate gyro.

7.1.3 Lock-in -- The phenomenon of lock-in has historically been a most prominent error source in the laser gyro and the most difficult to handle. The means for compensating lock-in has been the principal factor determining the configuration and performance of laser gyros from different manufacturers.

The phenomenon of laser-gyro lock-in arises because of imperfections in the lasing cavity, principally the mirrors, that produce backscattering from one laser beam into the other. (44) The resulting coupling action tends to pull the frequencies of the two beams together at low rates producing a scale-factor error. For rates below a threshold known as the lock-in rate, the two beams lock together at the same frequency producing no output (i.e., a dead-zone). Figure 17 illustrates the effect of lock-in on the output of the laser gyro as a function of steady input rate*.

The magnitude of the lock-in effect depends primarily on the quality of the mirrors. In general, lock-in rates on the order of 0.01 to 0.1 degree-per-second are the lowest levels achievable with today's laser gyro technology (with 0.63-micron laser wavelength). Compared with 0.01-degree-per-hour navigation requirements, this is a serious error source that must be overcome.

A straight-forward and effective approach for overcoming lock-in is mechanically dithering the laser block at high frequency through a stiff dither flexure suspension built into the gyro assembly. The spoked wheel-like structure in Figure 15 is a rotary spring. One spring on each side of the laser block suspends it from the center post. Piezoelectric transducers on one of the springs provide the dither-motor drive mechanism (Figure 14) to vibrate the lasing block at its resonant frequency about the input axis through a small angle but at high rates. The dither rate amplitude and acceleration are designed so that the dwell time in the lock-in zone is short such that lock-in will never develop. The result is a gyro that has continuous resolution over the complete rate range. The residual effect of lock-in is a negligible scale factor nonlinearity due to the averaging of the gyro input rate across the lock-in region (37), and a small random error in the gyro output (random rate noise) that is introduced each time the block passes through lock-in (at twice the dither frequency).

*Figure 17 illustrates the effect of lock-in under steady-state conditions (i.e., under relatively constant input rates). Lock-in is actually a nonlinear dynamic characteristic whose response is dependent on both the amplitude and frequency content of the gyro input rate. (37)

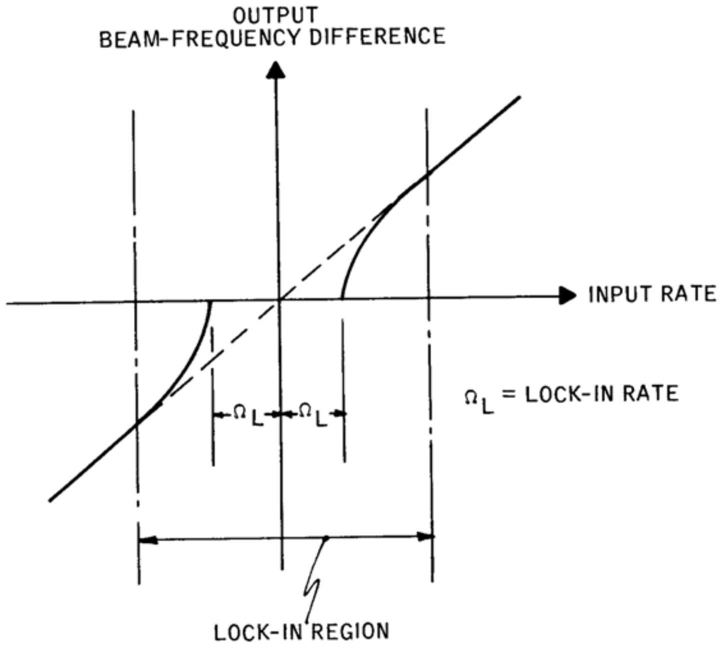


Figure 17. Laser gyro lock-in.

By mounting the readout reflector prism on the gyro case and the readout photodiodes on the block (Figure 13), a simple mechanism can be provided to remove the dither signal from the gyro output. If the gyro center of rotation is selected properly, the translation of the dither beam across the prism causes a fringe motion at the detector that identically cancels the dither rate sensed by the block. The result is an output signal that accurately measures the rotation of the gyro case, free from the dither oscillation. Alternatively, the readout-prism can be mounted with the readout-diodes directly on the gyro block, with a digital filter used to eliminate the unwanted dither motion from the gyro output. The penalty is the bandwidth limitation associated with the digital filter dynamic response.

7.1.4 Other Methods for Lock-in Compensation -- The original alternative to mechanical dither was the use of a Faraday cell within the laser cavity (37). A Faraday cell contains a magnetically active optical material whose index-of-refraction to circularly-polarized light can be altered by an applied magnetic field. Since laser gyros operate with plane-polarized laser beams, quarter wave plates must be included in the Faraday-cell to circularly polarize the light entering, and plane-polarize the light leaving the cell. By applying a magnetic field across the Faraday cell, a differential index-of-refraction shift is created between the clockwise and counterclockwise laser beams, producing a differential change in the optical path length between the two beams. A frequency difference or bias is thereby generated between the two beams with amplitude and phase determined by the amplitude and phase of the applied magnetic field. Typical Faraday-cell mechanizations have incorporated ac-coupled square-wave magnetic control-fields to washout bias errors associated with control-electronics offsets. The resulting bias, having known magnitude and phase is then easily removed from the gyro pulse-output circuitry by digital subtraction.

An alternate to the Faraday-cell approach is the magnetic-mirror concept (based on the transverse Kerr effect) in which a magnetically sensitive inner coating (e.g., iron) is applied to one of the laser mirrors. (39,45) By applying a magnetic field to the mirror transverse to the laser beam, a differential phase shift is introduced between the reflected clockwise and counterclockwise beams which appears as a differential path-length change around the cavity. The result is a bias imposed on the gyro output that is controllable by the applied magnetic field. Bias uncertainties can be compensated through use of an alternating biasing technique (such as the square-wave approach utilized with the Faraday cell). Additionally, the magnetic mirror can be operated in a saturated bias state to eliminate bias error susceptibility to stray magnetic fields, a problem with the Faraday cell which has generally required magnetic shielding around the gyro to minimize magnetically induced error effects.

An advantage for the Faraday-cell or magnetic-mirror concepts is the ability to develop lock-in bias compensation electrically without a mechanical dither flexure requirement for each gyro. As a result, high packaging densities are achievable through multi-gyro integration (e.g., Figure 16). Another advantage arises because of the ability to generate a square-wave dithered bias that has a low frequency and a rapid traversal rate through lock-in (i.e., short dwell time in the lock-in zone for each traversal, and few traversals per unit of time). Thus, lower random noise is generated from this potential error source (as contrasted with mechanically dithered units where, due to the inertial/spring physical characteristics of the gyro block/dither assembly, high traversal rates through lock-in to reduce random error each dither cycle tend to be accompanied by high dither frequencies, hence many random errors per unit time -- see subsection 7.1.3).

The principal difficulty with the Faraday-cell has been the introduction of thermally and acceleration-sensitive bias errors into the gyro through unpredictable birefringent and anisotropic effects in the Faraday cell. The latter error can be decreased by reducing the length of the Faraday cell (and its associated biasing capability). Reduction of bias capability, however, generates scale-factor nonlinearities due to the inability to keep the average rate into the gyro well outside of the lock-in region.

Little has been published on the error mechanisms associated with magnetic mirrors. Reference 45 indicates that magnetic mirrors designed for a large lock-in biasing capability also introduce large losses into the lasing cavity due to their accompanying low reflectivity. The loss effect is diluted as bias amplitude capability is reduced. Since higher gain and an accompanying degradation in gyro performance stability (see subsection 7.1.5) are required to overcome added cavity losses, this suggests that a tradeoff exists in the design of magnetic mirrors between increased gyro scale-factor nonlinearities (for low-bias-amplitude mirrors, hence less effective lock-in compensation) versus decreased gyro stability (for high-bias-amplitude mirrors). It also suggests that magnetic-mirror technology may be difficult to apply in 0.63-micron lasers (a higher accuracy gyro configuration compared to the 1.15-micron wavelength units but with lower available gain to overcome cavity losses; see subsection 7.1.5). Except for experimental models, laser gyros incorporating magnetic mirrors to date have only utilized the 1.15-micron transition, and have been implemented with lower amplitude lock-in biasing capabilities compared with mechanically dithered instruments. (39, 46)

Another approach for overcoming lock-in has been the multioscillator or differential laser gyro (DILAG) concept. (45, 47, 48, 49) This method also incorporates a Faraday bias cell, but in a manner that tends to cancel the effects of bias shift generated by the intrusion of the cell into the laser cavity. A polarizing crystal is used within the cavity to create two pairs of counter-rotating beams, each pair oppositely polarized from the other. Hence, two laser gyros are created in the same cavity, each being separable through use of a polaroid filter on the output. The effect of the opposite polarization between the two laser sets is to make each respond in the opposite sense to the applied Faraday bias. Hence, one gyro output becomes biased in the opposite direction from the other. Summing the two signals doubles the sensed rate signal and theoretically cancels the Faraday bias from the output, including the deleterious effects of bias uncertainties. As a result, high amplitudes of Faraday bias can be used, providing adequate capability for compensating lock-in. In addition, the need to use alternating bias is eliminated due to the cancellation of bias offset uncertainties at the gyro output.

The accuracy of the DILAG approach hinges on the degree to which error effects in the gyro pairs are equal and opposite. Little has been published in this regard in the open literature. One possible source of noncancelling bias error in the DILAG is anisotropic and birefringent effects in the polarizing crystal. Reference 50 suggests that the effect of off-nominal cavity tuning (i.e., operation off the center of the Doppler gain curve) can have a significant contribution to noncancelling bias errors in the DILAG. Because of the polarizing crystal and Faraday cell in the laser cavity, higher losses are present in the DILAG which must be compensated by higher gain. Decreased accuracy can thereby result (see subsection 7.1.5).

7.1.5 Laser Gyro Operating Wavelength -- Laser gyros have been designed for operation with 0.63-micron (visible red) or 1.15-micron (infrared) laser wavelengths. In general, the tradeoff between the two wavelength configurations has been higher accuracy but a more sophisticated design and manufacturing technology for the visible lasers, versus lower performance but simpler design and manufacturing methods for the infrared units.

From a performance standpoint, laser gyro lock-in, bias and scale-factor errors are generally lower for the 0.63-micron instruments. Lock-in is proportional to the operating wavelength squared (44), hence, other factors being equal, is a factor-of-four smaller for the 0.63-micron gyro. Laser gyro readout detectors (typically silicon) have a higher amplitude response to the 0.63-micron compared to the 1.15-micron wavelength, hence higher gains are generally required in 1.15-micron lasers for adequate output signal strength. Since laser gyro scale-factor error increases with laser gain (37, 44, 51) decreased scale-factor accuracy results. Langmuir flow also increases with increasing gyro gain (41), thus lower gyro bias stability is generally characteristic of 1.15-micron laser-gyro configurations.

Laser gain increases with increasing wavelength (38), hence higher gains are typically achievable with 1.15-micron units and cavity losses are more easily overcome (or conversely, cavity loss design and manufacturing requirements can be relaxed). For the 0.63-micron laser gyro, cavity design and manufacturing processes must be carefully controlled to assure that losses are stable and less than the available gain. From a mirror technology standpoint, the 1.15-micron laser dielectric mirror is typically simpler to design and manufacture, due to the lower sensitivity of its transmissibility characteristic with material parameter variations. The 0.63-micron mirror technology on the other hand can have significant transmissibility variations with parameter changes. Consequently 0.63-micron mirror materials must be more stable to maintain constant gain/loss characteristics in the laser cavity for repeatable gyro performance.

7.1.6 Size Versus Performance -- General scaling laws for laser gyros vary, depending upon gyro configuration and analytical error theory assumptions. Honeywell's experience with mechanically dithered units has been that lock-in and bias uncertainty vary inversely between the square and cube of the gyro path length, and scale-factor uncertainty varies inversely as the path length. (37, 51) Thus, laser gyro performance is heavily influenced by gyro size with the larger units being the most accurate.

## 7.2 Analytical Description and Error Model

Because the laser gyro is based on optical rather than inertial mass principles, the device has no acceleration-sensitive bias errors that corrupt its accuracy. Theoretically (without instrument imperfections), the laser gyro is an ideal single-degree-of-freedom incremental rate-integrating sensor.

The analytical model for the laser gyro parallels that for the single-degree-of-freedom floated gyro (see Eq. (8), (10), and (11)) with errors associated with mass properties removed

$$\omega_{OUTPUT} = (1 + \epsilon)(\omega_x + \gamma_z \omega_y - \gamma_y \omega_z) + \omega_B$$

$$\epsilon = \epsilon_o + f(|\omega_x|) + g(\omega_x) \tag{44}$$

$$\omega_B = B_o + n_1 + n_2$$

where

$\omega_{OUTPUT}$ = gyro-output signal

$\omega_x$ = gyro-input rate

$\epsilon$ = gyro scale-factor error

$\omega_B$ = gyro bias error

$\gamma_y, \gamma_z$ = misalignments of the gyro lasing plane relative to the nominal gyro input axis

$\omega_y, \omega_z$ = angular rotation rates of the gyro case normal to the input axis

$\epsilon_o$ = "fixed" scale-factor error

$f(|\omega_x|)$ = symmetrical (relative to positive and negative input rates) linearity error

$g(\omega_x)$ = generalized linearity error (containing symmetrical and asymmetrical components)

$B_o$ = "fixed" bias error

$n_1$ = random bias error with unbounded integral value

$n_2$ = random bias error with bounded integral value

It should be noted that the analytical model defined by Eq. (44) represents the net effective input/output relation for the laser gyro with control loops and lock-in compensation implemented. Analytical models for the "open-loop" gyro are available in the literature that define the dynamic characteristics of the lock-in effect (37, 44). In general, however, these models are valuable principally for gyro design; they are not useful for system-error-analysis purposes.

The "fixed" scale-factor-error coefficient ($\epsilon_o$) in Eq. (44) is caused principally by gain/loss variations in the laser cavity, laser path-length deviations from nominal due to manufacturing tolerances and, depending on design adequacy, residual thermal effects (anomalies in the path-length control loops in compensating residual thermal expansion of the Cervit laser cavity). The symmetrical scale-factor-error term ($f(|\omega_x|)$) is the residual effect of lock-in for laser gyros employing mechanical dither for compensation. (37) The $g(\omega_x)$ term is the residual effect of lock-in for gyros incorporating non-mechanical lock-in compensation. In general, the magnitude of the scale-factor linearity error for a given input rate is proportional to the degree to which the biased gyro input is removed from the lock-in region (on the average) divided by input rate being sensed (i. e., the linearity error is measured as a fraction of input rate). The width of the lock-in region is proportional to lock-in rate, thus, low scale-factor linearity error is achieved with a high ratio of applied bias to lock-in rate.

The $B_o$ fixed-bias term in the laser gyro is caused by circulating flow phenomena in the lasing cavity that cause differential optical path-length variations between the clockwise and counterclockwise laser beams (37, 41), forward-scattering effects caused by laser cavity interference with the laser (e. g., beam interractions with imperfect mirror surfaces) that produce differential phase shifts between the laser beams, and residual errors introduced by the lock-in compensation device. The latter effect is peculiar to laser gyros using nonmechanical lock-in compensation techniques.

The $n_1$ error is a white- or colored white-noise effect generated within the lasing cavity. A classical cause, in the case of mechanically-dithered laser gyros, is a random-angle error introduced each time the gyro input rate is cycled through the lock-in zone (twice each dither cycle). For laser gyros utilizing nonmechanical lock-in compensation, the $n_1$ random noise term is present, but its source is not as well understood. In general, $n_1$ is caused by random instabilities in the bias-producing mechanisms in the lasing cavity. The $n_1$ error is typically measured in terms of the root-mean-square value of its integral over a specified time period (that is long compared to the $n_1$ noise-process correlation-time). As with classical zero-mean random-noise processes, the average magnitude of the square of the integral of $n_1$ builds linearly with time; hence, the root-mean-square value builds as the square-root of time. The performance figure for $n_1$ is typically expressed in degrees-per-square-root-of-hour (deg/$\sqrt{hr}$, see Table 1).

The $n_2$ bounded-noise term (on an integral basis) is caused by scale-factor errors in the mechanism used to eliminate lock-in compensation bias from the output of laser gyros employing alternating bias. For mechanically dithered gyros with an off-block readout-prism mount for passive-mechanical bias removal (see subsection 7. 1. 3), $n_2$ is caused by an off-nominal center-of-dither rotation. For mechanically dithered gyros with block-mounted readout prism, $n_2$ is caused by anomalies or design limitations in the dynamic filter used for dither rate attenuation. For either mechanical dither compensation figuration, the $n_2$ effect is measured in terms of the root-mean-square value of its integral (i.e., seconds-of-arc), and is usually considered as a part of the gyro-output-pulse quantization uncertainty for error analysis purposes. For laser gyros employing alternating electro-optical bias for lock-in compensation, $n_2$ is caused by scale factor uncertainties in the applied electro-optical bias, hence, errors introduced in digitally subtracting an equivalent bias rate from the gyro pulse-output. For error analysis purposes, the effect can be modeled as a saw-tooth waveform with amplitude expressed in seconds of arc and period equal to the alternating bias period.

In general, the $B_o$, $\epsilon_o$, $\gamma_y$, $\gamma_z$ terms in Eq. (44) are measurable and predictable to a large extent for purposes of compensation. The stability of the measured error effects (over time and temperature) is heavily influenced by the gyro-mechanization approach utilized, particularly with regard to lock-in compensation. The remaining errors in Eq. (44) are generally unpredictable (in a practical sense) and controllable only through gyro design and manufacturing practices established to satisfy application requirements.

### 7.3 Performance and Application Areas

Because of its high rate capability that is independent of bias accuracy, performance insensitivity to acceleration, rugged construction, and inherently high reliability (due to the absence of moving parts), proposed utilization areas for the laser gyro have spanned the spectrum from benign to rugged environmental applications with low- to high-accuracy performance requirements. The versatility of the instrument is one of its principal attributes due to the potential for large-volume production with associated reductions in cost and increases in reliability that accompany large-scale production programs.

Performance figures compatible with 1-nmi/hr inertial navigator requirements (see Table 1) have been demonstrated with mechanically dithered triangular laser gyros with 0.63-micron wavelength and 5.7-inch size (each triangle leg) by gyro laboratory testing and system flight testing. (3, 7, 10, 52, 53) These performance capabilities have been achieved without thermal controls, through thermal and vibration exposures, from turn-on to turn-on, and over several years without calibration. The warm-up time for these instruments (as for all laser gyros) is negligible; full gyro operation is attained at the instant of turn-on including full performance capabilities compatible with Table 1 high accuracy requirements for the newer technology configurations. (10) Limited data under high-g sled tests have confirmed the predicted g-insensitivity of the device (54).

Performance capabilities of laser gyros utilizing nonmechanical bias for lock-in compensation have been more compatible with the lower accuracy (e.g., AHRS) applications (see Table 1). Laser gyros designed with magnetic-mirror technology using the 1.15-micron transition for AHRS-accuracy applications have readily achieved performance levels in the Table 1 AHRS category. (39, 42, 43, 46, 55) Laser gyros designed around the DILAG concept have utilized the 0.63-micron transition and have had performance goals compatible with the 1-nmi/hr INS requirements in Table 1. The limited test data available on the DILAG, however, suggest that further development is needed before the concept can be seriously considered for 1-nmi/hr applications (56). The additional complexity in implementing the concept (i.e., four mirrors, polarizing crystal, dual-gyro electronics and readout) (47) would appear to make the DILAG unattractive for the lower accuracy AHRS-class applications where its demonstrated performance level is acceptable.

Random noise for the laser gyro is one of its important error sources in 1-nmi/hr inertial navigation applications that must be overcome to achieve fast reaction times. High random noise extends the time for system-heading determination to filter the earth-rate signal from the gyro noise in establishing initial heading. (10) The 0.003-deg/$\sqrt{hr}$ figure in Table 1 is consistent with fast reaction times desired in advanced aircraft. Random noise for mechanically dithered laser gyros is principally a function of mirror quality and manufacturer experience. The technology level at Honeywell with a 0.63-micron wavelength transition is routinely achieving random-noise coefficients in the 0.002- to 0.008-deg/$\sqrt{hr}$ range. With the benefits of learning as laser gyro technology phases into production, 0.003-deg/$\sqrt{hr}$ should become standard performance.

Rate capabilities for laser gyros are inherently high, limited only by the noise/bandwidth characteristics of the readout electronics. Requirements in Table 1 are easily achieved with today's technology. The scale-factor accuracy of the 0.63-micron gyro is exceptionally high (10), meeting the Table-1 higher accuracy 5-ppm performance figure. The high rate and scale-factor accuracy capabilities of the laser gyro are principal reasons that the device is well suited for high-accuracy use in high-dynamic rate environments, an application area where torque-to-balance gyros have limited utility (due to scale-factor-accuracy limitations).

Sensor alignment accuracy for the laser gyro is determined by the structural stability of the mechanical interface between the lasing plane and the sensor mount. Notably absent is the misalignment caused by torque-loop servodynamic error (present with the torque-to-balance instruments) and the effect of pickoff null movement (present with all rotating mass gyros). Alignment accuracy capabilities of 5 seconds-of-arc (commensurate with Table 1 INS requirements) are readily achievable with mechanically dithered laser gyros. In the case of the nonmechanically-dithered gyro, utilization of the integrated multiple-gyro packaging design (e.g., Figure 16) provides exceptional alignment stability between gyro input axes for applications requiring high alignment accuracy in severe dynamic environments. (57, 58)

The deficiency of today's mechanically dithered laser gyro is its size. The GG1300 (Figure 15), the largest laser gyro produced by Honeywell, and which has demonstrated the highest performance levels thus far achieved with laser-gyro technology, has a 5.7-inch path length (each side of the lasing triangle) and is 115 cubic inches in volume. The newer-technology GG1342 laser gyro currently in development at Honeywell for 1-nmi/hr INS applications, has a 4.2-inch path length, and outside dimensions of 6.8 by 5.8 by 2.1 inches (or 84 cubic inches in volume). Comparable figures for the alternate high-accuracy strapdown momentum-wheel gyros are generally half the volume of the GG1342 (including electronics). For lower accuracy applications where nonmechanically dithered performance is adequate, the laser-gyro size disadvantage can be eliminated through integrated multiple-gyro packaging.

## 8. PENDULOUS ACCELEROMETER

Accelerometers utilized to date in strapdown attitude reference and navigation applications have almost exclusively been of the pendulous torque-to-balance design. (18) A typical pendulous accelerometer is shown in Figure 18. The unit consists of a hinged pendulum assembly, a moving-coil signal-generator/pickoff that senses angular movement of the pendulum from a nominally null position, and a permanent-magnet torque-generator that enables the pendulum to be torqued by electrical input. The torquer magnet is fixed to the accelerometer case, and the coil assembly is mounted to the pendulum. Delicate flex leads provide electrical access to the coil across the pendulum/case hinge junction. Electronics are included for pickoff readout and for generating current to the torquer.

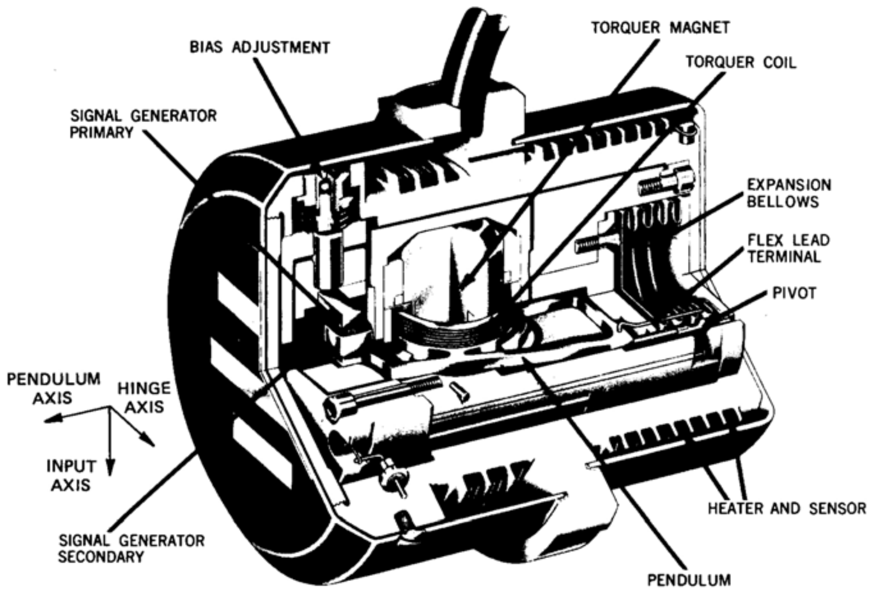


Figure 18. Honeywell GG177 fluid-damped pendulous accelerometer.

The device is operated in the caged mode by applying electrical current to the torquer at the proper magnitude and phasing to maintain the pickoff at null. Under these conditions, the electrically generated torque on the pendulum balances the dynamic torque generated by input acceleration normal to the pendulum plane. Hence, the electrical current through the torquer becomes proportional to the input acceleration, and is the output signal for the device.

### 8.1 General Design Considerations

Mechanization approaches for the pendulous accelerometer vary between manufacturers, but generally fall into two categories: fluid filled and dry units. Fluid-filled devices utilize a viscous fluid in the cavity between the pendulum and case for damping and partial flotation. The dry units use dry air, nitrogen, or electromagnetic damping.

Utilization of the fluid-filled approach generally simplifies the pendulum design due to the natural damping of pendulum resonances afforded by the fluid, the ability to achieve a given pendulosity with a larger pendulum assembly (due to the partial fluid flotation) with associated reductions in manufacturing toerlances, and the ease in achieving good damping in the torque-to-balance loop. The disadvantage of the fluid-filled concept is the addition of the fluid with its unique design and manufacturing problems (bellows assembly for fluid expansion, seals for the case and portions of the pendulum assembly, and filling the unit without introducing bubbles that deteriorate performance). The advantage of the dry accelerometer design is the elimination of the problems associated with the fluid. The disadvantage is a more exacting pendulum design (for a given level of performance) to achieve damping without fluid, and to enable device manufacture with generally tighter dimensional tolerances due to the direct transfer of pendulum manufacturing errors to device performance (i.e., without the attenuating effect of partial flotation afforded in the fluid-filled device).

The hinge element for the pendulous accelerometer is a flexible member that is stiff normal to the hinge line to maintain mechanical stability of the hinge axis relative to the case under dynamic loading, but flexible about the hinge line to minimize unpredictable spring restraint torques that cannot be distinguished from acceleration inputs. Materials selected for the hinge are chosen for low mechanical hysteresis to minimize unpredictable spring-torque errors. To minimize hysteresis effects, the hinge dimensions are selected to assure that hinge stresses under dynamic inputs and pendulum movement are well below the yield-stress for the hinge material.

Beryllium-copper has been a commonly used pendulum-hinge material due to its high ratio of yield-stress to Young's modulus (i.e., the ability to provide large flexures without exceeding material yield-stress). A popular low-cost design approach for dry accelerometers has utilized fused quartz for both the hinge and pendulum by etching the complete assembly from a single-piece quartz substrate (see Figure 19). Performance capabilities of the quartz-flexure hinge design have been limited, however, due to the relatively large flexure thickness (hence, spring effect) needed to avoid hinge-fracture under shock and dynamic loads, and the associated bias error that develops due to pickoff null movement (principally a function of temperature).

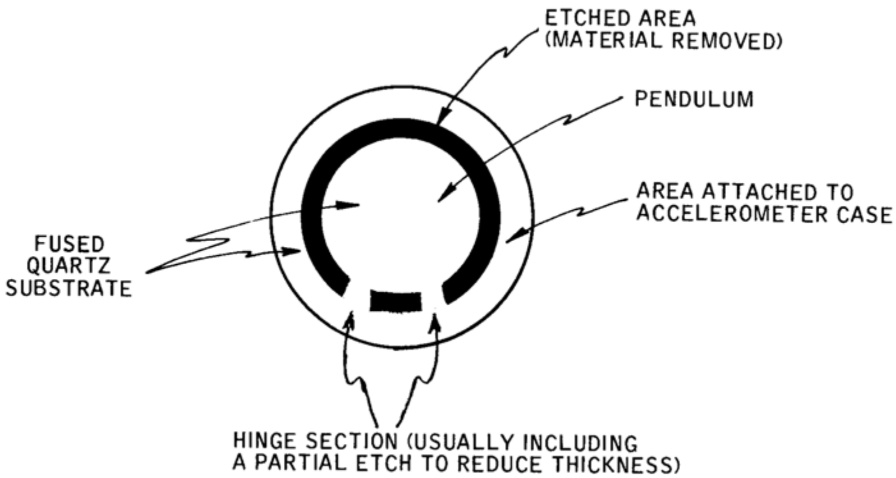


Figure 19. Quartz-flexure pendulum/hinge concept.

## 8.2 Analytical Description and Error Model

Consider the pendulum assembly for the pendulous accelerometer and define a coordinate frame for it with X normal to the plane of the pendulum, Y along the hinge axis, and Z along the pendulum axis (see Figure 20). A point B is defined on the hinge axis in the plane of symmetry of the pendulum, and length $\ell_{CG}$ is defined from B to the pendulum center of mass. Case-fixed coordinate axes are also defined to be nominally parallel to the pendulum axes except for small angular displacement $\theta$ of the pendulum relative to the case about the hinge axis (i.e., the angle sensed by the accelerometer pickoff). A reference point A is defined as fixed to case axes and lying on a line from point B through the pendulum center of mass when $\theta = 0$. An equation can now be derived for the accelerometer output in terms of the acceleration of the reference point A.

First group the forces on the pendulum into four categories

$$\underline{F}_P = \underline{F}_H + \underline{F}_D + \underline{F}_T + \underline{F}_e \tag{45}$$

where

$\underline{F}_P$ = net force on the pendulum

$\underline{F}_H$ = reaction force at the hinge

$\underline{F}_D$ = damping force (proportional to $\dot{\theta}$) provided by a damping mechanism designed into the instrument (e.g., electromagnetic)

$\underline{F}_T$ = force provided by the torque-generator

$\underline{F}_e$ = residual error forces created by instrument imperfections

The associated net moment applied to the pendulum about an axis parallel to the hinge axis (y) and through the pendulum center-of-mass is

$$M_{y_P} = [ -(\underline{\ell}_{CG} \times \underline{F}_H) + \underline{M}_s + \underline{M}_D^* + \underline{M}_T^* + \underline{M}_e^* ] \cdot \underline{u}_y \tag{46}$$

where

$M_{y_P}$ = Net y-axis moment on the pendulum about the center-of-mass

$\underline{M}_s$ = Spring torque about the hinge axis associated with the pendulum suspension mechanism

$\underline{M}_D^*, \underline{M}_T^*, \underline{M}_e^*$ = moments about the center of mass associated with $\underline{F}_D, \underline{F}_T$, and $\underline{F}_e$

$\underline{\ell}_{CG}$ = distance vector with magnitude $\ell_{CG}$ from point B to the pendulum center-of-mass

$\underline{u}_y$ = unit vector parallel to the hinge axis (y)

The form of the moment term associated with $\underline{F}_H$ in Eq. (46) is the simple cross-product relation indicated about the hinge axis because $\underline{\ell}_{CG}$ intersects the hinge line. Consequently, only the components of $\underline{F}_H$ along the hinge line and normal to the pendulum can have a moment about the center-of-mass and along $\underline{u}_y$. Since the moment arm for each of these $\underline{F}_H$ components is the same ($\underline{\ell}_{CG}$), the composite force vector $\underline{F}_H$ can be used in total without regard to the individual moment arms for the separate $\underline{F}_H$ hinge force components.

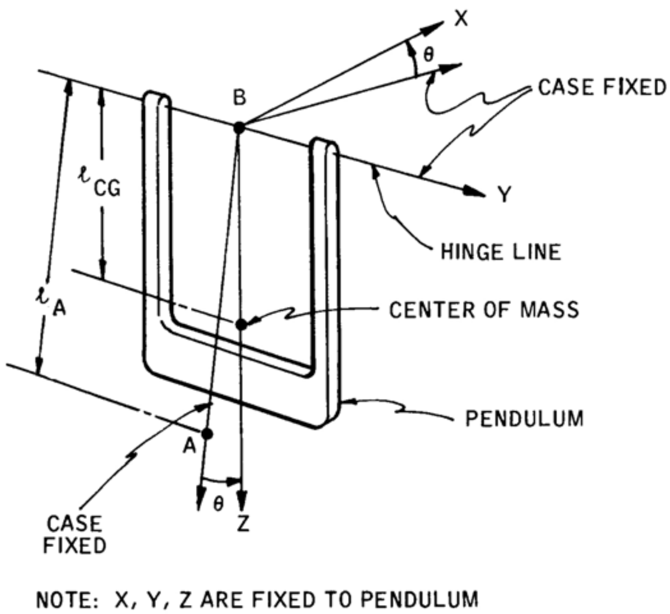


Figure 20. Pendulous-accelerometer coordinate frame definition.

With Eq. (45) for $\underline{F}_H$, Eq. (46) becomes

$$M_{y_P} = [ - (\underline{\ell}_{CG} \times \underline{F}_P) + \underline{M}_s + (\underline{M}_D^* + \underline{\ell}_{CG} \times \underline{F}_D) + (\underline{M}_T^* + \underline{\ell}_{CG} \times \underline{F}_T) + (\underline{M}_e^* + \underline{\ell}_{CG} \times \underline{F}_e)] \cdot \underline{u}_y = [ - (\underline{\ell}_{CG} \times \underline{F}_P) + \underline{M}_s + \underline{M}_D + \underline{M}_T + \underline{M}_e] \cdot \underline{u}_y \tag{47}$$

where

$\underline{M}_D, \underline{M}_T, \underline{M}_e$ = composite error moment terms in brackets [ ] in Eq. (47)

$M_{y_P}$ = net y-axis moment on the pendulum about the center-of-mass

The vector components in Eq. (47) are defined in pendulum axes as

$$\underline{F}_P = \begin{pmatrix} F_{x_P} \\ - \\ - \end{pmatrix}$$

$$\underline{\ell}_{CG} = \begin{pmatrix} 0 \\ 0 \\ \ell_{CG} \end{pmatrix}$$

$$\underline{M}_s = \begin{pmatrix} - \\ M_s \\ - \end{pmatrix}$$

$$\underline{M}_D = \begin{pmatrix} - \\ M_D \\ - \end{pmatrix}$$

$$\underline{M}_T = \begin{pmatrix} - \\ M_T \\ - \end{pmatrix}$$

$$\underline{M}_e = \begin{pmatrix} - \\ M_e \\ - \end{pmatrix}$$

with

$$M_s = - K\,\theta$$

$$M_D = - C\,\dot{\theta}$$

where

$K$ = pendulum spring-torque spring-constant

$C$ = pendulum angular motion ($\dot{\theta}$) damping coefficient

$M_T$ = pendulum torque provided by the torque-generator

$M_e$ = net error torque on the pendulum about the hinge axis

Substitution in Eq. (47) provides the equivalent scalar form for the net y-axis moment on the pendulum about the center-of-mass

$$M_{y_P} = -F_{x_P}\,\ell_{CG} - C\,\dot{\theta} - K\,\theta + M_T + M_e \tag{48}$$

The x-force and y-moment momentum-transfer relations for the pendulum are now introduced for the $M_{y_P}$ and $F_{x_P}$ terms in Eq. (48)

$$F_{x_P} = m\,a_{x_{CG}}$$

$$M_{y_P} = J_y\,(\dot{\omega}_y + \ddot{\theta}) + (J_x - J_z)\,\omega_x\,\omega_z \tag{49}$$

where

$m$ = pendulum mass

$J_x, J_y, J_z$ = pendulum moments of inertia about the pendulum center-of-mass along axes parallel to the pendulum x, y, and z axes

$a_{x_{CG}}$ = acceleration of the pendulum center-of-mass parallel to the pendulum x-axis

$\omega_x, \omega_y, \omega_z$ = inertial angular rate components of accelerometer case parallel to pendulum x, y, and z axes

The $a_{x_{CG}}$ term in Eq. (49) can be related to the x-axis acceleration of reference point A (see Figure 20). First define $\underline{\omega}$ as the angular velocity of the pendulum relative to inertial (nonrotating) space, $\underline{\omega}_C$ as the inertial rotation rate of the accelerometer case, and $\underline{\omega}_P$ as the rotation rate of the pendulum relative to the case (due to rotation about the hinge axis). The acceleration of the pendulum center of mass can be equated to the acceleration of point B on the hinge axis (see Figure 20) plus centripetal and angular acceleration effects

$$\underline{a}_{CG} = \underline{a}_B + \dot{\underline{\omega}} \times \underline{\ell}_{CG} + \underline{\omega} \times (\underline{\omega} \times \underline{\ell}_{CG}) \tag{50}$$

with

$$\underline{\omega} = \underline{\omega}_C + \underline{\omega}_P \tag{51}$$

and where

$\underline{a}_{CG}$ = acceleration of the pendulum center of mass

$\underline{a}_B$ = acceleration of point B on the accelerometer hinge axis

A similar expression can be written for the acceleration of point A on the accelerometer case

$$\underline{a}_A = \underline{a}_B + \dot{\underline{\omega}}_C \times \underline{\ell}_A + \underline{\omega}_C \times (\underline{\omega}_C \times \underline{\ell}_A) \tag{52}$$

where

$\underline{a}_A$ = acceleration of the case-fixed accelerometer reference point A

$\underline{\ell}_A$ = distance vector with magnitude $\ell_A$ from point B to point A

An equation for $\underline{a}_{CG}$ in terms of $\underline{a}_A$ is obtained by combining Eq. (50) to (52)

$$\begin{aligned} \underline{a}_{CG} = \; & \underline{a}_A - \dot{\underline{\omega}}_C \times \underline{\ell}_A - \underline{\omega}_C \times (\underline{\omega}_C \times \underline{\ell}_A) + (\dot{\underline{\omega}}_C + \dot{\underline{\omega}}_P) \times \underline{\ell}_{CG} \\ & + (\underline{\omega}_C + \underline{\omega}_P) \times [(\underline{\omega}_C + \underline{\omega}_P) \times \underline{\ell}_{CG}] \end{aligned} \tag{53}$$

The x-axis component of Eq. (53) in pendulum axes is the desired relationship between $a_{x_{CG}}$ in Eq. (49) and $a_{x_A}$ (the x-axis acceleration of the reference point A on the accelerometer case). The vector quantities in Eq. (53) are defined in terms of their X, Y, and Z components in pendulum axes as

$$\underline{\omega}_C = \begin{pmatrix} \omega_x \\ \omega_y \\ \omega_z \end{pmatrix}$$

$$\underline{\omega}_P \begin{pmatrix} 0 \\ \dot{\theta} \\ 0 \end{pmatrix}$$

$$\underline{\ell}_{CG} \begin{pmatrix} 0 \\ 0 \\ \ell_{CG} \end{pmatrix}$$

$$\underline{\ell}_A \begin{pmatrix} -\theta \ell_A \\ c \\ \ell_A \end{pmatrix}$$

Substituting in Eq. (53), neglecting $\theta\,\omega$ compared to $\omega$ terms, and evaluating for the x-axis components yields the desired relationship between $a_{x_{CG}}$ and $a_{x_A}$

$$a_{x_{CG}} = a_{x_A} - (\ell_A - \ell_{CG})\,\dot{\omega}_y - (\ell_A - \ell_{CG})\,\omega_x\,\omega_z + \ell_{CG}\,\ddot{\theta} \tag{54}$$

Equations (48), (49), and (54) in combination define the dynamic response relation for the pendulous accelerometer. Before combining, revised nomenclature and the effect of accelerometer misalignments are introduced.

The pendulosity (Q) of the accelerometer is defined as the product of the pendulum mass with the distance from the hinge axis to the pendulum center-of-mass

$$Q = m\, \ell_{CG} \tag{55}$$

The torque-generator torque is defined in terms of an equivalent command-acceleration with a scale-factor error; and the error torque is equated to an acceleration bias defined as the torque-generator command-acceleration needed to nullify the effect of the error torque on the pendulum

$$\begin{aligned} M_T &= \frac{Q}{(1+\epsilon)} a_T \\ M_e &= -\frac{Q}{(1+\epsilon)} a_B \end{aligned} \tag{56}$$

where

$a_T$ = torque-generator command-acceleration

$a_B$ = accelerometer bias

The case angular rate components in pendulum axes ($\omega_x$, $\omega_y$, $\omega_z$) can be related to acceleration components along nominal accelerometer axes. The pendulum is misaligned from the accelerometer case by the pickoff angle ($\theta$) and the accelerometer case may be misaligned from the nominal accelerometer axes, hence

$$\begin{aligned} a_{x_A} &= a_I + \gamma_P\, a_H - (\gamma_H + \theta)\, \omega_P \\ \omega_x &= \omega_I + \gamma_P\, \omega_H - (\gamma_H + \theta)\, \omega_P \\ \omega_y &= \omega_H + \gamma_I\, \omega_P - \gamma_P\, \omega_I \\ \omega_z &= \omega_P + (\gamma_H + \theta)\, \omega_I - \gamma_I\, \omega_H \end{aligned} \tag{57}$$

where

I, H, P = nominal accelerometer axes (I = input; H = hinge; P = pendulum; see Figure 18)

With Eq. (55) to (57), Eq. (48), (49), and (54) can be combined to yield the input/output equation for the pendulous accelerometer. Upon combination, rearrangement, and neglecting higher order terms, the result is

$$\begin{aligned} a_T = {} & (1+\epsilon)\, [a_I + \gamma_P\, a_H - (\gamma_H + \theta)\, a_P - (\ell_A - \ell_{CG} - \frac{J_y}{Q})\, \dot{\omega}_H \\ & - (\frac{J_z - J_x}{Q} + \ell_A - \ell_{CG})\, \omega_I\, \omega_P] + a_B + \frac{1}{Q}(J_H\, \ddot{\theta} + C\, \dot{\theta} + K\, \theta) \end{aligned} \tag{58}$$

where

$J_H$ = moment of inertia of the pendulum about the hinge axis (i.e., $J_H = J_y + m\, \ell_{CG}^2$)

Since $\ell_A$ (the distance to the acceleration measurement reference point) was arbitrarily defined, it can be selected to simplify the error model. A convenient selection nulls the $\dot{\omega}_H$ effect in Eq. (58)

$$\ell_A = \ell_{CG} + \frac{J_y}{Q} \tag{59}$$

It should be recognized that this selection corresponds to the center of percussion for the pendulum assembly. With Eq. (59), Eq. (58) becomes the final dynamic model form given below:

$$\begin{aligned} a_T = {} & (1+\epsilon)\, [a_I + \gamma_P\, a_H - (\gamma_H + \theta)\, a_P \\ & - \frac{(J_z + J_y - J_x)}{Q}\, \omega_I\, \omega_P] + a_B + \frac{1}{Q}\, (J_H\, \ddot{\theta} + C\, \dot{\theta} + K\, \theta) \end{aligned} \tag{60}$$

Equation (60) with (59) defines the input/output characteristic for the pendulous accelerometer. In operational usage, the accelerometer is operated in closed-loop fashion such that the command-acceleration ($a_T$) torquer input is used to maintain the pickoff angle at null. Eq. (59) and (60) are illustrated with this concept in block diagram form in Figure 21. Figure 21 shows that the accelerometer output $a_T$ is proportional to the input $a_I$ (plus error terms) with a bandwidth characteristic determined by the form of the torque-loop mechanization. Implementations commonly utilized for the accelerometer torque-loop electronics are the digital-rebalance pulse-on-demand concept, and the analog-rebalance followup-digitizer approach (see Section 4.).

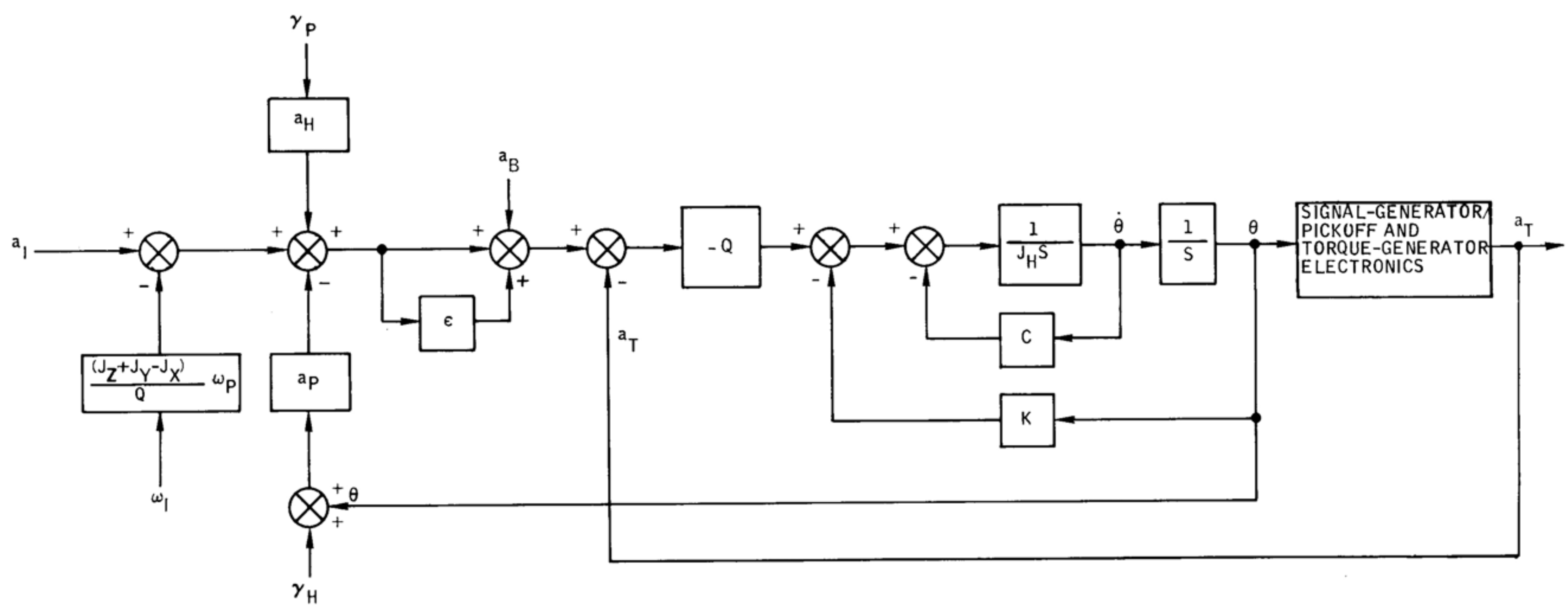


Figure 21. Pendulous-accelerometer analytical response diagram.

Error-input terms in Figure 21 for the pendulous accelerometer include the accelerometer mechanical misalignment errors ($\gamma_H$ and $\gamma_P$), spring-restraint (K) bias and misalignment error due to off-null pickoff angle $\theta$ (caused by pickoff-detector null bias and torque-loop dynamic effects), aniso-inertia angular-input error ($J_z + J_y - J_x$), torquer scale-factor error ($\epsilon$), and bias error $a_B$. Of these, the anisoinertia, spring restraint, and pickoff misalignment effects (due to torque-loop bandwidth limitations) are intrinsic to the basic instrument design; the remaining errors are caused by imperfections in the instrument manufacture compared to the ideal design configuration.

A key error source in the pendulous accelerometer is the K $\theta$ spring effect in Figure 21. If a significant spring constant K is generated as a result of the pendulum suspension design, care must be taken to assure that the null (under zero input) is stable. Otherwise, large error-torque variations will be generated that cannot be compensated. Variations in $\theta$ are caused by pickoff-detector null movement (mechanical movement and electrical bias shifts) and the resulting closed-loop torquing of the pendulum to an offset $\theta$ angle position.

The accelerometer-bias term is composed of several contributing factors; a typical error model is given by

$$a_B = C_0 + C_1 + C_2\, a_I\, a_P + n \tag{61}$$

where

$C_0$ = g-insensitive bias error

$C_1$ = bias error generated by vibration inputs (linear and angular) that is unmodelable for purposes of compensation

$C_2$ = anisoelastic error coefficient caused by unequal compliance (relative to the pivots) in the accelerometer pendulum assembly under g-loading along the pendulum and input axes

$n$ = stochastic random-bias error caused by randomly varying instabilities in the accelerometer assembly

A typical cause for the $C_0$ g-insensitive bias error is pickoff offset (e.g., caused by pickoff electrical null shift) in conjunction with residual spring torques in the pivots about the hinge line (caused by flex-leads for example). The equivalent error associated with the pivot spring and hysteresis effects in Figure 21 is usually included as part of the $C_0$ coefficient. The $C_1$ term has been included to account for the fluid dynamic or gas dynamic effects that are present in accelerometers utilizing fluid or gas (between the pendulum and case) for damping. The inertial and viscous properties of the fluid (or gas) as it interacts with the pendulum have been neglected in the development of Eq. (60) (and Figure 21).

The scale-factor error for the pendulous accelerometer includes linearity error effects and is typically modeled as

$$\epsilon = \epsilon_0 + \epsilon_1 \frac{a_I}{|a_I|} + \epsilon_2\, a_I + \epsilon_3\, a_I^2 \tag{62}$$

The terms in Eq. (62) directly parallel those for the floated-gyro scale-factor-error model (Eq. (10)) discussed previously.

Compensation for the pendulous accelerometer is designed to remove the predictable error terms from the output by measuring their values and using them in the system computer for sensor-output correction. The stability of the measured coefficients over time, temperature, vibration, input profile, and from turn-on to turn-on ultimately determines the device accuracy (and required calibration interval).

### 8.3 Performance and Application Areas

Both fluid-filled and dry versions of the pendulous accelerometer have been utilized in strapdown applications where performance in the Table 1 1-nmi/hr INS category has been required. One of the original strapdown applications for the device was in the velocity cut-off switch for several spacecraft launch vehicles (e.g., a dry unit was utilized on the original Agena upper-stage booster, and a fluid-filled unit was incorporated in the original Delta upper-stage vehicle). Fluid-filled versions are now in use on the advanced Agena and Delta inertial guidance systems. Fluid-filled units have recently demonstrated adequate performance in 1-nmi/hr long-term terrestrial cruise strapdown INS developmental flight tests (3, 4, 5) in moderate vibration environments without heaters utilizing temperature to compensate for thermally sensitive errors (principally scale-factor error and pickoff null instability). An advanced development model strapdown laser-gyro INS has recently been designed for general 1-nmi/hr application utilizing a fluid-filled accelerometer and has initiated developmental testing. (7)

Lower performance strapdown systems (e.g., tactical missile systems) in recent years have almost exclusively utilized the dry quartz-flexure design due to its low-cost benefits. Performance capabilities of the device in these applications have generally been compatible with Table 1 (AHRS) requirements without using heaters for temperature control. Use of the dry design in the higher performance areas has been limited, and has generally required heaters to stabilize performance; e.g., ATIGS. (7, 54) Temperature measurements can be used to compensate for predictable performance variations. However, for the dry quartz-flexure unit, the bias temperature-variations (e.g., pickoff null movement and flex-lead error-torques) have been too large to be accurately calibratable by temperature measurements alone, hence temperature control has been required to achieve high accuracy (with an accompanying reaction time penalty for warmup, and a cost penalty for temperature controls).

In severe vibrations (possibly amplified by sensor-assembly mounting-structure resonances) rectification of the anisoinertia, and particularly the pickoff-angle cross-coupling error, can produce bias deviations in the pendulous accelerometer (see Figure 21). The latter effect (also known as vibropendulous error), is produced by torque-loop dynamic error under high-frequency acceleration inputs (I), and the resulting cross-coupling of P-axis acceleration into the sensor output (i.e., a g-squared error effect). For I- and P-axis acceleration components at the same frequency, a rectification is possible, depending on the relative phasing of the acceleration components. Worst-case vibropendulous error occurs for acceleration vibration-vector inputs normal to the hinge line, and 45 degrees from the input axis. The magnitude of the vibropendulous effect depends on the bandwidth of the accelerometer loop relative to the vibration frequencies encountered. Bandwidths in the 100- to 300-Hz region are representative of fluid-filled accelerometers, which is generally wide enough to maintain the vibropendulous effect at a tolerable level for most applications (10 $\mu g/g^2$ for typical military vibration profiles including the input-vibration frequency-attenuation effect typically afforded by the strapdown sensor assembly mount). For the dry accelerometer configuration, vibropendulous effects have generally not been as much of a concern because loop bandwidths have been typically wider (e.g. - 800 Hz).

With regard to bandwidth effects, it should be noted that a disadvantage for the pendulous accelerometer in some applications is the need for wide bandwidth to reduce vibropendulous error. This limits the ability of the accelerometer pendulum to filter out high-amplitude vibration inputs that may be present on the input signal. As a result, current levels for the torque loop and associated digitizing electronics (see Section 4.) may be higher and more difficult to handle accurately.

## 9. CONCLUDING REMARKS

Several sensors are available today that generally meet strapdown system performance requirements, each with advantages and limitations, depending on the area of application. The ultimate selection of a sensor to meet particular requirements can be made only through a careful tradeoff evaluation that assesses reliability, maintainability, cost, size, weight, and power factors, as well as performance. One of the principal tradeoffs in the selection of a strapdown gyro are the potential advantages projected for the newer-technology instruments not yet in production (i.e., the electrostatic and laser gyros) versus the known capabilities and limitations of established production-gyro technology (i.e., the floated rate-integrating and tuned-rotor gyros). For the strapdown accelerometer, tradeoff selection alternatives will remain limited until new innovations are developed specifically for strapdown application that overcome the limitations in existing pendulous accelerometers originally designed for gimbaled application.

## 10. ACKNOWLEDGMENTS

I would like to express my appreciation to J. Killpatrick, F. Aronowitz, T. J. Podgorski, W. N. Johnson, and V. H. Aske for their valuable comments during the preparation of this paper.

## REFERENCES

1. Klass, Philip J., "Laser Gyro Reemerges as INS Contender," Aviation Week and Space Technology, 13 January 1975.

2. Klass, Philip J., "Laser Gyros Find Increased Applications," Aviation Week & Space Technology, 25 July 1977.

3. Developmental Test of the Honeywell Laser Inertial Navigation System (LINS), Final Report, Central Inertial Guidance Test Facility, 6585th Test Group, Holloman Air Force Base, Report ADTC-TR-75-74, November 1975.

4. Strapdown 727 Flight Test Summary Results, Boeing Report B-8182-5-48A, October 1975.

5. Strapdown 747 Flight Test Summary Results, Boeing Report B-8182-6-3A, January 1976.

6. Development Flight Testing of the N-57A Inertial Navigation System, , Central Inertial Guidance Test Facility, 6585th Test Group, Holloman Air Force Base, Report ADTC-TR-75-86, November 1975.

7. Bachman, K. L. and Carson, E. W., "Advanced Development Program for the Ring Laser Gyro Navigator," ION National Aerospace Meeting, Warminster, PA, 28 April 1976.

8. Investigation of Application of Two-Degree-of-Freedom Dry Tuned-Gimbal Gyroscopes to Strapdown Navigation Systems, Final Report, NASA Report CR-132419, April 1974.

9. Duncan, Robert R., "MICRON - A Strapdown Inertial Navigator Using Miniature Electrostatic Gyros," SAE Aerospace Control and Guidance Systems Committee, Paradise Valley, Arizona, 15-17 May 1974.

10. Savage, Paul G., "Laser Gyros in Strapdown Inertial Navigation Systems," IEEE 1976 Position Location and Navigation Symposium, San Diego, California, 1-3 November 1976.

11. Peterson, Roland, "Advantages of Gimbaled Inertial Navigation Systems," NAECON, Dayton, Ohio, 18-20 May 1976.

12. Dynamic Errors in Strapdown Inertial Navigation Systems, NASA Report CR-1962, December 1971.

13. Bortz, J. E., "A New Mathematical Formulation for Strapdown Inertial Navigation," IEEE Transactions on Aerospace and Electronic Systems, Volume AES-7, No. 1, January 1971.

14. Roantree, James P., "Advancements in Strapdown Navigation," NAECON, Dayton, Ohio, 1974.

15. Eberlein, A. J., "Inertial Navigation Interim Report," Honeywell Internal Interoffice Correspondence, 3 May 1972.

16. Pitman, George R. Jr., ed., Inertial Guidance, John Wiley and Sons, New York, 1962.

17. Leondes, Cornelius T., ed., Guidance and Control of Aerospace Vehicles, McGraw-Hill, 1963.

18. Macomber, George R. and Fernandes, Manuel, Inertial Guidance Engineering, Prentice-Hall, Englewood Cliffs, New Jersey, 1962.

19. Britting, Kenneth R., Inertial Navigation System Analysis, John Wiley and Sons, New York, 1971.

20. Wrigley, W., Hollister, W. M., and Denhard, W. G., "Gyroscopic Theory, Design, and Instrumentation," M. I. T. Press, 1969.

21. Flight Test of the Sign III Kalman Inertial Doppler System, Final Report, Central Inertial Guidance Test Facility, 6585th Test Group, Holloman Air Force Base, Report AFSWC-TR-71-94, April 1967.

22. Howe, Edwin W., "A Free Rotor Gyro," Symposium on Unconventional Inertial Sensors, Farmingdale, New York, 1963.

23. Savet, Paul H., "New Trends in Non-floated Precision Gyroscopes," Grumman Research Department Memorandum RM-247J, October 1964.

24. Craig, Robert J. G., "Theory of Operation of Elastically Supported Tuned Gyroscope," IEEE Transactions on Aerospace and Electronic Systems, Vol. AES-8, No. 3, May 1972.

25. Craig, Robert J. G., "Theory of Errors of a Multigimbal, Elastically Supported, Tuned Gyroscope," IEEE Transactions on Aerospace and Electronic Systems, Vol. AES-8, No. 3, May 1972.

26. Craig, Robert J. G., "Dynamically Tuned Gyros in Strapdown Systems," AGARD Conference Proceedings No. 116 on Inertial Navigation Components and Systems, AD-758 127, Paris, France, February 1973.

27. Kornbluth, B., "Derivation of And Test Techniques Used to Investigate Support Mechanism Problems Associated with the Litton Vibrator Gyro," Proc. ION/NASA Meeting on Problems in Inertial Guidance, 21-22 January 1970.

28. Shaw, Jack C., "Benefits of Strapdown Over Gimbal Systems for Aircraft Application," NAECON, Dayton, Ohio, 18-20 May 1976.

29. Harrington, Jr., Captain Edwin V., Bell, Jackie W., and Raroha, Major George H., "MIRA: A New Approach to Integrated Reference Systems," NAECON, Dayton, Ohio, 18-20 May 1976.

30. "Development Test Results of Boeing ISADS System," Informal Discussions with Jack C. Shaw (Boeing) regarding design experience during the development of the Boeing Integrated Strapdown Air Data System, a strapdown navigation system utilizing Teledyne tuned rotor gyros with Boeing-designed gyro electronics (Flight Test Results Reported in References 4 and 5).

31. Craig, Robert J. G., and Russel, James G., "Cost Considerations in a Strapdown Navigation System Using Dry-Tuned Instruments," INTERCON 1975, New York City, New York, 8-10 April 1975.

32. Moore, J. P., "Trident Electrostatically Suspended Gyro Monitor (ESGM)," SAE Aerospace Control and Guidance Systems Committee, Phoenix, Arizona, 17 May 1974.

33. Bold, N. T., Engebretson, H. J., and Moore, J. P., "Universal Marine System Gyro-ESG," ION Conference, Long Island, New York, 23-24 October 1973.

34. Warzynski, Captain Robert R. and Ringo, Ronald L., "The Evolution of ESG Technology," Agard Symposium, June 1971.

35. Eberlein, A. J., and Savage, P. G., Strapdown Cost Trend Study and Forecast, NASA Report CR-137585.

36. Killpatrick, Joseph, "The Laser Gyro," IEEE Spectrum, October 1967.

37. Aronowitz, Frederick, "The Laser Gyro," Laser Applications, Vol. 1, Academic Press, New York, 1971.

38. Garrett, C. G. B., "Gas Lasers," McGraw-Hill, 1967.

39. Morrison, Robert F., Laser Gyro Reaction Time Investigation Program, AFAL Report AFAL-TR-74-169, September 1974.

40. Jenkins, F.A., and White, H.E., Fundamentals of Optics, McGraw-Hill, 1950.

41. Podgorski, Ted J., and Aronowitz, Fred, "Langmuir Flow Effects in the Laser Gyro," IEEE Journal of Quantum Electronics, Vol. QE-4, No. 1, January 1968.

42. Morrison, R.F., Levinson, Dr. E., and Bryant Jr., B.L., "The SLIC-7 Laser Gyro, Inertial Guidance System," NAECON, Dayton, Ohio, 1977.

43. Morrison, R., Levinson, Dr. E., and McAdory, R., "The SLIC-15 Laser Gyro IMU for Mid-course Missile Guidance," ION National Aerospace Symposium, Warminster, Pennsylvania, 27-28 April 1976.

44. Aronowitz, Frederick, and Collins, R.J., "Mode Coupling Due to Back Scattering in a HeNe Traveling Wave Ring Laser," Applied Physics Letters, Vol. 9, No. 1, 1 July 1966.

45. Dewar, Dr. D., "The Laser Gyroscope," Royal Aeronautical Society, London, 12 January 1977.

46. Feldman, Julius, Gootkind, David, and Helfant, Stephan, Sperry ASLG 15 Laser-Gyro Performance and Error Model, Final Report, Charles Stark Draper Laboratory Report R-989, July 1976.

47. Roantree, James P., Burns, John E., and McAdory, Robert W., "Differential Laser Gyro Technology," NAECON, Dayton, Ohio, 1975.

48. Bresman, J., Cook, H., and Lysobey, D., "Differential Laser Gyro Development," ION National Aerospace Meeting, Warminster, Pennsylvania, 28 April 1976.

49. Mathews, J.B., "The Laser Gyro and its Impact on Guidance and Navigation Applications," 9th Annual Electro-Optics/Laser Conference, Anaheim, California, 25-27 October 1977.

50. Grant, D., Hambenne, J., Hutchings, T., Sanders, V., Scully, M., "A Multioscillator (Four-Mode) Ring Laser Gyro Report," NAECON, Dayton, Ohio, 1977.

51. Aronowitz, F., and Lim, W.L., "Positive Scale Factor Correction in the Laser Gyro," IEEE Journal of Quantum Electronics, Vol. QE-13, No. 5, May 1977.

52. Savage, Paul G., and Ignagni, Mario B., "Honeywell Laser Inertial Navigation System (LINS) Test Results," Ninth Joint Services Data Exchange Group for Inertial Systems, St. Petersburg, Florida, 18-19 November 1975.

53. Feldman, J., and Helfant, S., "A Laser Gyro Evaluation Plan and Test Results," NAECON, Dayton, Ohio, 1977.

54. Rocket Sled and Centrifuge Testing of the Advanced Tactical Inertial System (ATIGS), Central Inertial Test Facility, 6585th Test Group, Holloman Air Force Base, Report ADTC-TR-77-7, January 1977.

55. Pasik, Donald J., Gneses, Morris I., and Taylor, George R., "A Ring Laser Gyro Strapdown Inertial Navigation System: Performance Analysis and Test Results," AIAA Guidance and Control Conference, Boston, Massachusetts, 20-22 August 1975.

56. Stowell, W.K., McAdory, R.W., and Roantree, J.P., "Differential Laser Gyro," IEEE Southeast Conference, Clemson, South Carolina, 5-7 April 1976.

57. Laser Triad Rate Gyro, McDonnell Douglas Report G3236, August 1972.

58. "ABMDA UPSTAGE Experiment," Presentation to Congress by U.S. Department of Defense Directorate of Development, Research, and Engineering, Advanced Research Projects Agency, October 1972.

59. Scoville, A.E., and Yamron, J., "The Mechanization of a Strapdown Inertial System Based on Time-Modulated Torquing," AIAA/JACC Guidance and Control Conference, Seattle, Washington, 15-17 August 1966.

60. A Study of Critical Computational Problems Associated with Strapdown Inertial Navigation Systems, NASA Report CR-968, April 1968.

## NOTES

## INERTIAL NAVIGATION EQUATIONS

## NAV SEMINAR - LECTURE 1 NOTES

### CORIOLIS EQUATION

In several of the developments to follow, the Coriolis equation is utilized to relate rates of change of a vector's components as viewed in two coordinate frames rotating relative to one another. The Coriolis equation can be derived by considering an arbitrary vector $\underline{N}$ and its derivative in two coordinate frames, A and B. Frames A and B can be considered to have the same point of origin, but to be rotating relative to one another (B with respect to A) at angular velocity $\underline{\omega}_{AB}$.

We begin the development by defining a triad of orthogonal unit vectors fixed in coordinate frame B as $\underline{u}_X$, $\underline{u}_Y$, and $\underline{u}_Z$. Vector $\underline{N}$ can be decomposed into three components along each of these unit vectors as:

$$\underline{N} = N_X \, \underline{u}_X + N_Y \, \underline{u}_Y + N_Z \, \underline{u}_Z$$

where

$N_X, N_Y, N_Z$ = Scalar quantities representing the projections of $\underline{N}$ along $\underline{u}_X$, $\underline{u}_Y$, and $\underline{u}_Z$ respectively.

We now take the derivative of $\underline{N}$ as defined above as viewed in coordinate frame A:

$$\left(\frac{d}{dt}\underline{N}\right)_A = \left(\frac{d}{dt}N_X\right)_A \underline{u}_X + \left(\frac{d}{dt}N_Y\right)_A \underline{u}_Y + \left(\frac{d}{dt}N_Z\right)_A \underline{u}_Z + N_X\left(\frac{d\underline{u}_X}{dt}\right)_A + N_Y\left(\frac{d\underline{u}_Y}{dt}\right)_A + N_Z\left(\frac{d\underline{u}_Z}{dt}\right)_A \tag{1}$$

Because the $N_X$, $N_Y$, $N_Z$ quantities are scalars, their rates of change are equivalent in coordinate frames A or B. Hence,

$$\left(\frac{dN_X}{dt}\right)_A = \dot{N}_X \qquad \left(\frac{dN_Y}{dt}\right)_A = \dot{N}_Y \qquad \left(\frac{dN_Z}{dt}\right)_A = \dot{N}_Z \tag{2}$$

where

$\dot{(\;)}$ = The time derivative of the scalar quantity.

The rates of change of the unit vector terms in Equation (1) (viewed in the A frame) can be defined by reference to the following figure.

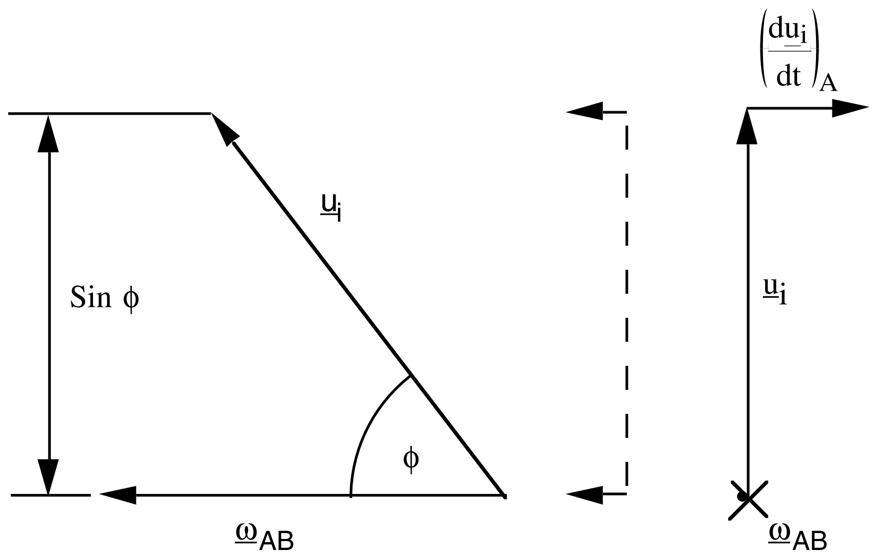


The figure defines one of the unit vectors in question ($\underline{u}_i$ with i = X, Y or Z) and the angular rotation vector $\underline{\omega}_{AB}$ defining the rotational rate of B relative to A. The angle between the two vectors is $\phi$ and the perpendicular distance from $\underline{u}_i$ to $\underline{\omega}_{AB}$ is sin $\phi$. Since $\underline{u}_i$ is a unit vector (constant amplitude) fixed to Frame B, it rotates with B relative to A at $\underline{\omega}_{AB}$ so that its rate of change (as viewed from Frame A) is perpendicular to $\underline{u}_i$ and $\underline{\omega}_{AB}$ with magnitude equal to $/\underline{w}_{AB}/\sin\phi$ (see figure). Mathematically, the rate of change is equivalent to the cross-product between $\underline{u}_i$ and $\underline{\omega}_{AB}$, hence:

$$\left(\frac{d\underline{u}_i}{dt}\right)_A = \underline{\omega}_{AB} \times \underline{u}_i$$

Substitution (with (2)) in (1) yields:

$$\begin{aligned}\left(\frac{d\underline{N}}{dt}\right)_A &= \dot{N}_X\,\underline{u}_X + \dot{N}_Y\,\underline{u}_Y + \dot{N}_Z\,\underline{u}_Z + N_X\left(\underline{\omega}_{AB}\times\underline{u}_X\right) + N_Y\left(\underline{\omega}_{AB}\times\underline{u}_Y\right) + N_Z\left(\underline{\omega}_{AB}\times\underline{u}_Z\right) \\ &= \dot{N}_X\,\underline{u}_X + \dot{N}_Y\,\underline{u}_Y + \dot{N}_Z\,\underline{u}_Z + \underline{\omega}_{AB}\times\underline{N}\end{aligned} \tag{3}$$

Because $\underline{u}$ is fixed in the B frame, the equivalent to (3) in the B Frame is:

$$\left(\frac{d\underline{N}}{dt}\right)_B = \dot{N}_X\,\underline{u}_X + \dot{N}_Y\,\underline{u}_Y + \dot{N}_Z\,\underline{u}_Z$$

Equation (3) thjereby reduces to:

$$\left(\frac{d\underline{N}}{dt}\right)_A = \left(\frac{d\underline{N}}{dt}\right)_B + \underline{\omega}_{AB}\times\underline{N} \tag{4}$$

Equation (4) is the general Coriolis equation that relates rates of change of an arbitrary vector $\underline{N}$ as viewed in coordinate frames A and B of similar origin but rotating relative to one another at $\underline{\omega}_{AB}$. This equation will now be used to derive the differential equation generally used to compute velocity in terrestrial cruise inertial navigation systems.

VELOCITY EQUATION

To derive the differential equation for determining velocity in terrestrial cruise inertial navigation systems, three coordinate frames are utilized:

I = The inertial frame, defined to be non-rotating.

E = The earth frame, defined to be fixed to the earth, hence rotating at earth's rate.

L = The local level frame, defined to have two of its axes parallel to the earth's surface beneath the vehicle. The third axis is parallel to the local vertical at the vehicle position.

We now define the velocity of interest in navigating relative to the earth as the rate of change of position as viewed in earth fixed (E) coordinates:

$$\underline{v} \overset{\Delta}{=} \left( \frac{d\underline{R}}{dt} \right)_E$$

where:

$\underline{v}$ = The velocity vector of interest.

$\underline{R}$ = The position vector to the vehicle (from earth's center).

The components of $\underline{v}$ along local level (L) coordinates are of interest since these define the horizontal and vertical components of velocity. It would be convenient if a differential equation for $\underline{v}$ could be developed in L-frame coordinates so that its integral would directly equal $\underline{v}$. Specifically, we seek an expression for $\left( \frac{d\underline{v}}{dt} \right)_L$.

As will be apparent subsequently, such an expression is a function of the vehicle acceleration sensed by on-board accelerometers. Through Newton's law, accelerometers sense rates of change of velocity in non-rotating inertial space. Hence, we might presume that the relationship we seek for the local level frame velocity rate involves rates of change of vectors in I-frame coordinates.

Using Coriolis Equation (4), the L-Frame derivative of $\underline{v}$ can be related to the rate of change of $\underline{v}$ as viewed in the I-frame through:

$$\left(\frac{d\underline{v}}{dt}\right)_L = \left(\frac{d\underline{v}}{dt}\right)_I - \underline{\omega} \times \underline{v} \tag{5}$$

where:

$\underline{\omega}$ = The rotation rate of the local vertical frame relative to the inertial frame. It is generated by vehicle motion over the earth, and earth's angular rate.

The $\left(\frac{d\underline{v}}{dt}\right)_I$ term in (5) can be developed by first defining $\underline{v}$ in terms of the rate of change of $\underline{R}$ as viewed in the I-frame. Again, using Coriolis,

$$\underline{v} = \left(\frac{d\underline{R}}{dt}\right)_E = \left(\frac{d\underline{R}}{dt}\right)_I - \underline{\Omega} \times \underline{R} \tag{6}$$

where:

$\underline{\Omega}$ = The rotation rate of the E frame relative to I (i.e., - earth's rotation rate vector).

Differentiating Equation (6) in the I-frame, and noting that $\underline{\Omega}$ is constant in inertial space, hence, its derivative is zero, yields:

$$\left(\frac{d\underline{v}}{dt}\right)_I = \left(\frac{d^2\underline{R}}{dt^2}\right)_I - \underline{\Omega} \times \left(\frac{d\underline{R}}{dt}\right)_I$$

Solving for $\left(\frac{d\underline{R}}{dt}\right)_I$ from Equation (6) and substituting in the latter $\left(\frac{d\underline{v}}{dt}\right)_I$ equation obtains:

$$\left(\frac{d\underline{v}}{dt}\right)_I = \left(\frac{d^2\underline{R}}{dt^2}\right)_I - \underline{\Omega} \times \left(\underline{v} + \underline{\Omega} \times \underline{R}\right) = \left(\frac{d^2\underline{R}}{dt^2}\right)_I - \underline{\Omega} \times \underline{v} - \underline{\Omega} \times \left(\underline{\Omega} \times \underline{R}\right)$$

We can now substitute the latter expression into Equation (5):

$$\left(\frac{d\underline{v}}{dt}\right)_L = \left(\frac{d^2\underline{R}}{dt^2}\right)_I - \underline{\Omega} \times \left(\underline{\Omega} \times \underline{R}\right) - \left(\underline{\Omega} + \underline{\omega}\right) \times \underline{v}$$

The $\left(\frac{d^2\underline{R}}{dt^2}\right)_I$ term above represents the total inertial acceleration of the vehicle and is equal to the sum of the local gravity vector $(\underline{g})$ and the specific force acceleration vector $(\underline{a}_{sf})$ sensed by accelerometers:

$$\left(\frac{d^2\underline{R}}{dt^2}\right)_I = \underline{g} + \underline{a}_{sf}$$

Hence:

$$\left(\frac{d\underline{v}}{dt}\right)_L = \underline{a}_{sf} + \underline{g} - \underline{\Omega} \times \left(\underline{\Omega} \times \underline{R}\right) - \left(\underline{\Omega} + \underline{\omega}\right) \times \underline{v} \tag{7}$$

We now observe that for a vehicle at rest relative to the earth, $\underline{v}$ and the rate of change of $\underline{v}$ in the local level frame is zero. Under these conditions, Equation (7) reduces to:

$$\underline{a}_{sf} + \underline{g} - \underline{\Omega} \times \left(\underline{\Omega} \times \underline{R}\right) = 0$$

or

$$\underline{a}_{sf} = -\left[\underline{g} - \underline{\Omega} \times \left(\underline{\Omega} \times \underline{R}\right)\right]$$

We also note that a plumb bob suspended in the vehicle at rest will be directed along the accelerometer sensed line of force. For this reason, the term in brackets in the latter expression is referred to as plumb bob gravity. Because it is a function only of position, it can be mapped and programmed into the system computer as a function of position. With this definition for gravity, Equation (7) assumes the final form:

$$\left(\frac{d\underline{v}}{dt}\right)_L = \underline{a}_{sf} + \underline{g}' - \left(\underline{\Omega} + \underline{\omega}\right) \times \underline{v} \tag{8}$$

where $\underline{g}'$ is plumb bob gravity defined by:

$$\underline{g}' = \underline{g} - \underline{\Omega} \times \left(\underline{\Omega} \times \underline{R}\right) \tag{8A}$$

Equation (8) is continuously integrated in the inertial navigation computer in L-Frame coordinates to evaluate $\underline{v}$.

The components of the $\underline{a}_{sf}$ term in Equation (8) represent accelerations that would be sensed by accelerometers with input axes directed along locally level navigation axes. In gimbaled inertial navigation systems, a gyro stabilized mechanical platform is instrumented and controlled to remain locally level and aligned with navigation axes. Accelerometers mounted on this platform provide the $\underline{a}_{sf}$ components directly. In strapdown systems where the accelerometers are mounted along vehicle axes, the components of $\underline{a}_{sf}$ must be calculated analytically from the accelerometer measurements using computed attitude data that defines the orientation of the orthogonal accelerometer axes (body axes) relative to local level navigation axes. The details of the strapdown computations will be discussed in a subsequent lecture.

The $\underline{\omega}$ angular rate vector in (8) represents the total inertial rotation rate of the local level navigation frame relative to inertial space. This parameter is used not only in Equation (8), but also to maintain the level orientation of the navigation coordinate frame used for the $\underline{a}_{sf}$ accelerometer reference. In the case of gimbaled systems, $\underline{\omega}$ is used as a rotation rate command to the gyro stabilized platform on which the accelerometers are mounted. In this way the platform is controlled to rotate at $\underline{\omega}$, hence remain locally level. In the case of strapdown systems, $\underline{\omega}$ is used in conjunction with strapdown gyro signals to calculate the orientation of the strapdown accelerometer axes (vehicle axes) relative to local level navigation coordinates.

The $\underline{\omega}$ vector used in Equation (8) and in maintaining the level orientation of the navigation reference is calculated in the system computer as the sum of the angular rate of the local level frame relative to the earth ($\underline{\rho}$) plus the rotation rate of the earth relative to inertial space ($\underline{\Omega}$):

$$\underline{\omega} = \underline{\Omega} + \underline{\rho} \tag{9}$$

The $\underline{\Omega}$ earth rate vector in (9) is calculated as a function of computed vehicle position (i.e., the horizontal and vertical components depend on latitude). The horizontal components of $\underline{\rho}$ in (9) are calculated from vehicle horizontal velocity (horizontal components of $\underline{v}$ determined by integrating Equation (8)). The vertical component of $\underline{\rho}$ is selected to simplify the position integration (to be discussed in a subsequent lecture).

The components of plumb-bob gravity ($\underline{g}'$) in Equation (8) are calculated in the system computer in local level navigation coordinates as a function of position. This computation is simplified by noting that by good fortune, plumb bob vertical (the direction of $\underline{g}'$) is also perpendicular to the earth's surface (within a few arc seconds). Hence, for a locally level navigation frame with vertical defined as perpendicular to the local earth surface, the horizontal components of $\underline{g}'$ can be accurately approximated by zero; i.e., not calculated. Such a vertical defined as being normal to the earth surface is called a <u>geodetic</u> vertical. A vertical defined as lying along a line to the center of the earth is a <u>geocentric</u> vertical. Because of earth's oblateness, geocentric and geodetic verticals at the same point on the earth surface can deviate by as much as 3 milliradians (depending on position location). Geodetic vertical is typically instrumented in inertial navigation systems for the navigation frame reference to simplify the gravity computation (as discussed above), and as will be discussed subsequently, to also simplify the computation of latitude.

NAV SEMINAR - LECTURE 2 NOTES

## INTEGRATION OF VERTICAL VELOCITY EQUATION

Integration of the vertical (z) component of Equation (8) generates the vertical velocity component $v_Z$. Altitude can be obtained from $v_Z$ by first defining an altitude vector ($\underline{h}$) as the distance along a perpendicular from the earth surface to the actual position:

$$\underline{h} \;=\; h\,\underline{u} \;=\; \underline{R} - \underline{R}_S$$

where

$h$ = altitude.

$\underline{u}$ = Unit vector along the local vertical, perpendicular to the local earth surface.

$\underline{R}_S$ = Position vector from earth's center to the local earth surface position.

Altitude rate can be obtained by applying Coriolis Equation (4) to rates of change of $\underline{h}$ as viewed in the earth and local level frames:

$$\left(\frac{d\underline{h}}{dt}\right)_L = \left(\frac{d\underline{h}}{dt}\right)_E - \underline{\rho} \times \underline{h} \quad \text{where}$$

$\underline{\rho}$ = The angular rate of the L-frame relative to the E-Frame.

Substituting for $\underline{h}$,

$$\left(\frac{d\underline{h}}{dt}\right)_L = \dot{h}\,\underline{u} - h\left(\frac{d\underline{u}}{dt}\right)_L = \left(\frac{d\underline{h}}{dt}\right)_E - h\left(\underline{\rho} \times \underline{u}\right)$$

Because $\underline{u}$ is along the local vertical and L is a locally vertical coordinate frame, $\underline{u}$ is constant in the L-Frame, and its rate of change in the L-Frame is zero. With this substitution, taking the dot product of the above expression with $\underline{u}$ yields:

$$\dot{h} \;=\; \underline{u} \cdot \left(\frac{d\underline{h}}{dt}\right)_E = \underline{u} \cdot \left(\frac{d\underline{R}}{dt}\right)_E - \underline{u} \cdot \left(\frac{d\underline{R}_S}{dt}\right)_E$$

or, with the definition for $\underline{v}$:

$$\dot{h} \;=\; \underline{u} \bullet \underline{v} - \underline{u} \bullet \left(\frac{d\underline{R}_S}{dt}\right)_E$$

Because $\underline{u}$ is locally perpendicular to the earth surface, the rate of change of $\underline{R}_S$ has no component along $\underline{u}$. Hence, the dot product of the $\underline{R}_S$ derivative with $\underline{u}$ in the latter expression is zero. The vertical component of $\underline{v}$ is $v_z$, therefore, the final expression for altitude rate is simply:

$$\dot{h} = v_z$$

A direct integration of the z component of $\left(\frac{d\underline{v}}{dt}\right)_L$ (from (8)) to obtain $v_z$, and integration of $v_z$ to obtain h, has a divergence characteristic to instrument and gravity modeling error due to the decrease in the magnitude of $\underline{g}'$ (see Equation (8)) with altitude. As a result, an acceleration measurement error (in $\underline{a}_{sf}$ in Equation (8)), say in the upward direction, creates an erroneous $v_z$ and h, also upward. The $\underline{g}'$ term, which is calculated in the navigation computer as a function of altitude, is thereby, reduced. From Equation (8), this further increases the error in $v_z$ upward. The situation progressively worsens as the resulting altitude error grows with an unbounded exponential divergence.

For short term flights (e.g., 5 minutes or less), the divergence characteristic of the vertical channel is not pronounced, and h can be obtained as a double integration of $\dot{v}_z$. For long duration (e.g., greater than 10 minutes) flights, however, the altitude divergence is generally unacceptable, and means must be incorporated to attenuate the unbounded altitude error growth. This is accomplished through use of a blending filter which slaves the z-channel computed altitude to an external measurement of altitude (typically a barometric altimeter). The following figure illustrates the concept.

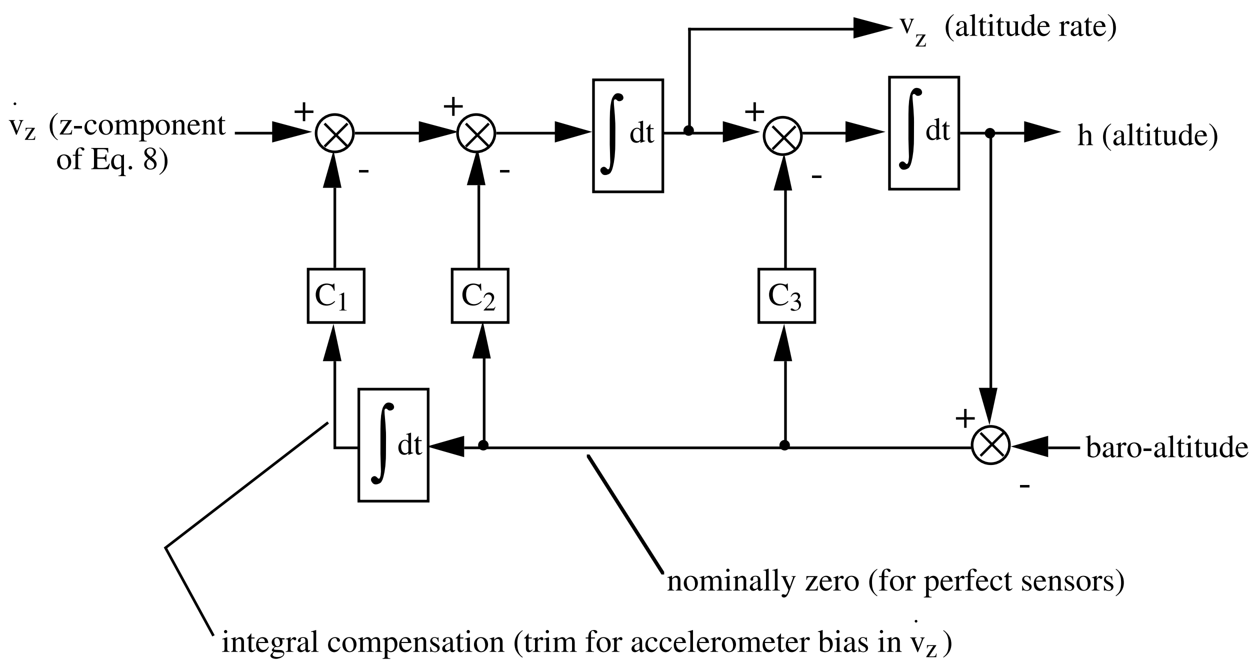


From the figure, the inertially derived altitude is compared with the baro altitude to derive an error signal which is fed back to the altitude and altitude rate integrators. The integrators are, thereby, servoed to maintain the altitude error signal near zero (on the average), thereby, preventing altitude divergence. The filter gains are low enough to prevent amplifying noise from the baro signal, and high enough to attenuate inertial sensor errors present on $\dot{v}_Z$. Integral compensation is included in the error feedback path to prevent build-up of an altitude offset in the servo loop due to accelerometer (hence, $\dot{v}_Z$) bias.

Note, that under ideal conditions, $\dot{v}_Z$ and the baro altitude signal are error free, and no error is generated in the feedback path. Thus, under these conditions, the feedback path, in effect, is disengaged, and the altitude is derived as the ideal double integration of $\dot{v}_Z$. Hence, the feedback loops only operate under error conditions. As a result, the blending filter displays the wide bandwidth performance of the inertially derived signal (double integration of $\dot{v}_Z$), the stable altitude characteristic of the baro altimeter, and through proper gain selection, attenuates the baro altimeter noise so that the final altitude output signal is a smooth measure of vehicle altitude.

## INTEGRATION OF HORIZONTAL VELOCITY CHANNEL EQUATIONS

The integration of the horizontal velocity components (X, Y) is accomplished with an appropriate integration algorithm to calculate the position of the vehicle over the earth. Because position over the earth is typically measured in units of angular rotation over the earth's surface, the horizontal velocity components are first converted to their equivalent angular rate form to represent the angular rotation rate of the local vertical as the vehicle travels over the earth. The angular rate components are then used as inputs to the position integration algorithm. Note that the vehicle transport angular rate components used for position integration are identically the horizontal components of $\underline{\rho}$ in Equation (9) of Lecture 1.

The following figure is a sketch of the earth illustrating latitude and longitude position for a particular vehicle location. Also shown in the sketch is the local level navigation coordinate frame. From the figure, it should be apparent that the angular orientation of the Z-axis (vertical) of the navigation frame relative to earth polar/equatorial coordinates is defined by latitude and longitude. Conversely, if the angular orientation of the Z-axis relative to earth coordinates is known, latitude and longitude can be determined. Thus, the calculation of vehicle position can be performed by calculating the angular orientation of the Z-axis of the navigation frame relative to the earth.

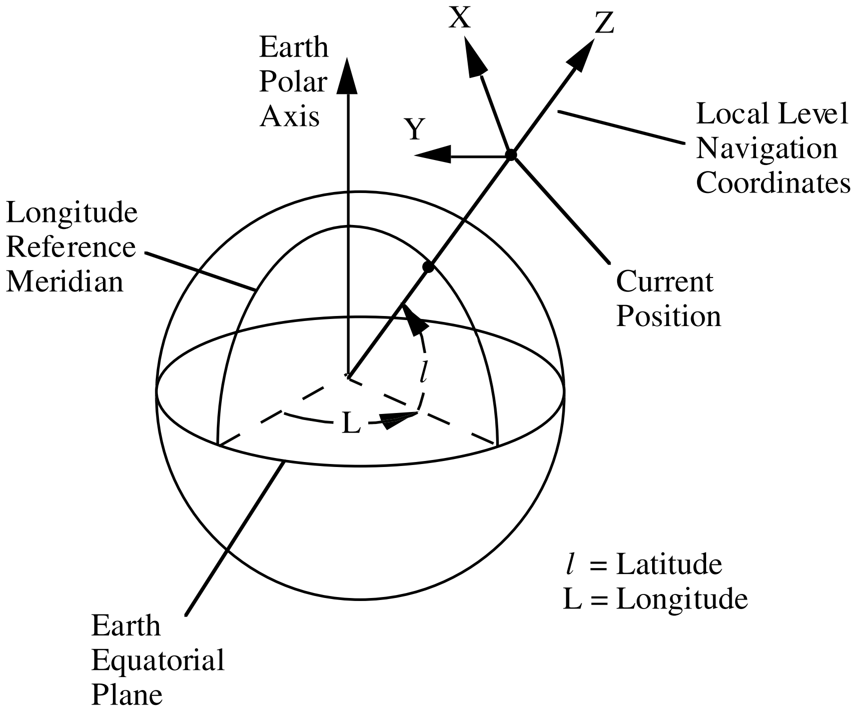


The calculation of the angular orientation of Z relative to earth coordinates is performed in an inertial navigation system as part of a general computation of the relative orientation between earth fixed and local level navigation axes. The angular attitude of the local level frame relative to earth fixed coordinates is typically defined in terms of the cosines of the angles between the axes of the two frames (i.e., direction cosines). The rate of change of these cosines is a function of the components of $\underline{\rho}$ discussed previously. A continuous integration of the cosine rate equations generates the local level navigation frame attitude relative to the earth, hence, the data from which latitude/longitude position can be analytically extracted. Additionally, the position direction cosines provide the data used in determining the azimuth (heading) orientation of the navigation axes relative to geographic North. As we shall see in a subsequent lecture, the azimuth angle is required to calculate velocity and heading data relative to North/East axes for system outputs. (Note that the horizontal velocity components generated by integrating Equation (8) are along local level navigation axes. Since the local level navigation frame is not necessarily aligned with North/East axes, a mathematical operation is required to generate the geographic North/East data from the navigation axis components.)

The position direction cosine rate equations can be derived by applying Coriolis Equation (4) to a unit vector $\underline{D}_j$ fixed to the earth along earth reference axes (along the Z polar axis or X, Y equatorial axes of the earth, each designated in general as j):

$$\left(\frac{d\underline{D}_j}{dt}\right)_E = 0 = \left(\frac{d\underline{D}_j}{dt}\right)_L + \underline{\rho} \times \underline{D}_j$$

In the above equation, the rate of change of vector $\underline{D}_j$ has been equated to zero in earth coordinates because it is by definition fixed to the earth. The latter equation is equivalently:

$$\left(\frac{d\underline{D}_j}{dt}\right)_L = -\underline{\rho} \times \underline{D}_j \tag{10}$$

The components of each $\underline{D}_j$ (j = 1, 2, or 3 for each earth frame axis) along local level (L) navigation axes are the cosines of the angles between $\underline{D}_j$ and navigation axes and are denoted for each $\underline{D}_j$ as:

$$\begin{pmatrix} d_{11} \\ d_{12} \\ d_{13} \end{pmatrix} \quad \begin{pmatrix} d_{21} \\ d_{22} \\ d_{23} \end{pmatrix} \quad \begin{pmatrix} d_{31} \\ d_{32} \\ d_{33} \end{pmatrix}$$

The components of Equation (10) for j = 1 and 2 are given by:

$$\begin{aligned}
\dot{d}_{11} &= d_{12}\,\rho_z - d_{13}\,\rho_y \\
\dot{d}_{12} &= d_{13}\,\rho_x - d_{11}\,\rho_z \\
\dot{d}_{13} &= d_{11}\,\rho_y - d_{12}\,\rho_x \\
\dot{d}_{21} &= d_{22}\,\rho_z - d_{23}\,\rho_y \\
\dot{d}_{22} &= d_{23}\,\rho_x - d_{21}\,\rho_z \\
\dot{d}_{23} &= d_{21}\,\rho_y - d_{22}\,\rho_x
\end{aligned} \tag{11}$$

Equations (11) are integrated in the inertial navigation system computer to continuously evaluate the $d_{ji}$ direction cosine elements. Inputs to Equations (11) are the components of $\underline{\rho}$.

As mentioned previously, the x, y horizontal components of $\underline{\rho}$ in Equation (11) are calculated from computed vehicle horizontal velocity. The vertical component of $\underline{\rho}$ can be arbitrarily selected to simplify the overall navigation equations. (Note that $p_z$, the vertical component of $\underline{\rho}$, only rotates the horizontal axes of the navigation coordinate frame about the vertical. The orientation of the vertical navigation frame axis relative to the earth is unaffected by $\rho_z$. Since vehicle position is determined only from the orientation of the vertical navigation frame axis relative to the earth (see previous figure), $\rho_z$ is not an inherent part of the position determination function, and can be selected based on other criteria.)

A logical choice for $\rho_Z$ might be to rotate the navigation axes so as to maintain a parallel alignment with earth North/East geographic axes. Such a navigation reference with X, Y aligned North/East is denoted as a latitude/longitude or geographic local level navigation coordinate frame. Velocity components calculated by integrating Equation (8) in local level geographic navigation coordinates will automatically lie along North/East/Vertical axes, the desired form for system output. Additionally, heading data defined by the azimuth orientation of the vehicle axes relative to the navigation frame will be referenced to North, another desirable feature for output. The geometry in the following figure demonstrates that the required value of $\rho_Z$ for a latitude/longitude navigation frame is given by:

$$\rho_Z = \rho_N \tan l \tag{12}$$

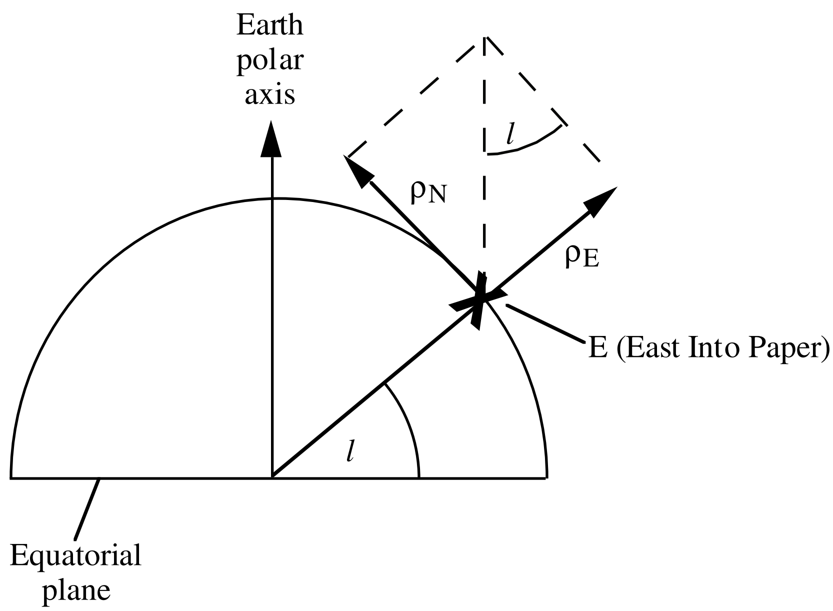


To maintain the E axis east in the previous figure, the precessional rate of the local level frame must be such that the component of $\underline{\rho}$ normal to E is parallel to the earth polar axis. Since it is only the component of $\underline{\rho}$ perpendicular to E that precesses E, this assures that the angular precession of E will occur in a plane parallel to the equator. If the E axis is also maintained horizontal by the horizontal components of $\underline{\rho}$, the E axis will thereby be forced to remain East. From the figure, the vector sum of the N and Z components of $\underline{\rho}$ define the component of $\underline{\rho}$ perpendicular to E. For the vector sum to be parallel to the polar axis, Equation (12) must be satisfied.

Equation (12) reveals that a singularity exists in the vertical component of $\underline{\rho}$ for a latitude/longitude frame near the poles ($l = \pm 90°$). Thus, use of such a system must be restricted to travel away from the poles to avoid introducing large errors in the local vertical navigation frame rotation rate, and hence, the attitude reference.

If we arbitrarily set $\rho_Z$ to zero, the implementation is denoted as a "wander azimuth" configuration. If $\rho_Z$ is set equal to $-\Omega_Z$ (i.e., $\omega_Z = 0$, see Equation (9)) a "free azimuth" implementation would result, so denoted from the gimbaled counter-part of not requiring an inertial torquing rate for the azimuth gyro (letting it run free). For either the wander azimuth or free azimuth approach, $\rho_Z$ is finite by definition for all locations on the earth. Since $\rho_X$ and $\rho_Y$ are also finite (equal to the horizontal component of vehicle angular motion over the earth), no singularities exist for $\underline{\rho}$, and the local level navigation frame precession rate is completely defined for all earth trajectories. The $\underline{\rho}$ singularity condition associated with the latitude/longitude local level frame approach is, thereby, avoided.

For the wander azimuth implementation, the azimuth rotation rate of the navigation frame relative to the earth is zero when the vehicle is stationary ($\underline{\rho} = 0$). For this condition, the azimuth angle between North and navigation level axes remains constant. Under vehicle translational motion, the azimuth orientation of the navigation frame wanders from North, hence the term "wander azimuth". The azimuth angle between navigation axes and North/East geographic axes is known as the "wander angle".

With $\rho_Z = 0$, Equations (11) for the wander azimuth implementation assume the simplified form:

$$
\begin{aligned}
\dot{d}_{11} &= -\, d_{13}\, \rho_Y \\
\dot{d}_{12} &= d_{13}\, \rho_X \\
\dot{d}_{13} &= d_{11}\, \rho_Y - d_{12}\, \rho_X \\
\dot{d}_{21} &= -\, d_{23}\, \rho_Y \\
\dot{d}_{22} &= d_{23}\, \rho_X \\
\dot{d}_{23} &= d_{21}\, \rho_Y - d_{22}\, \rho_X
\end{aligned}
\qquad (13)
$$

Note in Equations (13) that the position direction cosine rates are well behaved functions ($d_{ji}$'s, being cosines of angles, never exceed 1 in magnitude, and, as discussed previously, the components of $\rho_X$ and $\rho_Y$ are always finite.) Thus, the $d_{ji}$ quantities can be calculated from an integration of Equations (13) at all earth positions including the poles.

It should be noted at this point that a set of differential equations for latitude, longitude, and wander angle can also be derived which when integrated yield latitude/longitude/wander angle directly. Unfortunately, these equations suffer from a singularity condition at the poles similar to the problem noted previously for the latitude/longitude local level navigation frame implementation. Integration of these equations through a pole traversal results in a lost longitude and azimuth reference that is irrecoverable. One of the reasons for using direction cosines as the basic position reference parameters is to avoid singularities for all earth positions, thereby providing a complete global navigation capability.

The next two lectures will discuss how latitude, longitude, and wander angle are extracted from the integral of position direction cosine rate Equations (13), and how the $d_{ji}$'s in Equations (13) are initialized prior to engaging the integration function. Also to be discussed are the calculations of $\rho_x$, $\rho_y$ for Equations (9) and (13) from $v_x$ and $v_y$, the expressions for the $\Omega_x$, $\Omega_y$, $\Omega_z$ earth rate components in Equations (8) and (9) as functions of the $d_{ji}$'s, the calculation of the gravity term in Equation (8) as a function of altitude (h) and position ($d_{ji}$), and the equations used for calculating North/East velocity components from $v_x$ and $v_y$ using the wander angle data.

## METHOD OF LEAST WORK FOR TREATING EULER ROTATION OPERATIONS

For a vector A with components $A_x$, $A_y$, $A_z$ in one coordinate frame, find the A components in another frame (´) rotated from the first by angle $\psi$ about the Z axis (i.e., - the Z axes of both frames are coincident):

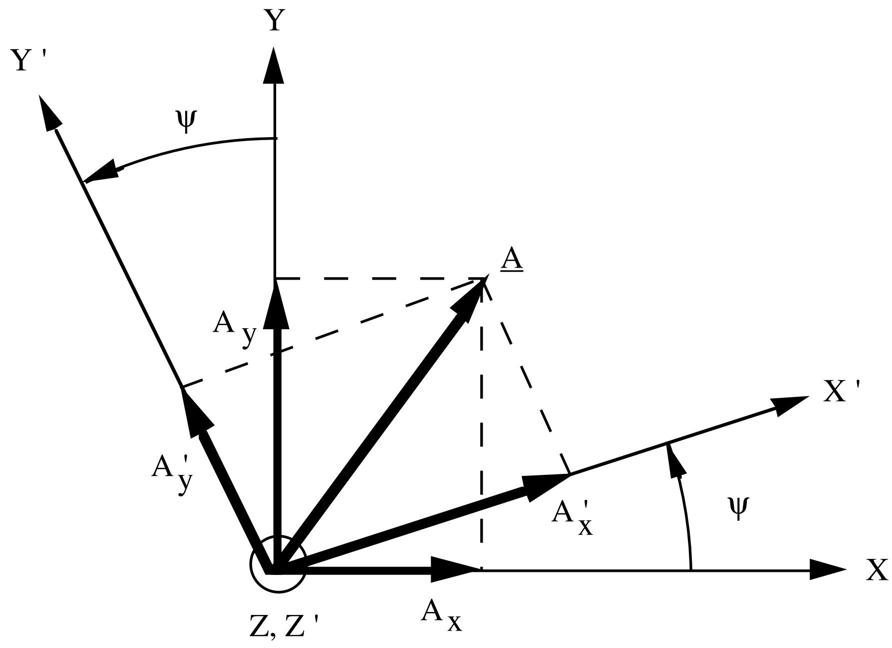


Given $A_x$, $A_y$, $A_z$, find $A_x'$, $A_y'$, $A_z'$. The solution is found by treating $A_x$, $A_y$, $A_z$ as independent vectors, finding their components individually in (´) coordinates, and summing the results:

$$
\begin{aligned}
A_x' &= A_x \cos\psi + A_y \sin\psi \\
A_y' &= A_y \cos\psi - A_x \sin\psi \\
A_z' &= A_z
\end{aligned}
\qquad (14)
$$

This can be represented by the signal flow diagram:

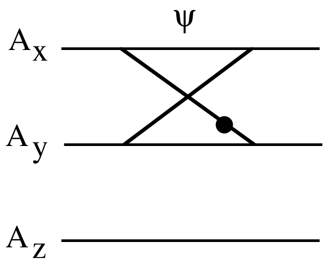


$$A_x' = A_x \cos\psi + A_y \sin\psi$$

$$A_y' = A_y \cos\psi - A_x \sin\psi$$

$$A_z' = A_z$$

which is interpreted as:

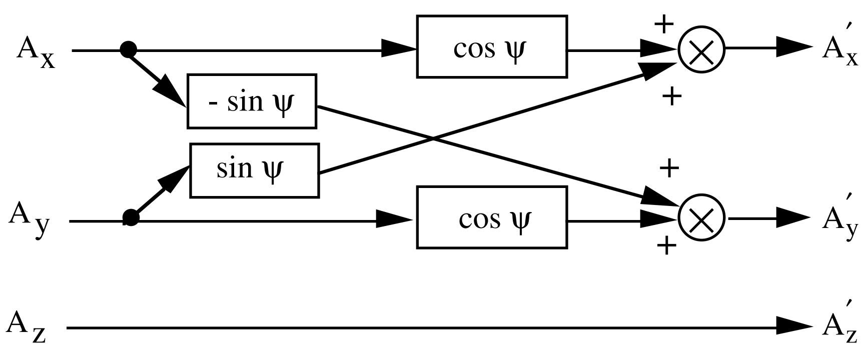


The horizontal lines between the crossed lines are treated as transmission paths with a gain of cos ψ. The crossed lines are treated as transmission paths with a gain of sin ψ. The dot (.) indicates minus (-) sin ψ. The straight path alone has unity gain. The $A_x´$, $A_y´$, $A_z´$ are derived from the top diagram by multiplying the A´s on the left by the gains along all paths to the A´s on the right. The result is Equations (14).

A similar derivation for X-axis (ϕ) and Y axis (θ) rotations yields:

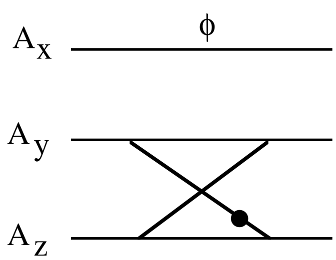


$$A_x' = A_x$$

$$A_y' = A_y \cos\phi + A_z \sin\phi$$

$$A_z' = A_z \cos\phi - A_y \sin\phi$$

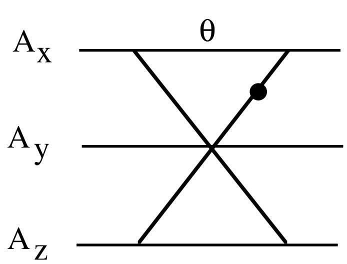


$$A_x' = A_x \cos\theta - A_z \sin\theta$$

$$A_y' = A_y$$

$$A_z' = A_z \cos\theta + A_x \sin\theta$$

A heading, pitch, roll Euler sequence, such as used for vehicle reference is given by:

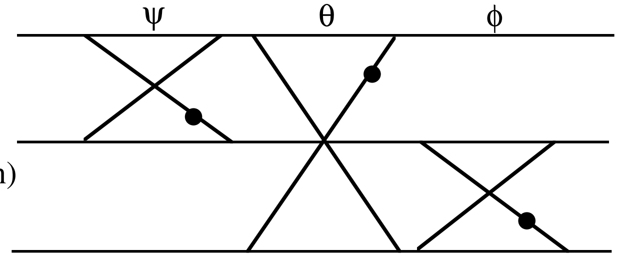


A vector $\underline{A}$ in the reference coordinate frame (x, y, z) has equivalent components in the vehicle frame (x´, y´, z´) equal to inputs at the left multiplied by all paths to the right. For example, for the y´ component:

$$A_y' = A_x\left(\cos\psi\sin\theta\sin\phi - \sin\psi\cos\phi\right)$$
$$+ A_y\left(\sin\psi\sin\theta\sin\phi + \cos\psi\cos\phi\right)$$
$$+ A_z\left(\cos\theta\sin\phi\right)$$

A similar set can be obtained for the $A_x$´, $A_z$´ components. It should be apparent that the terms in brackets represent the cosines of the angles between the two frames (i.e., between x and y', y and y', z and y' respectively). These are more commonly referred to as the direction cosines between the two coordinate frames. The above procedure allows one to easily derive an analytical expression between any left and right axis (any particular direction cosine) by tracing and summing all gains between the two points. Nine such elements exist. This is truly the method of least work for obtaining these expressions. Moreover, it is fun.

An interesting application of the technique is the determination of body rates (roll, pitch, yaw: p, q, r) from Euler angle rates ($\dot\phi$, $\dot\theta$, $\dot\psi$). This is obtained by noting that p, q, r is the net vector sum of each of the $\dot\phi$, $\dot\theta$, $\dot\psi$ effects acting simultaneously. By introducing each of the $\dot\phi$, $\dot\theta$, $\dot\psi$ vectors into the diagram at points where their vector form is known, and then tracing and summing to the right, p, q, r are determined. The $\dot\phi$, $\dot\theta$, $\dot\psi$ quantities are along X, Y, Z respectively in the intermediate frames where their Euler angles are defined. Thus:

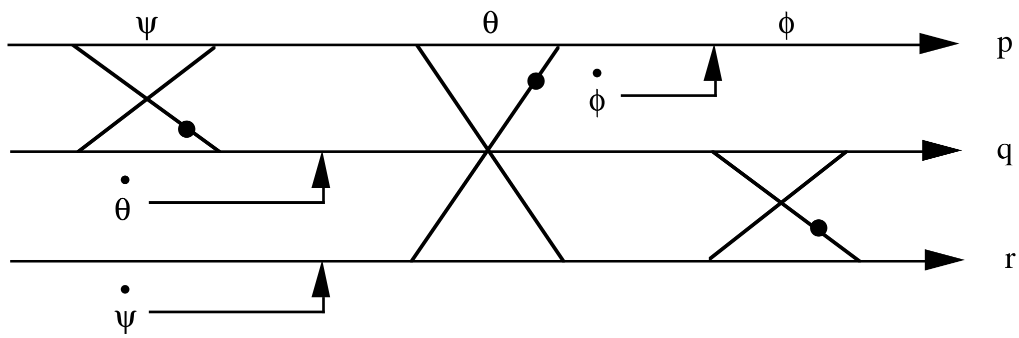


and

$$p = \dot{\phi} - \dot{\psi} \sin \theta$$
$$q = \dot{\theta} \cos \phi + \dot{\psi} \cos \theta \sin \phi$$
$$r = - \dot{\theta} \sin \phi + \dot{\psi} \cos \theta \cos \phi$$

What could be simpler (or more fun)?

The diagram works in the inverse direction also, provided that the three outputs are calculated at one coordinate frame position. The former diagram works ($A_x$, $A_y$, $A_z$ from $A_x'$, $A_y'$, $A_z'$). The latter diagram ($\dot{\phi}$, $\dot{\theta}$, $\dot{\psi}$ from p, q, r) is not directly reversible without some trickery (left as an exercise).

## APPLICATION TO THE NAVIGATION PROBLEM

The angular relationship between the local level coordinate frame and the earth fixed equatorial coordinate frame can be described by the Euler sequence: Y(+ΔL), X(-$l$), Z(+α) as illustrated by the diagram that follows and where:

| | | |
|---|---|---|
| $\Delta L$ | = | Longitude change since initiation of navigation. |
| $l$ | = | Current latitude. |
| $\alpha$ | = | The wander angle between north and the local level frame Y-axis. |
| $L_o$ | = | Initial longitude. |
| $l_o$ | = | Initial latitude. |

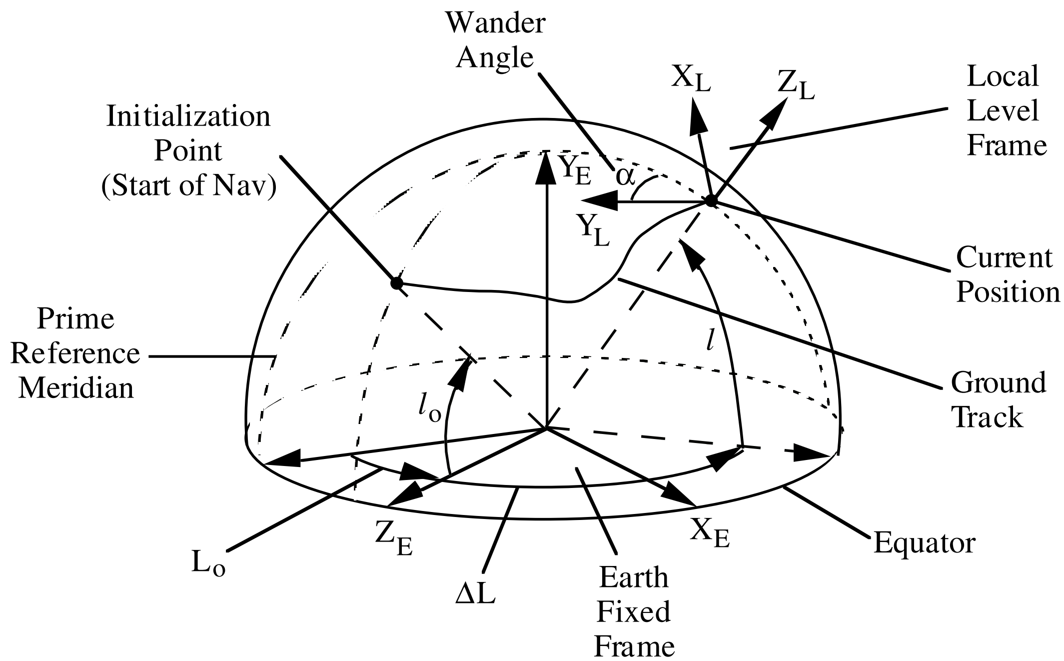


Using the Method of Least Work:

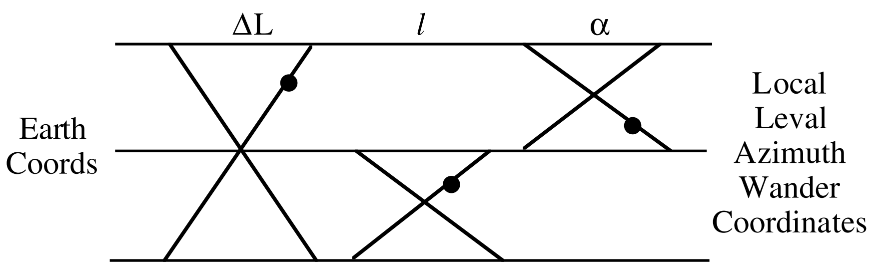


Note, the dot (•) is inverted on the $l$ because it is a minus X rotation.

We can now easily obtain a set of equations for the $d_{ji}$'s (direction cosines) between the earth frame and local level frame in terms of $\Delta L$, $l$, $\alpha$. These can then be equated to the d's (from the last lecture - Equations (13)), and the desired $\Delta L$, $l$, $\alpha$ quantities calculated for pilot display, etc. Using the "Method":

$$
\begin{aligned}
d_{11} &= \cos \Delta L \cos \alpha - \sin \Delta L \sin l \sin \alpha \\
d_{12} &= - \cos \Delta L \sin \alpha - \sin \Delta L \sin l \cos \alpha \\
d_{13} &= \sin \Delta L \cos l \\
d_{21} &= \cos l \sin \alpha \\
d_{22} &= \cos l \cos \alpha \\
d_{23} &= \sin l \\
d_{33} &= \cos \Delta L \cos l
\end{aligned}
\tag{15}
$$

from which:

$$\tan l = \frac{\sin l}{\cos l} = \frac{\sin l}{\sqrt{1 - \sin^2 l}} = \frac{d_{23}}{\sqrt{1 - d_{23}{}^2}} = \frac{d_{23}}{\sqrt{d_{21}^2 + d_{22}^2}}$$

$$\tan \alpha = \frac{d_{21}}{d_{22}}$$

$$\tan \Delta L = \frac{\sin \Delta L}{\cos \Delta L} = \frac{d_{13}}{d_{33}} = \frac{d_{13}}{d_{11}\, d_{22} - d_{21}\, d_{12}}$$

The latter equation (with $1 - d_{23}^2$ replaced by $d_{21}^2 + d_{22}^2$ and $d_{33}$ replaced by $d_{11}\, d_{22} - d_{21}\, d_{12}$) is used so that $d_{33}$ need not be calculated (note its absence in Equations (13)). The equality between $d_{33}$ and the cross-product follows from the definition of $\underline{D}_1$, $\underline{D}_2$ and $\underline{D}_3$ being orthogonal unit vectors along the Earth axes, and that, therefore,

$$\underline{D}_3 = \underline{D}_1 \times \underline{D}_2$$

$$\underline{D}_2 \cdot \underline{D}_2 = 1$$

The expressions for $d_{33}$ and $1 - d_{23}^2$ are obtained by carrying out the cross and dot products in component form using:

$$\underline{D}_1 = \begin{pmatrix} d_{11} \\ d_{12} \\ d_{13} \end{pmatrix} \qquad \underline{D}_2 = \begin{pmatrix} d_{21} \\ d_{22} \\ d_{23} \end{pmatrix} \qquad \underline{D}_3 = \begin{pmatrix} d_{31} \\ d_{32} \\ d_{33} \end{pmatrix}$$

The inverse trig functions give the desired results:

$$L = L_o + \Delta L = L_o + \tan^{-1} \frac{d_{13}}{d_{11}\, d_{22} - d_{21}\, d_{12}}$$

$$l = \tan^{-1} \frac{d_{23}}{\sqrt{d_{21}^2 + d_{22}^2}} \tag{16}$$

$$\alpha = \tan^{-1} \frac{d_{21}}{d_{22}}$$

Equations (16) are typically programmed in the navigation computer to evaluate L, $l$, and $\alpha$ from the computer D matrix elements. Note in Equation (16) that longitude is determined from an arc tan function of $d_{13}$ divided by $d_{33}$ (i.e., $d_{33} = d_{11}\, d_{22} - d_{21}\, d_{12}$). From Equation (15), both $d_{13}$ and $d_{33}$ approach zero at high and low latitudes ($l = \pm 90$ deg or cos $l = 0$). Hence, longitude at the poles is not defined. Thus, the equivalent of the singularity condition at the poles noted previously for latitude/longitude navigation coordinates also exists for longitude determination in the azimuth wander implementation. The key difference, however, is that for the latitude/longitude coordinate frame approach, the position reference is permanently destroyed; for the azimuth wander coordinate frame concept, the basic position data (the position direction cosines) remain intact through pole traversals, and longitude can again be read accurately after the traversal is completed. The latter singularity condition simply emphasizes the fact that longitude at either pole (a single point) is meaningless; latitude alone completely defines the pole position, and the latitude determination equation for the azimuth wander system is deterministic at the poles.

A similar singularity situation exists in the wander azimuth system for the wander angle extraction formula in Equations (16). Both $d_{21}$ and $d_{22}$ approach zero at high and low latitude ($l = \pm 90°$), hence, the wander angle becomes undefined at the poles. This is because the concept of heading relative to North vanishes at the poles (i.e., at the North pole all directions are South, and vise versa at the South pole). As for the longitude determination function in the wander azimuth system, the wander angle data is once again recoverable after the pole transversal is completed.

Returning to Equations (13), these are differential equations that must be integrated continuously in the flight computer to determine the d's. To begin the integration process, the d's must be initialized properly at entry into the navigate mode. The "Method" can be used to derive the equations used for d initialization. At initialization time, $\Delta L = 0$ (by definition), $l = l_o$ and $\alpha = \alpha_o$. A vector along the Y-axis of the Earth Frame, in particular, the earth rate vector, then, at initialization time, is given in local level navigation coordinates by:

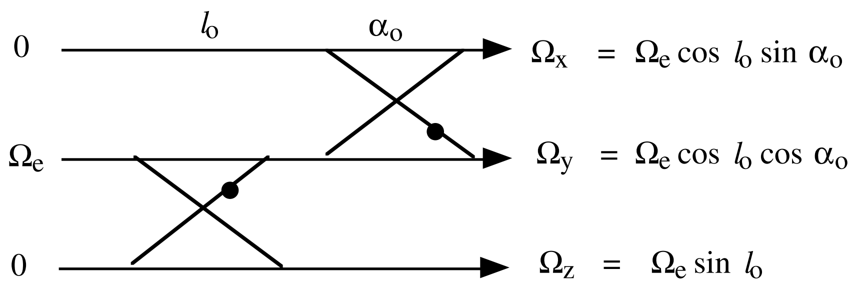


Also, the d elements at this time, from Equations (15) (or directly from the above diagram) are:

$$
\begin{aligned}
d_{11_o} &= d_{11_o} = \cos \alpha_o \\
d_{12_o} &= d_{12_o} = -\sin \alpha_o \\
d_{13_o} &= d_{13_o} = 0 \\
d_{21_o} &= \cos l_o \sin \alpha_o \\
d_{22_o} &= \cos l_o \cos \alpha_o \\
d_{23_o} &= \sin l_o
\end{aligned}
\tag{17}
$$

Defining normalized earth rate components as:

$$
\Omega_1 = \frac{\Omega_x}{\Omega_e} = \cos l_o \sin \alpha_o
$$

$$
\Omega_2 = \frac{\Omega_y}{\Omega_e} = \cos l_o \cos \alpha_o
$$

we obtain the final expressions for the $d_o$'s in terms of $\Omega_1$, $\Omega_2$, and $l_o$:

$$
\begin{aligned}
d_{11_o} &= \frac{\Omega_2}{\cos l_o} & \qquad d_{21_o} &= \Omega_1 \\
d_{12_o} &= -\frac{\Omega_1}{\cos l_o} & \qquad d_{22_o} &= \Omega_2 \\
d_{13_o} &= 0 & \qquad d_{23_o} &= \sin l_o
\end{aligned}
\tag{18}
$$

Equations (18) are initialization equations that would be executed at completion of alignment at the instant of entry into the navigate mode. The $l_o$ quantity is the initial latitude entered into the display. The $\Omega_1$, $\Omega_2$ quantities are calculated as the primary output from the alignment filter (and sometimes displayed to indicate alignment progress). It should be noted that if the accuracy penalty is acceptable, $l_o$ can actually be computed from $\Omega_1$, $\Omega_2$ without requiring a latitude input from the display:

$$\tan^2 l_o = \frac{\sin^2 l_o}{\cos^2 l_o} = \frac{1 - \cos^2 l_o}{\cos^2 l_o} = \frac{1}{\cos^2 l_o} - 1$$

$$= \frac{1}{\cos^2 l_o \left(\cos^2 \alpha_o + \sin^2 \alpha_o\right)} - 1 = \frac{1}{\Omega_1^2 + \Omega_2^2} - 1$$

$$/l_o/ = \tan^{-1} \sqrt{\frac{1}{\Omega_1^2 + \Omega_2^2} - 1}$$

The sign of $l_o$ is obtained by either knowing which hemisphere one is in at takeoff (North or South), or calculating $\Omega_3$, the normalized vertical component of earth rate, as an added part of the alignment process ($\Omega_3 = \frac{\Omega_z}{\Omega_e} = \sin\ l_o$) and using sign of $\Omega_3$ to determine $l_o$ polarity. The $\Omega_3$ term cannot be estimated to the same accuracy as $\Omega_1$, $\Omega_2$, but it can possibly be estimated to an accuracy sufficient for estimating its sign. The feasibility of the above method for calculating $l_o$ breaks down near the equator where $\Omega_1^2 + \Omega_2^2$ equals one and becomes insensitive to latitude variations. Near the equator, one may resort to the use of $\Omega_3$ directly for latitude determination, and suffer some performance degradation due to the reduced accuracy in estimating $\Omega_3$ (compared to $\Omega_1$, $\Omega_2$). The associated latitude estimation equation is:

$$l_o = \tan^{-1} \frac{\Omega_3}{\sqrt{\Omega_1^2 + \Omega_2^2}}$$

The basic problem associated with the idea of inertially calculating initial latitude lies in the added error produced in the system output. Since latitude is calculated using the system gyro and accelerometer data, errors in these instruments produce an initial latitude error. This is an additional error source that must now be accounted for in the system error budget. (Normally, initial latitude error is essentially zero, based on an accurate input to the system by the operator). For most applications, the added error is large enough to be intolerable. The utility of the $l_o$ self estimating concept may, therefore, prove more beneficial as a check against an erroneous pilot entry or to indicate a malfunctioning system, than as an absolute reference.

NAV SEMINAR - LECTURE 4 NOTES

DERIVATION OF ρ AND Ω EXPRESSIONS FOR EQUATIONS (8), (9), AND (13)

The components of $\underline{\rho}$ ($\rho_x$ and $\rho_y$; $\rho_z = 0$) are evaluated for the azimuth wander system by first considering their form in North/East geographic coordinates, and then transforming the result to azimuth wander coordinates. For geographic local level coordinates, the horizontal components of $\underline{\rho}$ are given by:

$$\rho_N = \frac{1}{r_L} v_E$$

$$\rho_E = -\frac{1}{r_l} v_N$$

where:

| | | |
|---|---|---|
| $\rho_N$, $\rho_E$ | = | North and East components of $\underline{\rho}$. |
| $v_N$, $v_E$ | = | North and East components of $\underline{v}$. |
| $r_L$, $r_l$ | = | The radii of curvature of the local horizontal in the East ($r_L$) and North ($r_l$) directions. The local horizontal is defined as the plane at the navigation altitude that is parallel to the earth's surface below the navigating vehicle. "Below" is defined as downward along a line from the navigating vehicle that passes perpendicularly through the earth's surface. |

The North/East geographic frame is rotated from the azimuth wander frame about the local vertical Z-axis by the wander angle (α). Thus:

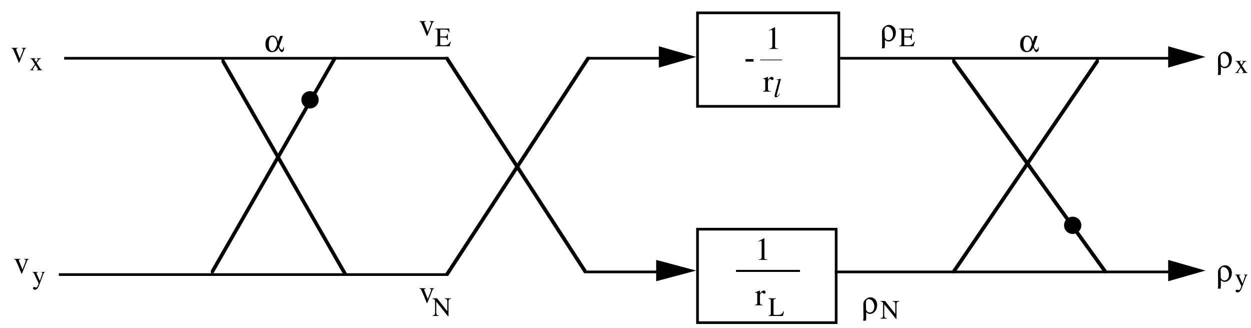


From the diagram:

$$\rho_x = v_x\left(\frac{\sin\alpha\cos\alpha}{r_L} - \frac{\sin\alpha\cos\alpha}{r_l}\right) + v_y\left(\frac{-\cos^2\alpha}{r_l} - \frac{\sin^2\alpha}{r_L}\right)$$

$$= v_x \sin\alpha\cos\alpha\left(\frac{1}{r_L} - \frac{1}{r_l}\right) - v_y\left(\frac{\cos^2\alpha}{r_l} - \frac{\sin^2\alpha}{r_L}\right)$$

If the earth were a perfect sphere, $r_L$ and $r_l$ would be equal to the radial distance from earth's center to the vehicle. Because the earth is an oblate spheroid, the expressions for $r_L$ and $r_l$ are more complex. From Appendix B in Pittman - <u>Inertial Guidance</u>, the values for $r_L$ and $r_l$ for zero altitude (on the earth's surface) can be accurately approximated by:

$$r_l = R_o\left[1 - e\left(2 - 3\sin^2 l\right)\right]$$
$$r_L = R_o\left(1 + e\sin^2 l\right)$$

where

$l$ = Vehicle geocentric latitude.

$R_o$ = The equatorial earth radius.

e = The ellipticity of the ellipse formed by the intersection of a meridian plane with the earth's surface. I.e.; the earth's surface is approximated as an ellipsoid of revolution where the earth polar axis is both the axis of symmetry of the ellipsoid and the minor axis of the ellipse used to generate the ellipsoid. The major axis of the ellipse lies in the earth's equatorial plane. The earth's surface is defined as the surface generated by revolving the ellipse about the earth polar axis.

For flights above the surface of the earth, the latter expression is modified to first order by setting the $R_o$ term equal to $R_o + h$ where:

h = Vehicle altitude.

Thus:

$$r_l = \left(R_o + h\right)\left[1 - e\left(2 - 3\sin^2 l\right)\right]$$
$$r_L = \left(R_o + h\right)\left(1 + e\sin^2 l\right)$$

Since e is small, and h is small relative to $R_o$, the $\frac{1}{r_l}$ and $\frac{1}{r_L}$ terms in the previous $\rho_x$ expression can be approximated by first order Taylor series expansions:

$$\frac{1}{r_l} \approx \frac{1}{R_o}\left[1 - \frac{h}{R_o} + e\left(2 - 3\sin^2 l\right)\right]$$

$$\frac{1}{r_L} \approx \frac{1}{R_o}\left(1 - \frac{h}{R_o} - e\sin^2 l\right)$$

and

$$\frac{1}{r_L} - \frac{1}{r_l} = -\frac{1}{R_o}\, e\left(\sin^2 l + 2 - 3\sin^2 l\right)$$

$$= -\frac{2e}{R_o}\left(1 - \sin^2 l\right) = -\frac{2e}{R_o}\cos^2 l$$

Substituting into the terms in the $\rho_x$ equation yields:

$$\sin\alpha\cos\alpha\left(\frac{1}{r_L} - \frac{1}{r_l}\right) = -\frac{2e}{R_o}\left(\sin\alpha\cos l\right)\left(\cos\alpha\cos l\right)$$

and

$$\frac{\cos^2\alpha}{r_l} + \frac{\sin^2\alpha}{r_L} = \frac{1}{R_o}\left[\cos^2\alpha\left(1 - \frac{h}{R_o} + e\left(2 - 3\sin^2 l\right)\right) + \sin^2\alpha\left(1 - \frac{h}{R_o} - e\sin^2 l\right)\right]$$

$$= \frac{1}{R_o}\left[\left(\cos^2\alpha + \sin^2\alpha\right)\left(1 - \frac{h}{R_o}\right) + e\cos^2\alpha\left(2 - 2\sin^2 l - \sin^2 l\right) - e\sin^2\alpha\sin^2 l\right]$$

$$= \frac{1}{R_o}\left(1 - \frac{h}{R_o} + 2e\cos^2\alpha\cos^2 l - e\cos^2\alpha\sin^2 l - e\sin^2\alpha\sin^2 l\right)$$

$$= \frac{1}{R_o}\left(1 - \frac{h}{R_o} + 2e\cos^2\alpha\cos^2 l - e\sin^2 l\right)$$

$$= \frac{1}{R_o}\left(1 - \frac{h}{R_o} + e\left[-2\cos^2\alpha\cos^2 l + 1 - \cos^2 l\left(\cos^2\alpha + \sin^2\alpha\right)\right]\right)$$

$$= \frac{1}{R_o}\left[1 - \frac{h}{R_o} - e\left(1 - 3\left(\cos\alpha\cos l\right)^2 - \left(\sin\alpha + \cos l\right)^2\right)\right]$$

With the above terms, the $\rho_x$ equation becomes:

$$\rho_x = -\frac{v_y}{R_o}\left[1 - \frac{h}{R_o} - e\left(1 - 3\left(\cos\alpha\cos l\right)^2 - \left(\sin\alpha\cos l\right)^2\right)\right]$$

$$-\frac{v_x}{R_o}\, 2e\left(\sin\alpha\cos l\right)\left(\cos\alpha\cos l\right)$$

The bracketed trigonometric terms in the latter equation are functions of geocentric latitude. Since each of these terms is multiplied by e, only a second order error (in e) is introduced into $\rho_x$ if they are approximated by their geodetic latitude derived counterparts as defined by $d_{21}$ and $d_{22}$ in Equations (15). (Note: Although the same symbol $l$ is used in Equations (15) and for the $\rho_x$ derivation above, $l$ in Equations (15) represents geodetic latitude while $l$ in the $\rho_x$ equation represents geocentric latitude. The difference between geodetic and geocentric latitudes is on the order of e, hence, an $e^2$ error is introduced in $\rho_x$ when geodetic latitude is used as an approximation.) Using $d_{21}$ and $d_{22}$ for the bracketed terms, the $\rho_x$ equation assumes the final form:

$$\rho_x = -\frac{v_y}{R_o}\left[1 - \frac{h}{R_o} - e\left(1 - 3\,d_{22}^2 - d_{21}^2\right)\right] - \frac{v_x}{R_o}\left(2\,e\,d_{21}\,d_{22}\right) \tag{19}$$

A similar derivation yields the following for $\rho_y$:

$$\rho_y = \frac{v_x}{R_o}\left[1 - \frac{h}{R_o} - e\left(1 - 3\,d_{21}^2 - d_{22}^2\right)\right] + \frac{v_y}{R_o}\left(2\,e\,d_{21}\,d_{22}\right) \tag{19A}$$

These are the desired expressions for the components of $\underline{\rho}$ in azimuth wander coordinates for the navigation computer (with $\rho_z = 0$).

The expression for the $\underline{\Omega}$ vector in Equations (8) and (9) in azimuth wander coordinates is obtained by multiplying the earth rate vector magnitude ($\Omega_e$) by the cosines of the angles between the earth polar axis (Y-axis in the earth frame) and the azimuth wander axes. The cosines are the $\underline{D_2}$ direction cosines ($d_{21}$, $d_{22}$, $d_{23}$).

Thus:

$$\underline{\Omega} = \begin{pmatrix} d_{21}\ \Omega_e \\ d_{22}\ \Omega_e \\ d_{23}\ \Omega_e \end{pmatrix} \tag{19B}$$

The $\underline{\omega}$ vector in Equation (8) is the sum of $\underline{\Omega}$ and $\underline{\rho}$ as shown in Equation (9). With $\rho_z = 0$ for azimuth wander navigation coordinates, and $\underline{\Omega}$ as defined above, $\underline{\omega}$ is given by:

$$\underline{\omega} = \begin{pmatrix} \omega_x \\ \omega_y \\ \omega_z \end{pmatrix} = \begin{pmatrix} \rho_x + d_{21}\,\Omega_e \\ \rho_y + d_{22}\,\Omega_e \\ d_{23}\,\Omega_e \end{pmatrix} \tag{19C}$$

As discussed previously, plumb-bob gravity lies approximately along the geodetic vertical, hence, for geodetic vertical navigation coordinates, $\underline{g}'$ in (8A) is:

$$\underline{g}' = \begin{pmatrix} 0 \\ 0 \\ -g_D \end{pmatrix}$$

where $g_D$ is the component of plumb-bob gravity downward along the geodetic vertical. The components of $\underline{a}_{sf}$ and $\underline{v}$ in (8) can be defined as:

$$\underline{a}_{sf} = \begin{pmatrix} a_x \\ a_y \\ a_z \end{pmatrix} \qquad \underline{v} = \begin{pmatrix} v_x \\ v_y \\ v_z \end{pmatrix}$$

Substitution of the latter expressions in (8) yields the equivalent component form in azimuth wander local level navigation coordinates in terms of parameters calculated in the navigation computer (or derived from measurements; i.e., - accelerations $a_x$, $a_y$, $a_z$).

$$\begin{aligned} \dot{v}_x &= a_x + 2\, d_{23}\, \Omega_e\, v_y - \left(2\, d_{22}\, \Omega_e + \rho_y\right) v_z \\ \dot{v}_y &= a_y + \left(2\, d_{21}\, \Omega_e + p_x\right) v_z - 2\, d_{23}\, \Omega_e\, v_x \\ \dot{v}_z &= a_z - g_D + \left(2\, d_{22}\, \Omega_e + \rho_y\right) v_x - \left(2\, d_{21}\, \Omega_e + \rho_x\right) v_y \end{aligned} \tag{20}$$

## CALCULATION OF PLUMB-BOB GRAVITY ($G_D$) FOR EQUATION (20)

Newton’s Law of Gravitation tells us that the magnitude of gravitational attraction from a point mass is inversely proportional to the square of the distance from the point mass. For a sphere with uniform mass distribution, the same law applies above the sphere with the distance factor measured to the center of the sphere. In the vicinity of a planet, such as the earth, the law is slightly modified due to the mass asymmetry that always exists in any real body. For the earth, the mass distribution is approximately symmetrical about the polar axis and essentially oblate (i.e., symmetrical above and below the equatorial plane). From Section 4.5 in Britting - Inertial Navigation Systems Analysis, earth’s gravitational acceleration, as determined by satellite orbit observations, can be accurately approximated for inertial navigation purposes by:

$$g = \frac{\mu}{R^2}\left(1 - \frac{3}{4}\, J_2 \left(1 - 3 \cos 2\, l\right)\right)$$

where

$R$ = The radial distance from earth’s center to the point where gravity is being measured.

$l$ = Geodetic latitude.

$J_2$ = An empirical constant equal to 0.00108.

$\mu$ = The average value of gravity at the equator times earth's equatorial radius squared.

The downward or negative Z-axis navigation coordinate component of plumb-bob gravity ($g_D$ in Equations (20)) equals g minus the vertical component of $-\underline{\Omega} \times (\underline{\Omega} \times \underline{R})$ (See Equation (8A)). Using (19B) with the $d_{ij}$'s as defined by (15), $\underline{\Omega}$ can be written as:

$$\underline{\Omega} = \begin{pmatrix} \Omega_e \cos l \sin \alpha \\ \Omega_e \cos l \cos \alpha \\ \Omega_e \sin l \end{pmatrix}$$

with in navigation coordinates,

$$\underline{R} = \begin{pmatrix} 0 \\ 0 \\ R \end{pmatrix}$$

The vertical (Z) component of $-\underline{\Omega} \times (\underline{\Omega} \times \underline{R})$ is:

$$R\, \Omega_e^2 \cos^2 l$$

so that:

$$g_D = \frac{\mu}{R^2}\left(1 - \frac{3}{4} J_2 (1 - 3 \cos 2\, l)\right) - R\, \Omega_e^2 \cos^2 l$$

From Appendix B of Pittman - Inertial Guidance, R at the surface of the earth can be accurately approximated as:

$$R = R_o \left(1 - e \sin^2 l\right)$$

where $R_o$ and e are as defined previously in this lecture, and $l$ is geocentric latitude (or approximately geodetic latitude).

Including the effect of altitude above the earth, the above expression for moderate altitudes (less than 100,000 feet) can be approximated as:

$$R = R_o \left(1 - e \sin^2 l\right) + h$$

Substituting in the $g_D$ equation, recognizing that e is small (approximately $\frac{1}{298}$) and that h is much less than $R_o$, and applying appropriate trigonometric manipulations yields the following:

$$g_D = \frac{\mu\left(1 - \frac{3}{4} J_2 (1 - 3\cos 2\,l)\right)}{R_o^2\left(\left(1 - e\sin^2 l\right) + \frac{h}{R_o}\right)^2} - \left[R_o\left(1 - e\sin^2 l\right) + h\right]\Omega_e^2\cos^2 l$$

$$\approx \frac{\mu}{R_o^2}\left(1 - \frac{3}{4} J_2\left[1 - 3\left(1 - 2\sin^2 l\right)\right] + 2\,e\sin^2 l - 2\frac{h}{R_o}\right)$$

$$- R_o\,\Omega_e^2\left(1 - e\sin^2 l + \frac{h}{R_o}\right)\cos^2 l$$

$$= \frac{\mu}{R_o^2}\left(1 + \frac{3}{2} J_2\left(1 - 3\sin^2 l\right) + 2\,e\sin^2 l - 2\frac{h}{R_o}\right)$$

$$- R_o\,\Omega_e^2\left(1 - e\sin^2 l + \frac{h}{R_o}\right)\cos^2 l$$

$$= \frac{\mu}{R_o^2}\left(1 - 2\frac{h}{R_o} + 2\,e\sin^2 l\right) + \frac{\mu}{R_o^2}\frac{3}{2} J_2\left(1 - 3\sin^2 l\right)$$

$$- R_o\,\Omega_e^2\left(1 - e\sin^2 l + \frac{h}{R_o}\right)\cos^2 l$$

$$= G_1\left(1 - 2\frac{h}{R_o} + 2\,e\sin^2 l\right) + G_2\left(1 - 3\sin^2 l\right) - G_3\left(1 - e\sin^2 l + \frac{h}{R_o}\right)\cos^2 l$$

where

$$G_1 = \frac{\mu}{R_o^2} = \text{Average gravity magnitude at earth's surface at the equator.}$$

$$G_2 = \frac{3}{2} J_2\,G_1 \qquad (20A)$$

$$G_3 = R_o\,\Omega_e^2$$

Using $d_{23}$ for $\sin l$ (from Equations (15)), the final expression for $g_D$ becomes:

$$g_D = G_1\left(1 - 2\frac{h}{R_o} + 2\,e\,d_{23}^2\right) + G_2\left(1 - 3\,d_{23}^2\right) - G_3\left(1 - e\,d_{23}^2 + \frac{h}{R_o}\right)\left(1 - d_{23}^2\right) \qquad (20B)$$

## VELOCITY COMPONENTS IN NORTH/EAST GEOGRAPHIC COORDINATES

Before summarizing, one additional set of expressions should be derived for output and display: the equations for the horizontal velocity components in North/East geographic coordinates. These can be expressed in two forms: as North/East components ($v_N$, $v_E$) along North/East axes directly, or in polar coordinate form as the ground speed magnitude ($v_G$) and track angle (TK) of the horizontal velocity vector relative to North. The following diagram illustrates the geometry involved. The relationship between $v_N$, $v_E$, TK, $v_G$ and $v_x$, $v_y$, $\alpha$ from the diagram are given in Equations (21).

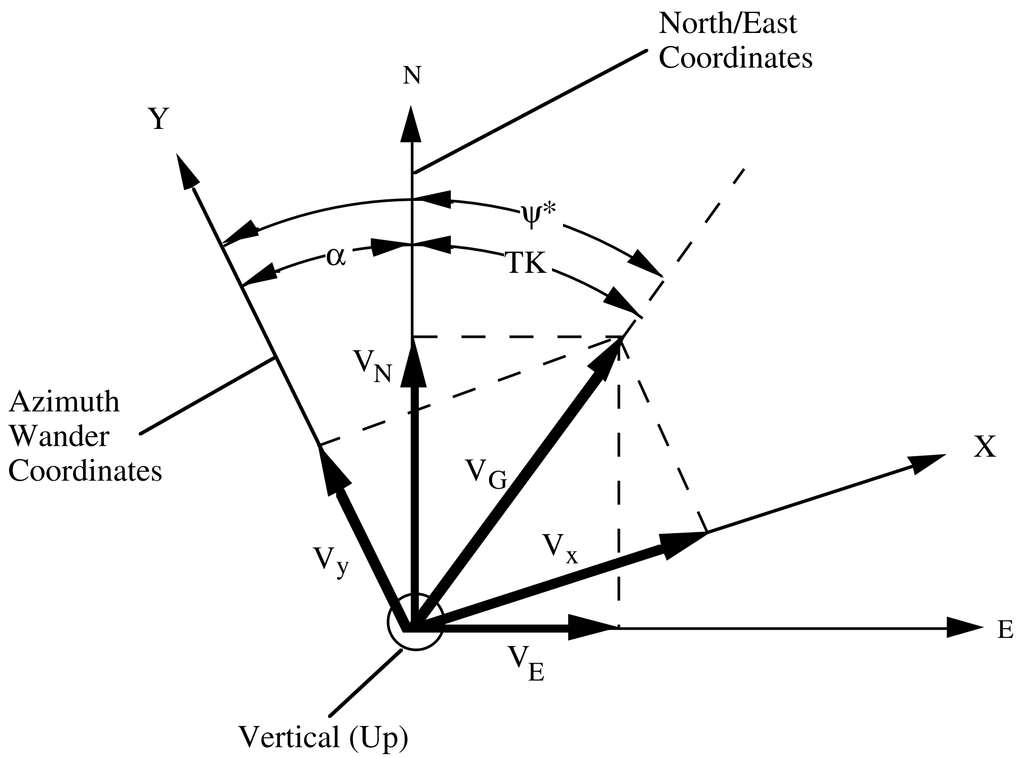


$$
\begin{aligned}
v_N &= v_y \cos\alpha + v_x \sin\alpha \\
v_E &= v_x \cos\alpha - v_y \sin\alpha \\
TK &= \psi^* - \alpha \\
\psi^* &= \tan^{-1}\frac{v_x}{v_y} \\
TK &= \tan^{-1}\frac{v_x}{v_y} - \alpha \\
V_G &= \sqrt{v_x^{\,2} + v_y^{\,2}}
\end{aligned}
\qquad (21)
$$

NAVIGATION EQUATION SUMMARY

The block diagram that follows summarizes the total computations involved in computing navigation data from acceleration (and baro altitude) measurements as given by Equations (13), (16), (19), (19A), (19C), (20), (20A), (20B), and (21), with the baro altitude channel from Lecture Notes 2, and initial conditions given by Equations (18) and $v_{x_o} = v_{y_o} = 0$.

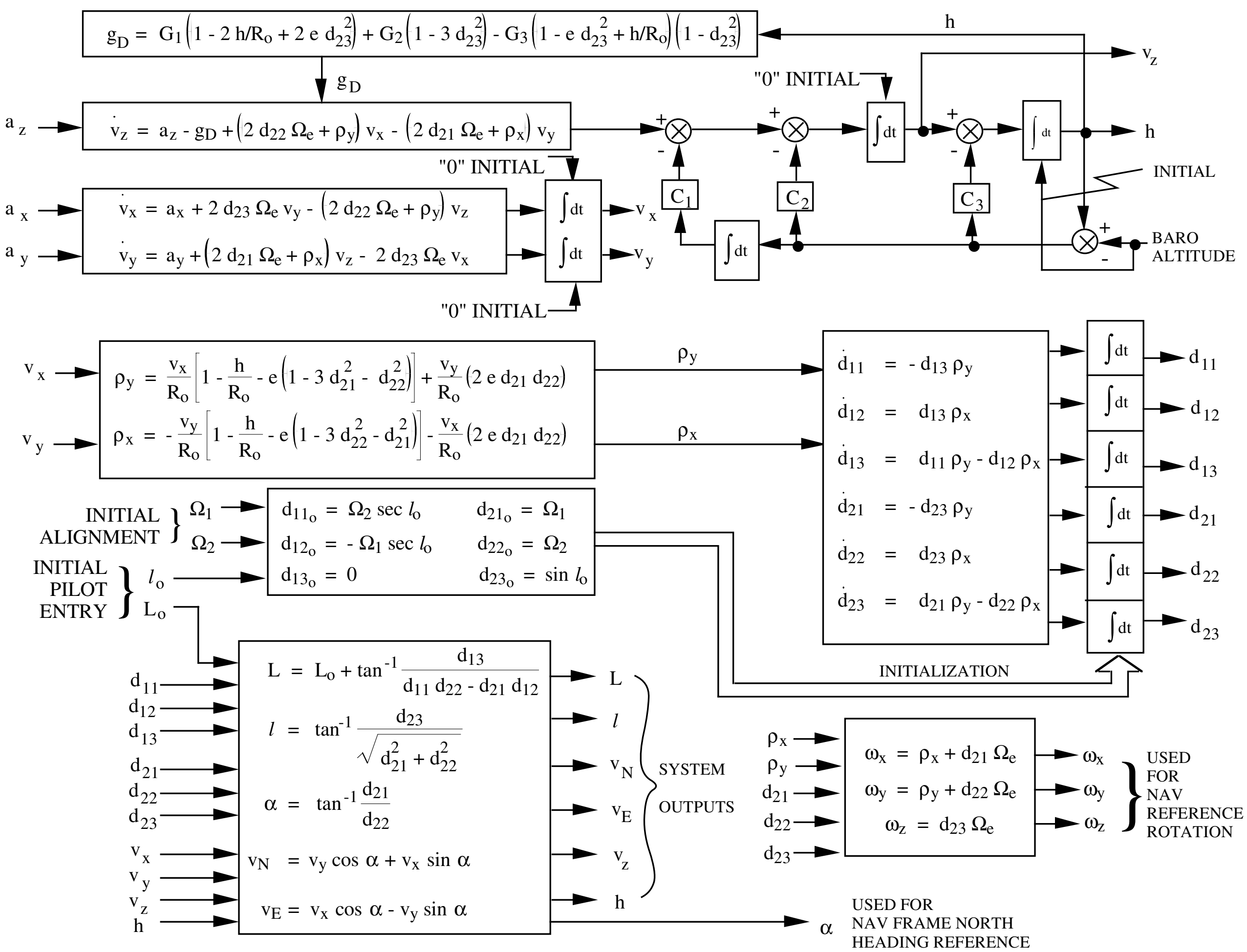


**NAVIGATION EQUATION SUMMARY**

## STRAPDOWN ATTITUDE REFERENCE EQUATIONS

LECTURE 5

LECTURE 6

LECTURE 7

LECTURE 8

LECTURE 9

Equations (20) are integrated in the navigation computer to evaluate the components of $\underline{v}$. These equations have the following form:

$$\dot{v}_x = a_x + (\text{Slowly varying or small terms - SVOST})$$

$$\dot{v}_y = a_y + (\text{SVOST})$$

$$\dot{v}_z = a_z + (\text{SVOST})$$

Their integrals can be written as:

$$v_x = \sum_n \int_{t_n}^{t_{n+1}} a_x \, dt + \sum_m \int_{t_m}^{t_{m+1}} (\text{SVOST}) \, dt$$

| | | | |
|---|---|---|---|
| Computer fast iteration summation | Integrals over fast iteration period | Computer slower iteration summation | Integrals over slower iteration period |

Similarly for $v_y$, $v_z$. The $\int_{t_m}^{t_{m+1}}$ (SVOST) dt term is usually approximated by a simple integration algorithm such as setting it equal to 1/2 the sum of the values of ( ) at the start and end of the iteration interval, times $\Delta t$ the iteration period. The first term needs more care in its evaluation for the case of strapdown systems because the $a_x$, $a_y$, $a_z$ terms are derived from body mounted accelerometers using computer derived attitude from the strapdown gyros. The attitude may be changing rapidly, and the equations for approximating $\int_{t_n}^{t_{n+1}} a_x \, dt$ (i.e., the algorithms for evaluating the integrals on a discrete basis in a digital computer) can be in error if care is not taken in their formulation. Neither can the algorithm be too complicated or the computer will be loaded down at the high iteration rate.

We wish to derive an algorithm for evaluating the integral of $\underline{a}^L$ over the computation interval. Define the quantity to be evaluated as:

$$\Delta \underline{v}_n^L = \int_{t_n}^{t_{n+1}} \underline{a}^L \, dt \tag{22}$$

Matrix
Vector
Notation

The vector of acceleration $(a_x, a_y, a_z)$
in local level coordinates.

L refers to local level navigation coordinates

The $\underline{a}$ term is needed in local level navigation axes but it is measured in body axes. To equate the components of $\underline{a}$ in these frames, we write:

Unit vectors and $\underline{a}$ components in the B frame (Body or Vehicle axes)

$$\underline{a} = a_{B_x} \underline{i}_B + a_{B_y} \underline{j}_B + a_{B_z} \underline{k}_B$$

$$= a_{L_x} \underline{i}_L + a_{L_y} \underline{j}_L + a_{L_z} \underline{k}_L$$

Unit vectors and $\underline{a}$ components in the L frame (Local Level axes)

Taking the dot product of both sides of the above with $\underline{i}_L$ yields:

$$a_{L_x} = \underline{a} \cdot \underline{i}_L = a_{B_x}(\underline{i}_L \cdot \underline{i}_B) + a_{B_y}(\underline{i}_L \cdot \underline{j}_B) + a_{B_z}(\underline{i}_L \cdot \underline{k}_B)$$

The terms in brackets are the cosines of the angles between the indicated unit vectors in the B and L frames. Identifying these as direction cosines we get,

$$a_{Lx} = C_{11}\, a_{B_x} + C_{12}\, a_{By} + C_{13}\, a_{B_z}$$

where $C_{12}$ is the (direction) cosine between L frame axis 1 ($\underline{i}_L$) and B frame axis 2 ($j_B$) (and similarly for $C_{11}$ and $C_{13}$).

Similarly, for $a_{Ly}$ and $a_{Lz}$:

$$a_{Ly} = C_{21}\, a_{B_x} + C_{22}\, a_{By} + C_{23}\, a_{B_z}$$

$$a_{Lz} = C_{31}\, a_{B_x} + C_{32}\, a_{By} + C_{33}\, a_{B_z}$$

or in matrix form:

$$\begin{pmatrix} a_{Lx} \\ a_{Ly} \\ a_{Lz} \end{pmatrix} = \begin{bmatrix} C_{11} & C_{12} & C_{13} \\ C_{21} & C_{22} & C_{23} \\ C_{31} & C_{32} & C_{33} \end{bmatrix} \begin{pmatrix} a_{Bx} \\ a_{By} \\ a_{Bz} \end{pmatrix}$$

or in matrix notation:

$$\underline{a}^L = C_B^L \; \underline{a}^B$$

$\underline{a}$ in L frame axes | Direction cosine matrix from B to L | $\underline{a}$ in B frame axes

Returning to Equation (22), then:

$$\Delta \underline{v}_n^L = \int_{t_n}^{t_{n+1}} \underline{a}^L dt = \int_{t_n}^{t_{n+1}} C_B^L \underline{a}^B \, dt \tag{22A}$$

The approximation can be made that $C_B^L$ in the latter equation can be approximated by its value half way through the interval (this assumption should be checked under the expected variations in $C_B^L$ for the maneuver profiles expected). Hence:

$$\Delta \underline{v}_n^L = C_B^L\left(t_{n+1/2}\right) \int_{t_n}^{t_{n+1}} \underline{a}^B dt = C_B^L\left(t_{n+1/2}\right) \Delta \underline{v}_n^B \tag{23}$$

where

$$\Delta \underline{v}_n^B = \int_{t_n}^{t_{n+1}} \underline{a}^B dt = \text{The strapdown accelerometer pulse counts over the iteration interval.}$$

To derive a simple expression for $C_B^L\left(t_{n+1/2}\right)$, lets first review some simple direction cosine matrix operations and identities.

For an arbitrary vector $\underline{V}$ and arbitrary coordinate frames D, E, and F,

$$\underline{v}^E = C_D^E \, \underline{v}^D$$

$$\underline{v}^F = C_E^F \, \underline{v}^E = C_E^F C_D^E \, \underline{v}^D$$

But $\quad \underline{v}^F = C_D^F \, \underline{v}^D$

Hence, $$C_D^F = C_E^F C_D^E \tag{24}$$

and

$$\underline{v}^E = C_D^E \, \underline{v}^D$$

$$\left(\underline{v}^E\right)^T = \left(C_D^E \, \underline{v}^D\right)^T = \left(\underline{v}^D\right)^T \left(C_D^E\right)^T$$

$$v^2 = \underline{v} \bullet \underline{v} = \underline{v}^E \bullet \underline{v}^E = \left(\underline{v}^E\right)^T \underline{v}^E = \left(\underline{v}^D\right)^T \left(C_D^E\right)^T C_D^E \, \underline{v}^D$$

$$v^2 = \underline{v}^D \bullet \underline{v}^D = \left(\underline{v}^D\right)^T \underline{v}^D$$

where T designates the transpose.

Thus, $\left(C_D^E\right)^T C_D^E = I$ (24A)

and

$$\left(C_D^E\right)^T = \left(C_D^E\right)^{-1}$$

Using (24) with F = D:

$$C_D^D = I = C_E^D \, C_D^E$$

Hence,

$$C_E^D = \left(C_D^E\right)^{-1}$$

and with (24A):

$$\left(C_D^E\right)^T = C_E^D \tag{25}$$

Returning to (23), using (24), and approximating L as constant over the iteration interval yields,

$$C_B^L\left(t_{n+1/2}\right) = C_{B(n)}^L \, C_{B(n+1/2)}^{B(n)} \tag{26}$$

Now look at:

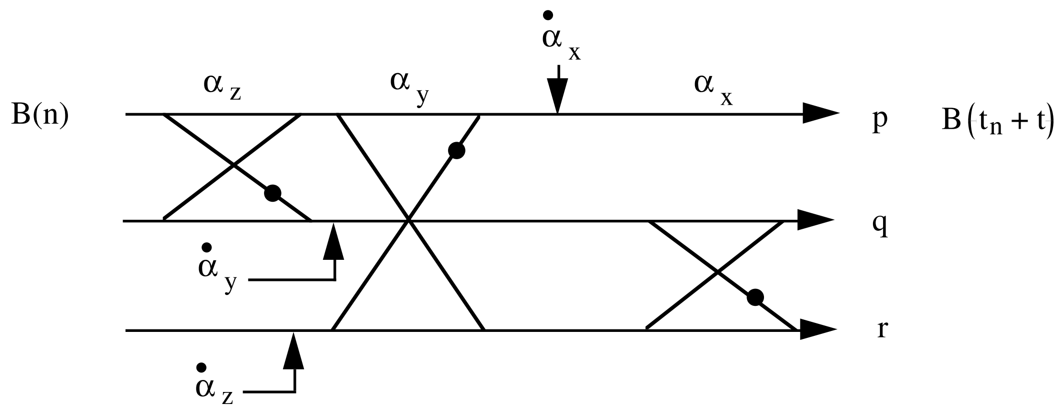


We assume that the sample time period is short enough that the $\alpha_x$, $\alpha_y$, $\alpha_z$ terms can be represented as small Euler rotations from time $t_n$ due to body rates (p, q, r) or their equivalents $\dot{\alpha}_x$, $\dot{\alpha}_y$, $\dot{\alpha}_z$ (with L assumed constant so all of the Euler motion can be attributed to body rates). Then, from the diagram:

$$p = \dot{\alpha}_x - \dot{\alpha}_z \sin\alpha_y$$

$$q = \dot{\alpha}_y \cos\alpha_x + \dot{\alpha}_z \cos\alpha_y \sin\alpha_x$$

$$r = \dot{\alpha}_z \cos\alpha_y \cos\alpha_x - \dot{\alpha}_y \sin\alpha_x$$

For a small sample period, $\alpha_x$, $\alpha_y$, $\alpha_z$ are small and:

$$\begin{aligned} p &\approx \dot{\alpha}_x \\ q &\approx \dot{\alpha}_y \\ r &\approx \dot{\alpha}_z \end{aligned} \tag{27}$$

or

$$\alpha_{x_n} = \int_{t_n}^{t_{n+1}} p \, dt$$

$$\alpha_{y_n} = \int_{t_n}^{t_{n+1}} q \, dt$$

$$\alpha_{z_n} = \int_{t_n}^{t_{n+1}} r \, dt$$

Also from the diagram, for small $\alpha_x$, $\alpha_y$, $\alpha_z$, the direction cosine matrix can be read by inspection at $t_{n+1}$:

$$C_{B(n+1)}^{B(n)} = \begin{bmatrix} 1 & -\alpha_{z_n} & \alpha_{y_n} \\ \alpha_{z_n} & 1 & -\alpha_{x_n} \\ -\alpha_{y_n} & \alpha_{x_n} & 1 \end{bmatrix} \qquad (27A)$$

If the body rates are fairly constant over the iteration period, it can be assumed that at ($t_{n+1/2}$), half the angles ($\alpha_{x_n}$, $\alpha_{y_n}$, $\alpha_{z_n}$) have been traversed. Hence:

$$C_{B(n+1/2)}^{B(n)} = \begin{bmatrix} 1 & -\frac{\alpha_{z_n}}{2} & \frac{\alpha_{y_n}}{2} \\ \frac{\alpha_{z_n}}{2} & 1 & -\frac{\alpha_{x_n}}{2} \\ -\frac{\alpha_{y_n}}{2} & \frac{\alpha_{x_n}}{2} & 1 \end{bmatrix} \qquad (28)$$

Returning to (23), with (26):

$$\Delta \underline{v}_n^L = C_{B(n)}^L C_{B(n+1/2)}^{B(n)} \Delta \underline{v}_n^B$$

With (28):

$$C_{B(n+1/2)}^{B(n)}\,\Delta\underline{v}_n^B = \begin{bmatrix} 1 & -\frac{\alpha_{z_n}}{2} & \frac{\alpha_{y_n}}{2} \\ \frac{\alpha_{z_n}}{2} & 1 & -\frac{\alpha_{x_n}}{2} \\ -\frac{\alpha_{y_n}}{2} & \frac{\alpha_{x_n}}{2} & 1 \end{bmatrix} \begin{pmatrix} \Delta v_{xn}^B \\ \Delta v_{yn}^B \\ \Delta v_{zn}^B \end{pmatrix}$$

$$= \begin{pmatrix} \Delta v_{xn}^B \\ \Delta v_{yn}^B \\ \Delta v_{zn}^B \end{pmatrix} + \frac{1}{2} \begin{bmatrix} 0 & -\alpha_{z_n} & \alpha_{y_n} \\ \alpha_{z_n} & 0 & -\alpha_{x_n} \\ -\alpha_{y_n} & \alpha_{x_n} & 0 \end{bmatrix} \begin{pmatrix} \Delta v_{xn}^B \\ \Delta v_{yn}^B \\ \Delta v_{zn}^B \end{pmatrix}$$

$$= \Delta\underline{v}_n^B + \frac{1}{2}\,\underline{\alpha}_n^B \times \Delta\underline{v}_n^B$$

where $\underline{\alpha}_n^B$ is the strapdown pulse count vector over the iteration interval:

$$\underline{\alpha}_n^B = \begin{pmatrix} \alpha_{x_n} \\ \alpha_{y_n} \\ \alpha_{z_n} \end{pmatrix} = \begin{pmatrix} \int_{t_n}^{t_{n+1}} p\,dt \\ \int_{t_n}^{t_{n+1}} q\,dt \\ \int_{t_n}^{t_{n+1}} r\,dt \end{pmatrix}$$

Thus,

$$\Delta\underline{v}_n^L = C_{B(n)}^L\left(\Delta\underline{v}_n^B + \frac{1}{2}\,\underline{\alpha}_n^B \times \Delta\underline{v}_n^B\right) \tag{29}$$

The cross-product term in Equation (29) has been denoted as “rotation compensation”. Equation (29) is a valid approximation for Equation (22A) in applications where $\underline{a}^B$ has little or no high frequency content relative to the $t_n$ to $t_{n+1}$ sampling frequency. For cases where high vibration frequency components are prevalent (such as in high frequency environment military applications) an alternate technique is required which can be derived from (22A) as illustrated below.

We first equate the $C_B^L$ term in Equation (22A) to the product of $C_B^L$ at $t_n$ with the transformation matrix relating body attitude at $t_n$ to body attitude at some general time t within the interval from $t_n$ to $t_{n+1}$:

$$C_B^L = C_{B(n)}^L C_B^{B(n)}$$

Equation (22A) then becomes:

$$\Delta \underline{v}_n^L = \int_{t_n}^{t_{n+1}} C_{B(n)}^L C_B^{B(n)} \underline{a}^B dt = C_{B(n)}^L \int_{t_n}^{t_{n+1}} C_B^{B(n)} \underline{a}^B dt \qquad (29A)$$

The $\underline{a}^B dt$ term in (29A) can be identified as a small increment of integrated body acceleration, or the accelerometer output pulse vector $d\underline{v}^B$:

$$d\underline{v}^B = \underline{a}^B dt$$

Substituting into the integral in (29A) using (27A):

$$C_B^{B(n)} \underline{a}^B dt = C_B^{B(n)} d\underline{v}^B = \begin{bmatrix} 1 & -\alpha_z & \alpha_y \\ \alpha_z & 1 & -\alpha_x \\ -\alpha_y & \alpha_x & 1 \end{bmatrix} d\underline{v}^B$$

$$= d\underline{v}^B + \begin{bmatrix} 0 & -\alpha_z & \alpha_y \\ \alpha_z & 0 & -\alpha_x \\ -\alpha_y & \alpha_x & 0 \end{bmatrix} d\underline{v}^B = d\underline{v}^B + \underline{\alpha}^B \times d\underline{v}^B$$

where

$$\underline{\alpha}^B = \begin{pmatrix} \alpha_x \\ \alpha_y \\ \alpha_z \end{pmatrix} = \begin{pmatrix} \int_{t_n}^{t} p\, dt \\ \int_{t_n}^{t} q\, dt \\ \int_{t_n}^{t} r\, dt \end{pmatrix} = \begin{pmatrix} \int_{t_n}^{t} d\alpha_x \\ \int_{t_n}^{t} d\alpha_y \\ \int_{t_n}^{t} d\alpha_z \end{pmatrix} = \int_{t_n}^{t} d\underline{\alpha}^B \tag{29B}$$

$\underline{\alpha}^B$ = Strapdown gyro pulse count vector from $t_n$ to general time t in the interval from $t_n$ to $t_{n+1}$.

$d\underline{\alpha}^B$ = A small increment of integrated body rate, or the instantaneous gyro output pulse vector.

Substituting in (29A):

$$\Delta\underline{v}_n^L = C_{B(n)}^L \int_{t_n}^{t_{n+1}} \left( d\underline{v}^B + \underline{\alpha}^B \times d\underline{v}^B \right)$$

or

$$\Delta\underline{v}_n^L = C_{B(n)}^L \left( \Delta\underline{v}^B + \int_{t_n}^{t_{n+1}} \underline{\alpha}^B \times \underline{dv}^B \right) \tag{29C}$$

with

$$\underline{\alpha}^B = \int_{T_n}^{t} d\underline{\alpha}^B \tag{29D}$$

Equation (29C) is the equivalent of Equation (29) used in applications where the body acceleration can have significant variations in the interval $t_n$ to $t_{n+1}$. The integral term in (29C) is denoted as sculling compensation. Note, that effective use of sculling compensation implies that the accelerometers utilized have sufficient bandwidth to accurately measure the high frequency components present in $d\underline{v}^B$. It should also be noted that the implementation of Equations (29C) and (29D) in a strapdown system would be accomplished as a high speed software function. In this manner, the high frequency content of $\underline{\alpha}^B$ and $d\underline{v}^B$ in the interval $t_n$ to $t_{n+1}$ can be accurately accounted for.

Now, lets look at deriving an equation to compute $C_B^L$. Start with:

$$C_B^L = C_I^L C_B^I \tag{30}$$

where I represents a non-rotating inertial coordinate frame. Look at $C_B^I$ first:

$$C_{B(n+1)}^I = C_{B(n)}^I C_{B(n+1)}^{B(n)}$$

$$= C_{B(n)}^I \begin{bmatrix} 1 & -\alpha_{z_n} & \alpha_{y_n} \\ \alpha_{z_n} & 1 & -\alpha_{x_n} \\ -\alpha_{y_n} & \alpha_{x_n} & 1 \end{bmatrix} = C_{B(n)}^I + C_{B(n)}^I \begin{bmatrix} 0 & -\alpha_{z_n} & \alpha_{y_n} \\ \alpha_{z_n} & 0 & -\alpha_{x_n} \\ -\alpha_{y_n} & \alpha_{x_n} & 0 \end{bmatrix}$$

$$\frac{C_{B(n+1)}^I - C_{B(n)}^I}{\Delta t} = C_{B(n)}^I \begin{bmatrix} 0 & -\alpha_{z_n} & \alpha_{y_n} \\ \alpha_{z_n} & 0 & -\alpha_{x_n} \\ -\alpha_{y_n} & \alpha_{x_n} & 0 \end{bmatrix} \frac{1}{\Delta t}$$

where $\Delta t$ is the time interval between $t_n$ and $t_{n+1}$. Letting $\Delta t$ approach 0 in the limit:

$$\frac{\alpha_{x_n}}{\Delta t} = \frac{\int_{t_n}^{t_{n+1}} p \, dt}{\Delta t} \approx p$$

$$\frac{\alpha_{y_n}}{\Delta t} \approx q$$

$$\frac{\alpha_{z_n}}{\Delta t} \approx r$$

Therefore:

$$\dot{C}_B^I = C_B^I \Omega_{IB}^B \tag{31}$$

where B is the body frame, IB designates the angular rate of the B frame relative to the non-rotating I frame, and $\Omega_{IB}^B$ is the skew symmetric form of the angular rate vector $\underline{\omega}_{IB}^B$:

$$\Omega_{IB}^{B} \overset{\Delta}{=} \begin{bmatrix} 0 & -r & q \\ r & 0 & -p \\ -q & p & 0 \end{bmatrix} = \text{Skew symmetric form of} \quad \underline{\omega}_{IB}^{B} \overset{\Delta}{=} \begin{pmatrix} p \\ q \\ r \end{pmatrix}$$

Note:

$$(\Omega)^T = -\Omega$$

Now look at $C_I^L$ in Equation (30). Start with the transpose. Using (25), the transpose is $C_L^I$. By a derivation similar to that leading to Equation (31), it can be shown that:

$$\dot{C}_L^I = C_L^I \, \Omega_{IL}^L$$

Taking the transpose:

$$\dot{C}_I^L = \left(\Omega_{IL}^L\right)^T C_I^L = -\Omega_{IL}^L \, C_I^L \qquad (32)$$

Taking the derivative of (30):

$$\dot{C}_B^L = \dot{C}_I^L \, C_B^I + C_I^L \, \dot{C}_B^I$$

Substituting (31) and (32),

$$\dot{C}_B^L = -\Omega_{IL}^L \, C_I^L \, C_B^I + C_I^L \, C_B^I \, \Omega_{IB}^B$$

or, with (30)

$$\dot{C}_B^L = C_B^L \, \Omega_{IB}^B - \Omega_{IL}^L \, C_B^L \qquad (33)$$

where

$\Omega_{IB}^B$ = Skew symmetric form of the angular rate vector $\underline{\omega}_{IB}^B$

$\Omega_{IL}^L$ = Skew symmetric form of $\underline{\omega}$ from navigation lecture notes (i.e., $\underline{\omega} = \underline{\rho} + \underline{\Omega}$).

Solving Equation (33) on an incremental basis without introducing computation error has been a key subject area for strapdown navigation. During the next lecture we'll discuss some of the solution approaches used.

$$\dot{C}_B^L = C_B^L \, \Omega_{IB}^B - \Omega_{IL}^L \, C_B^L \tag{33}$$

How can the above equation be integrated incrementally? Can the first portion on the right side be evaluated independently from the second portion? I.e., can the update of $C_B^L$ be divided into a high speed part associated with high body rates $\Omega_{IB}^B$, and a low speed part associated with local level frame rates $\Omega_{IL}^L$?

From the previous lecture, the above equation is equivalent to:

$$C_B^L = C_I^L \, C_B^I \tag{34}$$

$$\dot{C}_B^I = C_B^I \, \Omega_{IB}^B \tag{35}$$

$$\dot{C}_I^L = - \Omega_{IL}^L \, C_I^L \tag{36}$$

We now solve for $C_B^I$ and $C_I^L$ independently. Integrating (35) and (36):

$$C_{B(t)}^I = C_{B(n)}^I + \int_{t_n}^{t} C_{B(t)}^I \, \Omega_{IB}^B \, dt \tag{36A}$$

$$C_I^{L(\tau)} = C_I^{L(n)} - \int_{t_n}^{\tau} \Omega_{IL}^L \, C_I^{L(\tau)} \, d\tau \tag{36B}$$

where

$\tau, t$ = Running time after $t_n$.

(n), (t), ($\tau$) = Indicator of the position of frames B or L at times $t_n$, t or $\tau$.

Define:

$C_{B(t)}^{L(\tau)}$ = Orientation of frame L at time $\tau$ relative to frame B at time t.

Substituting from (36A) and (36B):

$$C_{B(t)}^{L(\tau)} = C_I^{L(\tau)} C_{B(t)}^I = \left( C_I^{L(n)} - \int_{t_n}^{\tau} \Omega_{IL}^L C_I^{L(\tau)} d\tau \right) C_{B(t)}^I$$

$$= C_I^{L(n)} C_{B(t)}^I - \int_{t_n}^{\tau} \Omega_{IL}^L C_I^{L(\tau)} C_{B(t)}^I d\tau \tag{36C}$$

$$= C_{B(t)}^{L(n)} - \int_{t_n}^{\tau} \Omega_{IL}^L C_{B(t)}^{L(\tau)} d\tau$$

Similarly, for $C_{B(t)}^{L(n)}$ in (36C), with (36A):

$$C_{B(t)}^{L(n)} = C_I^{L(n)} C_{B(t)}^I = C_I^{L(n)} C_{B(n)}^I + \int_{t_n}^{t} C_I^{L(n)} C_{B(t)}^I \Omega_{IB}^B dt$$

$$= C_{B(n)}^{L(n)} + \int_{t_n}^{t} C_{B(t)}^{L(n)} \Omega_{IB}^B dt \tag{36D}$$

Equations (36C) and (36D) can be interpreted as follows. Equation (36D) states that $C_{B(t)}^{L(n)}$ can be calculated by integrating the first part of Equation (33) from $t_n$ to t (say $t_{n+1}$). Equation (36C) states that $C_{B(t)}^{L(\tau)}$ (or $C_{B(n+1)}^{L(\tau)}$) can then be obtained by taking the result of the Equation (36D) integration and using it as the initial condition in integrating the second part of Equation (33). The result after integrating to $\tau = t_{n+1}$ is $C_{B(n+1)}^{L(n+1)}$ which constitutes a complete update of $C_B^L$. Thus, the integration of (33) can be performed in two steps if the following procedure is followed:

1. $$C_{B(t)}^{L_n} = C_{B_n}^{L_n} + \int_{t_n}^{t} C_{B(t)}^{L_n} \Omega_{IB}^B dt$$

   $$C_{B_{n+1}}^{L_n} = C_{B(t)}^{L_n} \left(t = t_{n+1}\right)$$

2. $$C_{B_{n+1}}^{L(t)} = C_{B_{n+1}}^{L_n} - \int_{t_n}^{t} \Omega_{IL}^L C_{B_{n+1}}^{L(\tau)} d\tau$$

   $$C_{B_{n+1}}^{L_{n+1}} = C_{B_{n+1}}^{L(t)} \left(t = t_{n+1}\right)$$

The above process implies that during step 1, the $\Omega_{IL}^{L}$ history in step 2 is being recorded so that it may be played back into the second step integral after step 1 is complete. This is a relatively simple matter because $\Omega_{IL}^{L}$ can be approximated by a constant over the interval when $\Omega_{IB}^{B}$ is being processed in step 1. The actual digital evaluation of step 2, then, is usually accomplished by a simple integration algorithm assuming a constant value of $\Omega_{IL}^{L}$ over the update interval. Since $\Omega_{IL}^{L}$ is small, little error results.

Let us now discuss how step 1 may be performed digitally; i.e., how to digitally integrate the following part of Equation (33) over an update interval in the digital computer:

$$\dot{C}_B^L = C_B^L \, \Omega_{IB}^B \tag{37}$$

Let's first expand (37) and note that its rows are independent:

$$\begin{aligned} \dot{C}_{i1} &= C_{i2}\,\omega_3 - C_{i3}\,\omega_2 \\ \dot{C}_{i2} &= C_{i3}\,\omega_1 - C_{i1}\,\omega_3 \\ \dot{C}_{i3} &= C_{i1}\,\omega_2 - C_{i2}\,\omega_1 \end{aligned} \tag{38}$$

where

$$\omega_1, \omega_2, \omega_3 \quad = \quad \text{Components of } \underline{\omega}_{IB}^{B}$$

Each row can be updated individually. Let's look at row i in general.

$$\underline{\dot{C}}_i^T = \underline{C}_i^T \, \Omega_{IB}^B$$

where $\underline{C}_i^T \equiv \left(C_{i1}, C_{i2}, C_{i3}\right)$ and $\underline{C}_i$ is the column vector formed from row i of C.

The transpose of $\underline{\dot{C}}_i^T$ is:

$$\underline{\dot{C}}_i = \left(\Omega_{IB}^B\right)^T \underline{C}_i = - \Omega_{IB}^B \, \underline{C}_i$$

Note: The transpose of $\Omega_{IB}^B$ equals its negative because it is skew symmetric.

We thereby obtain the Coriolis equivalent:

$$\dot{\underline{C}}_i = - \underline{\omega}_{IB}^{B} \times \underline{C}_i \tag{39}$$

Let's look at the integration of (39). First note that the angular rate vector $\underline{\omega}_{IB}^{B}$ in (39) is not available as a numerical value but only as integral counts from gyro pre-counters:

$$\underline{\alpha}_P^B = \int_{t_p}^{t_{p+1}} \underline{\omega}_{IB}^B \, dt \stackrel{\Delta}{=} \begin{pmatrix} \alpha_x \\ \alpha_y \\ \alpha_z \end{pmatrix} \tag{40}$$

where $t_p$, $t_{p+1}$ are gyro counter sample times. We might try the approximation that an integral of (39) may be evaluated by summing the following differences:

$$\Delta \underline{C}_{p+1} = - \underline{\alpha}_P^B \times \underline{C}_p \tag{41}$$

where the i has been dropped for convenience. Let's evaluate how well (41) approximates the true solution for the special case of $\alpha_x = \alpha_y = 0$ and $\alpha_z = + \varepsilon$ for the first sample and $-\varepsilon$ for the second. For this special case, (41) becomes:

$$\Delta C_{1p} = C_{2p}\, \alpha_{zp} = C_{2p}\, \varepsilon$$

$$\Delta C_{2p} = - C_{1p}\, \alpha_{zp} = - C_{1p}\, \varepsilon$$

$$C_{1p+1} = C_{1p} + \Delta C_{1p} = C_{1p} + C_{2p}\, \varepsilon$$

$$C_{2p+1} = C_{2p} + \Delta C_{2p} = C_{2p} - C_{1p}\, \varepsilon$$

$$\Delta C_{1p+1} = C_{2p+1}\, \alpha_{zp+1} = - C_{2p}\, \varepsilon + C_{1p}\, \varepsilon^2$$

$$\Delta C_{2p+1} = - C_{1p+1}\, \alpha_{zp+1} = C_{1p}\, \varepsilon + C_{2p}\, \varepsilon^2$$

$$C_{1p+2} = C_{1p+1} + \Delta C_{1p+1} = C_{1p} + C_{1p}\, \varepsilon^2$$

$$C_{2p+2} = C_{2p+1} + \Delta C_{2p+1} = C_{2p} + C_{2p}\, \varepsilon^2$$

residual errors

Since the net rotation was zero, the correct values for $C_1$ and $C_2$ at p + 2 should be the same as at p (i.e., $C_{1p}$ and $C_{2p}$). The above algorithm, however, results in an error equal to $\varepsilon^2$ times C. Since C is on the order of 1, this is equivalent to an error on the order of $1/2\, \varepsilon^2$ per iteration. On a drift rate basis:

$$\text{Drift} = \frac{\varepsilon^2}{2\,\Delta t_p} = \frac{\varepsilon}{2\,\Delta t_p}\,\varepsilon = \frac{1}{2}\,\omega\,\varepsilon$$

in which $\omega$ represents the angular rate magnitude. To eliminate the drift rate effect under limit cycle rate conditions, the use of a reversible first order algorithm has been used in the past. (The algorithms we are discussing thus far are called first order because they only contain $\alpha$ terms to the first power.) The reversible first order algorithm follows a computation format similar to the one described previously. It differs in that $C_1$ and $C_2$ are updated sequentially for $\alpha_z$ with the order of update dependent on the sign of $\alpha_z$. The $C_2$, $C_3$ and $C_3$, $C_1$ updates for $\alpha_x$, $\alpha_y$ (see (38)) would be processed in a similar manner, with the $\alpha$'s being processed into the C update, also in sequential fashion ($\alpha_x$, then $\alpha_y$, then $\alpha_z$). The update for $\alpha_z$ is:

| For $\alpha_z$ Plus | For $\alpha_z$ Minus |
|---|---|
| $\Delta C_{1p} = C_{2p}\,\alpha_{zp}$ | $\Delta C_{2p} = -\,C_{1p}\,\alpha_{zp}$ |
| $C_{1p+1} = C_{1p} + \Delta C_{1p}$ | $C_{2p+1} = C_{2p} + \Delta C_{2p}$ |
| $\Delta C_{2p} = -\,C_{1p+1}\,\alpha_{zp}$ | $\Delta C_{1p} = C_{2p+1}\,\alpha_{zp}$ |
| $C_{2p+1} = C_{2p} + \Delta C_{2p}$ | $C_{1p+1} = C_{1p} + \Delta C_{1p}$ |

Note: $\alpha_{zp}$ includes sign in this nomenclature. i.e., $\alpha_{zp} = -\,\varepsilon$ for a pulse of $\varepsilon$ magnitude in the negative sense.

It can be verified that for the sequence of $\alpha_z$ consisting of $+\varepsilon$ following by $-\varepsilon$, processing the above algorithm (first the left side, then the right) returns the C states to their correct initial conditions. In this respect, the reversible first order algorithm improves over the algorithm discussed previously.

Under general high rate conditions, the drift error in all first order algorithms is on the order of the formula given previously: $1/2\;\omega\,\varepsilon$.

For a computer computation frequency of f, the value for $\varepsilon$ when rotating at $\omega$ is:

$$\varepsilon = \frac{\omega}{f}$$

hence,

$$\text{Drift} = \left(\frac{1}{2}\,\frac{\omega}{f}\right)\omega$$

Thus, the effect of the first order algorithm is to generate a scale factor type error equal to $\frac{1}{2}\frac{\omega}{f}$. At 200 deg/sec rotation rate, with a computation rate of 2 KHz , the equivalent scale factor error is:

$$\frac{1}{2}\ \frac{200\ \text{deg/sec}}{57.3 \times 2000\ \text{Hz}} \times 10^6\ \text{ppm} \quad = \quad 873\ \text{ppm}$$

Compared to typical high accuracy strapdown rate sensing scale factor accuracy requirements of 5 ppm, this is clearly unacceptable. A higher iteration rate would reduce the error, but would also increase the computer throughput requirements.

All first order algorithms suffer inaccuracy at high rates unless the iteration rate is increased to an undesirably high level. The increased iteration rate, in turn, produces increased computer round-off error. In modern strapdown systems, higher order algorithms are used that have the combined effect of reversibility, high accuracy at high rates, and reasonable repetition rates (e.g., 100 - 200 Hertz) to minimize computer loading and round-off error build-up. The next lecture will develop the higher order attitude algorithms used with typical modern-day strapdown systems.

The update of the $C_B^L$ matrix for body inertial rotation (the $\Omega_{IB}^B$ part of Equation (33)) is typically accomplished over several intervals for each $\Omega_{IL}^L$ update; i.e., the $\Omega_{IB}^B$ portion might be updated at 100 Hertz while the $\Omega_{IL}^L$ portion is updated at 10 Hertz. The $\Omega_{IL}^L$ update can be approximated as:

$$C_{B(n+1)}^{L(n+1)} = C_{B(n+1)}^{L(n)} - \frac{\left(\Omega_{IL}^L(n) + \Omega_{IL}^L(n+1)\right) T_n}{2} C_{B(n+1)}^{L(n)} \tag{42}$$

where

$T_n$ = Update interval from $t_n$ to $t_{n+1}$

As discussed in the previous lecture, this approximation typically results in an acceptably small error because $\underline{\omega}_{IL}^L$ is small and slowly changing over the update period $T_n$.

The higher frequency update of $C_B^L$ due to body rates $\Omega_{IB}^B$ calculates the value of $C_B^L$ at the intermediate points between the $t_n$ and $t_{n+1}$ low frequency update times. Denoting the intermediate update times as $t_m$, $t_{m+1}$, $t_{m+2}$, etc. we can write a general sequence for the high frequency updating operation as:

$$\begin{aligned}
C_{B(m)}^{L(n)} &= C_{B(n)}^{L(n)} C_{B(m)}^{B(n)} \\
C_{B(m+1)}^{L(n)} &= C_{B(m)}^{L(n)} C_{B(m+1)}^{B(m)} \\
C_{B(m+2)}^{L(n)} &= C_{B(m+1)}^{L(n)} C_{B(m+2)}^{B(m+1)} \\
&\ \vdots \\
C_{B(n+1)}^{L(n)} &= C_{B(m+i)}^{L(n)} C_{B(n+1)}^{B(m+i)}
\end{aligned} \tag{43}$$

I.e., the $C_B^L$ update for $\Omega_{IB}^B$ consists of a series of intermediate updates of the form:

$$C_{B(m+1)}^{L(n)} = C_{B(m)}^{L(n)} C_{B(m+1)}^{B(m)}$$

The $C_{B(m)}^{L(n)}$ matrix is the value of $C_B^L$ from the last update; $C_{B(m+1)}^{B(m)}$ is the cosine matrix generated by $\Omega_{IB}^B$ that moves B from its orientation at $t_m$ to its orientation at $t_{m+1}$. Let's find an expression for $C^{B(m)}_{B(m+1)}$ for an angular rotation defined about a space fixed axis $\underline{u}$ through an angle $\phi$. For such a rotation definition, we will now derive an equation for $C^{B(m)}_{B(m+1)}$ in terms of $\underline{u}$ and $\phi^{*}$.

For the derivation, it is helpful to think of B(m) as a fixed reference frame R and the B(m+1) frame as rotated relative to R which we will denote as B (for the body frame). Hence:

$$C^{B(m)}_{B(m+1)} \stackrel{\Delta}{=} C^R_B \tag{43A}$$

Now, define an arbitrary vector $\underline{r}^B_o$ as fixed in the body frame. Clearly, in the R frame, this vector looks like:

$$\underline{r}^R_o = C^R_B \, \underline{r}^B_o \tag{43B}$$

Now, look at the geometry in the figure to determine $\underline{r}^R_o$ in terms of $\underline{r}^B_o$ after a rotation $\phi$ about the axis $\underline{u}$.

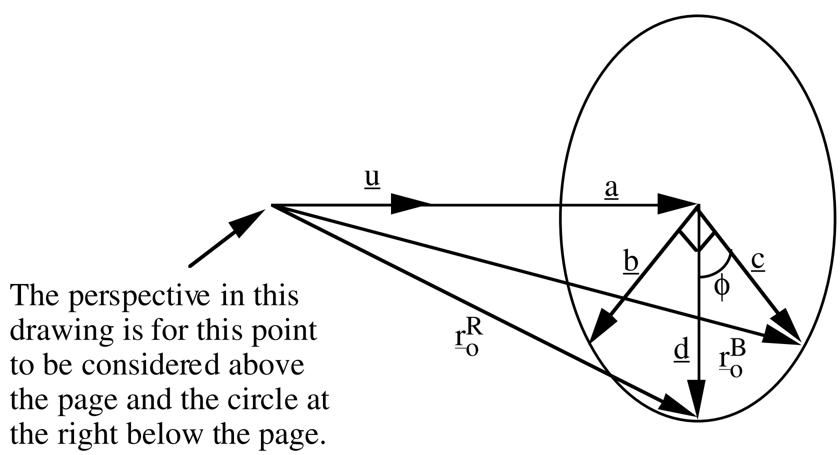


As $\underline{r}^B_o$ rotates about $\underline{u}$ through $\phi$, it traces a cone about $\underline{u}$. The tip of $\underline{r}^B_o$ traces a circular arc in the plane normal to $\underline{u}$. The vector $\underline{r}^R_o$ is equal to $\underline{r}^B_o$ after it has rotated through $\phi$ into the $\underline{r}^R_o$ position (i.e., in the R frame, $\underline{r}^B_o$ looks like it rotates to $\underline{r}^R_o$. In the B-Frame, $\underline{r}^B_o$ is constant

---

** Based on the geometrical method used by John E. Bortz, "A New Mathematical Formulation For Strapdown Inertial Navigation", IEEE Transactions On Aerospace and Electronic Systems, Volume AE5-7, No. 1, January 1971.

by definition). We also define vectors $\underline{b}$, $\underline{c}$, $\underline{d}$ as radii to the circle with $\underline{c}$, $\underline{d}$ intercepting $\underline{r}_o^B$ and $\underline{r}_o^R$, and $\underline{b}$ perpendicular to $\underline{c}$. Vector $\underline{a}$ is the projection of $\underline{r}_o^B$ along $\underline{u}$. Note that it is also the projection of $\underline{r}_o^R$ along $\underline{u}$. Considering $\underline{u}$ to be a unit vector, we can now write:

$$\underline{r}_o^R = \underline{a} + \underline{d} \tag{44}$$

$$\underline{a} = \left(\underline{r}_o^B \cdot \underline{u}\right) \underline{u} \tag{45}$$

$$\underline{c} = \underline{r}_o^B - \underline{a} = \underline{r}_o^B - \left(\underline{r}_o^B \cdot \underline{u}\right) \underline{u} \tag{46}$$

where $\underline{a}$ is the component of $\underline{r}_o^B$ along $\underline{u}$. From the diagram, $\underline{b}$ is defined to have the same magnitude as $\underline{c}$ and perpendicular to $\underline{c}$ and $\underline{u}$ with the same magnitude as $\underline{c}$. Thus, since $\underline{u}$ is defined as a unit vector,

$$\underline{b} = \underline{u} \times \underline{c}$$

or with (46),

$$\underline{b} = \underline{u} \times \underline{r}_o^B \tag{47}$$

Let's find an expression for $\underline{d}$ in terms of $\underline{b}$ and $\underline{c}$. Look into the circular plane:

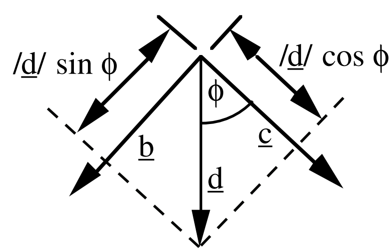


Vector $\underline{d}$ can be broken up into two parts: $/\underline{d}/ \cos\phi$ along $\underline{c}$, and $/\underline{d}/ \sin\phi$ along $\underline{b}$. Thus,

$$\underline{d} = /\underline{d}/ \sin\phi \underbrace{\frac{\underline{b}}{/\underline{b}/}}_{\substack{\text{unit} \\ \text{vector} \\ \text{along } \underline{b}}} + /\underline{d}/ \cos\phi \underbrace{\frac{\underline{c}}{/\underline{c}/}}_{\substack{\text{unit} \\ \text{vector} \\ \text{along } \underline{c}}}$$

But since $\underline{a}$, $\underline{b}$, and $\underline{c}$ are radii of the same circle:

$$/\underline{b}/ = /\underline{c}/ = /\underline{d}/$$

Thus:

$$\underline{d} \;=\; \underline{b}\sin\phi + \underline{c}\cos\phi \tag{48}$$

Combining (45) through (48) in (44):

$$\begin{aligned}
\underline{r}_o^R &= \left(\underline{r}_o^B \cdot \underline{u}\right)\underline{u} + \left(\underline{u}\times\underline{r}_o^B\right)\sin\phi + \left[\underline{r}_o^B - \left(\underline{r}_o^B \cdot \underline{u}\right)\underline{u}\right]\cos\phi \\
&= \left(1 - \cos\phi\right)\underline{u}\left(\underline{u}\cdot\underline{r}_o^B\right) + \sin\phi\left(\underline{u}\times\underline{r}_o^B\right) + \cos\phi\,\underline{r}_o^B
\end{aligned}$$

The vector triple product identity states:

$$\underline{A}\times\left(\underline{B}\times\underline{C}\right) \;=\; \left(\underline{A}\cdot\underline{C}\right)\underline{B} - \left(\underline{A}\cdot\underline{B}\right)\underline{C}$$

Hence:

$$\underline{u}\left(\underline{u}\cdot\underline{r}_o^B\right) \;=\; \underline{u}\times\left(\underline{u}\times\underline{r}_o^B\right) + \left(\underline{u}\cdot\underline{u}\right)\underline{r}_o^B \;=\; \underline{u}\times\left(\underline{u}\times\underline{r}_o^B\right) + \underline{r}_o^B$$

Thus:

$$\begin{aligned}
\underline{r}_o^R &= \left(1 - \cos\phi\right)\left[\underline{u}\times\left(\underline{u}\times\underline{r}_o^B\right) + \underline{r}_o^B\right] + \sin\phi\left(\underline{u}\times\underline{r}_o^B\right) + \cos\phi\,\underline{r}_o^B \\
&= \underline{r}_o^B + \sin\phi\left(\underline{u}\times\underline{r}_o^B\right) + \left(1 - \cos\phi\right)\underline{u}\times\left(\underline{u}\times\underline{r}_o^B\right)
\end{aligned}$$

In matrix form,

$$\begin{aligned}
\underline{r}_o^R &= \underline{r}_o^B + \sin\phi\left(\underline{u}\times\right)\underline{r}_o^B + \left(1 - \cos\phi\right)\left(\underline{u}\times\right)\left(\underline{u}\times\right)\underline{r}_o^B \\
&= \left[I + \sin\phi\left(\underline{u}\times\right) + \left(1 - \cos\phi\right)\left(\underline{u}\times\right)\left(\underline{u}\times\right)\right]\underline{r}_o^B
\end{aligned} \tag{49}$$

where

$\left(\underline{u}\times\right)$ = Skew symmetric form of $\underline{u}$, equivalent to a cross-product operator.

Comparing the above with (43B), we can write the equation for $C_B^R$ in terms of $\underline{u}$ and $\phi$:

$$C_B^R \;=\; I + \sin\phi\left(\underline{u}\times\right) + \left(1 - \cos\phi\right)\left(\underline{u}\times\right)\left(\underline{u}\times\right)$$

If we define:

$$\underline{\phi} \;\overset{\Delta}{=}\; \phi\,\underline{u} \qquad\qquad u \;=\; \frac{\underline{\phi}}{\phi}$$

we obtain:

$$C_B^R \;=\; I + \frac{\sin\phi}{\phi}\left(\underline{\phi}\times\right) + \frac{\left(1 - \cos\phi\right)}{\phi^2}\left(\underline{\phi}\times\right)\left(\underline{\phi}\times\right) \tag{50}$$

Equation (50) defines the direction cosine matrix equivalent to a rotation maneuver $\underline{\phi}$ ($\phi$ about a constant axis $\underline{u}$). We can look at $\underline{\phi}$ as another way of defining C through the (50) relationship. That is, for every C, there is a $\underline{\phi}$ that satisfies (50). This is a statement of the fact that a body can be rotated from one orientation to any other through a single rotation about a fixed axis in space. This combined axis rotation is defined by $\underline{\phi}$. Now, what if the rotation maneuver that created $C_B^R$ actually did occur as a fixed maneuver about a fixed axis? (Note - This doesn't have to be the case; $C_B^R$ could have been created by any arbitrary maneuver. After $C_B^R$ is formed, $\underline{\phi}$ is defined as that single axis maneuver that would have generated the same $C_B^R$ ). For a real single axis maneuver, $\underline{u}$ is along $\underline{\omega}$ (i.e. - the vehicle angular velocity axis which is fixed for the maneuver). Then:

$$\underline{u} \;=\; \frac{\underline{\omega}}{\omega} \qquad\qquad \underline{u} \cdot \underline{\omega} \;=\; \omega$$

$$\phi \;=\; \int_{t_m}^{t_{m+1}} \omega \, dt$$

$$\underline{\phi} \;=\; \underline{u}\,\phi \;=\; \int_{t_m}^{t_{m+1}} \underline{u}\,\omega \, dt \;=\; \int_{t_m}^{t_{m+1}} \underline{\omega} \, dt$$

$$\underline{\phi} \;=\; \int_{t_m}^{t_{m+1}} \underline{\omega} \, dt \;=\; \underline{\alpha} \;=\; \text{Gyro counts}$$

Thus, for an actual rotation maneuver about a fixed axis, $\underline{\phi}$ equals the gyro counts, and (50) with $\underline{\alpha}$ for $\underline{\phi}$ gives an exact solution for updating the $C_B^L$ matrix for the $\underline{\alpha}$ rotation.

Looking at (50) in more detail:

$$\underline{\phi} \overset{\Delta}{=} \begin{pmatrix} \phi_x \\ \phi_y \\ \phi_z \end{pmatrix} \qquad \phi^2 = \left( \phi_x^{\,2} + \phi_y^{\,2} + \phi_z^{\,2} \right)$$

$$\sin\phi = \phi - \frac{\phi^3}{3!} + \frac{\phi^5}{5!} - \cdots$$

$$\frac{\sin\phi}{\phi} = 1 - \frac{\phi^2}{3!} + \frac{\phi^4}{5!} - \cdots \text{ powers of } \phi^2$$

$$\cos\phi = 1 - \frac{\phi^2}{2!} + \frac{\phi^4}{4!} - \frac{\phi^6}{6!} + \cdots$$

$$\frac{1 - \cos\phi}{\phi^2} = \frac{1}{2!} - \frac{\phi^2}{4!} + \frac{\phi^4}{6!} - \cdots \text{ powers of } \phi^2$$

$$\left(\underline{\phi}\times\right) = \begin{bmatrix} o & -\phi_z & \phi_y \\ \phi_z & o & -\phi_x \\ -\phi_y & \phi_x & o \end{bmatrix}$$

$$\left(\underline{\phi}\times\right)\left(\underline{\phi}\times\right) = \left(\underline{\phi}\times\right)^2 = \begin{bmatrix} -\left(\phi_z^{\,2} + \phi_y^{\,2}\right) & \phi_x\,\phi_y & \phi_x\,\phi_z \\ \phi_x\,\phi_y & -\left(\phi_z^{\,2} + \phi_x^{\,2}\right) & \phi_y\,\phi_z \\ \phi_x\,\phi_z & \phi_y\,\phi_z & -\left(\phi_y^{\,2} + \phi_x^{\,2}\right) \end{bmatrix}$$

And (50) is (with 43A):

$$C_{B\,(m+1)}^{B\,(m)} = I + \left(1 - \frac{\phi^2}{3!} + \frac{\phi^4}{5!} \cdots\right) \begin{bmatrix} o & -\phi_z & \phi_y \\ \phi_z & o & -\phi_x \\ -\phi_y & \phi_x & o \end{bmatrix}$$

$$+ \left(\frac{1}{2!} - \frac{\phi^2}{4!} + \frac{\phi^4}{6!} \cdots\right) \begin{bmatrix} -\left(\phi_z^{\,2} + \phi_y^{\,2}\right) & \phi_x\,\phi_y & \phi_x\,\phi_z \\ \phi_x\,\phi_y & -\left(\phi_z^{\,2} + \phi_x^{\,2}\right) & \phi_y\,\phi_z \\ \phi_x\,\phi_z & \phi_y\,\phi_z & -\left(\phi_y^{\,2} + \phi_x^{\,2}\right) \end{bmatrix} \tag{51}$$

with

$$C_{B(m+1)}^{L(n)} = C_{B(m)}^{L(n)} \quad C_{B(m+1)}^{B(m)} \tag{51A}$$

The “order” of the algorithm depends on the number of terms carried in the series expansions.  A fifth order algorithm, for example, uses terms including the $\frac{\phi^4}{5!}$ and $\frac{\phi^2}{4!}$ terms.

If (51) is used with the body rate integrals for $\underline{\phi}$, (51) has to be iterated fairly rapidly to assure that the assumption of a non-rotating $\underline{\omega}$ vector is valid (say 1000 Hertz).  This restriction can be removed if a compensation term is first added to the body rate integrals to correct for $\underline{\omega}$ rotation motion (coning).  This is, in fact, the correct $\underline{\phi}$ vector to use (the use of the body rate integral for $\underline{\phi}$ is only an approximation).  For the next lecture, we will develop an expression for evaluating $\underline{\phi}$ in terms of $\underline{\omega}$, and show that it equals the integral of $\underline{\omega}$ plus terms proportional to $\underline{\phi} \times \underline{\omega}$ (i.e. - the portion of $\underline{\omega}$ perpendicular to $\underline{\phi}$, which is the coning effect).

## NAV SEMINAR - LECTURE 8 NOTES

This lecture deals with a general derivation of the rate of change of $\underline{\phi}$ without restrictions on $\underline{\omega}$ (such as in the last lecture where $\underline{\omega}$ was assumed non-rotating and $\underline{\phi}$, under those conditions, was shown to be equal to the integral of $\underline{\omega}$). We begin* with the expression for $C_B^R$ (Equation (50)):

$$C = I + f_1 \left(\underline{\phi}\times\right) + f_2 \left(\underline{\phi}\times\right)^2 \tag{52}$$

where for simplicity, the following definitions have been introduced:

$$C \overset{\Delta}{=} C_B^R \qquad f_1 = \frac{\sin \phi}{\phi} \qquad f_2 = \frac{1 - \cos \phi}{\phi^2} \tag{52A}$$

The transpose of (52) is:

$$\begin{aligned} C^T &= I + f_1 \left(\underline{\phi}\times\right)^T + f_2 \left(\underline{\phi}\times\right)^T \left(\underline{\phi}\times\right)^T \\ &= I - f_1 \left(\underline{\phi}\times\right) + f_2 \left(\underline{\phi}\times\right)^2 \end{aligned} \tag{53}$$

where use has been made that $\left(\underline{\phi}\times\right)$ is skew symmetric and, therefore,

$$\left(\underline{\phi}\times\right)^T = - \left(\underline{\phi}\times\right)$$

Combining (52) and (53) yields an expression for $\left(\underline{\phi}\times\right)$ in terms of C and $f_1$:

$$\frac{1}{2}\left(C - C^T\right) = f_1 \left(\underline{\phi}\times\right) \tag{54}$$

The C and $\left(\underline{\phi}\times\right)$ quantities can be viewed as continuous functions that are generated as the body moves from B(m) (or R from last lecture) to B(m+1) through a continuous set of attitudes determined by $\underline{\omega}_{IB}^B$. The value for C and $\left(\underline{\phi}\times\right)$ at B(m+1), then equals the values needed for the Equation (51) computer algorithm. The equation we seek for $\underline{\phi}$ is a differential equation defining how $\underline{\phi}$ changes from m to m+1. Integration over the interval

---

* Based on similar a formulation by John E. Bortz, “A New Mathematical Formulation For Strapdown Inertial Navigation”, IEEE Transactions On Aerospace and Electronic Systems, Volume AES-7, No. 1, January 1971.

from m to m+1 will yield the sought after general value of $\underline{\phi}$ for (51). In general, $\underline{\phi}$ will be a function of the instantaneous values of $\underline{\omega}$ and $\underline{\phi}$ (or C from Equation (52)) at any given time in the interval between m and m+1.

With this concept in mind, we differentiate (54) to obtain an expression for $\dot{\underline{\phi}}$ during the interval m and m+1 (Remember that (52) was derived strictly as a function of $\underline{\phi}$ without fixing the time at m+1. Therefore, it is completely valid to consider (52) as a general expression that defines how C is generated as $\underline{\phi}$ evolves continuously from m to a general running time in the interval from m to m+1):

$$\frac{1}{2}\left(\dot{C} - \dot{C}^{T}\right) = \dot{f}_1\left(\underline{\phi}\times\right) + f_1\left(\dot{\underline{\phi}}\times\right) \tag{55}$$

From the previous lecture, and extending to an arbitrary time point during the interval from m to m+1 (say m+i where i is a running time variable from m):

$$C_{B(m+i)}^{L(n)} = C_{B(m)}^{L(n)} \, C_{B(m+i)}^{B(m)} \tag{56}$$

The derivative of (56) with respect to running time from m is:

$$\dot{C}_{B(m+i)}^{L(n)} = C_{B(m)}^{L(n)} \, \dot{C}_{B(m+i)}^{B(m)} \tag{57}$$

From Equation (37) which expresses the general rate of change $C_B^L$ due to $\Omega_{IB}^B$:

$$\dot{C}_{B(m+i)}^{L(n)} = C_{B(m+i)}^{L(n)} \, \Omega_{IB}^{B}$$

or, with (56)

$$\dot{C}_{B(m+i)}^{L(n)} = C_{B(m)}^{L(n)} \, C_{B(m+i)}^{B(m)} \, \Omega_{IB}^{B} \tag{58}$$

Equating (57) and (58):

$$\dot{C}_{B(m+i)}^{B(m)} = C_{B(m+i)}^{B(m)} \, \Omega_{IB}^{B} \tag{59}$$

It should be clear from the last lecture and the definition of C given previously, that at m+i in the interval between m and m+1,

$$C_{B(m+i)}^{B(m)} = C_{B(i)}^{R} = C \tag{60}$$

Thus, with (59):

$$\dot{C} = C\left(\underline{\omega}\times\right) \tag{61}$$

where, for simplicity, $\underline{\omega}$ has been used for $\underline{\omega}_{IB}^{B}$, or in skew symmetric form:

$$\left(\underline{\omega}\times\right) \overset{\Delta}{=} \Omega_{IB}^{B}$$

We can now use (61) to obtain an expression for $\frac{1}{2}\left(\dot{C} - \dot{C}^T\right)$ in Equation (55). Using (52) for C in (61),

$$\dot{C} = \left(\underline{\omega}\times\right) + f_1\left(\underline{\phi}\times\right)\left(\underline{\omega}\times\right) + f_2\left(\underline{\phi}\times\right)^2\left(\underline{\omega}\times\right) \tag{62}$$

The transpose of (62) is:

$$\dot{C}^T = -\left(\underline{\omega}\times\right) + f_1\left(\underline{\omega}\times\right)\left(\underline{\phi}\times\right) - f_2\left(\underline{\omega}\times\right)\left(\underline{\phi}\times\right)^2 \tag{63}$$

One half the difference between (62) and (63) is:

$$\begin{aligned}\frac{1}{2}\left(\dot{C} - \dot{C}^T\right) = &\left(\underline{\omega}\times\right) + \frac{1}{2} f_1\left[\left(\underline{\phi}\times\right)\left(\underline{\omega}\times\right) - \left(\underline{\omega}\times\right)\left(\underline{\phi}\times\right)\right] \\ &+ \frac{1}{2} f_2\left[\left(\underline{\phi}\times\right)^2\left(\underline{\omega}\times\right) + \left(\underline{\omega}\times\right)\left(\underline{\phi}\times\right)^2\right]\end{aligned} \tag{64}$$

Equation (64) is an expression for the $\frac{1}{2}\left(\dot{C} - \dot{C}^T\right)$ term in (55). It can be simplified as follows. First, remember the vector triple product identity:

$$\left(\underline{A}_1 \times \underline{A}_2\right)\times \underline{A}_3 = \left(\underline{A}_1 \cdot \underline{A}_3\right)\underline{A}_2 - \left(\underline{A}_2 \cdot \underline{A}_3\right)\underline{A}_1$$

Now, look at the term multiplying $\frac{1}{2} f_1$ in (64), and multiply it by an arbitrary vector $\underline{V}$:

$$\left(\underline{\phi}\times\right)\left(\underline{\omega}\times\right)\underline{V} - \left(\underline{\omega}\times\right)\left(\underline{\phi}\times\right)\underline{V} = \underline{\phi}\times\left(\underline{\omega}\times\underline{V}\right) - \underline{\omega}\times\left(\underline{\phi}\times\underline{V}\right)$$

Using the vector triple product identity for each of the latter terms:

$$\underline{\phi}\times\left(\underline{\omega}\times\underline{V}\right) = -\left(\underline{\omega}\times\underline{V}\right)\times\underline{\phi} = -\left(\underline{\omega}\cdot\underline{\phi}\right)\underline{V} + \left(\underline{V}\cdot\underline{\phi}\right)\underline{\omega}$$

$$\underline{\omega}\times\left(\underline{\omega}\times\underline{V}\right) = -\left(\underline{\phi}\times\underline{V}\right)\times\underline{\omega} = -\left(\underline{\phi}\cdot\underline{\omega}\right)\underline{V} + \left(\underline{V}\cdot\underline{\omega}\right)\underline{\phi}$$

Subtracting the previous expressions yields

$$\underline{\phi} \times \left(\underline{\omega} \times \underline{V}\right) - \underline{\omega} \times \left(\underline{\phi} \times \underline{V}\right) = \left(\underline{V} \cdot \underline{\phi}\right) \underline{\omega} - \left(\underline{V} \cdot \underline{\omega}\right) \underline{\phi}$$

or with the vector triple product identity:

$$\underline{\phi} \times \left(\underline{\omega} \times \underline{V}\right) - \underline{\omega} \times \left(\underline{\phi} \times \underline{V}\right) = \left(\underline{\phi} \times \underline{\omega}\right) \times \underline{V}$$

and in matrix form:

$$\left(\underline{\phi}\times\right)\left(\underline{\omega}\times\right) \underline{V} - \left(\underline{\omega}\times\right)\left(\underline{\phi}\times\right) \underline{V} = \left(\underline{\phi} \times \underline{\omega}\right)^{*} \underline{V}$$

where

$(\quad)^{*}$ = The skew symmetric form of the vector in brackets.

Since $\underline{V}$ is arbitrary,

$$\left(\underline{\phi}\times\right)\left(\underline{\omega}\times\right) - \left(\underline{\omega}\times\right)\left(\underline{\phi}\times\right) = \left(\underline{\phi} \times \underline{\omega}\right)^{*} \tag{65}$$

The term multiplying $\frac{1}{2} f_2$ in (64) can be reduced in a similar manner:

$$\left(\underline{\phi}\times\right)^2 \left(\underline{\omega}\times\right) \underline{V} + \left(\underline{\omega}\times\right)\left(\underline{\phi}\times\right)^2 \underline{V} = \underline{\phi} \times \left[\underline{\phi} \times \left(\underline{\omega} \times \underline{V}\right)\right] + \underline{\omega} \times \left[\underline{\phi}\times \left(\underline{\phi} \times \underline{V}\right)\right]$$

$$\begin{aligned} \underline{\phi} \times \left[\underline{\phi} \times \left(\underline{\omega} \times \underline{V}\right)\right] &= \underline{\phi} \times \left[- \left(\underline{\phi} \cdot \underline{\omega}\right) \underline{V} + \left(\underline{\phi} \cdot \underline{V}\right) \underline{\omega}\right] \\ &= - \left(\underline{\phi} \cdot \underline{\omega}\right) \left(\underline{\phi} \times \underline{V}\right) + \left(\underline{\phi} \cdot \underline{V}\right) \left(\underline{\phi} \times \underline{\omega}\right) \end{aligned}$$

$$\begin{aligned} \underline{\omega} \times \left[\underline{\phi} \times \left(\underline{\phi} \times \underline{V}\right)\right] &= \underline{\omega} \times \left[- \left(\underline{\phi} \cdot \underline{\phi}\right) \underline{V} + \left(\underline{\phi} \cdot \underline{V}\right) \underline{\phi}\right] \\ &= - \phi^2 \left(\underline{\omega} \times \underline{V}\right) + \left(\underline{\phi} \cdot \underline{V}\right) \left(\underline{\omega} \times \underline{\phi}\right) \\ &= - \phi^2 \left(\underline{\omega} \times \underline{V}\right) - \left(\underline{\phi} \cdot \underline{V}\right) \left(\underline{\phi} \times \underline{\omega}\right) \end{aligned}$$

$$\underline{\phi} \times \left[\underline{\phi} \times \left(\underline{\omega} \times \underline{V}\right)\right] + \underline{\omega} \times \left[\underline{\phi} \times \left(\underline{\phi} \times \underline{V}\right)\right] = - \left(\underline{\phi} \cdot \underline{\omega}\right) \left(\underline{\phi} \times \underline{V}\right) - \phi^2 \left(\underline{\omega} \times \underline{V}\right)$$

or in matrix form:

$$\left(\underline{\phi}\times\right)^2 \left(\underline{\omega}\times\right) \underline{V} + \left(\underline{\omega}\times\right)\left(\underline{\phi}\times\right)^2 \underline{V} = - \left(\underline{\phi} \cdot \underline{\omega}\right) \left(\underline{\phi}\times\right) \underline{V} - \phi^2 \left(\underline{\omega}\times\right) \underline{V}$$

Since $\underline{V}$ is arbitrary:

$$\left(\underline{\phi}\times\right)^2 \left(\underline{\omega}\times\right) + \left(\underline{\omega}\times\right)\left(\underline{\phi}\times\right)^2 = - \left(\underline{\phi} \cdot \underline{\omega}\right) \left(\underline{\phi}\times\right) - \phi^2 \left(\underline{\omega}\times\right) \tag{66}$$

Substituting (65) and (66) in (64) and (55):

$$
\begin{aligned}
\frac{1}{2}\left(\dot{C} - \dot{C}^T\right) &= \left(\underline{\omega}\times\right) + \frac{1}{2} f_1 \left(\underline{\phi} \times \underline{\omega}\right)^* - \frac{1}{2} f_2 \left[\left(\underline{\phi} \cdot \underline{\omega}\right)\left(\underline{\phi}\times\right) + \phi^2 \left(\underline{\omega}\times\right)\right] \\
&= \dot{f}_1 \left(\underline{\phi}\times\right) + f_1 \left(\dot{\underline{\phi}}\times\right)
\end{aligned}
\tag{67}
$$

Each term in (67) contains a scalar times a vector skew symmetric matrix. We can, therefore, invert each element of the equation to find the equivalent vector form:

$$
f_1 \dot{\underline{\phi}} + \dot{f}_1 \underline{\phi} = \underline{\omega} + \frac{1}{2} f_1 \left(\underline{\phi} \times \underline{\omega}\right) - \frac{1}{2} f_2 \left[\left(\underline{\phi} \cdot \underline{\omega}\right) \underline{\phi} + \phi^2 \underline{\omega}\right] \tag{68}
$$

Equation (68) is almost to the form we are looking for relating $\underline{\omega}$ and $\underline{\phi}$ to $\dot{\underline{\phi}}$. We can simplify it further if we introduce the following definition for $\underline{\omega}$:

$$
\underline{\omega} = \omega_\phi \overbrace{\left(\underline{\phi} / \phi\right)}^{\text{unit vector along } \underline{\phi}} + \Delta\underline{\omega} \tag{69}
$$

where:

$\omega_\phi$ = The component of $\underline{\omega}$ along $\underline{\phi}$

$\Delta\underline{\omega}$ = The component of $\underline{\omega}$ perpendicular to $\underline{\phi}$.

Substituting (69) in (68):

$$
\begin{aligned}
f_1 \dot{\underline{\phi}} + \dot{f}_1 \underline{\phi} &= \underline{\omega} + \frac{1}{2} f_1 \left(\underline{\phi} \times \Delta\underline{\omega}\right) - \frac{1}{2} f_2 \left( \phi\, \omega_\phi \underline{\phi} + \phi\, \omega_\phi \underline{\phi} + \phi^2 \Delta\underline{\omega}\right) \\
&= \underline{\omega} + \frac{1}{2} f_1 \left(\underline{\phi} \times \Delta\underline{\omega}\right) - \frac{1}{2} f_2 \phi^2 \Delta\underline{\omega} - f_2 \phi\, \omega_\phi \underline{\phi}
\end{aligned}
\tag{70}
$$

In the previous equation, use was made by the definition of $\Delta\underline{\omega}$ that $\underline{\phi} \cdot \Delta\underline{\omega} = 0$. Also, that $\underline{\phi} \times \underline{\phi} = 0$.

We now take the dot product of (70) with $\underline{\phi}$. Using (69) for $\underline{\omega}$:

$$
f_1 \underline{\phi} \cdot \dot{\underline{\phi}} + \dot{f}_1 \phi^2 = \phi\, \omega_\phi - f_2 \phi^3 \omega_\phi \tag{71}
$$

where use has been made of the fact that $\underline{\phi} \times \Delta\underline{\omega}$ and $\Delta\underline{\omega}$ are perpendicular to $\underline{\phi}$ and that, therefore, their dot products with $\underline{\phi}$ are zero. The $\underline{\phi} \cdot \dot{\underline{\phi}}$ term can be reduced by:

$$\underline{\phi} \cdot \underline{\phi} = \phi^2$$

$$(\underline{\phi} \cdot \underline{\phi})^{\cdot} = \left(\dot{\underline{\phi}} \cdot \underline{\phi}\right) + \left(\underline{\phi} \cdot \dot{\underline{\phi}}\right) = 2\, \underline{\phi} \cdot \dot{\underline{\phi}} = 2\, \phi\, \dot{\phi}$$

$$\underline{\phi} \cdot \dot{\underline{\phi}} = \phi\, \dot{\phi}$$

Also, using (52A) for $f_1$:

$$\dot{f}_1 = \frac{\dot{\phi}\, \phi \cos\phi - \dot{\phi} \sin\phi}{\phi^2}$$

With (52A) for $f_1$ and $f_2$, and the latter identities, (71) becomes:

$$\dot{\phi} \sin\phi + \dot{\phi}\, \phi \cos\phi - \dot{\phi} \sin\phi = \phi\, \omega_\phi - \left(1 - \cos\phi\right) \phi\, \omega_\phi$$

or

$$\phi\, \dot{\phi} \cos\phi = \phi\, \omega_\phi \cos\phi$$

or for $\cos\phi \neq 0$

$$\phi\, \dot{\phi} = \phi\, \omega_\phi \tag{72}$$

Going back to (71), and introducing $\underline{\phi} \cdot \dot{\underline{\phi}} = \phi\, \dot{\phi}$ and (72):

$$f_1\, \phi\, \omega_\phi + \dot{f}_1\, \phi^2 = \phi\, \omega_\phi - f_2\, \phi^3\, \omega_\phi$$

or

$$\phi\, \omega_\phi \left(1 - f_1\right) - f_2\, \phi^3\, \omega_\phi - \dot{f}_1\, \phi^2 = 0 \tag{73}$$

Now go back to (70) and rearrange:

$$
\begin{aligned}
f_1 \, \dot{\underline{\phi}} \; &= \; f_1 \, \underline{\omega} + \left(1 - f_1\right) \underline{\omega} + \frac{1}{2} f_1 \left(\underline{\phi} \times \Delta\underline{\omega}\right) - \frac{1}{2} f_2 \, \phi^2 \, \Delta\underline{\omega} - f_2 \, \phi \, \omega_\phi \, \underline{\phi} - \dot{f}_1 \, \underline{\phi} \\
&= \; f_1 \, \underline{\omega} + \left(1 - f_1\right)\left(\omega_\phi \, \underline{\phi} / \phi + \Delta\underline{\omega}\right) + \frac{1}{2} f_1 \left(\underline{\phi} \times \Delta\underline{\omega}\right) - \frac{1}{2} f_2 \, \phi^2 \, \Delta\underline{\omega} - f_2 \, \phi \, \omega_\phi \, \underline{\phi} - \dot{f}_1 \, \underline{\phi} \\
&= \; f_1 \, \underline{\omega} + \frac{1}{2} f_1 \left(\underline{\phi} \times \Delta\underline{\omega}\right) + \left(1 - f_1 - \frac{1}{2} f_2 \, \phi^2\right) \Delta\underline{\omega} + \left[\left(1 - f_1\right) \phi \, \omega_\phi - f_2 \, \phi^3 \, \omega_\phi - \dot{f}_1 \, \phi^2\right] \underline{\phi} / \phi^2
\end{aligned}
$$

The large term in brackets is equal to zero from (73). Thus, dividing by $f_1$:

$$
\dot{\underline{\phi}} \; = \; \underline{\omega} + \frac{1}{2}\left(\underline{\phi} \times \Delta\underline{\omega}\right) - \left(1 - \frac{1}{f_1} + \frac{f_2 \, \phi^2}{2 \, f_1}\right) \Delta\underline{\omega} \tag{74}
$$

Using (52A) for the large term in brackets,

$$
\begin{aligned}
1 - \frac{1}{f_1} + \frac{f_2 \, \phi^2}{2 \, f_1} \; &= \; 1 - \frac{2 - f_2 \, \phi^2}{2 \, f_1} \; = \; 1 - \frac{1 + \cos \phi}{2 \, f_1} \\
&= \; 1 - \frac{\left(1 + \cos \phi\right) \phi}{2 \sin \phi} \; = \; 1 - \frac{\phi \sin \phi}{2 \left(1 - \cos \phi\right)}
\end{aligned} \tag{75}
$$

a trig identity
manipulation

The $\Delta\underline{\omega}$ term can be expressed in terms of $\underline{\omega}$ and $\underline{\phi}$. By definition,

$$
\begin{aligned}
\Delta\underline{\omega} \; &= \; \underline{\omega} - \omega_\phi \, \underline{\phi} / \phi \; = \; \underline{\omega} - \left(\underline{\omega} \cdot \underline{\phi} / \phi\right) \underline{\phi} / \phi \; = \; \underline{\omega} - \left(\underline{\omega} \cdot \underline{\phi}\right) \underline{\phi} / \phi^2 \\
&= \; \frac{1}{\phi^2}\left[\phi^2 \, \underline{\omega} - \left(\underline{\omega} \cdot \underline{\phi}\right) \underline{\phi}\right]
\end{aligned}
$$

Using the triple vector product identity and $\underline{\phi} \cdot \underline{\phi} = \phi^2$:

$$
\Delta\underline{\omega} \; = \; - \frac{1}{\phi^2}\left[\underline{\phi} \times \left(\underline{\phi} \times \underline{\omega}\right)\right] \tag{76}
$$

Using (75) and (76) in (74), then yields the final expression for $\dot{\underline{\phi}}$:

$$
\dot{\underline{\phi}} \; = \; \underline{\omega} + \frac{1}{2} \, \underline{\phi} \times \underline{\omega} + \frac{1}{\phi^2}\left(1 - \frac{\phi \sin \phi}{2 \left(1 - \cos \phi\right)}\right) \underline{\phi} \times \left(\underline{\phi} \times \underline{\omega}\right) \tag{77}
$$

Equation (77) is the general equation for $\dot{\underline{\phi}}$ which when integrated over the interval from m to m+1 yields the exact value of $\underline{\phi}$ to use in Equation (51). Note, that as the integration begins (with $\underline{\phi}$ initially zero), $\underline{\phi}$ is equal to the integral of $\underline{\omega}$ (i.e., - the second and third terms in the Equation (77) expression start out at zero). If $\underline{\omega}$ is constant, $\underline{\phi}$ will, therefore, be generated along $\underline{\omega}$, and the cross-products of $\underline{\omega}$ with $\underline{\phi}$ in the second and third terms will remain zero. Hence $\underline{\phi}$ will equal the integral of $\underline{\omega}$ for the entire interval. This is the approximation we discussed during the last lecture (i.e.: $\underline{\phi} \approx \int \underline{\omega}\, dt = \underline{\alpha}$). If the rotation of $\underline{\omega}$ during the generation of $\underline{\phi}$ is to be taken into account, the other terms in (77) must be utilized. Note that the third term is much smaller than the second term. If the trigonometric terms are expanded in a Taylor series, it can be shown that the trigonometric term in brackets times $\frac{1}{\phi^2}$ is equal to $\frac{1}{12}$ (to first order in $\phi^2$). Thus,

$$\frac{1}{\phi^2}\left(1 - \frac{\phi \sin \phi}{2\left(1\text{-}\cos \phi\right)}\right)\underline{\phi} \times \left(\underline{\phi} \times \underline{\omega}\right) = \frac{1}{12}\,\underline{\phi} \times \left(\underline{\phi} \times \underline{\omega}\right) + \text{higher order terms}$$

This is an order of magnitude smaller than $\frac{1}{2}\left(\underline{\phi} \times \underline{\omega}\right)$, and much smaller than even this due to the 1/12 (compared to 1/2) coefficient. Hence, the second term can be neglected in the coning equation. An additional approximation that can be used is that $\underline{\phi} \times \underline{\omega}$ can be approximated by $\underline{\alpha} \times \underline{\omega}$ where

$$\underline{\alpha} = \int_m \underline{\omega}\, dt$$

Thus, the $\dot{\underline{\phi}}$ equation can be approximated by:

$$\underline{\alpha} = \int_m \underline{\omega}\, dt$$

$$\Delta\underline{\phi} = \frac{1}{2}\int \left(\underline{\alpha} \times \underline{\omega}\, dt\right)$$

$$\underline{\phi} = \underline{\alpha} + \Delta\underline{\phi}$$

or,

$$
\begin{aligned}
\underline{\alpha} &= \int d\underline{\alpha} \\
\Delta\underline{\phi} &= \frac{1}{2}\int \left(\underline{\alpha} \times d\underline{\alpha}\right) \qquad (78) \\
\underline{\phi} &= \underline{\alpha} + \Delta\underline{\phi}
\end{aligned}
$$

where

$d\underline{\alpha}$ = The gyro output count vector

Equations (78) would be approximated by a digital integration algorithm that is iterated at high rate between the update intervals of Equation (51). This can be performed as a high speed software function in the central strapdown navigation computer or a separate high speed processor.

One of the fine tuning compensation terms commonly utilized with strapdown attitude reference algorithms is an orthonormality correction that corrects the direction cosine matrix for residual errors that may cause its rows and columns to deviate from orthogonality and normality. This could be caused, for example, by computer finite word length effects or truncation of the Equation (51) Taylor series under high rate inputs. The orthonormality correction is based on the fact that the rows (and columns) of the C matrix (relating body to local level coordinates - Equation (51)) represent unit vectors in one coordinate frame projected on the axes of another frame. Being unit vectors along orthogonal coordinate axes, their dot products with one another should be zero; being unit vectors, their dot products with themselves should equal one. Deviations from orthogonality and normality indicate an error effect that can be compensated on a regular basis to bring the C matrix elements into their nominally orthogonal/normal condition.

To derive the equation for the orthonormality update, we first write the relation for C (i.e., $C_B^L$) in terms of its rows $\underline{C}i$:

$$C = \begin{pmatrix} \underline{C}_1 \\ \underline{C}_2 \\ \underline{C}_3 \end{pmatrix}$$

Note: The bar under $\underline{C}i$ represents a row vector in this discussion which differs from the usual convention where under-bar represent a column vector.

Each $\underline{C}i$ represents a three element row vector equal (theoretically) to the projection into the body coordinate frame of a unit vector along local level coordinates. (e.g. - $\underline{C}_1$ represents a unit vector along the X (axis 1) local level coordinate axis, $\underline{C}_2$ along Y (axis 2), etc.). For the orthogonality condition to be met, the dot product of the $\underline{C}i$'s with one another should be zero. Lets look at a non-orthogonal condition between $\underline{C}_1$ and $\underline{C}_2$ and determine a correction that will achieve orthogonality.

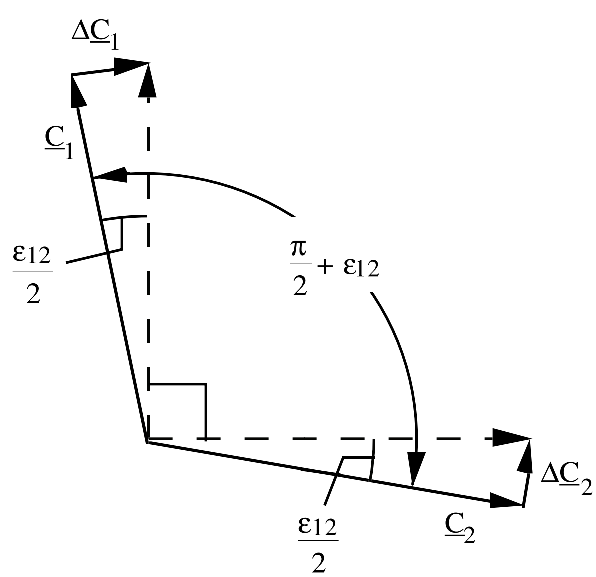

The figure shows $\underline{C}_1$ and $\underline{C}_2$ deviating from orthogonality (90 degrees) by the error angle $\varepsilon_{12}$. Since we have no reason to assume either $\underline{C}_1$ or $\underline{C}_2$ to be more likely in error, we assume they are equally likely and apply a correction of equal amount to each. The correction is to add a small vector amount ($\Delta\underline{C}_1$ and $\Delta\underline{C}_2$) to each that will rotate each by half of $\varepsilon_{12}$ so that a net $\varepsilon_{12}$ rotation between the two will be applied. The result after the rotations (dotted vectors) will achieve orthogonality. For small $\varepsilon_{12}$, $\Delta\underline{C}_1$ is parallel to $\underline{C}_2$ and $\Delta\underline{C}_2$ is parallel to $\underline{C}_1$ so that:

$$\Delta\underline{C}_1 = \frac{\varepsilon_{12}}{2}\underline{C}_2$$

$$\Delta\underline{C}_2 = \frac{\varepsilon_{12}}{2}\underline{C}_1$$

The $\varepsilon_{12}$ quantity is evaluated by taking the dot product of $\underline{C}_1$ with $\underline{C}_2$. The result, since both $\underline{C}_1$ and $\underline{C}_2$ are unity in magnitude to first order, equals the cosine of the angle between them:

$$\underline{C}_1 \cdot \underline{C}_2 = /\underline{C}_1/\ /\underline{C}_2/ \cos\left(\frac{\pi}{2} + \varepsilon_{12}\right)$$

$$= -/\underline{C}_1/\ /\underline{C}_2/ \sin\varepsilon_{12} \approx -/\underline{C}_1/\ /\underline{C}_2/\ \varepsilon_{12} = -\varepsilon_{12}$$

Hence:

$$\Delta\underline{C}_1 = -\frac{1}{2}\left(\underline{C}_1 \cdot \underline{C}_2\right)\underline{C}_2$$

$$\Delta\underline{C}_2 = -\frac{1}{2}\left(\underline{C}_1 \cdot \underline{C}_2\right)\underline{C}_1$$

Similarly, to correct for non-orthogonality between $\underline{C}_2$, $\underline{C}_3$ and $\underline{C}_3$, $\underline{C}_1$:

$$\Delta\underline{C}_2 = -\frac{1}{2}\left(\underline{C}_2 \cdot \underline{C}_3\right)\underline{C}_3$$

$$\Delta\underline{C}_3 = -\frac{1}{2}\left(\underline{C}_2 \cdot \underline{C}_3\right)\underline{C}_2$$

Correction for $\underline{C}_2$, $\underline{C}_3$ non-orthogonality

$$\Delta\underline{C}_3 = -\frac{1}{2}\left(\underline{C}_3 \cdot \underline{C}_1\right)\underline{C}_1$$

$$\Delta\underline{C}_1 = -\frac{1}{2}\left(\underline{C}_3 \cdot \underline{C}_1\right)\underline{C}_3$$

Correction for $\underline{C}_3$, $\underline{C}_1$ non-orthogonality

The total orthogonality correction is the sum of the above three sets:

$$\begin{aligned}
\Delta\underline{C}_1 &= -\frac{1}{2}\left(\underline{C}_1 \cdot \underline{C}_2\right)\underline{C}_2 - \frac{1}{2}\left(\underline{C}_1 \cdot \underline{C}_3\right)\underline{C}_3 \\
\Delta\underline{C}_2 &= -\frac{1}{2}\left(\underline{C}_2 \cdot \underline{C}_3\right)\underline{C}_3 - \frac{1}{2}\left(\underline{C}_2 \cdot \underline{C}_1\right)\underline{C}_1 \qquad (79) \\
\Delta\underline{C}_3 &= -\frac{1}{2}\left(\underline{C}_3 \cdot \underline{C}_1\right)\underline{C}_1 - \frac{1}{2}\left(\underline{C}_3 \cdot \underline{C}_2\right)\underline{C}_2
\end{aligned}$$

To adjust for normality error, we want to find a correction that modifies the magnitude of each $\underline{C}i$ without altering its direction. The correction should be such that after its application, the magnitude of $\underline{C}i$ equals one. The correction, therefore, has the following form:

$$\Delta\underline{C} = \varepsilon_{ii}\,\underline{C}_i \qquad (80)$$

For the magnitude of $\underline{C}_i$ to equal one after correction:

$$\left(\underline{C}_i + \Delta\underline{C}_i\right) \cdot \left(\underline{C}_i + \Delta\underline{C}_i\right) = 1$$

or, substituting for $\Delta\underline{C}_i$ and assuming small $\varepsilon_{ii}$:

$$\begin{aligned}
\left(\underline{C}_i + \varepsilon_{ii}\,\underline{C}_i\right) \cdot \left(\underline{C}_i + \varepsilon_{ii}\,\underline{C}_i\right) &= \left(1 + \varepsilon_{ii}\right)\underline{C}_i \cdot \left(1 + \varepsilon_{ii}\right)\underline{C}_i \\
&= \left(1 + \varepsilon_{ii}\right)^2 \underline{C}_i \cdot \underline{C}_i \approx \left(1 + 2\,\varepsilon_{ii}\right)\underline{C}_i \cdot \underline{C}_i = 1
\end{aligned}$$

or

$$\underline{C}_i \cdot \underline{C}_i = \frac{1}{1 + 2\,\varepsilon_{ii}} \approx 1 - 2\,\varepsilon_{ii}$$

or

$$\varepsilon_{ii} = -\frac{1}{2}\left(\underline{C}_i \cdot \underline{C}_i - 1\right)$$

Substituting in (80), we obtain the normality correction for each $\underline{C}i$:

$$\begin{aligned}
\Delta\underline{C}_1 &= -\frac{1}{2}\left[\left(\underline{C}_1 \cdot \underline{C}_1\right)\underline{C}_1 - \underline{C}_1\right] \\
\Delta\underline{C}_2 &= -\frac{1}{2}\left[\left(\underline{C}_2 \cdot \underline{C}_2\right)\underline{C}_2 - \underline{C}_2\right] \qquad (81) \\
\Delta\underline{C}_3 &= -\frac{1}{2}\left[\left(\underline{C}_3 \cdot \underline{C}_3\right)\underline{C}_3 - \underline{C}_3\right]
\end{aligned}$$

The sum of (79) with (81) is the combined orthogonality/normality correction algorithm:

$$\Delta\underline{C}_1 = -\frac{1}{2}\left[\underline{C}_1\left(\underline{C}_1 \cdot \underline{C}_1\right) + \underline{C}_2\left(\underline{C}_1 \cdot \underline{C}_2\right) + \underline{C}_3\left(\underline{C}_1 \cdot \underline{C}_3\right) - \underline{C}_1\right]$$

$$\Delta\underline{C}_2 = -\frac{1}{2}\left[\underline{C}_1\left(\underline{C}_2 \cdot \underline{C}_1\right) + \underline{C}_2\left(\underline{C}_2 \cdot \underline{C}_2\right) + \underline{C}_3\left(\underline{C}_2 \cdot \underline{C}_3\right) - \underline{C}_2\right]$$

$$\Delta\underline{C}_3 = -\frac{1}{2}\left[\underline{C}_1\left(\underline{C}_3 \cdot \underline{C}_1\right) + \underline{C}_2\left(\underline{C}_3 \cdot \underline{C}_2\right) + \underline{C}_3\left(\underline{C}_3 \cdot \underline{C}_3\right) - \underline{C}_3\right]$$

or in matrix form:

$$\begin{pmatrix} \Delta\underline{C}_1 \\ \Delta\underline{C}_2 \\ \Delta\underline{C}_3 \end{pmatrix} = -\frac{1}{2}\left[\begin{pmatrix} \underline{C}_1 \\ \underline{C}_2 \\ \underline{C}_3 \end{pmatrix}\left(\underline{C}_1^{\,T}\ \underline{C}_2^{\,T}\ \underline{C}_3^{\,T}\right)\begin{pmatrix} \underline{C}_1 \\ \underline{C}_2 \\ \underline{C}_3 \end{pmatrix} - \begin{pmatrix} \underline{C}_1 \\ \underline{C}_2 \\ \underline{C}_3 \end{pmatrix}\right]$$

$$= -\frac{1}{2}\left[\begin{pmatrix} \underline{C}_1 \\ \underline{C}_2 \\ \underline{C}_3 \end{pmatrix}\left(\underline{C}_1^{\,T}\ \underline{C}_2^{\,T}\ \underline{C}_3^{\,T}\right) - I\right]\begin{pmatrix} \underline{C}_1 \\ \underline{C}_2 \\ \underline{C}_3 \end{pmatrix}$$

where

$$I = \text{The identity matrix} = \begin{bmatrix} 1 & 0 & 0 \\ 0 & 1 & 0 \\ 0 & 0 & 1 \end{bmatrix}$$

or, in terms of C (see first equation in this set of notes):

$$\Delta C = \frac{1}{2}\left(I - C\,C^T\right)C \qquad (82)$$

Equation (82) is the correction to be applied to the $C_B^L$ matrix to bring the rows into orthogonality and normality. It is natural to ask if this is also the same expression that would have been obtained if we had derived the relation to orthogonalize and normalize the columns. The answer to this question is easily obtained by noting that the derivation of (82) placed no restriction on C as being $C_B^L$. The same result would have been obtained for any C, even the transpose of $C_B^L$. If the procedure was repeated for the rows of $C_B^L$ transposed, we would derive the equation for orthonormalizing the rows of $\left(C_B^L\right)^T$ or the columns of $C_B^L$. Clearly, the result would equal (82), with C replaced by $C^T$:

$$\Delta C^T = \frac{1}{2}\left[I - C^T\left(C^T\right)^T\right]C^T$$

or

$$\Delta C^T = \frac{1}{2}\left(I - C^T C\right) C^T \tag{83}$$

The transpose of the (83) is:

$$\Delta C = \frac{1}{2} C \left[I - C^T \left(C^T\right)^T\right] \tag{84}$$

or

$$\Delta C = \frac{1}{2} C \left(I - C^T C\right) = \frac{1}{2}\left(C - C\,C^T C\right) = \frac{1}{2}\left(I - C\,C^T\right) C \tag{85}$$

which is identical to (82). Hence (82) and (83) are equivalent and an orthonormalization of the columns or rows of C produces the identically same result.

Some of the other compensations typically utilized in strapdown inertial navigation systems are basic sensor error corrections, gyro quantization compensation and accelerometer size effect compensation. Sensor compensation takes the sensor counts as they enter the computer and corrects them for known sensor errors. For example, the x-axis gyro (and accelerometer) sensor compensation equation typically looks like:

$$\Delta\alpha_x = K_1 + K_2\,\alpha_x + K_3\,\alpha_y + K_4\,\alpha_z$$

where

$K_1$ is the sensor bias correction.

$K_2$ is the sensor scale factor correction

$K_3$, $K_4$ are sensor misalignment corrections

$\alpha_x$, $\alpha_y$, $\alpha_z$ are sensor input counts

$\Delta\alpha_x$ is the x-axis sensor error correction (to be added to $\alpha_x$)

For ring laser gyros, $K_1$ in general is an analytically defined function of measured gyro temperature, with the $K_2$, $K_3$, and $K_4$ coefficients fixed. For very high angular rate/high accuracy applications, the $K_2$ scale factor coefficient may also include temperature sensitive terms.

For the accelerometers, both $K_1$ (bias), $K_2$ (scale factor), and $K_3$, $K_4$ (misalignment) coefficients are generally analytically defined functions of measured accelerometer temperature. For high acceleration applications, the $K_2$ scale factor coefficient for the accelerometer may also contain acceleration sensitive terms based on accelerometer output measurements (to account for scale factor nonlinearity).

A quantization correction can be incorporated for a laser gyro that compensates for hysteresis and finite pulse size in the gyro readout logic. The average error introduced at turn-around is the total deadband (d) minus the gyro pulse size ($\varepsilon$). The compensation is to add this to the gyro count sample in the computer for each turn-around:

$$\Delta\alpha = \frac{d - \varepsilon}{2}\left[\text{sign}\left(\alpha_n\right) - \text{sign}\left(\alpha_{n-1}\right)\right]$$

where

$\alpha_n$ is the gyro count sample

$\alpha_{n-1}$ is the previous gyro count sample

sign ($\alpha_n$) equals 1 for $\alpha_n$ positive, and -1 for $\alpha_n$ negative

For motion in one direction $\alpha_n = \alpha_{n-1}$ and the above effect is zero. For a change in direction, the difference between the $\alpha_n$, $\alpha_{n-1}$ signs produce a "2" magnitude which when multiplied by $\frac{d - \varepsilon}{2}$ produces the desired d - $\varepsilon$ correction. The sense of the compensation is also correct (positive for a negative turn-around: $\alpha_n$ from + to - ; and negative for a positive turn-around). Quantization compensation can also be incorporated for an accelerometer depending on the type of accelerometer being used.

Accelerometer size effect compensation corrects for the fact that the three accelerometers cannot physically occupy the same space, hence, measure acceleration at slightly different points. Errors created by this effect are caused by angular motion and the resulting differences in centripetal and angular acceleration between the accelerometer locations:

$$\Delta a_i = \underline{u}_i \cdot \left[\dot{\underline{\omega}} \times l_j + \underline{\omega} \times \left(\underline{\omega} \times l_j\right)\right]$$

where

$\Delta a_i$ = The correction for the i$^{th}$ accelerometer

$\underline{u}_i$ = Unit vector along the i$^{th}$ accelerometer input axis

$\dot{\underline{\omega}}$ = Angular acceleration (computed from gyro sample differences)

$l_j$ = Linear distance from the i$^{th}$ accelerometer to the sensor assembly reference acceleration sensing point

$\underline{\omega}$ = Gyro sensed angular rate

## INTERFACE BETWEEN NAVIGATION AND STRAPDOWN REFERENCE EQUATIONS

Thus far we have not made a distinction between local level axes used for the $C_B^L$ reference and the local level axes used for navigation (i.e., the two frames have been assumed identical). The two frames may differ, however, in the definition of their X, Y, Z axes. Typically, the local level frame axes for $C_B^L$ are defined with Z down, while just the opposite is typically the case for the navigation frame Z axis. The X, Y axes for the two frames would be parallel, but X for the navigation frame would be the Y axis for the $C_B^L$ reference frame, and Y for the navigation frame would be X for the $C_B^L$ reference. Both frames, of course, are right handed.

The navigation coordinate frame selection in the above discussion is chosen so that calculated navigation parameters are represented in the normal Z axis up convention traditionally used in inertial navigation with positive wander angle defined as a rotation about a Z up vertical. The $C_B^L$ reference frame selection in the above discussion is chosen so that body angle reference data (described in the next section) follows normal attitude/heading reference conventions (i.e., heading is traditionally defined as a rotation about a Z down vertical).

Use of the two local level coordinate frame definitions does, however, cause some confusion at the interface between the navigation and strapdown attitude reference equations, requiring the following variable transformations:

$$\begin{pmatrix} a_x \\ a_y \\ a_z \end{pmatrix} = \begin{pmatrix} a_y \\ a_x \\ -a_z \end{pmatrix}$$

For navigation Equations (20) — From strapdown transformation Equation (29) or (29C)

$$\begin{pmatrix} \omega_x \\ \omega_y \\ \omega_z \end{pmatrix} = \begin{pmatrix} \omega_y \\ \omega_x \\ -\omega_z \end{pmatrix}$$

For $C_B^L$ update Equation (33) — From Equation (19C) of navigation computations

ATTITUDE/HEADING OUTPUTS

An important function in an inertial navigation system is its ability to provide attitude/heading output data to other vehicle systems. In the case of a gimbaled inertial system, this data is derived from resolvers mounted on the platform gimbal shafts. For a strapdown system, the attitude/heading data is derived from the direction cosine matrix relating body and Z down local level reference axes. The following diagram illustrates the relationship between the Euler angles typically used to represent attitude/heading.

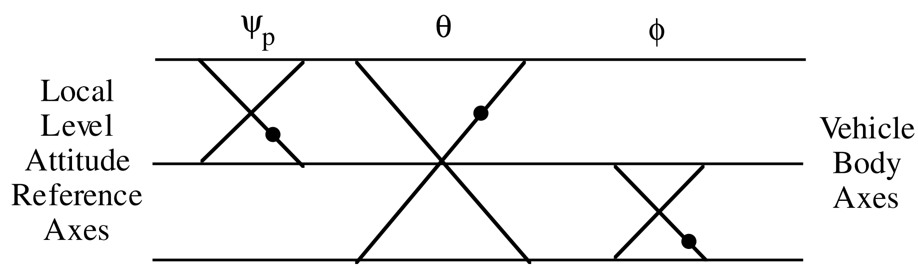


In the diagram:

$\psi_p$ = Vehicle heading angle relative to local level Z down reference axes (also known as "platform heading")

$\theta$ = Vehicle pitch angle

$\phi$ = Vehicle roll angle

The analytical relationship between $\psi_p$, $\theta$, $\phi$ and the $C_B^L$ direction cosine matrix elements can be written directly by inspection of the diagram as:

$$C_{11} = \cos\theta \cos\psi_p$$
$$C_{12} = -\cos\phi \sin\psi_p + \sin\phi \sin\theta \cos\psi_p$$
$$C_{13} = \sin\phi \sin\psi_p + \cos\phi \sin\theta \cos\psi_p$$

$$C_{21} = \cos\theta \sin\psi_p$$
$$C_{22} = \cos\phi \cos\psi_p + \sin\phi \sin\theta \sin\psi_p$$
$$C_{23} = -\sin\phi \cos\psi_p + \cos\phi \sin\theta \sin\psi_p$$

$$C_{31} = -\sin\theta$$
$$C_{32} = \sin\phi \cos\theta$$
$$C_{33} = \cos\phi \cos\theta$$

where

$$C_{ij} = \text{Element ij of } C_B^L.$$

From the above,

$$\cos\theta = \sqrt{C_{32}^2 + C_{32}^2}$$

So that the desired inverse relationships become:

$$\phi = \tan^{-1}\frac{C_{32}}{C_{33}}$$

$$\theta = \tan^{-1}\frac{-C_{31}}{\sqrt{C_{32}^2 + C_{32}^2}}$$

$$\psi_p = \tan^{-1}\frac{C_{21}}{C11}$$

In order to obtain heading relative to North rather than with respect to local level reference axes, it is necessary to correct $\psi_p$ for the wander angle ($\alpha$). Thus $\psi_N$ (vehicle true heading relative to true North) is given by:

$$\psi_N = \psi_p - \alpha$$

Note in the previous relationship, that the wander angle is subtracted from $\psi_p$ to obtain $\psi_N$. This is because the wander angle is defined relative to a Z up vertical (see Lecture 3) as contrasted with $\psi_N$ or $\psi_p$ which are defined relative to a Z down vertical (see previous section for further discussion on local level coordinate frame definitions).

It should also be noted that for pitch angles approaching ±90 degrees, both the numerator and denominator of the $\phi$ and $\psi_p$ arc tangent arguments approach zero, hence, $\phi$ and $\psi_p$ become undefined. This is simply a statement of the fact that for nose up or down attitudes, roll and heading are indistinguishable (i.e., heading is measured about the vertical and roll is measured about the vehicle longitudinal axis which is also vertical for $\theta = \pm 90$ degrees). A typical implementation of the $\phi$, $\psi$ output functions for $\theta$ near ±90 degrees is to hold them fixed at their last computed value until $\theta$ becomes once again sufficiently removed from the ±90 degrees singularity condition.

## QUATERNIONS

A course in strapdown navigation would not be complete without including a discussion on Quaternions. Quaternion parameters have found popular usage in strapdown applications for attitude referencing as contrasted with the direction cosine matrix attitude reference parameters described previously.

The attitude reference quaternion is based on the concept of the Euler axis of rotation that exists between two coordinate frames that have some arbitrary angular orientation relative to one another. The Euler axis is defined as the axis of rotation about which one coordinate frame can be rotated into the other. For any arbitrary attitude of one frame relative to the other, one unique Euler axis exists. The attitude quaternion associated with two coordinate frames is defined as a set of four parameters: three represent the components of a vector directed along the Euler axis between the two frames; the fourth is a scalar quantity. The length of the vector parameter equals the sine of $\beta/2$ where $\beta$ is the angle of rotation about the Euler axis that rotates one of the coordinate frames into the other; the scalar parameter equals the cosine of $\beta/2$.

The discussion to follow describes how the attitude reference quaternion can be used as an alternative to direction cosines in the strapdown attitude determination integration process, and in the transformation operation that converts body sensed accelerations to their equivalent local level navigation coordinate axis counterparts. Also to be addressed is a comparison between the relative advantages and disadvantages between the quaternion and the direction cosine matrix approaches for body attitude referencing in strapdown navigation applications.

To introduce the quaternion concept, let's begin the discussion in a somewhat unrelated field: complex numbers (as in Morse and Feshbach, Methods of Theoretical Physics). A complex number v is defined as having a real and imaginary part:

$$v = e\,i + h$$

where:

e, h = Scalar quantities

i = The imaginary number defined as the square root of minus one.

From the definition of i,

$$i\,i = -1$$

The complex number v can be thought of as a "two-vector" with components e and h in the complex plane. We will now demonstrate that another complex number u can be defined that can be used as an operator to rotate v through an angle $\phi$ in the complex plane. We also note that a rotation of a vector is equivalent mathematically to a vector transformation operation. Let's define u in general as

$$u = a\,i + d$$

The product w of u with v is:

$$w = u\,v = (a\,i + d)(e\,i + h) = a\,e\,i\,i + a\,h\,i + d\,e\,i + d\,h$$

$$= (e\,d + h\,a)\,i + (h\,d - e\,a)$$

Hence, the effect of the multiplication operation of u on v is to create a new complex number w with a real component (h d - e a) and an imaginary component (e d + h a).

If the components of u were defined as

$$a = \sin\phi \qquad d = \cos\phi$$

The u v product w would be:

$$w = (e\cos\phi + h\sin\phi)\,i + (h\cos\phi - e\sin\phi)$$

From the latter expression it should be apparent that the u v product vector represents vector v rotated by $\phi$ in the complex plane. Alternatively, w is equivalent to vector v projected along the axes of a new complex plane rotated by $\phi$ from the original (see following sketch).

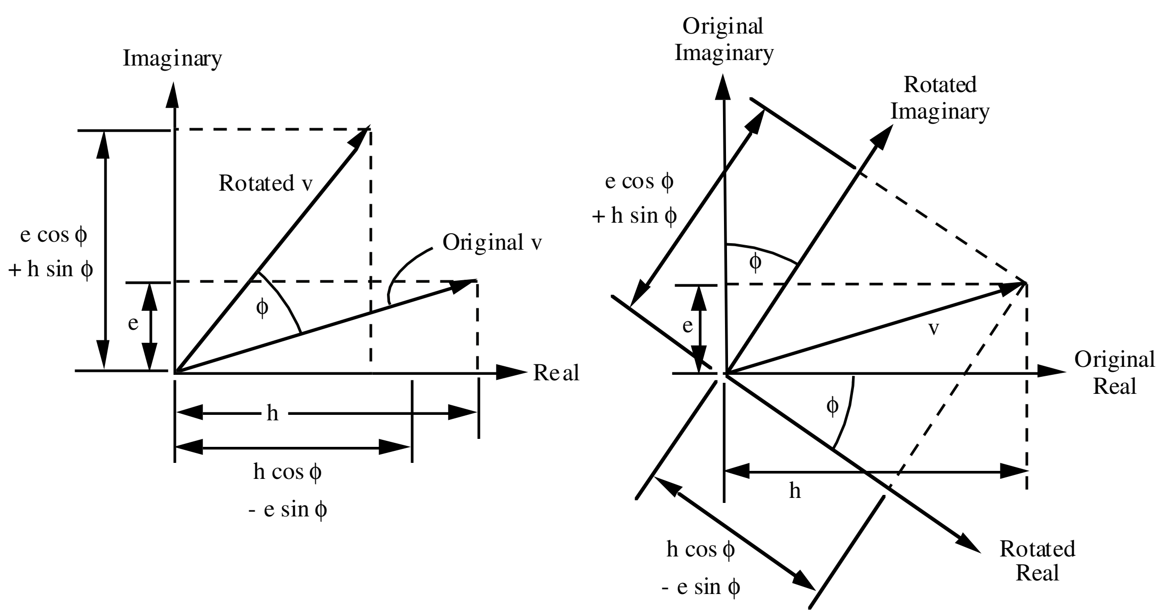


Thus, u = i sin $\phi$ + cos $\phi$ can be considered as an operator that transforms vector v into a new frame rotated by $\phi$ from the original frame.

Let's try to extend this concept into the world of three-dimensional vectors. If we now consider the i parameter to represent a unit vector along the x-axis of a three-dimensional coordinate frame, we can extend the concept of v to also include the j and k components (i.e., with y and z axis components) as a "four-vector":

$$v = e\,i + f\,j + g\,k + h$$

where

e, f, g = The conventional components of a vector in an x, y, z three-dimensional coordinate frame.

h = A fourth component (a scalar) which would normally be zero if v represented a typical 3-component vector, but which is carried as a scalar quantity (e.g., in a fourth dimension) for the present.

The u quantity is similarly expanded.

$$u = a\,i + b\,j + c\,k + d$$

We now define the rules of four-vector multiplication by extension of the complex number concept using a right-handed vector cross-product convention:

$$\begin{array}{lll} i\,i = -1 & j\,j = -1 & k\,k = -1 \\ i\,j = k & j\,k = i & k\,i = j \\ j\,i = -k & k\,j = -i & i\,k = -j \end{array}$$

With the above definitions, the product w of u with v is now given by:

$$\begin{aligned} w = u\,v &= (a\,i + b\,j + c\,k + d)(e\,i + f\,j + g\,k + h) \\ &= a\,e\,i\,i + a\,f\,i\,j + a\,g\,i\,k + a\,h\,i \\ &\quad + b\,e\,j\,i + b\,f\,j\,j + b\,g\,j\,k + b\,h\,j \\ &\quad + c\,e\,k\,i + c\,f\,k\,j + c\,g\,k\,k + c\,h\,k \\ &\quad + d\,e\,i + d\,f\,j + d\,g\,k + d\,h \\ &= (a\,h + d\,e + b\,g - c\,f)\,i \\ &\quad + (b\,h + d\,f + c\,e - a\,g)\,j \\ &\quad + (c\,h + d\,g + a\,f - b\,e)\,k \\ &\quad + (d\,h - a\,e - b\,f - c\,g) \end{aligned}$$

or in “Four-vector” matrix form:

$$\begin{pmatrix} e' \\ f' \\ g' \\ h' \end{pmatrix} = \begin{bmatrix} d & -c & b & a \\ c & d & -a & b \\ -b & a & d & c \\ -a & -b & -c & d \end{bmatrix} \begin{pmatrix} e \\ f \\ g \\ h \end{pmatrix} \qquad (85A)$$

where

$$w \overset{\Delta}{=} e'\,i + f'\,j + g'\,k + d'$$

To complete the analogy it would be ideal at this point if we could now equate the components of u to a three-dimensional vector transformation operation and demonstrate that the i, j, k components of w as defined above represent the transformed form of the i, j, k components of v. Unfortunately, the analogy breaks down to a certain extent and such a simple relationship for u is not quite possible. However, an equivalent expression for u can be found that does possess the desired vector transformation property, if we modify the u operation on v to be defined as

$$w \;=\; u\,v\,u^* \qquad \text{(85B)}$$

where

u* is the complex conjugate of u defined by:

$$u^* = -\,a\,i\,-\,b\,j\,-\,c\,k\,+\,d$$

Carrying out the v u* product in (85B) using the previously stated rules of four-vector multiplication yields:

$$v\,u^* \;=\; (ei + fj + gk + h)(-ai - bj - ck + d)$$

$$= \begin{matrix} (ed - ha - fc + gb)\,i \\ +\,(fd - hb - ga + ec)\,j \\ +\,(gd - hc - eb + fa)\,k \\ +\,(hd + ea + fb + gc) \end{matrix} \;=\; \begin{bmatrix} d & -c & b & -a \\ c & d & -a & -b \\ -b & a & d & -c \\ a & b & c & d \end{bmatrix} \begin{pmatrix} e \\ f \\ g \\ h \end{pmatrix}$$

and for the newly defined w given by (85B) we find with (85A):

$$w \;=\; u\,v\,u^* \;=\; \begin{bmatrix} d & -c & b & a \\ c & d & -a & b \\ -b & a & d & c \\ -a & -b & -c & d \end{bmatrix} \begin{bmatrix} d & -c & b & -a \\ c & d & -a & -b \\ -b & a & d & -c \\ a & b & c & d \end{bmatrix} \begin{pmatrix} e \\ f \\ g \\ h \end{pmatrix}$$

$$= \begin{bmatrix} (d^2 + a^2 - b^2 - c^2) & 2\,(ab - cd) & 2\,(ac + bd) & 0 \\ 2\,(ab + cd) & (d^2 + b^2 - c^2 - a^2) & 2\,(bc - ad) & 0 \\ 2\,(ac - bd) & 2\,(bc + ad) & (d^2 + c^2 - a^2 - b^2) & 0 \\ 0 & 0 & 0 & (a^2 + b^2 + c^2 + d^2) \end{bmatrix} \begin{pmatrix} e \\ f \\ g \\ h \end{pmatrix} \qquad \text{(85C)}$$

We now equate the components of u to the previously defined quaternion rotation parameters. If the Euler axis for the rotation operation in question is denoted as having i, j, k components of $l$, m and n, and the rotation magnitude is $\phi$, the four components of u are given by:

$$a \;=\; l\sin\frac{\phi}{2} \qquad b \;=\; m\sin\frac{\phi}{2} \qquad c \;=\; n\sin\frac{\phi}{2} \qquad d \;=\; \cos\frac{\phi}{2}$$

If we now define a vector $\underline{\phi}$ as lying along the Euler axis with magnitude $\phi$, we can also write:

$$l = \frac{\phi_x}{\phi} \qquad m = \frac{\phi_y}{\phi} \qquad n = \frac{\phi_z}{\phi}$$

where

$\phi_x, \phi_y, \phi_z$ = The components of $\underline{\phi}$.

Thus,

$$a = \frac{\phi_x}{\phi}\sin\frac{\phi}{2} \qquad b = \frac{\phi_y}{\phi}\sin\frac{\phi}{2}$$
$$c = \frac{\phi_z}{\phi}\sin\frac{\phi}{2} \qquad d = \cos\frac{\phi}{2} \tag{85D}$$

Substitution of (85D) into (85C) after application of appropriate trigonometric identities equates to:

$$w = \begin{bmatrix} 1-\left(\phi_y^2+\phi_z^2\right)\frac{(1-\cos\phi)}{\phi^2} & -\frac{\phi_z}{\phi}\sin\phi+\phi_x\phi_y\frac{(1-\cos\phi)}{\phi^2} & \frac{\phi_y}{\phi}\sin\phi+\phi_x\phi_z\frac{(1-\cos\phi)}{\phi^2} & 0 \\ \frac{\phi_z}{\phi}\sin\phi+\phi_x\phi_y\frac{(1-\cos\phi)}{\phi^2} & 1-\left(\phi_x^2+\phi_z^2\right)\frac{(1-\cos\phi)}{\phi^2} & -\frac{\phi_x}{\phi}\sin\phi+\phi_y\phi_z\frac{(1-\cos\phi)}{\phi^2} & 0 \\ -\frac{\phi_y}{\phi}\sin\phi+\phi_x\phi_z\frac{(1-\cos\phi)}{\phi^2} & \frac{\phi_x}{\phi}\sin\phi+\phi_y\phi_z\frac{(1-\cos\phi)}{\phi^2} & 1-\left(\phi_x^2+\phi_y^2\right)\frac{(1-\cos\phi)}{\phi^2} & 0 \\ 0 & 0 & 0 & 1 \end{bmatrix} \begin{pmatrix} e \\ f \\ g \\ h \end{pmatrix} \tag{85E}$$

The upper left $3 \times 3$ elements in (85E) are equivalent to:

$$I + \frac{\sin\phi}{\phi}\left(\underline{\phi}\times\right) + \frac{1-\cos\phi}{\phi^2}\left(\underline{\phi}\times\right)\left(\underline{\phi}\times\right)$$

This is identically the same expression derived in Lecture 7 (Equation (50)) for the direction cosine matrix between two coordinate frame rotated relative to one another by the rotation vector $\underline{\phi}$. It can be concluded that the quaternion operation defined by Equation (85B) with (85D) is equivalent to a vector transformation operation on the three vector components of v.

A Quaternion for Strapdown Body Attitude Referencing -- The previous discussion has introduced the concept of the quaternion and its relationship to the direction cosine matrix. For the strapdown attitude referencing problem, a quaternion representing the attitude orientation between body and local level navigation axes is computed through an integration process. The quaternion elements are then converted to their equivalent direction cosine form when required for strapdown vector transformation operations, or to evaluate Euler angle outputs.

If the quaternion relating body to local level navigation axes is defined as

$$q_B^L = \begin{pmatrix} a \\ b \\ c \\ d \end{pmatrix}$$

the equivalent to the $C_B^L$ direction cosine matrix was shown through equations (85C), (85E), and (50) to be:

$$C_B^L = \begin{bmatrix} \left(d^2 + a^2 - b^2 - c^2\right) & 2\left(ab - cd\right) & 2\left(ac + bd\right) \\ 2\left(ab + cd\right) & \left(d^2 + b^2 - c^2 - a^2\right) & 2\left(bc - ad\right) \\ 2\left(ac - bd\right) & 2\left(bc + ad\right) & \left(d^2 + c^2 - a^2 - b^2\right) \end{bmatrix} \qquad (85F)$$

As for the direction cosine updating operations discussed in Lecture 6, the quaternion integration process can be divided into two steps: updates for body motion, and updates for local level motion. The body motion updates are typically handled at a high rate (e.g., 100 Hz) using a high order algorithm, while the quaternion updates for navigation frame rotation can be accurately handled at a lower rate (e.g., 10 Hz) using a simpler first order algorithm.

Attitude Reference Quaternion Updating for Body Motion -- For body motion updating, let's define $q_B^L$ at two different times, $t_m$ and $t_{m+1}$, relative to the navigation frame attitude at time $t_n$. These values for $q_B^L$ will be denoted as $q_{B(m)}^{L(n)}$ and $q_{B(m+1)}^{L(n)}$ analogous to the direction cosine nomenclature in Lecture 7. Further, let's define another quaternion $h_{B(m+1)}^{B(m)}$ relating the body attitude at the $t_m$ and $t_{m+1}$ points. If the rotation angle vector $\underline{\phi}$ represents the Euler axis and angle relating the body attitude at times $t_m$ and $t_{m+1}$ we can write as in Equation (85D):

$$h^{B(m)}_{B(m+1)} = \begin{pmatrix} \dfrac{\phi_x}{\phi} \sin \dfrac{\phi}{2} \\ \dfrac{\phi_y}{\phi} \sin \dfrac{\phi}{2} \\ \dfrac{\phi_z}{\phi} \sin \dfrac{\phi}{2} \\ \cos \dfrac{\phi}{2} \end{pmatrix}$$

or in equivalent mixed vector/scalar notation,

$$h^{B(m)}_{B(m+1)} = \left(\underline{\phi} / \phi\right) \sin \frac{\phi}{2} + \cos \frac{\phi}{2} \tag{85G}$$

where

$$\underline{\phi} = \phi_x \, i + \phi_y \, j + \phi_z \, k$$

The components of $\underline{\phi}$ for (85G) are evaluated from gyro body axis data exactly as described in Lectures 7 and 8.

The problem we now pose for the quaternion body motion updating problem is: given $h^{B(m)}_{B(m+1)}$ from Equation (85G), how does one calculate the updated attitude quaternion $q^{L(n)}_{B(m+1)}$ from the previously calculated value $q^{L(n)}_{B(m)}$? The solution is obtained by observing the effect of the quaternion operator on an arbitrary four-vector v. The four-vector v can be defined in each of the coordinate frames of interest (L(n), B(m), and B(m+1)) as $v^{L(n)}$, $v^{B(m)}$, and $v^{B(m+1)}$. The relationship between the components of v in these frames is obtained by application of the quaternion transformation rule given by Equation (85B):

$$v^{B(m)} = h^{B(m)}_{B(m+1)} \, v^{B(m+1)} \left(h^{B(m)}_{B(m+1)}\right)^*$$

$$v^{L(n)} = q^{L(n)}_{B(m)} \, v^{B(m)} \left(q^{L(n)}_{B(m)}\right)^*$$

or, in combination:

$$v^{L(n)} = q^{L(n)}_{B(m)} \, h^{B(m)}_{B(m+1)} \, v^{B(m+1)} \left(h^{B(m)}_{B(m+1)}\right)^* \left(q^{L(n)}_{B(m)}\right)^*$$

The following conjugate product rule for quaternions can be easily demonstrated by component expansion and application of the four-vector product rules:

$$\left(h_{B(m+1)}^{B(m)}\right)^* \left(q_{B(m)}^{L(n)}\right)^* = \left(q_{B(m)}^{L(n)} \, h_{B(m+1)}^{B(m)}\right)^*$$

hence,

$$v^{L(n)} = q_{B(m)}^{L(n)} \, h_{B(m+1)}^{B(m)} \, v^{B(m+1)} \left(q_{B(m)}^{L(n)} \, h_{B(m+1)}^{B(m)}\right)^*$$

but,

$$v^{L(n)} = q_{B(m+1)}^{L(n)} \, v^{B(m+1)} \left(q_{B(m+1)}^{L(n)}\right)^*$$

therefore,

$$q_{B(m+1)}^{L(n)} = q_{B(m)}^{L(n)} \, h_{B(m+1)}^{B(m)} \qquad (85H)$$

Equations (85G) and (85H) define how the attitude quaternion $q_B^L$ is updated from cycle to cycle in the system computer as a function of the body rotation angle vector $\underline{\phi}$ determined as in Lectures 7 and 8 from gyro input data.

<u>Attitude Reference Quaternion Updating for Local Level Motion</u> -- Let's now define $r_{L(n+1)}^{L(n)}$ as another rotation quaternion relating the local navigation frame attitude at times $t_n$ and $t_{n+1}$:

$$r_{L(n+1)}^{L(n)} = \left(\underline{\theta}/\theta\right) \sin\frac{\theta}{2} + \cos\frac{\theta}{2} \qquad (85I)$$

where $\underline{\theta}$ is defined as the Euler axis rotation vector in local level coordinates that rotates the L frame from its orientation at $t_n$ into its orientation at $t_{n+1}$. We also note at this point that the inverse quaternion $r_{L(n)}^{L(n+1)}$ is given by:

$$r_{L(n)}^{L(n+1)} = - \left(\underline{\theta}/\theta\right) \sin\frac{\theta}{2} + \cos\frac{\theta}{2} \qquad (85J)$$

The latter relationship becomes obvious when one recognizes that the Euler axis in frames L(n) and L(n+1) have identical components (i.e., the Euler axis is the axis about which L(n) revolves into L(n+1); hence, the Euler axis is stationary in the L frame as L rotates from its $t_n$ orientation L(n) into its $t_{n+1}$ orientation L(n+1)). The angle value for the rotation from $t_{n+1}$ to $t_n$, of course, is the negative of the angle value for a rotation from $t_n$ to $t_{n+1}$. Thus, the justification for (85J) compared to (85I).

We now apply the test vector v (as for body motion updating ) to q and r to determine the relationship between $q_{B(n)}^{L(n)}$ and $q_{B(n)}^{L(n+1)}$ in terms of $r_{L(n)}^{L(n+1)}$ .

$$v^{L(n+1)} = r_{L(n)}^{L(n+1)} \; q_{B(n)}^{L(n)} \; v^{B(n)} \left( r_{L(n)}^{L(n+1)} \; q_{B(n)}^{L(n)} \right)^*$$

but,

$$v^{L(n+1)} = q_{B(n)}^{L(n+1)} \; v^{B(n)} \left( q_{B(n)}^{L(n+1)} \right)^*$$

therefore,

$$q_{B(n)}^{L(n+1)} = r_{L(n)}^{L(n+1)} \; q_{B(n)}^{L(n)} \qquad (85K)$$

Equation (85K) with (85J) shows how the quaternion $q_B^L$ is updated for local level frame motion. The $\underline{\theta}$ vector in (85J) can be approximated to first order (as in Lecture 7) as the time interval $T_n$ between $t_n$ and $t_{n+1}$ times the average value of the local level navigation frame angular rate over the $t_n$ to $t_{n+1}$ interval:

$$\underline{\theta} = \left( \underline{\omega}_{IL}^{L}(n) + \underline{\omega}_{IL}^{L}(n+1) \right) \frac{T_n}{2} \qquad (85L)$$

<u>Differential Equation for the Body Attitude Reference Quaternion</u> - A differential equation for the body attitude quaternion can also be derived from Equations (85G), (85H), (85J), and (85K) by analyzing the case where $q_B^L$ is updated by a body rotation and navigation frame rotation over a given time interval. From (85H), the change $\Delta_B$ in $q_B^L$ due to the body rotation h is:

$$\Delta_B \left( q_B^L \right) = q_{B(m)}^{L(n)} \, h_{B(m+1)}^{B(m)} - q_{B(m)}^{L(n)} = q_{B(m)}^{L(n)} \left( h_{B(m+1)}^{B(m)} - 1 \right)$$

From Equation (85K), the change $\Delta_L$ in $q_B^L$ due to navigation frame rotation is:

$$\Delta_L \left( q_B^L \right) = r_{L(n)}^{L(n+1)} \; q_{B(n)}^{L(n)} - q_{B(n)}^{L(n)} = \left( r_{L(n)}^{L(n+1)} - 1 \right) q_{B(n)}^{L(n)}$$

For the same time intervals (i.e., equivalencies between m and n), the total change $\Delta$ in $q_B^L$ is the sum of the latter two expressions:

$$\Delta q_B^L = q_{B(n)}^{L(n)} \left( h_{B(n+1)}^{B(n)} - 1 \right) + \left( r_{L(n)}^{L(n+1)} - 1 \right) q_{B(n)}^{L(n)} \qquad (85M)$$

We now return to equations (85G) and (85J) for h and r to evaluate the previous (h-1) and (r-1) terms over a small time interval ($t_n$ to $t_{n+1}$) such that $\underline{\phi}$ and $\underline{\theta}$ are small:

$$h_{B(n+1)}^{B(n)} - 1 = \left(\underline{\phi}/\phi\right) \sin\frac{\phi}{2} + \cos\frac{\phi}{2} - 1 \approx \left(\underline{\phi}/\phi\right)\frac{\phi}{2} + 1 - 1 = \frac{1}{2}\,\underline{\phi}$$

$$r_{L(n)}^{L(n+1)} - 1 \approx -\frac{1}{2}\,\underline{\theta}$$

Using the shorthand $q_B^L$ for $q_{B(n)}^{L(n)}$, (85M) then becomes:

$$\Delta\, q_B^L = \frac{1}{2}\, q_B^L\, \underline{\phi} - \frac{1}{2}\, \underline{\theta}\, q_B^L$$

We now divide the latter expression by the time interval for the $q_B^L$ change ($\Delta t$) and let $\Delta t$ go to zero in the limit to obtain an expression for $\dot{q}_B^L$.

$$\dot{q}_B^L = \frac{1}{2}\, q_B^L \left(\lim_{\Delta t \to 0} \frac{1}{\Delta t}\, \underline{\phi}\right) - \frac{1}{2}\left(\lim_{\Delta t \to 0} \frac{1}{\Delta t}\, \underline{\theta}\right) q_B^L$$

From Lectures 5 through 8 it should be clear that:

$$\left(\lim_{\Delta t \to 0} \frac{1}{\Delta t}\, \underline{\phi}\right) = \underline{\omega}_{IB}^{B} \qquad\qquad \left(\lim_{\Delta t \to 0} \frac{1}{\Delta t}\, \underline{\theta}\right) = \underline{\omega}_{IL}^{L}$$

Therefore,

$$\dot{q}_B^L = \frac{1}{2}\, q_B^L\, \underline{\omega}_{IB}^{B} - \frac{1}{2}\, \underline{\omega}_{IL}^{L}\, q_B^L \qquad (85N)$$

Equation (85N) is the differential equation describing the rate of change of the body attitude quaternion in terms of strapdown gyro sensed rates $\left(\underline{\omega}_{IB}^{B}\right)$ and calculated local level navigation frame rotation rates $\left(\underline{\omega}_{IL}^{L}\right)$. Equation (85N) directly parallels the equivalent relationship for the $C_B^L$ direction cosine matrix rate given by Equation (33). Note that Equation (85N) is a four-vector equation that must abide by the rules of four-vector multiplication if it is to be expanded in terms of its components. As an exercise, it is interesting to look at the component form of (85m). If we define:

$$\underline{\omega}_{IB}^{B} = \begin{pmatrix} \omega_x \\ \omega_y \\ \omega_z \\ 0 \end{pmatrix} \qquad \underline{\omega}_{IL}^{L} = \begin{pmatrix} \omega_1 \\ \omega_2 \\ \omega_3 \\ 0 \end{pmatrix}$$

with, as before:

$$q_B^L = \begin{pmatrix} a \\ b \\ c \\ d \end{pmatrix}$$

Equation (85N) becomes:

$$\begin{pmatrix} \dot{a} \\ \dot{b} \\ \dot{c} \\ \dot{d} \end{pmatrix} = \frac{1}{2}\begin{bmatrix} d & -c & b & a \\ c & d & -a & b \\ -b & a & d & c \\ -a & -b & -c & d \end{bmatrix}\begin{pmatrix} \omega_x \\ \omega_y \\ \omega_z \\ 0 \end{pmatrix} - \frac{1}{2}\begin{bmatrix} 0 & -\omega_3 & \omega_2 & \omega_1 \\ \omega_3 & 0 & -\omega_1 & \omega_2 \\ -\omega_2 & \omega_1 & 0 & \omega_3 \\ -\omega_1 & -\omega_2 & -\omega_3 & 0 \end{bmatrix}\begin{pmatrix} a \\ b \\ c \\ d \end{pmatrix}$$

or

$$\begin{pmatrix} \dot{a} \\ \dot{b} \\ \dot{c} \\ \dot{d} \end{pmatrix} = \frac{1}{2}\begin{bmatrix} d & -c & b \\ c & d & -a \\ -b & a & d \\ -a & -b & -c \end{bmatrix}\begin{pmatrix} \omega_x \\ \omega_y \\ \omega_z \end{pmatrix} - \frac{1}{2}\begin{bmatrix} d & c & -b \\ -c & d & a \\ b & -a & d \\ -a & -b & -c \end{bmatrix}\begin{pmatrix} \omega_1 \\ \omega_2 \\ \omega_3 \end{pmatrix}$$

or equivalently:

$$\begin{pmatrix} \dot{a} \\ \dot{b} \\ \dot{c} \\ \dot{d} \end{pmatrix} = \frac{1}{2}\begin{bmatrix} 0 & (\omega_z + \omega_3) & -(\omega_y + \omega_2) & (\omega_x - \omega_1) \\ -(\omega_z + \omega_3) & 0 & (\omega_x + \omega_1) & (\omega_y - \omega_2) \\ (\omega_y + \omega_2) & -(\omega_x + \omega_1) & 0 & (\omega_z - \omega_3) \\ -(\omega_x - \omega_1) & -(\omega_y - \omega_2) & -(\omega_z - \omega_3) & 0 \end{bmatrix}\begin{pmatrix} a \\ b \\ c \\ d \end{pmatrix}$$

<u>Comparisons Between Quaternion Parameters and Direction Cosines for Strapdown Body Attitude Referencing</u> -- The tradeoff between direction cosines versus quaternion parameters as the primary attitude reference data in strapdown inertial systems has been a

popular area of debate between strapdown analysts in the past. In its original form, the tradeoff centered on the relative accuracy between the two methods in accounting for body angular motion. These tradeoffs invariable evolved from the differential equation form of the direction cosine and quaternion updating Equations (33) and (85N) investigating the accuracy of equivalent algorithms for integrating these equations in a digital computer under hypothesized body angular motion. Invariably, the body motion investigated was coning motion at various frequencies relative to the computer update frequency. For these early studies, the tradeoffs generally demonstrated that for comparable integration algorithms, the quaternion approach generated solutions that more accurately replicated the true coning motion for situations where the coning frequency was within a decade of the computer update frequency.

As presented in these lecture notes, both the quaternion and direction cosine updating algorithms have been based on processing of a body angle motion vector $\underline{\phi}$ which already accounts for coning motion (as discussed in Lectures 7 and 8). These updating algorithms (Equations (85H) with (85G) for the quaternion and (51A) with (51) for direction cosines) represent exact solutions for the attitude updating process for a given input angle vector $\underline{\phi}$. Consequently, the question of accuracy for different body motion can no longer be considered a viable tradeoff area. The principle tradeoffs that remain between the two approaches are the computer memory and throughput requirements associated with each in a strapdown navigation system.

In order to assess the relative computer memory and throughput requirements for quaternion parameters versus direction cosines, the composite of all computer requirements for each must be assessed. In general, these can be grouped into four major computational areas:

1. Basic updating algorithm

2. Normalization and orthogonalization algorithms

3. Algorithms for conversion to the direction cosine matrix form needed for acceleration transformation and Euler angle extraction

4. Initialization algorithms

• Basic Updating Algorithms - The basic updating algorithm for the quaternion parameter is somewhat simpler than for direction cosines as expansion of equations (85H) and (85G) compared with (51A) and (51) would reveal. This results in both a throughput and memory advantage for the quaternion approach. Part of this advantage arises because only four quaternion elements have to be updated compared to nine for direction cosines. The advantage is somewhat diminished if it is recognized that only two rows of direction cosines (i.e., 6 elements) need actually be updated since the third row can then be easily derived from the other two by a cross-product operation.

• Normalization And Orthogonalization Algorithms - The normalization and orthogonalization operations associated with direction cosines are given by Equation (82). For the quaternion parameters, a normalization operation can also be defined that maintains the sum of the squares of the quaternion elements at unity (i.e., from Equation (85D), the ideal quaternion has this property). It can be demonstrated following a procedure similar to that leading to the normalization portion (Equation (81)) of the direction cosine orthonormalization operations, that the quaternion normalization equation is given by:

$$\Delta q \;=\; -\frac{1}{2}\left(a^2 + b^2 + c^2 + d^2 - 1\right) q \;=\; -\frac{1}{2}\left(q\, q^* - 1\right) q \qquad \text{(85P)}$$

where

$a, b, c, d$ = The four quaternion elements

$\Delta q$ = The correction to q which when added to q, normalizes q (i.e., sets the sum of the squares of the elements to unity).

Equation (85P) for the quaternion is generally simpler to implement than Equation (82) for direction cosines. If only two rows of the direction cosines matrix are updated (as described in the previous section) Equation (82) reduces to three algebraic operations: the dot product of each row with itself for normalization, and the dot product between the two rows for orthogonalization. The resulting computations are half that dictated by (82), but are still more than required by (85P) for the quaternion. Since the orthonormalization operations would in general be iterated at low rate (as discussed in Lecture 7), no throughput advantage results for the quaternion. Some memory savings may be realized, however.

A key factor that must be addressed relative to orthonormalization tradeoffs is whether or not orthonormalization is actually needed at all. Clearly, if the direction cosine or quaternion updating algorithms were implemented perfectly, orthonormalization would not be required. It is the author's contention that, in fact, the accuracy requirements for strapdown systems dictate that strapdown attitude updating software cannot tolerate any errors whatsoever (compared to sensor error effects). Therefore, if the attitude updating software is designed for negligible drift and scale factor error (compared to sensor errors) it will also implicitly exhibit negligible orthogonalization and/or normalization errors.

• Algorithms For Conversion To The Direction Cosine Matrix - If the basic calculated attitude data is direction cosines directly, no conversion process is required. For cases where only two rows of direction cosines are updated, the third row must be generated by the cross-product between the two rows calculated. For example:

$$\begin{aligned} C_{31} &= C_{12}\, C_{23} - C_{13}\, C_{22} \\ C_{32} &= C_{13}\, C_{21} - C_{11}\, C_{23} \\ C_{33} &= C_{11}\, C_{22} - C_{12}\, C_{21} \end{aligned} \qquad \text{(85Q)}$$

For quaternion parameters, Equations (85F) must be implemented to develop the direction cosine matrix, a significantly more complex operation compared with (85P) for the two-row direction cosine approach. Since direction cosine elements are generally required at high rate (for acceleration transformation and Euler angle output extraction) both a throughput and memory penalty is accrued for the quaternion approach.

• Initialization Algorithms - Initialization equations for direction cosines will be discussed in Lecture 11. In general, the method to be described is based on a measurement or a normalized acceleration vector, and equating this to the third row of the directional cosine matrix. The other two rows are then initialized to be orthogonal to the third at an attitude about the third that simplifies system testing. If the same technique were applied when using quaternion parameters, the direction cosine elements would first be calculated similarly, followed by an inverse of Equations (85F) (i.e., a direction cosine to quaternion conversion). With this approach, the quaternion initialization process would be more complex since it would include the same direction cosine initialization steps (or a good portion thereof) plus the conversion to the quaternion format.

Alternatively, a dynamic erection algorithm can be established that "closes-the-loop" on the quaternion/conversion-to-cosines/acceleration-transformation equations by implementing the $\underline{\omega}_{IL}^{L}$ vector term in equations (85N). The $\underline{\omega}_{IL}^{L}$ vector would be controlled to rotate q so that the resulting horizontal components of the transformed acceleration vector are nulled. When horizontal null is achieved, the quaternion attitude is leveled, hence, initialized. (It should be noted that a similar technique can also be used with direction cosines rather than the direct approach described in Lecture 11). The disadvantage with the servo dynamic approach to initial erection is that it is somewhat slower than the direct approach described in Lecture 11, and does not allow positive control of the azimuth orientation of the resulting wander azimuth coordinate frame. Some inefficiencies are thereby produced in the process of converting vector data from the resulting wander azimuth coordinates to a more tractible frame for test data interpretation.

It can be concluded that the initialization algorithms for quaternion parameters are at best equal to direction cosines (for the less preferred dynamic erection approach) and at worst, more complex than direction cosines for the direct initial erection approach. The net result is a memory penalty for the quaternion approach (throughput is not a handicap during initialization operations).

• Tradeoff Conclusions - From the above qualitative discussion, it is difficult to draw hard conclusions regarding a preference for direction cosines versus quaternion parameters for attitude referencing in strapdown inertial systems. Pros and cons exist for each in the different tradeoff areas. Quantitative comparisons based on actual software sizing and computer loading studies have led to similar inconclusive results. Fortunately, today's computer technology is such that the slight advantage that one attitude parameter approach may have over the other in any particular application is insignificant compared with the composite total strapdown inertial system throughput and memory software requirement. Hence ultimate selection of the attitude approach can be safely made based on "analyst's choice". On this basis, it is the author's opinion that the use of quaternion parameters introduces an additional and unnecessary conceptual detail into the strapdown computational process and that therefore, direction cosines, the attitude form ultimately required for other computational operations, is the preferred attitude updating approach.

## STRAPDOWN ATTITUDE REFERENCE EQUATION SUMMARY

The overall summary of the strapdown attitude update and accelerometer transformation calculations based on direction cosine body attitude referencing is illustrated by the block diagram on the following page. This portion of the software interfaces with the navigation equation block diagram of Lecture 4. Its net effect is identical to the interface that a gimbaled platform would have with the navigation equations. Hence, the term “electronic gimbal” has been used to define this computational element. The diagram includes representative iteration rates for the computational elements that might be utilized in modern day strapdown inertial navigation systems. This diagram summarizes the material presented in Lectures 5 to 9. For the next lecture we’ll discuss the effect of uncompensated sensor errors and how they propagate into navigational errors in the system computer.

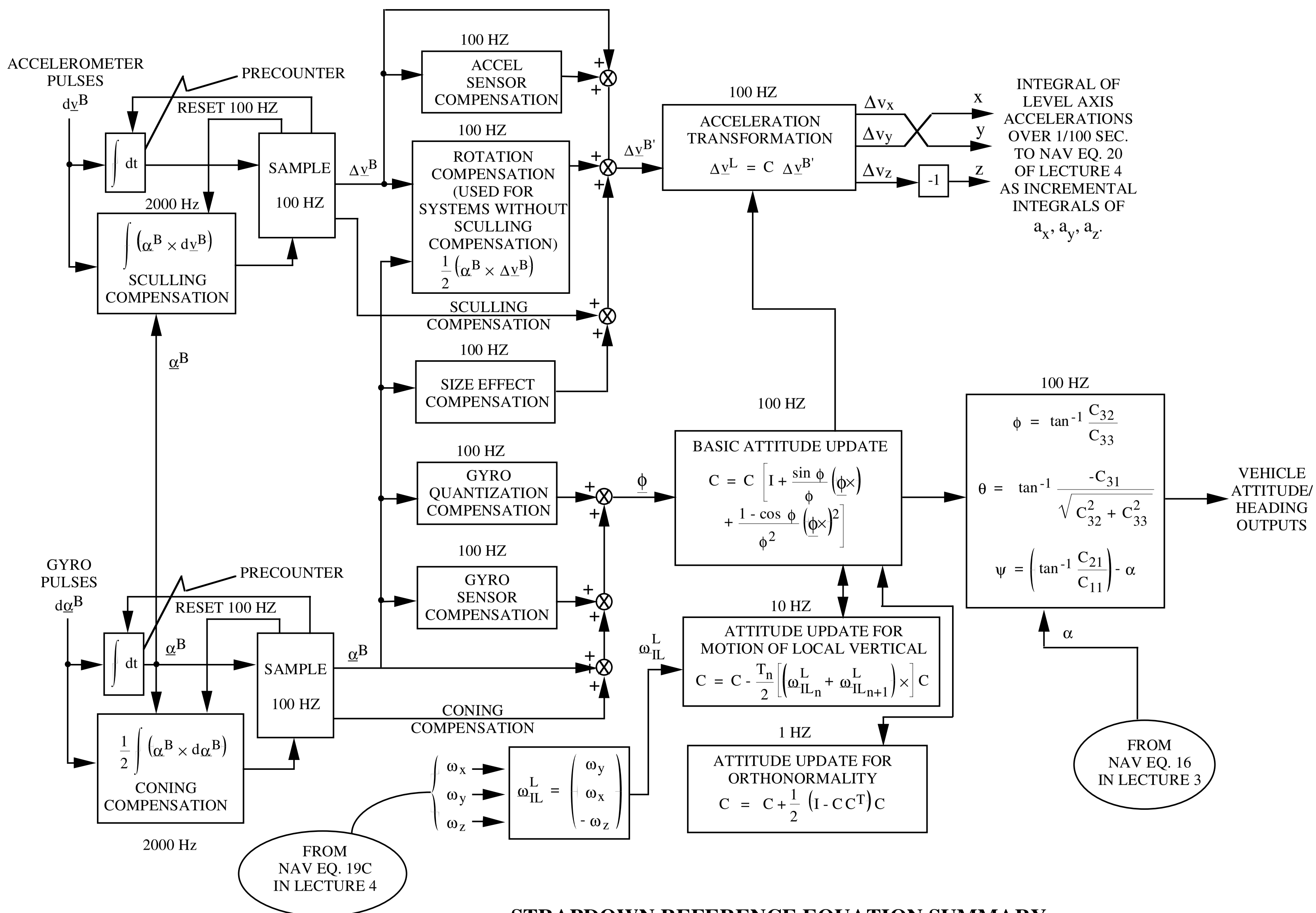


**STRAPDOWN REFERENCE EQUATION SUMMARY**

## NOTES

# STRAPDOWN INS ERROR CHARACTERISTICS

LECTURE 10

## NAV SEMINAR - LECTURE 10 NOTES

The previous nine lectures discussed the theory of strapdown inertial navigation assuming that perfect measurements of rate and acceleration were attainable with the strapdown gyro and accelerometer sensors. In reality, the sensors are not perfect and their actual outputs are in error from the true rate and acceleration inputs. Since the strapdown computer has no way of distinguishing perfect from imperfect measurements, it processes the imperfect measurements, assuming that no errors exist (i.e., using the equations developed in Lectures 1 - 9). As a result, the computer outputs deviate from the true navigation solution. This lecture discusses the characteristics of the navigation errors generated in the computer due to sensor input errors. Before proceeding, the definition of sensor error must be clearly defined. By sensor error, we mean the unknown error in the sensor output that is not corrected by the compensation terms discussed in Lecture 9. These can be caused by sensor compensation errors (due to imperfect calibration measurements), sensor error instabilities (unaccountable variations in the sensor errors from turn-on to turn-on over long term, for example), or imperfect forms of the compensation equations (errors in our basic understanding or modelability of the sensor errors being compensated).

We begin by defining an analytical model for the computational process being performed on the sensor signals (a composite of the basic strapdown navigation equations developed in the previous lectures). Since we are considering the strapdown computation equations as "transfer functions" for the sensor errors (into navigational error) we need only include the dominant terms in the equations for error analysis purposes (e.g., small effects such as earth's oblateness can be neglected). To simplify the discussion, only horizontal short term navigation errors will be considered, hence, inclusion of the vertical baro control loop is omitted. The figure on the following page provides the analytical model. It represents a summary of Equations (8), (13), and (33) developed previously with the following changes in nomenclature:

$C_J^K$ = The direction cosine matrix from J to K frame coordinates (i.e., transforms a vector from the J-frame to the K-frame). In our case the direction cosine matrices used are: $C_B^L$ from the B (body) frame to the L (local level) frame and $C_L^E$ from the L-frame to the E (earth) frame (previously identified as D in Lecture Notes 2).

$\underline{\omega}_{JK}^{L}$ = The angular rate of frame K relative to frame J as seen in the L-frame. Since $\underline{\omega}_{JK}$ is a vector quantity, it can be evaluated in any coordinate set (say the L-frame) to obtain numerical values for its components in this coordinate frame. For our case, the vectors we are dealing with are $\underline{\omega}_{IB}^{B}$, $\underline{\omega}_{IE}^{E}$, $\underline{\omega}_{IE}^{L}$, $\underline{\omega}_{EL}^{L}$ (i.e., the body rate relative to inertial space as measured in body axes sensed by gyros, the earth rate relative to inertial space as measured in the earth and local level frames, and the rotation rate of the

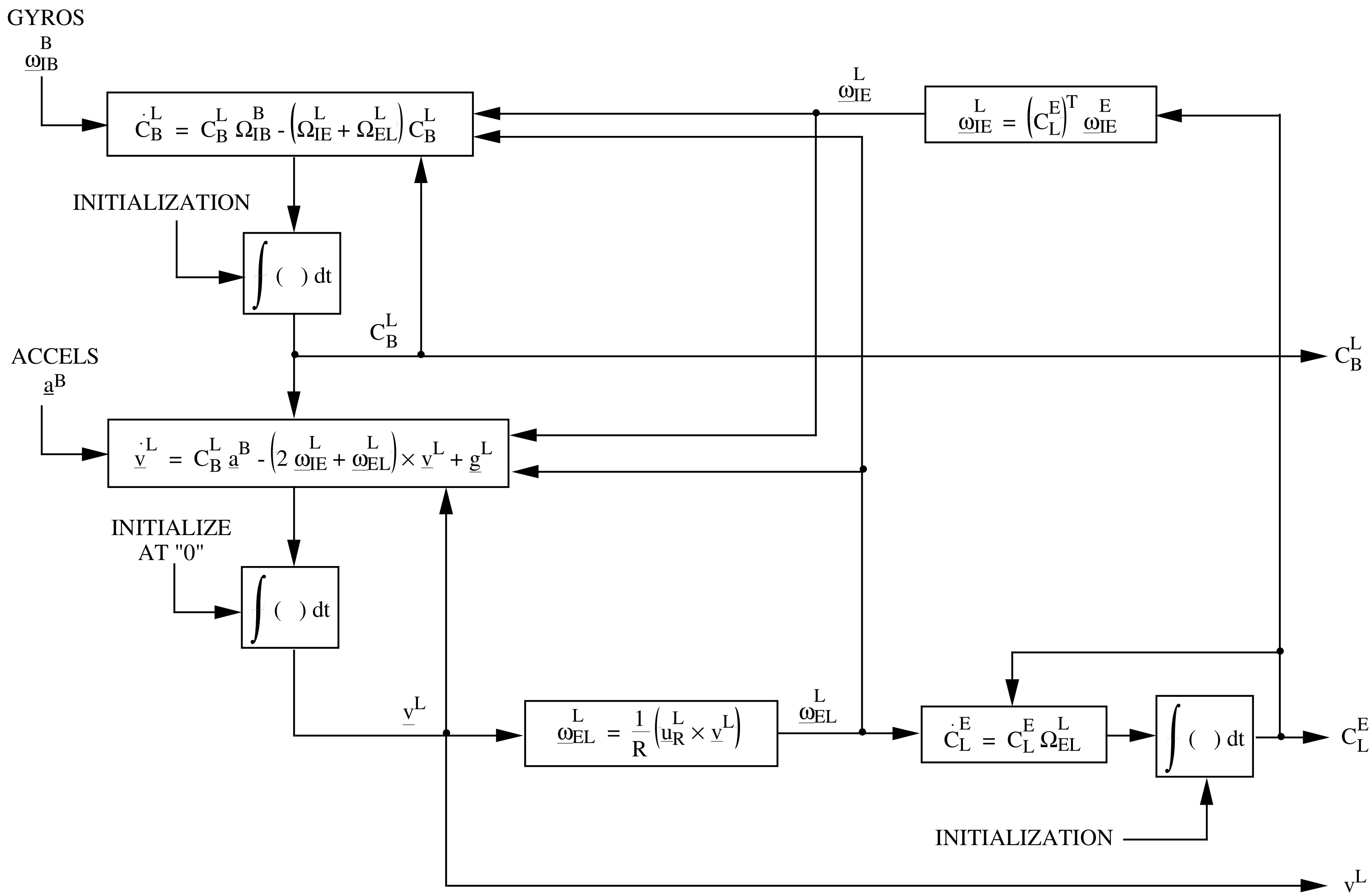


**FIGURE 1 - STRAPDOWN NAVIGATOR COMPUTATION FLOW**

local level frame relative to the earth frame as measured in the local level frame.) The second and fourth quantities were previously identified (in Lecture 2) as $\underline{\rho}$ and $\underline{\Omega}$.

$\underline{a}^B$ = Specific force acceleration vector (sensed by accelerometers) as measured in body axes (i.e., strapdown accels).

$\underline{v}^L$ = Vehicle velocity relative to the earth as measured in local level axes ($\underline{v}$ in Lecture 1).

$\underline{g}^L$ = Apparent gravity in local level coordinates ($\underline{g}'$ in Lecture 1).

$\Omega^L_{JK}$ = Skew symmetric form of $\underline{\omega}^L_{JK}$.

R = Earth's radius.

$\underline{u}^L_R$ = Unit vector upward along the local vertical as measured in local level axes (i.e., having x, y components of zero and z component of one).

The equation for $\underline{\omega}^L_{EL}$ in the figure is the simplified form of Equations (19) (e neglected) with $\rho_z = 0$ (i.e., azimuth wander implementation). The equation for $\underline{\omega}^L_{IE}$ in the figure is the basic vector transformation relation used in the equations leading to Equation (20). The $\underline{\omega}^E_{IE}$ vector is a known quantity (i.e., earth's rate equals $\omega_e$ along y and zero along x and z in the earth frame - Lecture Notes 3).

In order to ascertain the effects of errors in $\underline{\omega}^B_{IB}$ and $\underline{a}^B$ on the computational elements in the previous figure, we must define actual gyro and accelerometer measurements of these quantities (that include sensor errors) as:

$$\overset{*}{\underline{\omega}}{}^B_{IB} \quad \text{and} \quad \overset{*}{\underline{a}}{}^B$$

with associated sensor errors as:

$$\underset{\text{Gyro Error}}{\delta\underline{\omega}^B_{IB}} \overset{\Delta}{=} \underset{\text{Gyro Output}}{\overset{*}{\underline{\omega}}{}^B_{IB}} - \underset{\text{Gyro Input}}{\underline{\omega}^B_{IB}}$$

$$\underset{\text{Accel Error}}{\delta\underline{a}^B} \overset{\Delta}{=} \underset{\text{Accel Output}}{\overset{*}{\underline{a}}{}^B} - \underset{\text{Accel Input}}{\underline{a}^B}$$

The computed navigation parameters in the actual system (with $\overset{*}{\underline{\omega}}{}_{IB}^{B}$ and $\overset{*}{\underline{a}}{}^{B}$ inputs) are identical in form with those in the figure and will be denoted similarly, but superscripted with an (*), i.e.:

$$\overset{*}{C}{}_B^L,\ \overset{*}{\underline{v}}{}^L,\ \overset{*}{C}{}_L^E,\ \text{etc.}$$

The associated errors in these quantities are defined as the differences between them and the correct values calculated with perfect (error free) sensor inputs (i.e., with $\underline{\omega}_{IB}^{B}$ and $\underline{a}^{B}$ as in the figure):

$$\delta C_B^L \;=\; \overset{*}{C}{}_B^L - C_B^L \qquad \delta\underline{v}^L \;=\; \overset{*}{\underline{v}}{}^L - \underline{v}^L \qquad \text{etc.}$$

A set of equations relating the sensor errors ($\delta\underline{\omega}^B$ and $\delta\underline{a}^B$) to the navigation parameter errors ($\delta C_B^L$, etc.) can be obtained by subtracting the equations in the diagram (the perfect error free set) from the equivalent form of the same equations, (with the * parameters containing errors and erroneous sensor inputs $\overset{*}{\underline{\omega}}{}_{IB}^{B}$, $\overset{*}{\underline{a}}{}^{B}$), and introducing the definitions given previously for the resulting differences (errors). The result can be put in block diagram form as illustrated by Figure 2 representing the error model for the system. If the error diagram is compared with the original total computation flow diagram it should be apparent that the two equation sets are similar in form since the latter represents the differential of the former. It should also be apparent that two new variables have been introduced ($\underline{\phi}^L$, $\underline{e}^L$) which represent the errors in the $\overset{*}{C}{}_B^L$ and $\overset{*}{C}{}_L^E$ matrices. These new variables represent small angular error vector quantities. Their relationship with the errors in the cosine matrices can be understood through the following example.

Consider an arbitrary vector $\underline{V}$ expressed in body axes ($\underline{V}^B$). Its form in local level axes ($\underline{V}^L$) is:

$$\underline{V}^L \;=\; C_B^L\,\underline{V}^B \tag{86}$$

The computed form of the same relation in the navigation computer would be:

$$\overset{*}{\underline{V}}{}^L \;=\; \overset{*}{C}{}_B^L\,\overset{*}{\underline{V}}{}^B \tag{87}$$

Defining computed errors (as before) as:

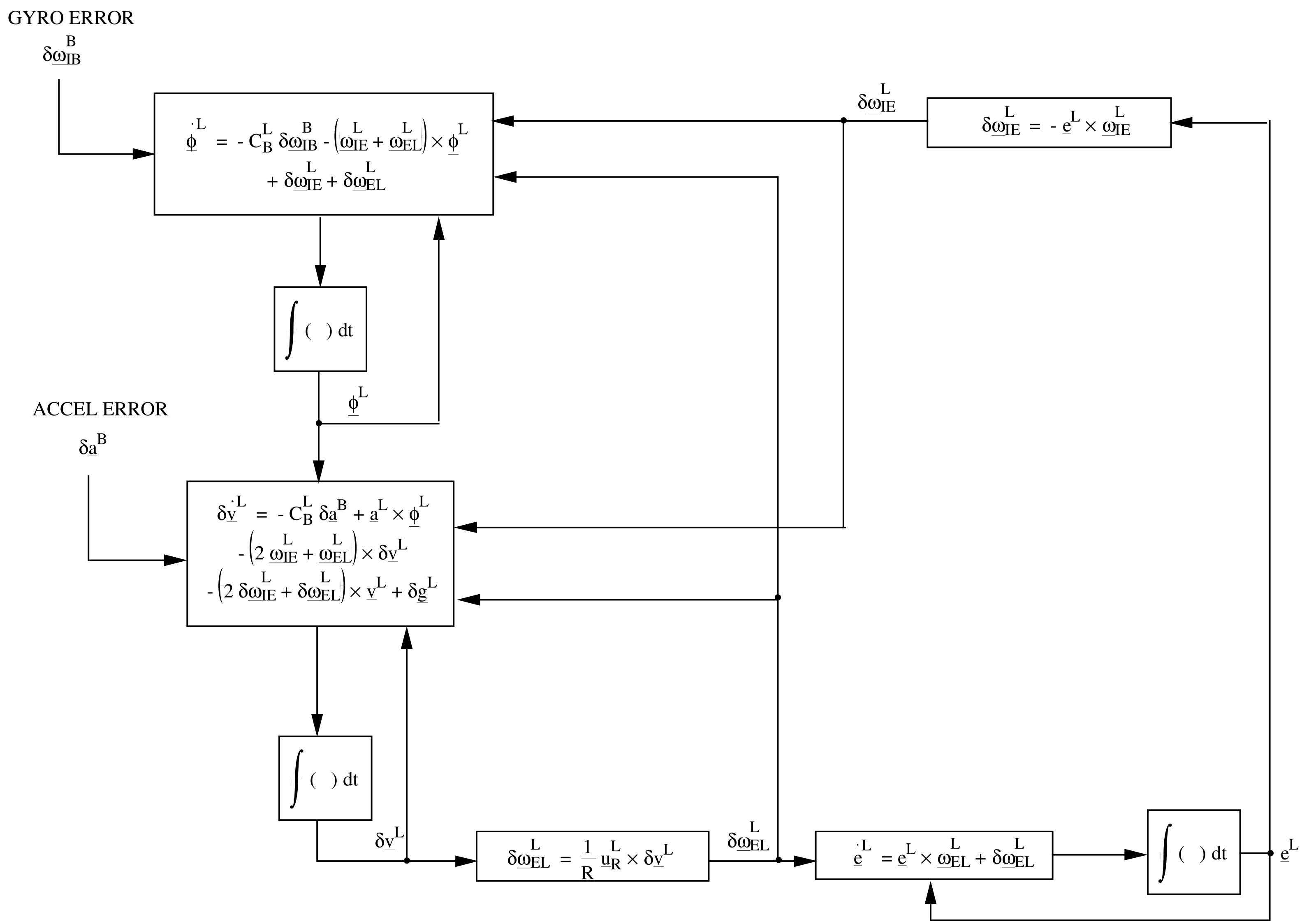


FIGURE 2 - STRAPDOWN NAVIGATOR ERROR DIAGRAM

$$\delta \underline{V}^L = \overset{*}{\underline{V}}{}^L - \underline{V}^L$$

$$\delta \underline{V}^B = \overset{*}{\underline{V}}{}^B - \underline{V}^B$$

$$\delta C_B^L = \overset{*}{C}{}_B^L - C_B^L$$

Then

$$\begin{aligned} \overset{*}{\underline{V}}{}^L &= \underline{V}^L + \delta \underline{V}^L \\ \overset{*}{\underline{V}}{}^B &= \underline{V}^B + \delta \underline{V}^B \\ \overset{*}{C}{}_B^L &= C_B^L + \delta C_B^L \end{aligned} \tag{88}$$

Substituting (88) in (87) and introducing (86) obtains the expression for $\delta \underline{V}^L$ in terms of $\delta \underline{V}^B$ and $\delta C_B^L$ (i.e., the error equation):

$$\begin{aligned} \underline{V}^L + \delta \underline{V}^L &= \left(C_B^L + \delta C_B^L\right)\left(\underline{V}^B + \delta \underline{V}^B\right) \\ &= C_B^L \, \underline{V}^B + \delta C_B^L \, \underline{V}^B + C_B^L \, \delta \underline{V}^B \\ &\qquad + \delta C_B^L \, \delta \underline{V}^B \text{ (second order and negligible)} \\ &= \underline{V}^L + \delta C_B^L \, \underline{V}^B + C_B^L \, \delta \underline{V}^B \end{aligned}$$

or

$$\delta \underline{V}^L = \delta C_B^L \, \underline{V}^B + C_B^L \, \delta \underline{V}^B \tag{89}$$

To obtain an equivalent expression for $\delta C_B^L$, we define $\overset{*}{C}{}_B^L$ as the combination of $C_B^L$ followed by an additional error rotation matrix:

$$\overset{*}{C}{}_B^L \overset{\Delta}{=} C_L^{\overset{*}{L}} \, C_B^L \tag{90}$$

where:

$C_L^{\overset{*}{L}}$ = Small rotation direction cosine matrix relating the nominal level frame (L) and the computed level frame ($\overset{*}{L}$) orientation. For this case, B is assumed fixed and L (or $\overset{*}{L}$) is referenced to it. It is equally valid to consider L fixed and B (or $\overset{*}{B}$) defined relative to it. The choice depends on which coordinate frame the error is more conveniently defined for error analysis purposes.

Expanding (90):

$$\overset{*}{C}{}_B^L = (I - I + C_L^{\overset{*}{L}}) C_B^L = C_B^L - (I - C_L^{\overset{*}{L}}) C_B^L$$

With (88),

$$\delta C_B^L = - (I - C_L^{\overset{*}{L}}) C_B^L \tag{91}$$

In Lecture Notes 5, we observed that a small rotation direction cosine matrix could be expressed as:

$$C_L^{\overset{*}{L}} = \begin{bmatrix} 1 & \phi_z & -\phi_y \\ -\phi_z & 1 & \phi_x \\ \phi_y & -\phi_x & 1 \end{bmatrix}^L$$

where

$\phi_x, \phi_y, \phi_z$ = Small angular rotations about the L-frame x, y, z axes between the $\overset{*}{L}$ and L frames (the rotation of $\overset{*}{L}$ relative to L). Note that the signs are inverted in the $C_L^{\overset{*}{L}}$ expression above (compared to $C_{B(n+1)}^{B(n)}$ in Lecture 5) because the angles now are from L to $\overset{*}{L}$ (compared with the inverse of B(n) to B(n+1) in Lecture 5).

Alternatively, the above is:

$$C_L^{L*} = \begin{bmatrix} 1 & 0 & 0 \\ 0 & 1 & 0 \\ 0 & 0 & 1 \end{bmatrix} - \begin{bmatrix} 0 & -\phi_z & \phi_y \\ \phi_z & 0 & -\phi_x \\ -\phi_y & \phi_x & 0 \end{bmatrix}^L = I - \left(\underline{\phi}^L \times\right) \tag{92}$$

where

$\left(\underline{\phi}^L \times\right)$ = Skew symmetric cross product operator form of the vector $\underline{\phi}^L$ where:

$$\underline{\phi}^L = \begin{pmatrix} \phi_x \\ \phi_y \\ \phi_z \end{pmatrix}^L$$

The cross-product convention is used because, as is easily verified by the above definition of $\left(\underline{\phi}^L \times\right)$, its product with an arbitrary vector $\underline{V}^L$ is equivalent to the cross-product of the vector with $\underline{\phi}^L$:

$$\left(\underline{\phi}^L \times\right) \underline{V}^L \overset{\Delta}{=} \underline{\phi}^L \times \underline{V}^L \tag{93}$$

Substituting (92) in (91):

$$\delta C_B^L = -\left[ I - I + \left(\underline{\phi}^L \times\right) \right] C_B^L = -\left(\underline{\phi}^L \times\right) C_B^L \tag{94}$$

Now substitute (94) in (89):

$$\delta \underline{V}^L = -\left(\underline{\phi}^L \times\right) C_B^L \underline{V}^B + C_B^L \delta \underline{V}^B$$

Which, with (86) and (93) is:

$$\delta \underline{V}^L = -\left(\underline{\phi}^L \times\right) \underline{V}^L + C_B^L \delta \underline{V}^B \qquad \text{or}$$

$$\boxed{\delta \underline{V}^L = -\underline{\phi}^L \times \underline{V}^L + C_B^L \delta \underline{V}^B} \tag{95}$$

Equation (95) is the error form of (86) that is equivalent to (89). The difference is that the angular error vector $\underline{\phi}^L$ is used to represent the rotation error in $C_B^L$. From (95) it should be apparent that this is equivalent to a rotation of the vector $\underline{V}^L$ by the angle $\underline{\phi}^L$ (i.e., this is the effect of the cross-product operation) which is also the effect of rotating $\underline{V}^B$ through a $C_B^L$ that is in error.

The latter technique is utilized in deriving the error block diagram (shown previously) from the basic navigation equations. The $\underline{\phi}^L$ vector in the diagram represents the angular error in the $C_B^L$ matrix, the $\underline{e}^L$ vector represents the angular error vector in the $C_E^L$ matrix. The $\underline{\delta g}^L$ term is the error in $\underline{g}^L$ (due to local gravity anomalies and errors in the gravity model used in the system, typically on the order of 20 μg's). A complete derivation of the error equations is contained in Appendix B at the end of these Lecture Notes.

We can now analyze the error block diagram to determine the system error response ($\delta\underline{v}^L$, $\underline{\phi}^L$, $\underline{e}^L$) to system input errors ($\delta\underline{\omega}_{IB}^B$, $\delta\underline{a}^B$, $\delta\underline{g}^L$). In terms of navigation parameters:

$\delta\underline{v}^L$ = Error in the system computed velocity.

$\underline{\phi}^L$ = Error in the system computed attitude.

$\underline{e}^L$ = Error in the system computed position in terms of angular deviation (arc minutes or nautical miles for the horizontal components). The vertical component of $\underline{e}^L$ is related to the wander angle error and is not normally of interest for error analysis purposes.

To investigate the principal short term (1-2 hour) characteristics of the system, most of the terms in the error block diagram can be neglected to obtain the simplified form in the following figure.

The associated error differential equations are:

$$\dot{\underline{\phi}}^L = -C_B^L\,\delta\underline{\omega}_{IB}^B - \left(\underline{\omega}_{IE}^L + \underline{\omega}_{EL}^L\right)\times\underline{\phi}^L + \delta\underline{\omega}_{EL}^L$$

$$\delta\dot{\underline{v}}^L = C_B^L\,\delta\underline{a}^B + \underline{a}^L\times\underline{\phi}^L$$

$$\delta\underline{\omega}_{EL}^L = \frac{1}{R}\left(\underline{u}_R^L\times\delta\underline{v}^L\right) \qquad (96)$$

$$\underline{\omega}_{EL}^L = \frac{1}{R}\left(\underline{u}_R^L\times\underline{v}^L\right)$$

$$\dot{\underline{e}}^L = \delta\underline{\omega}_{EL}^L$$

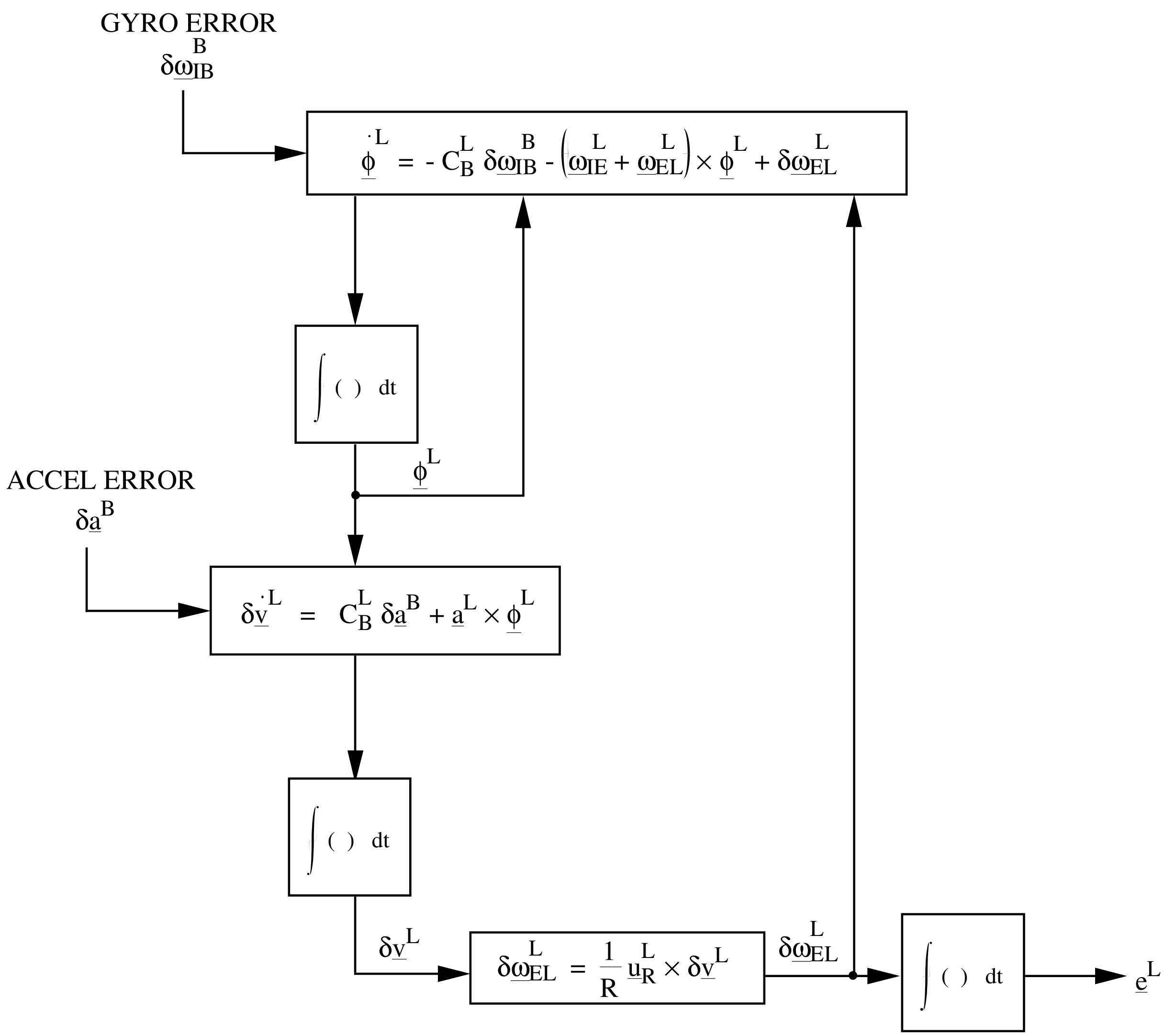


**FIGURE 3 - SIMPLIFIED STRAPDOWN NAVIGATOR ERROR DIAGRAM**

Equations (96) can be rearranged to a form that lends itself more simply to qualitative analysis. We first differentiate $\delta\underline{\omega}_{EL}^{L}$ and substitute $\delta\dot{\underline{v}}^{L}$:

$$\delta\dot{\underline{\omega}}_{EL}^{L} = \frac{1}{R}\left(\underline{u}_{R}^{L} \times \delta\dot{\underline{v}}^{L}\right) = \frac{1}{R}\,\underline{u}_{R}^{L} \times \left(C_{B}^{L}\,\delta\underline{a}^{B} + \underline{a}^{L} \times \underline{\phi}^{L}\right)$$

$$= \frac{1}{R}\left[\underline{u}_{R}^{L} \times \left(C_{B}^{L}\,\delta\underline{a}^{B}\right) + \underline{u}_{R}^{L} \times \left(\underline{a}^{L} \times \underline{\phi}^{L}\right)\right]$$

Applying the triple vector product identity (see Lecture 8):

$$\underline{u}_{R}^{L} \times \left(\underline{a}^{L} \times \underline{\phi}^{L}\right) = -\left(\underline{a}^{L} \times \underline{\phi}^{L}\right) \times \underline{u}_{R}^{L} = -\left(\underline{u}_{R}^{L} \cdot \underline{a}^{L}\right)\underline{\phi}^{L} + \left(\underline{u}_{R}^{L} \cdot \underline{\phi}^{L}\right)\underline{a}^{L}$$

Hence:

$$\delta\dot{\underline{\omega}}_{EL}^{L} = \frac{1}{R}\left[\underline{u}_{R}^{L} \times \left(C_{B}^{L}\,\delta\underline{a}^{B}\right) + \left(\underline{u}_{R}^{L} \cdot \underline{\phi}^{L}\right)\underline{a}^{L} - \left(\underline{u}_{R}^{L} \cdot \underline{a}^{L}\right)\underline{\phi}^{L}\right] \qquad (96A)$$

If we define $\delta\underline{v}^{L}$ as having a vertical ($\delta v_{R}$) and horizontal ($\delta\underline{v}_{H}^{L}$) component, we can write:

$$\delta\underline{v}^{L} = \delta v_{R}\,\underline{u}_{R}^{L} + \delta\underline{v}_{H}^{L}$$

$$\delta\underline{\omega}_{EL}^{L} = \frac{1}{R}\left(\underline{u}_{R}^{L} \times \delta\underline{v}^{L}\right) = \frac{1}{R}\left(\underline{u}_{R}^{L} \times \delta\underline{v}_{H}^{L}\right)$$

$$\underline{u}_{R}^{L} \times \delta\underline{\omega}_{EL}^{L} = \frac{1}{R}\,\underline{u}_{R}^{L} \times \left(\underline{u}_{R}^{L} \times \delta\underline{v}_{H}^{L}\right) = -\frac{1}{R}\,\delta\underline{v}_{H}^{L} \qquad (96B)$$

$$\delta\underline{v}_{H}^{L} = -R\left(\underline{u}_{R}^{L} \times \delta\underline{\omega}_{EL}^{L}\right)$$

Similarly,

$$\underline{\omega}_{EL}^{L} = \frac{1}{R}\left(\underline{u}_{R}^{L} \times \underline{v}_{H}^{L}\right) \qquad (96C)$$

where:

$\underline{v}_{H}^{L}$ = The horizontal component of $\underline{v}^{L}$.

With (96A, B, C), (96) becomes equivalently:

$$\begin{aligned}
\dot{\underline{\phi}}^L &= -\,C_B^L\,\delta\underline{\omega}_{IB}^B - \left(\underline{\omega}_{IE}^L + \underline{\omega}_{EL}^L\right)\times\underline{\phi}^L + \delta\underline{\omega}_{EL}^L \\
\delta\dot{\underline{\omega}}_{EL}^L &= \frac{1}{R}\left[\underline{u}_R^L \times \left(C_B^L\,\delta\underline{a}^B\right) + \left(\underline{u}_R^L \cdot\ \underline{\phi}^L\right)\underline{a}^L - \left(\underline{u}_R^L \cdot\ \underline{a}^L\right)\underline{\phi}^L\right] \\
\delta\underline{v}_H^L &= R\left(\underline{u}_R^L \times \delta\underline{\omega}_{EL}^L\right) \\
\underline{\omega}_{EL}^L &= \frac{1}{R}\left(\underline{u}_R^L \times \underline{v}_H^L\right) \\
\dot{\underline{e}}^L &= \delta\underline{\omega}_{EL}^L
\end{aligned} \tag{97}$$

We now introduce the idea of vertical and horizontal components for $\underline{a}^L$ and $\underline{\phi}^L$. If the upward vertical component of $\underline{a}^L$ is approximated by g (i.e., essentially horizontal flight), we can write:

$$\underline{\phi}^L = \phi_R\,\underline{u}_R^L + \underline{\phi}_H^L$$

Vertical Components — Horizontal Components

$$\underline{a}^L = g\,\underline{u}_R^L + \underline{a}_H^L$$

Application to the terms in (97) yields:

$$\left(\underline{u}_R^L \cdot\ \underline{\phi}^L\right)\underline{a}^L - \left(\underline{u}_R^L \cdot\ \underline{a}^L\right)\underline{\phi}^L = \phi_R\left(\underline{a}_H^L + g\,\underline{u}_R^L\right) - g\left(\underline{\phi}_H^L + \phi_R\,\underline{u}_R^L\right) = \phi_R\,\underline{a}_H^L - g\,\underline{\phi}_H^L$$

$$\underline{\omega}_{EL}^L \times \underline{\phi}^L = \frac{1}{R}\left(\underline{u}_R^L \times \underline{v}_H^L\right)\times\left(\underline{\phi}_H^L + \phi_R\,\underline{u}_R^L\right) \approx \frac{1}{R}\left(\underline{u}_R^L \times \underline{v}_H^L\right)\times\phi_R\,\underline{u}_R^L = \frac{1}{R}\,\phi_R\,\underline{v}_H^L$$

$$\underline{\omega}_{IE}^L \times \underline{\phi}^L = \underline{\omega}_{IE}^L \times\left(\underline{\phi}_H^L + \phi_R\,\underline{u}_R^L\right) \approx \phi_R\,\underline{\omega}_{IE}^L \times \underline{u}_R^L$$

In the latter equations, the approximation has been made that $\phi_R$ (the vertical component of $\underline{\phi}^L$, or the heading error) is generally larger than $\underline{\phi}_H^L$. Substituting into (97) then obtains:

$$\dot{\underline{\phi}}^L = \dot{\underline{\phi}}_H^L + \dot{\phi}_R\, \underline{u}_R^L = -\, C_B^L\, \delta\underline{\omega}_{IB}^B - \phi_R\, \underline{\omega}_{IE}^L \times \underline{u}_R^L - \frac{1}{R}\, \phi_R\, \underline{v}_H^L + \delta\underline{\omega}_{EL}^L$$

$$\delta\dot{\underline{\omega}}_{EL}^L = \frac{1}{R}\left[\underline{u}_R^L \times \left(C_B^L\, \delta\underline{a}^B\right) + \phi_R\, \underline{a}_H^L - g\, \underline{\phi}_H^L\right]$$

It should be clear from the above that $\delta\underline{\omega}_{EL}^L$ is a horizontal vector (i.e., the $\underline{u}_R^L \times (\ )$ term is horizontal since it is perpendicular to $\underline{u}_R^L$, and the other components are horizontal by definition). Similarly, the $\underline{\omega}_{IE}^L \times \underline{u}_R^L$ term in the $\dot{\underline{\phi}}^L$ equation is horizontal. With these factors in mind, the $\dot{\underline{\phi}}^L$ equation can be divided into two parts by taking the dot product with $\underline{u}_R^L$ (for the vertical part), and subtracting this from the $\dot{\underline{\phi}}^L$ total equation to obtain the horizontal part:

$$\dot{\phi}_R = -\, \underline{u}_R^L \cdot \left(C_B^L\, \delta\underline{\omega}_{IB}^B\right)$$

$$\dot{\underline{\phi}}_H^L = -\, C_B^L\, \delta\underline{\omega}_{IB}^B + \underline{u}_R^L \cdot \left(C_B^L\, \delta\underline{\omega}_{IB}^B\right) \underline{u}_R^L - \phi_R\, \underline{\omega}_{IE}^L \times \underline{u}_R^L - \frac{1}{R}\, \phi_R\, \underline{v}_H^L + \delta\underline{\omega}_{EL}^L$$

With the latter simplifications, (97) becomes the final form:

$$\dot{\phi}_R = -\, \underline{u}_R^L \cdot \left(C_B^L\, \delta\underline{\omega}_{IB}^B\right)$$

$$\dot{\underline{\phi}}_H^L = -\, C_B^L\, \delta\underline{\omega}_{IB}^B + \underline{u}_R^L \cdot \left(C_B^L\, \delta\underline{\omega}_{IB}^B\right) \underline{u}_R^L - \phi_R\, \underline{\omega}_{IE}^L \times \underline{u}_R^L - \frac{1}{R}\, \phi_R\, \underline{v}_H^L + \delta\underline{\omega}_{EL}^L$$

$$\delta\dot{\underline{\omega}}_{EL}^L = \frac{1}{R}\left[\underline{u}_R^L \times \left(C_B^L\, \delta\underline{a}^B\right) + \phi_R\, \underline{a}_H^L - g\, \underline{\phi}_H^L\right] = \delta\dot{\underline{\omega}}_{EL_H} \tag{98}$$

$$\delta\underline{v}_H^L = -\, R\left(\underline{u}_R^L \times \delta\underline{\omega}_{EL}^L\right) = -\, R\left(\underline{u}_R^L \times \delta\underline{\omega}_{EL_H}^L\right)$$

$$\dot{\underline{e}}^L = \delta\underline{\omega}_{EL}^L = \delta\underline{\omega}_{EL_H}^L = \dot{\underline{e}}_H^L$$

Equations (98) are shown in block diagram form on the next page. The block diagram is now in a convenient form to analyze the characteristic response of the system errors.

We first observe that a closed dynamic loop exists containing two integrators with a negative loop gain of g/R. This should be recognizable as an undamped oscillator with natural frequency $\omega_o$ given by:

$$\omega_o = \sqrt{g/R}$$

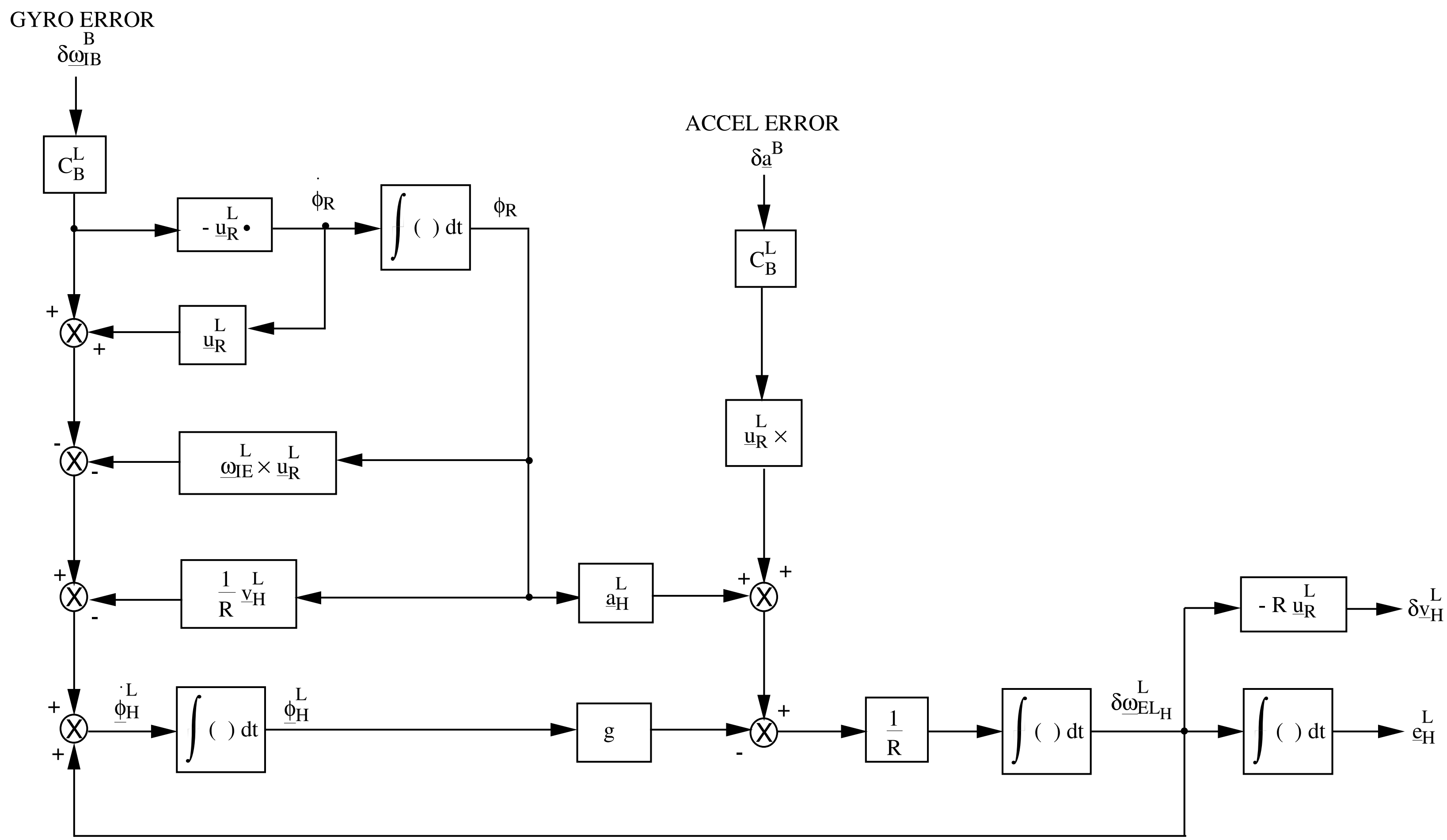


**FIGURE 4 - SIMPLIFIED STRAPDOWN NAVIGATOR ERROR ANALYSIS DIAGRAM**

Numerically, $\omega_o = \frac{2\pi}{84}$ radians per minute corresponding to a period of 84 minutes. This is the so called Schuler frequency. The characteristic response of the errors in an inertial navigation system contain the dynamics of the Schuler oscillation as remnants of imperfections in the system operating through the navigation equations.

For the case of constant sensor errors and system parameters ($\underline{v}_H^L$, $\underline{\omega}_{IE}^L$), the response of the horizontal system errors ($\underline{\phi}_H^L$, $\delta\underline{v}_H^L$, and $\underline{e}_H^L$) can be obtained qualitatively from the diagram by inspection, as illustrated by the qualitative response curves sketched on the next following page.

The associated error equations (solutions to differential Equations (98)) can be shown to be:

$$\begin{aligned}
\underline{\phi}_H^L \;=\; & \underline{\phi}_{H_o}^L \cos\omega_o t - \phi_{R_o}\left(\underline{\omega}_{IE}^L \times \underline{u}_R^L\right)\frac{\sin\omega_o t}{\omega_o} + \delta\underline{\omega}_{EL_{Ho}}^L \frac{\sin\omega_o t}{\omega_o} \\
& - \left[C_B^L\,\delta\underline{\omega}_{IB}^B - \underline{u}_R^L \cdot \left(C_B^L\,\delta\underline{\omega}_{IB}^B\right)\right]\frac{\sin\omega_o t}{\omega_o} \\
& + \left[\underline{u}_R^L \cdot \left(C_B^L\,\delta\underline{\omega}_{IB}^B\right)\right]\left(\underline{\omega}_{IE}^L \times \underline{u}_R^L + \frac{1}{R}\,\underline{v}_H^L\right)\frac{\left(1 - \cos\omega_o t\right)}{\omega_o^2} \\
& + \underline{u}_R^L \times \left(C_B^L\,\delta\underline{a}^B\right)\frac{1}{g}\left(1 - \cos\omega_o t\right)
\end{aligned}$$

$$\begin{aligned}
\delta\underline{\omega}_{EL}^L \;=\; & \delta\underline{\omega}_{EL_o}^L \cos\omega_o t - \underline{\phi}_{H_o}^L\omega_o \sin\omega_o t + \phi_{R_o}\left[\left(\underline{\omega}_{IE}^L \times \underline{u}_R^L\right)\left(1 - \cos\omega_o t\right) + \frac{1}{R}\underline{v}_H^L\right] \\
& + \left[C_B^L\,\delta\underline{\omega}_{IB}^B - \underline{u}_R^L \cdot \left(C_B^L\,\delta\underline{\omega}_{IB}^B\right)\right]\left(1 - \cos\omega_o t\right) \\
& - \left[\underline{u}_R^L \cdot \left(C_B^L\,\delta\underline{\omega}_{IB}^B\right)\right]\left(\underline{\omega}_{IE}^L \times \underline{u}_R^L + \frac{1}{R}\,\underline{v}_H^L\right)\left(t - \frac{\sin\omega_o t}{\omega_o}\right) \qquad (99) \\
& + \underline{u}_R^L \times \left(C_B^L\,\delta\underline{a}^B\right)\frac{\omega_o}{g}\sin\omega_o t
\end{aligned}$$

$$\begin{aligned}
\underline{e}^L \;=\; & \underline{e}_o^L - \underline{\phi}_{H_o}^L\left(1 - \cos\omega_o t\right) + \delta\underline{\omega}_{EL_o}^L\frac{\sin\omega_o t}{\omega_o} + \phi_{R_o}\left[\left(\underline{\omega}_{IE}^L \times \underline{u}_R^L\right)\left(t - \frac{\sin\omega_o t}{\omega_o}\right)\right. \\
& \left. + \frac{1}{R}\,\underline{v}_H^L\, t\right] + \left[C_B^L\,\delta\underline{\omega}_{IB}^B - \underline{u}_R^L \cdot \left(C_B^L\,\delta\underline{\omega}_{IB}^B\right)\right]\left(t - \frac{\sin\omega_o t}{\omega_o}\right) \\
& - \left[\underline{u}_R^L \cdot \left(C_B^L\,\delta\underline{\omega}_{IB}^B\right)\right]\left(\underline{\omega}_{IE}^L \times \underline{u}_R^L + \frac{1}{R}\,\underline{v}_H^L\right)\left(\frac{t^2}{2} - \frac{\left(1 - \cos\omega_o t\right)}{\omega_o^2}\right) \\
& + \underline{u}_R^L \times \left(C_B^L\,\delta\underline{a}^B\right)\frac{1}{g}\left(1 - \cos\omega_o t\right)
\end{aligned}$$

with

$$\delta\underline{v}_H^L = - R \left(\underline{u}_R^L \times \delta\underline{\omega}_{EL}^L\right)$$

$$\delta\underline{\omega}_{EL_o}^L = \frac{1}{R}\left(\underline{u}_R^L \times \delta\underline{v}_{H_o}^L\right) \tag{99A}$$

In generating the solutions to the Equations (98) differential equations it was assumed that $\underline{a}_H^L$ (see Figure 4 diagram) was such as to generate $\underline{v}_H^L$ rapidly (instantaneously) at the start of flight (t = 0) and from then on to equal zero (i.e., approximating an acceleration to a cruise velocity $\underline{v}_H^L$ and then maintaining $\underline{v}_H^L$). The effect in the Figure 4 block diagram is to immediately build up a signal on the $\delta\underline{\omega}_{EL}^L$ value of $\phi_{R_o} \frac{1}{R} \underline{v}_H^L$ due to transmission of $\phi_{R_o}$ through $\underline{a}_H^L$ at t = 0. The $\delta\underline{\omega}_{EL}^L$ value of $\phi_{R_o} \frac{1}{R} \underline{v}_H^L$ is then fed back into the $\underline{\phi}_H^L$ integrator, canceling the $\phi_{R_o}$ transmission to $\underline{\phi}_H^L$ through the $\frac{1}{R} \underline{v}_H^L$ block. The result is that the Schuler transient associated with $\phi_{R_o} \frac{1}{R} \underline{v}_H^L$ is effectively blocked and a constant ramp is produced at $\underline{e}^L$ (the effect on $\delta\underline{v}^L$ is to produce a constant offset error).

By analyzing the Equations (99) solutions the following can be ascertained regarding the behavior of the navigation system error characteristics. Again, it should be remembered that these considerations are approximations and are valid for the early flight phases (first hour or two).

1. The effect of horizontal gyro drift components ($C_B^L\ \delta\underline{\omega}_{IB}^B$ with the vertical component removed) is to generate an unbounded position error ($\underline{e}^L$) with average slope proportional to the gyro drift. Quantitatively, 0.01 degree per hour gyro drift produces $0.01 \times 60$ arc min per hour or 0.6 nmph (nautical miles per hour) position drift ($\underline{e}^L$). This is the reason that inertial navigation system require 0.01 degree per hour gyros to meet 1 nmh requirements.

2. Horizontal gyro drift produces an offset Schuler oscillation in the velocity error ($\delta\underline{\omega}_{EL}^L$ can be considered as the velocity error in arc min per hour or knots) with the Schuler oscillation amplitude and offset both equal to the gyro drift (i.e., a Schuler oscillation from zero to twice the gyro drift). For 0.01 degree per hour drift, the peak velocity error is $0.01 \times 2 \times 60 = 1.2$ knots, occurring at 42 minutes from t = 0.

3. Horizontal gyro drift produces a sinusoidal error in the platform attitude with a peak amplitude equal to the drift rate divided by the Schuler frequency (4.46

rad/hr). For a 0.01 degree per hour drift, attitude errors of $0.01 \times 60/4.46 = 0.15$ arc min are generated. Platform horizontal attitude errors ($\underline{\phi}_H^L$), in general, are insignificant compared, for example, to the error in knowing the attitude of the sensor assembly relative to the vehicle axes (several arc min).

4. Vertical gyro drift rates generate a linear unbounded velocity error build-up ($\delta\underline{\omega}_{EL}^L$) and parabolic position error build-up. Typically (for 1-2 hr flights) the effect is small compared to the effect of horizontal gyro drift. For example, for a 0.01 degree per hour drift rate, 600 knots cruise velocity ($\underline{v}_H^L$), and 10 degree/hour horizontal earth rate effect $\underline{\omega}_{IE}^L \times \underline{u}_R^L$, the error in $\delta\underline{\omega}_{EL}^L$ after 1 hour is approximately $(0.01/57.3) \times \sqrt{(600)^2 + (10 \times 60)^2} \times 1 \text{ hr} \approx 0.2$ nmph. The associated position error ($\underline{e}^L$) is 0.1 nm.

5. The effect of initial heading error is similar to gyro drift through a coupling of earth's rate and translational velocity effects (i.e., the navigation solution is initially generated in an offset direction with the offset given by $\phi_{R_o}$). Quantitatively, a 1 milliradian error with 600 knots vehicle velocity and 10 degree per hour horizontal earth rate results in an equivalent gyro drift of $1 \times 10^{-3} \times \sqrt{(10)^2 + (600/60)^2} = 0.014$ degree/hour. A heading alignment error of 1 milliradian or less is required for 1 nmph (0.01 degree per hour gyro) inertial navigation accuracy.

6. The effect of accelerometer error is to generate bounded Schuler oscillations in the attitude, velocity, and position errors. Quantitatively, a 50 μg accelerometer bias generates a 0 to 100 μradian ($100 \times 10^{-6} \times 57.3 \times 60 = 0.36$ arc min) Schuler attitude and position ($\underline{\phi}_H^L$, $\underline{e}^L$) oscillation and a $(0.36/2) \times 4.46 = 0.7$ knot velocity oscillation ($\omega_o = 4.46$ rad/hr). To keep velocity errors low, accelerometer errors are typically selected to be less than 50 μg's.

7. The effect of initial attitude errors ($\underline{\phi}_{H_o}^L$) is similar to the effect of accelerometer error with a micro-g producing the same quantitative effect as a microradian. Hence, good vertical alignment (order of 50 μrad) is required to keep velocity errors down.

8. The effect of initial velocity errors is to produce a bounded Schuler oscillation in the system errors that, for systems initialized at a stationary position ( e.g., aircraft at land based airports) is negligible compared to other error sources (because the initial velocity error is typically very small (less than 0.1 fps) and its effect is bounded in position growth).

One of the most serious error effects in strapdown navigation systems is the effect of sensor-to-sensor misalignment errors. In the error diagram, these effects are wrapped up in the basic sensor errors themselves ($\delta\underline{\omega}_{IB}^{B}$, $\delta\underline{a}^{B}$). The effect of a gyro misalignment is to introduce a coupling of rate from another axis (orthogonal to the gyro input axis) into the gyro sensing axis. Under high rotation rates, a significant error can result. Since high rate maneuvers are typically of short duration, it is better to think of the error in terms of its net integrated effect over the maneuver period (i.e., the effect on $\underline{\phi}^{L}$ in the error block diagram due to the integration of $C_B^L\ \delta\underline{\omega}_{IB}^{B}$ when $\delta\underline{\omega}_{IB}^{B}$ contains misalignment cross coupling errors). In general, the effect of a misalignment is to introduce an error on the order of the misalignment into $\underline{\phi}^{L}$ each time the vehicle rotates through one radian. However, because these effects add vectorially, and because of the distortion of $C_B^L$ to the error before it is integrated to obtain $\underline{\phi}^{L}$, the composite of several rotation maneuvers can add or subtract. For example, a 180 degree rotation about a single vehicle axis generates a net $\underline{\phi}^{L}$ error equal to twice the misalignment error. A 360 degree rotation about a single vehicle axis, on the other hand, results in zero net error, as would (+) followed by a (-) rotation of equal magnitude about the same axis. A 360 degree rotation about an axis skewed relative to the sensor axes (a simultaneous pitch/yaw rotation for example) produces a net $\underline{\phi}^{L}$ error due to sensor misalignment. A combination of sequential maneuvers about different axes produces a composite of canceling and additive effects that are a function of the maneuver history and misalignments. In general, the particular maneuver profiles anticipated must be analyzed to determine the effects of particular sensor misalignments, and to determine whether a net error in $\underline{\phi}^{L}$ results in the vertical axis ($\phi_R$) or the more critical (from a velocity accuracy standpoint) horizontal axes ($\underline{\phi}_H^{L}$). Typical strapdown inertial navigation systems achieve 15 μrad alignment stabilities from sensor-to-sensor axes. For a 180 degree maneuver, with 15 μrads misalignment, the worst case effect is to generate a Schuler velocity oscillation of ± 0.6 fps. For applications where extensive maneuvering may exist and where high velocity accuracy is needed, the 15 μrad figure may be somewhat marginal. Future advancements in sensor mount design may make it possible to achieve better than 15 μrad alignment accuracy which, in turn, will broaden the spectrum of maneuvering application areas where strapdown technology is viable.

**NOTES**

**STRAPDOWN INS INITIAL ALIGNMENT**

LECTURE 11

## NAV SEMINAR - LECTURE 11 NOTES

In this lecture we will discuss the initial alignment process associated with strapdown inertial navigation systems. These are the computational equations utilized after system turn-on to establish the initial value for the C matrix (or $C_B^L$) in Lectures 5-9, and the initial values of $\Omega_1$ and $\Omega_2$ (the estimated level earth rates components in the local level frame) used in Lecture 3 to initialize the wander angle, hence, the D matrix.

The basic principal utilized with all inertial systems (strapdown or gimbaled) for quasi-stationary self-alignment (without external inputs) is to align the vertical with sensed acceleration, and to align the azimuth based on sensed earth rate. The assumption used is that the vehicle carrying the inertial system is essentially stationary during the alignment process so that sensed acceleration is basically along the local vertical (i.e., vehicle disturbances are transitory and can be filtered out). Aligning the vertical of the reference platform (the analytical C matrix in the case of a strapdown system) with the sensed acceleration, therefore, levels the platform. The initial platform heading is established by measuring earth rate in the leveled frame and using the knowledge that the plane containing the local vertical and the sensed earth rate vector is a meridian plane (i.e., lies North/South). Hence, the angle between the leveled reference frame and the computed meridian plane defines the initial azimuth (or wander angle in a wander azimuth implementation approach).

For most inertial navigation systems, leveling and heading initialization is divided into two phases: coarse alignment and fine alignment. During coarse alignment, the platform is rapidly erected to an approximately level condition (within a degree or so). Fine alignment is the process of fine tuning the vertical alignment (to an accuracy of less than 50 μrad) and simultaneously determining the azimuth alignment by earth rate measurements. For strapdown systems, coarse alignment can be performed extremely rapidly since erection is an analytical process in the computer, unrestricted by finite rotation rate limitations associated with real gimbaled platforms containing inertia and gyro torquing rate limitations. The azimuth alignment process for both strapdown and gimbaled systems can be virtually identical, with the exception of special filters in the alignment estimation equations that may be tailored to handle noise effects peculiar to the actual hardware elements in the system (e.g., random walk in laser gyros). The following is a discussion of typical strapdown coarse and fine alignment techniques.

### COARSE ALIGNMENT

Coarse alignment is achieved by measuring the components of the sensed acceleration vector in vehicle axes and using this measurement to estimate the initial value of the $C_B^L$ (or C) matrix in Lectures 5-9. Recall from Lectures 5-9 that the rows of C are equal to unit vectors along local level frame (L) axes projected on body (vehicle axes). That is:

$$C = \begin{pmatrix} \underline{C}_1^T \\ \underline{C}_2^T \\ \underline{C}_3^T \end{pmatrix}$$

where $\underline{C}_i$ is a column vector whose components are the elements in C matrix row i. $\underline{C}_3$ represents the projection of a unit vertical vector on body axes. (Note: In these lectures, the L Frame reference for $C_B^L$ is defined to have Z axis down whereas for navigation velocity/position calculations, the L Frame is defined with Z axis up. See Lecture 9 - Interface Between Navigation And Strapdown Reference Equations section for more discussion.) The coarse alignment process uses measured body acceleration as sensed by the accelerometers to develop a first estimate of $\underline{C}_3$. For a stationary vehicle the sensed acceleration vector $\underline{a}^B$ is along $\underline{C}_3$ and equal in magnitude to g (directed upward). Hence, neglecting the effects of small vehicle vibrations, we can write:

$$\underline{a}^B \approx -g\,\underline{C}_3$$

where $\underline{C}_3$ is defined as downward, hence the negative sign. Equivalently,

$$\underline{C}_3 \approx -\frac{1}{g}\,\underline{a}^B$$

The coarse alignment of $\underline{C}_3$ is based on the latter equation except that $\underline{a}^B$ is estimated as an integral of $\underline{a}^B$ over a short time interval T divided by T. Hence, the initial estimate for $\underline{C}_3$ is, in component form:

$$\begin{aligned} C_{31} &= -\frac{1}{g\,T}\int_o^T a_x\,dt \\ C_{32} &= -\frac{1}{g\,T}\int_o^T a_y\,dt \\ C_{33} &= -\frac{1}{g\,T}\int_o^T a_z\,dt \end{aligned} \qquad (100)$$

The initial course alignment values for $\underline{C}_2$ and $\underline{C}_3$ can be selected arbitrarily to satisfy other desirable constraints (such as simplifying calibration measurements for example), provided that the basic properties of C are maintained (i.e., orthogonality and normality).

A simple specification for defining the second direction cosine row ($\underline{C}_2$) is that the component along the X-axis ($C_{21}$) be zero. The advantage in this approach is that for initial orientations of the strapdown sensor assembly with Y-axis or Z-axis down, $C_{21}$ becomes a direct measure of Y or Z gyro integrated drift rate during fine alignment (and navigation) under static conditions. That is, for either of these orientations, the cosine of the angle between the level Y-axis and the computed body X-axis should remain at the initial condition after coarse alignment (i.e, zero). A value differing from zero is due to drift rate from the gyro along the vertical axis, and the value of $C_{21}$ becomes equal to the integrated gyro drift rate since coarse alignment completion. This is a useful relationship for measuring gyro drift in the laboratory. Thus, the initial value for $C_{21}$ is:

$$C_{21} = 0 \tag{101}$$

For $\underline{C}_2$ to be perpendicular to $\underline{C}_3$, their dot product must be zero:

$$\underline{C}_2 \cdot \underline{C}_3 = C_{21}\,C_{31} + C_{22}\,C_{32} + C_{23}\,C_{33} = C_{22}\,C_{32} + C_{23}\,C_{33} = 0 \tag{102}$$

Equation (102) is satisfied by:

$$\begin{aligned} C_{22} &= K\,C_{33} \\ C_{23} &= -\,K\,C_{32} \end{aligned} \tag{103}$$

Where K is a constant selected to normalize $\underline{C}_2$ (i.e., the sum of the squares of its elements should be unity). Based on this criterion, it is easily verified that $K = \sqrt{C_{32}^2 + C_{33}^2}$ so that the initial values for $\underline{C}_2$ are:

$$\begin{aligned} C_{21} &= 0 \\ C_{22} &= C_{33} / \sqrt{C_{32}^2 + C_{33}^2} \\ C_{23} &= -\,C_{32} / \sqrt{C_{32}^2 + C_{33}^2} \end{aligned} \tag{104}$$

The coarse initialization of $\underline{C}_1$ is trivial once $\underline{C}_2$ and $\underline{C}_3$ is known. The cross-product of $\underline{C}_2$ with $\underline{C}_3$ provides $\underline{C}_1$ directly (i.e., a unit vector perpendicular to $\underline{C}_2$ and $\underline{C}_3$):

$$\begin{aligned} C_{11} &= C_{22}\,C_{33} - C_{23}\,C_{32} \\ C_{12} &= C_{23}\,C_{31} - C_{21}\,C_{33} \\ C_{13} &= C_{21}\,C_{32} - C_{22}\,C_{31} \end{aligned} \tag{105}$$

The above procedure for coarse leveling the C matrix works as long as $\underline{C}_3$ has components along Y and Z ($C_{32}$, $C_{33}$), thereby defining non-zero values for $C_{22}$ and $C_{23}$

in Equations (104). If $C_{32}$, $C_{33}$ are near zero, the procedure breaks down because Equation (104) becomes indetermanent (i.e., a singularity condition exists). Under these conditions, a different set of logic must be used. It is easily verified from Equations (100), that the $C_{32} = C_{33} = 0$ condition corresponds to the total acceleration vector being directed along X (i.e., X up or down). From Equation (100), the test for encroachment on this condition is that $/C_{31}/$ be near unity. A $/C_{31}/$ greater than 0.85 condition can be utilized to signal the need for a revised set of erection logic. Under these conditions, $C_{23}$ can be set to zero (rather than $C_{21}$ as in (101)) and proceed as before:

$$\underline{C}_2 \cdot \underline{C}_3 \;=\; C_{21}\, C_{31} + C_{22}\, C_{32} + C_{23}\, C_{32} \;=\; C_{21}\, C_{31} + C_{22}\, C_{32} \;=\; 0$$

Proceeding:

$$\begin{aligned} C_{21} &= \;K\, C_{32} \\ C_{22} &= -\, K\, C_{31} \\ C_{23} &= \;0 \end{aligned}$$

The initial $\underline{C}_2$ for the normalization routine, therefore, is:

$$\begin{aligned} C_{21} &= C_{32} \,/ \sqrt{C_{31}^2 + C_{32}^2} \\ C_{22} &= -\, C_{31} \,/ \sqrt{C_{31}^2 + C_{32}^2} \qquad (106) \\ C_{23} &= 0 \end{aligned}$$

Equation (105) is used as before to evaluate $\underline{C}_3$.

It should be noted that for X down, and $C_{31}$ greater than 0.85 so that (106) is used for initial $\underline{C}_2$), $C_{23}$ becomes a direct measure of X-gyro drift (i.e., the movement of the computed Z-body axis relative to the Y-level axis after completion of coarse alignment). This was the motivation for specifying the $C_{23} = 0$ condition for $C_{31}$ greater than 0.85.

## FINE ALIGNMENT

The fine alignment process is, in a sense, the inverse of the navigation process. Referring to Figure 1 of the previous lecture, the velocity ($\underline{v}^L$) is determined in an inertial navigation system during the navigation mode by processing sensed gyro and acceleration measurements, and computed earth rate and attitude matrix elements ($\underline{\omega}_{IE}^L$, $C_B^L$). In the alignment process, the problem is to estimate the attitude matrix and earth rate components such that the computed velocity ($\underline{v}^L$) satisfies known statistical constraints imposed during alignment (i.e., for ground alignment, $\underline{v}^L$ has zero average horizontal components with short term fluctuations due to vehicle buffeting by wind, fuel loading, etc.). Figure 4A on the next page illustrates this concept.

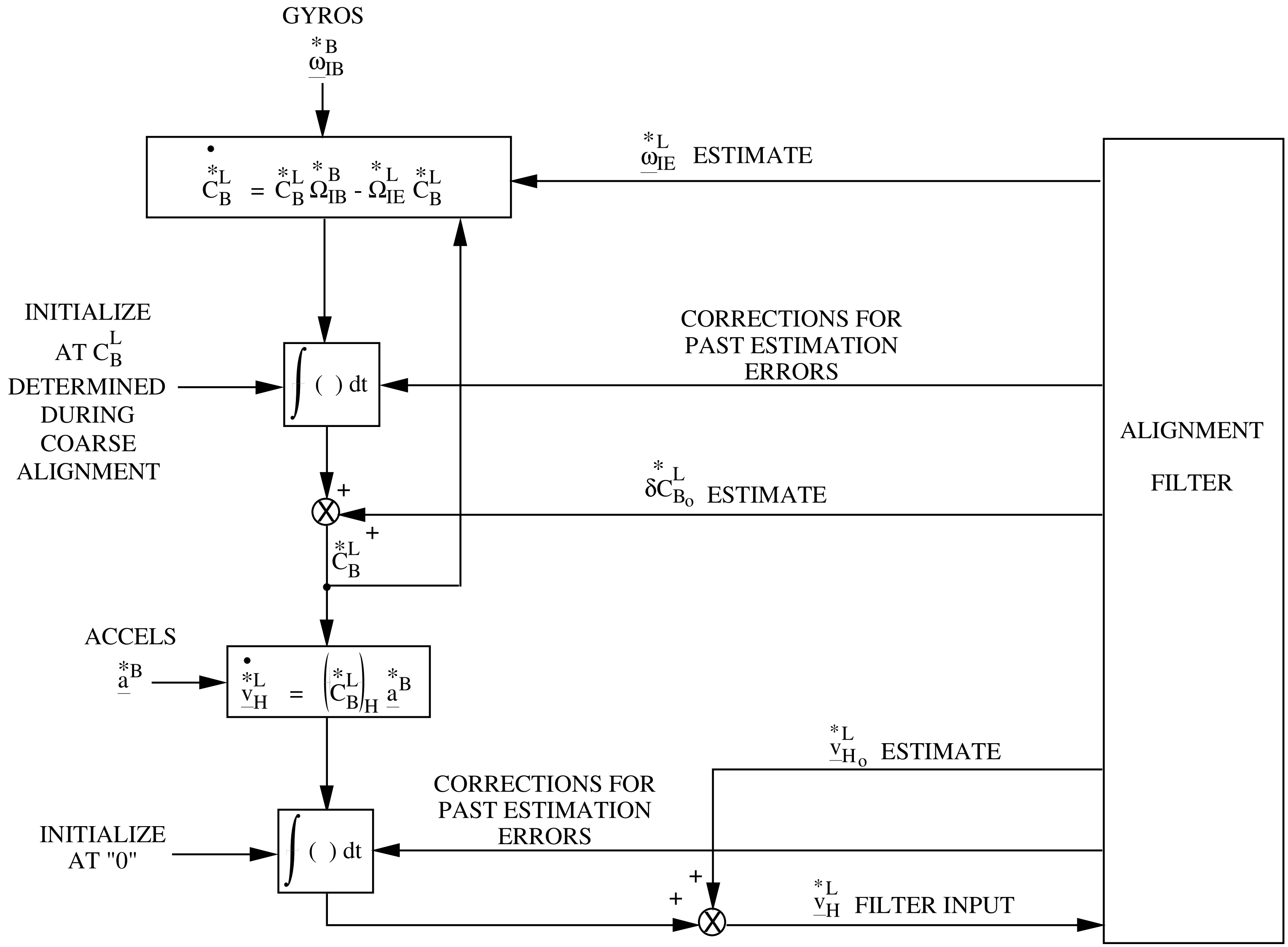


**FIGURE 4A - FINE ALIGNMENT LOOP CONCEPT**

If we compare Figure 4A with Figure 1 of the previous lecture, we note that the computations for the horizontal components of $\underline{v}^L$ are identical, except that the earth rate signals for $C_B^L$ update, the initial $C_B^L$ error (due to coarse leveling errors) at start of fine alignment, and the initial value of horizontal velocity ($\underline{v}_{H_0}^L$) are now estimated by the alignment filter based on the computed value of $\underline{v}_H^L$ and its comparison (in the alignment filter) against normally anticipated velocity conditions (approximately zero with random variations). In addition, because the vehicle is stationary on the average during alignment, the $\underline{\omega}_{EL}^L$ and $\underline{v}^L$ terms in the Figure 1 $\dot{C}_B^L$ and $\dot{\underline{v}}^L$ equations are approximately zero, hence, neglected in the equivalent Figure 4A computations. The alignment filter also computes updates for the $\overset{*}{C}{}_B^L$ and $\overset{*}{\underline{v}}{}_H^L$ integrators to compensate for the accumulated effect of past errors in the $\overset{*}{\underline{\omega}}{}_{IE}^L$ and $\delta\overset{*}{C}{}_{B_o}^L$ estimates generated by the alignment filter.

In Figure 4A, the (*) star notation has been utilized (as contrasted with Figure 1) to indicate that the quantities so annotated are real measurements and associated computation variables that contain sensor errors and their resulting effects on the computation process. This notation will be expanded upon subsequently when we analyze the effect of sensor errors on alignment accuracy. The $\left(\overset{*}{C}{}_B^L\right)_H$ quantity in Figure 4A represents the horizontal rows of $\overset{*}{C}{}_B^L$ (i.e., - the two rows that generate the horizontal level coordinate frame components of a body frame vector being transformed through it). It should also be noted in Figure 4A that the estimate of initial velocity $\left(\overset{*}{\underline{v}}{}_{Ho}^L\right)$ is included in the alignment process, but is neglected in the navigation process (i.e., the initial velocity for the navigation mode in Figure 1 of the previous lecture is equated to zero). The reason for this is that for the navigation problem, the initial velocity under ground alignment conditions is generally negligible compared with typical (2 - 3 fps) velocity accuracy requirements. For the alignment problem where the output is a very fine measurement of earth rate under noisy conditions, the same velocity error can affect the azimuth alignment accuracy. Consequently, it is accounted for during the alignment process to improve on azimuth determination accuracy. (It should be noted that the initial value of velocity for navigation could be estimated from $\overset{*}{\underline{v}}{}_H^L$ (see Figure 4A) at completion of alignment for a refinement in navigation accuracy.)

The implementation of the alignment filter in Figure 4A is accomplished using a linear filter with time varying gains. The gain schedules are selected to minimize the reaction time (settling time) of the alignment process on the one hand, and minimize alignment errors due to system noise and vehicle acceleration disturbances on the other (i.e., the classical filter noise/bandwidth tradeoff). Figure 5 is an analytical description of the alignment filter (within the dotted lines) and its interface with the velocity determination

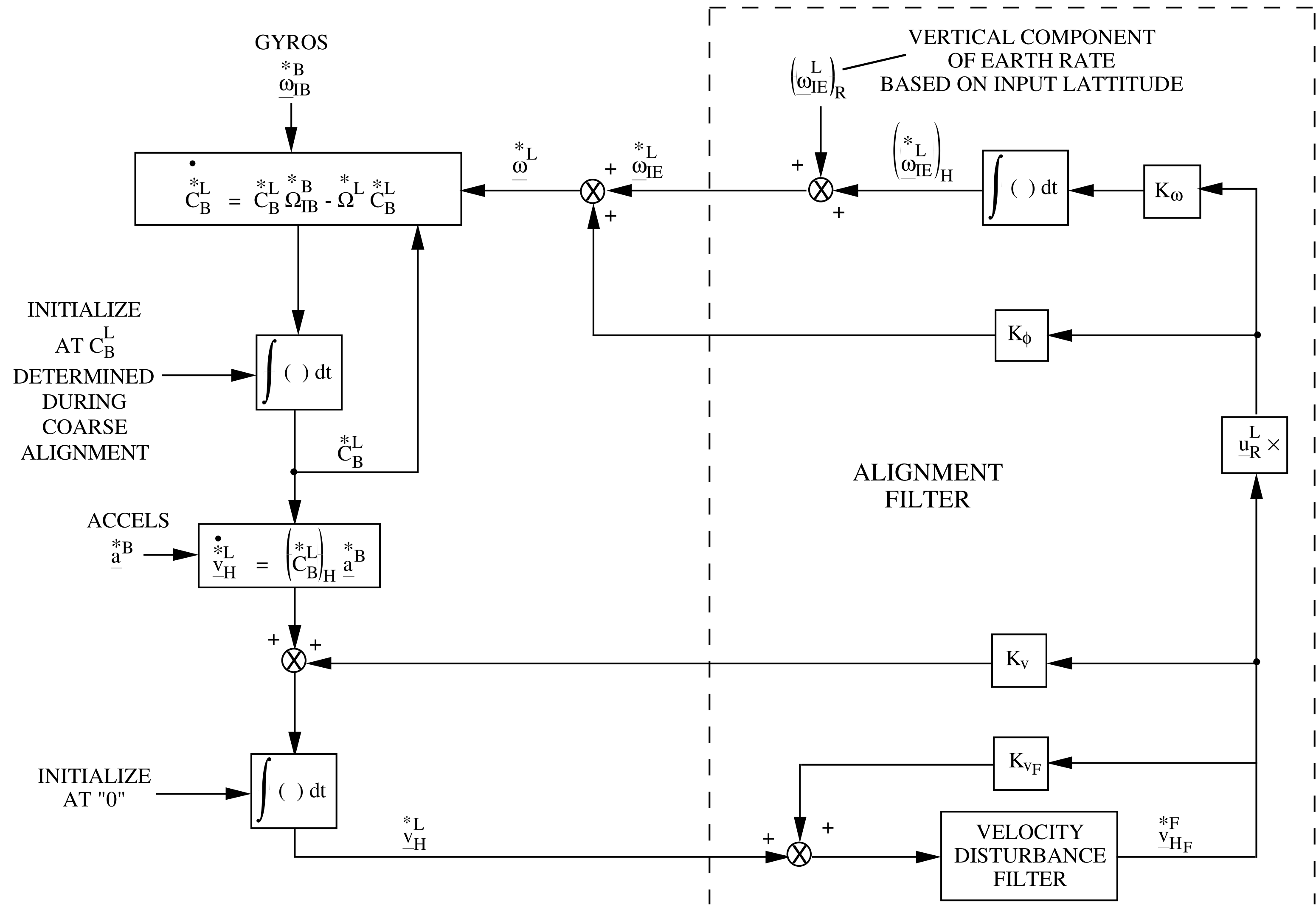


**FIGURE 5 - MODIFIED FINE ALIGNMENT LOOP ANALYTICS**

($\overset{*}{\underline{v}}{}_H^L$) computation (compare with Figure 4A). The comparison between Figures 4A and 5 show a small variation between the filter interfaces. The difference is that separate filter outputs are shown in Figure 4A for compensating $C_B^L$ errors and correcting for past estimation errors accumulating on the $\overset{*}{C}{}_B^L$ and $\overset{*}{\underline{v}}{}_H^L$ integrators. In Figure 5, these functions are applied through an addition to the inputs of the integrators through the $K_\phi$ and $K_v$ gains. In the case of $K_\phi$, the corrections to $\overset{*}{C}{}_B^L$ are achieved by augmenting the $\overset{*}{C}{}_B^L$ level axis frame rotation rate signal. It should be clear that the resulting resets of $\overset{*}{C}{}_B^L$ and $\overset{*}{\underline{v}}{}_H^L$ can be implemented to achieve the identical result in Figure 5 as in Figure 4A.

The internal structure of the alignment filter in Figure 5 contains a velocity disturbance filter (to attenuate the effects of vehicle acceleration disturbances on alignment accuracy), thereby allowing a higher loop gain (i.e., faster alignment time) for equivalent performance. Also included is an integral controller to generate the level earth rate estimate, the output from the alignment process for initial heading determination (see Lecture 3). The vertical component of earth rate is then added to the horizontal component estimate to obtain the total earth rate signal for $\dot{\overset{*}{C}}{}_B^L$ input. The vertical earth rate component is determined from the initial latitude insertion to the system (equal to earth's rate times sine latitude - see Lecture 3). A feedback around the velocity disturbance filter is included to compensate for the build-up of errors created from previous filter estimation errors propagating into $\overset{*}{\underline{v}}{}_H^L$, hence into the filter. The $\left(K_\Omega, K_\phi, K_v, K_{vF}\right)$ gains in Figure 5 are time varying functions based on Kalman filter theory (next lecture).

Assuming that filter convergence is achieved, the response of the Figure 5 estimation loop will result in a leveling of $\overset{*}{C}{}_B^L$ and a generation of $\overset{*}{\underline{\omega}}{}_{IE}^L$ that maintains $\overset{*}{C}{}_B^L$ stationary (this has to be true for $\overset{*}{\underline{v}}{}_H^L$ to be stationary - i.e., which is the steady state). This condition can only be achieved by the correct (leveled) value of $\overset{*}{C}{}_B^L$ and the correct value of the earth rate estimates.

To gain a deeper understanding of the dynamics of the alignment loop, the equivalent error diagram associated with Figure 5 is shown in Figure 6. The indicated error quantities are identical to the values introduced in the previous lecture (See Figures 2 and 4). The Figure 5 and 6 diagrams are equivalent. Figure 6 shows the response of the filter loop in terms of the errors in $C_B^L$ (i.e., $\underline{\phi}_H^L$, $\phi_R$) and measured horizontal acceleration $\underline{a}_H^L$

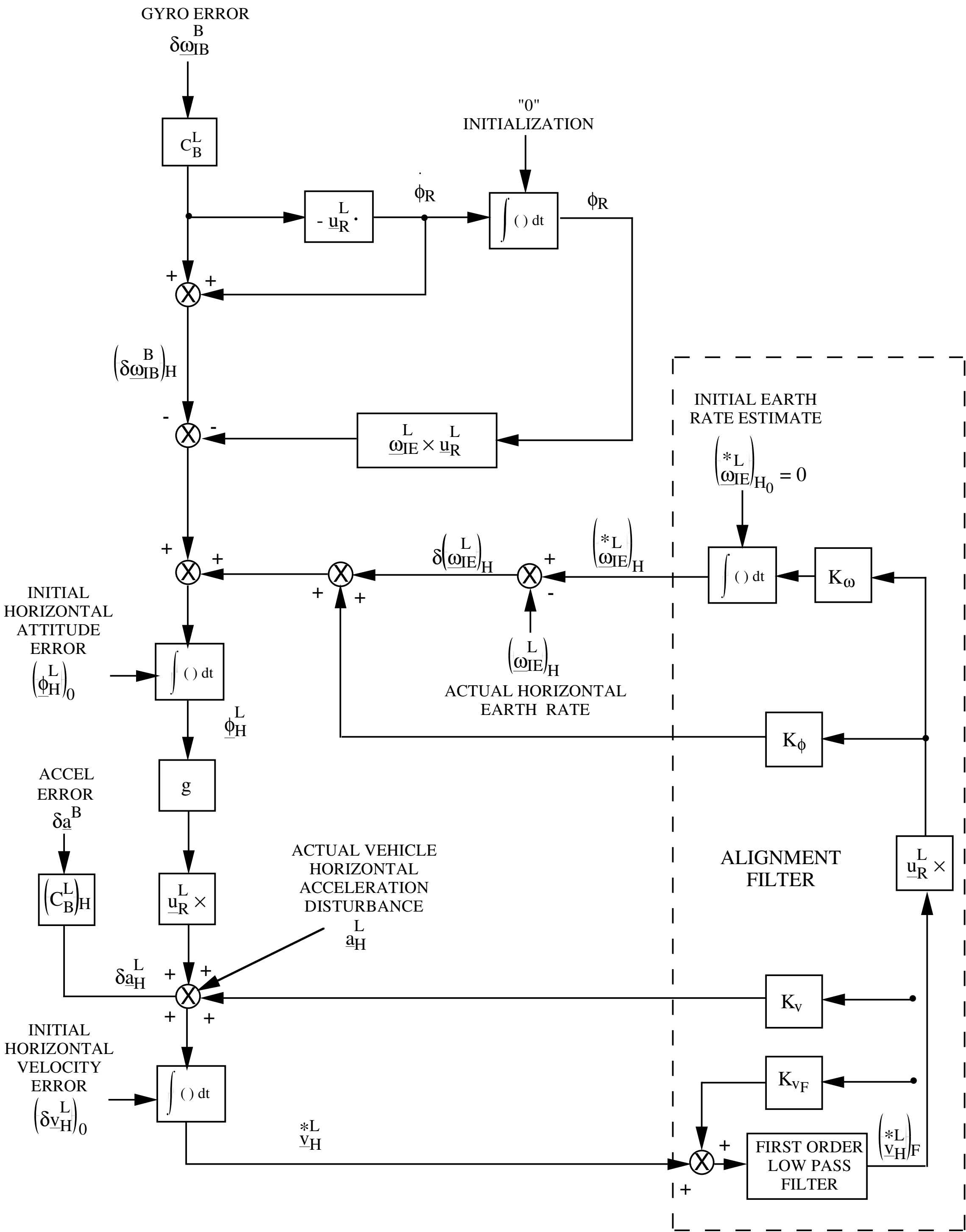


**FIGURE 6 - FINE ALIGNMENT LOOP ERROR DIAGRAM**

(i.e., $\delta \underline{a}_H^L$), and their effect on the $\overset{*}{\underline{v}}{}_H^L$ input to the filter and associated filter response outputs. In developing the Figure 6 diagram, the definitions of $\overset{*}{\underline{v}}{}_H^L$ and the horizontal components of $\overset{*}{\underline{\omega}}{}_{IE}^L$ were utilized:

$$\overset{*}{\underline{v}}{}_H^L = \dot{\underline{v}}_H^L + \delta \dot{\underline{v}}_H^L = \underline{a}_H^L + \delta \underline{a}_H^L$$

$$\left(\overset{*}{\underline{\omega}}{}_{IE}^L\right)_H = \left(\underline{\omega}_{IE}^L\right)_H + \left(\delta \underline{\omega}_{IE}^L\right)_H$$

Before analyzing the qualitative response of the Figure 6 loop, it is first noted that the effect of the $\left(\underline{u}_R^L \times\right)$ operator is to rotate the input vector by 90 deg about the vertical (i.e., a horizontal vector east becomes a horizontal vector north with identical magnitude). The effect of two successive $\left(\underline{u}_R^L \times\right)$ operations is to introduce a 180 deg vector rotation. This is equivalent to reversing the direction of the input vector, or applying a gain of -1. If we now look at Figure 6, it is to be noted that $\left(\underline{u}_R^L \times\right)$ appears twice as one traverses the closed loop. Hence, the net effect is to produce a negative gain (-1) in the overall estimation loop.

A qualitative inspection of Figure 6 reveals that the alignment loop is a fourth order control loop (3 integrators and 1 first order filter) in each of the two horizontal axes. It should be apparent that adequate flexibility exists in the estimation loop gains $\left(K_\Omega, K_\phi, K_v, K_{vF}\right)$ to achieve stable estimation loop performance (i.e., eliminating initial leveling errors $\left(\underline{\phi}_H^L\right)$ and reaching a steady state estimate for the earth term $\left(\overset{*}{\underline{\omega}}{}_{IE}^L\right)_H$). The selection of these gains for optimum convergence will be discussed in the next lecture. For now, we will assume that a set of stabilizing gains can be developed that will produce a stable estimation loop that, therefore, will reach a steady state condition. The steady state condition (after initial transients have decayed to zero) will contain random signals (produced by sensor noise and vehicle acceleration disturbance inputs) superimposed on a steady state solution created by fixed sensor errors. The remainder of this lecture deals with the analysis of the steady state solution terms.

To determine the effects of constant sensor input errors on the steady state alignment, we apply the principal of linear superposition and analyze the Figure 6 steady loop response to each constant sensor input (i.e., the sensor noise and vehicle horizontal disturbance effects are assumed to be zero). The effects of the noise and disturbance inputs can then be analyzed separately (assuming zero constant sensor inputs) and the results combined with the individual fixed sensor input results to obtain the total solution.

We begin by analyzing the steady state solution to all constant sensor inputs except for the $\dot{\phi}_R$ terms produced by vertical gyro drift (this will be discussed later). For $\dot{\phi}_R$ assumed zero, the steady state solution to Figure 6 with fixed sensor inputs will result in a condition where the inputs to all the integrators are zero (i.e., the steady state is achieved when the integrator outputs are constant or zero). The input to the $\left(\underline{\omega}_{IE}^{*L}\right)_H$ integrator being zero is equivalent to:

$$\left(\underline{v}_H^{*L}\right)_{F_{SS}} = 0 \qquad\qquad \underline{\text{Note}}\text{: SS = Steady State}$$

With the latter condition, the $\delta\underline{v}_H^L$ integrator input equal to zero condition yields:

$$g\,\underline{u}_R^L \times \left(\underline{\phi}_H^L\right)_{SS} + \left(C_B^L\right)_H \delta\underline{a}^B = 0$$

or, taking the cross-product with $\underline{u}_R^L$ and remembering that $\left(\underline{u}_R^L \times\right)\left(\underline{u}_R^L \times\right) = -1$, obtains:

$$-\,g\left(\underline{\phi}_H^L\right)_{SS} + \underline{u}_R^L \times \left[\left(C_B^L\right)_H \delta\underline{a}^B\right] = 0$$

or

$$\left(\underline{\phi}_H^L\right)_{SS} = \underline{u}_R^L \times \frac{1}{g}\left(C_B^L\,\delta\underline{a}^B\right) \tag{107}$$

Hence, the state leveling error $\left(\underline{\phi}_H^L\right)_{SS}$ is equal to the horizontal accelerometer bias component expressed in g’s, i.e., 15 μg accelerometer bias error produces 15 μrad initial platform tilt.

Now, looking at the input to the $\underline{\phi}_H^L$ integrator and equating it to zero in the steady state:

$$\left(\delta\underline{\omega}_{IE}^L\right)_H - \left(\delta\underline{\omega}_{IB}^L\right)_H = 0$$

or

$$\left(\delta\underline{\omega}_{IE}^L\right)_H = \left(\delta\underline{\omega}_{IB}^L\right)_H \tag{108}$$

Hence, the steady state earth rate estimation error is equal to the horizontal component of gyro drift. This translates into an initial heading error for the navigation mode due to use of erroneous $\left(\underline{\omega}_{IE}^{*L}\right)_H$ estimates in determining the initial wander angle. Using the nomenclature of Lecture 3, let's calculate what the initial wander angle error is due to erroneous $\left(\overset{*}{\underline{\omega}}{}^{L}_{IE}\right)_H$. We first write algebraic expressions for the horizontal components including error effects:

$$\overset{*}{\Omega}_x = \Omega_x + \delta\Omega_x = \Omega_x + \delta\overset{*}{\omega}_x$$
$$\overset{*}{\Omega}_y = \Omega_y + \delta\Omega_y = \Omega_y + \delta\overset{*}{\omega}_y \qquad (109)$$

where $\delta\overset{*}{\omega}_x$, $\delta\overset{*}{\omega}_y$ are components of $\left(\delta\underline{\omega}^{L}_{IB}\right)_H$ (i.e., level axis gyro drift rate components). From Lecture 3, the initial wander angle is established implicitly through the D matrix initialization:

$$\overset{*}{d}_{21_o} = \overset{*}{\Omega}_x / \Omega_e$$

$$\overset{*}{d}_{22_o} = \overset{*}{\Omega}_y / \Omega_e$$

The associated initial wander angle is:

$$\overset{*}{\alpha}_o = \tan^{-1}\left(\overset{*}{d}_{21_o} / \overset{*}{d}_{22_o}\right) = \tan^{-1}\left(\overset{*}{\Omega}_x / \overset{*}{\Omega}_y\right)$$

The differential of the latter expression yields the error in $\overset{*}{\alpha}_o$ due to errors in $\overset{*}{\Omega}_x / \overset{*}{\Omega}_y$:

$$\delta\alpha_o = \delta \tan^{-1}\left(\Omega_x / \Omega_y\right) = \frac{1}{1 + \left(\Omega_x / \Omega_y\right)^2}\ \delta\left(\Omega_x / \Omega_y\right)$$
$$= \frac{1}{1 + \left(\Omega_x / \Omega_y\right)^2}\ \frac{\Omega_y\ \delta\Omega_x - \Omega_x\ \delta\Omega_y}{\Omega_y^2} = \frac{\Omega_y\ \delta\Omega_x - \Omega_x\ \delta\Omega_y}{\Omega_y^2 + \Omega_x^2} \qquad (110)$$

From Lecture 3:

$$\Omega_x = \Omega_e \cos l_o \sin \alpha_o$$
$$\Omega_y = \Omega_e \cos l_o \cos \alpha_o \qquad (111)$$

where

$\Omega_e$ = Earth's rate magnitude and $l_o$ is initial latitude.

With (111),

$$\Omega_x^2 + \Omega_y^2 \;=\; \Omega_e^2 \left(\cos^2 l_o \sin^2\alpha_o + \cos^2 l_o \cos^2\alpha_o\right) \;=\; \Omega_e^2 \cos^2 l_o$$

$$\Omega_y\, \delta\Omega_x - \Omega_x\, \delta\Omega_y \;=\; \Omega_e \cos l_o \left(\delta\Omega_x \cos\alpha_o - \delta\Omega_y \sin\alpha_o\right)$$

Then (110) with (109) yields the desired expression of initial wander angle error in terms of gyro horizontal fixed bias during alignment:

$$\delta\alpha_o \;=\; \frac{\delta\overset{*}{\omega}_x \cos\alpha_0 - \delta\overset{*}{\omega}_y \sin\alpha_o}{\Omega_e \cos l_o} \tag{112}$$

Equation (112) shows that the initial wander angle error (i.e., the error in knowing the L Frame orientation relative to north, hence, also the negative of the initial heading error) equals the east component of gyro bias (the numerator in (112)) divided by earth rate times cosine latitude. Quantitatively, for east gyro bias of 0.01 degree per hr, and a 45 degree latitude, the initial wander angle error is:

$$\frac{0.01}{0.707 \times 15} \approx \;\text{1 milliradian}$$

From the previous lecture, this error provides the equivalent of the 0.01 deg per hr gyro bias acting during navigation.

We now return to the $\dot{\phi}_R$ term in Figure 6 (vertical gyro drift rate) that was not included in the above analysis. As can be seen from Figure 6, this term has the effect of a ramp input to the alignment loop. The response of the earth rate estimation error $\left(\delta\underline{\omega}_{IE}^{L}\right)_H$ is a function of the loop gains. In general, as will now be illustrated, for typical alignment times of 5 minutes, the effect of $\phi_R$ is small enough to be ignored. For example, for a gyro drift of 0.01 deg/hr, $\phi_R$ after 5 minutes equals approximately 10 µrads. The cross-coupling of this effect into the estimation loop (through $\underline{\omega}_{IE}^{L} \times \underline{u}_R^{L}$) is to introduce a drift rate with magnitude on the order of 10 µrad × 15 deg/hr ≈ 0.00015 deg/hr. Clearly, this is negligible compared to a 0.01 deg per hr gyro bias in $\delta\underline{\omega}_{IB}^{L}$. The 10 mrad error in $\phi_R$ introduces a heading error in the direction cosine matrix which is also clearly negligible compared to the 1 milliradian heading error developed from $\delta\underline{\omega}_{IB}^{L}$ (Equation (112)). Hence, the effect of vertical gyro drift on initial alignment is negligible as stipulated.

We conclude this lecture with a discussion of the correlation that exists between the errors that are present during navigation (discussed in the last lecture), and the initial alignment errors described in this lecture which also produce navigation error. Since gyro and accelerometer bias directly determine the heading and vertical alignment accuracy, we should expect that these initialization errors and their subsequent propagation into navigation error are strongly related to the direct effects of gyro and accelerometer bias during navigation.

We return to Equations (107) and (112) that define the final alignment errors. In order to differentiate between the navigation and alignment phases of flight, the $C_B^L$ matrix is designated as $C_{B_o}^L$ during alignment (implies a stationary fixed attitude. Note - This is not always true). With this nomenclature and the definition for $\left(\delta\underline{\omega}_{IB}^L\right)_H$ as given in Figure 6, these equations can be written in the equivalent form:

$$\begin{aligned} \left(\underline{\phi}_H^L\right)_o &= \underline{u}_R^L \times \frac{1}{g}\left(C_{B_o}^L\, \delta\underline{a}_o^B\right) \\ \delta\alpha_o &= \frac{1}{\Omega_e \cos l_o}\, \underline{u}_E^L \cdot \left(C_{B_o}^L\, \delta\underline{\omega}_{IB_o}^B\right) \end{aligned} \qquad (113)$$

Where $\underline{u}_E^L$ is a unit vector in the easterly direction as seen in the local level frame (i.e., the indicated dot product is the component of $\delta\underline{\omega}_{IB}^L$ in the east direction as defined algebraically by Equation (112)). The associated error in initializing the D matrix (see Lecture 3) or $\underline{e}^L$ (see previous lecture) is $\delta\alpha_o$ around the vertical direction. Hence,

$$\underline{e}_o^L = \delta\alpha_o\, \underline{u}_R^L = \frac{1}{\Omega_e \cos l_o}\left[\underline{u}_E^L \cdot \left(C_{B_o}^L\, \delta\underline{\omega}_{IB_o}^B\right)\right] \underline{u}_R^L \qquad (114)$$

Let's now return to the basic strapdown navigator error diagram (Figure 2 of the last lecture). With $\underline{e}^L$ initialized as in (114), the initial value of $\delta\underline{\omega}_{IE}^L$ generated during navigation is given by:

$$\delta\underline{\omega}_{IE_0}^L = -\, \underline{e}_o^L \times \underline{\omega}_{IE_o}^L = -\, \frac{1}{\Omega_e \cos l_o}\left[\underline{u}_E^L \cdot \left(C_{B_o}^L\, \delta\underline{\omega}_{IB_o}^B\right)\right]\left(\underline{u}_R^L \times \underline{\omega}_{IE_o}^L\right)$$

Defining $\underline{\omega}_{IE}^L$ as containing north and vertical components, the cross-product term can be expanded as follows:

$$\underline{\omega}_{IE_o}^L = \Omega_e \cos l_o\, \underline{u}_N^L + \Omega_e \sin l_o\, \underline{u}_R^L$$

$$\underline{u}_R^L \times \underline{\omega}_{IE_o}^L = \Omega_e \cos l_o \left(\underline{u}_R^L \times \underline{u}_N^L\right) = -\, \Omega_e \cos l_o\, \underline{u}_E^L$$

where $\underline{u}_N^L$ and $\underline{u}_E^L$ are unit vectors north and east, respectively. The previous development recognizes that the cross-product between unit vectors in the north and vertical directions is a unit vector along an easterly line. Now substituting in the $\delta\underline{\omega}_{IE_o}^L$ equation obtains:

$$\delta\underline{\omega}_{IE_o}^L = \left[\underline{u}_E^L \cdot \left(C_{B_o}^L\ \delta\underline{\omega}_{IB_o}^B\right)\right] \underline{u}_E^L \tag{115}$$

Hence, the effect on the initial wander angle initialization error (initial heading error) is to introduce a rotation rate error in the direction cosine rate equations during the first hour or so of navigation equal to the east component of gyro drift during alignment. From Figure 2, the net effective drift rate in the $\dot{\underline{\phi}}^L$ equation (the sum of the gyro error and $\delta\underline{\omega}_{IE}^L$ terms) is equal to:

$$- C_B^L\ \delta\underline{\omega}_{IB}^B + \left[\underline{u}_E^L \cdot \left(C_{B_o}^L\ \delta\underline{\omega}_{IB_o}^B\right)\right] \underline{u}_E^L$$

If $C_B^L$ equals $C_{B_o}^L$ (i.e., the vehicle attitude during navigation equals its attitude during alignment) and $\delta\underline{\omega}_{IB}^B$ equals $\delta\underline{\omega}_{IB_o}^B$ (no additional gyro errors are introduced as a result of navigation), the net effect of the above expression is to cancel the easterly gyro error effects on navigation error build-up. Since rate errors from the gyros are not constant, the above effect is only partially true. Nevertheless it is an important characteristic of strapdown inertial navigation systems that should be understood, particularly during laboratory testing (i.e., for a stationary system, a large portion of the gyro drift east will be canceled and the predominant error will be north causing an east-west velocity and position error. Gyro random drift masks this effect to some extent).

A similar effect exists from the $\left(\underline{\phi}_H^L\right)_o$ term (Equation (113)). If $\underline{a}^L$ in Figure 2 is approximated by $g\ \underline{u}_R^L$, the cross-product with $\underline{\phi}^L$ in the $\delta\dot{\underline{v}}^L$ equation becomes initially (with (113)):

$$\underline{a}^L \times \underline{\phi}^L \approx g\ \underline{u}_R^L \times \underline{\phi}_o^L = g\ \underline{u}_R^L \times \left(\underline{\phi}_H^L\right)_o = g\ \underline{u}_R^L \times \left[\underline{u}_R^L \times \frac{1}{g}\left(C_{B_o}^L\ \delta\underline{a}_o^B\right)\right] = -\left(C_{B_o}^l\ \delta\underline{a}_o^B\right)_H$$

In Figure 2, this term is added to the acceleration error in the $\delta\dot{\underline{v}}^L$ equation. The sum of the two terms, therefore, is:

$$C_B^L\ \delta\underline{a}^B + \underline{a}^L \times \underline{\phi}^L = C_B^L\ \delta\underline{a}^B - \left(C_{B_o}^L\ \delta\underline{a}_o^B\right)_H$$

As with the gyro drift, the net horizontal effect is zero if the attitude of the vehicle is the same during navigation as during alignment (assuming the accelerometer error remains the same). (The vertical error is not canceled, however, vertical navigation errors are typically clamped by a baro-altimeter in inertial navigation systems). The result is that horizontal navigation error build-up due to accelerometer error in strapdown systems is canceled by the initial vertical alignment error, if the navigation orientation matches the orientation during alignment.  This characteristic is particularly important when interpreting navigation errors in laboratory testing and for system calibration.

## NOTES

# KALMAN FILTERING TECHNIQUES

LECTURE 12

NAV SEMINAR - LECTURE 12 NOTES

This lecture deals with the design of the gains for the alignment filter discussed in the last lecture. The method to be used is the "minimum variance" (Kalman filter) approach which generates "optimal" gains that result in the lowest error (in a statistical) sense for the variables in the estimation loops. In order to develop the gain equations, we return to Figure 6 of the previous lecture and recast the problem into a discrete form for compatibility with the discrete operations of the digital computer performing the alignment function.

To analyze the filter in Figure 6 for optimal gain determination, it is convenient to think of the estimation loop updating process as being composed of two basic steps: (1) The propagation of errors around the loop between filter updates, and (2) The actual measurement and updating of the loop variable estimates through application of the alignment filter gains. These two steps occur on an iterative basis in the digital computer performing the alignment function. The first step is an open loop propagation of the error variables in the estimation loop (i.e., with gains of zero), the second step is an impulsive correction to the variables, occurring at the filter iteration frequency. Step 1 is illustrated in Figure 7.

Comparing Figure 7 to Figure 6, it should be apparent that both are equivalent for zero gains (between filter updates) except that the $\dot{\phi}_R$ portion of the Figure 6 diagram has been eliminated in Figure 7 since its effect is negligible (see previous lecture). To simplify the diagram, Figure 7 only shows the local level versions of the sensor input error ( - $\left(\delta \underline{a}^L\right)_H$ and $\left(\delta \underline{\omega}_{IB}^L\right)_H$). In addition, Figure 7 represents the earth rate estimation error $\left(\delta \underline{\omega}_{IE}^L\right)_H$ as the output of the free integrator (i.e., a constant). From Figure 6, this representation is equivalent to the assumption that $K_\omega$ (the earth rate estimation gain) is zero (between filter updates), and that $\left(\delta \underline{\omega}_{IE}^L\right)_H$ is constant. The latter condition is satisfied because the alignment is being performed at a stationary location.

As discussed in the last lecture, the alignment loop gains are designed to reach steady state conditions rapidly in the presence of random disturbances in the estimation loop. The steady state condition is a function of fixed sensor errors (discussed in the previous lecture) and is independent of the alignment gains. Consequently, in the gain determination analysis, the only error effects that need be considered in Figure 7 are those associated with initial vertical alignment uncertainties, initial earth rate component estimation uncertainties and random noise. The dominant noise sources involved for ring laser gyro strapdown inertial navigation systems are:

- Laser gyro - Laser gyro random noise and pulse quantization error.

- Accelerometer - Accelerometer pulse quantization error.

- Acceleration Disturbances - Vehicle wind buffeting and stores/fuel loading effects that produce random accelerometer outputs.

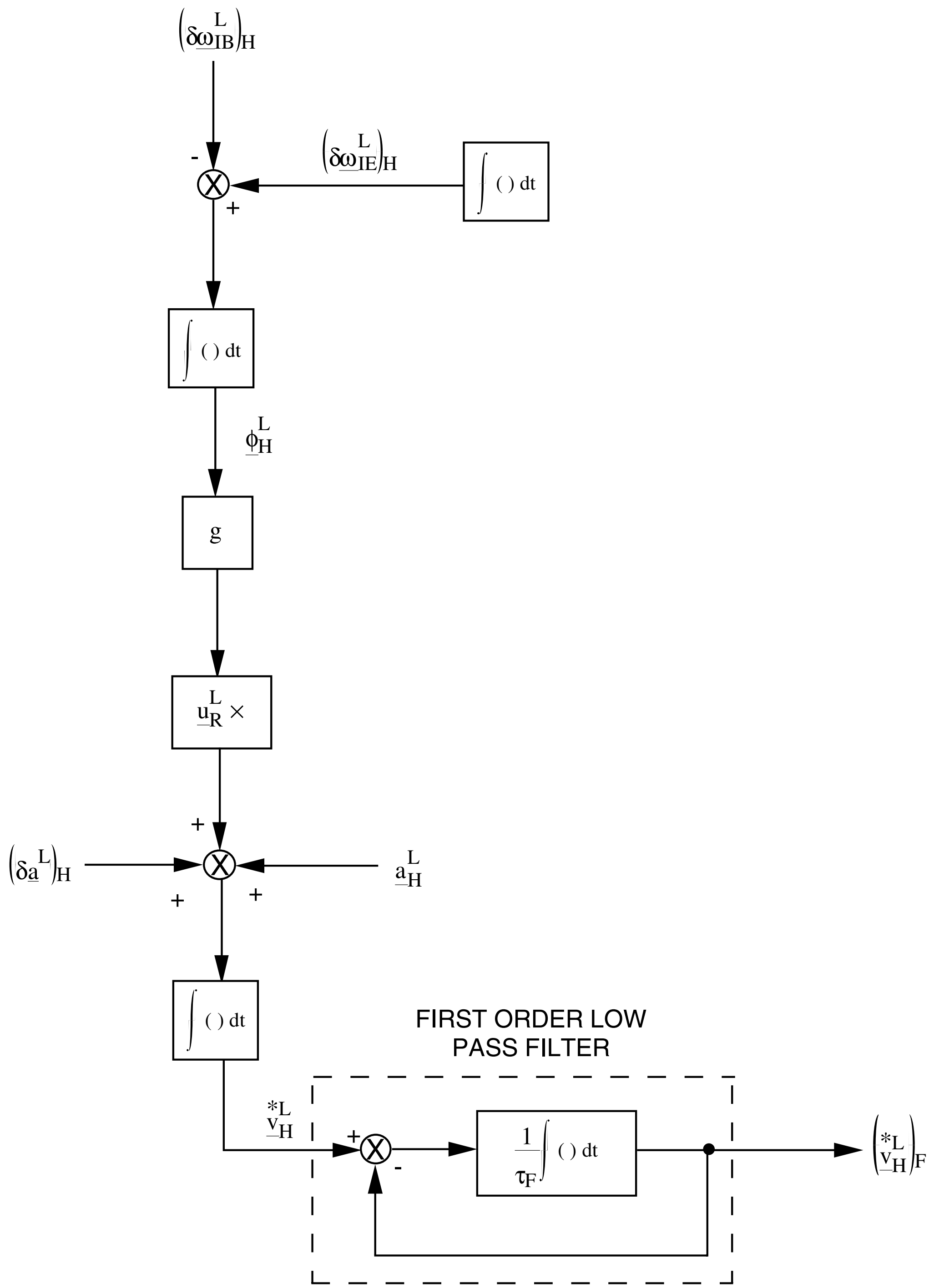


**FIGURE 7 - ERROR PROPAGATION BETWEEN FILTER UPDATES**

These effects can be introduced into the Figure 7 diagram as illustrated in Figure 8. (The i.c. terms in Figure 8 refers to “initial conditions”.) If Figure 8 is compared with Figure 7 it will be noted that gyro random noise ($\underline{n}_{GR}$) is shown as a rate error entering the $\underline{\phi}_H^L$ integrator (as would be expected), but that the gyro quantization noise ($\underline{n}_{GQ}$) sums into the $\underline{\phi}_H^L$ integrator output. A similar effect is to be noted for the accelerometer quantization noise ($\underline{n}_{AQ}$) which sums into the velocity integrator output (rather than the input as may have been expected from Figure 7). Quantization noise is an error associated with the digitization of the sensor output signals. The sensor digitization process is actually an integration process; ie., the digitization outputs represent quantized increments of <u>integrated</u> sensor input. The quantization noise represents the uncertainty in the integrated sensor signal due to the quantization of the digitizer pulse size (i.e., until a pulse is actually output, the integrated sensor signal is only known within a one pulse resolution). The above discussion serves to illustrate that the quantization noise effect is an uncertainty in the knowledge of integrated sensor input, hence, its effect is modeled in Figure 8 as an uncertainty in the integrated sensor signals, or as errors in the $\underline{\phi}_H^L$ and $\underline{v}_H^{*L}$ integrator outputs.

A model has also been incorporated in Figure 8 to account for the dynamics of the vehicle random acceleration motion ($\underline{a}_H^L$). As can be seen in the Figure, $\underline{a}_H^L$ is modeled as a second order response to a disturbance noise ($\underline{n}_D$) representing vehicle acceleration noise due to wind gusts, stores/fuel loading, etc.. The $K_D$, $C_D$ dynamic response constants represent the aircraft/landing gear dynamics associated with “stationary” vehicle response to the dynamic acceleration inputs. As shall be seen subsequently, the model for the vehicle disturbances need only be approximately known, principally to categorize the bandwidth and root-mean-square amplitude characteristics of the disturbance velocity $\underline{v}_H^L$. The simplified second order model in Figure 8 is sufficient for our purposes of determining optimal filter gains.

We now redraw Figure 8 to separate the contributions to $\left(\underline{v}_H^{*L}\right)_F$ (the filtered value of $\underline{v}_H^{*L}$) into two parts: those caused by system errors, and those caused by vehicle disturbances. This separation will be useful later on when we will recognize that the vehicle disturbance effects are only approximately modelable, and not accurately predictable.

Figure 9 is the redrawn version of Figure 8 with the above separation. The output $\left(\underline{v}_H^{*L}\right)_F$ is the input to the filter gains in Figure 6. This signal will hereafter be referred to as “the measurement” for compatibility with optimal estimation theory nomenclature. Upon comparison, it should be clear that Figures 8 and 9 are dynamically equivalent relative to the effects on “the measurement.” The difference between the figures is that the attenuation filter dynamics are shown applied separately to the system and vehicle disturbance inputs in Figure 9 (rather than in total as in Figure 8). The individual

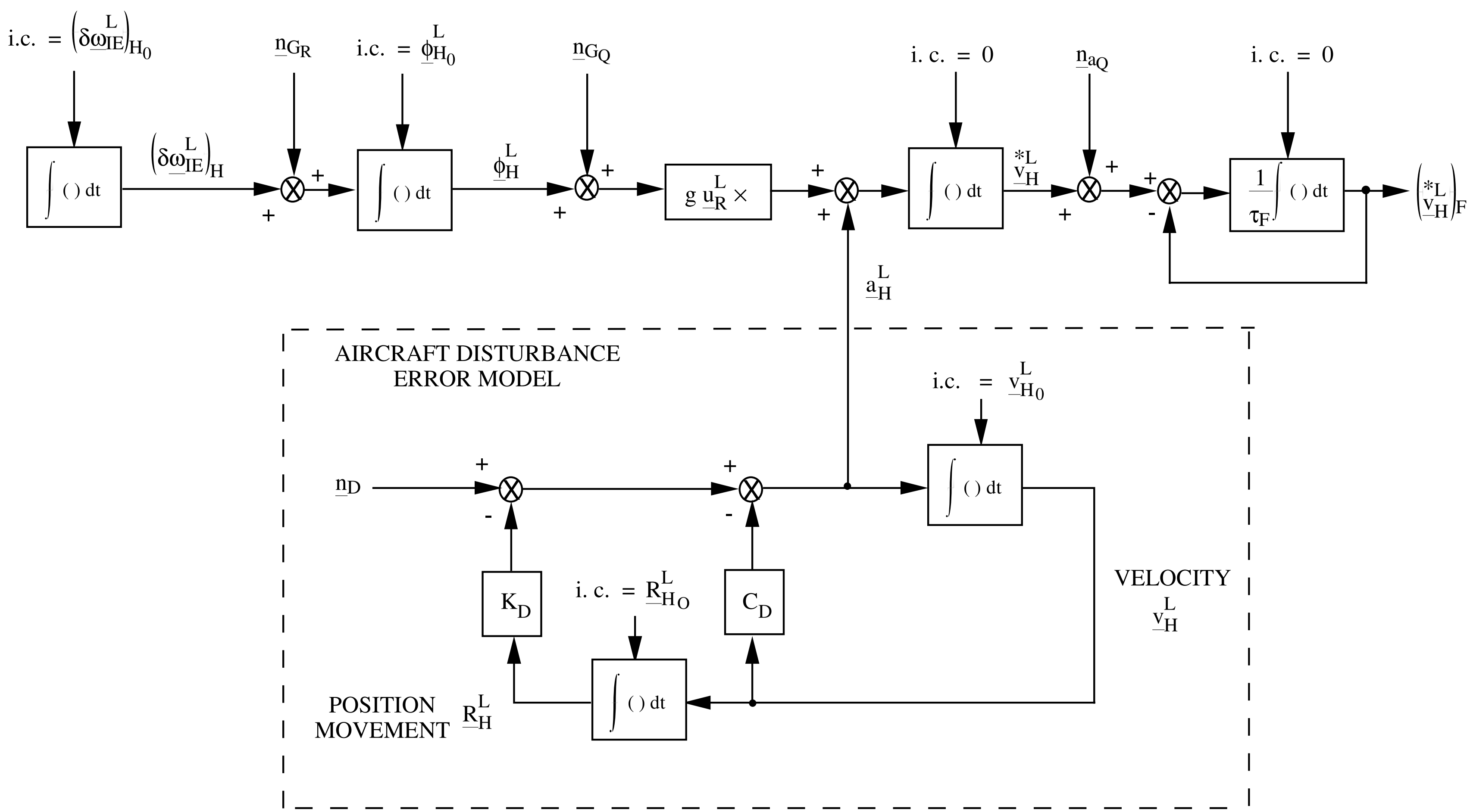


**FIGURE 8 - ALIGNMENT LOOP ERRORS BETWEEN FILTER UPDATES**

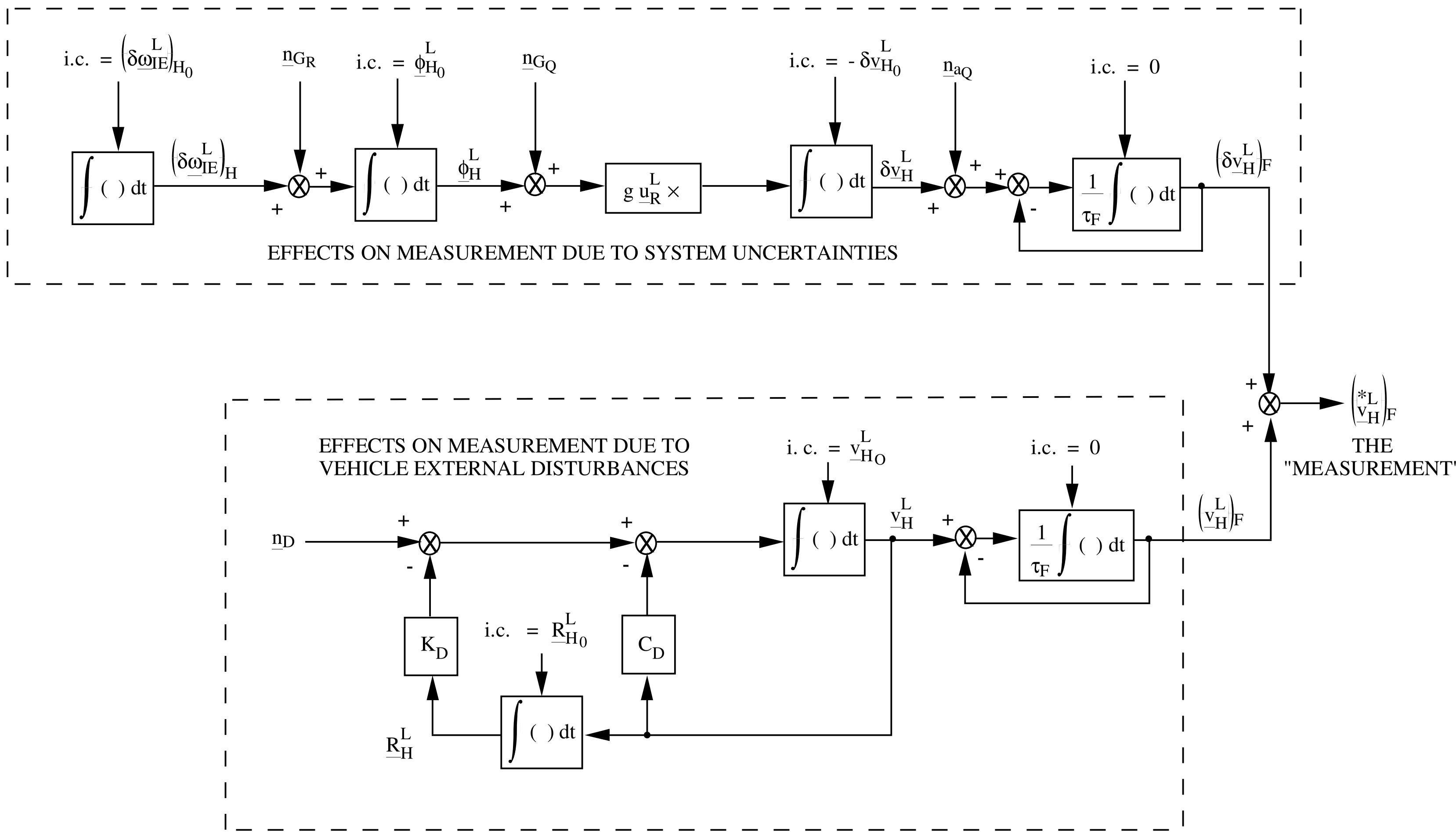


**FIGURE 9 - REVISED ALIGNMENT LOOP ERROR FLOW BETWEEN FILTER UPDATES**

attenuation filter outputs in Figure 9 are denoted as $\left(\delta \underline{v}_H^L\right)_F$ and $\left(\underline{v}_H^L\right)_F$. Their sum is the Figure 8 filter output $\left(\underline{v}_H^{*L}\right)_F$ or the "measurement".

## STATE VECTOR NOTATION

In the analyses to follow, it is convenient to adopt a more compact nomenclature. To do this we first write the differential equations that correspond to Figure 9:

$$\left(\delta \dot{\underline{\omega}}_{IE}^L\right)_H = 0$$

$$\dot{\underline{\phi}}_H^L = \left(\delta \underline{\omega}_{IE}^L\right)_H + \underline{n}_{GR}$$

$$\delta \dot{\underline{v}}_H^L = g\, \underline{u}_R^L \times \left(\underline{\phi}_H^L + \underline{n}_{G_Q}\right)$$

$$\left(\delta \dot{\underline{v}}_H^L\right)_F = \frac{1}{\tau_F}\left[ - \left(\delta \underline{v}_H^L\right)_F + \delta \underline{v}_H^L + \underline{n}_{aQ}\right] \tag{116}$$

$$\dot{\underline{v}}_H^L = - C_D\, \underline{v}_H^L - K_D\, \underline{R}_H^L + \underline{n}_D$$

$$\dot{\underline{R}}_H^L = \underline{v}_H^L$$

$$\left(\dot{\underline{v}}_H^L\right)_F = \frac{1}{\tau_F}\left[ - \left(\underline{v}_H^L\right)_F + \underline{v}_H^L\right]$$

with the "measurement":

$$\left(\underline{v}_H^{*L}\right)_F = \left(\underline{v}_H^L\right)_F + \left(\delta \underline{v}_H^L\right)_F \tag{117}$$

We now define the “state vector” as the vector of dynamic variables being analyzed. Referring to Equations (116), the state vector $\underline{X}$ is defined as:

$$\underline{X} \overset{\Delta}{=} \begin{pmatrix} \left(\delta\underline{\omega}_{IE}^{L}\right)_H \\ \underline{\phi}_H^L \\ \delta\underline{v}_H^L \\ \left(\delta\underline{v}_H^L\right)_F \\ \underline{v}_H^L \\ \underline{R}_H^L \\ \left(\underline{v}_H^L\right)_F \end{pmatrix} \tag{117A}$$

We also define the "process noise" vector $\underline{n}$ as the driving function input to Equations (116):

$$\underline{n} \overset{\Delta}{=} \begin{pmatrix} \underline{n}_{GR} \\ \underline{n}_{GQ} \\ \underline{n}_{aQ} \\ \underline{n}_D \end{pmatrix} \tag{117B}$$

with the associates "state dynamic matrix" A and "process noise dynamic coupling matrix" G defined as:

$$A \overset{\Delta}{=} \begin{bmatrix} 0 & 0 & 0 & 0 & 0 & 0 & 0 \\ 1 & 0 & 0 & 0 & 0 & 0 & 0 \\ 0 & g\left(\underline{u}_R^L \times\right) & 0 & 0 & 0 & 0 & 0 \\ 0 & 0 & \frac{1}{\tau_F} & -\frac{1}{\tau_F} & 0 & 0 & 0 \\ 0 & 0 & 0 & 0 & -C_D & -K_D & 0 \\ 0 & 0 & 0 & 0 & 1 & 0 & 0 \\ 0 & 0 & 0 & 0 & \frac{1}{\tau_F} & 0 & -\frac{1}{\tau_F} \end{bmatrix} \tag{117C}$$

$$G \stackrel{\Delta}{=} \begin{bmatrix} 0 & 0 & 0 & 0 \\ I & 0 & 0 & 0 \\ 0 & g\left(\underline{u}_R^L \times\right) & 0 & 0 \\ 0 & 0 & \frac{1}{\tau_F} I & 0 \\ 0 & 0 & 0 & I \\ 0 & 0 & 0 & 0 \\ 0 & 0 & 0 & 0 \end{bmatrix} \tag{117D}$$

where I is the identity matrix and:

$$\dot{\underline{X}} = A\,\underline{X} + G\,\underline{n} \tag{118}$$

Equation (118) is the equivalent state vector form of Equation (116). Note, that Equation (118) can also be viewed as a general differential equation set where $\underline{X}$, A, $\underline{n}$ and G are arbitrarily selected to represent the particular set of differential equations being analyzed.

We now introduce the concept of a generalized measurement of $\underline{X}$ as an input to an estimation filter (in our case, the alignment filter). Denoting the measurement vector as $\underline{Z}$, we define:

$$\underline{Z} = H\,\underline{X} + \underline{v} \tag{119}$$

where H is the "measurement matrix" that defines the combination of $\underline{X}$ elements that comprises the "measurement", and $\underline{v}$ is the “measurement noise” vector. The measurement noise is defined as the noise introduced in the process of making the measurement. For our case (Equation (117)), the measurement vector is:

$$\underline{Z} = \left(\underline{v}_H^L\right)_F + \left(\delta\underline{v}_H^L\right)_F \tag{119A}$$

so that, with the definition of $\underline{X}$ given previously (and (119)):

$$H = \begin{bmatrix} 0 & 0 & 0 & I & 0 & 0 & I \end{bmatrix} \tag{119B}$$

Equation (117) shows that our model has zero measurement noise. To keep the analysis a little more general, however, we will utilize Equation (119) with $\underline{v}$ included. If you like, you can consider $\underline{v}$ as computer round-off error associated with $\left(\underline{v}_H^{*L}\right)$ in (117). This is a legitimate measurement noise effect (however, in reality, it is small, and negligible in our case compared, for example, with $\underline{v}_H^L$).

## DISCRETE PROPAGATION EQUATION FORM

Equations (118) and (119) define the propagation of the state vector variables between filter updates, and the associated measurement for the filter at the time of update. Let us now recast the differential state vector propagation Equation (118) into its equivalent discrete form for compatibility with discrete computer operations. To do this, we define $\underline{X}$ after the last filter update as $\underline{X}_{n-1}$, and $\underline{X}$ just before the current filter update as $\underline{X}_n$. The equivalent discrete form of (118) relates $\underline{X}_n$ to $\underline{X}_{n-1}$ and is given by:

$$\underline{X}_n = F_n \, \underline{X}_{n-1} + \underline{w}_n \tag{120}$$

In Equation (120), $F_n$ is called the "state transition matrix." $F_n$ represents the normalized homogeneous solution to Equation (118) (i.e., with $\underline{n}$ zero) at the current time ($t_n$) due to unity initial conditions at the last filter update (at $t_{n-1}$). Multiplication by the known initial conditions at $t_{n-1}$ (namely $\underline{X}_{n-1}$) generates the contribution to $\underline{X}_n$ due to the dynamic propagation of $\underline{X}_{n-1}$ through Equation (118). The $\underline{w}_n$ term in (120) represents the particular solution to (118) created by $\underline{n}$ acting over the interval from $t_{n-1}$ to $t_n$. It can be shown that $F_n$ and $\underline{w}_n$ are related to the Equation (118) terms through:

$$\dot{F}(t,\ \tau) = A\,F(t,\ \tau) \qquad\qquad F(\tau, \tau) = I$$

$$F_n = F\left(t_n, t_{n-1}\right) \tag{120A}$$

$$\underline{w}_n = \int_{t_{n-1}}^{t} F\left(t_n, \tau\right) G(\tau)\, \underline{n}(\tau)\, d\tau$$

$F_n$ is the solution to the differential equation given above at $t_n$ with unity matrix initial conditions at $t_{n-1}$. Time $\tau$ in the above expressions is an arbitrary time in the interval $t_{n-1}$ to $t_n$. The $\underline{w}_n$ vector is the integrated effect at time $t_n$ of differential changes in $\underline{X}$ created at time $\tau$ by $\underline{n}$ acting over the differential time $d\tau$. Multiplication of $G(\tau)\, \underline{n}(\tau)\, d\tau$ by $F\left(t_n, \tau\right)$ translates the resulting change in $\underline{X}$ at $\tau$ to its effect at $t_n$ (i.e., accounts for the dynamical propagation of $d\underline{X}(\tau)$ through the dynamics of differential Equation (118)).

Equation (120) is the discrete form of Equation (118) that relates $\underline{X}$ between discrete filter update times $t_{n-1}$ and $t_n$. The measurement Equation (119) can be similarly stated as a measurement at discrete (n) times. Hence, the discrete model for the propagation dynamics between updates and the measurement can be summarized as:

$$\underline{X}_n = F_n \, \underline{X}_{n-1} + \underline{w}_n$$
$$\underline{Z}_n = H_n \, \underline{X}_n + \underline{v}_n \qquad (121)$$

GENERALIZED FILTER STRUCTURE

Let us now synthesize a generalized updating equation for the alignment filter based on the application of a generalized gain matrix to the measurement $\underline{Z}$. The result will ultimately be the filter gain matrix utilized by the alignment filter to correct $\underline{X}$ for the current iteration cycle. In developing the generalized updating equation, however, let us generalize a little bit further so that our results will be applicable to a broader class of applications. To do this, we introduce the concept of an "estimate" as contrasted with a "reset." An "estimate" is an estimation of the state vector $\underline{X}$ based on the measurement $\underline{Z}$ and past estimates of $\underline{X}$. A "reset" is the modification of $\underline{X}$ based on the estimate. For our case, since we wish $\underline{X}$ to be zero, the reset is simply a subtraction of the $\underline{X}$ estimate from the computer quantities containing the $\underline{X}$ error (e.g., $C_B^L$ and $\underline{v}_H^L$. See Figure 5 of the last lecture). Hence, for this case, the estimated value of $\underline{X}$ becomes zero after the reset is applied. For some applications, it may not be possible to directly reset some of the $\underline{X}$ elements, or it may not be desirable to reset them to zero (e.g., control to a specified offset condition may be required). To be more general, let us assume that $\underline{X}$ is updated as a result of the $\underline{X}$ estimate by a general filter control variable $\underline{u}$ which we will select to fit the requirements of the particular problem being analyzed. Hence, we can write that the effect of the filter on $\underline{X}$ at each update time is to modify $\underline{X}$ as:

$$\underline{X} = \underline{X} + \underline{u}$$

where $\underline{u}$ is the control variable based on filter measurements and other system constraints. Hence, (121) becomes the modified form:

$$\underline{X}_n = F_n \, \underline{X}_{n-1} + F_n \, \underline{u}_{n-1} + \underline{w}_n$$
$$\underline{Z}_n = H_n \, \underline{X}_n + \underline{v}_n \qquad (122)$$

Equation (122) includes the effect of system dynamics ($F_n$) translating the control change in $\underline{X}$ applied at $t_{n-1}$ ($\underline{u}_{n-1}$) to present time $t_n$, just prior to the $t_n$ filter update cycle.

We now introduce the concept of the "estimate" of $\underline{X}$ and the associated generalized estimation and control equations:

$\overset{*}{\underline{X}}_n(-)$ = The estimate for $\underline{X}_n$ at the measurement time $t_n$

$\overset{*}{\underline{X}}_n(+)$ = The improved estimate for $\underline{X}_n$ due to processing the measurement $\underline{Z}_n$ in the estimation filter we will be synthesizing.

We now synthesize the generalized estimation and control equations to be:

$$\underline{u}_{n-1} = f(\overset{*}{\underline{X}}_{n-1}(+) \text{ and other command constraints})$$

$$\overset{*}{\underline{X}}_n(-) = F_n \overset{*}{\underline{X}}_{n-1}(+) + F_n \underline{u}_{n-1}$$

$$\overset{*}{\underline{Z}}_n = H_n \overset{*}{\underline{X}}_n(-) \qquad (123)$$

$$\overset{*}{\underline{X}}_n(+) = \overset{*}{\underline{X}}_n(-) - K_n \left(\overset{*}{\underline{Z}}_n - \underline{Z}_n\right)$$

where

$\overset{*}{\underline{Z}}_n$ = The estimate for $\underline{Z}_n$

$K_n$ = Generalized estimation gain matrix.

If (123) is compared with (122), the principal for the filter structure should be apparent. The estimate for $\underline{X}_n$ before the $t_n$ update ( $\overset{*}{\underline{X}}_n(-)$) is based on the value after the last update ( $\overset{*}{\underline{X}}_{n-1}(+)$) modified by the state transition matrix, plus the transition effect at $t_n$ of the control vector $\underline{u}_{n-1}$ applied at $t_{n-1}$ (after the last update). The $\underline{u}_{n-1}$ vector is indicated to be a function of the best estimate of $\underline{X}$ after the last update ( $\overset{*}{\underline{X}}_{n-1}(+)$ ) plus some other command constraints peculiar to the particular problem at hand. From Equation (122), the $\overset{*}{\underline{X}}_n(-)$ equation in (123) is clearly the best estimate for $\underline{X}$ at $t_n$ based on all available information. Since $\underline{w}_n$ is an unknown random vector in (122), its presence cannot be accounted for in (123) prior to the $t_n$ measurement $\underline{Z}_n$. Hence, the $\overset{*}{\underline{X}}_n(-)$ estimation equation does not include the effect of $\underline{w}_n$ in (122) (i.e., our best estimate is to assume it is zero or equally likely to be any positive or negative value). The $\underline{Z}_n$ measurement provides the additional information needed at $t_n$ to improve the $\overset{*}{\underline{X}}_n(-)$ estimate. The estimate for $\underline{Z}_n$ (i.e., $\overset{*}{\underline{Z}}_n$) in (123) is what we would expect $\underline{Z}_n$ to be (see Equation (122)) based on our best estimate of $\underline{X}$ when we make the $\underline{Z}_n$ measurement ( $\overset{*}{\underline{X}}_n(-)$). Since $\underline{Z}_n$ contains unpredictable measurement noise ($\underline{v}_n$), and because $\overset{*}{\underline{X}}_n(-)$ will differ from $\underline{X}_n$ due to estimation errors, $\overset{*}{\underline{Z}}_n$ will also differ from $\underline{Z}_n$. The difference between $\overset{*}{\underline{Z}}_n$ and $\underline{Z}_n$

in Equations (123) is our measure of the accuracy in the estimation of $\underline{X}$. Hence, the measurement "residual" ($\overset{*}{\underline{Z}}_n$ - $\underline{Z}_n$) is utilized in a negative feedback sense to update the $\overset{*}{\underline{X}}$ estimate (generate $\overset{*}{\underline{X}}_n(+)$). The gain matrix $K_n$ amplifies and distributes the feedback into the $\overset{*}{\underline{X}}$ elements to achieve some degree of optimality in the revised estimate (to be discussed subsequently). The above sequence is summarized in Figure 10 (refer to Equations (122) and (123)).

Note, in Figure 10 that if the control law is for $\underline{u}_{n-1}$ to equal the negative of the $\underline{X}$ estimate ($\underline{u}_{n-1} = - \overset{*}{\underline{X}}_{n-1}$), the revised estimate for $\underline{X}$ (after application of $\underline{u}_{n-1}$) will be zero (i.e., the best estimate for $\underline{X}$ will be controlled to zero). Under these conditions, the $F_n$ and $H_n$ feedback paths in the filter portion of Figure 9 become zero. The result is that the $\underline{Z}_n$ measurement through the $K_n$ gain becomes fed back directly to control the real $\underline{X}$ process equations. This is the configuration we will ultimately use in the alignment problem for the error parameters in the error state vector ($\left(\delta\underline{\omega}_{IE}^{L}\right)_H$, $\underline{\phi}_H^L$, $\delta\underline{v}_H^L$, $\left(\delta\underline{v}_H^L\right)_F$ as in Figure 6). For now, we will retain the Figure 10 $\underline{u}_{n-1}$ control law configuration for generality.

## OPTIMAL GAIN DETERMINATION

The filter design problem is to select the gain matrix in Equations (123) (and Figure 10) such that the error in our estimate of $\underline{X}$ is minimized in a statistical sense. More specifically, we seek a gain matrix that will minimize the variance in the error in $\overset{*}{\underline{X}}$ after each update. To formulate the problem mathematically, we first define the estimation error as simply:

$$\Delta\underline{X} \overset{\Delta}{=} \overset{*}{\underline{X}} - \underline{X}$$

At time $t_n$, using the notation of the previous section, the estimation error before and after the update is:

$$\Delta\underline{X}_n(-) = \overset{*}{\underline{X}}_n(-) - \underline{X}_n$$

$$\Delta\underline{X}_n(+) = \overset{*}{\underline{X}}_n(+) - \underline{X}_n$$

We now also define the covariance matrix associated with $\Delta\underline{X}_n$ as:

$$P_n \overset{\Delta}{=} E\left(\Delta\underline{X}_n \, \Delta\underline{X}_n^T\right)$$

where

E = The expected value operator (i.e., average statistical value)

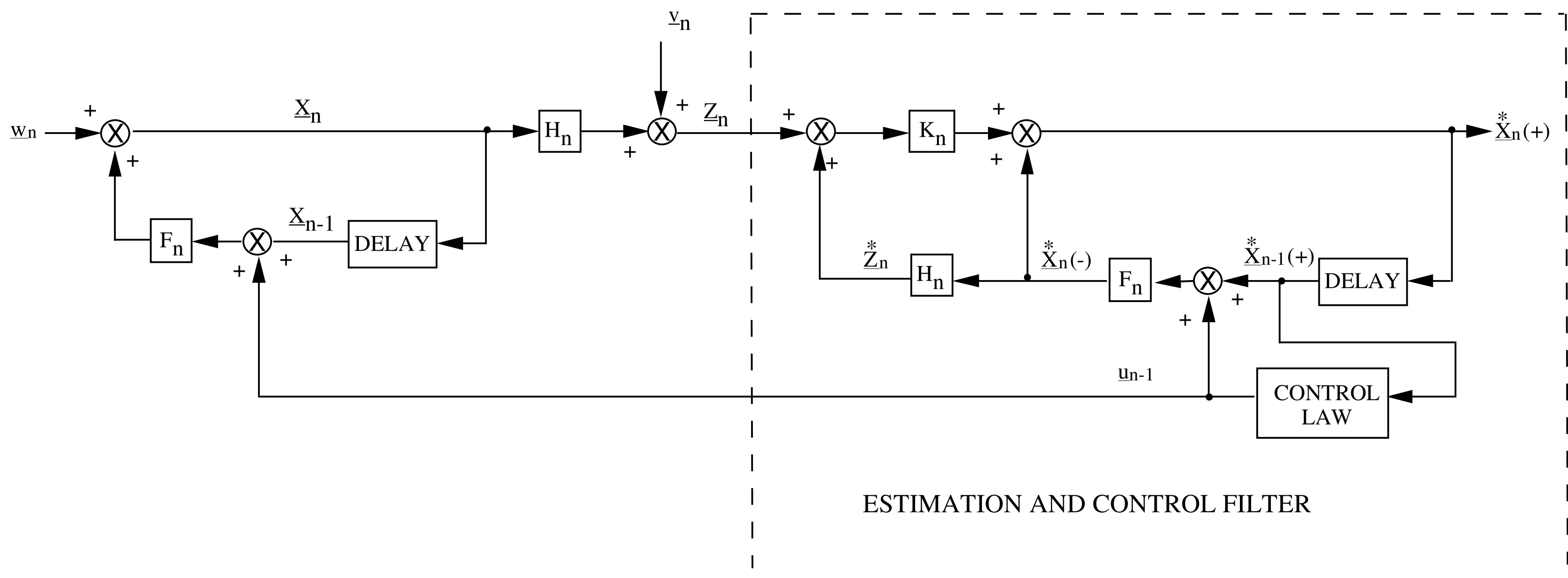


**FIGURE 10 - GENERALIZED DISCRETE FILTER STRUCTURE**

Expanding the $P_n$ definition finds:

$$P_n = \begin{bmatrix} E\left(\Delta X_1^2\right) & E\left(\Delta X_1\,\Delta X_2\right) & E\left(\Delta X_1\,\Delta X_3\right) & \cdots \\ E\left(\Delta X_2\,\Delta X_1\right) & E\left(\Delta X_2^2\right) & E\left(\Delta X_2\,\Delta X_3\right) & \cdots \\ E\left(\Delta X_3\,\Delta X_1\right) & E\left(\Delta X_3\,\Delta X_2\right) & E\left(\Delta X_3^2\right) & \cdots \\ \vdots & \vdots & \vdots & \end{bmatrix}_n$$

where

$\Delta X_1, \Delta X_2$, etc. = The elements of $\Delta\underline{X}$.

The above expression for P shows that the diagonal elements equal the variances for the elements of $\Delta\underline{X}$ (i.e., the mean squared values) and the off-diagonal terms equal the covariances. It should also be apparent that $P_n$ is a symmetrical matrix, hence, it equals its transpose:

$$P_n^T = P_n \tag{124}$$

The covariance matrix concept has been introduced as the measure of uncertainty in $\overset{*}{\underline{X}}_n$ (i.e., the statistics of its error characteristics). The basis for selecting the gain matrix $K_n$ in Equations (123) will be to minimize $P_n$ after the update. We now return to Equations (123) to derive an expression for $P_n(+)$ ($P_n$ after the update) in terms of $P_n(-)$ ($P_n$ before the update), the statistics of the measurement noise, and the general gain matrix $K_n$.

We begin by subtracting $\underline{X}_n$ from both sides of the Equations (123) update expression and introduce (122) for $\underline{Z}_n$:

$$\begin{aligned} \overset{*}{\underline{X}}_n(+) - \underline{X}_n &= \overset{*}{\underline{X}}_n(-) - \underline{X}_n + K_n\left(H_n\,\underline{X}_n + \underline{v}_n - H_n\,\overset{*}{\underline{X}}_n(-)\right) \\ &= \overset{*}{\underline{X}}_n(-) - \underline{X}_n - K_n\,H_n\left(\overset{*}{\underline{X}}_n(-) - \underline{X}_n\right) + K_n\,\underline{v}_n \end{aligned}$$

Introducing the definition for the estimation error $\Delta\underline{X}$ as given previously:

$$\begin{aligned} \Delta\underline{X}_n(+) &= \Delta\underline{X}_n(-) - K_n\,H_n\,\Delta\underline{X}_n(-) + K_n\,\underline{v}_n \\ &= \left(I - K_n\,H_n\right)\Delta\underline{X}_n(-) + K_n\,\underline{v}_n \end{aligned} \tag{124A}$$

We now utilize the definition for the $\Delta\underline{X}$ covariance matrix to develop the statistical equivalent of the above.

$$P_n(+) \overset{\Delta}{=} E\left(\Delta\underline{X}_n(+)\,\Delta\underline{X}_n(+)^T\right)$$

Substituting for $\Delta\underline{X}_n(+)$ and expanding:

$$\begin{aligned}
P_n(+) &= E\left\{\left[\left(I - K_n H_n\right)\Delta\underline{X}_n(-) + K_n\,\underline{v}_n\right]\left[\left(I - K_n H_n\right)\Delta\underline{X}_n(-) + K_n\,\underline{v}_n\right]^T\right\} \\
&= E\left[\left(I - K_n H_n\right)\Delta\underline{X}_n(-)\,\Delta\underline{X}_n^T(-)\left(I - K_n H_n\right)^T\right] \\
&\quad + E\left(K_n\,\underline{v}_n\,\underline{v}_n^T\,K_n^T\right) + E\left[\left(I - K_n H_n\right)\Delta\underline{X}_n(-)\,\underline{v}_n^T\,K_n^T\right] \\
&\quad + E\left[K_n\,\underline{v}_n\,\Delta\underline{X}_n^T(-)\left(I - K_n H_n^T\right)\right] \\
&= \left(I - K_n H_n\right)E\left(\Delta\underline{X}_n(-)\,\Delta\underline{X}_n^T(-)\right)\left(I - K_n H_n\right)^T + K_n\,E\left(\underline{v}_n\,\underline{v}_n^T\right)K_n^T \\
&\quad + \left(I - K_n H_n\right)E\left(\Delta\underline{X}_n(-)\,\underline{v}_n^T\right)\underline{K}_n^T + K_n\,E\left(\underline{v}_n\,\Delta\underline{X}_n^T(-)\right)\left(I - K_n H_n\right)^T
\end{aligned}$$

The $E\left(\Delta\underline{X}_n(-)\,\Delta\underline{X}_n^T(-)\right)$ expression above should be recognized as the $\Delta\underline{X}$ covariance matrix prior to the update $P_n(-)$. The $E\left(\underline{v}_n\,\underline{v}_n^T\right)$ expression is defined as the measurement noise covariance matrix:

$$R_n \overset{\Delta}{=} E\left(\underline{v}_n\,\underline{v}_n^T\right) \tag{124B}$$

In order to evaluate the $\Delta\underline{X}_n(-)$, $\underline{v}_n$ product terms we have to specify the correlation characteristics of the measurement noise $\underline{v}_n$. We assume that $\underline{v}_n$ is a "white" sequence (in n) (i.e., $\underline{v}$ at $t_n$ is uncorrelated with $\underline{v}$ at any other time $t_m$). Mathematically:

$$E\left(\underline{v}_n\,\underline{v}_m^T\right) = R_n\,\delta_{nm}$$

where

$\delta_{nm}$ is the Kronecker that, by definition, satisfies:

$$\begin{aligned}
\delta_{nm} &= 0 \quad \text{for } n \neq m \\
&= 1 \quad \text{for } n = m
\end{aligned}$$

Since $\underline{v}_n$ is uncorrelated from past values of $\underline{v}_m$, past measurements ($\underline{Z}_n$) are uncorrelated with $\underline{v}_n$. Since the past measurements were used to generate $\overset{*}{\underline{X}}_n(-)$ (see Figure 10), we can conclude that $\overset{*}{\underline{X}}_n(-)$ is also uncorrelated with $\underline{v}_n$. Hence:

$$E\left(\underline{v}_n\, \Delta\underline{X}_n^T(-)\right) = 0$$

$$E\left(\underline{v}_n\, \Delta\underline{X}_n^T(-)\right) = 0$$

With the latter results, the previous covariance update equation becomes the simplified form:

$$P_n(-) = \left(I - K_n H_n\right) P_n(-) \left(I - K_n H_n\right)^T + K_n R_n K_n^T \tag{125}$$

Equation (125) relates the uncertainty in $\overset{*}{\underline{X}}$ after the update with the uncertainty before the update as a result of applying an update using $K_n$ with a measurement containing noise. The $\overset{*}{\underline{X}}$ uncertainty is represented by the covariance matrix $P_n$ and the noise characteristics of the measurement are contained in the $R_n$ covariance matrix.

We can now pose the $K_n$ design problem as the selection of $K_n$ to minimize $P_n(+)$ (i.e., to minimize the uncertainty in $\overset{*}{\underline{X}}$ after the update, or equivalently, minimize the variance of the error in $\overset{*}{\underline{X}}$ after the update).

To determine the optimal $K_n$ that minimizes $P_n(+)$ in (125), we first expand (125) as follows:

$$\begin{aligned}
P_n(+) &= P_n(-) - K_n H_n P_n(-) - P_n(-) \left(K_n H_n\right)^T \\
&\qquad + K_n H_n P_n(-) \left(K_n H_n\right)^T + K_n R_n K_n^T \\
&= P_n(-) + K_n \left(H_n P_n(-) H_n^T + R_n\right) K_n^T \\
&\qquad - K_n \left(P_n^T(-) H_n^T\right) - P_n(-) H_n^T K_n^T \\
&= P_n(-) + K_n \left(H_n P_n(-) H_n^T + R_n\right) K_n^T \\
&\qquad - K_n \left(P_n(-) H_n^T\right)^T - P_n(-) H_n^T K_n^T
\end{aligned}$$

In the previous expression, the substitution of $P_n(-)$ equaling its transpose (Equation (124)) was made. In order to simplify the algebra to follow we define $A_n$ and $B_n$ as the coefficients in the latter equation:

$$\begin{aligned}
A_n &\overset{\Delta}{=} H_n P_n(-) H_n^T + R_n \\
B_n &\overset{\Delta}{=} P_n(-) H_n^T
\end{aligned} \tag{126}$$

so that:

$$P_n(+) = P_n(-) + K_n A_n K_n^T - K_n B_n^T - B_n K_n^T \quad (127)$$

We now make an observation on the form of (127) as contrasted, for example, with a term of the form:

$$\left(K_n - D_n\right) C_n \left(K_n - D_n\right)^T = K_n C_n K_n^T - K_n C_n D_n^T - D_n C_n K_n^T + D_n C_n D_n^T$$

or, for $C_n$ symmetrical such that $C_n = C_n^T$:

$$\begin{aligned} &\left(K_n - D_n\right) C_n \left(K_n - D_n\right)^T \\ &\qquad = K_n C_n K_n^T - K_n \left(D_n C_n\right)^T - D_n C_n K_n^T + D_n C_n D_n^T \end{aligned} \quad (128)$$

If (127) is compared with (128) it should be clear that the two are identical in form, except for the $D_n C_n D_n^T$ and $P_n$ (-) terms. That is, for $C_n$ and $D_n$ defined as follows, the two expressions are equivalent if (127) is corrected for $P_n(-)$ and $D_n C_n D_n^T$.

$$\begin{aligned} C_n &= A_n \\ D_n C_n &= B_n \end{aligned} \quad (129)$$

or

$$D_n = B_n C_n^{-1} = B_n A_n^{-1}$$

We must now check that $C_n = A_n$ is symmetrical since the expansion form (128) assumed this. A look at (126) reveals that this is indeed the case. $A_n$ is composed of a symmetrical matrix (the covariance matrix $R_n$) plus a symmetrical matrix ($P_n(-)$) modified by $H_n$ and $H_n^T$. It is easily verified that $H_n P_n(-) H_n^T$ is symmetrical by proving that it equals its transpose:

$$\left(H_n P_n(-) H_n^T\right)^T = H_n P_n(-)^T \ H_n^T = H_n P_n (-) H_n^T$$

Hence, since both elements of $A_n$ are symmetrical, $A_n$ is symmetrical. We now use (129) to rewrite (127) as:

$$P_n(+) = P_n(-) + K_n C_n K_n^T - K_n \left(D_n C_n\right)^T - D_n C_n K_n^T$$

which, with the (128) identity is:

$$P_n(+) = P_n(-) + \left(K_n - D_n\right) C_n \left(K_n - D_n\right)^T - D_n C_n D_n^T$$

With (129),

$$P_n(+) = P_n(-) - B_n \left(B_n A_n^{-1}\right)^T + \left(K_n - B_n A_n^{-1}\right) A_n \left(K_n - B_n A_n^{-1}\right)^T \qquad (130)$$

Equation (130) is in a form that can now be used to define the optimum $K_n$ that minimizes $P_n(+)$ by inspection. Before this is done, however, the properties of the last term must be understood. The form of this term is similar to the $P_n$ term in $A_n$ Equation (126) discussed previously. We will soon show that this expression always has positive terms along the diagonal. Hence, since it is added to $P_n(-)$ in (130) to form $P_n(+)$, it increases the magnitude of the diagonal elements in $P_n$. Since the diagonal elements in $P_n$ represent the variances of the $\overset{*}{\underline{X}}$ element errors, we wish the diagonal elements in $P_n(+)$ to be minimized through the updating process. Since the last term in (130) only increases $P_n(+)$, and since $K_n$ only appears in this term in the $P_n(+)$ equation, we can conclude that the optimum value for $K_n$ that minimizes $P_n(+)$ is that value that sets the last term in (130) to zero. From (130), this value is seen by inspection to be:

$$K_n = B_n A_n^{-1}$$

or with (126):

$$K_n = P_n(-) H_n^T \left(H_n P_n(-) H_n^T + R_n\right)^{-1} \qquad (131)$$

Equation (131) is the optimal gain which will generate a minimum variance estimate for $\overset{*}{\underline{X}}$ after the update is applied (as specified in Equation (123) and Figure 10).

It is noted in passing, that if the gain for the filter is calculated according to Equation (131), Equation (125) for Pn(+) can be simplified by expansion and substitution. Beginning with the analytical expansion following Equation (125), and substituting (131):

$$\begin{aligned} P_n(+) &= P_n(-) + K_n \left(H_n P_n(-) H_n^T + R_n\right) K_n^T - K_n \left(P_n(-) H_n^T\right)^T - P_n(-) H_n^T K_n^T \\ &= P_n(-) + P_n(-) H_n^T K_n^T - K_n \left(P_n(-) H_n^T\right)^T - P_n(-) H_n^T K_n^T \\ &= P_n(-) - K_n \left(P_n(-) H_n^T\right)^T \end{aligned}$$

Expanding the transposed term in brackets and recognizing that $P_n(-)$ equals its transpose yields:

$$P_n(+) = P_n(-) - K_n H_n P_n(-)$$

or

$$P_n(+) = \left(I - K_n H_n\right) P_n(-) \qquad (131A)$$

Equation (131A) is equivalent to Equation (125) for cases where $K_n$ satisfies Equation (131). In applying (131A), it is important to recognize that it is based on an exact application (and computation) of (131). For the more general case where $K_n$ is not exactly calculated according to the optimal (131) expression, Equation (125) should be used. For the development to follow, Equation (125) is used in general throughout (although (131A) could have been used in some instances to simplify the equations).

We now go back a step and prove that the last term in (130) does indeed always have positive diagonal elements as stipulated in our logic for selecting $K_n$. If we define the $K_n - B_n A_n^{-1}$ term as $G_n$ for simplicity, the last term in (130) is, with (126):

$$\begin{aligned}
&\left(K_n - B_n A_n^{-1}\right) A_n \left(K_n - B_n A_n^{-1}\right)^T \\
&\qquad = G_n A_n G_n^T = G_n \left(H_n P_n(-) H_n^T + R_n\right) G_n^T \\
&\qquad = G_n H_n P_n(-) H_n^T G_n^T + G_n R_n G_n^T \\
&\qquad = G_n H_n P_n(-) \left(G_n H_n\right)^T + G_n R_n G_n^T
\end{aligned}$$

Each of the two terms in the above expression consists of a covariance matrix ($P_n(-)$ or $R_n$) pre and post multiplied by a matrix and its transpose. Let's look at the $G_n R_n G_n^T$ term as an example and reintroduce the definition for $R_n$:

$$G_n R_n G_n^T = G_n E\left(\underline{v}_n \underline{v}_n^T\right) G_n^T = E\left[\left(G_n \underline{v}_n\right)\left(G_n \underline{v}_n\right)^T\right]$$

The $G_n \underline{v}_n$ term in the above expression is also a vector (say $\underline{Y}_n$) so that

$$G_n R_n G_n^T = E\left(\underline{Y}_n \underline{Y}_n^T\right)$$

If the above expression is expanded in component form (as we did for $P_n$ previously) it will be obvious that the diagonal elements are the variances (or mean squared values) of the $\underline{Y}_n$ elements. Hence, the diagonal elements are positive. A similar argument also applies for the $G_n H_n P_n(-) \left(G_n H_n\right)^T$ term, hence, its diagonal elements are also positive. It is concluded that the sum of these terms (the last term in (130)) must, therefore, also have positive diagonal elements, thereby, validating the assumption used previously in selecting $K_n$.

In order to use (131) to determine $K_n$, we must know the values of $H_n$, $R_n$, and $P_n(-)$. The former two matrices represent our basic understanding of the measurement process; they represent the model for the measurement and the measurement noise. The last term ($P_n(-)$) is a dynamic variable that is the result of past filter updates since the filtering process was initiated. In order to determine the value for $P_n(-)$ we must keep track of these changes in $P_n$ that have been accrued over past filtering cycles. Changes in $P_n$ occur from three sources: 1. The filtering updating operation (as defined by Equation (125)), 2. The change in $P_n$ between filter update cycles due to the dynamical interaction between the state vector elements, and 3. The effect of integrated process noise on the actual $\underline{X}$

vector that is unknown by the filter between measurements (see Equations (122)). We will now derive an equation for the second and third effects.

Equation (125) defines the change in $P_n$ over an update cycle ($P_n(+)$ as a function of $P_n(-)$). What we now seek is an expression for $P_n(-)$ in terms of $P_n$ after the last filter update ($P_{n-1}(+)$). To do this we return to Equations (123) and concentrate on the expression defining the estimate of $\underline{X}$ before the update $\overset{*}{\underline{X}}_n(-)$ in terms of the estimate for $\underline{X}$ after the last update $\overset{*}{\underline{X}}_n(+)$. The covariance matrix propagation associated with this relationship is the equation we desire, linking $P_n(-)$ to $P_{n-1}(+)$. From Equations (123), the estimate for $\overset{*}{\underline{X}}_n(-)$ is:

$$\overset{*}{\underline{X}}_n(-) = F_n \overset{*}{\underline{X}}_{n-1}(+) + F_n \underline{u}_{n-1}$$

From (122), the actual $\underline{X}$ vector expression over the same interval is:

$$\underline{X}_n = F_n \underline{X}_{n-1} + F_n \underline{u}_{n-1} + \underline{w}_n$$

Subtracting the latter two expressions yields:

$$\overset{*}{\underline{X}}_n(-) - \underline{X}_n = F_n (\overset{*}{\underline{X}}_{n-1}(+) - \underline{X}_{n-1}) - \underline{w}_n$$

or, with the definition for the estimation error $\Delta\underline{X}$,

$$\Delta\underline{X}_n(-) = F_n \Delta\underline{X}_{n-1}(+) - \underline{w}_n \tag{131B}$$

The covariance matrix expression associated with the latter equation is:

$$\begin{aligned} P_n(-) &= E\left(\Delta\underline{X}_n(-)\, \Delta\underline{X}_n^T(-)\right) \\ &= E\left[\left(F_n \Delta\underline{X}_{n-1}(+) - \underline{w}_n\right)\left(F_n \Delta\underline{X}_{n-1}(+) - \underline{w}_n\right)^T\right] \\ &= F_n E\left(\Delta\underline{X}_{n-1}(+)\, \Delta\underline{X}_{n-1}^T(+)\right) F_n^T + E\left(\underline{w}_n\, \underline{w}_n^T\right) \\ &\quad - F_n E\left(\Delta\underline{X}_{n-1}(+)\, \underline{w}_n^T\right) - E\left(\underline{w}_n\, \Delta\underline{X}_{n-1}^T(+)\right) F_n^T \end{aligned}$$

The first expected value term in the above expression should be recognized as the covariance of $\Delta\underline{X}$ after the last filter update (i.e., $P_{n-1}(+)$). The second term is the covariance matrix associated with the integrated process noise from $t_{n-1}$ to $t_n$. We define:

$$Q_n \overset{\Delta}{=} E\left(\underline{w}_n\, \underline{w}_n^T\right) \tag{131C}$$

Because $\underline{w}_n$ represents the integrated effect of $\underline{n}$ process noise on $\Delta\underline{X}_n$ over the $t_{n-1}$ to $t_n$ time interval , it is uncorrelated with $\underline{X}$ and its uncertainty $\Delta\underline{X}$ at time $t_{n-1}$ or earlier. Because $\underline{n}$ is white noise, it is uncorrelated with $\underline{X}$ and its uncertainty $\Delta\underline{X}$ prior to or at time $t_{n-1}$. Hence,

$$E\left(\Delta\underline{X}_{n-1}(+)\ \underline{w}_n^T\right) = 0$$

$$E\left(\underline{w}_n\ \Delta\underline{X}_{n-1}^T(+)\right) = 0$$

Substituting the above results into the $P_n(-)$ expression yields the desired relationship between $P_n(-)$ and $P_{n-1}(+)$:

$$P_n(-) = F_n\, P_{n-1}(+)\, F_n^T + Q_n \tag{132}$$

Equations (125) and (132) describe the propagation of $P_n$ between updates and over an update. With Equation (131) for $K_n$, this set enables the optimal gain matrix to be calculated on a continuous basis for the estimation filter (Figure 10). These results are summarized in Figure 11.

It is to be noted in Figure 11, that the optimal gain determination requires an open loop updating of the covariance matrix P based on its value for the previous interval. An integration process is implied by this operation that must be initialized at the start of the filtering process. The initial value of P (i.e., $P_o$) is determined by the best estimate (on a root-mean-square basis) of the variances (and covariances) associated with the errors in the state vector $\underline{X}$ at the start of alignment. One of the advantages (and shortcomings) of the minimum variance approach is that it is based on knowing what the initial uncertainty in $\underline{X}$ is (as manifested in $P_o$). In addition, knowledge of the statistics of the process and measurement noise (as manifested in $Q_n$ and $R_n$) is required. If these statistical parameters are known (and they usually are), the Figure 11 gain formula yields excellent filter performance. On the other hand, if $Q_n$, $R_n$ and $P_o$ are unknown (or have large uncertainties), performance deficiencies can be introduced.

To be assured that reasonable performance will be achievable with the possible variations that may be experienced in $R_n$, $Q_n$, and $P_o$ from what was assumed in the filter design, digital simulation analyses are required. Such simulation studies are designed to obtain a set of $R_n$, $Q_n$, $P_o$ that yield good filter performance over the range of anticipated variations in these parameters that may actually be experienced in practice.

Another point should be noted regarding the form of Figure 11 for filter performance analyses. The performance of the filter is completely characterized on a statistical basis from instant to instant by the covariance matrix P. Hence, in the process of calculating the gain, the covariance performance of all of the filter estimated states (the elements of $\underline{X}$), are also determined. Statistical analyses of the filter performance using a digital simulation, therefore, need only simulate the Figure 11 loop. Note, that the Figure 11 covariance update equations are general for any gain $K_n$ (see derivation), not only for the optimal gain. Gains determined on the basis of off-nominal $Q_n$, $R_n$, $P_o$ can also be

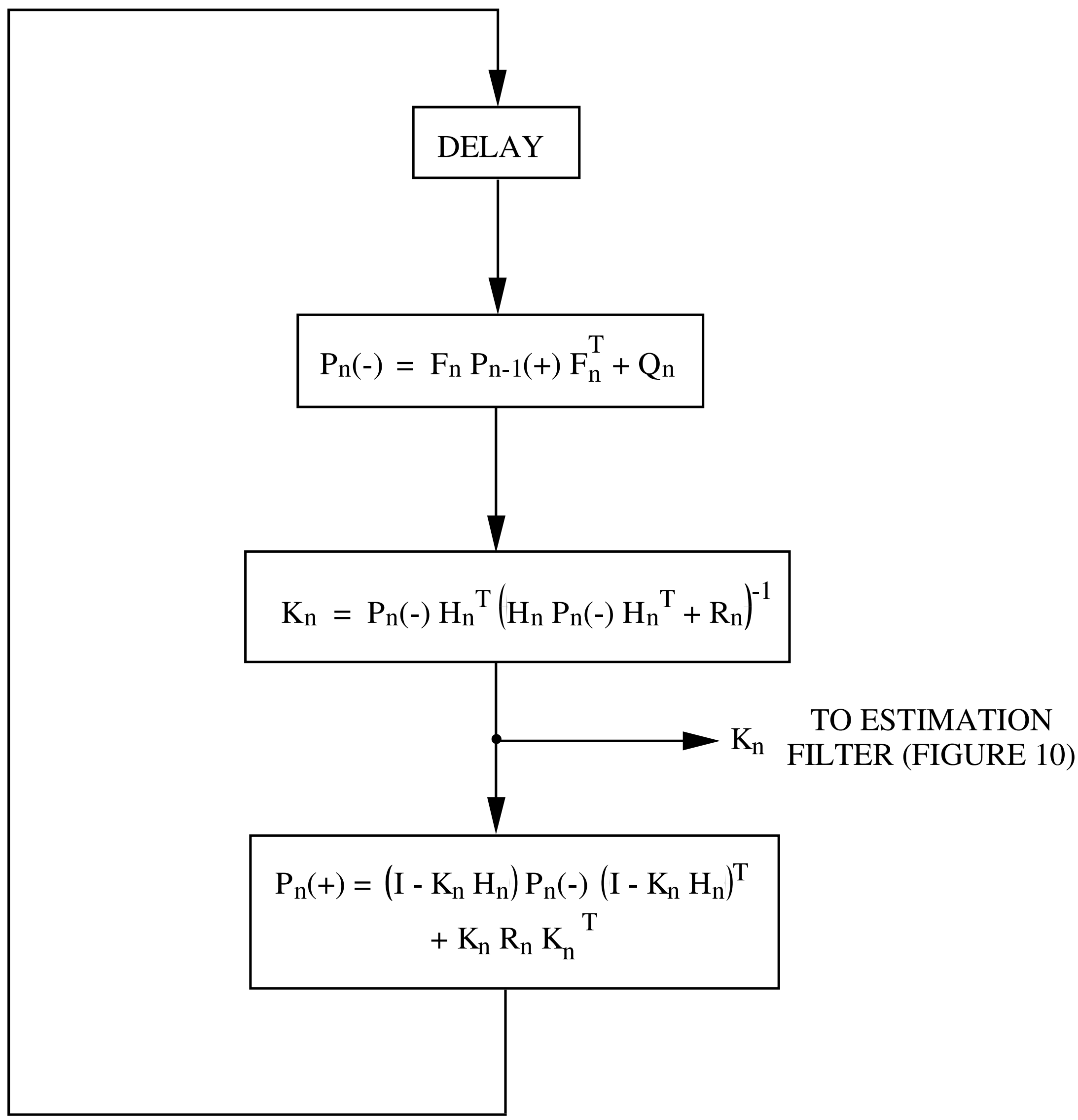


**FIGURE 11 - OPTIMAL GAIN DETERMINATION**

utilized in Figure 11 if the $K_n$ block is replaced by the equivalent block for off-nominal gain determination. Such an approach is illustrated in Figure 11A. The starred quantities are the assumed off-nominal filter gain design parameters. The non-starred quantities represent the actual statistics of the filter operation that would be experienced when applying the off-nominal parameter based gains.

In the more general case, the analytical model used for the estimation filter in the flight computer (Figures 10 and 11) may not only deviate from reality in $Q_n$, $R_n$ and $P_o$, but may also contain inaccuracies in its state dynamics matrix model ($F_n$), its measurement matrix model ($H_n$), and in the number of states it accounts for. The analysis of these effects deals with the performance characteristics of "suboptimal" filters (filters that have the general optimal gain determination and estimation structure, but with inaccuracies in the system model, either due to uncertainties in the actual model, or due to approximations intentionally introduced to reduce the analytical complexity of the flight software required for implementation). The equivalent to Figure 11A for determining suboptional filter performance in the more general case can be derived following the same methodology used in developing Equations (122) to (132).

We begin by defining the analytical model of the system states assumed in the flight computer:

$$\overset{*}{\underline{X}}_n (-) = \overset{*}{F}xx_n \overset{*}{\underline{X}}_{n-1} (+) + \overset{*}{F}xx_n \underline{u}_{n-1} \tag{132A}$$

where

$\overset{*}{\underline{X}}$ = The flight computer estimation filter state vector before (-) and after (+) a filter update.

$\overset{*}{F}xx$ = The state transition matrix for $\overset{*}{\underline{X}}$ assumed in the flight computer.

$\underline{u}$ = The $\underline{X}$ control vector used to modify $\underline{X}$ at each Kalman update cycle (following the $\overset{*}{\underline{X}}$ update).

The estimation filter update equation is:

$$\begin{aligned} \overset{*}{\underline{Z}} &= \overset{*}{H}_{xn} \overset{*}{\underline{X}}_n(-) \\ \overset{*}{\underline{X}}_n(+) &= \overset{*}{\underline{X}}_n(-) - K_n \left( \overset{*}{\underline{Z}}_n - \underline{Z}_n \right) \end{aligned} \tag{132B}$$

where

$\underline{Z}$ = The actual measurement vector (obtained from actual system measurements).

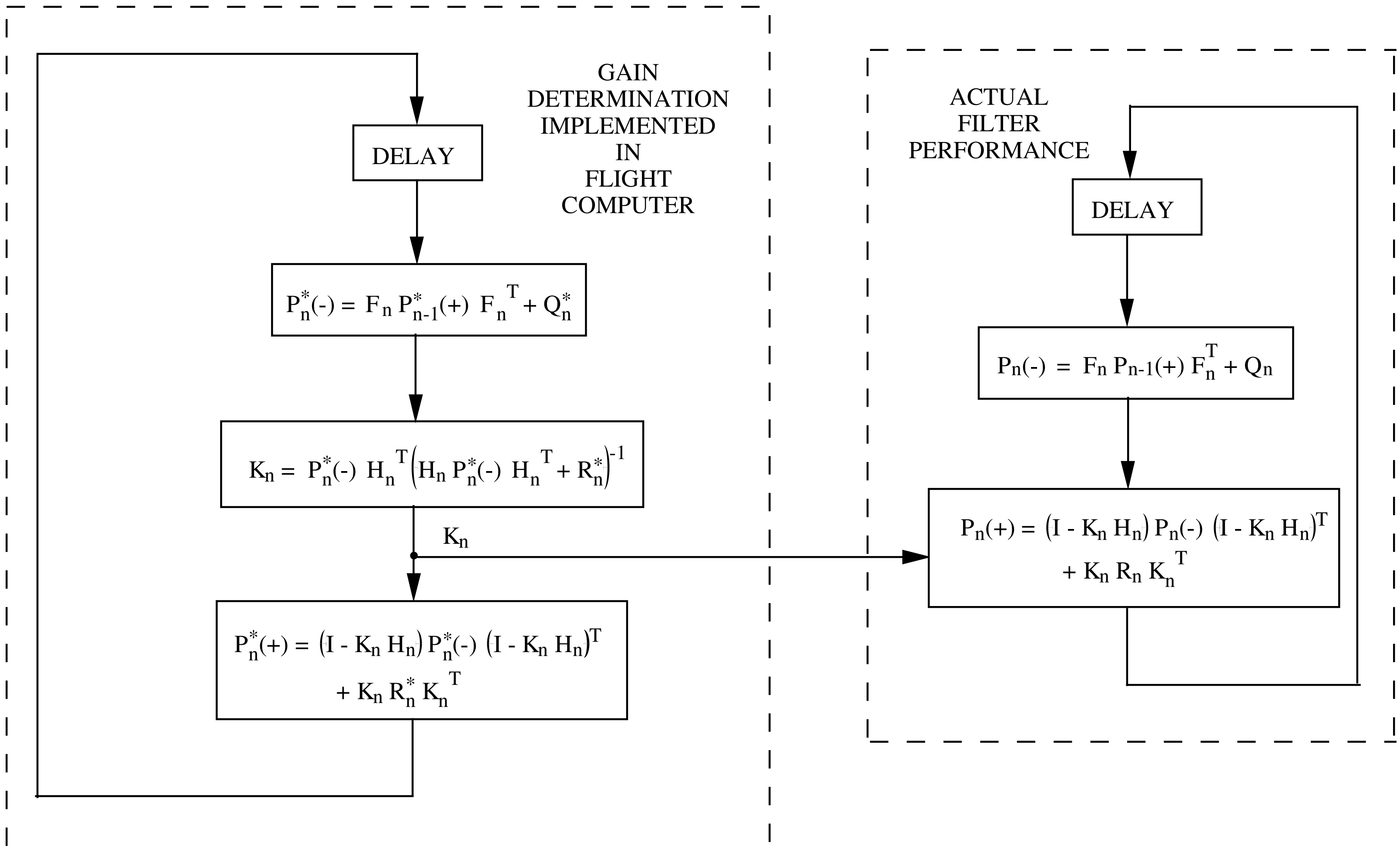


**FIGURE 11A - FILTER PERFORMANCE MODEL WITH OFF-NOMINAL GAINS FOR SIMULATION ANALYSES**

$\overset{*}{\underline{Z}}$ = The flight computer estimate for the filter input measurement (based on the assumed analytical model for $\underline{X}$).

$\overset{*}{H}_x$ = The flight computer model for the measurement matrix.

K = The "optimal" gain matrix used in the computer estimation filter, typically calculated as shown in the left hand portion of Figure 11A.

We now define the actual system analytical model as:

$$\underline{X}_n = F_{xx_n}\,\underline{X}_{n-1} + F_{xy_n}\,\underline{Y}_{n-1} + \underline{w}_{x_n} + F_{xx_n}\,\underline{u}_{n-1}$$
$$\underline{Y}_n = F_{yy_n}\,\underline{Y}_{n-1} + F_{yx_n}\,\underline{X}_{n-1} + \underline{w}_{y_n} + F_{yx_n}\,\underline{u}_{n-1} \qquad (132C)$$
$$\underline{Z}_n = H_{x_n}\,\underline{X}_n + H_{y_n}\,\underline{Y}_n + \underline{v}_n$$

where:

$\underline{X}$ = The actual state vector (approximated by $\overset{*}{\underline{X}}$ in the flight computer estimation filter).

$\underline{Y}$ = The vector of additional actual states not accounted for in the flight computer filter.

$F_{xx}, F_{xy}, F_{yx}, F_{yy}$ = $\underline{X}$, $\underline{Y}$ state dynamic matrix elements ($F_{xx}$ is approximated by $\overset{*}{F}_{xx}$ in the flight computer).

$\underline{w}_x, \underline{w}_y$ = $\underline{X}$, $\underline{Y}$ state integrated input process noise vectors.

$\underline{v}$ = Measurement noise.

$H_x, H_y$ = Actual system measurement matrices ($H_x$ is approximated by $\overset{*}{H}_x$ and $H_y$ is assumed to be zero in the flight computer filter).

The error in the flight computer $\underline{X}$ estimate is defined as before (in the steps leading to Equation (124A)):

$$\Delta\underline{X} \overset{\Delta}{=} \overset{*}{\underline{X}} - \underline{X}$$

The value for $\Delta\underline{X}$ immediately following an update is derived by combining equations (132B) and the $\underline{Z}$ measurement formula from Equations (132C):

$$\Delta\underline{X}_n(+) = \overset{*}{\underline{X}}_n(+) - \underline{X}_n = \overset{*}{\underline{X}}_n(-) - K_n (\overset{*}{\underline{Z}}_n - \underline{Z}_n) - \underline{X}_n$$

$$= \overset{*}{\underline{X}}_n(-) - \underline{X}_n + K_n \left(H_{x_n} \underline{X}_n + H_{y_n} \underline{Y}_n + \underline{v}_n - \overset{*}{H}_{x_n} \overset{*}{\underline{X}}_n(-)\right)$$

$$= \Delta\underline{X}_n(-) + K_n \left(- \overset{*}{H}_{x_n} \overset{*}{\underline{X}}_n(-) + \overset{*}{H}_{x_n} \underline{X}_n - \overset{*}{H}_{x_n} \underline{X}_n + H_{x_n} \underline{X}_n + H_{y_n} \underline{Y}_n + \underline{v}_n\right)$$

$$= \Delta\underline{X}_n(-) + K_n \left(- \overset{*}{H}_{x_n} \Delta\underline{X}_n(-) - (\overset{*}{H}_{x_n} - Hx_n) \underline{X}_n + H_{y_n} \underline{Y}_n + \underline{v}_n\right)$$

or

$$\Delta\underline{X}_n(+) = (I - K_n \overset{*}{H}_{x_n}) \Delta\underline{X}_n(-) + K_n \underline{v}_n - K_n (\overset{*}{H}_{x_n} - H_{x_n}) \underline{X}_n + K_n H_{y_n} \underline{Y}_n \qquad (132D)$$

where

I = The identity matrix with the same dimension as $\underline{X}$ or $\Delta\underline{X}$

The error immediately preceding an update is derived by combining Equation (132A) with the dynamic propagation formulas in Equations (132C):

$$\begin{aligned}\Delta\underline{X}_n(-) &= \overset{*}{\underline{X}}_n(-) - \underline{X}_n = \overset{*}{F}_{xx_n} \overset{*}{\underline{X}}_{n-1}(+) + \overset{*}{F}_{xx_n} \underline{u}_{n-1} - F_{xx_n} \underline{X}_{n-1} \\ &\quad - F_{xy_n} \underline{Y}_{n-1} - \underline{w}_{x_n} - F_{xx_n} \underline{u}_{n-1} \\ &= \overset{*}{F}_{xx_n} \Delta\underline{X}_{n-1}(+) + (\overset{*}{F}_{xx_n} - F_{xx_n}) \underline{X}_{n-1} - F_{xy_n} \underline{Y}_{n-1} - \underline{w}_{x_n} \\ &\quad + (\overset{*}{F}_{xx_n} - F_{xx_n}) \underline{u}_{n-1}\end{aligned} \qquad (132E)$$

It is convenient at this point to hypothesizes a form for the control vector $\underline{u}$. For inertial navigation estimation problems $\underline{u}$ is typically a linear function of the estimated state vector $\overset{*}{\underline{X}}$:

$$\underline{u} = - L \overset{*}{\underline{X}} = - L \left(\underline{X} + \Delta\underline{X}\right)$$

where

L = The control matrix.

Substituting in (132E) yields the final form:

$$\Delta\underline{X}_n(-) \;=\; \overset{*}{F}_{xx_n}\,\Delta\underline{X}_{n-1}(+) + (\overset{*}{F}_{xx_n} - F_{xx_n})\,\underline{X}_{n-1} - F_{xy_n}\,\underline{Y}_{n-1} - \underline{w}_{x_n}$$

$$- (\overset{*}{F}_{xx_n} - F_{xx_n})\,L_n\left(\underline{X}_{n-1} + \Delta\underline{X}_{n-1}(+)\right)$$

or

$$\Delta\underline{X}_n(-) \;=\; \left[\overset{*}{F}_{xx_n} - (\overset{*}{F}_{xx_n} - F_{xx_n})\,L_n\right]\Delta\underline{X}_{n-1}(+)$$

$$+ (\overset{*}{F}_{xx_n} - F_{xx_n})\,(I - L_n)\,\underline{X}_{n-1} - F_{xy_n}\,\underline{Y}_{n-1} - \underline{w}_{x_n} \qquad (132F)$$

The $\underline{X}$, $\underline{Y}$ dynamic propagation formulas can also be expanded using the latter definition for $\underline{u}$:

$$\underline{X}_n \;=\; F_{xx_n} - \left(I - L_n\right)\underline{X}_{n-1} + F_{xy_n}\,\underline{Y}_{n-1} - F_{xx_n}\,L_n\,\Delta\underline{X}_{n-1}(+) + \underline{w}_{x_n}$$

$$\underline{Y}_n \;=\; F_{yy_n}\,\underline{Y}_{n-1} + F_{yx_n}\left(I - L_n\right)\underline{X}_{n-1} - F_{yx_n}\,L_n\,\Delta\underline{X}_{n-1}(+) + \underline{w}_{y_n} \qquad (132G)$$

Equations (132D), (132F) and (132G) can now be converted to a more familiar form if we define an augmented state vector with associated dynamics, integrated process noise increment, measurement model, and update gain matrix as follows:

$$\underline{X}' = \begin{pmatrix} \Delta\underline{X} \\ \underline{X} \\ \underline{Y} \end{pmatrix} \qquad\qquad \underline{w}' = \begin{pmatrix} \underline{w}_x \\ -\underline{w}_x \\ -\underline{w}_y \end{pmatrix}$$

$$F' = \begin{bmatrix} [\overset{*}{F}_{xx} - (\overset{*}{F}_{xx} - F_{xx})\,L] & (\overset{*}{F}_{xx} - F_{xx})\,(I - L) & -F_{xy} \\ -F_{xx}\,L & F_{xx}\,(I - L) & F_{xy} \\ -F_{yx}\,L & F_{yx}\,(I - L) & F_{yy} \end{bmatrix} \qquad (132H)$$

$$H' = \begin{bmatrix} Hx & (\overset{*}{H}x - Hx) & -Hy \end{bmatrix} \qquad K' = J\,K \qquad J = \begin{pmatrix} I \\ 0 \\ 0 \end{pmatrix}$$

Using the above definitions, Equations (132D), (132F) and (132G) simplify to the following familiar forms:

$$\underline{X}'_n(-) \;=\; F'_n\,\underline{X}'_{n-1}(+) - \underline{w}'_n$$

$$\underline{X}'_n(+) \;=\; \left(I' - K'_n\,H'_n\right)\underline{X}'_n(-) + K'_n\,\underline{v}_n \qquad (132I)$$

where

$I' =$ The identity matrix with the same dimension as $\underline{X}'$

Equations (132I) are identical in form to Equations (124A) and (131A). Hence, the covariance equivalents of (132I) should also be identical in form to Equations (125) and (132) (the covariance equivalents of (124A) and (131A)). Thus, from (124A) and (131A):

$$P_n'(-) = F_n' P_{n-1}'(+) F_n'^T + Q_n'$$
$$P_n'(+) = \left(I' - K_n' H_n'\right) P_n'(-) \left(I' - K_n' H_n'\right)^T + K_n' R_n K_n'^T \qquad (132J)$$

where

$$R = E\left(\underline{v}\,\underline{v}^T\right)$$

$$Q' = E\left(\underline{w}'\,\underline{w}'^T\right) = E\left\{\begin{pmatrix} \underline{w}_x \\ -\underline{w}_x \\ -\underline{w}_y \end{pmatrix} \begin{bmatrix} \underline{w}_x^T & -\underline{w}_x^T & -\underline{w}_y^T \end{bmatrix}\right\}$$

$$= E\begin{bmatrix} \underline{w}_x\underline{w}_x^T & -\underline{w}_x\underline{w}_x^T & -\underline{w}_x\underline{w}_y^T \\ -\underline{w}_x\underline{w}_x^T & \underline{w}_x\underline{w}_x^T & \underline{w}_x\underline{w}_y^T \\ -\underline{w}_y\underline{w}_x^T & \underline{w}_y\underline{w}_x^T & \underline{w}_y\underline{w}_y^T \end{bmatrix} = \begin{bmatrix} Q_{xx} & -Q_{xx} & -Q_{xy} \\ -Q_{xx} & Q_{xx} & Q_{xy} \\ -Q_{xy}^T & Q_{xy}^T & Q_{yy} \end{bmatrix} \qquad (132K)$$

$$Q_{xx} = E\left(\underline{w}_x\,\underline{w}_x^T\right)$$
$$Q_{yy} = E\left(\underline{w}_y\,\underline{w}_y^T\right)$$
$$Q_{xy} = E\left(\underline{w}_x\,\underline{w}_y^T\right)$$

$$P' = E\left(\underline{X}'\,\underline{X}'^T\right) = E\left\{\begin{pmatrix} \Delta\underline{X} \\ \underline{X} \\ \underline{Y} \end{pmatrix} \begin{bmatrix} \Delta\underline{X}^T & \underline{X}^T & \underline{Y}^T \end{bmatrix}\right\}$$

(Continued)

$$= E \begin{bmatrix} \Delta\underline{X}\,\Delta\underline{X}^T & \Delta\underline{X}\,\underline{X}^T & \Delta\underline{X}\,Y^T \\ \underline{X}\,\Delta\underline{X}^T & \underline{X}\,\underline{X}^T & \underline{X}\,Y^T \\ \underline{Y}\,\Delta\underline{X}^T & \underline{Y}\,\underline{X}^T & \underline{Y}\,Y^T \end{bmatrix} = \begin{bmatrix} P_{\Delta X \Delta X} & P_{X \Delta X} & P_{Y \Delta X} \\ P_{X \Delta X} & P_{XX} & P_{XY} \\ P_{Y \Delta X}{}^T & P_{XY}{}^T & P_{YY} \end{bmatrix}$$

(132K)
(Concluded)

$$P_{\Delta X \Delta X} = E\left(\Delta\underline{X}\,\Delta\underline{X}^T\right) \qquad P_{XX} = E\left(\underline{X}\,\underline{X}^T\right)$$
$$P_{X \Delta X} = E\left(\underline{X}\,\Delta\underline{X}^T\right) \qquad P_{XY} = E\left(\underline{X}\,\underline{Y}^T\right)$$
$$P_{Y \Delta X} = E\left(\underline{Y}\,\Delta\underline{X}^T\right) \qquad P_{YY} = E\left(\underline{Y}\,\underline{Y}^T\right)$$

The performance of the suboptimal filter is defined by the covariance of the error vector $\Delta\underline{X}$ (i.e., by $P_{\Delta X \Delta X} = E\left(\Delta\underline{X}\,\Delta\underline{X}^T\right)$, the upper diagonal elements in the Equations (132K) $P'$ matrix formula). Symbolically,

$$P_{\Delta X \Delta X} = J^T P' J \tag{132L}$$

where J is as defined in Equations (132H).

Figure 11B depicts Equations (132J) with (132L) in block diagram form. The $K_n$ gain matrix is shown being generated as in Figure 11A from the reduced state flight computer filter model estimate for the system covariance characteristics (the assumed statistics of $\overset{*}{\underline{X}}$ with its assumed state transition matrix, input noise matrix, measurement matrix, measurement noise matrix, and covariance matrix initialization).

An alternate to the Figure 11B suboptimal analytical configuration separates the control from the error propagation equations such that Equations (132A) and (132C) become equivalently:

$$\overset{*}{\underline{X}}_{n-1}(++) = \overset{*}{\underline{X}}_{n-1}(+) + \underline{u}_{n-1}$$
$$\overset{*}{\underline{X}}_n(-) = \overset{*}{F}_{xx_n}\,\overset{*}{\underline{X}}_{n-1}(++) \tag{132M}$$

$$\underline{X}_{n-1}(++) = \underline{X}_{n-1} + \underline{u}_{n-1}$$
$$\underline{Y}_{n-1}(++) = \underline{Y}_{n-1}$$
$$\underline{X}_n = F_{xx_n}\,\underline{X}_{n-1}(++) + F_{xy_n}\,\underline{Y}_{n-1}(++) + \underline{w}_{x_n} \tag{132N}$$
$$Y_n = F_{yy_n}\,\underline{Y}_{n-1}(++) + F_{yx_n}\,\underline{X}_{n-1}(++) + \underline{w}_{y_n}$$

where

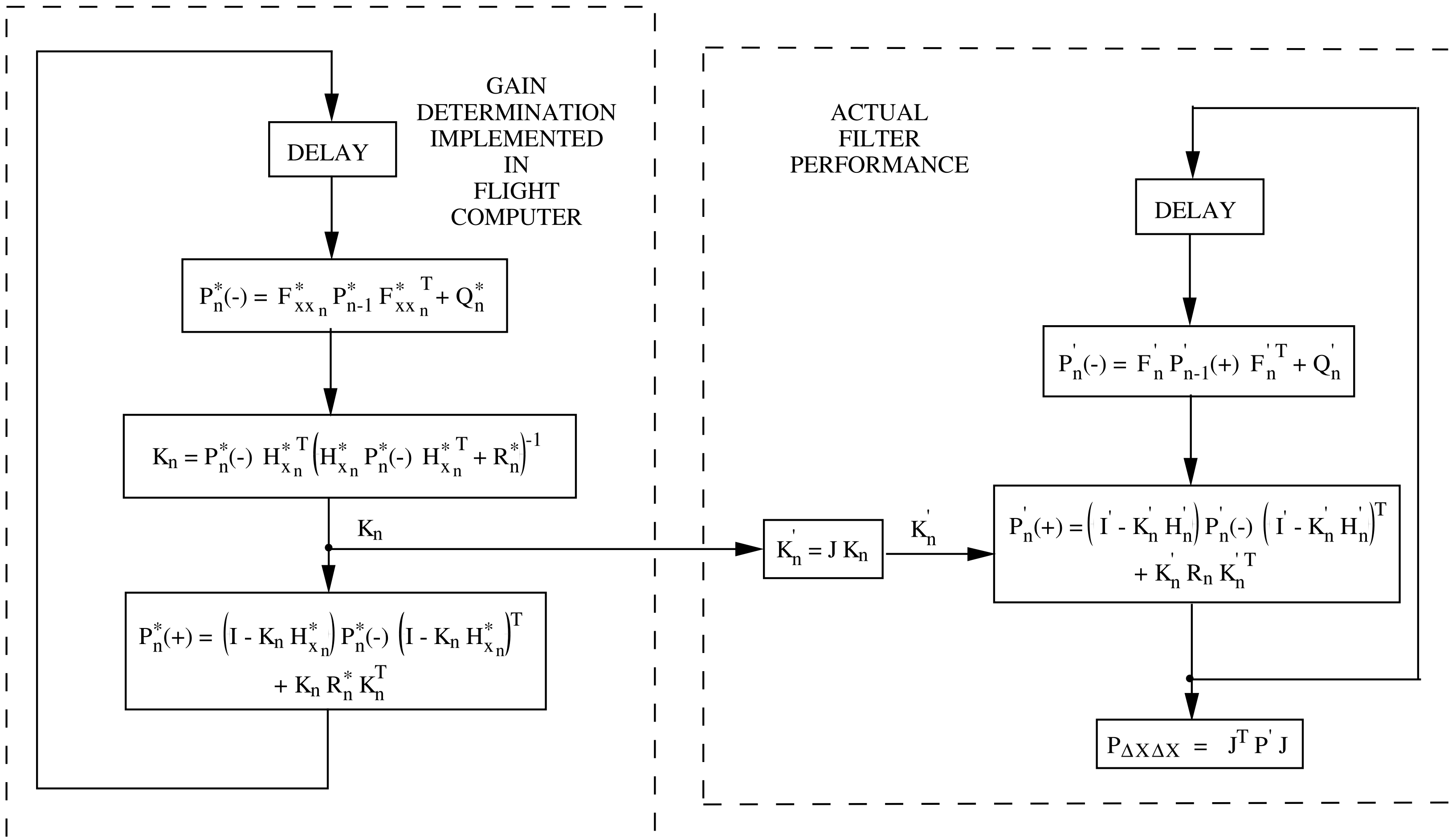


**FIGURE 11B - GENERALIZED SUBOPTIMAL KALMAN FILTER PERFORMANCE MODEL FOR SIMULATION ANALYSES**

(++) = Reference to conditions immediately after application of the control vector which is immediately after the Kalman estimate is made.

The $\underline{X}$ equations in (132M) and (132N) can then be combined using the previous definition for $\Delta\underline{X} = \overset{*}{\underline{X}} - \underline{X}$ to obtain:

$$\Delta\underline{X}_{n-1}(++) = \Delta\underline{X}_{n-1}(+) \tag{132O}$$

$$\begin{aligned}\Delta\underline{X}_n(-) &= \overset{*}{F}_{xx_n}\, \overset{*}{\underline{X}}_{n-1}(++) - F_{xx_n}\, \underline{X}_{n-1}(++) - F_{xy_n}\, \underline{Y}_{n-1}(++) - \underline{w}_{x_n} \\ &= \overset{*}{F}_{xx_n}\, \Delta\overset{*}{\underline{X}}_{n-1}(++) + (\overset{*}{F}_{xx_n} - F_{xx_n})\, \underline{X}_{n-1}(++) - F_{xy_n}\, \underline{Y}_{n-1}(++) - \underline{w}_{x_n}\end{aligned}$$

Introducing $\underline{u} = - L\, \overset{*}{\underline{X}} = - L\left(\underline{X} + \Delta\underline{X}\right)$, Equations (132N) with (132O) become:

$$\begin{aligned}\Delta\underline{X}_{n-1}(++) &= \Delta\underline{X}_{n-1}(+) \\ \underline{X}_{n-1}(++) &= - L_n\, \Delta\underline{X}_{n-1}(+) + \left(I - L_n\right) \underline{X}_{n-1}(+) \\ \underline{Y}_{n-1}(++) &= \underline{Y}_{n-1}(+) \\ \Delta\underline{X}_n(-) &= \overset{*}{F}_{xx_n}\, \Delta\underline{X}_{n-1}(++) + (\overset{*}{F}_{xx_n} - F_{xx_n})\, \underline{X}_{n-1}(++) - F_{xy_n}\, \underline{Y}_{n-1}(++) - \underline{w}_{x_n} \\ \underline{X}_n(-) &= F_{xx_n}\, \underline{X}_{n-1}(++) + F_{xy_n}\, \underline{Y}_{n-1}(++) - \underline{w}_{x_n} \\ \underline{Y}_n(-) &= F_{yy_n}\, \underline{Y}_{n-1}(++) + F_{yx_n}\, \underline{X}_{n-1}(++) + \underline{w}_{y_n}\end{aligned} \tag{132P}$$

Using definitions similar to those employed in Equations (132H), Equations (132P) can be written in the augmented form:

$$\begin{aligned}\underline{X}'_{n-1}(++) &= F''_n\, \underline{X}'_{n-1}(+) \\ \underline{X}'_n(-) &= F'''_n\, \underline{X}'_{n-1}(++) - \underline{w}'_n\end{aligned} \tag{132Q}$$

where

$$
\underline{X}' = \begin{pmatrix} \Delta\underline{X} \\ \underline{X} \\ \underline{Y} \end{pmatrix} \qquad \underline{w}' = \begin{pmatrix} \underline{w}_x \\ -\underline{w}_x \\ -\underline{w}_y \end{pmatrix}
$$

$$
F'' = \begin{bmatrix} I & 0 & 0 \\ -L & (I - L) & 0 \\ 0 & 0 & I \end{bmatrix} \tag{132R}
$$

$$
F''' = \begin{bmatrix} \overset{*}{F}_{xx} & (\overset{*}{F}_{xx} - F_{xx}) & -F_{xy} \\ 0 & F_{xx} & F_{xy} \\ 0 & F_{yx} & F_{yy} \end{bmatrix}
$$

The companion covariance propagation equations are:

$$
\begin{aligned}
P'_{n-1}(++) &= F''_n \, P'_{n-1}(+) \, F''^{T}_n \\
P'_n(-) &= F'''_n \, P'_{n-1}(++) \, F'''^{T}_n + Q'_n
\end{aligned} \tag{132S}
$$

where P´ and Q´ are as defined previously in Equations (132K).

Equations (132S) with the covariance update equation in (132J) form an alternate to the (132J) suboptimal covariance matrix propagation equations. Figure 11C illustrates how the actual filter performance would be evaluated with this approach using the actual system calculated gain $K_n$ (as in Figure 11B).

Figures 11B or 11C with Equations (132H), (132K), and (132R) can be used to evaluate the suboptimal covariance performance ($P_{\Delta x \Delta x}$) of an estimation and control filter implemented in flight software for the general case where the flight computer state vector model differs from the "real world" in its dynamic characteristics, measurement characteristics, number of states in the overall model, as well as variations in the process noise and initial covariance amplitudes.

Figures 10 and 11 define the general structure of the classical discrete Kalman filter with state variable control. Figures 11A, 11B, and 11C define covariance methods that are useful for analyzing the performance of such Kalman filters in "real world" environments.

Kalman filtering is a general estimating technique that is not only applicable to the specific inertial navigation alignment problem we are addressing; as we shall see at the end of this lecture, it is a general concept that can be applied to a large class of estimating problems encountered with digital systems including the broader problem of inertial navigation system aiding.

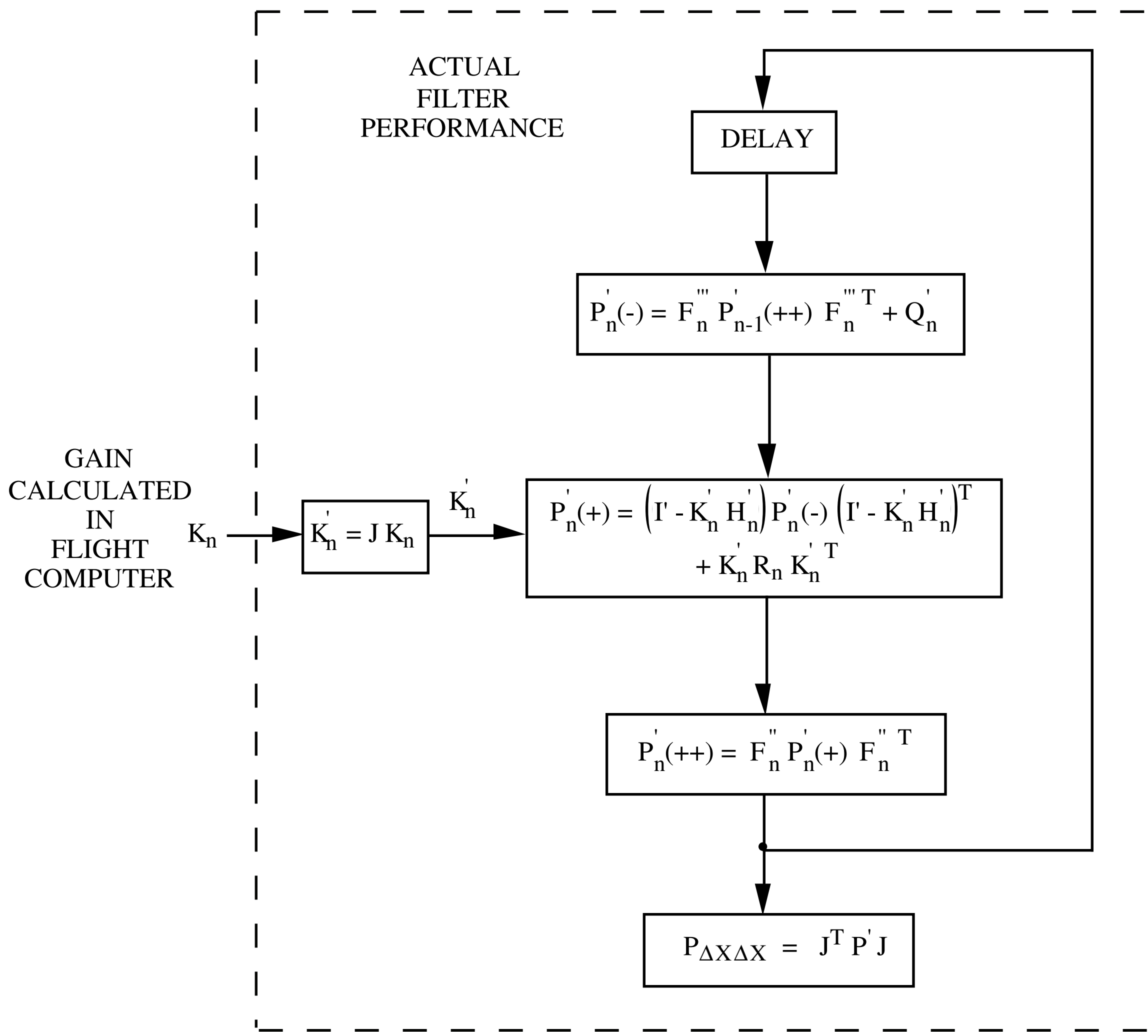


**FIGURE 11C - ALTERNATE GENERALIZED SUBOPTIMAL KALMAN FILTER PERFORMANCE MODEL FOR SIMULATION ANALYSES**

## APPLICATION TO THE FINE ALIGNMENT PROBLEM

Let us now return to our problem of performing the strapdown fine alignment function and apply the Figure 10 and 11 Kalman filter optimal gain approach developed in the previous paragraphs. Returning to Equation (117A) which defines the state vector for the fine alignment problem, we note that the top four state vector elements are system induced errors, whereas the bottom three are environmentally induced effects (see Figure 9). We also recall that the environmentally induced effects are only approximately modelable, as contrasted with the system induced errors, which are accurately understood, hence, modelable. In addition, the externally induced effects generally have wider bandwidth characteristics than the system errors, which are, therefore, attenuated to a larger extent by the pre-filter installed in the system software that operates on $\underline{v}_H^{*L}$, the sum of the system and environmentally induced effects (see Figures 5 and 6). This, of course, was the reason for inserting the pre-filter: so that "the measurement" is a stronger measure of system errors (the quantities of interest) rather than external effects (i.e., to increase signal-to-noise ratio). The above discussion sets forth the rationale for not attempting to estimate the environmentally induced effects as part of the alignment filter operations (i.e., not estimating the last three elements in Equation (117A)). It can be verified that if the model we assume for the environmental disturbance is accurate, neglecting to estimate the disturbance state variables adds virtually no error to our filter performance results. On the other hand, if our model for the disturbance state variables is inaccurate, not estimating the disturbance effects avoids the potential of significant filter inaccuracies caused by a bad mismatch between the actual disturbance and the model we are using for the external environment.

Not estimating the disturbance effects does not mean that we neglect their presence completely. We still account for their presence on a statistical sense in the covariance matrix (P) used in Figure 11 to determine the optimal gains. The way we implement the "no estimate" constraint is simply to set the gain elements associated with the disturbance estimates to zero in Figure 11. Since there is no coupling between the system and environmentally induced state variables between filter updates (see Figure 9), setting the update gain for the environmental state estimates to zero completely uncouples their effects in Figure 10 from the estimates of the system error states. Consequently, estimated environmental state variables in Figure 10 can be eliminated without changing the filter performance results.

The final simplification is to set the control vector $\underline{u}_{n-1}$ equal to the negative of the $\underline{X}$ estimate at (n-1) (i.e., correcting the $\underline{X}$ states being estimated to zero so that the best estimate for them is controlled to zero continuously). With this philosophy, from Equations (117A), the control law sets:

$$\left(\delta\underline{\omega}_{IE}^{*L}\right)_H = 0 \qquad \underline{\phi}_H^{*L} = 0 \qquad \delta\underline{v}_H^{*L} = 0 \qquad \left(\delta\underline{v}_H^{*L}\right)_F = 0$$

Since, based on all the available information these are the best estimates for the system error variables, we can conclude that this is our best control of the actual system error states.

With the latter simplifications, Figures 10 and 11 can be put into the equivalent Figure 12 form. Comparing Figure 12 with 11 it is to be noted that the Figure 10 estimation filter dynamics $F_n$ and $H_n$ within the filter are absent in Figure 12. This, of course, is due to our selection of $\underline{u}_{n-1}$ to equal - $\overset{*}{\underline{X}}_{n-1}$ (see Figure 10). The prime (´) notation for $\underline{X}$ signifies those elements of $\underline{X}$ being estimated. Hence:

$$\underline{X}' = \begin{pmatrix} \left(\delta\underline{\omega}_{IE}^{L}\right)_H \\ \underline{\phi}_H^L \\ \delta\underline{v}_H^L \\ \left(\delta\underline{v}_H^L\right)_F \end{pmatrix} \tag{133}$$

The double prime (") indicates the elements of $\underline{X}$ not being estimated (i.e., the disturbance state variables:

$$\underline{X}'' = \begin{pmatrix} \underline{v}_H^L \\ \underline{R}_H^L \\ \left(\underline{v}_H^L\right)_F \end{pmatrix} \tag{134}$$

The associated state transition and integrated process noise vectors $\left(F_n', F_n'', \underline{w}_n', \underline{w}_n''\right)$ are those elements of $F_n$ and $\underline{w}_n$ in Equation (120) associated with $\underline{X}'$ and $\underline{X}''$ Since $\underline{X}'$ and $\underline{X}''$ are uncoupled, such a separation is readily achievable. The measurement matrices $H_n'$, $H''_n$ are compatible with (133), (134), and (119A), and are given by:

$$\begin{aligned} H_n' &= \begin{bmatrix} 0 & 0 & 0 & 1 \end{bmatrix} \\ H_n'' &= \begin{bmatrix} 0 & 0 & 1 \end{bmatrix} \end{aligned} \tag{135}$$

The $K_n'$ gain matrix is the optimal gain matrix of Figure 11 associated with the $\underline{X}'$ states being estimated. The J matrix equates the elements of $K_n$ (in Figure 11) associated with $\underline{X}''$ to zero. The J´ matrix discards the zero elements of $K_n$ associated with $\underline{X}''$ so that the remainder $K_n'$ is only for updating $\underline{X}'$. Hence:

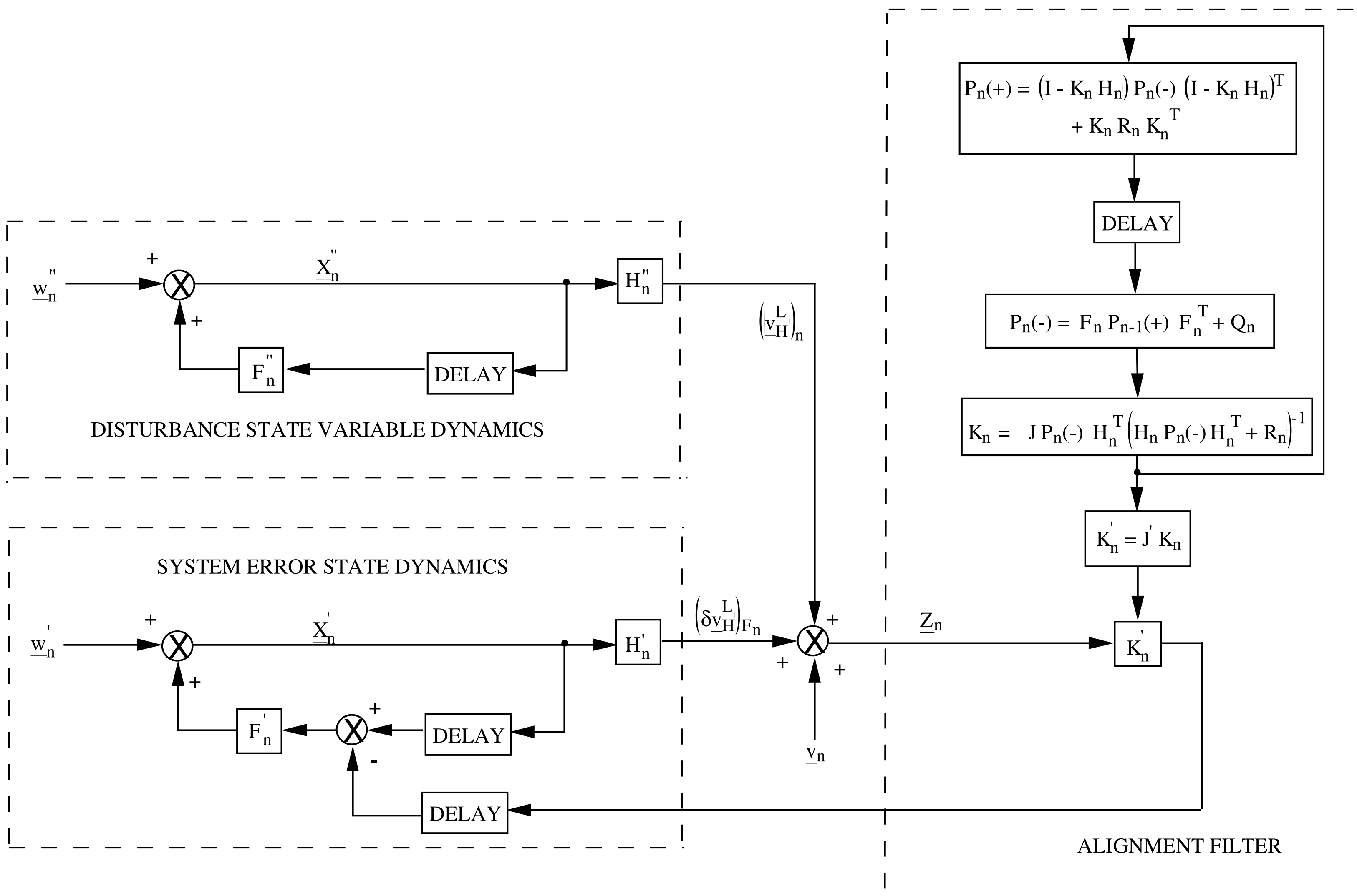


**FIGURE 12 - FINE ALIGNMENT DISCRETE KALMAN FILTER**

$$
J = \begin{bmatrix} 1 & 0 & 0 & 0 & 0 & 0 & 0 \\ 0 & 1 & 0 & 0 & 0 & 0 & 0 \\ 0 & 0 & 1 & 0 & 0 & 0 & 0 \\ 0 & 0 & 0 & 1 & 0 & 0 & 0 \\ 0 & 0 & 0 & 0 & 0 & 0 & 0 \\ 0 & 0 & 0 & 0 & 0 & 0 & 0 \\ 0 & 0 & 0 & 0 & 0 & 0 & 0 \end{bmatrix} \qquad J' = \begin{bmatrix} 1 & 0 & 0 & 0 & 0 & 0 & 0 \\ 0 & 1 & 0 & 0 & 0 & 0 & 0 \\ 0 & 0 & 1 & 0 & 0 & 0 & 0 \\ 0 & 0 & 0 & 1 & 0 & 0 & 0 \end{bmatrix} \tag{136}
$$

The other matrices in the alignment filter are those described previously in Equations (119B), (121), (124A), and (131A). Since there is no significant "measurement" noise for the alignment problem as formulated, the measurement noise vector $\underline{v}_n$ and covariance matrix $R_n$ can be equated to zero. If Figure 12 is compared with Figure 6 (and 7) it should be apparent that Figure 12 is the equivalent discrete form of Figure 6, and that the $K_n$ matrix of Figure 12 is the Figure 6 $K_\Omega$, $K_\phi$, $K_V$, $K_{VF}$ gain array utilized in the flight computer.

One final note regarding the implementation of Figure 12 in the flight computer. If Equations (136), (119B), (121), (124A), (131A), (117A,B,C), (118), and (120A) are reviewed, it is to be noted that the matrices involved in the Figure 12 gain determination are constant (except for P and K which are the dependent variables generated as a time function from the fixed matrices and the initial conditions set for P). Hence, the Figure 12 gain determination loop will generate the same gains as a function of time for all alignments. It can be concluded that if the resulting gains are determined once on a laboratory computer as a function of time, they can then theoretically be programmed into the flight computer as a time scheduled function with equivalent flight computer alignment filter results. It should be realized, however, that in more general Kalman filter applications, the gain determination will depend on variable navigation parameters for which the stored gain schedule approach is no longer valid.

## GENERALIZED KALMAN FILTER APPLICATIONS

The general Kalman filter structure as represented in Figures 10 and 11 can be applied to a variety of problems, not only to the alignment problem we have been dealing with. One of the principal advantages of the approach is that it allows the blending of information from several different sources to develop the optimum estimate from all sources combined. One of the classical applications of this latter approach has been in the blending of navigational information from several different sources on a vehicle to obtain an optimum navigational estimate. The result is a navigation estimate that has all of the high accuracy qualities of the input navigational devices, but with many of the poorer performance characteristics removed. When an inertial navigation system is one of the sources of navigational data feeding the Kalman filter, the total integrated system is known as a Kalman aided inertial system, or a hybrid aided inertial system.

As an example of a Kalman aided system, consider a system composed of an inertial navigator (INS), a doppler radar, and an Omega receiver. The INS provides self contained low noise wide bandwidth data; however, due to sensor errors, the position errors present in the output are unbounded, and velocity errors are present with Schuler oscillations that tend to build in amplitude with mission time. The doppler radar, on the other hand, generally has high quality bounded velocity information (typically in error by 0.1% of actual velocity), but the data is noisy and needs filtering. As a result, bandwidth characteristics are degraded. In addition, the doppler data is erroneous during maneuvering flight, and for a military application, doppler radar is radiating and not desirable for security reasons as an operating condition over unfriendly territory.

Navigational position data obtained by integrating the doppler velocity data (a heading reference is implied in the doppler system output) also has an unbounded characteristic on the same order as the INS. The Omega receiver, on the other hand, has bounded position errors (on the order of one mile), but without direct velocity data as an output. Deriving velocity data from Omega position changes yields too noisy an output, even with filtering. (Stand alone Omega systems may utilize a heading reference and air speed as the basic velocity reference, with the Omega position data used to update the velocity signal in a blending filter similar to the one we utilized for the vertical INS channel using the baro altimeter). A disadvantage of Omega is the possibility of black-out periods for extended times during the mission due to low signal to noise ratios from the Omega receiver.

A Kalman aided system utilizing the above three navigational devices would have the wide bandwidth low noise characteristics of the INS, the high quality velocity accuracy of the doppler (with noise removed) and the bounded position error characteristics of the Omega receiver. If an accurate model for the INS sensor errors (as well as the attitude/position/velocity error model - see Lecture 10) is incorporated for the Kalman filter states, the filter will estimate the INS sensor errors, which can then be utilized (through the $\underline{u}_{n-1}$ control vector in Figure 10) to calibrate the sensors in flight. With the INS calibrated, improved INS performance is achievable if the Omega becomes too noisy to be usable, or the doppler data cannot be used due to vehicle maneuvering, or because it is shut down for security reasons. Under these conditions, the integrated system can operate with only the INS in a pure inertial mode, until the other sensor data is restored. The $H_n$ measurement matrix in Figure 10 would be controlled by the filter software to reflect which (if any) measurements from the three navigation devices are being processed. The Kalman filter covariance matrix would be updated in Figure 11 with the $H_n$ as configured throughout the mission, thereby providing an accurate indication of the error conditions in all navigation devices, even when they are not being measured.

With the Kalman filter providing the blending function as described above, it should also be apparent that the integrated system achieves a degree of optimality from a redundancy standpoint. Each navigation device can also be considered as a back-up for the Omega. When all are operating, the Kalman filter provides the optimum estimate for the navigational state based on all estimates. For the case where one device (or two) fails, the filter will continue to provide the best navigation estimate based on the data available from the remaining operating input devices.

Figure 13 is a generalized diagram for the above described integrated Kalman aided inertial system. The measurement for the Kalman filter is obtained by subtracting navigation signals between the input devices so that a measure of the device errors is input to the filter (recall that the measurement vector $\underline{Z}_n$ is used as a measure of system errors. If the system is perfect, $\underline{Z}_n$ should be zero, except for measurement noise).

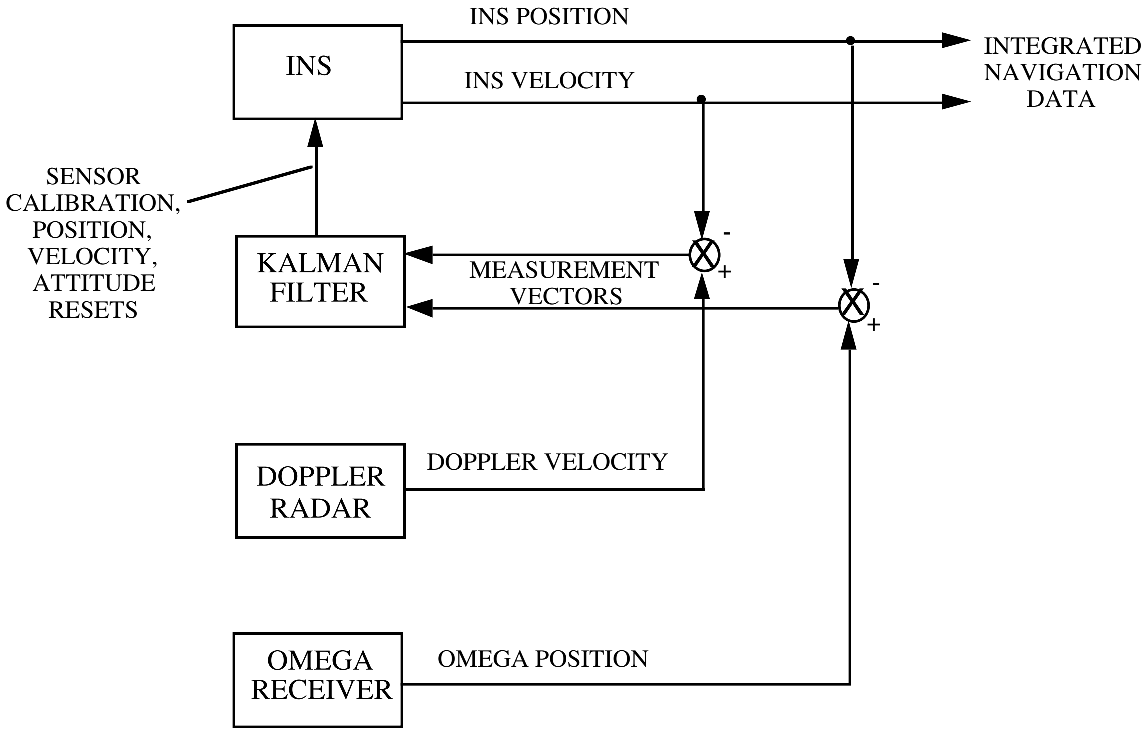


**FIGURE 13 - EXAMPLE OF A HYBRID AIDED INERTIAL NAVIGATION SYSTEM**

Note in Figure 13 that the INS is being updated (with $\underline{u}_{n-1}$) from the filter so that its output becomes the best estimate directly. In this type of implementation, the INS is considered the primary reference that is updated by the other devices. The Kalman filter for such an approach, may be a part of the INS computer. Depending on the application, other configurations are obviously possible. The Kalman filter structure in Figure 13, of course, would be as shown in Figures 10 with 11 for the gain determination. The error models used for the gain determination would account for all of the significant error states and noise variables in the sensing devices, and in the measurement process.

One final note regarding the Figure 13 configuration. With the Kalman aided inertial configuration indicated, the inertial system is in a continual state of being updated in terms of sensor calibration as well as position, velocity, and attitude accuracy (assuming that measurements are being processed). With this arrangement, therefore, the initial alignment process described previously can also be included. Hence, the initial alignment would become another filter submode, with the measurement brought in as indicated in Figure 13. Thus, the distinction between the alignment and navigation modes would disappear. All modes would be navigation modes, with the measurement and Kalman filter state variables configured to handle the particular mission assignment (initial alignment, pure inertial, Doppler-inertial, Omega-inertial, doppler-Omega-inertial etc.). A doppler dead-reckoning mode could also be implemented by augmenting the doppler in Figure 13 with a position integration, and updating the doppler position/velocity readings with Kalman estimates of the errors in these quantities determined during prior aided operations. Note, that an in-air alignment mode is also achievable with this system by merely entering the doppler-inertial mode with the initial covariance matrix in the Kalman filter set to correspond to the larger uncertainty in a misaligned platform. The Kalman update cycle will then reset the INS attitude along with the other parameters to achieve the proper attitude reference accuracy, hence, achieve alignment.

## NOTES

**LECTURE NOTES APPENDICES**

APPENDIX A - DERIVATION OF STRAPDOWN
INERTIAL NAVIGATION EQUATIONS

APPENDIX B - DERIVATION OF ERROR EQUATIONS FOR
STRAPDOWN INERTIAL NAVIGATION SYSTEMS

**NOTES**

# APPENDIX A

## DERIVATION OF STRAPDOWN INERTIAL NAVIGATION EQUATIONS

This appendix provides a rigorous derivation of the continuous form strapdown inertial navigation differential equations.

### Nomenclature

The following general nomenclature is used in this appendix:

$A, A_1, A_2, A_3$ = Arbitrary coordinate frames.

E Frame = Earth fixed coordinate frame used for position location definition.

L Frame = Navigation coordinate frame having its Z axis parallel to the upward vertical at the local earth surface referenced position location point on the earth's surface. Used for integrating acceleration into velocity, for defining the angular orientation of the local vertical in the E Frame and for describing the strapdown sensor coordinate frame orientation.

B Frame = Strapdown inertial sensor coordinates ("body frame") with axes parallel to nominal right handed orthogonal sensor input axes.

I Frame = Non-rotating inertial coordinate frame used as the reference for angular rate sensor measurements.

$\underline{V}$ = Vector without specific coordinate frame designation.

$\underline{V}^A$ = Column matrix with elements equal to the projection of $\underline{V}$ on Frame A axes.

$C_{A_2}^{A_1}$ = Direction cosine matrix that transforms a vector from its $A_2$ Frame projection form to its $A_1$ Frame projection form.

$\underline{\omega}_{A_1 A_2}$ = Angular rate of coordinate Frame $A_2$ relative to coordinate Frame $A_1$. When $A_1$ is the inertial I Frame, $\underline{\omega}_{A_1 A_2}$ is the angular rate measured by angular rate sensors mounted on Frame $A_2$.

$\Omega_{A_1 A_2}^{A_3}$ = Skew symmetric (or cross-product) form of $\underline{\omega}_{A_1 A_2}^{A_3}$ represented by the square matrix $\begin{bmatrix} 0 & -\omega_{Z_{12}}^{3} & \omega_{Y_{12}}^{3} \\ \omega_{Z_{12}}^{3} & 0 & -\omega_{X_{12}}^{3} \\ -\omega_{Y_{12}}^{3} & \omega_{X_{12}}^{3} & 0 \end{bmatrix}$ where $\omega_{X_{12}}^{3}$, $\omega_{Y_{12}}^{3}$, $\omega_{Z_{12}}^{3}$ are the components of $\underline{\omega}_{A_1A_2}^{A_3}$. The matrix product of $\Omega_{A_1A_2}^{A_3}$ with another $A_3$ Frame vector equals the cross-product of $\underline{\omega}_{A_1A_2}^{A_3}$ with the vector in the $A_3$ Frame. Because $\Omega_{A_1A_2}^{A_3}$ is skew symmetric, its transpose equals its negative.

$\dot{( )} = \frac{d( )}{dt}$ = Derivative with respect to time.

General Coriolis Relationship Between Unit Vectors In Rotating Coordinate Frames

Consider a unit vector $\underline{u}_{A_1}$ along one of the axes of a coordinate Frame $A_1$. Define its components in another coordinate Frame $A_2$ as the column vector $\underline{u}_{A_1}^{A_2}$. Now, assume that coordinate Frame $A_1$ is rotating relative to Frame $A_2$ at angular velocity $\underline{\omega}_{A_2A_1}$. Define the components of $\underline{\omega}_{A_2A_1}$ in Frame $A_2$ as the column vector $\underline{\omega}_{A_2A_1}^{A_2}$. Further, assume that the angle between $\underline{u}_{A_1}^{A_2}$ and $\underline{\omega}_{A_2A_1}^{A_2}$ is $\alpha$. Figure A-1 depicts the geometry involved as viewed in Frame 2.

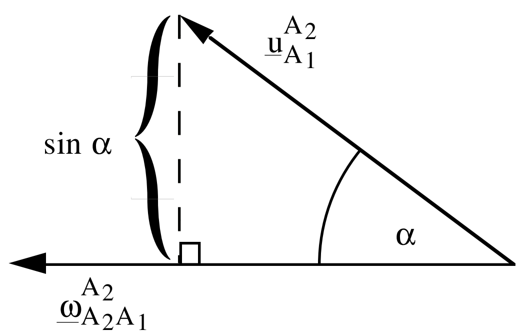


FIGURE A1 - GEOMETRY INVOLVED

The magnitude of the rate of change of $\underline{u}_{A_1}^{A_2}$ is equal to the component of $\underline{u}_{A_1}^{A_2}$ perpendicular to $\underline{\omega}_{A_2A_1}^{A_2}$ times the magnitude of $\underline{\omega}_{A_2A_1}^{A_2}$. From Figure A-1, since $\underline{u}_{A_1}^{A_2}$ is a unit vector, its component perpendicular to $\underline{\omega}_{A_2A_1}^{A_2}$ is sin α and:

$$\left|\dot{\underline{u}}_{A_1}^{A_2}\right| = \left|\underline{\omega}_{A_2A_1}^{A_2}\right| \sin\alpha$$

From Figure A-1, the direction of $\underline{\dot{u}}^{A_2}_{A_1}$ is perpendicular to $\underline{\omega}^{A_2}_{A_2 A_1}$ and $\underline{u}^{A_2}_{A_1}$, into the plane of the paper. From the definition of the cross-product between two vectors, the above magnitude and direction properties of $\underline{\dot{u}}^{A_2}_{A_1}$ show that:

$$\underline{\dot{u}}^{A_2}_{A_1} = \underline{\omega}^{A_2}_{A_2 A_1} \times \underline{u}^{A_2}_{A_1}$$

Defining the rotation rate of Frame $A_2$ relative to Frame $A_1$ as $\underline{\omega}^{A_2}_{A_1 A_2}$, and noting that:

$$\underline{\omega}^{A_2}_{A_1 A_2} = - \underline{\omega}^{A_2}_{A_2 A_1}$$

allows us to write the equivalent form:

$$\boxed{\underline{\dot{u}}^{A_2}_{A_1} = - \underline{\omega}^{A_2}_{A_1 A_2} \times \underline{u}^{A_2}_{A_1} \qquad \text{(A-1)}}$$

Equation (A-l) is the fundamental Coriolis relationship defining the rates of change of the components of a unit vector $\underline{u}^{A_2}_{A_1}$ (fixed in one coordinate Frame $A_1$) as measured in another coordinate Frame $A_2$ rotating relative to $A_1$ at angular velocity $\underline{\omega}^{A_2}_{A_1 A_2}$.

Body Direction Cosine Rate Equation

The direction cosine matrix relating body to local level navigation coordinates is defined as $C^L_B$, which can be related to an inertial non-rotating coordinate frame (I) through:

$$C^L_B = C^L_I \, C^I_B$$

where

$C^L_I$, $C^I_B$ = Direction cosine matrices relating the inertial (I) frame to the local level frame (L) and the body frame (B).

The derivative of the latter expression is:

$$\dot{C}^L_B = C^L_I \, \dot{C}^I_B + \dot{C}^L_I \, C^I_B \qquad \text{(A-2)}$$

The rows of $C_B^I$ represent unit vectors along the I Frame coordinate axes as projected into the B Frame:

$$C_B^I = \begin{bmatrix} \left(\underline{u}_{I1}^B\right)^T \\ \left(\underline{u}_{I2}^B\right)^T \\ \left(\underline{u}_{I3}^B\right)^T \end{bmatrix} = \left(\underline{u}_{I1}^B, \underline{u}_{I2}^B, \underline{u}_{I3}^B\right)^T \qquad \text{(A-3)}$$

where

$\underline{u}_{Ij}^B$ = The column vector whose elements represent the B Frame components of a unit vector along the $j^{th}$ I Frame coordinate axis.

Taking the derivative of (A-3) obtains:

$$\dot{C}_B^I = \left(\dot{\underline{u}}_{I1}^B, \dot{\underline{u}}_{I2}^B, \dot{\underline{u}}_{I3}^B\right)^T$$

Applying (A-1):

$$\dot{\underline{u}}_{Ij}^B = - \underline{\omega}_{IB}^B \times \underline{u}_{Ij}^B$$

or

$$\dot{\underline{u}}_{Ij}^B = - \Omega_{IB}^B \, \underline{u}_{Ij}^B$$

Substituting:

$$\begin{aligned} \dot{C}_B^I &= - \left[\Omega_{IB}^B \left(\underline{u}_{I1}^B, \underline{u}_{I2}^B, \underline{u}_{I3}^B\right)\right]^T \\ &= - \left(\underline{u}_{I1}^B, \underline{u}_{I2}^B, \underline{u}_{I3}^B\right)^T \, \Omega_{IB}^{B\,T} \\ &= \left(\underline{u}_{I1}^B, \underline{u}_{I2}^B, \underline{u}_{I3}^B\right)^T \, \Omega_{IB}^B \end{aligned}$$

where use has been made of the fact that the transpose of a skew symmetric matrix equals the negative of the matrix.

With (A-3),

$$\dot{C}_B^I = C_B^I \, \Omega_{IB}^B \qquad \text{(A-4)}$$

A similar development for $\dot{C}_L^I$ obtains:

$$\dot{C}_L^I = C_L^I \; \Omega_{IL}^L$$

Taking the transpose yields the $\dot{C}_I^L$ term in (A-2):

$$\dot{C}_I^L = - \Omega_{IL}^L \; C_I^L \qquad \text{(A-5)}$$

Substituting (A-4) and (A-5) into (A-2) yields:

$$\dot{C}_B^L = C_I^L \left( C_B^I \; \Omega_{IB}^B \right) - \left( \Omega_{IL}^L \; C_I^L \right) C_B^I$$

or, upon recombining the matrix elements:

$$\boxed{\dot{C}_B^L = C_B^L \; \Omega_{IB}^B - \Omega_{IL}^L \; C_B^L \qquad \text{(A-6)}}$$

Equation (A-6) relates the rate of change of the body-to-local level navigation frame direction cosine matrix to inertial rotation rates of the body as measured in body axes (by strapdown gyros) and inertial rotation rates of the navigation frame as computed in navigation frame axes.

Position Direction Cosine Rate Equation

The horizontal position of an inertial navigation system (INS) over the earth can be defined in terms of a direction cosine matrix $C_L^E$ relating earth fixed axes (E) to the locally level navigation coordinate frame axes (L). The rate of change of $C_L^E$ is related to the rotation rate of L with respect to the E Frame. Following the development procedure utilized for the body axis direction cosine rates, the $C_L^E$ rate equation can be similarly obtained:

$$C_L^E = \left( \underline{u}_{E1}^L, \underline{u}_{E2}^L, \underline{u}_{E3}^L \right)^T$$

$$\dot{C}_L^E = \left( \dot{\underline{u}}_{E1}^L, \dot{\underline{u}}_{E2}^L, \dot{\underline{u}}_{E3}^L \right)^T$$

$$\dot{\underline{u}}_{Ej}^L = - \Omega_{EL}^L \; \underline{u}_{Ej}^L$$

$$\dot{C}_L^E = - \left[ \Omega_{EL}^L \left( \underline{u}_{E1}^L, \underline{u}_{E2}^L, \underline{u}_{E3}^L \right) \right]^T = \left( \underline{u}_{E1}^L, \underline{u}_{E2}^L, \underline{u}_{E3}^L \right)^T \Omega_{EL}^L$$

$$\dot{C}_L^E = C_L^E\,\Omega_{EL}^L \tag{A-7}$$

Angular Rates Of The Earth And Local Level Frames

The inertial angular rate of the local level frame ($\underline{\omega}_{IL}^L$ in Equation (A-6)) is computed as the sum of the angular rate of L relative to E and the rotation rate of E relative to I:

$$\underline{\omega}_{IL}^L = \underline{\omega}_{IE}^L + \underline{\omega}_{EL}^L \tag{A-8}$$

The $\underline{\omega}_{IE}^L$ term in (A-8) represents the earth rotation rate vector as seen in local level coordinates. It is related to the equivalent component vector in earth coordinates through the direction cosine matrix relating local level and earth coordinates axes ($C_L^E$):

$$\underline{\omega}_{IE}^L = C_E^L\,\underline{\omega}_{IE}^E \tag{A-9}$$

The $\underline{\omega}_{EL}^L$ term in (A-8) is equal to the sum of its horizontal and vertical components. The vertical component is a function of the type of local level navigation frame utilized (e.g., wander azimuth, free azimuth, or North/East geographic). The horizontal component of $\underline{\omega}_{EL}^L$ is produced by the translation of the local level navigation frame over the earth. For a spherical earth, the magnitude of the associated angular rotation rate of the local vertical (the horizontal component of $\underline{\omega}_{EL}^L$) equals the horizontal component of velocity divided by the distance from earth's center to the vehicle. The direction of the horizontal angular rate vector is perpendicular to the velocity vector. The above effects can be expressed analytically as:

$$\underline{\omega}_{EL}^L = \frac{1}{R}\left(\underline{u}_R^L \times \underline{v}^L\right) + \rho_R\,\underline{u}_R^L \tag{A-10}$$

where

$\underline{v}$ = Translational velocity of the navigation frame relative to earth.

$R$ = Distance from earth's center to the INS (for a spherical earth).

$\underline{u}_R$ = Unit vector along the position vector from earth center to the current INS position.

$\rho_R$ = Terrestrial angular rate of the local level navigation frame (L) about $\underline{u}_R$.

For a true oblate earth model, Equation (A-10) has the more general form:

$$\underline{\omega}^L_{EL} = \underline{\rho}^L_H + \rho_{Vert}\, \underline{u}^L \qquad \text{(A-11)}$$

where

$\underline{\rho}^L_H$ = Horizontal component of $\underline{\omega}^L_{EL}$ required to maintain horizontal navigation coordinate axes in the presence of $\underline{v}^L$

$\underline{u}^L$ = Unit vector perpendicular to the surface of the earth along the local vertical.

$\rho_{Vert}$ = Terrestrial angular rate of the local level navigation frame (L) about the geodetic local geodetic vertical.

The $\underline{\rho}^L_H$ term is a function of $\underline{v}^L$ and the local curvature of the earth's surface.

Velocity Rate Equation

The velocity of interest in inertial navigation is the time rate of change of position relative to earth fixed coordinates. The velocity vector is defined in earth coordinates as:

$$\underline{v}^E \overset{\Delta}{=} \dot{\underline{R}}^E \qquad \text{(A-12)}$$

where

$\underline{v}^E$ = Column vector representing the velocity vector of interest projected along earth frame axes.

$\underline{R}^E$ = Column vector representing the position vector from earth's center to the INS as viewed in earth coordinate axes.

The components of $\underline{v}$ in local level frame (L) coordinates are the values needed for internal system computer usage and (with appropriate conversion routines) for navigation data outputs. The L Frame components of $\underline{v}$ are related to the earth frame components by the E to L direction cosine matrix through:

$$\underline{v}^L = C_E^L \, \underline{v}^E \tag{A-13}$$

The derivative of (A-13) is:

$$\dot{\underline{v}}^L = \dot{C}_E^L \, \underline{v}^E + C_E^L \, \dot{\underline{v}}^E \tag{A-14}$$

The $\dot{C}_E^L$ term in (A-14) is the transpose of (A-7):

$$\dot{C}_E^L = \left(\Omega_{EL}^L\right)^T C_E^L = - \Omega_{EL}^L \, C_E^L \tag{A-15}$$

where it is recognized that $\Omega_{EL}^L$ is skew symmetric, hence its transpose equals its negative.

The $\dot{\underline{v}}^E$ term in (A-14) can be developed by first operating on (A-12):

$$\underline{v}^E = \dot{\underline{R}}^E = \frac{d}{dt}\left(C_I^E \, \underline{R}^I\right) = C_I^E \, \dot{\underline{R}}^I + \dot{C}_I^E \, \underline{R}^I$$

Through a development similar to that leading to (A-4),

$$\dot{C}_I^E = C_I^E \, \Omega_{EI}^I = - C_I^E \, \Omega_{IE}^I \tag{A-16}$$

where it is recognized that $\Omega_{IE}^I$ is the negative of $\Omega_{EI}^I$. Hence,

$$\underline{v}^E = C_I^E \left(\dot{\underline{R}}^I - \Omega_{IE}^I \, \underline{R}^I\right) \tag{A-17}$$

The $\dot{\underline{v}}^E$ term for (A-14) is now obtained from the derivative of (A-17):

$$\begin{aligned} \dot{\underline{v}}^E &= C_I^E \left(\ddot{\underline{R}}^I - \dot{\Omega}_{IE}^I \, \underline{R}^I - \Omega_{IE}^I \, \dot{\underline{R}}^I\right) + \dot{C}_I^E \left(\dot{\underline{R}}^I - \Omega_{IE}^I \, \underline{R}^I\right) \\ &= C_I^E \left(\ddot{\underline{R}}^I - \Omega_{IE}^I \, \dot{\underline{R}}^I\right) + \dot{C}_I^E \left(\dot{\underline{R}}^I - \Omega_{IE}^I \, \underline{R}^I\right) \end{aligned} \tag{A-18}$$

The $\dot{\Omega}_{IE}^I$ term in the latter expression has been equated to zero due to the constancy of earth's rotation rate. With (A-16), (A-18) becomes:

$$\begin{aligned}\dot{\underline{v}}^E &= C_I^E\left(\ddot{\underline{R}}^I - \Omega_{IE}^I\,\dot{\underline{R}}^I - \Omega_{IE}^I\,\dot{\underline{R}}^I + \Omega_{IE}^I\,\Omega_{IE}^I\,\underline{R}^I\right)\\ &= C_I^E\left(\ddot{\underline{R}}^I - 2\,\Omega_{IE}^I\,\dot{\underline{R}}^I + \Omega_{IE}^I\,\Omega_{IE}^I\,\underline{R}^I\right)\end{aligned} \tag{A-19}$$

The $\dot{\underline{R}}^I$ term in (A-19) can be related to $\underline{v}$ through (A-17). Transformation of (A-17) to the I Frame (multiplication by $C_E^I$) and rearrangement yields:

$$\dot{\underline{R}}^I = \underline{v}^I + \Omega_{IE}^I\,\underline{R}^I$$

Substitution into (A-19) obtains:

$$\begin{aligned}\dot{\underline{v}}^E &= C_I^E\left[\ddot{\underline{R}}^I - 2\,\Omega_{IE}^I\left(\underline{v}^I + \Omega_{IE}^I\,\underline{R}^I\right) + \Omega_{IE}^I\,\Omega_{IE}^I\,\underline{R}^I\right]\\ &= C_I^E\left(\ddot{\underline{R}}^I - \Omega_{IE}^I\,\Omega_{IE}^I\,\underline{R}^I - 2\,\Omega_{IE}^I\,\underline{v}^I\right)\end{aligned} \tag{A-20}$$

The $\ddot{\underline{R}}^I$ term in (A-20) is the total inertial acceleration of the INS. This can be equated to the sum of gravitational acceleration ($\underline{g}_o$) and specific force acceleration ($\underline{a}_{SF}$), the latter representing the acceleration produced by contact forces that is sensed by accelerometers:

$$\ddot{\underline{R}}^I = \underline{g}_o^I + \underline{a}_{SF}^I$$

Equation (A-20) then becomes:

$$\dot{\underline{v}}^E = C_I^E\left(\underline{a}_{SF}^I + \underline{g}_o^I - \Omega_{IE}^I\,\Omega_{IE}^I\,\underline{R}^I - 2\,\Omega_{IE}^I\,\underline{v}^I\right) \tag{A-21}$$

We now define:

$$\underline{g}^I \overset{\Delta}{=} \underline{g}_o^I - \Omega_{IE}^I\,\Omega_{IE}^I\,\underline{R}^I$$

The $\underline{g}$ vector is the negative of the specific force acceleration that would be measured by accelerometers at rest relative to the earth at radius vector $\underline{R}$. The direction of $\underline{g}$ is along the line a stationary plumb bob would take at position location $\underline{R}$ (i.e., stationary relative to the earth). For this reason, $\underline{g}$ is sometimes referred to as plumb bob gravity. With this definition, (A-21) assumes the simpler form:

$$\dot{\underline{v}}^E = C_I^E\left(\underline{a}_{SF}^I + \underline{g}^I - 2\,\Omega_{IE}^I\,\underline{v}^I\right) \tag{A-22}$$

We can now substitute (A-22) and (A-15) into (A-14) to obtain the following for $\dot{\underline{v}}^L$:

$$
\begin{aligned}
\dot{\underline{v}}^L &= -\Omega_{EL}^L \; C_E^L \; \underline{v}^E + C_E^L \; C_I^E \left(\underline{a}_{SF}^I + \underline{g}^I - 2\,\Omega_{IE}^I \; \underline{v}^I\right) \\
&= -\Omega_{EL}^L \; \underline{v}^L + C_I^L \left(\underline{a}_{SF}^I + \underline{g}^I - 2\,\Omega_{IE}^I \; \underline{v}^I\right) \\
&= -\Omega_{EL}^L \; \underline{v}^L + \underline{a}_{SF}^L + \underline{g}^L - 2\,\Omega_{IE}^L \; \underline{v}^L
\end{aligned}
$$

Introducing the cross-product vector notation into the latter expression and combining terms yields the final expression for $\dot{\underline{v}}^L$:

$$
\boxed{\dot{\underline{v}}^L = \underline{a}_{SF}^L + \underline{g}^L - \left(\underline{\omega}_{EL}^L + 2\,\underline{\omega}_{IE}^L\right) \times \underline{v}^L \qquad \text{(A-23)}}
$$

The $\underline{a}_{SF}^L$ term in (A-23) is obtained by transforming data measured in aircraft body axes to local level coordinates using the body (B) to local level (L) direction cosine matrix:

$$
\boxed{\underline{a}_{SF}^L = C_B^L \, \underline{a}_{SF}^B \qquad \text{(A-24)}}
$$

<u>Altitude Rate Equation</u>

The equation for altitude rate is obtained from the defining equations for altitude:

$$
\begin{aligned}
\underline{h}^L &= h\,\underline{u}^L = \underline{R}^L - \underline{R}_s^L \\
h &= \left(\underline{R}^L - \underline{R}_s^L\right) \bullet \underline{u}^L
\end{aligned}
\qquad \text{(A-25)}
$$

where

$h$ = Altitude

$\underline{u}^L$ = Unit vector (in L Frame axes) that is perpendicular (along the local geodetic vertical) to the earth surface and is directed through the local $\underline{R}^L$ position point. By the definition of the L Frame, $\underline{u}^L$ is along the L Frame vertical axis.

$\underline{h}^L$ = Altitude vector.

$\underline{R}_s^L$ = Position vector from earth center to the earth surface point where $\underline{u}^L$ emanates.

The altitude rate is the derivative of h in (A-25):

$$\dot{h} = \left(\dot{\underline{R}}^{L} - \dot{\underline{R}}_{s}^{L}\right) \bullet \underline{u}^{L} \tag{A-26}$$

where it is recognized that the rate of change of $\underline{u}^L$ is zero because it is defined as a unit vector along the L-Frame vertical axis (hence, its derivative in the L-Frame is zero).

We can also write:

$$\begin{aligned} \underline{R}^{L} &= C_{E}^{L}\,\underline{R}^{E} \\ \underline{R}_{s}^{L} &= C_{E}^{L}\,\underline{R}_{s}^{E} \end{aligned} \tag{A-27}$$

The derivative of (A-27) is:

$$\begin{aligned} \dot{\underline{R}}^{L} &= C_{E}^{L}\;\dot{\underline{R}}^{E} + \dot{C}_{E}^{L}\;\underline{R}^{E} \\ \dot{\underline{R}}_{s}^{L} &= C_{E}^{L}\;\dot{\underline{R}}_{s}^{E} + \dot{C}_{E}^{L}\;\underline{R}_{s}^{E} \end{aligned} \tag{A-28}$$

The $\dot{C}_E^L$ term in (A-28) is the transpose of (A-7). From the definition of $\omega_{EL}^L$, its transpose equals its negative, hence:

$$\dot{C}_{E}^{L} = -\,\Omega_{EL}^{L}\,C_{E}^{L} \tag{A-29}$$

Substituting (A-29) and (A-12) in (A-28):

$$\begin{aligned} \dot{\underline{R}}^{L} &= C_{E}^{L}\;\underline{v}^{E} - \Omega_{EL}^{L}\,C_{E}^{L}\;\underline{R}^{E} \\ \dot{\underline{R}}_{s}^{L} &= C_{E}^{L}\;\dot{\underline{R}}_{s}^{E} - \Omega_{EL}^{L}\,C_{E}^{L}\;\underline{R}_{s}^{E} \end{aligned} \tag{A-30}$$

or

$$\begin{aligned} \dot{\underline{R}}^{L} &= \underline{v}^{L} - \underline{\omega}_{EL}^{L} \times \underline{R}^{L} \\ \dot{\underline{R}}_{s}^{L} &= C_{E}^{L}\,\dot{\underline{R}}_{s}^{E} - \underline{\omega}_{EL}^{L}\,\underline{R}_{s}^{L} \end{aligned} \tag{A-31}$$

Substituting (A-31) with (A-25) into (A-26) yields:

$$
\begin{aligned}
\dot{h} &= \left[\underline{v}^L - C_E^L \, \dot{\underline{R}}_s^E - \underline{\omega}_{EL}^L \times \left(\underline{R}^L - \underline{R}_s^L\right)\right] \bullet \underline{u}^L \\
&= \left[\underline{v}^L - C_E^L \, \dot{\underline{R}}_s^E - h \left(\underline{\omega}_{EL}^L \times \underline{u}^L\right)\right] \bullet \underline{u}^L \qquad \text{(A-32)} \\
&= \underline{v}^L \bullet \underline{u}^L - \left(C_E^L \, \dot{\underline{R}}_s^E\right) \bullet \underline{u}^L
\end{aligned}
$$

From the definition of $\underline{R}_s^E$ as a vector from earth's center to the local earth surface, changes in $\underline{R}_s^E$ produced by vehicle translation must be horizontal along the earth surface. As such, the second term in Equation (A-32) is identically zero. (Note: This can also be demonstrated analytically through a very complicated development.) The final equation for altitude rate, therefore, is:

$$
\boxed{\dot{h} = \underline{v}^L \bullet \underline{u}^L} \qquad \text{(A-33)}
$$

Strapdown Inertial Navigation Equation Summary

The strapdown inertial navigation equations are given by Equations (A-6), (A-7), (A-9), (A-10), (A-11), (A-23), (A-24), and (A-33), and are summarized below for easy reference:

$$
\begin{aligned}
\dot{C}_B^L &= C_B^L \, \Omega_{IB}^B - \left(\Omega_{IE}^L + \Omega_{EL}^L\right) C_B^L \\
\underline{\omega}_{IE}^L &= C_E^L \, \underline{\omega}_{IE}^E \\
\underline{\omega}_{EL}^L &= \frac{1}{R}\left(\underline{u}_R^L \times \underline{v}^L\right) + \rho_R \, \underline{u}_R^L \qquad \text{for a spherical earth} \\
& \qquad\qquad\qquad\qquad\qquad\qquad\qquad\qquad \text{(A-34)} \\
\underline{\omega}_{EL}^L &= \underline{\rho}_H^L + \rho_{Vert} \, \underline{u}^L \qquad \text{for a general oblate earth} \\
\dot{\underline{v}}^L &= C_B^L \, \underline{a}_{SF}^B + \underline{g}^L - \left(\underline{\omega}_{EL}^L + 2\underline{\omega}_{IE}^L\right) \times \underline{v}^L \\
\dot{C}_L^E &= C_L^E \, \Omega_{EL}^L \\
\dot{h} &= \underline{v}^L \bullet \underline{u}^L
\end{aligned}
$$

# APPENDIX B

## DERIVATION OF ERROR EQUATIONS FOR STRAPDOWN INERTIAL NAVIGATION SYSTEMS

This appendix derives the error equations for strapdown inertial navigation systems. The results are generalized to the extent that they can be applied to any of the traditional types of local level navigation implementations (e.g., wander azimuth, free azimuth, or North/East geographic).

### Nomenclature

The following general nomenclature is used in this appendix:

$A, A_1, A_2, A_3$ = Arbitrary coordinate frames.

E Frame = Earth fixed coordinate frame used for position location definition.

L Frame = Navigation coordinate frame having its Z axis parallel to the upward vertical at the local earth surface referenced position location point on the earth's surface. Used for integrating acceleration into velocity, for defining the angular orientation of the local vertical in the E Frame and for describing the strapdown sensor coordinate frame orientation.

B Frame = Strapdown inertial sensor coordinates ("body frame") with axes parallel to nominal right handed orthogonal sensor input axes.

I Frame = Non-rotating inertial coordinate frame used as the reference for angular rate sensor measurements.

$\underline{V}$ = Vector without specific coordinate frame designation.

$\underline{V}^A$ = Column matrix with elements equal to the projection of $\underline{V}$ on Frame A axes.

$C_{A_2}^{A_1}$ = Direction cosine matrix that transforms a vector from its $A_2$ Frame projection form to its $A_1$ Frame projection form.

$\underline{\omega}_{A_1A_2}$ = Angular rate of coordinate Frame $A_2$ relative to coordinate Frame $A_1$. When $A_1$ is the inertial I Frame, $\underline{\omega}_{A_1A_2}$ is the angular rate measured by angular rate sensors mounted on Frame $A_2$.

$\Omega_{A_1A_2}^{A_3}$ = Skew symmetric (or cross-product) form of $\underline{\omega}_{A_1A_2}^{A_3}$ represented by the square matrix $\begin{bmatrix} 0 & -\omega_{Z_{12}}^{3} & \omega_{Y_{12}}^{3} \\ \omega_{Z_{12}}^{3} & 0 & -\omega_{X_{12}}^{3} \\ -\omega_{Y_{12}}^{3} & \omega_{X_{12}}^{3} & 0 \end{bmatrix}$ where $\omega_{X_{12}}^{3}$, $\omega_{Y_{12}}^{3}$, $\omega_{Z_{12}}^{3}$ are the components of $\underline{\omega}_{A_1 A_2}^{A_3}$. The matrix product of $\Omega_{A_1 A_2}^{A_3}$ with another $A_3$ Frame vector equals the cross-product of $\underline{\omega}_{A_1 A_2}^{A_3}$ with the vector in the $A_3$ Frame. Because $\Omega_{A_1 A_2}^{A_3}$ is skew symmetric, its transpose equals its negative.

$I$ = Identity matrix.

$\dot{(\ )} = \dfrac{d(\ )}{dt}$ = Derivative with respect to time.

$\underline{v}$ = Velocity relative to the earth.

$h$ = Altitude above the earth's surface.

$\underline{g}$ = Plumb-bob gravity.

$\underline{a}_{SF}$ = Specific force acceleration (acceleration produced by contact forces, not gravitation). Strapdown accelerometers measure $\underline{a}_{SF}$ in the B Frame.

$\underline{u}_R$ = Unit vector upward along the the radial vector from earth's center.

$R$ = Radial distance from earth's center to the INS.

$\rho_R$ = vertical component of $\underline{\omega}_{EL}^{L}$ transport rate.

Strapdown Inertial Navigation Equations

The differential equations of kinematic motion of a vehicle traveling relative to the earth that are typically instrumented in a strapdown inertial navigation system (INS) are derived in Appendix A (Equations (A-34)) and have the following form:

$$
\begin{aligned}
&\dot{C}_B^L = C_B^L\, \Omega_{IB}^B - \left(\Omega_{IE}^L + \Omega_{EL}^L\right) C_B^L \\
&\underline{\omega}_{IE}^L = C_E^L\, \underline{\omega}_{IE}^E \\
&\underline{\omega}_{EL}^L = \frac{1}{R}\left(\underline{u}_R^L \times \underline{v}^L\right) + \rho_R\, \underline{u}_R^L \qquad \text{for a spherical earth} \\
&\dot{\underline{v}}^L = C_B^L\, \underline{a}_{SF}^B + \underline{g}^L - \left(\underline{\omega}_{EL}^L + 2\,\underline{\omega}_{IE}^L\right) \times \underline{v}^L \\
&\dot{C}_L^E = C_L^E\, \Omega_{EL}^L \\
&\dot{h} = \underline{v}^L \bullet \underline{u}_R^L
\end{aligned}
\qquad \text{(B-1)}
$$

The spherical earth form of the Equation (A-34) $\underline{\omega}_{EL}^L$ equation has been used in (B-1) as an approximation for error model determination. In addition, the approximation has been made that the unit vector along the geodetic vertical $\underline{u}^L$ is parallel to the unit vector along the radius vector from earth's center $\underline{u}_R^L$, hence, $\underline{u}_R^L$ is utilized for both and treated as a constant. These approximations produce second order error effects that are generally negligible for error analysis purposes.

## Strapdown Navigation System Error Equations

A strapdown inertial navigation system attempts to continuously evaluate Equations (B-1) in an on-board navigation computer using strapdown gyros and accelerometers to measure the $\underline{\omega}_{IB}^B$ and $\underline{a}_{SF}^B$ quantities. The accuracy for such an implementation is dependent primarily on the accuracy of the inertial sensor measurements (i.e. - computer errors can be designed out of the error budget by careful software development and use of a computer with sufficient word length and speed).

Inertial sensor errors propagate through the navigation equations, producing navigation errors that contain the dynamic characteristics of Equations (B-1). Equations for the navigation errors can be derived by differencing Equations (B-1) with the same form of these equations implemented in the on-board flight computer that include sensor errors. The equations executed in the INS computer are defined as:

$$\dot{\hat{C}}{}^L_B = \hat{C}^L_B \, \tilde{\Omega}^B_{IB} - \left(\hat{\Omega}^L_{IE} + \hat{\Omega}^L_{EL}\right) \hat{C}^L_B$$

$$\hat{\underline{\omega}}{}^L_{IE} = \hat{C}^L_E \, \hat{\underline{\omega}}{}^E_{IE}$$

$$\hat{\underline{\omega}}{}^L_{EL} = \frac{1}{\hat{R}} \left(\hat{\underline{u}}{}^L_R \times \hat{\underline{v}}{}^L\right) + \hat{\rho}_R \, \hat{\underline{u}}{}^L_R \qquad \text{(B-2)}$$

$$\dot{\hat{\underline{v}}}{}^L = \hat{C}^L_B \, \tilde{\underline{a}}{}^B_{SF} + \hat{\underline{g}}{}^L - \left(\hat{\underline{\omega}}{}^L_{EL} + 2 \, \hat{\underline{\omega}}{}^L_{IE}\right) \times \hat{\underline{v}}{}^L$$

$$\dot{\hat{C}}{}^E_L = \hat{C}^E_L \, \hat{\Omega}^L_{EL}$$

$$\dot{\hat{h}} = \hat{\underline{v}}{}^L \bullet \hat{\underline{u}}{}^L_R$$

where

$\wedge$ = Designation that the quantity indicated is a numerical array that has been generated as a result of calculations in the INS computer.

$\sim$ = Designation for a sensor measurement of the quantity indicated (i.e. - containing sensor errors).

The navigation error quantities of interest are the errors in $\hat{C}^L_B$, $\hat{\underline{v}}{}^L$, $\hat{C}^E_L$ and $\hat{h}$ defined as:

$$\delta C^L_B \stackrel{\Delta}{=} \hat{C}^L_B - C^L_B$$

$$\delta \underline{v}^L \stackrel{\Delta}{=} \hat{\underline{v}}{}^L - \underline{v}^L \qquad \text{(B-3)}$$

$$\delta C^E_L \stackrel{\Delta}{=} \hat{C}^E_L - C^E_L$$

$$\delta h \stackrel{\Delta}{=} \hat{h} - h$$

Errors in the sensor measurements and the other variables in Equations (B-2) are defined similarly:

$$
\begin{aligned}
\delta\tilde{\underline{\omega}}^{B}_{IB} &\triangleq \tilde{\underline{\omega}}^{B}_{IB} - \underline{\omega}^{B}_{IB} \qquad & \delta\underline{\omega}^{L}_{EL} &\triangleq \hat{\underline{\omega}}^{L}_{EL} - \underline{\omega}^{L}_{EL} \\
\delta\tilde{\underline{a}}^{B}_{SF} &\triangleq \tilde{\underline{a}}^{B}_{SF} - \underline{a}^{B}_{SF} & \delta\underline{g}^{L} &\triangleq \hat{\underline{g}}^{L} - \underline{g}^{L} \\
\delta\Omega^{L}_{IE} &\triangleq \hat{\Omega}^{L}_{IE} - \Omega^{L}_{IE} & \delta\rho_{R} &\triangleq \hat{\rho}_{R} - \rho_{R} \\
\delta\underline{\omega}^{L}_{IE} &\triangleq \hat{\underline{\omega}}^{L}_{IE} - \underline{\omega}^{L}_{IE} & \delta R &\triangleq \hat{R} - R \\
\delta\Omega^{L}_{EL} &\triangleq \hat{\Omega}^{L}_{EL} - \Omega^{L}_{EL} & &
\end{aligned}
\qquad \text{(B-4)}
$$

It is to be noted that no errors have been defined for $\hat{\underline{u}}^{L}_{R}$ and $\hat{\underline{\omega}}^{E}_{IE}$ . The errors in these quantities are identically zero because the values used for them in the computer are not calculated, but are constants equal to the true values.

$$
\begin{aligned}
\hat{\underline{u}}^{L}_{R} - \underline{u}^{L}_{R} &= 0 \\
\hat{\underline{\omega}}^{E}_{IE} - \underline{\omega}^{E}_{IE} &= 0
\end{aligned}
\qquad \text{(B-5)}
$$

A set of error propagation equations relating (B-3) and (B-4) can now be obtained by differencing Equations (B-1) with (B-2), introducing the Equation (B-3), (B-4), and (B-5) relationships, and dropping second order (error squared) terms:

$$\delta\dot{C}_B^L = \delta C_B^L\, \Omega_{IB}^B + C_B^L\, \delta\tilde{\Omega}_{IB}^B$$

$$- \left(\delta\Omega_{IE}^L + \delta\Omega_{EL}^L\right) C_B^L - \left(\Omega_{IE}^L + \Omega_{EL}^L\right) \delta C_B^L$$

$$\delta\dot{\underline{v}}^L = \delta C_B^L\, \underline{a}_{SF}^B + C_B^L\, \delta\tilde{\underline{a}}_{SF}^B - \left(2\, \delta\underline{\omega}_{IE}^L + \delta\underline{\omega}_{EL}^L\right) \times \underline{v}^L$$

$$- \left(2\, \underline{\omega}_{IE}^L + \underline{\omega}_{EL}^L\right) \times \delta\underline{v}^L + \delta\underline{g}^L$$

(B-6)

$$\delta\dot{C}_L^E = \delta C_L^E\, \Omega_{EL}^L + C_L^E\, \delta\Omega_{EL}^L$$

$$\delta\dot{h} = \underline{u}_R^L \bullet \delta\underline{v}^L$$

$$\delta\underline{\omega}_{IE}^L = \delta C_E^L\, \underline{\omega}_{IE}^E$$

$$\delta\underline{\omega}_{EL}^L = \frac{1}{R}\left(\underline{u}_R^L \times \delta\underline{v}^L\right) - \frac{\delta R}{R^2}\left(\underline{u}_R^L \times \underline{v}^L\right) + \delta\rho_R\, \underline{u}_R^L$$

Equations (B-6) can be converted into a more tractable form by introducing the concept of small angle vector rotations as the cause for the $\delta C$ errors:

$$\hat{C}_B^L = \left(I - \Gamma^L\right) C_B^L \qquad \Rightarrow \qquad \delta C_B^L = -\,\Gamma^L\, C_B^L$$

$$\hat{C}_E^L = \left(I - E^L\right) C_E^L \qquad \Rightarrow \qquad \delta C_E^L = -\,E^L\, C_E^L \tag{B-7}$$

$$\hat{C}_L^E = \left(\hat{C}_E^L\right)^T = C_L^E\left(I + E^L\right) \qquad \Rightarrow \qquad \delta C_L^E = C_L^E\, E^L$$

where

$\underline{\gamma}^L$ = The small angle rotation vector error associated with $\delta C_B^L$.

$\underline{e}^L$ = The small angle rotation vector associated with $\delta C_L^E$ .

$\Gamma^L$, $E^L$ = Skew symmetric operators associated with $\underline{\gamma}^L$ and $\underline{e}^L$. See Nomenclature section at front of this appendix for definition of skew symmetric form of general angular velocity vectors. The $\Gamma^L$, $E^L$ skew symmetric forms of $\underline{\gamma}^L$, $\underline{e}^L$ are defined similarly.

Using (B-7), the $\delta\underline{\omega}_{IE}^{L}$ equation in set (B-6) is:

$$\delta\underline{\omega}_{IE}^{L} = - E^{L} C_{E}^{L} \underline{\omega}_{IE}^{E} = - E^{L} \underline{\omega}_{IE}^{L} = - \underline{e}^{L} \times \underline{\omega}_{IE}^{L} \tag{B-8}$$

The error model for $\delta\underline{g}^{L}$ in the Equations (B-6) $\delta\dot{\underline{v}}^{L}$ expression is the variation in $\underline{g}^{L}$ in Equations (B-1) from true gravity. Variations are produced by altitude error (error in R) and true gravity variations from the model used in the computer. The $\underline{g}^{L}$ term in Equations (B-1) can be defined in general as a simple inverse square law gravity model plus a correction that accounts for the deviation of gravity from the simplified inverse square model:

$$\boxed{\underline{g}^{L} = - g_{o} \frac{R_{o}^{2}}{R^{2}} \underline{u}_{R}^{L} + \Delta\underline{g}^{L}} \tag{B-9}$$

where

$g_o$ = Simplified inverse square gravitation model magnitude on the earth surface.

$R_o$ = Earth's radius.

$R$ = Distance from earth center to the INS.

$\Delta\underline{g}^{L}$ = Correction to inverse square model that accounts for earth mass distribution effects and earth angular rotation centripetal acceleration (See Appendix A definition for gravity in Equation (A-22)).

The $\delta\underline{g}^{L}$ term in the Equations (B-6) $\delta\dot{\underline{v}}^{L}$ expression is the differential of (B-9):

$$\delta\underline{g}^{L} = 2\, g_{o} \frac{R_{o}^{2}}{R^{3}} \delta R + \delta\Delta\underline{g}^{L} \approx \frac{2g}{R} \delta h\, \underline{u}_{R}^{L} + \delta\underline{g}_{M}^{L} \tag{B-10}$$

where

$g$ = Gravity magnitude at INS.

$\delta\underline{g}_{M}^{L}$ = Unmodeled gravity error (produced, for example, by local gravity anomalies).

Equation (B-10) includes the variation of the inverse square term in (B-9) with altitude, but excludes variations in the $\Delta \underline{g}^L$ term with altitude as negligible. Equation (B-10) also includes the very good approximation that the error in R is equal to the error in h:

$$\delta R \approx \delta h \tag{B-11}$$

Using (B-7), (B-8) and (B-10), the $\dot{\underline{\delta v}}^L$ equation in set (B-6) becomes:

$$\begin{aligned} \delta\dot{\underline{v}}^L = {} & C_B^L \, \delta\underline{\tilde{a}}_{SF}^B - \underline{\gamma}^L \times \underline{a}_{SF}^L - \left(2\, \underline{\omega}_{IE}^L + \underline{\omega}_{EL}^L\right) \times \delta\underline{v}^L \\ & - \left( \delta\underline{\omega}_{EL}^L - 2\, \underline{e}^L \times \underline{\omega}_{IE}^L \right) \times \underline{v}^L + \frac{2\, g}{R}\, \delta h\, \underline{u}_R^L + \delta\underline{g}_M^L \end{aligned} \tag{B-12}$$

Substituting (B-7) into the $\delta\dot{C}_L^E$ equation in set (B-6) yields:

$$\dot{C}_L^E \, E^L + C_L^E \, \dot{E}^L = C_L^E \, E^L \, \Omega_{EL}^L + C_L^E \, \delta\Omega_{EL}^L$$

But, from Equation (B-1):

$$\dot{C}_L^E = C_L^E \, \Omega_{EL}^L$$

Therefore,

$$C_L^E \, \dot{E}^L = C_L^E \, E^L \, \Omega_{EL}^L - C_L^E \, \Omega_{EL}^L \, E^L + C_L^E \, \delta\Omega_{EL}^L$$

or,

$$\dot{E}^L = \left(E^L \, \Omega_{EL}^L - \Omega_{EL}^L \, E^L\right) + \delta\Omega_{EL}^L$$

The term in brackets can be reduced to simpler form by application of the triple vector product identity:

$$\left(\underline{V}_1 \times \underline{V}_2\right) \times \underline{V}_3 = \left(\underline{V}_1 \bullet \underline{V}_3\right) \underline{V}_2 - \left(\underline{V}_2 \bullet \underline{V}_3\right) \underline{V}_1 \tag{B-13}$$

where

$\underline{V}_1, \underline{V}_2, \underline{V}_3 \quad = \quad$ Arbitrary vectors

Multiplying the term in brackets by an arbitrary vector ($\underline{V}_3$) yields:

$$(\ )\,\underline{V}_3 = E^L\,\Omega_{EL}^L\,\underline{V}_3 - \Omega_{EL}^L\,E^L\underline{V}_3$$

or in the equivalent vector form:

$$(\ )\,\underline{V}_3 = \underline{e}^L \times \left(\underline{\omega}_{EL}^L \times \underline{V}_3\right) - \underline{\omega}_{EL}^L \times \left(\underline{e}^L \times \underline{V}_3\right)$$

Applying the triple vector product identity to the terms on the right:

$$\begin{aligned}(\ )\,\underline{V}_3 &= \left(\underline{e}^L \bullet \underline{V}_3\right)\underline{\omega}_{EL}^L - \left(\underline{e}^L \bullet \underline{\omega}_{EL}^L\right)\underline{V}_3 - \left(\underline{\omega}_{EL}^L \bullet \underline{V}_3\right)\underline{e}^L + \left(\underline{\omega}_{EL}^L \bullet \underline{e}^L\right)\underline{V}_3 \\ &= \left(\underline{e}^L \bullet \underline{V}_3\right)\underline{\omega}_{EL}^L - \left(\underline{\omega}_{EL}^L \bullet \underline{V}_3\right)\underline{e}^L\end{aligned}$$

which, with the Equation (B-13) triple vector product identity, becomes:

$$(\ )\,\underline{V}_3 = \left(\underline{e}^L \times \underline{\omega}_{EL}^L\right) \times \underline{V}_3$$

or in matrix form:

$$(\ )\,\underline{V}_3 = \left(\underline{e}^L \times \underline{\omega}_{EL}^L\right)^* \underline{V}_3$$

where

$(\ )^*$ = Designation for skew symmetric form of the vector in brackets. See Notation section at the start of this appendix for the definition of a vector skew symmetric form applied to angular rate vectors. The $(\ )^*$ notation uses the same skew symmetric form applied to an arbitrary vector.

Since $\underline{V}_3$ is arbitrary,

$$(\ ) = E^L\,\Omega_{EL}^L - \Omega_{EL}^L\,E^L = \left(\underline{e}^L \times \underline{\omega}_{EL}^L\right)^*$$

Thus:

$$\dot{E}^L = \left(\underline{e}^L \times \underline{w}_{EL}^L\right)^* + \delta\Omega_{EL}^L$$

or

$$\boxed{\dot{\underline{e}}^L = \underline{e}^L \times \underline{\omega}_{EL}^L + \delta\underline{\omega}_{EL}^L \qquad \text{(B-14)}}$$

The $\delta\dot{C}_B^L$ expression in Equations (B-6) is similarly reduced by applying $\delta\underline{\omega}_{EL}^L$ from Equation (B-6) and Equations (B-7) - (B-8):

$$\delta\dot{C}_B^L = -\dot{\Gamma}^T C_B^L - \Gamma^T \dot{C}_B^L = -\Gamma^L C_B^L \Omega_{IB}^B + C_B^L \delta\tilde{\Omega}_{IB}^B$$

$$-\left(\delta\Omega_{IE}^L + \delta\Omega_{EL}^L\right) C_B^L + \left(\Omega_{IE}^L + \Omega_{EL}^L\right)\Gamma^L C_B^L$$

From Equations (B-l):

$$\dot{C}_B^L = C_B^L \Omega_{IB}^B - \left(\Omega_{IE}^L + \Omega_{EL}^L\right) C_B^L$$

Hence,

$$\begin{aligned}
\dot{\Gamma}^L C_B^L &= -\Gamma^L\left[C_B^L \Omega_{IB}^B - \left(\Omega_{IE}^L + \Omega_{EL}^L\right) C_B^L\right] \\
&\quad + \Gamma^L C_B^L \Omega_{IB}^B - C_B^L \delta\tilde{\Omega}_{IB}^B + \left(\delta\Omega_{IE}^L + \delta\Omega_{EL}^L\right) C_B^L - \left(\Omega_{IE}^L + \Omega_{EL}^L\right)\Gamma^L C_B^L \\
&= \Gamma^L\left(\Omega_{IE}^L + \Omega_{EL}^L\right) C_B^L - \left(\Omega_{IE}^L + \Omega_{EL}^L\right)\Gamma^L C_B^L \\
&\quad - C_B^L \delta\tilde{\Omega}_{IB}^B + \left(\delta\Omega_{IE}^L + \delta\Omega_{EL}^L\right) C_B^L
\end{aligned}$$

or

$$\begin{aligned}
\dot{\Gamma}^L &= \Gamma^L\left(\Omega_{IE}^L + \Omega_{EL}^L\right) - \left(\Omega_{IE}^L + \Omega_{EL}^L\right)\Gamma^L - C_B^L \delta\tilde{\Omega}_{IB}^B C_L^B + \delta\Omega_{IE}^L + \delta\Omega_{EL}^L \\
&= \left[\underline{\gamma}^L \times \left(\underline{\omega}_{IE}^L + \underline{\omega}_{EL}^L\right)\right]^* - C_B^L \delta\tilde{\Omega}_{IB}^B C_L^B + \delta\Omega_{IE}^L + \delta\Omega_{EL}^L
\end{aligned}$$

It can be shown that:

$$C_B^L \delta\tilde{\Omega}_{IB}^B C_L^B = \left(C_B^L \delta\underline{\omega}_{IB}^B\right)^*$$

Hence,

$$\dot{\Gamma}^L = \left[\underline{\gamma}^L \times \left(\underline{\omega}_{IE}^L + \underline{\omega}_{EL}^L\right)\right]^* - \left(C_B^L \underline{\delta\omega}_{IB}^B\right)^* + \delta\Omega_{IE}^L + \delta\Omega_{EL}^L$$

or, in vector form:

$$\dot{\underline{\gamma}}^L = \underline{\gamma}^L \times \left(\underline{\omega}_{IE}^L + \underline{\omega}_{EL}^L\right) - C_B^L \underline{\delta\tilde{\omega}}_{IB}^B + \delta\underline{\omega}_{IE}^L + \delta\underline{\omega}_{EL}^L$$

or with Equation (B-8):

$$\dot{\underline{\gamma}}^L = \underline{\gamma}^L \times \left(\underline{\omega}_{IE}^L + \underline{\omega}_{EL}^L\right) - C_B^L\, \delta\underline{\tilde{\omega}}_{IB}^B - \underline{e}^L \times \underline{\omega}_{IE}^L + \delta\underline{\omega}_{EL}^L \qquad \text{(B-15)}$$

The $\delta\underline{\omega}_{EL}^L$ term in Equations (B-12), (B-14), and (B-15) is the expression in Equations (B-6) with (B-11) for $\delta R$:

$$\delta\underline{\omega}_{EL}^L = \frac{1}{R}\left(\underline{u}_R^L \times \delta\underline{v}^L\right) - \frac{\delta h}{R^2}\left(\underline{u}_R^L \times \underline{v}^L\right) + \delta\rho_R\, \underline{u}_R^L \qquad \text{(B-16)}$$

Equations (B-12), (B-14), (B-15), (B-16) and (B-6) for $\delta\dot{h}$ constitute the error expressions for Equations (B-l) in terms of sensor errors $\delta\underline{\tilde{a}}_{SF}^B$ and $\delta\underline{\tilde{\omega}}_{IB}^B$. Equations (B-3), (B-4), and (B-7) provide the definition for error terms $\delta\underline{v}^L$, $\underline{\gamma}^L$, $\underline{e}^L$, $\delta h$ in terms of the parameters calculated in the navigation computer. These equations are summarized below:

$$\begin{aligned}
\dot{\underline{\gamma}}^L &= \underline{\gamma}^L \times \left(\underline{\omega}_{IE}^L + \underline{\omega}_{EL}^L\right) - C_B^L\, \delta\underline{\tilde{\omega}}_{IB}^B - \underline{e}^L \times \underline{\omega}_{IE}^L + \delta\underline{\omega}_{EL}^L \\
\delta\underline{\omega}_{EL}^L &= \frac{1}{R}\left(\underline{u}_R^L \times \delta\underline{v}^L\right) - \frac{\delta h}{R^2}\left(\underline{u}_R^L \times \underline{v}^L\right) + \delta\rho_R\, \underline{u}_R^L \\
\delta\dot{\underline{v}} &= C_B^L\, \delta\underline{\tilde{a}}_{SF}^B - \underline{\gamma}^L \times \underline{a}_{SF}^L - \left(2\, \underline{\omega}_{IE}^L + \underline{\omega}_{EL}^L\right) \times \delta\underline{v}^L \\
&\quad - \left(\delta\underline{\omega}_{EL}^L - 2\, \underline{e}^L \times \underline{\omega}_{IE}^L\right) \times \underline{v}^L + \frac{2\,g}{R}\, \delta h\, \underline{u}_R^L + \delta\underline{g}_M^L \qquad \text{(B-17)} \\
\dot{\underline{e}}^L &= \underline{e}^L \times \underline{\omega}_{EL}^L + \delta\underline{\omega}_{EL}^L \\
\delta\dot{h} &= \underline{u}_R^L \bullet \delta\underline{v}^L
\end{aligned}$$

Equations (B-17) constitute an error model for a strapdown Iinertial navigation system that can be used for covariance simulation or Kalman filter design purposes. A disadvantage in these equations is that they compute position in terms of four parameters, the $\underline{\varepsilon}^L$ vector and

$\delta h$. The vertical component of $\underline{e}^L$, in particular, is a redundant angle that only appears as a consequence of the definition of the error parameters in locally level L Frame coordinates (i.e., the vertical component of $\underline{e}^L$ is the L Frame azimuth error). On the other hand, if the position error states are not significant enough to be included (e.g., in a Kalman filter design), the $\underline{\varepsilon}^L$ and $\delta h$ error states need not be included, hence, the above noted disadvantage disappears.

Error Equation Revisions To Simplify Position Error State Model

For situations where the position error states are to be included, and the redundant $\underline{\varepsilon}^L$ vertical error state is to be eliminated, a different definition can be used for the error parameters that avoids the need to explicitly calculate the vertical component of $\underline{e}^L$. The method is to define the basic attitude, velocity and position errors in earth (E Frame) coordinates:

$$\hat{C}_B^E = \left(I - \Psi^E\right) C_B^E \qquad \Rightarrow \qquad \delta C_B^E \overset{\Delta}{=} \hat{C}_B^E - C_B^E = -\Psi^E \, C_B^E$$

$$\delta \underline{V}^E = \hat{\underline{v}}^E - \underline{v}^E \qquad \text{(B-18)}$$

$$\delta \underline{R}^E \overset{\Delta}{=} \hat{\underline{R}}^E - \underline{R}^E$$

where

$C_B^E$ = Direction cosine matrix between body (B) and earth (E) coordinates.

$\Psi^E$ = Skew symmetric form of $\underline{\psi}^E$ defined below.

$\underline{\psi}^E$ = Angular error in $C_B^E$.

$\underline{R}$ = Position vector from earth's center to the INS.

We also note that:

$$C_B^E = C_L^E \, C_B^L \qquad \text{(B-19)}$$

so that:

$$\delta C_B^E = \delta C_L^E \, C_B^L + C_L^E \, \delta C_B^L \qquad \text{(B-20)}$$

Substituting $\delta C_L^E$ and $\delta C_B^L$ from (B-7) into (B-20) and the result with (B-19) into the Equation (B-18) $\Psi^E$ expression shows after rearrangement that:

$$\begin{aligned}\Psi^E &= -\left(\delta C_L^E\, C_B^L + C_L^E\, \delta C_B^L\right)\left(C_B^E\right)^T \\ &= -\left(C_L^E\, E^L\, C_B^L - C_L^E\, \Gamma^L\, C_B^L\right)\left(C_B^L\right)^T\left(C_L^E\right)^T \\ &= C_L^E\left(\Gamma^L - E^L\right)\left(C_L^E\right)^T\end{aligned}$$

or:

$$\left(C_L^E\right)^T \Psi^E\, C_L^E = \Gamma^L - E^L \qquad \text{(B-21)}$$

Recognizing the operation on the left as a similarity transformation from E to L, Equation (B-21), then, is equivalent to:

$$\boxed{\underline{\psi}^L = \underline{\gamma}^L - \underline{e}^L} \qquad \text{(B-22)}$$

An equation relating $\delta\underline{V}^E$ to $\delta\underline{v}^L$ is derived by first recognizing that:

$$\begin{aligned}\hat{\underline{v}}^E &= \hat{C}_L^E\, \hat{\underline{v}}^L \\ \underline{v}^E &= C_L^E\, \underline{v}^L \\ \hat{C}_L^E &= C_L^E + \delta C_L^E\end{aligned} \qquad \text{(B-23)}$$

Substituting (B-23) in the $\delta\underline{V}^E$ expression in (B-18) and applying the definition for $\delta\underline{v}^L$ from Equation (B-3), we obtain to first order

$$\begin{aligned}\delta\underline{V}^E &= \hat{C}_L^E\, \hat{\underline{v}}^L - C_L^E\, \underline{v}^L = \left(C_L^E + \delta C_L^E\right)\hat{\underline{v}}^L - C_L^E\, \underline{v}^L \\ &= C_L^E\left(\hat{\underline{v}}^L - \underline{v}^L\right) + \delta C_L^E\, \underline{v}^L = C_L^E\, \delta\underline{v}^L + \delta C_L^E\, \underline{v}^L\end{aligned} \qquad \text{(B-24)}$$

Substituting $\delta C_L^E$ from (B-7) into (B-24) yields:

$$\delta\underline{V}^E = C_L^E\left(\delta\underline{v}^L + E^L\, \underline{v}^L\right) = C_L^E\left(\delta\underline{v}^L + \underline{e}^L \times \underline{v}^L\right) \qquad \text{(B-25)}$$

If we now define:

$$\delta \underline{V}^L \overset{\Delta}{=} C_E^L \, \delta \underline{V}^E \qquad \text{(B-26)}$$

Equation (B-25) becomes:

$$\delta \underline{V}^L = \delta \underline{v}^L + \underline{e}^L \times \underline{v}^L \qquad \text{(B-27)}$$

An equation relating $\delta \underline{R}^E$ to $\underline{e}^L$ and h is obtained by first defining $\underline{R}$ in the E Frame by its magnitude and the unit vector along its direction $\underline{u}_R^E$:

$$\underline{R}^E = R \, \underline{u}_R^E$$

where

R = Radial distance from the center of the earth to the vehicle.

Then:

$$\delta \underline{R}^E = \hat{R} \, \hat{\underline{u}}_R^E - R \, \underline{u}_R^E \qquad \text{(B-28)}$$

The $\underline{u}_R^E$ vectors are calculated by transforming $\underline{u}_R^L$ through the $C_L^E$ matrix:

$$\hat{\underline{u}}_R^E = \hat{C}_L^E \, \hat{\underline{u}}_R^L = \hat{C}_L^E \, \underline{u}_R^L$$

$$\underline{u}_R^E = C_L^E \, \underline{u}_R^L$$

Substitution into (B-28) yields to first order:

$$\delta \underline{R}^E = \left(R + \delta R\right)\left(C_L^E + \delta C_L^E\right) \underline{u}_R^L - R \, C_L^E \, \underline{u}_R^L \approx R \, \delta C_L^E \, \underline{u}_R^L + \delta R \, C_L^E \, \underline{u}_R^L$$

where $\delta C_L^E$ and $\delta R$ are defined previously in Equations (B-3) and (B-4). Now apply $\delta C_L^E$ in terms of $E^L$ as defined in (B-7):

$$\delta \underline{R}^E = R \, C_L^E \, E^L \, \underline{u}_R^L + \delta R \, C_L^E \, \underline{u}_R^L$$

Treating $\delta\underline{R}^E$ as a position error vector evaluated in the E Frame, we transform to the L Frame to find its defined L Frame equivalent:

$$\delta\underline{R}^L \overset{\Delta}{=} C_E^L \, \delta\underline{R}^E \qquad \text{(B-29)}$$

With (B-29), the previous equation becomes:

$$\delta\underline{R}^L = R \, E^L \, \underline{u}_R^L + \delta R \, \underline{u}_R^L$$

or in vector form

$$\delta\underline{R}^L = R \left( \underline{\varepsilon}^L \times \underline{u}_R^L \right) + \delta R \, \underline{u}_R^L \qquad \text{(B-30)}$$

The vertical component of $\delta\underline{R}^L$ is the dot product of (B-30) with $\underline{u}_R^L$. As expected it equals $\delta R$. Subtracting the $\delta R \, \underline{u}_R^L$ vertical component from (B-30) yields the horizontal component of $\delta\underline{R}^L$:

$$\delta\underline{R}_H^L = R \left( \underline{e}^L \times \underline{u}_R^L \right) \qquad \text{(B-31)}$$

where

$\delta\underline{R}_H^L$ = Horizontal component of $\delta\underline{R}^L$.

Equations (B-11), (B-22), (B-27), (B-30) and (B-31) summarized below are equivalency relationships for the new $\underline{\psi}^L$, $\delta\underline{V}^L$, $\delta\underline{R}^L$ error parameters in terms of the original error parameters $\underline{\gamma}^L$, $\delta\underline{v}^L$, $\underline{e}^L$, $\delta h$.

$$\underline{\psi}^L = \underline{\gamma}^L - \underline{e}^L$$

$$\delta\underline{V}^L = \delta\underline{v}^L + \underline{e}^L \times \underline{v}^L$$

$$\delta\underline{R}^L = R\left(\underline{e}^L \times \underline{u}^L_R\right) + \delta R\ \underline{u}^L_R \qquad \text{(B-32)}$$

$$\delta\underline{R}^L_H = R\left(\underline{e}^L \times \underline{u}^L_R\right)$$

$$\delta R = \delta h$$

Differential equations for the new error parameters are now obtained by substituting (B-32) (with equivalent inverse relationships) into error Equations (B-17).

The $\dot{\underline{\psi}}^L$ equation is obtained by differencing $\dot{\underline{\gamma}}^L$, $\dot{\underline{e}}^L$ in Equations (B-17) and applying the $\underline{\psi}^L$ equivalency expression (and its derivative) from Equations (B-32):

$$\dot{\underline{\psi}}^L = \underline{\psi}^L \times \left(\underline{\omega}^L_{IE} + \underline{\omega}^L_{EL}\right) - C^L_B\ \delta\tilde{\underline{\omega}}^B_{IB} \qquad \text{(B-33)}$$

The $\delta\dot{\underline{V}}^L$ equation is derived by first differentiating the (B-32) $\delta\underline{V}^L$ expression:

$$\delta\dot{\underline{V}}^L = \delta\dot{\underline{v}}^L + \dot{\underline{e}}^L \times \underline{v}^L + \underline{e}^L \times \dot{\underline{v}}^L$$

and then substituting for $\dot{\underline{v}}^L$, $\delta\dot{\underline{v}}^L$ and $\dot{\underline{e}}^L$ from Equations (B-1and (B-17) with $\delta\underline{v}^L$ in terms of $\delta\underline{V}^L$ from the rearranged (B-32) $\delta\underline{V}^L$ expression. The result is:

$$\delta\dot{\underline{V}}^L = C_B^L\,\delta\underline{\tilde{a}}_{SF}^B - \underline{\gamma}^L \times \underline{a}_{SF}^L - \left(2\underline{\omega}_{IE}^L + \underline{\omega}_{EL}^L\right) \times \left(\delta\underline{V}^L - \underline{e}^L \times \underline{v}^L\right)$$

$$- \left(\delta\underline{\omega}_{EL}^L - 2\,\underline{e}^L \times \underline{\omega}_{IE}^L\right) \times \underline{v}^L + \frac{2g}{R}\,\delta h\,\underline{u}_R^L + \delta\underline{g}_M^L + \left(\underline{e}^L \times \underline{\omega}_{EL}^L + \delta\underline{\omega}_{EL}^L\right) \times \underline{v}^L$$

$$+ \underline{e}^L \times \left[C_B^L\,\underline{a}_{SF}^B - \left(2\,\underline{\omega}_{IE}^L + \underline{\omega}_{EL}^L\right) \times \underline{v}^L + \underline{g}^L\right]$$

$$= C_B^L\,\delta\underline{\tilde{a}}_{SF}^B - \left(\underline{\gamma}^L - \underline{e}^L\right) \times \underline{a}^L + \underline{e}^L \times \underline{g}^L - \left(2\,\underline{\omega}_{IE}^L + \underline{\omega}_{EL}^L\right) \times \delta\underline{V}^L + \frac{2g}{R}\,\delta h\,\underline{u}_R^L + \delta\underline{g}_M^L$$

$$+ \left(2\,\underline{\omega}_{IE}^L + \underline{\omega}_{EL}^L\right) \times \left(\underline{e}^L \times \underline{v}^L\right) + \left[\underline{e}^L \times \left(2\,\underline{\omega}_{IE}^L + \underline{\omega}_{EL}^L\right)\right] \times \underline{v}^L$$

$$- \underline{e}^L \times \left[\left(2\,\underline{\omega}_{IE}^L + \underline{\omega}_{EL}^L\right) \times \underline{v}^L\right]$$

The last three terms in the above expression can be shown to sum to identically zero by application of the triple vector product identity (Equation (B-13)) to each term and summing results.

Substituting $\underline{\psi}^L$, $\delta R$ from (B-32) for $(\underline{\gamma}^L - \underline{e}^L)$, $\delta h$ then yields:

$$\delta\dot{\underline{V}}^L = C_B^L\,\delta\underline{\tilde{a}}_{SF}^B - \underline{\psi}^L \times \underline{a}_{SF}^L + \underline{e}^L \times \underline{g}^L - \left(2\,\underline{\omega}_{IE}^L + \underline{\omega}_{EL}^L\right) \times \delta\underline{V}^L + \frac{2g}{R}\,\delta R\,\underline{u}_R^L + \delta\underline{g}_M^L$$

For error analysis purposes, the $\underline{\Delta g}^L$ term in $\underline{g}^L$ Equation (B-9) can be ignored. Then $\underline{g}^L$ is along $\underline{u}_R^L$ and the $\underline{e}^L \times \underline{g}^L$ term in the latter expression becomes:

$$\underline{e}^L \times \underline{g}^L = -\,g\left(\underline{e}^L \times \underline{u}_R^L\right)$$

Using the $\delta\underline{R}_H^L$ equivalency from (B-32) we then find that:

$$\underline{e}^L \times \underline{g}^L = -\,\frac{g}{R}\,\delta\underline{R}_H^L$$

so that the $\delta\dot{\underline{V}}^L$ equation assumes the final form:

$$\boxed{\delta\dot{\underline{V}}^L = C_B^L\,\delta\underline{\tilde{a}}_{SF}^B - \underline{\psi}^L \times \underline{a}_{SF}^L - \frac{g}{R}\,\delta\underline{R}_H^L - \left(2\,\underline{\omega}_{IE}^L + \underline{\omega}_{EL}^L\right) \times \delta\underline{V}^L + \frac{2g}{R}\,\delta R\,\underline{u}_R^L + \delta\underline{g}_M^L \qquad \text{(B-34)}}$$

It remains to develop a $\delta \underline{R}$ position error rate equation to replace the $\dot{\underline{e}}^L$, $\delta \dot{h}$ set in (B-17). The $\delta \underline{R}$ position error rate is developed by first differentiating the $\delta \underline{R}^E$ definition equation in set (B-18):

$$\delta \dot{\underline{R}}^E = \hat{\dot{\underline{R}}}^E - \dot{\underline{R}}^E \tag{B-35}$$

The velocity vector $\underline{v}$ is defined in Appendix A (Equation (A-12)) as follows:

$$\underline{v}^E = \dot{\underline{R}}^E \tag{B-36}$$

hence,

$$\hat{\underline{v}}^E = \hat{\dot{\underline{R}}}^E \tag{B-37}$$

Substituting (B-36) and (B-37) in (B-35), and introducing the definition for $\delta \underline{V}^E$ from (B-18) shows that:

$$\delta \dot{\underline{R}}^E = \delta \underline{V}^E \tag{B-38}$$

From (B-29) we also know that:

$$\delta \underline{R}^L \stackrel{\Delta}{=} C_E^L \, \delta \underline{R}^E \tag{B-39}$$

or upon differentiation:

$$\delta \dot{\underline{R}}^L = \dot{C}_E^L \, \delta \underline{R}^E + C_E^L \, \delta \dot{\underline{R}}^E \tag{B-40}$$

Substituting the transpose of $\dot{C}_L^E$ from (B-1) for $\dot{C}_E^L$ and using (B-38) for $\delta \dot{\underline{R}}^E$ shows that:

$$\delta \dot{\underline{R}}^L = - \Omega_{EL}^L \left(C_L^E\right)^T \delta \underline{R}^E + C_E^L \, \delta \underline{V}^E \tag{B-41}$$

Applying the Equation (B-26), (B-29) definitions for $\delta \underline{V}^L$, $\delta \underline{R}^L$ to (B-41) then yields the desired equation for $\delta \dot{\underline{R}}^L$:

$$\boxed{\delta \dot{\underline{R}}^L = \delta \underline{V}^L - \underline{\omega}_{EL}^L \times \delta \underline{R}^L} \tag{B-42}$$

Equations (B-33), (B-34) and (B-42), summarized below, constitute the strapdown inertial navigation error equations in terms of the new error parameters $\underline{\psi}^L$, $\delta\underline{V}^L$, $\delta\underline{R}^L$. These equations are completely equivalent to strapdown navigation error equations (B-17) based on the original error parameters $\underline{\gamma}^L$, $\delta\underline{v}^L$, $\underline{e}^L$, $\delta h$. The equivalency between the new and original navigation error parameters is provided by Equations (B-32).

$$
\begin{aligned}
\dot{\underline{\psi}}^L &= \underline{\psi}^L \times \left(\underline{\omega}_{IE}^L + \underline{\omega}_{EL}^L\right) - C_B^L \, \widetilde{\delta\underline{\omega}}_{IB}^B \\
\delta\dot{\underline{V}}^L &= C_B^L \, \delta\tilde{\underline{a}}_{SF}^B - \underline{\psi}^L \times \underline{a}_{SF}^L - \frac{g}{R} \, \delta\underline{R}_H^L \\
&\quad - \left(2 \, \underline{\omega}_{IE}^L + \underline{\omega}_{EL}^L\right) \times \delta\underline{V}^L + \frac{2\,g}{R} \, \delta R \, \underline{u}_R^L + \delta\underline{g}_M^L \qquad \text{(B-43)} \\
\delta\dot{\underline{R}}^L &= \delta\underline{V}^L - \underline{\omega}_{EL}^L \times \delta\underline{R}^L
\end{aligned}
$$

## NOTES

**LATER PAPERS**

1984 PAPER - ADVANCES IN STRAPDOWN SYSTEMS

1984 PAPER - STRAPDOWN SYSTEM ALGORITHMS

**NOTES**

# ADVANCES IN STRAPDOWN SENSORS

Paul G Savage
President
Strapdown Associates, Inc.
Woodbridge Plaza, Suite 150
10201 Wayzata Blvd
Minnetonka, Minnesota 55343

Presented in Athens-Greece,
Rome-Italy and Copenhagen-Denmark
as part of
AGARD Lecture Series No. 133
ADVANCES IN STRAPDOWN INERTIAL SYSTEMS

May, 1984

**ADVANCES IN STRAPDOWN SENSORS**

By

Paul G. Savage
President
Strapdown Associates, Inc.
Woodbridge Plaza, Suite 150
10201 Wayzata Blvd.
Minnetonka, Minnesota 55343

SUMMARY

This paper reviews the advances that have taken place in strapdown sensor technology since 1978. It is intended as an update to the paper on Strapdown Sensors presented as part of AGARD Lecture Series 95 in 1978 (1). Principal areas addressed in strapdown gyro technology are the state-of-the-art in mainstream floated rate-integrating and tuned-rotor strapdown gyros, performance advances in laser gyros, special design considerations associated with mechanically dithered laser gyros, the state-of-the-art in magnetic mirror and multioscillator laser gyros, present and projected application areas for laser gyros related to size, performance and cost, the theory of operation and state-of-the-art in fiber-optic rate sensor technology, and the fundamental distinctions between the laser gyro and fiber-optic rate sensor. Basic areas addressed in strapdown accelerometer technology are performance advances in pendulous accelerometers, and the theory of operation and state-of-the-art in vibrating beam accelerometer technology.

## 1. INTRODUCTION

The state-of-the-art in strapdown sensor technology has advanced considerably since 1978, particulary in the higher accuracy performance categories. Ring laser gyros designed by several manufacturing groups have demonstrated their ability to meet the requirements for 1 nmph inertial navigation. Laser gyros are now in operational use on several major aircraft programs, and have demonstrated reliabilities in the field that are exceeding user goals. Advanced development programs have been initiated to extend the performance capabilities of the ring laser gyro into the class needed for 0.1 nmph navigation.

Conventional floating rate-integrating and tuned-rotor gyro technology has been increasingly applied in the moderate to low performance strapdown areas. These instruments continue to provide a good alternative to the ring laser gyro in applications requiring small size and low cost, where lower performance is acceptable. A new optical rate sensor technology based on the use of fiber-optics has emerged over the past few years as a lower cost/reduced performance alternative to the ring laser gyro. Simultaneously, ring laser gyro development activities have been directed at cost and size reduction to extend its applicability range into the moderate performance areas.

Strapdown accelerometer technology continues to be principally based on the pendulous electrically servoed accelerometer design approach. Design refinements since 1978 have upgraded the performance of this instrument and somewhat reduced its cost. It continues to remain compatible in cost and performance with requirements in most strapdown application areas (in proportion to the cost of the gyro and computing elements that are also contained in a strapdown system). To meet cost targets for the future, a vibrating beam accelerometer technology is being developed as a lower cost alternative to the pendulous accelerometer.

This paper reviews each of the instruments discussed above, with emphasis on the performance capabilites, problem areas, and applications where they have been used or planned for use since 1978. For each instrument, a brief discussion is also included which describes its principal of operation. Analytical descriptions and detailed design considerations for the floated rate-integrating gyro, tuned-rotor gyro, ring laser gyro, and pendulous accelerometer have been provided in the AGARD Lecture Series 95 paper on Strapdown Sensors (1), and are not repeated here. Error characteristics for the fiber-optic rate sensor and vibrating beam accelerometer are presented, but from a qualitative standpoint, because the performance characteristics of these devices have not been sufficiently disclosed in the open literature to allow detailed accurate analytical modeling that accounts for the important critical error sources, particularly those that are environmentally induced and which change over time and operating cycles.

A generalized error budget is also provided for reference at the beginning of the paper which attempts to define typical gyro and accelerometer performance requirements for four types of strapdown inertial systems.

## 2. SENSOR PERFORMANCE REQUIREMENTS

Table 1 defines typical accuracy requirements for strapdown sensors in four application areas: the classical 1 nmph inertial navigator, a higher performance advanced 0.1 nmph inertial navigator, a lower performance strapdown attitude heading reference system (AHRS), and a still lower performance tactical missile midcourse guidance system. The performance categories depicted in Table 1 are considered typical for most strapdown sensor applications today and in the immediate future. Table 1 should be used as a reference to categorize typical sensor performance requirements during discussions on individual sensor capabilities.

TABLE 1 - TYPICAL STRAPDOWN SENSOR PERFORMANCE REQUIREMENTS

| Performance Parameter | 0.1 nmph INS | 1.0 nmph INS | AHRS | Tactical Missile Midcourse Guidance |
|---|---|---|---|---|
| Gyro Bias Uncertainty (deg/hr) | 0.001 | 0.01 | 1.0(0.1)* to 10 | 5 to 30 |
| Gyro Random Noise ($deg/hr^{1/2}$)** | 0.0005 | 0.002 | 0.01 | 0.1 |
| Gyro Scale-Factor Uncertainty (ppm) | 1 | 5 | 200 | 1000 |
| Gyro Alignment Uncertainty (arc sec) | 1 | 2 | 200 | 300 |
| Accelerometer Bias Uncertainty (μg) | 10 | 40 | 1000 | 1000 |
| Accelerometer Scale-Factor Uncertainty (ppm) | 50 | 200 | 1000 | 1000 |
| Accelerometer Alignment Uncertainty(sec) | 2 | 7 | 200 | 300 |
| Accelerometer Bias Trending (μg/sec) | 0.003 | 0.01 | NA(0.1)* | NA |

* For AHRS with an earth rate gyro-compass heading determination requirement. Other figure shown is for AHRS with heading slaved to magnetic flux heading detector.

** This error source is a characteristic principally of laser gyros.

## 3. SINGLE-DEGREE-OF-FREEDOM FLOATED RATE-INTEGRATING GYRO

The floated rate-integrating gyro (1, 4, 5) pictured schematically in Figure 1 is the gyro with the longest production history and is the original high-accuracy gimbaled-platform gyro. The device consists of a cylindrical hermetically sealed momentum-wheel/spinmotor assembly (float) contained in a cylindrical hermetically sealed case. The float is interfaced to the case by a precision suspension assembly that is laterally rigid (normal to the cylinder axis) but allows "frictionless" angular movement of the float relative to the case about the cylinder axis. The cavity between the case and float is filled with a fluid that serves the dual purpose of suspending the float at neutral buoyancy, and providing viscous damping to resist relative float-case angular motion about the suspension axis.

A ball-bearing or gas-bearing synchronous-hysteris spinmotor is utilized in the float to maintain constant rotor spinspeed, hence constant float angular momentum. A signal-generator/pickoff provides an electrical output signal from the gyro proportional to the angular displacement of the float relative to the case. An electrical torque generator provides the capability for applying known torques to the float about the suspension axis proportional to an applied electrical input current. Delicate flex leads are used to transmit electrical signals and power between the case and float.

Under applied angular rates about the input axis, the gyro float develops a precessional rate about the output axis (rotation rate of the angle sensed by the signal-generator/pickoff, see Figure 1). The pickoff-angle rate generates a viscous torque on the float about the output axis (due to the damping fluid) which sums with the electrically applied torque-generator torque to precess the float about the input axis at the gyro input rate. The pickoff-angle rate thereby becomes proportional to the difference between the input rate and the torque-generator precessional rate, hence, the pickoff angle becomes proportional to the integral of the difference between the input and torque-generator rates.

To operate the gyro in a strapdown mode, the pickoff angle is electrically servoed to null by the torque generator which is driven by the signal-generator/pickoff output (through suitable compensation and amplifer electronics). The time integral of the difference between the input and torque-generator precessional rates is thereby maintained at zero, and the integral of the torque-generator rate becomes proportional to the integral of the input rate. Thus, the integral of the torque-generator electrical current provides a measure of the integral of input rate for a rate-gyro strapdown inertial navigation system.

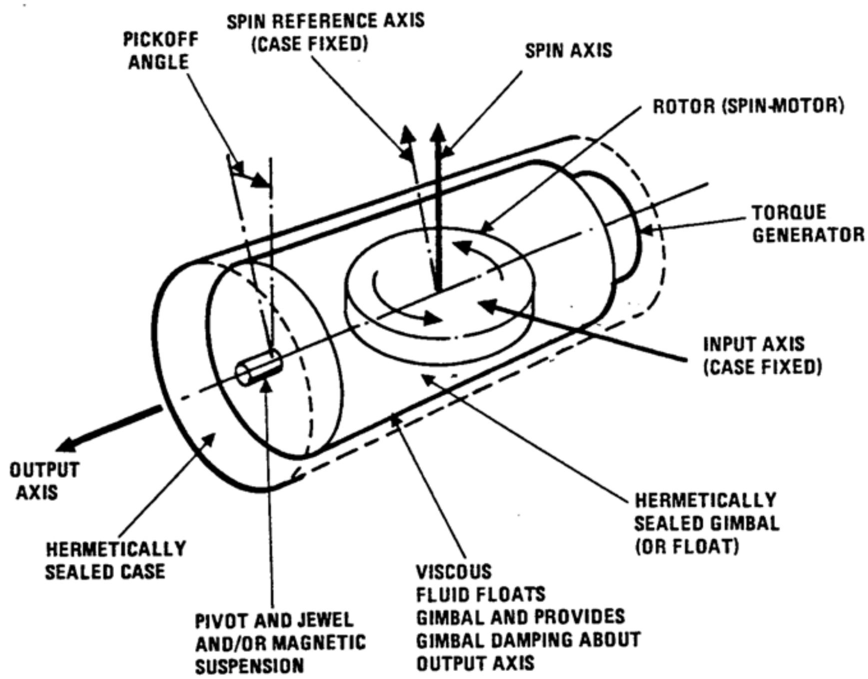


Figure 1 - Single-degree-of-freedom floated rate-integrated gyro concept.

### 3.1 Performance And Application Areas

Application areas for the strapdown floated rate-integrating gyro (RIG) have been primarily in the lower performance (5 to 30 deg/hr bias accuracy) areas where small-size low angular momentum units meet performance requirements, and costs are competetive with alternative gyro mechanization approaches (e.g., the tuned-rotor gyro). The floatation fluid suspension in the RIG makes the device extremely rugged, hence, provides a natural suitability to those lower performance application areas where high vibrations and shock are prevalent.

Low cost tactical missile midcourse inertial guidance has been a continuing application area for the strapdown RIG. Standard Missile-2, Harpoon, Phoenix, and recently AMRAAM, are examples of tactical missile systems that incorporate strapdown RIG's for midcourse guidance and stabilization/control. Strapdown RIG's have also been used in some applications to implement a short term navigation reference between updates from a higher accuracy navigation device. Examples are motion compensation for airborne radar systems (using the aircraft INS as the "outer-loop" reference), and to generate short term navigation data between precision radio navigation position fixes for aircraft test instrumentation purposes (e.g., ACMR - Air Combat Maneuvering Range).

Higher performance application areas for the strapdown RIG have remained limited due to their higher cost for comparable performance compared to the strapdown tuned-rotor or ring laser gyros.

## 4. TUNED-ROTOR GYRO

The tuned-rotor gyro (1, 6, 7, 8, 9, 10) is the most advanced gyro in large-scale production today for aircraft 1-nmi/hr gimbaled platforms. Due to its simplicity (compared to the floated rate-integrating gyro), the tuned-rotor gyro is theoretically lower in cost and more reliable. A drawing of a representative tuned-rotor gyro is presented in Figure 2. Figure 3 is a schematic illustration of the gyro rotor assembly.

The gyro consists of a momentum wheel (rotor) connected by a flexible gimbal to a case-fixed synchronous-hysteresis ball-bearing spinmotor drive shaft. The gimbal is attached to the motor and rotor through members that are torsionally flexible but laterally rigid. A two-axis variable-reluctance signal-generator/pickoff is included that measures the angular deviation of the rotor (in two axes) relative to the case (to which the motor is attached). Also included is a two-axis permanent-magnet torque generator that allows the rotor to be torqued relative to the case on current command. The torquer magnets are attached to the rotor, and the torquer coils are attached to the gyro case.

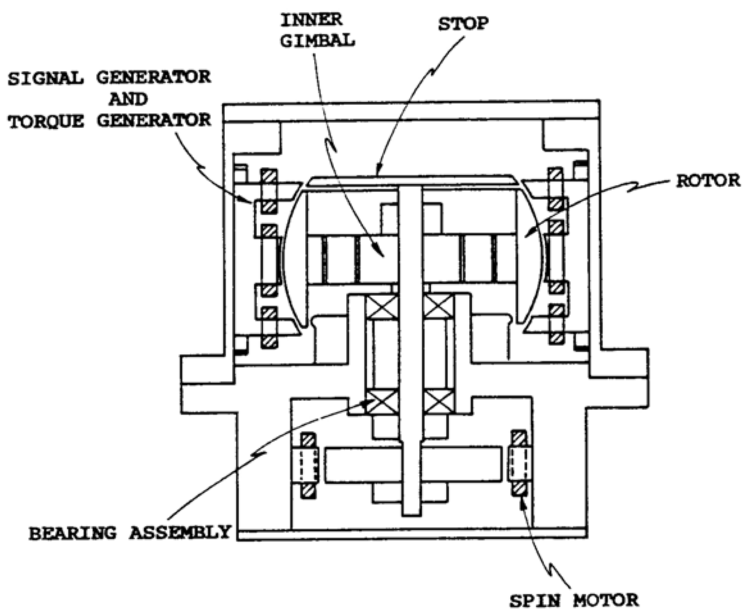


Figure 2 - Typical tuned-rotor gyro configuration.

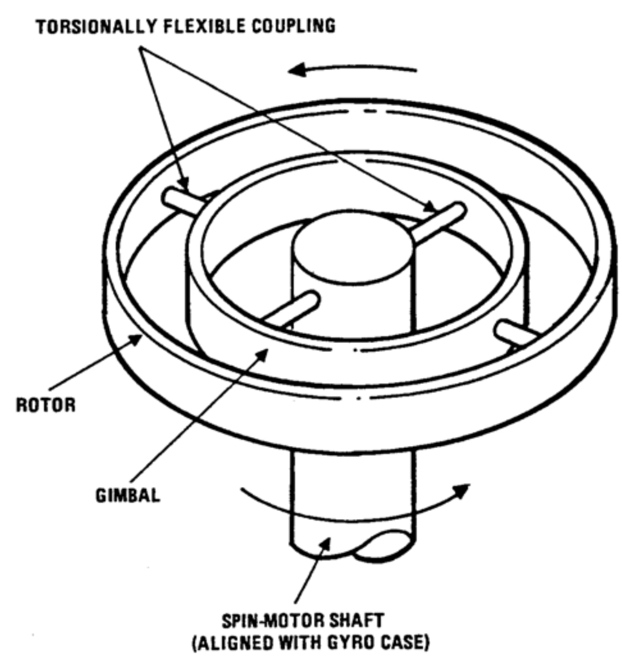


Figure 3 - Tuned-rotor gyro rotor assembly.

As for all angular-momentum-based rate-sensing devices, the key design feature of the gyro is the means by which it can contain the reference momentum (the spinning rotor), without introducing torques (drift rates) in the process. For the tuned-rotor gyro, the method is linked to the dynamic effect of the flexible gimbal attachment between the rotor and the motor. Geometrical reasoning reveals that when the rotor is spinning about an axis that deviates in angle from the motor-shaft axis, the gimbal is driven into a cyclic oscillation in and out of the rotor plane at twice the rotor frequency. Dynamic analysis shows that the reaction torque on the rotor to sustain this motion has a systematic component along the angular-deviation vector that is proportional to the angular displacement, but that acts as a spring with a negative spring constant. The flexible pivots between the rotor and gimbal, on the other hand, provide a similar spring torque to the rotor, but of the opposite sign. Hence, to free the rotor from systematic torques associated with the angular displacement, it is only necessary to design the gimbal pivot springs such that their effect cancels the inverse spring effect of the gimbal. The result (tuning) is a rotor suspension that is insensitive to angular movement of the case.

Use of the tuned-rotor gyro in a strapdown mode parallels the technique used for the floated rate-integrating gyro. Exceptions are that damping must be provided electrically in the caging loop, as there is no fluid, and that the gyro must be caged in two axes simultaneously. The latter effect couples the two caging loops together due to the gyroscopic cross-axis reaction of the rotor to applied torques.

## 4.1 Performance And Application Areas

Application areas for the strapdown tuned-rotor gyro (TRG) have been primarily in the medium performance areas where small-size low angular momentum units have acceptable accuracy, are lower in cost compared with comparable size/performance ring laser gyro technology, and where bias accuracy compared to equivalent cost RIG units is superior. The inherent simplicity in design of the dry rotor suspension concept for the TRG which lowers its production cost, also limits its usefulness in high vibration/shock environments where rotor resonances can potentially be excited (producing sensor error and, in extreme cases, device failure). Current design improvements for the TRG are being directed at extending its vibration capability while retaining accuracy.

The strapdown AHRS (attitude-heading reference system) has been a primary application area for the strapdown TRG for commercial aircraft, military drones, and most recently, torpedoes. One of the larger potential application areas for the strapdown TRG is for the military aircraft strapdown AHRS where small size and low cost are key requirements, and not yet achievable with ring laser gyro technology.

Two current application areas of interest for the strapdown TRG are for tactical missile midcourse guidance and helicopter or torpedo strapdown AHRS. Small-size low-cost versions of the strapdown TRG have been developed as a competitor to the RIG for the tactical missile midcourse guidance application. Potential vibration/shock susceptability of the TRG is an area of concern for the tactical missile application, but is being addressed by TRG design groups. Shock requirements for torpedo application of the TRG have been handled through use of elastomeric isolators between the TRG sensor assembly and torpedo mounting plate. The helicopter AHRS application imposes a bias stability requirement of 0.1 deg/hr on the TRG which is not achievable today with small size low cost units.

The 0.1 deg per hour helicopter AHRS requirement stems from the need to determine heading prior to takeoff by earth-rate gyro-compassing to an accuracy of 0.5 degrees. This translates into a gyro accuracy requirement of 0.1 deg/hr to detect the direction of horizontal earth rate (at 45 deg latitude) to 0.01 radians (i.e., 0.5 degrees). Typical small-size low-cost TRG's have bias accuracies over long term of 1 to 2 deg/hr. To achieve the 0.1 deg/hr requirement, a turn-table is needed to position the TRG at different orientations relative to the earth rate vector during initial alignment operations. In this way, repeatable gyro biases can be measured and separated from earth rate measurements, and earth rate measurements to the required 0.1 deg per hour accuracy become achievable. The turn-table also provides the means for calibrating the heading gyro scale factor prior to takeoff. The use of such a turn-table as an integral part of a strapdown TRG system for the helicopter AHRS is considered standard practice today.

### 4.1.1 Design Considerations In A Dynamic Environment

Use of a strapdown TRG (or RIG) in a dynamic vibration environment must address the basic question of wide versus narrow bandwidth for the torque-rebalance loop. If a significant angular vibration environment exists, the loop bandwidth must be broad enough to measure real angular rates that integrate into attitude/heading (33, 34). On the other hand, if the bandwidth is to broad, undesirable high frequency sensor error effects will be amplified and passed as output data to the attitude integration process, generating attitude error. In the case of the tuned-rotor gyro, undamped rotor wobble effects near spin frequency limit the maximum bandwidth that is practically achievable to approximately 80Hz. The minimum torque-rebalance bandwidth is selected so that the gyro rate signal outputs, when integrated, generate attitude data that:

1. Accurately accounts for the accelerometer attitude under combined angular/linear vibration environments (i.e. - sculling (33, 34)).

2. Accurately accounts for multiaxis angular vibration rates that rectify into attitude drift (i.e., coning (33, 34)).

In the case of the TRG, Item 2 is achievable with lower bandwidth than with the RIG because of the inherent nature of the TRG being an attitude sensing instrument (i.e., the pickoff signals measure the true attitude orientation of the gyro case relative to the rotor). As such, attitude errors in the TRG generated by low bandwidth limits, are theoretically recoverable (with a time delay) by proper torque-loop rebalance logic. This contrasts with the RIG torque-loop because the pickoff signal in the RIG represents the integrated input rate (not attitude). As such, the RIG bandwidth must be broad enough to accurately measure all significant multiaxis angular vibrations so that the true attitude can be properly constructed in the attitude integration process. Both the RIG and TRG bandwidths have comparable requirements to satisy Item 1.

One of the principal error mechanisms for torque-rebalance gyros under dynamic environments is torquer heating effects. In addition to producing scale factor errors in the gyro output, bias errors can be produced by associated thermal gradient effects across the instrument. In the case of the gyro scale factor error, much of the temperature induced effect can be eliminated by temperature measurement and modeling correction in the strapdown computer. Unfortunately, for the tuned-rotor gyro, because the torquer magnet is attached to the spinning rotor, direct temperature measurements are difficult to achieve due to the problem of making electrical measurements across the spinning rotor bearings (without resorting to slip-rings and attendent potential reliability problems).

In order to reduce the scale factor error variation with temperature, TRG manufacturers have developed new magnet materials (e.g., doped sumarium cobalt) which has a lower scale factor error as a function of temperature. The penalty is reduced magnet strength, hence, a larger magnet to generate the same torque capability. Note, that the torquer heating effect under angular vibration can also be reduced by lowering the bandwidth of the torque-rebalance loop. In the case of the TRG, this technique has been used in helicopter applications as a compromise between sensor error amplification versus output signal attenuation error. Because the TRG is more tolerant of low bandwidth operation (see previous discussion on Item 2 requirements), a reasonable compromise can usually be found. However, the bandwidth selection then becomes sensitive to vehicle installation and operating condition. In general, no true optimum solution is possible.

Scale factor errors in strapdown gyros under maneuvering flight conditions can rectify into attitude drift in the strapdown system computer (2, 34). The classical effect is through continuous turning in one direction that generates a net attitude error proportional to the product of the scale factor error with the net angle traversed. Cyclic maneuvers can also produce net attitude error buildup; asymmetrical scale factor errors rectify under oscillatory rates about the gyro input axis, symmetrical scale factor errors rectify under multiaxis rates that are phased ninety degrees apart (between axes). The classical case of the latter effect is the "jinking maneuver" which consists of cyclic patterns of roll right, turn right, roll left, turn left. In the case of the tuned-rotor gyro, the scale factor error effect must be assessed to assure compliance to accuracy requirements for the particular application being considered. Reduction of the gyro torquer scale factor temperature coefficient in future versions should broaden the areas of applicability for the instrument in a dynamic environment.

## 5. RING LASER GYRO

Unlike the gyros that utilize rotating mass for angular-measurement reference, the laser gyro operating principal is based on the relativistic properties of light (1, 11, 12, 14). The device has no moving parts; hence, it has the potential for extremely high reliability.

Figure 4 depicts the basic operating elements in a laser gyro: a closed optical cavity containing two beams of correlated (single-frequency) light. The beams travel continuously between the reflecting surface of the cavity in a closed optical-path; one beam travels in the clockwise direction, the other in the counterclockwise direction, each occupying the same physical space in the cavity. The light beams are generated from the lasing action of a helium-neon gas discharge within the optical cavity. The reflecting surfaces are dielectric mirrors designed to selectively reflect the frequency associated with the heluim-neon transition being used.

To understand the operation of the laser gyro, consider the effect of cavity rotation on an observer rotating with the cavity. Relative to the observer, it takes longer for a photon of light to traverse the distance around the optical path in the direction of rotation than in the direction opposite to the rotation. This effect is interpreted by the observer as a lengthening of the net optical path length in the direction of rotation, and a shortening of the path length in the opposite direction. Because the laser beam is self-resonating, it is a continuous beam that propagates around the cavity, closing on itself without discontinuity. As a result, the effect of the self-resonance is to maintain a fixed integral number of light wave lengths around the cavity. Under input angular rate, the increase in optical path length experienced by the beam traveling in the direction of rotation, must therefore

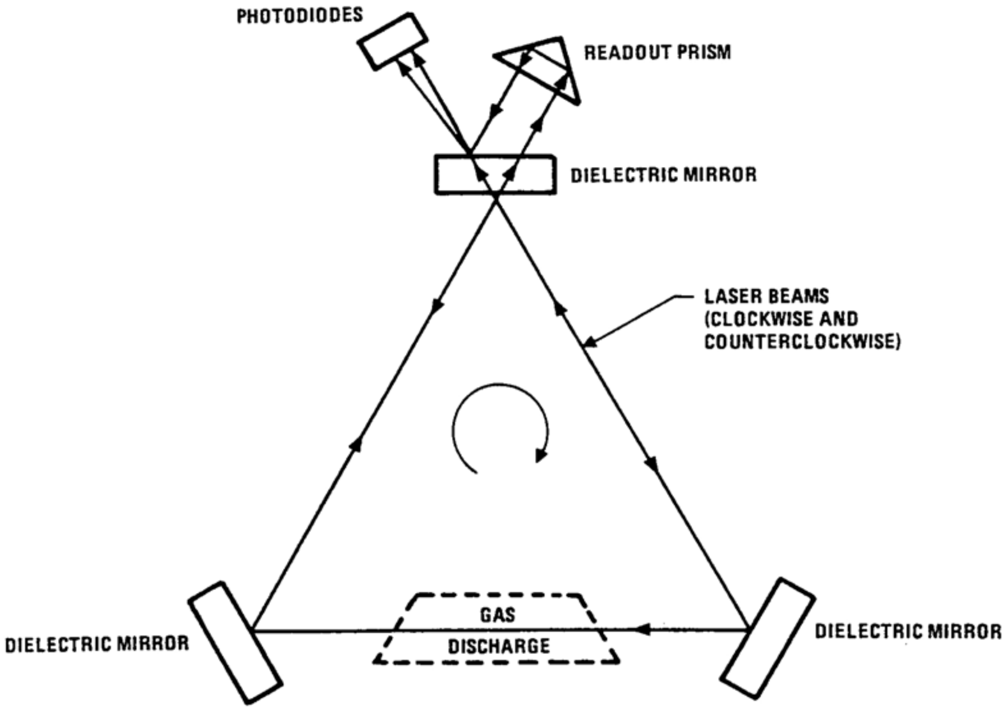


Figure 4 - Laser gyro operating elements.

be accompanied by a proportional increase in wavelength to maintain the same integral number of waves around the lengthened cavity. The converse is true for the beam traveling opposite to the direction of rotation. Thus, a wavelength difference is established between the oppositely directed beams proportional to the optical path length change, hence, proportional to the input angular rate. Because the speed of light is constant, the wavelength difference is accompanied by a frequency difference between the two beams in the opposite sense. Hence, a frequency difference is generated between the two beams that is proportional to input rotation rate.

The frequency difference is measured in the laser gyro by allowing a small percentage of the laser radiation to escape through one of the mirrors (Figure 4). An optical prism is typically used to reflect one of the beams such that it crosses the other in almost the same direction at a small angle (wedge angle). Due to the finite width of the beams, the effect of the wedge angle is to generate an optical fringe pattern in the readout zone. When the frequencies between the two laser beams are equal (under zero angular rate input conditions), the fringes are stationary relative to the observer. When the frequencies of the two beams are different (under rotational rates), the fringe pattern moves relative to the observer at a rate and direction proportional to the frequency difference (i.e., proportional to the angular rate). More importantly, the passage of each fringe indicates that the integrated frequency difference (integrated input rate) has changed by a specified increment. Hence, each fringe passage is a direct indication of an incremental integrated rate movement, the exact form of the output needed for a rate-gyro strapdown navigation system.

Digital integrated-rate-increment pulses are generated from the laser gyro from the outputs of two photodiodes mounted in the fringe area and spaced 90 degrees apart (in fringe space). As the fringes pass by the diodes, sinusiodal output signals are generated, with each cycle of a sine wave corresponding to the movement of one fringe over the diodes. By observing which diode output is leading the other (by 90 degrees), the direction of rotation is determined. Simple digital-pulse triggering and direction logic operating on the photodiode outputs convert the sinusoidal signal to digital pulses for computer input.

The analytical relationship between the fringe angle change and integrated rate input angle change (11, 12, 34) is given by:

$$\Delta\phi = \frac{8\,\pi\,A}{\lambda\,L}\,\Delta\theta \qquad (1)$$

where

$\Delta\phi$ = Gyro fringe angle output change (Note: $\Delta\phi = 2\pi$ for a movement of one fringe across the output photodiode).

A = Area enclosed by the laser beam.

L = Perimeter of the laser beam path.

$\lambda$ = Laser wavelength (e.g., 0.63 micron).

$\Delta\theta$ = Integrated input rate into the gyro (Note: $\Delta\theta = 2\pi$ for a complete 360 degree input rotation angle).

The "pulse size" for the laser gyro is the value of $\Delta\theta$ for which $\Delta\theta = 2\pi$ (i.e., the input angle which produces a full fringe movement of $2\pi$ across the photodiode output detector). It is easily verified that for an equilateral triangle laser gyro with 12.6 inch perimeter (4.2 inches per side), the pulse size for a 0.63 micron laser (typical of today's technology) is 2 arc seconds.

The digital pulse output logic can be mechanized to output a pulse each time a full fringe has passed across the diode (e.g., by triggering on the positive going zero crossing from one of the readout photodiodes). For this approach, the gyro output pulse scaling would equal the "pulse-size" defined above. Alternatively, gyro output pulses can be triggered at the positive and negative-going zero crossings from each of the two photodiodes to achieve an output pulse scaling that is four times finer than the basic full-fringe "pulse-size". Both of the latter approaches are used today.

## 5.1 Construction

Figure 5 illustrates a typical laser gyro mechanization concept. A single piece structure (typically Zerodur, a ceramic glass material) is used to contain the helium-neon gas, with the lasing mirrors and electrodes forming the seals. High voltage (typically 1500 volts) applied across the electrodes (one cathode and two anodes) maintains the helium-neon gas mixture in an ionized state, thereby providing the required laser pumping action. High-quality optical seals are used to avoid introducing contaminants into the helium-neon mixture, which would degrade performance and ultimately limit life-time.

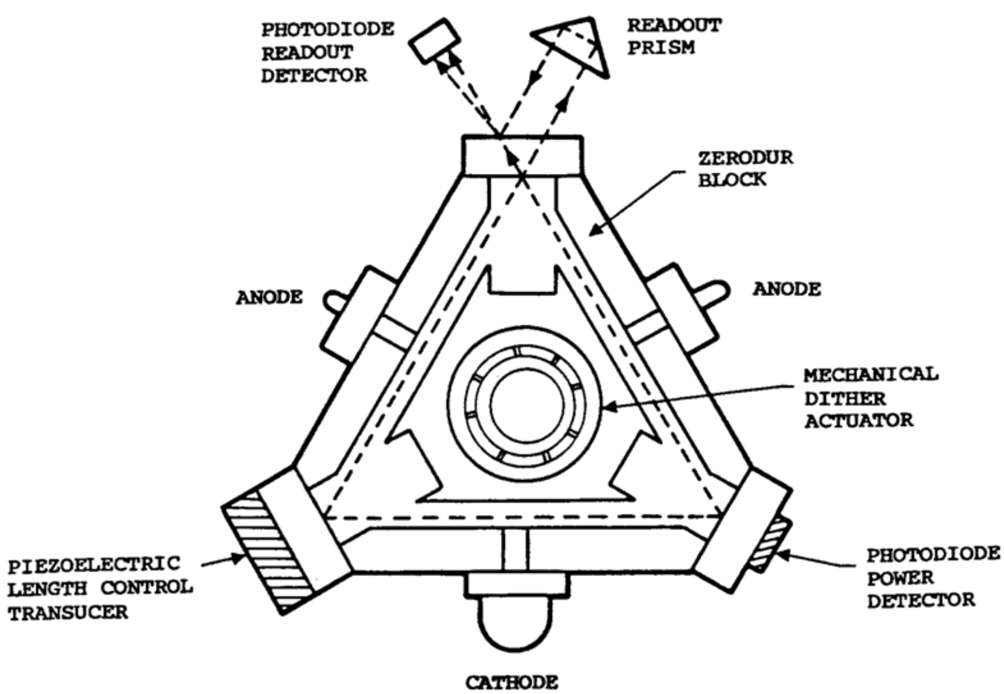


Figure 5 - Laser-gyro block assembly.

The accuracy of the laser gyro depends on the manner in which the laser beams are affected by the influences of the lasing cavity. A key requirement in this regard is that the average of the clockwise and counterclockwise path lengths around the lasing triangle be constant. Many of the error characteristics in the laser gyro vary as a function of average path length (12), hence, stabilizing average path length also implicitly stabilizes performance. Zerodur is used to construct the laser gyro optical cavity due to its low coefficient of thermal expansion, hence, high degree of path-length stability.

To compensate for residual remaining path-length variations, a piezoelectric transducer is mounted on one of the laser gyro mirror substrates (see Figure 5). Actuation of the transducer by a control voltage flexes the mirror substrate to effect a path-length change. The control signal for the transducer is designed to maintain peak average power in the lasing beams. Because average beam power varies cyclically with path-length multiples of laser wavelength, maintaining peak lasing power implicitly controls the average path-length to a constant value. The average beam power is detected in the laser gyro by a photodiode mounted on one of the mirrors that senses a small percentage of the combined radiation from the clockwise and counterclockwise beams.

### 5.1.1 Square Versus Triangular Ring Laser Gyros

Figure 6 illustrates a square laser gyro geometry utilizing four mirrors (as contrasted with the three-mirror triangular configuration in Figure 5). Both geometries are used today by competing ring laser gyro manufacturers. The rationale espoused by proponents of the triangular versus square geometry can be summarized as follows: Proponents of the triangular geometry point to the three-mirror configuration as having the minimum mirror count to form an enclosed laser ring. As a result mirror costs per gyro are minimized, and lock-in (a performance deficiency in the laser gyro to be discussed in the next section) is reduced due to the minimum number of scatterers (the mirrors) in the laser beam path. From a manufacturing standpoint, the proponents of the triangle point out that alignment of the mirrors on the gyro block is simplified (hence, cost reduced) because the triangle geometry is self-aligning in the lasing plane (through use of one curved mirror), and alignment out of the lasing plane is readily achieved by out-of-plane adjustment of the curved mirror during device assembly.

Proponents of the square laser gyro geometry consider the additional mirror cost a negligible penalty when technology advances are taken into account. The additional alignment requirement for the fourth mirror in a square is identified as a benefit by square gyro proponents due to the added flexibility it affords to adjust beam/cavity positioning, and thereby optimize performance. Another performance advantage identified for the square

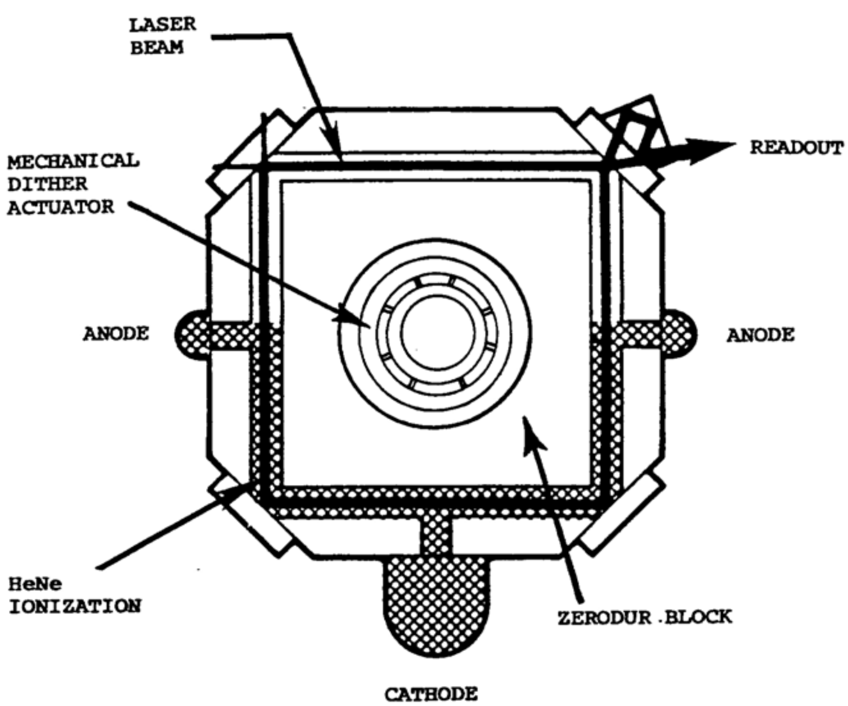


Figure 6 - Square laser gyro configuration.

is its higher area-to-perimeter ratio compared to a triangle of the same size, which directly increases accuracy. The area-to-perimeter ratio (see Equation (1)) is the primary parameter in the device that impacts performance (12, 13, 17). Proponents of the square also point to the lower angle of incidence at the laser beam/mirror interface which reduces back-scattering per mirror. The net result is a combined mirror reduction in back-scattering which more than compensates for the additional mirror scattering, hence, reduces overall gyro lock-in. Finally, from a manufacturing standpoint, square laser gyro enthusiasts claim simpler tooling and machining for square compared to triangular devices, hence, reduced production costs.

Triangular laser gyro proponents acknowledge a performance penalty due to the less favorable area-to-perimeter ratio and beam-incidence geometry. However, they claim that this advantage is minor and will be largely overcome by technology advances. Additionally, triangle proponents argue that when the gyro electrodes (size and geometry) are taken into account, no real size advantage exists for the square gyro configuration. From a machining standpoint, triangle proponents claim no advantage exists for any particular geometry once tooling is complete and experience has been attained.

At this stage in the laser gyro development cycle, it is not clear whether one geometry is superior to another as a general rule.

### 5.2 Lock-In

The phenomenon of lock-in continues to be the most prominent error source in the laser gyro and the most difficult to handle. The means for compensating lock-in has been the principal factor determining the configuration and performance of laser gyros from different manufacturers.

The phenomenon of laser gyro lock-in arises because of imperfections in the lasing cavity, principally the mirrors, that produce back-scattering from one laser beam into the other (13). The resulting coupling action tends to pull the frequencies of the two beams together at low rates producing a scale-factor error. For slowly changing rates below a threshold known as the lock-in rate, the two beams lock together at the same frequency producing no output (i.e., a dead zone). Figure 7 illustrates the effect of lock-in on the output of the laser gyro as a function of input rate for slowly changing input rate conditions. The magnitude of the lock-in effect depends primarily on the quality of the mirrors. In general, lock-in rates on the order of 0.01 to 0.1 degree-per-second are the lowest levels achievable with today's laser gyro technology (with 0.63-micron laser wavelength). Compared with 0.01 deg/hr navigation requirements, this is a serious error source that must be overcome.

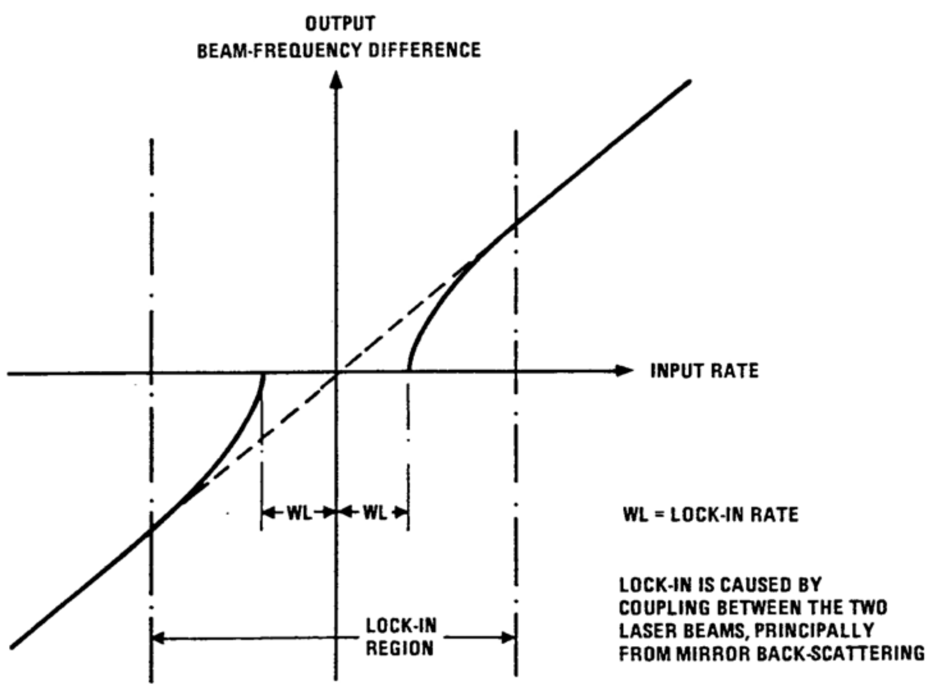


Figure 7 - Laser gyro lock-in.

Under dynamic input rates that rapidly pass through the lock-in region, the effect of lock-in is to introduce a small angle error in the gyro output as the lock-in zone is traversed, but still retaining sensitivity to input rate while in the lock-in region (i.e., no hard dead-zone develops as in Figure 7 (12, 13, 16). The latter effect underlies the basic principal behind adding cyclic high rate bias to the laser gyro as a means for circumventing the lock-in dead-zone effect, and converting it into a random angle error added to the gyro output each time the biased gyro input cycles through the lock-in region. The principal method being used today to generate the oscillating bias in the laser gyro is mechanical dither.

### 5.2.1 Mechanical Dither

With mechanical dither, the oscillating bias into the laser gyro is achieved by mechanically vibrating the gyro block at high frequency about its input axis through a stiff dither flexure suspension built into the gyro assembly. The spoked-like structures in Figures 5 and 6 conceptually illustrate such a flexure that is attached to the laser block (on the outside) and to the gyro case/mount (on the inside) by metal rings that are connected to each other by flexible metal reeds. Piezoelectric transducers attached to the reeds provide the dither drive mechanism to vibrate the gyro block at its resonant frequency about the input axis. One piezoelectric transducer is mechanized as a dither angle readout detector and used as the control signal to generate voltage into the drive piezo's to sustain a specified dither amplitude. The dither angle amplitude and acceleration are designed so that the dwell time in the lock-in zone is short so that hard lock-in will never develop. The result is a gyro that has continuous resolution over the complete input rate range. The residual effect of lock-in is a small random angle error in the gyro output that is introduced each time the gyro passes through lock-in (at twice the dither frequency). This is the principal source of random noise in mechanically dithered laser gyros. The relationship between laser gyros random noise, lock-in, and dither rate is ideally given by (15):

$$\sigma_R = \frac{\Omega_L}{(\Omega_D K)^{1/2}} \qquad (2)$$

where

$\sigma_R$ = Gyro random noise (or "random walk") coeffieient (deg/hr$^{1/2}$)

$\Omega_L$ = Lock-in rate

$\Omega_D$ = Dither rate amplitude

K = Gyro output scale factor in fringes per input revolution (i.e., the reciprocal of the gyro "pulse size" discussed previously, times $2\pi$)

For typical values of $\sigma_R$ = 0.002 deg/hr$^{1/2}$, $\Omega_L$ = 0.03 deg/sec, and K = 648,000 (i.e., 2 arc sec pulse size), equation (2) can be used to show that $\Omega_D$ = 72 deg/sec. To achieve sufficient lateral stiffness, the dither spring is designed such that the frequency of the dither motion is on the order of 400 hz. The associated dither cycle amplitude (corresponding to 72 deg/sec dither rate) is 103 arc sec (or 206 arc sec peak-to-peak). Equation (2) is based on the assumption that the angle error generated in the gyro output is uncorrelated from dither cycle to cycle. In practice this is not perfectly achievable, and somewhat larger dither amplitudes are required than predicted by equation (2). Nevertheless, the figures presented previously are generally representative of typical mechanical dither requirements.

Once mechanical dither is incorporated for lock-in compensation, means must be provided to remove the oscillating bias signal from the gyro output (so the that the gyro output represents the motion of the sensor assembly to which the gyro is mounted). Figure 5 illustrates the "case mounted readout" method of optically cancelling the dither from the output. By mounting the readout reflecting prism and photodiodes on the gyro case (i.e., off the gyro block) the translational movement of the gyro block relative to the case (caused by dither) will generate fringe motion at the photodiodes. This purely geometrical effect can be made to cancel the fringe movement produced by the laser block sensed dither angular motion through proper selection of the rotational center for the mechanical dither mount. The result is a photodiode output signal that responds to rotation of the gyro case and not relative movement between the dithering gyro relative to the case.

The alternative to "case-mounted readout" is "block-mounted readout" as illustrated in Figure 6. With this approach the gyro readout optics are mounted directly to the gyro block. Relative movement between the block and case is removed by measurement and substraction, or by filtering. In the measurement/substraction approach, a transducer (typically electromagnetic) is used to electrically measure the instantaneous angle between the gyro block and case. The electrical signal is then digitized and subtracted from the gyro pulse output for dither motion compensation. With the filter approach, a digital filter is used to filter signals near and above the dither frequency from the gyro output.

The result is a cancellation of the unwanted dither rate between the gyro block and case. The penalty is attenuation of real oscillating rates of the gyro case which, if significant, must be accurately measured for processing in the strapdown computer. Use of the filter approach is only valid for relatively benign environment applications where it can be assured that the only angular rate signals that need to be measured have frequency content well below the dither frequency.

5.2.1.1 <u>Mechanical Dither Design Complications</u> - Orginally touted as a simple solution to the lock-in problem with no deleterious side effects, the mechanical dither concept applied in practice has been found to be the source of several subtle mechanical coupling error mechanisms that must be designed for at the three-gyro system level for solution (19, 34). It must be realized at the onset, however, that these complications are directly proportional to the magnitude of dither motion required for lock-in compensation. As lock-in rates are reduced, dither amplitudes can be reduced proportionally (see equation (2)), and design solutions for the effects described below can be more easily achieved.

The basic problem with mechanical dither stems from a kinematic property of three-axis rotary motion that cyclic rates in two orthogonal axes, if at the same frequency but phase shifted by ninety degrees, will produce a real constant attitude rate about the third axis (33, 34). The effect, known as "coning", if present, must be measured as cyclic rate signals by the strapdown gyros, and delivered to the strapdown computer so that the true drift about the third axis will be properly calculated. The problem arises when gyro output errors are also being generated at the same frequency as the real rates to be measured. Cyclic error signals from the gyro in one axis, in combination with errors or real cyclic rates from the gyro in one of the other orthogonal axes, will produce a vector rate profile which appears as coning, but is false ("pseudo-coning" is the nonmenclature typically used to describe this phenonemon). Since the composite gyro output signals (real plus error) are processed in the same computer used to measure real coning motion, a pseudo-coning error will be created in the strapdown computer as a false drift rate about the "third" axis. Filtering the gyro signals to remove the output error oscillations is not acceptable if real cyclic motion is present, since the true drift caused by the real cyclic coning motion will not be properly measured and accounted for.

In the case of mechanically dithered laser gyros, a potential source of real high frequency coning in a strapdown system is the reaction torque of the gyro dither drives into the sensor assembly (the sensor assembly typically consists of a metal casting to which the gyros and accelerometers are mounted). To minimize dither reaction torque resonance effects, and to provide compliance for thermal expansion, most RLG sensor assemblies are mechanically isolated from the system chassis by elastomeric isolators (34). To generate coning motion, equal angular rate vibration frequencies must exist simultaneously in two orthogonal axes. Dither induced vibrations from nominally orthogonal laser gyros into the sensor assembly can become frequency correlated between axes if mechanical coupling exists between the axes (e.g., principal moment-of-inertia axes of the sensor assembly not parallel to gyro input axes). The mechanical coupling mechanisms tend to pull the dither frequencies in orthogonal axes together, thereby creating real coning at dither frequency. Hence, even if single gyro dither frequencies are separate, the mechanical coupling can shift the frequencies toward each other, thereby creating correlated frequency components between axes, or coning. Another source of real high frequency coning is linear random vibrations into the strapdown system that produce correlated frequency rotary sensor assembly motion in orthogonal axes due to sensor assembly/elastomeric mount asymmetries.

The real coning motion effects described above would not be a problem in themselves, since laser gyros have the bandwidth and sensitivity required for accurate measurement of these effects. The problem arises from pseudo-coning created at dither frequency, also due to dither mechanical interaction. A classical example is sensor assembly bending induced by the dither reaction torque which produces false gyro outputs at dither frequency (e.g., due to bending in the mechanism used to measure and remove gyro block/case relative angular dither motion from the gyro output, or gyro mount twisting about the gyro input axis).

Exacting and sophisticated mechanical design techniques must be used in the overall sensor, sensor assembly, and sensor assembly mount to assure that pseudo-coning effects are negligible below the frequencies where real coning exists and has to be measured (33, 34). The coning computation algorithm in the strapdown computer (33) can then be run at an iteration rate that is only high enough to measure the real coning motion frequency effects (i.e., so that high frequency pseudo-coning effects are attenuated). Classical techniques utilized to minumize pseudo-coning effects are to design for stiffness in the sensor assembly, design for mechanical symmetry in the sensor assembly to minimize mechanical dither cross-coupling between gyro axes, and to assure sufficient gyro dither frequency separation so that the tendency for frequency pulling together is minimized. If performed properly, a total design can be acheived that meets overall system requirements under external vibration. Proper design is more easily achieved for benign vibration environments (e.g., commerical aircraft).

5.2.2 Magnetic Mirror Bias

The magnetic-mirror concept is a nonmechanical biasing technique based on the transverse magneto-optic Kerr effect (14, 18, 21). A special inner coating (e.g., ferromagnetic metal) is applied to one of the laser gyro mirrors which, when magnetized normal to the plane of incidence by an applied magnetic field, imparts a nonreciprocal (i.e., opposite) phase shift between the clockwise and counterclockwise laser beams. This produces an apparant differential path-length shift between the laser beams which generates a frequency difference or output rate. The result is a bias imposed on the gyro output that is controllable by the applied magnetic field. Bias uncertainties are compensated through use of alternating bias control (i.e., square-wave dithering of the applied magnetic field). The magnetic field intensity is set at a high enough level to operate the magnetic mirror in a saturated state. In this way, bias shifts generated by stray magnetic fields are minimized.

The advantage of the magnetic mirror is the elimination of the need for mechanical dither, its associated design complications, and size/weight penalties. A problem area for the magnetic mirror has been difficulties in generating a large enough bias for the 0.63 micron laser gyro due to low reflectance of the ferromagnetic coating (14, 20). The resulting loss must be compensated by higher gain in the laser helium-neon discharge. For the 0.63 micron laser, high gain cannot be tolerated because the laser begins to resonate unwanted mode shapes that deteriorate performance. The net result is that the magnetic mirror biasing capability must be diluted by appropriate layering of dielectric coatings on the mirror to recover reflectance. The net bias levels achieved with this approach have not been sufficient to adequately compensate lock-in. (It should be noted that ferromagnetic magnetic mirror technology has been successfully applied to the lesser accurate 1.15 micron laser gyro which can be operated at a higher gain before multimoding problems develop (24)). Another problem area for magnetic mirror technology has been the introduction of residual nonrecipocal phase shifts between the incident laser beams that are temperature sensitive. The result is a bias instability that is temperature sensitive and which produces turn-on transients.

Recent work on laser gyro magnetic mirror technology has concentrated on the development of a garnet magnetic mirror in which the dielectric layer coatings on the laser mirror are made with a transparent garnet film that produces nonreciprocal phase shift to incident light on application of a magnetic field (20). The result has been that the loss effect (associated with the ferromagnetic magnetic mirror technology) has been significantly reduced so that high bias levels can be achieved with 0.63 micron lasers. Current design work is concentrating on doping the garnet material to reduce the effect of residual nonreciprocal temperature sensitive phase shifts that have remained with the new garnet mirror technolgy. Engineering personnel associated with these developments are predicting a breakthrough within the next year based on experimental results achieved to date on doped garnet coatings.

### 5.2.3 Multioscillator Laser Gyro

Conventional two-beam (clockwise and counterclockwise) laser gyros are designed to amplify plane polarized laser light (i.e., in which the electric vector normal to the laser beam is either perpendicular to the lasing plane (S-polarization) or in the lasing plane (P-polarization). Triangular lasers typically use the former polarization while square laser gyros typically use the latter. In the case of the multioscillator laser gyro (26, 27), circular polarization is used in which both S and P modes are simultaneously excited, but at one quarter wavelength phase shifted from one another. The result is a combined electric vector polarization that spirals between S and P, denoted as circular polarization. Right circularly polarized (RCP) or left circularly polarized (LCP) light is generated by creating a plus or minus quarter wavelength shift between the S and P waves, thereby creating a right or left sense spiralling electric vector wave.

In the multioscillator, both RCP and LCP laser beams are created in the same cavity, each with clockwise and counterclockwise components (i.e., a four-beam laser gyro). The two polarization states are excited by a reciprocal polarization rotator (e.g., a quartz crystal) in the beam path that imparts an additional spiral rotation to the circularly polarized light, and which operates identically on both the clockwise and counterclockwise components of the RCP or LCP beams (i.e., recriprocal). The additional rotation adds to the sprialling for the RCP beam and retards the spiraling of the LCP beam. The effect of the added rotation on the RCP beam is to resonate the light components with decreased wavelength such that a net spiral angle reduction is acheived around the beam path to match the spiral angle increase across the rotator. As a result, the RCP beam (both the clockwise and counterclockwise components) are up-shifted in frequency (proportional to the wavelength decrease). The opposite effect is created in the LCP light which is down-shifted in frequency by the same amount that the RCP light frequency is up-shifted. As for the two-beam laser gyro, each polarization state (RCP or LCP) contains a clockwise (CW) and a counterclockwise (CCW) beam component. Hence, two sets of CW and CCW beams are established, one RCP and the other LCP, each operating at a different center frequency. Each set is used to generate an independent output signal equal to the frequency difference between the CW and CCW beams. As for the two-beam laser gyro, the frequency difference output from each polarization state is proportional to input rotation rate. Also, as for the two-beam laser gyro, the frequency difference output from the RCP and LCP lasers experience lock-in which pull the CW and CCW frequencies together at low input rates.

In order to overcome lock-in, a nonreciprocal polarization rotator is introduced into the beam path which rotates circularly polarized light in the opposite sense for clockwise compared to counterclockwise beams. Hence, a frequency shift is imparted between the clockwise and counterclockwise beams (i.e., a bias) for both the RCP and LCP light. The frequency difference is maintained at a high enough level to remain far from the lock-in region under frequency shifts produced by angular rate inputs. The common means for introducing the nonreciprocal bias in the multioscillator laser gyro has been through use of a Faraday rotator consisting of a piece of amporphous glass placed in the beam path with a magnetic field applied across it parallel to the beam. The resulting Faraday effect introduces the desired frequency bias on the circularly polarized light that is in the opposite sense for the LCP compared to the RCP light beams. As a result, the RCP beam output (i.e., the difference between the clockwise and counterclockwise RCP beam frequencies) is positively biased, while the LCP beam frequency difference output is negatively biased by an equal amount.

By summing the outputs from the RCP and LCP beam sets, the input rate sensitivity is doubled, while the Faraday bias effect is cancelled. The cancelling of the bias by summing both outputs eliminates the need for alternating bias to compensate for Faraday rotator gain uncertainties. Elimination of the oscillating bias eliminates a main source of laser gyro random noise (i.e., dithering through the lock-in region). Hence, the random noise in the multioscillator is lower, and closer to the theroretical limit created by random gain and loss of photons from the laser beams (25, 26).

5.2.3.1 Principal Error Sources - The basic principal behind lock-in compensation in the multioscillator laser gyro relies on the Faraday bias (and Faraday bias uncertainties) being equal between the two laser beam sets so that they cancel one another. In practice, this is not totally true, to a large degree because the operating frequencies of the left and right circularly polarized laser sets are different by design. This frequency difference causes each to behave slightly differently to the Faraday bias, producing a net residual error when combined. The error is both temperature and magnetically sensitive, requiring some degree of magnetic shielding and temperature measurement compensation.

Another source of bias error in the multioscillator is variations in the lock-in characteristic between the right and left circularly polarized beams. Even through the Faraday bias keeps the lasers well outside of the lock-in region, small scale factor nonlinearitics still exist at the bias point caused by lock-in. Because the lock-in rates for the two beam sets differ, when the gyro outputs are summed, the residual lock-in error effects at the bias point do not cancel. The resulting bias error created is temperature sensitive and can have unpredictable varations over time.

Multioscillator design groups claim that the above effects are for the most part, predictable and can be compensated sufficiently for satisfactory operation in high accuracy applications.

Two areas where serious errors can develop and are not easily compensated arise from anisotropic and birefringence effects introduced in the light beams as they pass through a quartz crystal reciprocal polarization rotator and Faraday nonreciprocal rotator. The net effect is to introduce unpredictable nonreciprocal path length variation between all four beams which are temperature, acceleration and magnetically sensitive.

Recent advances in multioscillator design techniques have replaced the quartz crystal reciprocal polarization rotator with an out-of-plane beam path geometry that rotates the laser beam by optical reflection at the mirrors (thereby, mimicking the rotational effect of the quartz crystal) (27). The result is elimination of birefringence effects originally created by the presence of the quartz crystal in the beam path. Current work on the multioscillator is addressing improved methods for providing nonreciprocal polarization rotation that have small and more predictable error characteristics than were achieved with original Faraday rotator design configurations.

## 5.3 Laser Gyro Performance And Application Areas

Over the past 6 years, the ring laser gyro (RLG) has progressed from advanced development into full scale production in 1-nmph strapdown inertial navigation applications. The successful 1-nmph laser gyro system programs to date have utilized the 0.63 micron transition with mechanical dither. Systems in the 1-nmph range have been developed by several competing manufacturing groups for both commerical and military application.

Performance advances in RLG technology have been rapid. Continuing advances in laser gyro mirror technology has reduced lock-in (and random noise) by more than an order of magnitude over the past eight years. Lock-in rates lower than 0.0003 deg/hr$^{1/2}$ have been reported. Advanced development programs are now in progress to design laser gyros with performance capabilities required for 0.1 nmph navigation applications.

Principal problems remaining with RLG technology are size and weight for the high performance applications, and size, weight, and cost for the lower accuracy applications. For the higher performance applications, the total weight of an RLG strapdown inertial navigation system is typically 30% higher than its comparable gimbaled system counterpart. Significant cost, reliability, and reaction time benefits for the RLG system, however, make it an attractive alternative to the traditional gimbaled system. It is generally conceded that laser gyro performance in the lower accuracy AHRS and tactical missile midcourse guidance application areas is superior to the competing strapdown RIG or TRG strapdown technologies, however, size, weight, and cost advantages for the RIG or TRG with acceptable performance are prevailing factors today that continue to restrict entry of the RLG into the lower performance application areas.

Performance advances in future RLG's may make it possible to build smaller, lighter weight laser gyro systems for the lower performance market. Advances in nonmechanically dithered RLG technology may make it possible in the future to build a a small size cost/performance competetive integrated 3-axis laser gyro sensor assembly (1, 24) in a single Zerodur structure using interleaved laser paths to reduce net size/weight. If advances in mirror technology continue to reduce lock-in rates and associated dither amplitude requirements, mechanically dithered RLG system size/weight will also be reduced in the future. Production learning is expected to be the determining factor that will decide the degree to which laser gyro production costs will be reduced in the future to be competitive with the lower performance RIG and TRG strapdown sensors. For the higher performance strapdown applications areas, strapdown RIG and TRG manufacturer's generally conceed that the ring laser gyro is now the industry standard, and not a viable competition area for higher performance but more expensive versions of strapdown TRG or RIG technology.

## 6. FIBER-OPTIC ROTATION RATE SENSOR

One of the newer rate sensor technologies that has emerged over the past few years is the fiber-optic rotation rate sensor (28). The concept for the device is illustrated in Figure 8. Light generated from a suitable light source at a specified design frequency is transmitted through a fiber-optic coil. The light beam is first split by a beam-splitter so that half the radiation traverses the coil in the clockwise (CW) direction, and half in the counterclockwise (CCW) direction. The emerging light from both ends of the coil are then recombined at the beam splitter, and transmitted onto a photodetector. The photodetector output power is proportional to the average intensity of the recombined light.

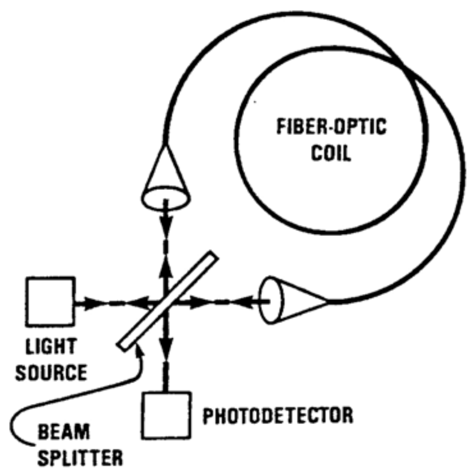


Figure 8 - Basic fiber-optic rotation rate sensor concept

Under rotation of the device about an axis normal to the plane of the fiber-optic coil, the effective optical path length is changed for the CW compared to the CCW beams in a manner similar to the ring laser gyro. In the direction of rotation, the path length increases (i.e., a photon of light has to traverse the length of the coil plus the distance that the coil has been rotated during the traversal period). In the direction opposite to the rotation, the light traverses the length of the coil, minus the distance that the coil has been rotated during the traversal period. The difference between the CCW and CW optical path lengths, then, is twice the distance of rotation, or:

$$\Delta L = 2 \frac{L}{C} \frac{D}{2} \omega = \frac{L\,D}{C} \omega$$

where

L = Total fiber length

D = Diameter of coil (assumed circular)

$\Delta L$ = Difference between CW and CCW optical path-lengths

$\omega$ = Input angular rate

C = Speed of light

This corresponds to a phase shift between the CW and CCW light beams emerging from the coil given by :

$$\Delta\phi \quad = \quad 2\pi \frac{\Delta L}{\lambda} = 2\pi \frac{L\ D}{C\ \lambda}\ \omega \tag{3}$$

where

$\lambda$ = Wavelength of light source

Thus, the phase angle between the emerging light beams becomes proportional to the input angular rate. This contrasts with the ring laser gyro resonator for which the phase angle change is proportional to the integral of the input rate (see Equation (1)). Hence, the fiber-optic rotation sensor is a "rate gyro" while the laser gyro is a "rate integrating gyro". The other difference between the two sensors is that the laser gyro CW and CCW beam frequencies are shifted from each other proportional to the input rotation rate (due to the self-resonance of the laser); the frequencies for the CW and CCW beams in the fiber-optic rate sensor remain equal under rotation rates.

The photodetector in Figure 8 is used to sense the phase shift between the CW and CCW beams. The amplitude of the combined beams at the photodiode equals the sum of the individual beam amplitudes, including the phase shift factor. The result is a combined beam intensity which is maximum for $\Delta\phi = 0$ and mininum (zero) for $\Delta\phi = \pi$ (i.e., varies as $\cos^2 (\Delta\phi/2)$). The photodetector output is proportional to the light intensity, hence, also varies approximately as $\cos^2 (\Delta\phi/2)$.

In order to achieve high sensitivity (high scale factor), the length L of the fiber coil is large. A typical value of L = 400 meters with D = 0.1 meters and $\lambda$ = 0.82 microns produces a $\Delta\phi$ from equation (3) of approximately one radian at 1 rad/sec input rate.

## 6.1 Practical Design Refinements

As depicted in Figure 8, the fiber-optic rotation rate sensor has fundamental error mechanisms that make it impractical to implement. Among these are large scale factor errors associated with photodetector scale factor uncertainties, light source intensity variations, and light amplitude losses in the fiber; loss of rate sensitivity around zero input rate (due to the $\cos^2 (\Delta\phi/2)$ output characteristic of the photodetector; phase angle variations due to mechanical movement between the beam splitter and fiber that produce changes in path length between the CW and CCW beams; and polarization state differences between the CW and CCW beams that produce phase shifts due to nonreciprocal birrefringence and anisotropic effects in the fiber material that are aggravated by environmental exposure. To overcome these fundamental problems, recent fiber-optic rotation sensor configurations (28) have adopted refined interface and control elements such as those depicted in Figure 9.

In Figure 9, the discrete component beam-splitter in Figure 8 is replaced by fiber-optic couplers which consist of integrated fiber-optic junctions that split entering beams 50% to the left and 50% to the right. A polarizer (28) is included to suppress unwanted polarization states in the light. The fiber itself is specifically manufactured to preserve a single polarization state (28) ("polarization preserving fiber"). In this manner, nonreciprocal fiber-beam interractions are suppressed.

A light source (typically a super-luminiscent diode such as Galium Arsenide) transmits narrow frequency bandwidth light* into the fiber that splits into CW and CCW components at the coupler junction. Acousto-optic shifters (A/O) (such as Bragg cells**) at the end of

---

*Note - Original fiber-optic sensors used laser light. One of the major technological break-throughs for the fiber-optic sensor was replacement of the coherent laser light with a broader spectrum source. The result was a significant reduction in nonreciprocal beam/fiber interraction error mechanisms due to the shorter correlation distance for the broader spectrum light (28, 29).

**Note - A Bragg cell (28) is typically mechanized as a piezoelectric device that imparts an acoustical vibration transverse to the light beam at its input drive frequency. The result is a bending of the light (by the "Bragg angle") with an accompanying frequency shift in the light passing through the cell equal to the Bragg cell drive frequency.

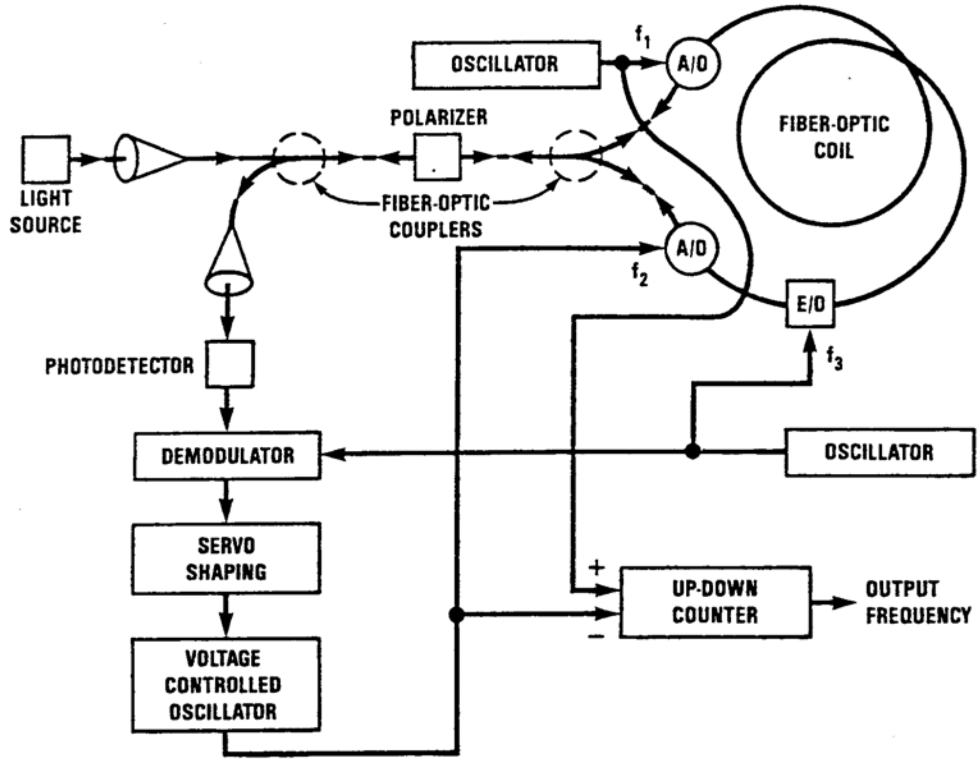


Figure 9 - Improved fiber-optic rotation rate sensor configuration.

the fiber coil are then used to generate a controlled phase shift in the light illuminating the photodector.

To function properly, each Bragg cell in Figure 9 must be biased at a large offset frequency $F_1$ (typically 20 $MH_z$). A Bragg cell mounted at one end of the coil is driven directly at the bias frequency $F_1$ (see Figure 9) which up-shifts the light leaving the cell by $F_1$ from the light entering the cell. The light entering from the left (the clockwise CW beam in Figure 9) must traverse the length of the coil at the up-shifted frequency before it leaves the coil and illuminates the photodetector. The beam entering from the right (the counterclockwise CCW beam in Figure 9), on the other hand, immediately leaves the coil and illuminates the detector after it is frequency up-shifted. The net result is that the CW beam travels a further distance at the up-shifted frequency than the CCW beam, thereby generating a net phase shift between the CW and CCW beams at the photodetector proportional to $F_1$ and the coil length.

The Bragg cell at the opposite end of the coil is driven at $F_2$ which generates a phase shift at the photodiode in the opposite sense to that created by the $F_1$ Bragg cell. The $F_2$ frequency is controlled in servo fashion to maintain the photodetector output at peak power (i.e., zero net phase angle). Under zero input angular rate, the $F_2$ servo drives $F_2$ to equal $F_1$ (i.e., so that equal and opposite phase shifts are created that cancel one-another). Under input angular rate, the servo creates a frequency difference between $F_2$ and $F_1$, the device output in Figure 9, proportional to the input angular rate (that generates an equivalent phase shift at the readout to null the phase shift created by input rotation). It is easily demononstrated that the frequency difference generated to achieve a net zero phase angle is given by:

$$F_2 - F_1 = \frac{4A}{\lambda \ell}\, \omega \tag{5}$$

where

$\ell$ = Length around one coil of the fiber (which typically consists of several coils).

If equation (5) is compared with equation (1) for the laser gyro resonator, it should be clear that they are identical on an integral basis (i.e., the frequency difference pulse count cycles from equation (5) times $2\pi$ radians/cycle is proportional to the input angle by the same factor that, in equation (1), relates RLG output fringe angle change to input angle change.

Figure 9 also includes an electro-optic phase shifter (E/O) driven at frequency $F_3$ at one end of the fiber, which imparts an oscillating path length change to the CW and CCW beams passing through (Note: The E/O is typically mechanized as a piezoelectric actuated "stretcher" which physically changes the length of the fiber by introducing stresses in the fiber proportional to applied voltage (28, 29). This induces an equivalent phase shift in the light). Because the E/O driver is at one end of the coil, the light beam passing out of the coil delivers the phase shift effect first to the photodetector. The beam traveling in the opposite direction has to traverse a longer length of fiber to the photodetector, hence, delivers its phase shift, by an equal amount, later. The delay creates an alternating phase bias at the photodiode mixed beam output, generating an oscillation of the output about the peak power point. By comparing the positive half cycle output decrease with the negative cycle decrease, a linear signal can be generated proportional to the average deviation of the input light phase angle difference from zero. The linear signal is generated in the phase sensitive demodulator shown in Figure 9 driven by $F_3$. The result is a signal out of the demodulator that is linearly proportional to the $\Delta\phi$ phase deviation from zero, thereby eliminating the $\cos^2(\Delta\phi/2)$ sensitivity problem around $\Delta\phi = 0$ that exists without the E/O device.

The basic advantages for the Figure 9 compared to the Figure 8 mechanization approach are the elimination of the discrete light/beam-splitter/fiber junctions, thereby reducing phase shift errors caused by mechanical movement; elimination of the photodetector zero-phase angle sensitivity problem through use of the E/O demodulator; and, through the closed-loop servo operation that maintains the phase angle signal at null, elimination of scale factor errors associated with light source intensity, optical intensity losses in the fiber and beam-splitters, and photodetector scale factor uncertainties.

## 6.2 Development Status And Application Areas

The basic motivation behind the development of the fiber-optic rate sensor was to design a low cost alternative to the ring laser gyro that was inherently void of lock-in problems. The resonant characteristic of the laser gyro which regenerates its light source by stimulated emission, is the transfer mechanism that couples the CW and CCW beams together from back-scatter, producing lock-in. For the fiber-optic rate sensor, the light source is external to the sensing ring, hence, does not amplify the effects of back-scatter. As a result, the lock-in phenomenon associated with the laser gyro is absent in the fiber-optic sensor. This has been proven experimentally (29). The rationale behind the projected low cost of the fiber-optic sensor is that use of fiber-optics and integrated-optics technologies should reduce labor hours associated with device manufacture. It also assumes continuing reductions in the cost of high quality optical fiber which has been occuring over the past few years. From a performance standpoint, the fiber-optic rotation sensor is not expected to compete with the high performance laser gyro for accuracy, but is envisioned as a competitor to the lower cost autopilot, and eventually tactical missile and AHRS quality gyros.

Much has been accomplished since 1976 when the fiber-optic rotation sensor concept was originally conceived. To a large degree, these accomplishments are summarized by the evolution of the concept from its original form (in Figure 8) to its more refined practical form (in Figure 9). Nevertheless, much remains to be accomplished before this device can be considered a serious competitor with mature low cost conventional spinning wheel gyro technology or new lower cost/medium performance laser gyro technology. The device has still to be designed into a practical form that is producible at low cost, and which achieves overall performance goals over opertional environments in a reasonable form factor. To a large extent the development status reflects the level of funding committment assigned by individual groups toward device development. Although many small funded activities have existed over the past 8 years, few dedicated programs have been heavily funded. From another standpoint, the funding limits could reflect lack of confidence by funding agencies in the new technology, or a lack of available funds to pursue new technologies after completing heavy investments in recent technologies that are only now entering large scale production (e.g., the laser gyro).

Some of the technical problems that remain for the fiber-optic rotation rate sensor (28) include larger than desired size (2 to 4 inches in diameter) for the fiber-optic ring to avoid introducing beam interractions with the fiber walls under tight fiber turns; scale factor errors due to photodiode output frequency variations with temperature; bias errors associated with photodiode output frequency side-bands creating phase offsets at the photodetector; bias errors created from large required Bragg cell drive frequency offsets coupled with variations in the CW and CCW Bragg biased coil lengths due to off-nominal variations between the Bragg cell distances to the fiber-optic coupler (see Figure 9); bias errors associated with the E/O demodulator electronics loop; bandwidth limits associated with the closed-loop operation in Figure 9; and increasing complexity of the sensor configuration to resolve problem areas. Virtually no data has been published on the performance of the fiber-optic rate sensor under dynamic environments. One of the principal potentional error mechanisms for the device (as for all angular rate sensing instruments) is bias error created under dynamic temperature, mechanical vibration, acoustic vibration, acceleration, and magnetic enviroments. Fiber-optic rate sensor enthusiasts remain confident that these problems can be resolved, given time and funding. For evidence they point to the significant performance advances made over the past eight years, where the fiber-optic rate sensor has progressed from an original concept that could barely detect earth's rate, to current technology versions that have demonstrated milli-earth-rate sensitivities (29).

## 7. PENDULOUS ACCELEROMETER

The pendulous accelerometer (Figure 10) (1) consists of a hinged pendulum assembly, a moving-coil signal-generator/pickoff that senses angular movement of the pendulum from a nominally null position, and a permanent-magnet torque-generator that enables the pendulum to be torqued by electrical input. The torquer magnet is fixed to the accelerometer case, and the coil assembly is mounted to the pendulum. Delicate flex leads provide electrical access to the coil across the pendulum/case hinge junction. Electronics are included for pickoff readout and for generating current to the torquer.

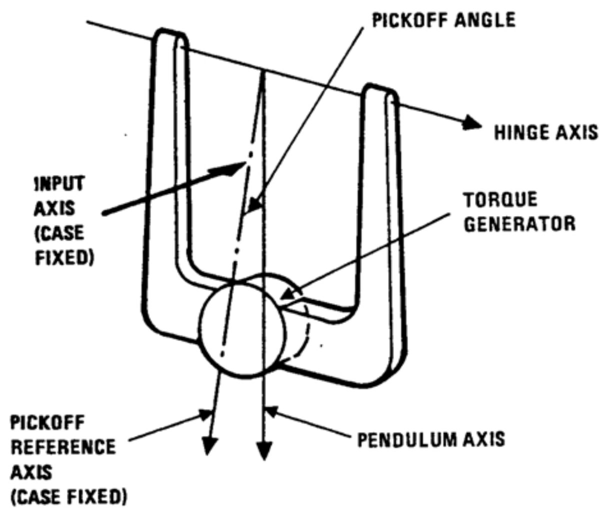


Figure 10 - Electrically servoed pendulous accelerometer concept.

The device is operated in the captured mode by applying electrical current to the torquer at the proper magnitude and phasing to maintain the pickoff at null. Under these conditions, the electrically generated torque on the pendulum balances the dynamic torque generated by input acceleration normal to the pendulum plane. Hence, the electrical current through the torquer becomes proportional to input acceleration, and is the output signal for the device.

Mechanization approaches for the pendulous accelerometer (1) vary between manufacturers but generally fall into two categories: fluid filled and dry units. Fluid-filled devices utilize a viscous fluid in the cavity between the pendulum and case for damping and partial floatation. The dry units use dry air, nitrogen, or electromagnetic damping.

The hinge element for the pendulous accelerometer is a flexible member that is stiff normal to the hinge line to maintain mechanical stability of the hinge axis relative to the case under dynamic loading, but flexible about the hinge line to minimize unpredictable spring restraint torques that cannot be distinguished from acceleration inputs. Materials selected for the hinge are chosen for low mechanical hysteresis to minimize unpredictable spring-torque errors. To minimize hystersis effects, the hinge dimensions are selected to assure that hinge stresses under dynamic inputs and pendulum movement are well below the yield-stress for the hinge material. Beryllium-copper has been a commonly used pendulum-hinge material due to its high ratio of yield-stress to Young's modulus (i.e., the ability to provide large flexures without exceeding material yield-stress). Another successful design approach for dry accelerometers has utilized fused quartz for both the hinge and pendulum by etching the complete assembly from a single-piece quartz substrate (1).

### 7.1 Performance And Application Areas

The pendulous accelerometer continues to be the primary mechanization approach being used for almost all strapdown applications. Design refinements over the past 6 years now provide units from several manufacturers that meet 1.0 nmph strapdown inertial navigation requirements in heaterless configurations. The heaterless configuration operates without temperature controls and achieves its accuracy through thermal modeling of the sensor errors in the strapdown system computer based on temperature measurements taken with temperature probes mounted within the sensing unit. The heaterless accelerometer configuration has been perfected within recent years for operation with ring laser gyros which are also operated heaterless using direct path-length control to stabilize performance (Note: Use of heaters to control temperature and stabilize performance with the ring laser gyro is impractical due to the long thermal time constant of the Zerodur material from which it is constructed, and the associated reaction time penalty that would be introduced from turn-on until temperature/performance stabilization. Laser gyro performance variations with temperature are also compensated by thermal modeling). It is highly fortunate that pendulous accelerometer designs originally developed for heated operation (to stabilize performance), have been predictable enough thermally, to allow accurate characterization over their complete temperature range by analytical modeling using temperature measurements. Hence, major design refinements for heaterless operation have not been necessary.

Most accelerometers today are of the dry pendulous metal flexure hinge variety (1). Design refinements in quartz hinge design configurations (1) (most notably in the plating technology used to conduct current across the hinge into the pendulum-mounted torquer coil to minimize hysteresis) have provided a rugged unit that meets 1.0 nmph strapdown inertial navigation accuracy requirements.

Experimental pendulous accelerometers have recently provided indications that identifiable futher design refinements will make it possible to achieve the accuracy improvements needed for the advanced 0.1 nmph INS applications. Advanced engineering develoment programs are currently being funded (at a fairly modest level) to develop and evaluate these performance improvements.

Unit costs for the pendulous accelerometer, although acceptable, still remain higher than desirable, particularly in the higher accuracy applications. Competitive sourcing in some applications has created the environment needed to reduce costs to some extent through design, manufacturing, and test improvements. Increased production volume has added to cost reduction through learning and improved tooling/automation techniques. However, the production volume has not been sufficient to develop the automatic manufacturing technologies needed to make major in-roads in cost reduction. Nevertheless, the pendulous accelerometer cost is acceptable for most applications, compared to the cost of other strapdown system elements.

## 8. TORQUE-LOOP MECHANIZATION APPROACHES FOR TORQUE REBALANCE INSTRUMENTS

The implementation of the torque loop for the torque-to-balance instruments (e.g., floated rate-integrating gyro, tuned-rotor gyro, pendulous accelerometer) continue to be mechanized using different approaches, depending on manufacter: digital pulse-rebalance or analog-rebalance with follow-up pulse-rebalance logic, using pulse-on-demand or pulse-width-modulated forced limit-cycle techniques (1). Little data has been published on the performance of these electrical circuits, an unfortunate circumstance, particulary since their accuracy is a key contributor to the overall performance of the intrument they are designed to operate with. Performance data advertized as representative of particular sensors does not always include the effect of the digital pulse-rebalance circuity (i.e., the data was taken on an analog basis at the basic instrument level). This becomes of greater concern when one considers the more demanding application areas that can require dynamic ranges (maximum input versus bias accuracy) in the $10^6$ to $10^7$ category.

## 9. THE VIBRATING BEAM ACCELEROMETER

Much of the cost for conventional pendulous electrically-servoed accelerometers is associated with the torque-generator and electronics needed to close-the-loop on the instrument and generate precision pulse outputs representing quantized increments of integrated input acceleration (1). The vibrating beam accelerometer replaces the torque-rebalance mechanism with an open-loop direct-digital-output transducer based on quartz-crystal oscillator technology (30, 31, 32). The concept is depicted in Figure 11.

In Figure 11, two quartz-crystal beams are mounted symmetrically back-to-back so that each axially supports a proof mass pendulum. Each beam is vibrated at its resonant frequency by an electronics loop in a manner similar to the method used to sustain amplitude in quartz-crytal oscillator clock references. In the absence of acceleration along the

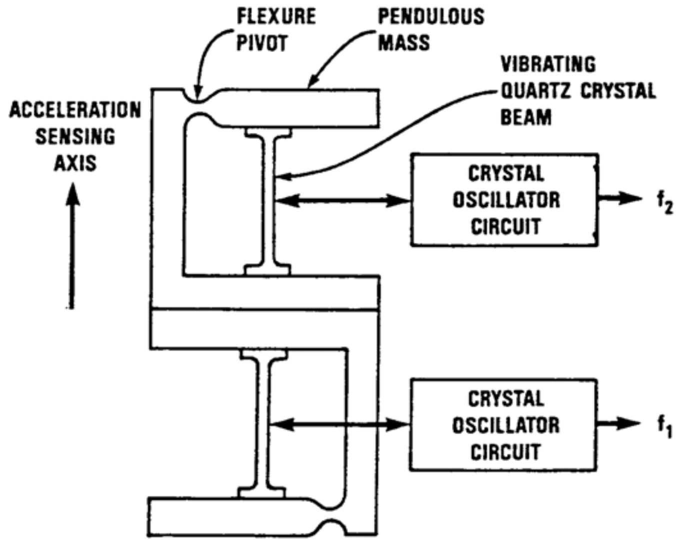


Figure 11 - Vibrating beam accelerometer concept.

acceleration sensing axis, both beams are selected to nominally resonate at the same frequency. Under applied acceleration, one beam is placed in compression and the other in tension by the inertial reaction of the pendulous proof masses. This produces an increase in frequency for the beam in tension, and a decrease in frequency for the beam in compression. The frequency difference ($F_2 - F_1$ in Figure (11)) is a direct digital output proportional to the input acceleration.

The symmetrical arrangement of the beams produces a cancellation of several error effects that would exist for one beam mounted individually. Error effects that are nominally cancelled include nominal beam frequency variations with temperature and aging, asymmetrical scale factor nonlinearities, anisoinertia errors (1), and vibropendulous errors (1) that are common between the individual beam assemblies.

## 9.1 Design Considerations And Application Areas

The vibrating beam accelerometer is being designed as a lower cost alternative to the conventional pendulous electrically-servoed accelerometer for strapdown applications. Cost reductions are expected to be achieved through elimination of the complex electro-mechanical assembly associated with the pendulous accelerometer torque-generator, and elimination of complex torque-to-balance and pulse quantizer readout electronics.

The ultimate success of the vibrating beam accelerometer will depend on whether its accuracy capabilities will approach those of mature technology pendulous accelerometers at a competetive price. Error mechanisms in the vibrating beam accelerometer arise from unpredictable variations between the two beam assemblies that are temperature, vibration sensitive and which vary over time. One of the more important error mechanisms that must be dealt with in the design of the unit is the potentional problem of mechanical coupling between the beam assemblies that pull the frequencies together under low input acceleration (an effect similar to lock-in for laser gyros). The result is a detection threshold for the unit that is a function of the strength of the mechanical coupling. The key to the design of an accurate vibrating beam accelerometer lies in the ability to isolate one crytsal beam from the other. One approach being used to achieve isolation is through application of a dual-beam construction (32) for each of the crystal beam assemblies as illustrated in Figure 12.

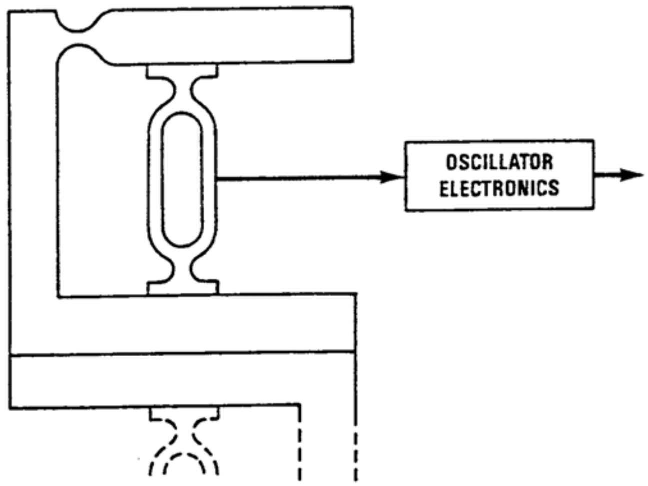


Figure 12 - Dual-beam crystal oscillator concept.

In Figure 12, each beam assembly is composed of an integral dual-beam arrangement in which the beam elements vibrate in opposition (180 degrees out of phase). The resulting counter-vibration allows each beam movement to be counter-acted mechanically by the other such that no net vibration is transmitted into the mount (i.e., similar to a tuning fork). The result is that mechanical coupling mechanisms between the independent dual-beam assemblies are minimized.

A problem area being addressed in the design of the vibrating beam accelerometer is the output resolution. Typical mechanizations are based on using crystals with a 40 KHz center frequency (zero input acceleration) with 10% variation over the design acceleration range. Hence, the inherent maximum frequency output of the device (beam frequency difference) under maximum input acceleration is typically 5 to 10 KHz. For the higher accuracy applications, this resolution is generally too coarse (by at least an order of magnitude under certain conditions). In order to enhance the basic resolution, design techniques being investigated include using time measurement between frequency difference pulses as the output, or use of digital phase-lock loop external circuity to generate higher frequency waveforms whose integral tracks the frequency difference output signal.

The vibrating beam accelerometer is still in its development stage with units becoming available for evaluation by test groups this year. Developmental test results reported to date have been encouraging. It is too early at this time to predict what the ultimate cost/performance of the device will be compared to mature pendulous accelerometer technology.

## 10. CONCLUDING REMARKS

Over the past six years, the laser gyro has emerged as the rate sensor most suitable for the high performance strapdown applications. Floated rate-integrating and tuned-rotor gyro technologies continue to be the most suitable rate sensors for the low-to-medium performance/low-cost application areas where small size is also important. It is expected that cost and size reductions for the laser gyro will broaden its applicability range in the future so that it will eventually dominate the medium accuracy performance areas as well. It is too early to predict whether the laser gyro will ever be of a low enough cost to successfully compete in the lower accuracy tactical missile application areas.

Pendulous accelerometer technology continues to be the main stay for strapdown applications. Performance advances and some cost reductions over the past few years have enabled this instrument to remain compatible with overall strapdown system cost/performance goals. To generate a significant cost reduction for strapdown accelerometers, the vibrating beam accelerometer is receiving attention by some development groups. Time will tell whether the cost/performance of this instrument will successfully compete with pendulous accelerometers in the future.

## 11. ACKNOWLEDGEMENTS

I would like to express my appreciation to engineering personnel in the following organizations who participated in valuable technical discussions on strapdown sensor technology during the preparation of this paper. These discussions provided the primary source of technical information for the paper.

Honeywell Avionics Division, Minneapolis, MN
Litton Guidance & Control Systems, Woodland Hills, CA
Naval Research Laboratory, Washington, DC
Raytheon Equipment Development Laboratories, Sudbury, MA
Rockwell Autonetics, Anaheim, CA
Singer Kearfott, Wayne, NJ
Sperry Gyroscope, Great Neck, NY
Sundstrand Data Control, Redmond, WA
Sundstrand Optical Technologies, Newbury Park, CA

## REFERENCES

1. Savage, Paul G., "Strapdown Sensors", "AGARD Lecture Series No. 95: Strapdown Inertial Systems - Theory And Applications", June 1978.

2. Savage, Paul G., "Laser Gyros In Strapdown Inertial Navigation Systems", IEEE PLANS, Hilton Inn, San Diego, CA, November 1 - 3, 1976

3. Dynamic Errors in Strapdown Inertial Navigation Systems, NASA Report CR-1962, December 1971.

4. Wrigley, W., Hollister, W.M., and Denhard, W.G.,"Gyroscopic Theory, Design, and Instrumentation", M.I.T. Press, 1969.

5. Macomber, George R., and Fernandes, Manuel, Inertial Guidance Engineering, Prentice-Hall, Englewood Cliffs, New Jersey, 1962.

6. Howe, Edwin W., "A Free Rotor Gyro", Symposium on Unconventional Inertial Sensors, Farmingdale, New York, 1963.

7. Savet, Paul H., "New Trends in Non-floated Precision Gyroscopes", Grumman Research Department Memorandum RM-247J, October 1964.

8. Craig, Robert J.G., "Theory of Operation of Elastically Supported Tuned Gyroscope", IEEE Transactions on Aerospace and Electronic Systems, Vol. AES-8, No. 3, May 1972.

9. Craig, Robert J.G., "Theory of Errors of a Multigimbal, Elastically Supported, Tuned Gyroscope", IEEE Transactions on Aerospace and Electronic Systems, Vol. AES-8, No. 3, May 1972.

10. Craig, Robert J.G., Dynamically Tuned Gyros in Strapdown Systems", AGARD Conference Proceedings No. 116 on Inertial Navigation Components and Systems, AD-758 127, Paris, France, February 1973.

11. Killpatrick, Joseph, "The Laser Gyro", IEEE Spectrum, October 1967.

12. Aronowitz, Frederick, "The Laser Gyro", Laser Applications, Vol. 1, Academic Press, New York, 1971.

13. Aronowitz, Frederick, and Collins R.J., "Mode Coupling Due to Back Scattering in a HeNe Traveling Wave Ring Laser", Applied Physics Letters, Vol. 9, No. 1, 1 July 1966.

14. Dewar, Dr. D., "The Laser Gyroscope", Royal Aeronautical Society, London, 12 January 1977.

15. Hammons, Seridan W., and Ashby, Val J., "Mechanically Dithered RLG At The Quantum Limit", 0547-3578/82/0000-0388 Copyright 1982 IEEE.

16. Hutchings, T.J., and Stjern, D.C., "Scale Factor Non-Linearity of a Body Dithered Laser gyro", IEEE NAECON, 1978, Vol. 2, Pg. 549.

17. Hutchings, T., "Development And Test of A Small Body Dithered Laser Gyro", Electro-Optics/Laser 77 Conference & Exposition, Anaheim, CA, Oct. 25-27, 1977.

18. Henery, R.D., Whitcomb, E.C., and Vescial, F., "Ferrimagnetic Garnets As Laser Gyro Faraday Elements", Electro-Optics/Laser 77 Conference & Exposition, Anaheim, CA, Oct. 25-27, 1977.

19. Mark, John G., Ebner, Robert E., and Brown, Alison K., "Design of RLG Inertial Systems For High Vibration", IEEE PLANS, Atlantic City, NJ, December 6-9, 1982.

20. McClure, R.E., and Vaher E., "An Improved Ring Laser Bias Element", CH1336-7/78/0000-0544 Copyright 1978 IEEE.

21. McClure, R.E., "An Electrical Equivalent Circuit For The Tranverse Mangeto-Optic Effect In Thin Magnetic Films", International Magnetics Conference, Boston, MA, April 24, 1980.

22. Freiser, M.J., "A Survey of Magneto-Optics Effects", IEEE Transactions on Magnetics MAG-4, 152, 1968.

23. Dillon, Jr., J.F., "Magneto-Optical Properties of Magnetic Garnets", Physics of Magnetic Garnets, pp 379-415, A. Paoletti, ed; North Holland, 1978.

24. Morrison, R.F., Levinson, Dr. E., and Bryant Jr., B.L., "The SLIC-7 Laser Gyro, Inertial Guidance System", NAECON, Dayton, Ohio, 1977.

25. Dorshner, Terry A., Hermann, A. Haus, Holz, Michael, Smith, Irl W., and Statz, Hermann, "Laser Gyro At Quantum Limit", IEEE Journal of Quantum Electronics, Vol QE-16, No. 12, December 1980.

26. Mathews, James B., Gneses, Morris I., and Berg, Dennis S., "A High Resolution Laser Gyro", NAECON May 16-18, 1978, Dayton, Ohio.

27. Statz, H., Dorschner, Terry A., Holz, M., and Smith, Irl W., The Multioscillator Ring Laser Gyroscope, Raytheon Research Division Technical Report T-1096, January, 1983.

28. Ezekiel, S., and Arditty, H.J., ed. Fiber-Optic Rotation Sensors, Proceedings of the First International Conference, M.I.T., Cambridge, MA, November 9-11, 1982; Published in Springer Series in Optical Sciences, Vol. 32, Schawlow, Arthur L., ed., Springer-Verlag Berlin Heidelberg New York 1982.

29. Burns, W.K., Moeller, R.P., Villarruel, C.A., and Abebe, M., "Fiber-Optic Gyroscope with Polarization-Holding Fiber", Optics Letters, Vol. 8, No. 10, October 1983.

30. Albert, William C., and Weber Raymond E., "Vibrating Beam Accelerometer For Strapdown Applications", IEEE PLANS, Atlantic City, NJ, December 6-9, 1982.

31. Albert, William C., "Vibrating Quartz Crystal Beam Accelerometer", Copyright ISA, 1982, ISBN: 0-87664-689-5.

32. Gogic, A.M., and Peters, R.B., "Description And Test Methods For A Frequency Output Accelerometer", Inertial Navigation Test Symposium, Holloman AFB, 1983.

33. Savage, P.G., "Strapdown System Algorithms", AGARD Lecture Series No. 133: Advances In Strapdown Inertial Systems", May 1984.

34. Savage, P.G., Introduction To Strapdown Inertial Systems, June 1, 1983 (Third Printing), and Introduction To Strapdown Inertial Navigation Systems - Supplemental Material, November 14, 1983; Third Strapdown Associates Open Seminar On Strapdown Inertial Navigation Systems, Marquette Inn, Minneapolis, MN, Nov. 14-18, 1983.

## NOTES

# STRAPDOWN SYSTEM ALGORITHMS

Paul G. Savage
President
Strapdown Associates, Inc.
Woodbridge Plaza, Suite 150
10201 Wayzata Blvd.
Minnetonka, Minnesota 55343

Presented in Athens, Greece;
Rome, Italy; and Copenhagen, Denmark;
As Part Of
AGARD Lecture Series No. 133
ADVANCES IN STRAPDOWN INERTIAL SYSTEMS
May, 1984

# STRAPDOWN SYSTEM ALGORITHMS

Paul G. Savage
President
Strapdown Associates, Inc.
Woodbridge Plaza, Suite 150
10201 Wayzata Blvd.
Minnetonka, Minnesota 55343

## SUMMARY

This paper addresses the attitude determination, acceleration transformation, and attitude/heading output computational operations performed in modern-day strapdown inertial navigation systems. Contemporary algorithms are described for implementing these operations in real-time computers. The attitude determination and acceleration transformation algorithm discussions are based on the two-speed approach in which high frequency coning and sculling effects are calculated with simplified high speed algorithms, with results fed into lower speed higher order algorithms. This is the approach that is typically used in most modern-day strapdown systems. Design equations are included for evaluating the performance of the strapdown computer algorithms as a function of computer execution speed and sensor assembly vibration amplitude/frequency/phase environment.

Both direction cosine and quaternion based attitude algorithms are described and compared in light of modern-day algorithm accuracy capabilities. Orthogonality and normalization operations are addressed for potential attitude algorithm accuracy enhancement. The section on attitude data output algorithms includes a discussion on roll/heading Euler angle singularities near high/low pitch angle conditions.

## 1. INTRODUCTION

The concept of strapdown inertial navigation was originated more than thirty years ago, largely from an analytical standpoint. The theoretical analytical expressions for processing strapdown inertial sensor data to develop attitude, velocity, and position information were reasonably well understood in the form of continuous matrix operations and differential equations. The implementation of these equations in a digital computer, however, was invariably keyed to severe throughput limitations of original airborne digital computer technology. As a result, many of the strapdown computational algorithms originated during these early periods were inherently limited in accuracy, particularly under high frequency dynamic motion. A classical test for algorithm accuracy during this early period was how well the algorithm computed attitude under cyclic coning motion as the coning frequency approached the computer update cycle frequency.

In the late 1960's and early 1970's, several analytical efforts addressed the problem of splitting the strapdown computation process into low and high speed sections

(7, 8, 10). The low speed section contained the bulk of the computational equations, and was designed to accurately account for low frequency large amplitude dynamic motion effects (e.g., vehicle maneuvering). The high speed computation section was designed with a small set of simple algorithms that would accurately account for high frequency small amplitude dynamic motion (e.g., vehicle vibrations). Splitting the computational process in this manner allowed the bulk of the strapdown algorithms to be iterated at reasonable speeds compatible with computer throughput limitations. The high speed algorithms were simple enough that they could be mechanized individually with special purpose electronics, or as a minor high speed loop in the main processor.

Over the past ten years, the structure of most strapdown algorithms has evolved into this two speed structure. The techniques have been refined today so that fairly straight-forward analytical design methods can be used to define algorithm analytical forms and computational rates to achieve required levels of performance in specified dynamic environments.

This paper describes the algorithms used today in most modern-day strapdown inertial navigation systems to calculate attitude and transform acceleration vector measurements from sensor to navigation axes. The algorithms for integrating the transformed accelerations into velocity and position data are not addressed because it is believed that these operations are generic to inertial navigation in general, not only strapdown inertial navigation.

For the algorithms discussed, the analytical basis is presented together with a discussion on general design methodology used to develop the algorithms for compatibility with particular user accuracy and environmental requirements.

## 2. STRAPDOWN COMPUTATION OPERATIONS

Figure 1 depicts the computational elements implemented by software algorithms in typical strapdown inertial navigation systems. Input data to the algorithms is provided from a triad of strapdown gyros and accelerometers. The gyros provide precision measurements of strapdown sensor coordinate frame ("body axes") angular rotation rate relative to nonrotating inertial space. The accelerometers provide precision measurements of 3-axis orthogonal specific force acceleration along body axes.

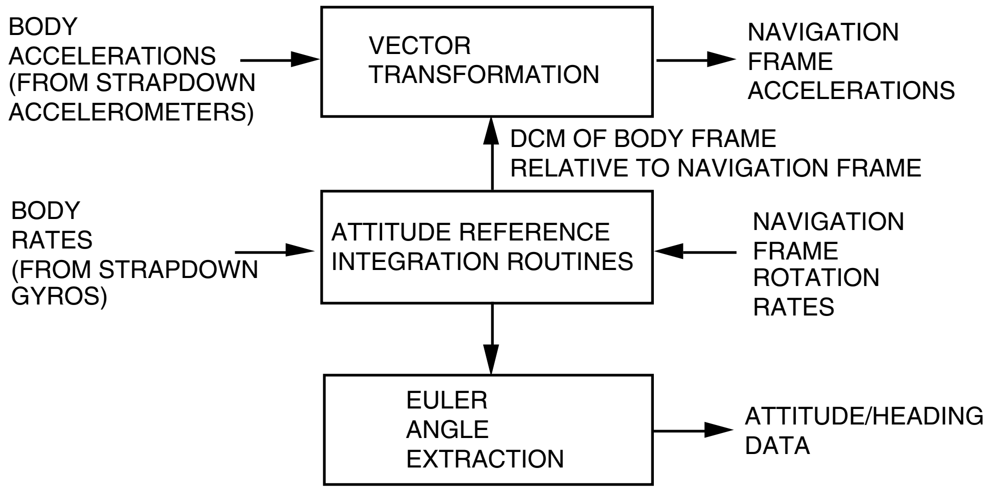


FIGURE 1 - STRAPDOWN ATTITUDE REFERENCE OPERATIONS

The strapdown gyro data is processed on an iterative basis by suitable integration algorithms to calculate the attitude of the body frame relative to navigation coordinates. The rotation rate of the navigation frame is an input to the calculation from the navigation section of the overall computation software. Typical navigation coordinate frames are oriented with the z-axis vertical and the x, y, axes horizontal.

The attitude information calculated from the gyro and navigation frame rate data is used to transform the accelerometer specific force vector measurements in body axes to their equivalent form in navigation coordinates. The navigation frame specific force accelerations are then integrated in the navigation software section to calculate velocity and position. The velocity/position computational algorithms are not unique to the strapdown mechanization concept, hence, are not treated in this paper. Several texts treat the velocity/position integration algorithms in detail (1, 2, 3, 4, 12).

Figure 1 also shows an Euler Angle Extraction function as part of the strapdown attitude reference operations. This algorithm is used to convert the calculated attitude data into an output format that is more compatible with typical user requirements (e.g., roll, pitch, heading Euler angles).

## 3. STRAPDOWN ATTITUDE INTEGRATION ALGORITHMS

The attitude information in strapdown inertial navigation systems is typically calculated in the form of a direction cosine matrix or as an attitude quaternion. The direction cosine matrix is a three-by-three matrix whose rows represent unit vectors in navigation axes projected along body axes. As such, the element in the $i^{th}$ row and $j^{th}$ column represents the cosine of the angle between the navigation frame i-axis and body frame j-axis. The quaternion is a four-vector whose elements are defined analytically (5, 9) as follows:

$$
\begin{aligned}
a &= \left(\alpha_x/\alpha\right)\sin\left(\alpha/2\right) \\
b &= \left(\alpha_y/\alpha\right)\sin\left(\alpha/2\right) \\
c &= \left(\alpha_z/\alpha\right)\sin\left(\alpha/2\right) \\
d &= \cos\left(\alpha/2\right)
\end{aligned}
\tag{1}
$$

where

$\alpha_x, \alpha_y, \alpha_z$ = Components of an angle vector $\underline{\alpha}$.

$\alpha$ = Magnitude of $\underline{\alpha}$.

The $\underline{\alpha}$ vector is defined to have direction and magnitude such that if the navigation frame was rotated about $\underline{\alpha}$ through an angle $\alpha$, it would be rotated into alignment with the body frame. The $\underline{\alpha}$ rotation angle vector and its quaternion equivalent (a, b, c, d, from equations (1)), or the direction cosine matrix, uniquely define the attitude of the body axes relative to navigation axes.

## 3.1 Direction Cosine Updating Algorithms

### 3.1.1 Direction Cosine Updating Algorithm For Body Rotations

The direction cosine matrix can be updated for body frame gyro sensed motion in the strapdown computer by executing the following classical direction cosine matrix chain rule algorithm on a repetitive basis:

$$C(m+1) = C(m)\ A(m) \tag{2}$$

where

C(m) = Direction cosine matrix relating body to navigation axes at the $m^{th}$ computer cycle time.

A(m) = Direction cosine matrix that transforms vectors from body coordinates at the $(m+1)^{th}$ computer cycle to body coordinates at the $m^{th}$ computer cycle.

It is well known (9) that:

$$A(m) = I + f_1\left(\underline{\phi}\times\right) + f_2\left(\underline{\phi}\times\right)^2 \tag{3}$$

where

$$f_1 = \frac{\sin \phi}{\phi} = 1 - \phi^2/3! + \phi^4/5! - \cdots$$

$$f_2 = \frac{1 - \cos \phi}{\phi^2} = 1/2! - \phi^2/4! + \phi^4/6! - \cdots$$

$$\phi^2 = \phi_x 2 + \phi_y 2 + \phi_z 2 \tag{4}$$

$$\left(\underline{\phi}\times\right) \overset{\Delta}{=} \begin{bmatrix} 0 & -\phi_z & \phi_y \\ \phi_z & 0 & -\phi_x \\ -\phi_y & \phi_x & 0 \end{bmatrix}$$

$I = 3 \times 3$ identity matrix

$\phi_x, \phi_y, \phi_z$ = Components of $\underline{\phi}$.

$\underline{\phi}$ = Angle vector with direction and magnitude such that a rotation of the body frame about $\underline{\phi}$ through an angle equal to the magnitude of $\underline{\phi}$ will rotate the body frame from its orientation at computer cycle m to its orientation at computer cycle m+1. The $\underline{\phi}$ vector is computed for each computer cycle m by processing the data from the strapdown gyros. The algorithm for computing $\underline{\phi}$ will be described subsequently.

The “order” of the algorithm defined by equations (2) through (4) is determined by the number of terms carried in the $f_1$, $f_2$ expansions. A fifth order algorithm, for example, retains sufficient terms in $f_1$ and $f_2$ such that A(m) contains all $\underline{\phi}$ term products out to fifth order. Hence, $f_1$ would be truncated after the $\phi^4$ term and $f_2$ would be truncated after the $\phi^2$ term to retain fifth order accuracy in A(m). The order of accuracy required is determined by system accuracy requirements under maximum rate input conditions when $\underline{\phi}$ is a maximum. The computation iteration rate is typically selected to assure that $\underline{\phi}$ remains small at maximum rate (e.g., 0.1 radians). This assures that the number of terms required for accuracy in the $f_1$, $f_2$ expansions will be reasonable.

### 3.1.2 Direction Cosine Updating Algorithm For Navigation Frame Rotations

Equation (2) is used to update the direction cosine matrix for gyro sensed body frame motion. In order to update the direction cosines for rotation of the navigation coordinate frame, the following classical direction cosine matrix chain rule algorithm is used:

$$C(n+1) = B(n)\, C(n) \tag{5}$$

where

$B(n)$ = Direction cosine matrix that transforms vectors from navigation axes at computer cycle n to navigation axes at computer cycle (n+1).

The equation for B(n) parallels equation (3):

$$B(n) = I - (\underline{\theta}\times) + 0.5(\underline{\theta}\times)^2 \tag{6}$$

with

$$\left(\underline{\theta}\times\right) \overset{\Delta}{=} \begin{bmatrix} 0 & -\theta_z & \theta_y \\ \theta_z & 0 & -\theta_x \\ -\theta_y & \theta_x & 0 \end{bmatrix} \tag{7}$$

where

$\theta_x, \theta_y, \theta_z$ = Components of $\underline{\theta}$.

$\underline{\theta}$ = Angle vector with direction and magnitude such that a rotation of the navigation frame about $\underline{\theta}$ through an angle equal to the magnitude of $\underline{\theta}$ will rotate the navigation frame from its orientation at computer cycle n to its orientation at computer cycle n+1. The $\underline{\theta}$ vector is computed for each computer cycle n by processing the navigation frame rotation rate data from the navigation software section (12)

It is important to note that the n cycle (for navigation frame rotation) and m cycle (for body frame rotation) are generally different, n typically being executed at a lower iteration rate than m. This is permissible because the navigation frame rotation rates are considerably smaller than the body rates, hence, high execution rates are not needed to maintain $\underline{\theta}$ small to reduce the order of the iteration algorithm. The algorithm represented by equations (5) and (6) is second order in $\underline{\theta}$. Generally, first order is of sufficient accuracy, and the $(\underline{\theta}\times)^2$ term need not be carried in the actual software implementation.

## 3.2 Quaternion Updating Algorithm

### 3.2.1 Quaternion Transformation Properties

The updating algorithms for the attitude quaternion can be developed through an investigation of its vector transformation properties (5, 9). We first introduce nomenclature that is useful for describing quaternion algebraic operations. Referring to equation (1), the quaternion with components a, b, c, d, can be described as:

$$u = ai + bj + ck + d \tag{8}$$

where

a, b, c = Components of the "vector" part of the quaternion.

i, j, k = Quaternion vector operators analogous to unit vectors along orthogonal coordinate axes.

d = "Scalar" part of the quaternion.

We also define rules for quaternion vector operator products as:

$$\begin{array}{lll} ii = -1 & ij = k & ji = -k \\ jj = -1 & jk = i & kj = -i \\ kk = -1 & ki = j & ik = -j \end{array}$$

With the above definitions, the product w of two quaternions (u and v) becomes:

$$\begin{aligned} w = uv &= (ai + bj + ck + d)\,(ei + fj + gk + h) \\ &= aeii + afij + agik + ahi \\ &\quad + beji + bfjj + bgjk + bhj \\ &\quad + ceki + cfkj + cgkk + chk \\ &\quad + dei + dfj + dgk + dh \\ &= (ah + de + bg - cf)\, i \\ &\quad + (bh + df + ce - ag)\, j \\ &\quad + (ch + dg + af - be)\, k \\ &\quad + (dh - ae - bf - cg) \end{aligned}$$

or in "Four-vector" matrix form:

$$w \stackrel{\Delta}{=} \begin{vmatrix} e' \\ f' \\ g' \\ h' \end{vmatrix} = \begin{bmatrix} d & -c & b & a \\ c & d & -a & b \\ -b & a & d & c \\ -a & -b & -c & d \end{bmatrix} \begin{vmatrix} e \\ f \\ g \\ h \end{vmatrix}$$

We also define the "complex conjugate" of the general quaternion u in equation (8) as:

$$u^* \stackrel{\Delta}{=} -ai - bj - ck + d$$

We now define a quaternion operator h(m) for the body angle change $\underline{\phi}$ over computer cycle m as:

$$h(m) \;=\; \begin{vmatrix} \left(\phi_x/\phi\right) \sin\left(\phi/2\right) \\ \left(\phi_y/\phi\right) \sin\left(\phi/2\right) \\ \left(\phi_z/\phi\right) \sin\left(\phi/2\right) \\ \cos\left(\phi/2\right) \end{vmatrix} \tag{9}$$

where the elements in the above column matrix refer to the i, j, k, and scalar components of h. We also define a general vector $\underline{v}$ with components $v_x$, $v_y$, $v_z$, and a corresponding quaternion v having the same vector components with a zero scalar component:

$$v \;=\; \begin{vmatrix} v_x \\ v_y \\ v_z \\ 0 \end{vmatrix}$$

Using the above definitions and the general rules for quaternion algebra, it is readily demonstrated by substitution and trigonometric manipulation that:

$$v' \overset{\Delta}{=} h(m)\, v\, h(m)^* \;=\; A'(m)\, v \tag{10}$$

where

$$A'(m) \overset{\Delta}{=} \begin{bmatrix} A(m) & 0 \\ 0 & 0 \end{bmatrix} \qquad v' \overset{\Delta}{=} \begin{vmatrix} v_x' \\ v_y' \\ v_z' \\ 0 \end{vmatrix} \qquad A(m) \;=\; \text{As defined in (3)}$$

Equation (10), therefore, is the quaternion form of the vector transformation equation that transforms a vector from body coordinates at computer cycle (m+1) to body coordinates at computer cycle m:

$$\underline{v}' \;=\; A(m)\; \underline{v} \tag{11}$$

where

$\underline{v}'$, $\underline{v}$ = “Three-vector” form of v' and v (i.e., with components $v_x'$, $v_y'$, $v_z'$ and $v_x$, $v_y$, $v_z$).

$\underline{v}$ = The general vector $\underline{v}$ in body coordinates at computer cycle (m+1).

$\underline{v}'$ = The general vector $\underline{v}$ in body coordinates at computer cycle m.

### 3.2.2 Quaternion Updating Algorithm For Body Motion

Equation (10) with its equation (11) dual can be used to define analogous vector transformation operations between body coordinates and navigation coordinates at computer cycle m as:

$$
\begin{aligned}
v'' &= q(m)\, v'\, q(m)^* \\
\underline{v}'' &= C(m)\ \underline{v}'
\end{aligned}
\tag{12}
$$

where

q(m) = Quaternion relating body axes to navigation axes at computer cycle m.

$\underline{v}'$ = The vector $\underline{v}$ in navigation coordinates.

$\underline{v}''$ = The vector $\underline{v}$ in body coordinates at computer cycle m.

$v', v''$ = Quaternion ("Four vector") form of $\underline{v}'$, $\underline{v}''$.

The q quaternion has four elements (i.e., a, b, c, d) that are updated for body motion $\underline{\phi}$ at each computer cycle m. The updating equation is easily derived by substituting equation (10) into (12):

$$\underline{v}'' = q(m)\, h(m)\, v\, h(m)^*\, q(m)^*$$

Using the definition for the quaternion complex conjugate, it is readily demonstrated that:

$$h(m)^*\, q(m)^* = \big(q(m)\, h(m)\big)^*$$

Thus,

$$\underline{v}'' = q(m)\, h(m)\, v\, \big(q(m)\, h(m)\big)^*$$

But we can also write the direct expression:

$$\underline{v}'' = q(m+1)\, v\, q(m+1)^*$$

Therefore, by direct comparison of the latter two equations:

$$q(m+1) = q(m)\, h(m) \tag{13}$$

Equation (13) is the quaternion equivalent to direction cosine updating equation (2). For computational purposes, h(m) as defined in equations (9) is equivalently:

$$h(m) = \begin{vmatrix} f_3\ \phi_x \\ f_3\ \phi_y \\ f_3\ \phi_z \\ f_4 \end{vmatrix}$$

$$f_3 = \frac{\sin\left(\phi/2\right)}{\phi} = 0.5\left(1 - \left(0.5\phi\right)^2/3! + \left(0.5\phi\right)^4/5! - \cdots\right)$$

$$f_4 = \cos\left(\phi/2\right) = 1 - \left(0.5\phi\right)^2/2! + \left(0.5\phi\right)^4/4! - \cdots) \tag{14}$$

$$\left(0.5\phi\right)^2 = 0.25\left(\phi_x 2 + \phi_y 2 + \phi_x 2\right)$$

The "order" of the equation (13) and (14) updating algorithm depends on the order of $\phi$ terms carried in h which depends on the truncation point used in $f_3$ and $f_4$. The rationale for selecting the algorithm order and associated algorithm iteration rate is directly analogous to selection of the direction cosine updating algorithm order (discussed previously).

### 3.2.3 Quaternion Updating Algorithm For Navigation Frame Rotation

Equation (13) with (14) is used to update the quaternion for body frame motion sensed by gyros. In order to update the quaternion for rotation of the navigation coordinate frame, an algorithm analogous to equation (5) (for the direction cosine matrix) is used with a navigation frame rotation quaternion r:

$$q(n+1) = r(n)\ q(n)$$

$$r(n) = \begin{vmatrix} -0.5\ \theta_x \\ -0.5\ \theta_y \\ -0.5\ \theta_z \\ 1-0.5\left(\theta/2\right)^2 \end{vmatrix} \tag{15}$$

$$\left(\theta/2\right)^2 = 0.25\left(\theta_x 2 + \theta_y 2 + \theta_x 2\right)$$

where

$\theta_x, \theta_y, \theta_z$ = Components of $\underline{\theta}$ as defined previously for equations (6) and (7).

The development of equation (15) parallels the development of (13). The equation for r(n) is a truncated form of the theoretical exact analytical expression (analogous to the second order truncated form of equation (14)). The $\theta^2$ term in equation (15) generally is not required for accuracy (due to the smallness of $\underline{\theta}$ in typical applications).

As for the direction cosine updating algorithm for navigation frame motion, the equivalent quaternion updating algorithm (equation (15)) updating cycle n need not be processed as fast as the body rate cycle m to maintain equivalent accuracy. This is due to the considerably smaller navigation frame rotation rates compared to body rotation rates.

### 3.2.4 Equivalencies Between Direction Cosine And Quaternion Elements

The analytical equivalency between the elements of the direction cosine matrix and the attitude quaternion can be derived by direct expansion of equations (12). If we define the elements of q as:

$$q = \begin{vmatrix} a \\ b \\ c \\ d \end{vmatrix}$$

equation (12) becomes after expansion, factorization of v', and neglecting the scalar part of the v'' and v' quaternion vectors (i.e., carrying only the vector components of $\underline{v}''$ and $\underline{v}'$):

$$\underline{v}'' = \begin{bmatrix} \left(d^2 + a^2 - b^2 - c^2\right) & 2\,(ab - cd) & 2\,(ac + bd) \\ 2\,(ab + cd) & \left(d^2 + b^2 - c^2 - a^2\right) & 2\,(bc - ad) \\ 2\,(ac - bd) & 2\,(bc + ad) & \left(d^2 + c^2 - a^2 - b^2\right) \end{bmatrix} \underline{v}' \qquad (16)$$

Defining C in equation (12) as:

$$C = \begin{bmatrix} C_{11} & C_{12} & C_{13} \\ C_{21} & C_{22} & C_{23} \\ C_{31} & C_{32} & C_{33} \end{bmatrix}$$

equation (16) when compared with (12) shows that:

$$C_{11} = d^2 + a^2 - b^2 - c^2$$

$$C_{12} = 2\,(ab - cd)$$

$$C_{13} = 2\,(ac + bd)$$

$$C_{21} = 2\,(ab + cd)$$

$$C_{22} = d^2 + b^2 - c^2 - a^2$$

$$C_{23} = 2\,(bc - ad)$$

$$C_{31} = 2\,(ac - bd) \qquad (17)$$

$$C_{32} = 2\,(bc + ad)$$

$$C_{33} = d^2 + c^2 - a^2 - b^2$$

The converse of equation (17) is somewhat more complicated. Using the property (from equation (1)) that:

$$a^2 + b^2 + c^2 + d^2 = 1$$

the converse of equation (17) can be shown (11) to be computable from the following sequence of operations:

$$T_r = C_{11} + C_{22} + C_{33}$$

$$P_1 = 1 + 2C_{11} - T_r$$

$$P_2 = 1 + 2C_{22} - T_r$$

$$P_3 = 1 + 2C_{33} - T_r$$

$$P_o = 1 + T_r$$

If $P_1 = \max(P_1, P_2, P_3, P_o)$, then:

$$a = 0.5\, P_1^{1/2}\, \mathrm{sign}\left(a_{previous}\right)$$

$$b = \left(C_{21} + C_{12}\right)/4a$$

$$c = \left(C_{13} + C_{31}\right)/4a \qquad (18)$$

$$d = \left(C_{32} - C_{23}\right)/4a$$

(Continued)

If $P_2 = \max(P_1, P_2, P_3, P_o)$, then:

$$
\begin{aligned}
b &= 0.5\, P_2^{1/2}\, \mathrm{sign}\left(b_{previous}\right) \\
c &= \left(C_{32} + C_{23}\right)/4b \\
d &= \left(C_{13} - C_{31}\right)/4b \\
a &= \left(C_{21} + C_{12}\right)/4b
\end{aligned}
$$

If $P_3 = \max(P_1, P_2, P_3, P_o)$, then:

$$
\begin{aligned}
c &= 0.5\, P_3^{1/2}\, \mathrm{sign}\left(c_{previous}\right) \\
d &= \left(C_{21} - C_{12}\right)/4c \\
a &= \left(C_{13} + C_{31}\right)/4c \\
b &= \left(C_{32} + C_{23}\right)/4c
\end{aligned}
\qquad \begin{matrix}(18)\\ \text{(Concluded)}\end{matrix}
$$

If $P_o = \max(P_1, P_2, P_3, P_o)$, then:

$$
\begin{aligned}
d &= 0.5\, P_o^{1/2}\, \mathrm{sign}\left(d_{previous}\right) \\
a &= \left(C_{32} - C_{23}\right)/4d \\
b &= \left(C_{13} - C_{31}\right)/4d \\
c &= \left(C_{21} - C_{12}\right)/4d
\end{aligned}
$$

## 3.3 The Computation of $\underline{\phi}$

### 3.3.1 Continuous Form

The $\underline{\phi}$ "body attitude change" vector is calculated by processing data from the strapdown gyros. Under situations where the angular rotation rate vector (sensed by the gyros) lies along a fixed direction (i.e., is nonrotating in inertial space), the $\underline{\phi}$ vector is equal to the simple integral of the angular rate vector over the time interval from computer cycle m to computer cycle (m+1):

$$\underline{\phi} = \int_{t_m}^{t_{m+1}} \underline{\omega}\, dt \qquad \text{for cases when } \underline{\omega} \text{ is nonrotating.} \tag{19}$$

where

$\underline{\omega}$ = Angular rate vector sensed by the strapdown gyros.

Under general motion conditions (when $\underline{\omega}$ may be rotating), equation (19) has the more complex form (as derived in (10) or alternatively, in Appendix A):

$$\underline{\alpha}\,(t) = \int_{t_m}^{t} \left( \underline{\omega} + 1/2\ \underline{\alpha} \times \underline{\omega} + \frac{1}{\alpha^2} \left( 1 - \frac{\alpha \sin\alpha}{2\ (1\text{-}\cos\alpha)} \right) \underline{\alpha} \times \left( \underline{\alpha} \times \underline{\omega} \right) \right) dt$$

$$\underline{\phi} = \underline{\alpha} \left( t = t_{m+1} \right) \tag{20}$$

It can verified by power series expansion that to first order,

$$\left( 1/\alpha^2 \right) \left( 1 - \frac{\alpha \sin\alpha}{2\ (1\text{-}\cos\alpha)} \right) \approx \frac{1}{12}$$

Hence, $\underline{\alpha}\,(t)$ in equation (20), to third order accuracy in $\alpha$ can be approximated by:

$$\underline{\alpha}\,(t) \approx \int_{t_m}^{t} \left( \underline{\omega} + 1/2\ \underline{\alpha} \times \underline{\omega} + \frac{1}{12}\ \underline{\alpha} \times \left( \underline{\alpha} \times \underline{\omega} \right) \right) dt \tag{21}$$

A second order expression for $\underline{\alpha}\,(t)$ can be obtained from (21) by dropping the 1/12 term. An even simpler expression for $\underline{\alpha}\,(t)$ is obtained by dropping the 1/12 term and approximating the $\underline{\alpha}$ term in the integral by the direct integral of $\underline{w}$:

$$\underline{\beta}\,(t) = \int_{t_m}^{t} \underline{\omega}\, dt$$

$$\delta\,\underline{\beta}\,(t) = 1/2 \int_{t_m}^{t} \underline{\beta} \times \underline{\omega}\, dt \tag{22}$$

$$\underline{\phi} = \underline{\beta} \left( t{=}t_{m+1} \right) + \underline{\delta\beta} \left( t{=}t_{m+1} \right)$$

An interesting characteristic about equation (22) is that its accuracy is in fact comparable to that of third order equation (21). In other words, the simplifying assumption of replacing $\alpha$ with $\beta$ in the 1/2 $\underline{\alpha} \times \underline{\omega}$ term is in fact equivalent to introducing an error in equation (21) that to third order, equals the $\frac{1}{12}\ \underline{\alpha} \times \left( \underline{\alpha} \times \underline{\omega} \right)$ term.

This property can be verified by simulation as well as analytical expansion under hypothesized angular motion conditions.

Equation (22) is the equation that is mechanized in software in most modern-day strapdown inertial navigation systems to calculate $\underline{\phi}$. It can be demonstrated analytically and by simulation that for representative vehicle angular motion and vibration, equation (22) faithfully calculates $\underline{\phi}$ to accuracy levels that are compatible with high performance strapdown inertial navigation system requirements.

For situations where $\underline{\omega}$ is nonrotating, the $\underline{\delta\beta}$ term in (22) is zero and $\underline{\phi}$ equals the simple time integral or $\underline{\omega}$ over the computer interval m (i.e., the equation (19) approximation). For situations where $\underline{\omega}$ is rotating (a situation defined analytically as "coning"), the $\underline{\delta\beta}$ term is nonzero and must be calculated and used as a correction to the $\underline{\omega}$ integral to properly calculate $\underline{\phi}$.

It is important to note that the accuracy by which equation (22) approximates (20) is dependent on $\underline{\phi}$ being small (e.g., less than 0.1 radian). In order to protect the accuracy of this approximation, the computer iteration rate must be high enough that $\underline{\phi}$ remains small under maximum vehicle rotation rate conditions.

### 3.3.2 Recursive Algorithm Form

The implementation of equation (22) in a digital computer implies that a higher speed integration summing operation be performed during each body motion attitude update cycle. A computational algorithm for the integration function can be derived by first rewriting equation (22) in the equivalent incremental updating form:

$$\underline{\beta}\,(t) = \underline{\beta}\,(l) + \int_{t_l}^{t} \underline{\omega}\, dt$$

$$\underline{\delta\beta}\,(l+1) = \underline{\delta\beta}\,(l) + 1/2 \int_{t_l}^{t_{l+1}} \underline{\beta}(t) \times \underline{\omega}\, dt \qquad (23)$$

$$\underline{\beta}\,(l+1) = \underline{\beta}\left(t=t_{l+1}\right)$$

$$\underline{\phi} = \underline{\beta}\left(t=t_{m+1}\right) + \underline{\delta\beta}\left(t=t_{m+1}\right)$$

with initial conditions:

$$\underline{\beta}\left(t=t_m\right) = 0$$

$$\underline{\delta\beta}\left(t=t_m\right) = 0 \tag{24}$$

where

$l$ = High speed computer cycle within the m body rate update cycle.

The integrals in (23) can be replaced by analytical forms that are compatible with gyro input data processing if $\underline{\omega}$ is replaced by a generalized time series expansion. For equations (23), it is sufficient to approximate $\underline{\omega}$ over the $l$ to $l$+1 time interval as a constant plus a linear ramp:

$$\underline{\omega} \approx \underline{A} + \underline{B}\left(t - t_l\right) \tag{25}$$

where

$\underline{A}, \underline{B}$ = Constant vectors.

Substituting (25) in (23), and recognizing with the equation (25) approximation that:

$$\underline{A}\left(t_{l+1} - t_l\right) = 1/2\left(\underline{\Delta\theta}(l) + \underline{\Delta\theta}(l\text{-}1)\right)$$

$$1/2\,\underline{B}\left(t_{l+1} - t_l\right)^2 = 1/2\left(\underline{\Delta\theta}\,(l) - \underline{\Delta\theta}(l\text{-}1)\right)$$

where by definition:

$$\underline{\Delta\theta}(l) \overset{\Delta}{=} \int_{t_l}^{t_{l+1}} \underline{\omega}\, dt$$

yields the desired final form for the $\underline{\phi}$ updating algorithm:

$$\underline{\delta\beta}(l+1) = \underline{\delta\beta}(l) + 1/2\left(\underline{\beta}\,(l) + 1/6\,\underline{\Delta\theta}(l\text{-}1)\right) \times \underline{\Delta\theta}(l)$$

$$\underline{\Delta\theta}(l) = \int_{t_l}^{t_{l+1}} \underline{\omega}\, dt = \sum_{t_l}^{t_{l+1}} \underline{d\theta}$$

$$\underline{\beta}(l+1) = \underline{\beta}(l) + \underline{\Delta\theta}(l) \tag{26}$$

$$\underline{\phi} = \underline{\beta}\left(t=t_{m+1}\right) + \underline{\delta\beta}\left(t=t_{m+1}\right)$$

with initial conditions:

$$\underline{\beta}\left(t=t_m\right) \overset{\Delta}{=} \underline{\beta}\,(l=0) \;=\; 0$$

$$\underline{\delta\beta}\left(t=t_m\right) \overset{\Delta}{=} \underline{\delta\beta}\,(l=0) \;=\; 0$$

where

$\underline{d\theta}$ = Gyro output pulse vector. Each component (x, y, z) represents the occurrence of a rotation through a specified fixed angle increment about the gyro input axis.

$\underline{\Delta\theta}$ = Gyro output pulse vector count from $l$ to $l$+1.

The computational algorithm described by equation (26) is used on a recursive basis to calculate $\underline{\phi}$ once each m cycle. After $\underline{\phi}$ is calculated, the $\underline{\beta}$ and $\underline{\delta\beta}$ functions are reset for the next m cycle $\underline{\phi}$ calculation. The iteration rate for $l$ within m is maintained at a high enough rate to properly account for anticipated dynamic $\underline{\omega}$ motion effects. Section 6. describes analytical techniques that can be used to assess the adequacy of the iteration rate under dynamic angular rate conditions.

## 3.4 The Computation of θ

The $\underline{\theta}$ vector in equations (6) and (15) is computed as a simple integral of navigation frame angular rate over the n cycle iteration period:

$$\underline{\theta} \;=\; \int_{t_n}^{t_{n+1}} \underline{\Omega}\, dt \tag{27}$$

where

$\underline{\Omega}$ = Navigation frame rotation rate as calculated in the navigation software section (12).

Standard recursive integration algorithms can be used to calculate $\underline{\theta}$ in equation (27) (e.g., trapezoidal) over the time interval from n to n+1. The update rate for the integration algorithm is selected to be compatible with software accuracy requirements in the anticipated dynamic maneuver environment for the user vehicle.

## 3.5 Orthogonality And Normalization Algorithms

Most strapdown attitude computation techniques periodically employ self-consistency correction algorithms as an outer-loop function for accuracy enhancement. If the basic attitude data is computed in the form of a direction cosine matrix, the self-consistency check is that the rows should be orthogonal to each other and equal to unity in magnitude. This condition is based on the fact that the rows of the direction cosine matrix represent unit vectors along orthogonal navigation coordinate frame axes as projected in body axes. For the quaternion, the self-consistency check is that the sum of the squares of the quaternion elements be unity (this can be verified by operation on equation (1)).

### 3.5.1 Direction Cosine Orthogonalization And Normalization

The test for orthogonality between two direction cosine rows is that the dot product be zero. The error condition, then is:

$$E_{ij} = C_i C_j^T \tag{28}$$

where

$C_i =$ $i^{th}$ row of C

$C_j =$ $j^{th}$ row of C

$T =$ Transpose

A calculated orthogonality error $E_{ij}$ can be corrected by rotating $C_i$ and $C_j$ relative to each other about an axis perpendicular to both by the error angle $E_{ij}$. Since it is not known whether $C_i$ or $C_j$ is in error, it is assumed that each are equally likely to be generating the error, and each is rotated by half of $E_{ij}$ to correct the error. Hence, the orthogonality correction algorithm is:

$$\begin{aligned} C_i(n+1) &= C_i(n) - 1/2\ E_{ij}\ C_j(n) \\ C_j(n+1) &= C_j(n) - 1/2\ E_{ij}\ C_i(n) \end{aligned} \tag{29}$$

It is easily verified using (29) that an orthogonality error $E_{ij}$ originally present in $C_i$ (n) and $C_j$ (n) is no longer present in $C_i$ (n+1) and $C_j$ (n+1) after application of equation (29).

The unity condition of $C_i$ (i.e., normality) can be tested by comparing the magnitude squared of $C_i$ with unity:

$$E_{ii} = C_i C_i^T - 1 \tag{30}$$

A measured normality error $E_{ii}$ can be corrected with:

$$C_i(n+1) = C_i(n) - 1/2\ E_{ii}\ C_i(n) \tag{31}$$

Equations (28) through (31) can be used to measure and correct orthogonality and normalization errors in the direction cosine matrix. In combined matrix form, the overall measurement/correction operation is sometimes written as:

$$C_{n+1} = C_{n+1/2} \left( I - C_n C_n^T \right) C_n \tag{32}$$

3.5.1.1 Rows or Columns - The previous discussion addressed the problem of orthogonalizing and nomalizing the rows of a direction cosine matrix C. In combined form, equation (32) shows that the correction is:

$$\delta C = 1/2 \left( I - CC^T \right) C \tag{33}$$

Equation (33) can be operated upon by premultiplication with C postmultiplication by $C^T$, and combining terms. The result is:

$$\delta C = 1/2\, C \left( I - C^T C \right) \tag{34}$$

The $\left( I - C^T C \right)$ term in (34) is the error matrix based on testing orthogonality and normality of the columns of C. Thus, if the rows of C are orthonormalized (i.e., dC is nulled), the columns of C will also be implicitly orthonormalized. The inverse applies if the columns are directly orthonormalized with (34). The question that remains is, which is preferred? The answer is related to the real time computing problem associated with the calculation and correction of orthogonalization and normalization errors.

Ideally, the orthogonalization and normalization operations are performed as an outer loop function in a strapdown navigation computer so as not to impact computer throughput requirements. A computational organization that facilities such an approach divides the orthonormalization operations into submodules that are executed on successive passes in the outer-loop software path. A logical division of the orthonormalization operations into submodules is as defined by equations (28), (29), (30), and (31).

This implies that measurement and correction of orthogonalization and normalization effects are performed at different times in the computing cycle. Such an approach is only valid if the orthogonality and normalizations errors (i.e., $E_{ij}$ and $E_{ii}$) remain reasonably stable as a function of time.

To assess the time stability of the orthogonality/normalization error is to investigate the rate of change of the bracketed terms in equations (33) and (34). For convenience, these will be defined as:

$$\begin{aligned} E_R &\stackrel{\Delta}{=} \left( I - CC^T \right) \\ E_C &\stackrel{\Delta}{=} \left( I - C^T C \right) \end{aligned} \tag{35}$$

The time derivative of (35) is:

$$\dot{E}_R = \dot{C}C^T - C\dot{C}^T$$
$$\dot{E}_C = \dot{C}^T C - C^T\dot{C} \tag{36}$$

Expressions for $\dot{C}$ and $\dot{C}^T$ can be developed by returning to equations (2), (3), (5), and (6). These equations can be rearranged to show that over a given time interval, the change in C is given by:

$$\Delta C = C\,(A - I) + (B - I)\,C$$

which with (3) and (4) becomes to first order:

$$\Delta C = C\,(\underline{\phi}\times) - (\underline{\theta}\times)\,C \tag{37}$$

Dividing by the time interval for the change in C, recognizing that $\underline{\phi}$ and $\underline{\theta}$ are approximately integrals of $\underline{\omega}$ and $\underline{\Omega}$ over the time interval, and letting the time interval go to zero in the limit, yields the classical equation for the rate of change of C:

$$\dot{C} = C\,(\underline{\omega}\times) - (\underline{\Omega}\times)\,C \tag{38}$$

where

$(\underline{\omega}\times), (\underline{\Omega}\times)$ = Skew symmetric matrix form of vectors $\underline{\omega}$, $\underline{\Omega}$.

The transpose of (38) is:

$$\dot{C}^T = (\underline{\omega}\times)\,C^T + C^T\,(\underline{\Omega}\times) \tag{39}$$

We now substitute (38) and (39) into (36). After combining terms and applying equations (35), the final result is:

$$\dot{E}_R = E_R\,(\underline{\Omega}\times) - (\underline{\Omega}\times)\,E_R$$
$$\dot{E}_C = E_C\,(\underline{\omega}\times) - (\underline{\omega}\times)\,E_C \tag{40}$$

Equations (40) show that the rate of change of $E_R$ is proportional to $E_R$ and the navigation frame rotation rate $\underline{\Omega}$, whereas the rate of change of $E_C$ is proportional to $E_C$ and the body rotation rate $\underline{\omega}$. Since $\underline{\omega}$ is generally much larger than $\underline{\Omega}$, $\dot{E}_C$ is generally larger than $\dot{E}_R$. It can be concluded that $E_R$ is more stable over time, hence, orthornormalizing the direction cosine matrix rows (based on the $E_R$ measurement) is the preferred computational approach if the real time computing problem is taken into account.

### 3.5.2 Quaternion Normalization

The quaternion is normalized by measuring its magnitude squared compared by unity, and adjusting each element proportionally to correct the normalization error. The normalization error is given by:

$$E_q = q\, q^* - 1 \tag{41}$$

It is easily verified using the rules for quaternion algebraic that $E_q$ equals the sum of the squares of the elements of q minus 1. The correction algorithm is given by:

$$q_{(n+1)} = q_{(n)} - 1/2\, E_q\, q_{(n)} \tag{42}$$

## 3.6 Direction Cosine Versus The Quaternion For Body Attitude Referencing

The tradeoff between direction cosine versus quaternion parameters as the primary attitude reference data in strapdown inertial systems has been a popular area of debate between strapdown analysts over the past three decades. In its original form, the tradeoff centered on the relative accuracy between the two methods in accounting for body angular motion. These tradeoffs invariably evolved from the differential equation form of the direction cosine and quaternion updating equations and investigated the accuracy of equivalent algorithms for integrating these equations in a digital computer under hypothesized body angular motion. Invariably, the body motion investigated was coning motion at various frequencies relative to the computer update frequency. For these early studies, the tradeoffs generally demonstrated that for comparable integration algorithms, the quaternion approach generated solutions that more accurately replicated the true coning motion for situations where the coning frequency was within a decade of the computer update frequency.

As presented in this paper, both the quaternion and direction cosine updating algorithms have been based on processing of a body angle motion vector $\underline{\phi}$ which accounts for all dynamic motion effects including coning. These updating algorithms (equation (2) and (3) for direction cosines and (13) and (14) for the quaternion) represent exact solutions for the attitude updating process for a given input angle vector $\underline{\phi}$. Consequently, the question of accuracy for different body motion can no longer be considered a viable tradeoff area. The principle tradeoffs that remain between the two approaches are the computer memory and throughput requirements associated with each in a strapdown navigation system.

In order to assess the relative computer memory and throughput requirements for quaternion parameters versus direction cosines, the composite of all computer requirements for each must be assessed. In general, these can be grouped into three major computational areas:

1. Basic updating algorithm

2. Normalization and orthogonalization algorithms

3. Algorithms for conversion to the direction cosine matrix form needed for acceleration transformation and Euler angle extraction

Basic Updating Algorithms - The basic updating algorithm for the quaternion parameters is somewhat simpler than for direction cosines as expansion of equations (2) and (3) compared with (13) and (14) would reveal. This results in both a throughput and memory advantage for the quaternion approach. Part of this advantage arises because only four quaternion elements have to be updated compared to nine for direction cosines. The advantage is somewhat diminished if it is recognized that only two rows of direction cosines (i.e., 6 elements) need actually be updated since the third row can then be easily derived from the other two by a cross-product operation (i.e., the third row represents a unit vector along the z-axis of the navigation frame as projected in body axes. The first two rows represent unit vectors along x and y navigation frame axes. The cross-product of unit vectors along x and y navigation axes equals the unit vector along the z-navigation axis).

Normalization And Orthogonalization Algorithms - The normalization and orthogonalization operations associated with direction cosines are given by equation (28) through (31). The quaternion normalization equation is given by equations (41) and (42).

The normalization equation for the quaternion is generally simpler to implement than the orthogonalization and normalization equations for the direction cosines. If only two rows of the direction cosine matrix are updated (as described in the previous paragraph) the direction cosine orthogonalization and normalization operations required are half that dictated by (28) through (31), but are still more than required by (41) and (42) for the quaternion. Since the orthonormalization operations would in general be iterated at low rate, no throughput advantage results for the quaternion. Some memory savings may be realized, however.

A key factor that must be addressed relative to orthonormalization tradeoffs is whether or not orthonormalization is actually needed at all. Clearly, if the direction cosine or quaternion updating algorithms were implemented perfectly, orthonormalization would not be required. It is the author’s contention that, in fact, the accuracy requirements for strapdown systems dictate that strapdown attitude updating software cannot tolerate any errors whatsoever (compared to sensor error effects). Therefore, if the attitude updating software is designed for negligible drift and scale factor error (compared to sensor errors) it will also implicitly exhibit negligible orthogonalization and/or normalization errors.

The above argument is valid if the effect of orthonormalization errors in strapdown attitude data is no more detrimental to system performance than other software attitude error effects. This is in fact the case, as detailed error analyses would reveal. Since modern-day general purpose computers used in today’s strapdown inertial navigation systems have the capability to implement attitude updating algorithms essentially perfectly within a reasonable throughput and memory requirement, it is the author's opinion that orthonormalization error correction should not be needed, hence, is not a viable tradeoff area relative to the use of quaternion parameters versus direction cosines.

Algorithms For Conversion To The Direction Cosine Matrix - If the basic calculated attitude data is direction cosines directly, no conversion process is required. For cases where only two rows of direction cosines are updated, the third row must be generated by the cross-product between the two rows calculated. For example:

$$\begin{aligned} C_{31} &= C_{12}\,C_{23} - C_{13}\,C_{22} \\ C_{32} &= C_{13}\,C_{21} - C_{11}\,C_{23} \\ C_{33} &= C_{11}\,C_{22} - C_{12}\,C_{21} \end{aligned} \tag{43}$$

For quaternion parameters, equation (17) must be implemented to develop the direction cosine matrix, a significantly more complex operation compared with (43) for the two row direction cosine approach. Since direction cosine elements are generally required at high rate (for acceleration transformation and Euler angle output extraction) both a throughput and memory penalty is accrued for the quaternion approach. The penalty is compounded if the calculated direction cosine outputs are required to greater than single precision accuracy (including computational round-off error). For noise-free acceleration transformation operations (such as may be needed to effect an accurate system calibration) double-precision accuracy is needed. The result is that equation (17) for the quaternion versus (43) for direction cosines would have to be implemented in double-precision imposing a significant penalty for the more complex quaternion conversion process.

Tradeoff Conclusions - From the above qualitative discussion, it is difficult to draw hard conclusions regarding a preference for direction cosines versus quaternion parameters for attitude referencing in strapdown inertial systems. Pros and cons exist for each in the different tradeoff areas. Quantitative comparisons based on actual software sizing and computer loading studies have led to similar inconclusive results. Fortunately, today's computer technology is such that the slight advantage one attitude parameter approach may have over the other in any particular application is insignificant compared with composite total strapdown inertial system throughput and memory software requirements. Hence, ultimate selection of the attitude approach can be safely made based on "analyst's choice".

## 4. STRAPDOWN ACCELERATION TRANSFORMATION ALGORITHMS

The acceleration vector measurement from the accelerometers in a strapdown inertial system is transformed from body to navigation axes through a mechanization of the classical vector transformation equation:

$$\underline{a}^N = C\,\underline{a} \tag{44}$$

where

$\underline{a}$ = Specific force acceleration measured in body axes by the strapdown accelerometers.

$\underline{a}^N$ = Specific force acceleration with components evaluated along navigation axes.

The implementation of equation (44) is accomplished on a repetitive basis as a recursive algorithm in a digital computer such that its integral properties are preserved at the computer cycle times. In this manner, the velocity which is formed from the integral of (44) will be accurate under dynamic conditions in which $\underline{a}^N$ may have erratic high frequency components. The recursive algorithm for (44) must account for the effects of body rotation (and secondarily, rotation of the navigation coordinate frame) as well as variations in $\underline{a}$ over the computer iteration period.

## 4.1 Acceleration Transformation Algorithm That Accounts For Body Rotation Effects

To develop an algorithm for equation (44) that preserves its integral properties, we begin with its integral over a computer cycle:

$$\underline{u}^N = \int_{t_m}^{t_{m+1}} C\, \underline{a}\, dt \tag{45}$$

where

$\underline{u}^N$ = Change in integral of equation (44) (or specific force velocity change) over a computer cycle m

The velocity vector in the navigation computer is generated by summing the $\underline{u}^N$'s corrected for Coriolis and gravity effects.

The C matrix in (45) is a continuous function of time in the interval from $t_m$ to $t_{m+1}$. An equivalent form for C in terms of its value at the computer update time (m) is:

$$C = C(m)\, A(t) \tag{46}$$

where

$C(m)$ = Value of C at $t_m$

$A(t)$ = Direction cosine matrix that transform vectors from body axes at time t to the body attitude at the start time for the computation interval $t_m$.

Equation (46) with the definition of A(t) above accounts for the effect of gyro sensed body motion over the computer interval. The next section will discuss the correction used to account for the small rotation of the navigation frame over the computer interval.

Substituting (46) in (45) and expanding:

$$\underline{u}^N = C(m) \int_{t_m}^{t_{m+1}} A(t)\, \underline{a}\, dt$$

We now use a first order approximation for A(t) as given in equation (3), with $\underline{\phi}$ treated as a function of time in the interval as defined to first order in equation (22):

$$\underline{\phi}(t) \approx \underline{\beta}(t) = \int_{t_m}^{t} \underline{\omega}\, dt$$

Thus,

$$A(t) \approx I + \left(\underline{\beta}(t) \times\right) \tag{47}$$

and

$$\underline{u}^N \approx C(m) \int_{t_m}^{t_{m+1}} \left(I + \left(\underline{\beta}(t) \times\right)\right) \underline{a}\, dt$$

$$= C(m) \int_{t_m}^{t_{m+1}} \underline{a}\, dt + \int_{t_m}^{t_{m+1}} \left(\underline{\beta}(t) \times \underline{a}\right) dt$$

We now define

$$\underline{u} \stackrel{\Delta}{=} \int_{t_m}^{t_{m+1}} \underline{a}\, dt$$

Hence,

$$\underline{u}^N = C(m) \left(\underline{u} + \int_{t_m}^{t_{m+1}} \left(\underline{\beta}(t) \times \underline{a}\right) dt\right) \tag{48}$$

with

$$\underline{\beta}(t) = \int_{t_m}^{t} \underline{\omega}\, dt$$

$$\underline{u} = \int_{t_m}^{t_{m+1}} \underline{a}\, dt$$

An alternative form of (48) can also be derived through direct application of the integration by parts rule to the integral term in the equation (48) $\underline{u}^N$ expression:

$$\underline{u}^N = C(m) \left( \underline{u} + 1/2\, \underline{\beta} \times \underline{u} + 1/2 \int_{t_m}^{t} \left( \underline{\beta}(t) \times \underline{a} + \underline{u}(t) \times \underline{\omega} \right) dt \right) \tag{49}$$

with

$$\underline{\beta}(t) = \int_{t_m}^{t} \underline{\omega}\, dt \qquad \underline{\beta} = \underline{\beta}\left(t{=}t_{m+1}\right)$$

$$\underline{u}(t) = \int_{t_m}^{t} \underline{a}\, dt \qquad \underline{u} = \underline{u}\left(t{=}t_{m+1}\right)$$

Equations (48) and (49) are algorithmic forms of equation (44) that can be used to calculated $\underline{u}^N$ in the strapdown computer exactly (within the approximation of equation (47)). These equations show that the specific force velocity change in navigation coordinates is approximately equal to the integrated output from the strapdown accelerometer ($\underline{u}$) over the computer cycle, times the direction cosine matrix which was valid at the previous computer update time. Correction terms are applied to account for body rotation. In general, the correction term involves an integral of the interactive effects of angular $\underline{\omega}$ and linear $\underline{a}$ motion over the update cycle. The integral terms have been coined “sculling” effects.

The equation (49) form of the $\underline{u}^N$ equation includes a 1/2 $\underline{\beta} \times \underline{u}$ term which can be evaluated at $t_{m+1}$ as the simple cross-product of integrated gyro and accelerometer measurements (i.e., without a dynamic integral operation). Furthermore, it is easily demonstrated that for approximately constant angular rates and accelerations over the computer cycle, the integral term in (49) is identically zero. This forms the basis for an approximate form of (49) which is valid under benign flight conditions (i.e., using equation (49) without including the integral term ). The 1/2 $\underline{\beta} \times \underline{u}$ term in (49) is sometimes denoted as “rotation compensation.”

### 4.1.1 Incremental Form of Transformation Operations and Sculling Terms

In a severe dynamic environment, equations (48) or (49) would be implemented explicitly with the integral terms mechanized as a high speed digital algorithmic operation within the $t_m$ to $t_{m+1}$ update cycle. The integral terms we are dealing with are from (48) and (49):

$$
\begin{aligned}
\underline{S}_1 &\overset{\Delta}{=} \int_{t_m}^{t_{m+1}} \left(\underline{\beta}(t) \times \underline{a}\right) dt \\
\underline{S}_2 &\overset{\Delta}{=} 1/2 \int_{t_m}^{t_{m+1}} \left(\underline{\beta}(t) \times \underline{a} + \underline{u}(t) \times \underline{\omega}\right) dt
\end{aligned}
\tag{50}
$$

With the equation (50) definitions, (48) and (49) become:

$$\underline{u}^N = C(m) \left(\underline{u} + \underline{S}_1\right) \tag{51}$$

or

$$\underline{u}^N = C(m) \left(\underline{u} + 1/2\, \underline{\beta} \times \underline{u} + \underline{S}_1\right) \tag{52}$$

Recursive algorithms for $\underline{S}_1$ or $\underline{S}_2$ can be derived by first rewriting (50) in the equivalent form:

$$
\begin{aligned}
\underline{\beta}(t) &= \underline{\beta}(l) + \int_{t_l}^{t} \underline{\omega}\, dt \\
\underline{u}(t) &= \underline{u}(l) + \int_{t_l}^{t} \underline{a}\, dt \\
\underline{\gamma}_1(l+1) &= \underline{\gamma}_1(l) + \int_{t_l}^{t_{l+1}} \left(\underline{\beta}(t) \times \underline{a}\right) dt \\
\underline{\gamma}_2(l+1) &= \underline{\gamma}_2(l) + 1/2 \int_{t_l}^{t_{l+1}} \left(\underline{\beta}(t) \times \underline{a} + \underline{u}(t) \times \underline{\omega}\right) dt
\end{aligned}
\qquad
\begin{aligned}
\underline{\beta}(l+1) &= \underline{\beta}\left(t = t_{l+1}\right) \\
\underline{u}(l+1) &= \underline{u}\left(t = t_{l+1}\right) \\
\underline{S}_1 &= \underline{\gamma}_1\left(t = t_{m+1}\right) \\
\underline{S}_2 &= \underline{\gamma}_2\left(t = t_{m+1}\right)
\end{aligned}
\tag{53}
$$

with initial conditions

$$
\begin{aligned}
&\underline{\beta}\left(t{=}t_m\right) \;=\; 0 \\
&\underline{u}\left(t{=}t_m\right) \;=\; 0 \\
&\underline{\gamma}_1\left(t{=}t_m\right) \;=\; 0 \\
&\underline{\gamma}_2\left(t{=}t_m\right) \;=\; 0
\end{aligned}
\qquad (54)
$$

where

$l$ = High speed computer cycle within m lower speed computation cycle.

The integrals in (53) can be replaced by analytical forms that are compatible with gyro and accelerometer input data processing if $\underline{\omega}$ and $\underline{a}$ are replaced by a generalized time series expansion. For equations (53), it is sufficient to approximate $\underline{\omega}$ and $\underline{a}$ over the $l$ to $l$+1 time interval as constants. Using this approximation in (53) yields the final algorithm forms. For $\underline{S}_1$, the companion to equation (51), the algorithm is:

$$
\begin{aligned}
&\underline{\gamma}_1\left(l{+}1\right) \;=\; \underline{\gamma}_1\left(l\right) + \left(\underline{\beta}(l) + 1/2\;\underline{\Delta\theta}\left(l\right)\right) \times \underline{\Delta v}(l) \\
&\underline{\beta}\left(l{+}1\right) \;=\; \underline{\beta}(l) + \underline{\Delta\theta}\left(l\right)
\end{aligned}
$$

where

$$
\underline{\Delta\theta}(l) \;=\; \int_{t_l}^{t_{l+1}} \underline{\omega}\,dt \;=\; \sum_{t_l}^{t_{l+1}} \underline{d\theta}
$$

$$
\underline{\Delta v}(l) \;=\; \int_{t_l}^{t_{l+1}} \underline{a}\,dt \;=\; \sum_{t_l}^{t_{l+1}} \underline{dv}
$$

and

$$
\underline{S}_1 = \underline{\gamma}_1\left(t{=}t_{m+1}\right) \qquad (55)
$$

For equation (51):

$$
\begin{aligned}
&\underline{u}\,(l{+}1) \;=\; \underline{u}\,(l) + \Delta v(l) \\
&\underline{u} \;\stackrel{\Delta}{=}\; \underline{u}\left(t{=}t_{m+1}\right)
\end{aligned}
$$

with initial conditions:

$$\underline{\beta}\left(t{=}t_m\right) \overset{\Delta}{=} \underline{\beta}\,(l{=}0) = 0$$

$$\underline{\gamma}_1\left(t{=}t_m\right) \overset{\Delta}{=} \underline{\gamma}_1\,(l{=}0) = 0$$

where

$\underline{d\theta}$, $\underline{dv}$ = Gyro and accelerometer output pulse vectors. Each component (x, y, z) represents the occurrence of a rotation through a specified angle about the gyro input axis (for $\underline{d\theta}$ components) or an acceleration through a specific force velocity change along the accelerometer input axis (for $\underline{dv}$ components).

$\underline{\Delta\theta}$, $\underline{\Delta v}$ = Gyro and accelerometer pulse vector counts from $l$ to $l$+1.

For the alternative $\underline{S}_2$ form, the companion to equation (52), the algorithm is:

$$\underline{\gamma}_2\,(l{+}1) = \underline{\gamma}_2\,(l) + 1/2\left(\underline{\beta}(l) \times \underline{\Delta v}(l) + \underline{u}(l) \times \underline{\Delta\theta}\,(l)\right)$$

$$\underline{\beta}\,(l{+}1) = \underline{\beta}(l) + \Delta\theta\,(l)$$

$$\underline{u}\,(l{+}1) = \underline{u}(l) + \underline{\Delta v}(l)$$

where

$$\underline{\Delta\theta}(l) = \int_{t_l}^{t_{l+1}} \underline{\omega}\,dt = \sum_{t_l}^{t_{l+1}} \underline{d\theta}$$

$$\underline{\Delta u}(l) = \int_{t_l}^{t_{l+1}} \underline{a}\,dt = \sum_{t_l}^{t_{l+1}} \underline{dv} \qquad (56)$$

and

$$\underline{S}_2 = \underline{\gamma}_2\left(t{=}t_{m+1}\right)$$

For equations (52):

$$\underline{\beta} = \underline{\beta}\left(t{=}t_{m+1}\right)$$

$$\underline{u} = \underline{u}\left(t{=}t_{m+1}\right)$$

with initial conditions:

$$\underline{\beta}\left(t{=}t_m\right) \overset{\Delta}{=} \underline{\beta}\left(l{=}0\right) = 0$$

$$\underline{u}\left(t{=}t_m\right) \overset{\Delta}{=} \underline{u}\left(l{=}0\right) = 0$$

$$\underline{\gamma}_2\left(t{=}t_m\right) \overset{\Delta}{=} \underline{\gamma}_2\left(l{=}0\right) = 0$$

Equations (51) with (55), or (52) with (56) are computational algorithms that can be used to calculate the navigation frame specific force velocity changes. Two iteration rates are implied: a basic m cycle rate, and a higher speed *l* cycle rate within each m cycle.

The m cycle rate is selected to be high enough to protect the approximation of neglecting the $\left(\underline{\beta}(t)\times\right)^2$ term in A(t) (contrast equation (47) with the equation (3) exact form for A). This design condition is typically evaluated under maximum expected linear acceleration/angular rate envelope conditions for the particular application. Typically, the m cycle rate required for accuracy in the attitude updating algorithms is also sufficient for accuracy requirements in the m cycle of the acceleration transformation algorithms.

The *l* cycle rate within m is set high enough to properly account for anticipated composite dynamic $\underline{\omega}$, $\underline{a}$ effects. Section 6. describes analytical techniques that can be used to assess the adequacy of the $\underline{S}$ iteration rate for the sculling computation under dynamic input conditions.

### 4.1.3 Acceleration Transformation Algorithms Based on Quaternion Attitude Data

Equations (51) or (52) were based on the use of direction cosine data (C) in the strapdown computer. If the basic attitude data is calculated in the form of a quaternion, the equivalent C matrix for transformation can be calculated using equations (17). Alternatively, the quaternion data can be applied directly in the implementation of the transformation operation through application of equation (12) to equations (51) and (52):

$$u^N = q(m)\left(u + S_1\right)q(m)^* \tag{57}$$

or

$$\begin{aligned} u^N &= q(m)\left(u + S_2'\right)q(m)^* \\ S_2' &\overset{\Delta}{=} 1/2\,\underline{\beta}\times\underline{u} + \underline{S}_2 \end{aligned} \tag{58}$$

where u and the terms in the middle brackets are the quaternion form of the vector of the same nomenclature defined as having the first three terms (i.e., vector components) equal to the vector elements, and the fourth scalar term equal to zero. The $\underline{S}_1$ and $\underline{S}_2$ terms are calculated as defined by equations (55) and (56).

## 4.2 Acceleration Transformation Algorithm Correction For Navigation Frame Rotations

The acceleration transformation algorithms represented by equation (51), (52) or (57), (58) with (55), (56) neglects the effect of navigation frame rotation. In general, this is a minor correction term that can be easily accounted for at the n cycle update rate (i.e., the computer cycle rate used to update the attitude data for the effect of navigation frame rotations). It can be shown through a development similar to that leading to equation (52), that the correction algorithm for local navigation frame motion is given to first order by:

$$\underline{\Delta u}^N(n) = -1/2\ \underline{\theta} \times \underline{v}\ (n) \tag{59}$$

where

$\underline{\Delta u}^N(n)$ = Correction to the value of $\underline{u}^N$ computed in the m cycle that occurs at the current n cycle time. (Note: the m cycle is within the lower speed n cycle time frame).

$\underline{v}\ (n)$ = Summation of $\underline{u}(m)$ over the n cycle update period.

$\underline{\theta}$ = Integral of the navigation frame angular rotation rate over the n cycle period (as described in Sections 3.1.2 and 3.4)

## 5. EULER ANGLE EXTRACTION ALGORITHMS

If the body attitude relative to navigation axes is defined in terms of three successive Euler angle rotations ψ, θ, φ about axes z, y, x respectively (from navigation to body axes), it can be readily demonstrated (9) that the relationship between the direction cosine elements and Euler angles is given by:

$$
\begin{aligned}
C_{11} &= \cos\theta \cos\psi \\
C_{12} &= -\cos\phi \sin\psi + \sin\phi \sin\theta \cos\psi \\
C_{13} &= \sin\phi \sin\psi + \cos\phi \sin\theta \cos\psi \\
C_{21} &= \cos\theta \sin\psi \\
C_{22} &= \cos\phi \cos\psi + \sin\phi \sin\theta \sin\psi \\
C_{23} &= -\sin\phi \cos\psi + \cos\phi \sin\theta \sin\psi \\
C_{31} &= -\sin\theta \\
C_{32} &= \sin\phi \cos\theta \\
C_{33} &= \cos\phi \cos\theta
\end{aligned}
\tag{60}
$$

For conditions where $|\theta| \neq \pi/2$ the inverse of equations (60) can be used to evaluate the Euler angles from the direction cosines:

$$
\begin{aligned}
\phi &= \tan^{-1} \frac{C_{32}}{C_{33}} \\
\theta &= -\tan^{-1} \frac{C_{31}}{\sqrt{\left(1 - C_{31}\, 2\right)}} \\
\psi &= \tan^{-1} \frac{C_{21}}{C_{11}}
\end{aligned}
\tag{61}
$$

For situations where $|\theta|$ approaches $\pi/2$, the $\phi$ and $\psi$ equations in (61) become indeterminate because the numerator and denominator approach zero simultaneously (see equations (60)). Under these conditions, an alternative equation for $\phi$, $\psi$ can be developed by first applying trigonometric algebra to equations (60) to obtain:

$$
\begin{aligned}
C_{23} + C_{12} &= \left(\sin\theta - 1\right) \sin\left(\psi + \phi\right) \\
C_{13} - C_{22} &= \left(\sin\theta - 1\right) \cos\left(\psi + \phi\right) \\
C_{23} - C_{12} &= \left(\sin\theta + 1\right) \sin\left(\psi - \phi\right) \\
C_{13} + C_{22} &= \left(\sin\theta + 1\right) \cos\left(\psi - \phi\right)
\end{aligned}
\tag{62}
$$

Taking appropriate reciprocals of sine, cosine terms in (62) and applying the inverse tangent function:

For $\theta$ near $+\pi/2$

$$\psi - \phi = \tan^{-1} \frac{C_{23} - C_{12}}{C_{13} + C_{22}}$$

(63)

For $\theta$ near $-\pi/2$

$$\psi + \phi = \pi + \tan^{-1} \frac{C_{23} + C_{12}}{C_{13} - C_{22}}$$

Equations (63) can be used to obtain expressions for the sum or difference of $\psi$ and $\phi$ under conditions where $|\theta|$ is near $\pi/2$. Explicit separate solutions for $\psi$ and $\phi$ cannot be found under the $|\theta| = \pi/2$ condition because $\psi$ and $\phi$ both become angle measures about parallel axes (about vertical), hence, measure the same angle (i.e., a degree of rotational freedom is lost, and only two Euler angles, $|\theta| = \pm\pi/2$ and $\psi$ or $\phi$ define the body to navigation frame attitude). Under $|\theta|$ near $\pi/2$ conditions, $\phi$ or $\psi$ can be arbitrarily selected to satisfy another condition, with the unspecified variable calculated from (63). As an example, $\psi$ might be set to a constant at the value it had from equations (61) when the $|\theta|$ near $\pi/2$ region was entered. This selection avoids jumps in $\psi$ as the solution equation is transitioned from the (61) to the (63) form.

## 6. ALGORITHM PERFORMANCE ASSESSMENT

The division of the attitude updating and acceleration transformation algorithms into high and low speed loops for body motion effects (*l* and m rates) provides for flexibility in selection of the iteration rates to maintain overall algorithm accuracy at system specified performance levels. The *l* and m rate algorithms have been designed such that the high rate *l* loop consists of simple computations that can be iterated at the high rate needed to properly account for high frequency vibration effects. The m rate loop algorithms, on the other are more complicated, based on computationally exact solutions.

Iteration rates for the m loop are selected to maintain accuracy under maximum maneuver induced motion conditions. The m loop iteration rate to maintain accuracy under maximum maneuver conditions can be easily evaluated analytically, or by simulation, through comparison of the actual algorithm solution with the Taylor series truncated forms selected for system mechanization. Iteration rates for the *l* loop are selected to maintain accuracy under anticipated vibratory environmental conditions.

### 6.1 Vibration Environment Assessment

A fundamental calculation that should be performed prior to the analysis of *l* loop algorithm iteration rate requirements is an assessment of the dynamic inputs that must be measured by the algorithms. In essence, this consists of an evaluation of the continuous (i.e., infinitely fast iteration rate) form of the algorithms in question under dynamic input conditions. The specific continuous form equations of interest are equations (22) for $\underline{\delta\beta}$ and (50) for $\underline{S}_1$ or $\underline{S}_2$.

#### 6.1.1 $\underline{\delta\beta}$ Dynamic Environment Assessment (Coning)

We repeat equations (22) for $\underline{\delta\beta}$ evaluated at $t = t_{m+1}$:

$$\underline{\beta}(t) = \int_{t_m}^{t} \underline{\omega}\, dt$$

$$\underline{\delta\beta}\left(t{=}t_{m+1}\right) = 1/2 \int_{t_m}^{t_{m+1}} \underline{\beta}(t) \times \underline{\omega}\, dt \tag{64}$$

and analyze the solution for $\underline{\delta\beta}\left(t{=}t_{m+1}\right)$ under general motion at frequency f in axes x and y with angular amplitudes $\theta_x$, $\theta_y$ and relative phase angle $\phi$ such that:

$$\int_{0}^{t} \underline{\omega}\, dt = \left(\theta_x \sin(2\pi f t),\ \theta_y \sin(2\pi f t+\phi),\ 0\right)^T$$

$$\underline{\omega} = 2\pi f \left(\theta_x \cos(2\pi f t),\ \theta_y \cos(2\pi f t+\phi),\ 0\right)^T \tag{65}$$

Substituting (65) in (64), expanding through application of appropriate trigonometric identities, and carrying out the indicated integrals analytically between the assigned limits, yields zero for the x, y components and the following for the z component of $\underline{\delta\beta}\left(t{=}t_{m+1}\right)$:

$$\delta\beta_z\left(t{=}t_{m+1}\right) = \pi\, \theta_x\, \theta_y \left(\sin\phi\right) f \left(\left(t_{m+1} - t_m\right) - \frac{\sin 2\pi f\left(t_{m+1} - t_m\right)}{2\pi f}\right)$$

Defining the m cycle time interval as $T_m$, the latter expression is equivalently:

$$\delta\beta_z = \pi\,\theta_x\,\theta_y\left(\sin\phi\right) f\,T_m\left(1 - \frac{\sin 2\pi f T_m}{2\pi f T_m}\right) \tag{66}$$

Hence, even though the $\underline{\omega}$ rate is cyclic in two axes as defined by equation (65) in x and y, the value for $\delta\beta_z$ is a constant proportional to the sine of the phase angle between the x, y angular vibrations. Under conditions where $\phi = 0$ (defined as "rocking" motion), $\delta\beta_z$ is zero. Under conditions where $\phi = \pi/2$, $\delta\beta_z$ is maximum. The equation (65) rate when $\phi = \pi/2$ has been termed "coning motion" due to the characteristic response of the z axis under this motion which describes a cone in inertial space.

Equation (66) can be converted into a "drift rate" form by dividing the $\delta\beta_z$ angle by the time interval $T_m$ over which it was evaluated:

$$\delta\dot{\beta}_z = \pi\,\theta_x\,\theta_y\left(\sin\phi\right) f\left(1 - \frac{\sin 2\pi f T_m}{2\pi f T_m}\right) \tag{67}$$

Equation (67) is a fundamental equation that can be used to assess the magnitude of $\delta\dot{\beta}_z$ that must be accounted for by the $\delta\beta$ computer algorithm under discrete frequency input conditions. If $\delta\dot{\beta}_z$ is small relative to system performance requirements, it can be neglected, and the *l* loop algorithm for $\delta\beta$ need not be implemented.

Equation (67) describes how $\delta\dot{\beta}_z$ can be calculated for a discrete input vibration frequency f. In a more general case, the input rate is composed of a mixture of frequencies in x and y at different phase angles $\phi$ for each. If the source of the generalized angular vibration is random input noise to the strapdown system, the x, y motion is colored by the transmission characteristics of the noise input to the x, y angular response. A more general development of equation (67) that accounts for the latter effects shows that the comparable equation for $\delta\dot{\beta}_z$ is given by:

$$\delta\dot{\beta}_z = \int_0^\infty \omega\,A_x(\omega)\,A_y(\omega)\,\sin\left(\phi_{Ay}(\omega) - \phi_{Ax}(\omega)\right)\left(1 - \frac{\sin \omega T_m}{\omega T_m}\right) P_{nn}(j\omega)\,d\omega \tag{68}$$

where

$A_x(\omega)$, $A_y(\omega)$ = Amplitude of the transfer function relating system input vibration noise to angular attitude response of the sensor assembly about the x, y axes.

$\phi_{Ax}(\omega)$, $\phi_{Ay}(\omega)$ = Phase of the transfer function relating system input vibration noise to angular attitude response of the sensor assembly about the x, y axes.

$P_{nn}(j\omega)$ = Power spectral density of input vibration noise.

$\omega$ = Fourier frequency (rad/sec)

Note: Mean squared vibration energy = $\int_0^\infty P_{nn}(j\omega)\, d\omega$

Equation (68) can be used to assess the extent of random spectrum dynamic angular environment to be measured by the $\delta\beta$ computational algorithm. The $\delta\dot{\beta}_z$ value calculated by (68) measures the composite correlated coning drift in the sensor assembly that must be calculated to accurately account for the actual motion present. If the $\delta\dot{\beta}_z$ magnitude calculated from (68) is small compared to other systems error budget effects, the mechanization of an algorithm to calculate $\delta\beta$ is not needed (i.e., can be approximated by zero).

The extension of equations (67) and (68) to y, z or z, x axis angular vibration motion should be obvious.

### 6.1.2 $\underline{S}_1$, $\underline{S}_2$ Dynamic Environment Assessment (Sculling)

We repeat equations (50) with $\underline{u}$ and $\underline{\beta}$ from (48) and (49):

$$
\begin{aligned}
\underline{\beta}(t) &= \int_{t_m}^{t} \underline{\omega}\, dt \\
\underline{u}(t) &= \int_{t_m}^{t} \underline{a}\, dt \\
\underline{S}_1 &= \int_{t_m}^{t_{m+1}} \left(\underline{\beta}(t) \times \underline{a}\right) dt \qquad\qquad (69) \\
\underline{S}_2 &= 1/2 \int_{t_m}^{t_{m+1}} \left(\underline{\beta}(t) \times \underline{a} + \underline{u}(t) \times \underline{\omega}\right) dt
\end{aligned}
$$

and analyze the $\underline{S}_1$, $\underline{S}_2$ solutions under general cycle motion at frequency f in axes x, y with angular amplitude $\theta_x$ about axis x and acceleration amplitude $D_y$ along axis y at relative phase $\phi$ such that:

$$\int_0^t \underline{\omega}\, dt = \left(\theta_x \sin(2\pi f t), 0, 0\right)^T$$

$$\underline{\omega} = \left(2\pi f\, \theta_x \cos(2\pi f t), 0, 0\right)^T \tag{70}$$

$$\underline{a} = \left(0, D_y \sin(2\pi f t + \phi), 0\right)^T$$

Substituting (70) in (69), expanding through application of appropriate trigonometric identities, and carrying out the indicated integrals analytically between the assigned limits, yields zero for the x, y components and the following for the z component of $\underline{S}_1$ and $\underline{S}_2$:

$$S_{2z} = 1/2\, T_m\, \theta_x\, D_y \left(\cos\phi\right)\left(1 - \frac{\sin \pi f T_m}{2\pi f T_m}\right) \tag{71}$$

$$S_{1z} = 1/2\left(\underline{\beta} \times \underline{u}\right)_z + S_{2z} \tag{72}$$

where

$$\left(\underline{\beta} \times \underline{u}\right)_z = \text{z - component of } \underline{\beta} \times \underline{u} \text{ evaluated at } t = t_{m+1}.$$

Hence, even though the $\underline{\omega}$ and $\underline{a}$ inputs are cyclic in two axes as defined in equations (70), the value for $S_{2z}$ is a constant proportional to the cosine of the phase angle between the x angular vibration and y linear acceleration vibration. Under conditions where $\phi = \pi/2$, $S_{2z}$ is zero. Under conditions where $\phi = 0$, $S_{2z}$ is a maximum. Equation (70) motion when $\phi = 0$ has been termed "sculling motion" due to the analogy with the characteristic angular movement and acceleration forces imparted to a single oar used to propel a boat from the stern. Note also that $S_{1z}$ is equal to $S_{2z}$ plus the correction term (rotation compensation) measured as the cross-product of the sample angular rate and linear acceleration integrals taken over the m computation cycle. (See equations (48) and (49) for definitions).

Equation (71) for $S_{2z}$ can be converted into an "acceleration bias" form by dividing the velocity change correction $S_{2z}$ by the time interval $T_m$ over which it was evaluated:

$$\dot{S}_{2z} = 1/2\;\theta_x\, D_y \left(\cos\phi\right)\left(1 - \frac{\sin 2\pi f T_m}{2\pi f T_m}\right) \tag{73}$$

Equation (73) (with (72) for $S_{1z}$) is a fundamental equation that can be used to assess the magnitude of $\dot{S}_{2z}$ that must be accounted for by the $S_1$ or $S_2$ computer algorithm under discrete frequency input conditions. If $\dot{S}_{2z}$ is small relative to system performance requirements, it can be neglected, and the *l* loop algorithm for calculating $S_1$ or $S_2$ need not be implemented. Under the latter conditions, $S_1$ would be set equal to the cross-product term in (72) which makes the basic equation (51) and (52) transformation algorithms identical.

Equation (73) describes how $\dot{S}_{2z}$ can be calculated with a discrete input vibration frequency f for angular motion about x and linear motion along y. In a more general case, the input rates and accelerations are composed of mixtures of angular and linear motion about x and y at different frequencies and relative phase angles. If the source of the generalized vibration motion is random input noise to the strapdown system, the x, y angular and linear motion is colored by the transmission characteristics of the noise input to the x, y angular and linear response. A more general development of equation (73) that accounts for the latter effects show that the comparable equation for $\dot{S}_{2z}$ is given by:

$$\dot{S}_{2z} = \int_0^{\infty} \Big(A_y(\omega)\, B_x(\omega) \cos\big(\phi_{Ay}(\omega) - \phi_{Bx}(\omega)\big) - A_x(\omega)\, B_y(\omega) \cos\big(\phi_{Ax}(\omega) - \phi_{By}(\omega)\big)\Big) \left(1 - \frac{\sin\omega T_m}{\omega T_m}\right) P_{nn}(j\omega)\, d\omega \tag{74}$$

where

$A_x(\omega)$, $A_y(\omega)$,
$\phi_{Ax}(\omega)$, $\phi_{Ay}(\omega)$, = As defined previously.
$P_{nn}(j\omega)$, $\omega$

$B_x(\omega)$, $B_y(\omega)$, = x, y amplitude/phase linear acceleration response of the
$\phi_{Bx}(\omega)$, $\phi_{By}(\omega)$ sensor assembly to the input vibration.

Equation (74) can be used to assess the extent of random spectrum dynamic motion environment to be measured by the $S_1$ or $S_2$ computational algorithms. The $\dot{S}_{2z}$ value calculated by (74) measures the composite correlated sculling acceleration bias in the sensor assembly that must be calculated to accurately account for the actual motion present. If the $\dot{S}_{2z}$ magnitude calculated from (74) is small compared to other system error budget effects, the mechanization of an algorithm to calculate $S_1$ or $S_2$ in the high rate *l* loop is not needed (i.e., $S_2$ can be approximated by zero in (52) or $S_1$ can be set equal to the cross-product term in (52)).

The extension of equations (73) and (74) for y, z or z, x axis vibration motion should be obvious.

## 6.2 Algorithm Accuracy Assessment.

The accuracy of the computation algorithm for $\underline{\delta\beta}$ or $\underline{S}_1$, $\underline{S}_2$ can be assessed by comparing their solutions to the comparable continuous form solutions developed in Section 6.1 under identical input conditions.

### 6.2.1 $\underline{\delta\beta}$ Coning Algorithm Error Assessment

The computational algorithm for calculating $\underline{\delta\beta}$ in a strapdown system is given by equation (26). A measure of the accuracy of the equation (26) algorithm can be obtained by analytically calculating the solution generated from (26) under assumed cyclic motion and comparing this result to the equivalent solution obtained from the idealized continuous algorithm described in Section 6.1. For a discrete frequency vibration input, the equation (65) motion can be used analytically in equation (26) to calculate the algorithm solution for $\underline{\delta\beta}$ at $t = t_{m+1}$ (i.e., analogous to the equation (67) solution for the continuous (infinitely fast) algorithm. After much algebraic manipulation, it can be demonstrated that the algorithm solution for $\underline{\delta\beta}$ as calculated from equation (26) under equation (65) input motion, has zero x, y components, with a z component rate given by:

$$\dot{\delta\beta}_{zALG} = \pi \, f \, \theta_x \, \theta_y \left(\sin \phi\right) \left( \left(1 + 1/3 \left(1 - \cos 2\pi f T_l\right)\right) \frac{\sin 2\pi f T_l}{2\pi f T_l} - \frac{\sin 2\pi f T_m}{2\pi f T_m} \right) \tag{75}$$

where

$\dot{\delta\beta}_{zALG}$ = Recursive algorithm solution for $\delta\beta_z$ rate

$T_l$ = Time interval for high speed $l$ computer iteration cycle

Equation (75) for the $\underline{\delta\beta}$ discrete recursive algorithm solution of equation (26) is directly analogous to the equation (67) solution of the equation (22) continuous $\underline{\delta\beta}$ algorithm. It is easily verified that (75) reduces to (67) as $T_l$ approaches zero.

The error in the $\underline{\delta\beta}$ algorithm is measured by the difference between (67) and (75); i.e.:

$$e\left(\dot{\delta\beta}_z\right) = \pi \, f \, \theta_x \, \theta_y \left(\sin \phi\right) \left( \left(1 + 1/3 \left(1 - \cos 2\pi f T_l\right)\right) \frac{\sin 2\pi f T_l}{2\pi f T_l} - 1 \right) \tag{76}$$

where

$$e\left(\delta\dot{\beta}_z\right) = \text{ Error rate in the equation (26) algorithm.}$$

Equation (76) can be used to assess the error in the equation (26) $\underline{\delta\beta}$ algorithm caused by finite iteration rate (i.e., the effect of $T_l$) under discrete frequency input conditions.

Under random vibration input conditions, the equation (26) algorithm can be analyzed to obtain the more general solution for the $\delta\beta_{zALG}$ rate:

$$\begin{aligned}\delta\dot{\beta}_{zALG} = \int_o^\infty & \omega\, A_x(\omega)\, A_y(\omega) \sin\left(\phi_{Ay}(\omega) - \phi_{Ax}(\omega)\right) \\ & \times\left(\left(1 + 1/3\,(1 - \cos\omega T_l)\right)\frac{\sin\omega T_l}{\omega T_l} - \frac{\sin\omega T_m}{\omega T_m}\right) P_{nn}(j\omega)\, d\omega\end{aligned} \tag{77}$$

The $\delta\beta$ algorithm error under random inputs is the difference between the equation (77) discrete solution and the equivalent continuous equation (68) solution form. The result is:

$$\begin{aligned}e\left(\delta\dot{\beta}_z\right) = \int_o^\infty & \omega\, A_x(\omega)\, A_y(\omega) \sin\left(\phi_{Ay}(\omega) - \phi_{Ax}(\omega)\right) \\ & \times\left(\left(1 + 1/3\,(1 - \cos\omega T_l)\right)\frac{\sin\omega T_l}{\omega T_l} - 1\right) P_{nn}(j\omega)\, d\omega\end{aligned} \tag{78}$$

Equations (76) and (78) can be used to assess the error in the equation (26) $\underline{\delta\beta}$ algorithm caused by finite iteration rate under discrete or random vibration input conditions. The extension of equations (76) and (78) to y, z or z, x axis effects should be obvious.

### 6.2.2 $\underline{S}$ Sculling Algorithm Error Assessment

The computational algorithm for calculating $\underline{S}_1$ or $\underline{S}_2$ is given by equations (55) and (56). A measure of the accuracy of these algorithms can be obtained by analytically calculating the solution generated from (55) or (56) under assumed cyclic motion and comparing the result to the equivalent solution obtained from the continuous algorithm as described in Section 6.1.2. For a discrete frequency vibration input, the equation (70) motion can be used analytically in equation (55) and (56) to calculate the algorithm solution for $\underline{S}_1$, $\underline{S}_2$ (i.e., analogous to the equation (72) and (73) solution for the continuous (infinitely fast) algorithms). After much algebraic manipulation, it can be demonstrated that the algorithm solution for $\underline{S}_1$ and $\underline{S}_2$ as calculated from equations (55) and (56) under equation (70) input motion, has zero x, y components, with a z component rate given by:

$$\dot{S}_{2zALG} = 1/2\ \theta_x\ D_y \left(\cos\ \phi\right)\left(\frac{\sin\ 2\pi f T_l}{2\pi f T_l} - \frac{\sin\ 2\pi f T_m}{2\pi f T_m}\right) \tag{79}$$

$$S_{1zALG} = 1/2 \left(\underline{\beta} \times \underline{u}\right)_z + S_{2zALG} \tag{80}$$

where

$S_{1zALG}, S_{2zALG}$ = Recursive algorithm solutions for $S_{1z}$, $S_{2z}$.

Equations (79) and (80) for the $\underline{S}_1$, $\underline{S}_2$ discrete recursive algorithm solution is directly analogous to the equations (73) and (72) solution to the continuous $\underline{S}_1$, $\underline{S}_2$ algorithm. It is easily verified that (79) and (80) reduce to (73) and (72) as $T_l$ approaches zero.

The error in the $\underline{S}_1$, $\underline{S}_2$ algorithm is measured by the difference between (79), (80) and (73), (72); i.e.,

$$e\left(\dot{S}_{1z}\right) = e\left(\dot{S}_{2z}\right) = 1/2\ \theta_x\ D_y \left(\cos\ \phi\right)\left(1 - \frac{\sin\ 2\pi f T_l}{2\pi f T_l}\right) \tag{81}$$

where

$e\left(\dot{S}_{1z}\right), e\left(\dot{S}_{2z}\right)$ = Error rate in the equation (55) and (56) algorithm solutions.

Equation (81) can be used to assess the error in the equation (55) and (56) algorithms caused by finite iteration rate (i.e., the effect of $T_l$) under discrete frequency input conditions.

Under random vibration input conditions, the equation (55) and (56) algorithms can be analyzed to obtain the more general solution for $S_{1z}$, $S_{2z}$:

$$\dot{S}_{2z} = \int_o^\infty \Big(A_y(\omega)\ B_x(\omega) \cos\left(\phi_{Ay}(\omega) - \phi_{Bx}(\omega)\right) \tag{82}$$

$$- A_x(\omega)\ B_y(\omega) \cos\left(\phi_{Ax}(\omega) - \phi_{By}(\omega)\right)\Big)\left(\frac{\sin\ \omega T_l}{\omega T_l} - \frac{\sin\ \omega T_m}{\omega T_m}\right) P_{nn}\ (j\omega)\ d\omega$$

$$S_{1z} = 1/2 \left(\underline{\beta} \times \underline{u}\right)_z + S_{2z}$$

The $S_{1z}$, $S_{2z}$ algorithm error under vibration is the difference between the equation (82) discrete solutions and the equivalent continuous equation (74) with (72) forms:

$$e\left(\dot{S}_{1z}\right) = e\left(\dot{S}_{2z}\right) = \int_o^\infty \Big(A_y(\omega)\, B_x(\omega) \cos\left(\phi_{Ay}(\omega) - \phi_{Bx}(\omega)\right) - A_x(\omega)\, B_y(\omega) \cos\left(\phi_{Ax}(\omega) - \phi_{By}(\omega)\right)\Big) \left(1 - \frac{\sin \omega T_l}{\omega T_l}\right) P_{nn}\,(j\omega)\, d\omega \tag{83}$$

Equation (82) and (83) can be used to assess the error in the equation (55) and (56) algorithms caused by finite iteration rate under discrete or random vibration input conditions. The extension of equation (83) to y, z or z, x axis effects should be obvious.

## 7. CONCLUDING REMARKS

The strapdown computational algorithms and associated design considerations presented in this paper are representative of the algorithms being used in most modern-day strapdown inertial navigation systems. The unique characteristic of the attitude and transformation algorithms presented is the separation of each into a complex low speed and simple high speed computation section. Due to the simplicity of the high speed calculations they can be executed at the high rates necessary to properly account for high frequency but generally low amplitude vibratory effects without posing an insurmountable throughput burden on the computer. The lower speed calculations which contain the bulk of the computational equations can then be executed at a fairly modest update rate selected to properly account for lower frequency but larger magnitude maneuver induced motion effects. Perhaps the principal advantage of the algorithm forms presented, is their ability to be analyzed for accuracy using straight-forward analytical techniques. This allows the algorithms to be easily tailored and evaluated for given applications as a function of anticipated dynamic environments and user accuracy requirements.

## REFERENCES

1. Pitman, George R. Jr., ed., Inertial Guidance, John Wiley and Sons, New York, 1962.

2. Leondes, Cornelius T., ed., Guidance and Control of Aerospace Vehicles, McGraw-Hill, 1963.

3. Macomber, George R. and Fernandes, Manuel, Inertial Guidance Engineering, Prentice-Hall Englewood Cliffs, New Jersey, 1962.

4. Britting, Kenneth R., Inertial Navigation System Analysis, John Wiley and Sons, New York, 1971.

5. Morse, Philip M. and Feshback, Herman, Methods of Theoretical Physics, McGraw-Hill, 1953.

6. A Study of Critical Computational Problems Associated with Strapdown Inertial Navigation Systems, NASA Report CR-968, April 1968.

7. Savage, P.G., "A New Second-Order Solution for Strapped-Down Attitude Computation", AIAA/JACC Guidance & Control Conference, Seattle, Washington, August 15-17, 1966.

8. Jordan, J.W., "An Accurate Strapdown Direction Cosine Algorithm", NASA TN D-5384, September 1969.

9. Mckern, Richard A., A Study of Transformation Algorithms For Use In A Digital Computer, Massachusetts Institute of Technology Master's Thesis, Department of Aeronautics and Astronatics, January 1968.

10. Bortz J.E., "A New Mathematical Formulation for Strapdown Inertial Navigation", IEEE Transactions on Aerospace and Electronic Systems, Volume AES-7, No. 1, January 1971.

11. Shepperd, Stanley W., "Quaternion from Rotation Matrix", AIAA Journal of Guidance and Control, Vol. 1, No. 3 May-June 1978.

12. Savage, P.G., Introduction To Strapdown Inertial Navigation Systems, June 1, 1983 (Third Printing); Third Strapdown Associates Open Seminar on Strapdown Inertial Navigation Systems, Marquette Inn, Minneapolis, Minnesota, November 14-18, 1983.

## APPENDIX A

## DERIVATION OF $\dot{\underline{\phi}}$ EQUATION

A differential equation for the rate of change of the $\underline{\phi}$ vector can be derived from the equivalent quaternion rate equation. The quaternion h in equations (13) and (14) is the quaternion equivalent to the $\underline{\phi}$ rotation angle vector. A differential equation for h can be derived from the incremental equivalent to (13) that describes how h changes over a short time period $\Delta t$ (from $t_l$ to $t_{l+1}$) within the larger time interval from $t_m$ to $t_{m+1}$:

$$h\,(l+1) = h(l)\,p(l) \tag{A1}$$

where

$$P = \begin{vmatrix} g_3 \, \alpha_x \\ g_3 \, \alpha_y \\ g_3 \, \alpha_z \\ g_4 \end{vmatrix} \tag{A2}$$

$$g_3 = \frac{\sin\left(\alpha/2\right)}{\alpha} \qquad\qquad g_4 = \cos\left(\alpha/2\right)$$

$\underline{\alpha}$ = Rotation angle vector associated with the small rotation of the body over the short computer time interval from $l$ to $l$+1 within the larger interval from m to m+1.

$\alpha_x, \alpha_y, \alpha_z, \alpha$ = Components and magnitude of $\underline{\alpha}$.

Equation (A1) is equivalently:

$$\frac{h\,(l+1) - h(\,l)}{\Delta t} = h(l)\,\frac{p(\,l) - 1}{\Delta t}$$

$$\Delta t \overset{\Delta}{=} t_{l+1} - t_l \tag{A3}$$

The basic definition of angular rate states that for small $\Delta t$,

$$\underline{\alpha} \approx \underline{\omega}\,\Delta t$$

$$\alpha \approx \omega\,\Delta t \tag{A4}$$

Hence, for small $\Delta t$, $\underline{\alpha}$ is small, and therefore, from (A2),

$$g_3 \approx 1/2$$

$$g_4 \approx 1 - \frac{\alpha^2}{2} \approx 1 - \frac{\omega^2\,\Delta t^2}{2} \tag{A5}$$

Using mixed vector/scalar notation, substitution of (A4) and (A5) in (A2) yields:

$$p = g_3\,\underline{\alpha} + g_4 \approx 1/2\,\underline{\omega}\,\Delta t + 1 - \frac{\omega^2\,\Delta t^2}{2}$$

Substituting in (A3) obtains:

$$\frac{h\,(l+1) - h(\,l)}{\Delta t} \approx h(l)\left(1/2\,\underline{\omega} + 1/2\,\omega^2\,\Delta t\right)$$

In the limit as $\Delta t \rightarrow 0$ , the latter reduce to the derivative form:

$$\dot{h} = 1/2\,h\,\underline{\omega} \qquad \text{(A6)}$$

We now return to (14) and express h as a function of $\underline{\phi}$ in mixed vector/scalar notation:

$$h = f_3\,\underline{\phi} + f_4$$

$$f_3 = \frac{\sin\left(\phi/2\right)}{\phi} \qquad \text{(A7)}$$

$$f_4 = \cos\left(\phi/2\right)$$

Substituting in (A6),

$$\dot{h} = 1/2\,f_3\,\underline{\phi}\,\underline{\omega} + 1/2\,f_4\,\underline{\omega} \qquad \text{(A8)}$$

It is readily demonstrated by algebraic expansion and using the rules of quaternion algebra that $\underline{\phi}\,\underline{\omega}$ in (A8) is equivalently:

$$\underline{\phi}\,\underline{\omega} = \underline{\phi} \times \underline{\omega} - \underline{\phi} \cdot \underline{\omega}$$

Differentiation of (A7) shows that:

$$\dot{h} = \dot{f}_3\,\underline{\phi} + f_3\,\dot{\underline{\phi}} + \dot{f}_4$$

$$\dot{f}_3 = 1/2\,\frac{\cos\,\phi/2}{\phi}\,\dot{\phi} - \frac{\sin\,\phi/2}{\phi^2}\,\dot{\phi} = \frac{\dot{\phi}}{\phi}\left(1/2\,f_4 - f_3\right)$$

$$\dot{f}_4 = -\,1/2\left(\sin\phi/2\right)\dot{\phi} = -\,1/2\,\phi\,\dot{\phi}\,f_3$$

Hence, with (A8),

$$\dot{h} = f_3 \dot{\underline{\phi}} + \frac{\dot{\phi}}{\phi}\left(1/2\ f_4 - f_3\right) \underline{\phi} - 1/2\ \phi \dot{\phi}\ f_3$$

$$= 1/2\ f_3 \left(\underline{\phi} \times \underline{\omega}\right) - 1/2\ f_3 \underline{\phi} \cdot \underline{\omega} + 1/2\ f_4 \underline{\omega}$$

Dividing by $f_3$ and solving for $\dot{\underline{\phi}}$:

$$\begin{aligned} \dot{\underline{\phi}} = {} & 1/2 \frac{f_4}{f_3} \underline{\omega} + 1/2 \left(\underline{\phi} \times \underline{\omega}\right) \\ & - \frac{\dot{\phi}}{\phi}\left(1/2 \frac{f_4}{f_3} - 1\right) \underline{\phi} - 1/2\ \phi \dot{\phi} - 1/2\ \underline{\phi} \cdot \underline{\omega} \end{aligned} \tag{A9}$$

Equation (A9) is now separated into its vector and scalar components:

$$\begin{aligned} \dot{\underline{\phi}} &= 1/2 \frac{f_4}{f_3} \underline{\omega} + 1/2 \left(\underline{\phi} \times \underline{\omega}\right) - \frac{\dot{\phi}}{\phi}\left(1/2 \frac{f_4}{f_3} - 1\right) \underline{\phi} \\ 1/2\ \phi \dot{\phi} &= 1/2\ \underline{\phi} \cdot \underline{\omega} \end{aligned} \tag{A10}$$

The scalar equation is equivalently:

$$\frac{\dot{\phi}}{\phi} = \frac{1}{\phi^2} \underline{\phi} \cdot \underline{\omega}$$

Substituting in the vector part of (A10) yields:

$$\dot{\underline{\phi}} = 1/2 \frac{f_4}{f_3} \underline{\omega} + 1/2 \left(\underline{\phi} \times \underline{\omega}\right) - \frac{1}{\phi^2}\left(1/2\ \frac{f_4}{f_3} - 1\right)\left(\underline{\phi} \cdot \underline{\omega}\right) \underline{\phi}$$

Using the vector triple product rule, it is easily demonstrated that:

$$\left(\underline{\phi} \cdot \underline{\omega}\right) \underline{\phi} = \underline{\phi} \times \left(\underline{\phi} \times \underline{\omega}\right) + \phi^2\ \underline{\omega}$$

Substituting:

$$\dot{\underline{\phi}} = 1/2 \frac{f_4}{f_3} \underline{\omega} + 1/2\ \underline{\phi} \times \underline{\omega} - \left(1/2\ \frac{f_4}{f_3} - 1\right) \underline{\omega} + \frac{1}{\phi^2}\left(1 - \frac{f_4}{2f_3}\right) \underline{\phi} \times \left(\underline{\phi} \times \underline{\omega}\right)$$

Combining terms:

$$\dot{\underline{\phi}} = \underline{\omega} + 1/2\, \underline{\phi} \times \underline{\omega} + \frac{1}{\phi^2}\left(1 - \frac{f_4}{2f_3}\right) \underline{\phi} \times \left(\underline{\phi} \times \underline{\omega}\right)$$

Using the definition for $f_4$ and $f_3$ from (A7), it can be shown by trigonometric manipulation that the bracketed coefficient in the latter expression is equivalently:

$$1 - \frac{f_4}{2f_3} = \frac{1}{\phi^2}\left(1 - \frac{\phi \sin \phi}{2\left(1 - \cos \phi\right)}\right)$$

Substitution yields the final expression for $\dot{\underline{\phi}}$:

$$\dot{\underline{\phi}} = \underline{\omega} + 1/2\, \underline{\phi} \times \underline{\omega} + \frac{1}{\phi^2}\left(1 - \frac{\phi \sin \phi}{2\left(1 - \cos \phi\right)}\right) \underline{\phi} \times \left(\underline{\phi} \times \underline{\omega}\right) \tag{A11}$$

Equation (20) in the main text is the integral form of (A11) over a computer cycle (from $t_m$ to $t_{m+1}$).

## NOTES

# NOTES